

Tony L. Schmitz · K. Scott Smith

Machining Dynamics

Frequency Response to Improved
Productivity

Second Edition



Machining Dynamics

Tony L. Schmitz • K. Scott Smith

Machining Dynamics

Frequency Response to Improved Productivity

Second Edition



Springer

Tony L. Schmitz
Department of Mechanical Engineering
and Engineering Science
University of North Carolina at Charlotte
Charlotte, NC, USA

K. Scott Smith
Department of Mechanical Engineering
and Engineering Science
University of North Carolina at Charlotte
Charlotte, NC, USA

ISBN 978-3-319-93706-9 ISBN 978-3-319-93707-6 (eBook)
<https://doi.org/10.1007/978-3-319-93707-6>

Library of Congress Control Number: 2018950061

© Springer International Publishing AG, part of Springer Nature 2019
This work is subject to copyright. All rights are reserved by the Publisher, whether the whole or part
of the material is concerned, specifically the rights of translation, reprinting, reuse of illustrations,
recitation, broadcasting, reproduction on microfilms or in any other physical way, and transmission or
information storage and retrieval, electronic adaptation, computer software, or by similar or dissimilar
methodology now known or hereafter developed.

The use of general descriptive names, registered names, trademarks, service marks, etc. in this
publication does not imply, even in the absence of a specific statement, that such names are exempt
from the relevant protective laws and regulations and therefore free for general use.

The publisher, the authors, and the editors are safe to assume that the advice and information in this book
are believed to be true and accurate at the date of publication. Neither the publisher nor the authors or the
editors give a warranty, express or implied, with respect to the material contained herein or for any errors
or omissions that may have been made. The publisher remains neutral with regard to jurisdictional claims
in published maps and institutional affiliations.

This Springer imprint is published by the registered company Springer Nature Switzerland AG
The registered company address is: Gewerbestrasse 11, 6330 Cham, Switzerland

Preface

The goal of this book is to demonstrate the importance of considering the role of process dynamics in machining performance. We based the book on graduate courses in mechanical vibrations and manufacturing that we have previously offered, but also included aspects of our research programs in machining dynamics and precision engineering. We developed the text to be applied in a traditional 15-week course format. It is appropriate for upper division and graduate level engineering students, as well as for the practicing engineer.

In this second edition, we have expanded the original seven chapters into eight and have added significant content. The additional content is summarized here. New exercises are also provided for each chapter.

- Chapter 1—This chapter is updated to include new manufacturing capabilities and current interest in Industry 4.0.
- Chapter 2—New topics include the eddy current damper as a physical realization of viscous damping (Sect. 2.1.4) and compensation for the phase error introduced by a time delay in frequency response function measurements (Sect. 2.6).
- Chapter 3—The additions to turning dynamics are modulated tool path turning (Sect. 3.6) and process damping (Sect. 3.7).
- Chapter 4—The milling dynamics description now includes (1) the use of periodic sampling to establish a metric that automatically differentiates between stable and unstable behavior for the milling time domain simulation (Sect. 4.4.5); (2) cutting force coefficients determination using an instantaneous force, nonlinear optimization method (Sect. 4.7.3); and (3) process damping (Sect. 4.8).
- Chapter 5—Minor text updates are included for this chapter, which investigates the influence of forced vibrations during stable milling on part geometric accuracy.
- Chapter 6—The additions are new code to enable stable and unstable milling signals to be heard (MATLAB® sound function, Example 6.3) and the renamed Sect. 6.4 (Period- n Bifurcations) with content on milling bifurcations, Poincaré maps, bifurcation diagrams, and stability maps.

- Chapter 7—Two new sections are added. These are (1) Sect. 7.7 Accelerometer Mass Compensation, which describes the use of Receptance Coupling Substructure Analysis to increase frequency response function measurement accuracy; and (2) Sect. 7.8 Thin Rib Dynamics, which applies Receptance Coupling Substructure Analysis to model the change in stiffness and natural frequency as material is removed by milling for thin, near net shape ribs.
- Chapter 8—This chapter on machining tribology is new to the second edition. It includes sections on Geometry, Forces, and Temperature (Sect. 8.1), Tool Life (Sect. 8.2), Cutting Fluids (Sect. 8.3), and the Relationship to Machining Dynamics (Sect. 8.4).

A key aspect of this book is the inclusion of functional MATLAB[®] code (in the form of m-files). We use this code to support numerical examples throughout the text and demonstrate the analytical and time domain algorithms we have described within the individual chapters. We organized the code by chapter and named the files according to the example that they support. To demonstrate the naming convention, Example 3.6 has three supporting programs: p_3_6_1.m, p_3_6_2.m, and p_3_6_3.m that are used to develop the book figures. Another special feature we have included is the ***For Instance*** and ***In a Nutshell*** explanations of selected topics for the non-mathematical reader.



We conclude by acknowledging the many contributors to this text. This naturally includes our instructors, colleagues, collaborators, and students. Among these, we'd like to particularly recognize the contributions of J. Tlusty, J. Ziegert, M. Davies, T. Burns, J. Pratt, G.S. Duncan, V. Ganguly, C. Tyler, J. Karandikar, M. Rubeo, A. Honeycutt, and R. Copenhaver.

Charlotte, NC
Charlotte, NC
July 2018

Tony L. Schmitz
K. Scott Smith

Contents

1	Introduction	1
1.1	The Big Picture	2
1.2	A Brief Review	4
1.3	Road Map	4
	References	5
2	Modal Analysis	7
2.1	Single Degree of Freedom Free Vibration	8
2.1.1	Free Vibration	8
2.1.2	Forced Vibration	9
2.1.3	Self-Excited Vibration	10
2.1.4	Lumped Parameter Model: No Damping	10
2.1.5	Viscous Damping	13
2.1.6	Coulomb Damping	16
2.1.7	Solid Damping	17
2.1.8	Lumped Parameter Model: Viscous Damping	17
2.2	Single Degree of Freedom Forced Vibration	19
2.3	Two Degree of Freedom Free Vibration	25
2.4	Two Degree of Freedom Forced Vibration	35
2.4.1	Modal Analysis	36
2.4.2	Complex Matrix Inversion	40
2.5	System Identification	42
2.5.1	Modal Fitting	42
2.5.2	Model Definition	47
2.5.3	Modal Truncation	49
2.6	Modal Testing Equipment	52
2.6.1	Force Input	53
2.6.2	Vibration Measurement	54

2.7	Measurement Uncertainties	58
	Exercises	59
	Appendix: Orthogonality of Eigenvectors	63
	References	65
3	Turning Dynamics	67
3.1	Turning Description	67
3.2	Regenerative Chatter in Turning	70
3.3	Stability Lobe Diagrams	73
3.4	The Oriented FRF	83
3.5	Turning Time Domain Simulation	91
3.5.1	Chip Thickness Calculation	91
3.5.2	Force Calculation	93
3.5.3	Displacement Calculation	94
3.5.4	Multiple Degree of Freedom Modeling	99
3.6	Modulated Tool Path Turning	101
3.6.1	Stability Analysis	104
3.6.2	Experimental Demonstration	108
3.7	Process Damping	114
3.7.1	Process Damping Description	115
3.7.2	Stability Algorithm	117
	Exercises	123
	References	126
4	Milling Dynamics	129
4.1	Milling Description	129
4.1.1	Tooth Passing Frequency	137
4.1.2	Multiple Teeth in the Cut	140
4.2	Regenerative Chatter in Milling	142
4.3	Stability Lobe Diagrams	145
4.3.1	Average Tooth Angle Approach	145
4.3.2	Oriented FRF	147
4.3.3	Fourier Series Approach	154
4.4	Milling Time Domain Simulation with Straight Teeth	164
4.4.1	Chip Thickness Calculation	164
4.4.2	Force Calculation	167
4.4.3	Displacement Calculation	167
4.4.4	Simulation Summary and Implementation	168
4.4.5	Periodic Sampling	175
4.5	Milling Time Domain Simulation with Helical Teeth	178
4.6	Ball Milling Time Domain Simulation with Helical Teeth	186
4.7	Experimental Cutting Force Coefficients	190
4.7.1	Updated Force Model	190
4.7.2	Linear Regression	193
4.7.3	Nonlinear Optimization	196
4.7.4	Experimental Techniques	198

4.8	Process Damping	199
4.8.1	Process Damping Description	199
4.8.2	Stability Algorithm	200
	Exercises	207
	Appendix: Reformulation of Fourier Series Eigenvalue Problem	209
	References	211
5	Surface Location Error in Milling	213
5.1	Surface Location Error	213
5.2	Frequency Domain Solution	216
5.2.1	Fourier Force Model	217
5.2.2	Frequency Domain Surface Location Error	219
5.2.3	Variation in Surface Location Error with Axial Location	225
5.2.4	Combining Stability and Surface Location Error in a Single Diagram	228
5.3	Cycloidal Tool Path Time Domain Simulation	229
	Exercises	236
	Appendix: Fourier Force Series Coefficients	237
	References	238
6	Special Topics in Milling	241
6.1	Frequency Content of Milling Signals	241
6.2	Runout	256
6.2.1	Simulation Modification	259
6.3	Variable Teeth Spacing	262
6.3.1	Simulation Updating	262
6.4	Period- n Bifurcations	265
6.4.1	Poincaré Maps	270
6.4.2	Bifurcation Diagrams	270
6.4.3	Stability Maps	271
6.5	Uncertainty Propagation	274
	Exercises	276
	References	278
7	Tool Point Dynamics Prediction	283
7.1	Motivation	284
7.2	Basic Receptance Coupling	284
7.2.1	Two Component Rigid Coupling	285
7.2.2	Two Component Flexible Coupling	289
7.2.3	Two Component Flexible, Damped Coupling	296
7.3	Advanced Receptance Coupling	302
7.4	Beam Receptances	308
7.5	Assembly Receptance Predictions	316
7.6	Tool-Holder-Spindle-Machine Receptance Predictions	322
7.6.1	Spindle-Machine Receptances	327

7.7	Accelerometer Mass Compensation	331
7.8	Thin Rib Dynamics	333
	Exercises	338
	References	340
8	Machining Tribology	345
8.1	Geometry, Forces, and Temperature	347
8.2	Tool Life	359
8.3	Cutting Fluids	370
8.4	Relationship to Machining Dynamics	373
	Exercises	374
	References	375
Index		377

Chapter 1

Introduction



You have to learn the rules of the game. And then you have to play better than anyone else.

—Albert Einstein

Advanced manufacturing in the twenty-first century has embraced revolutionary new technology and approaches that are changing the face of discrete part production. Game-changing innovations for increased manufacturing capabilities include additive manufacturing, hybrid manufacturing, the digital thread and twin, and Industry 4.0 to name a few. Additive manufacturing (AM) methods include fused deposition modeling, where a filament is extruded to form the part layers; selective laser sintering, where powder is sintered locally by a high energy source; and stereolithography, where a solid part is produced from a photosensitive liquid bath by photopolymerization. These processes can be coupled with a post-printing machining step to produce the desired accuracy and surface finish from near net shape geometries in hybrid manufacturing (HM = additive + subtractive).

AM and HM are receiving significant attention in industry due to the associated design freedom and inherent three-dimensional digital part representation. The digital thread, or communication framework that enables seamless data flow and an integrated view of manufacturing processes, is therefore a closely related topic. Within the digital thread, parts to be manufactured are first described by the designer using a digital solid model that is developed using computer-aided design (CAD) software. Numerically controlled machine instructions for additive and subtractive manufacturing, as well as other processes, are produced using computer-aided manufacturing (CAM) software. This digital domain data is partnered with the physical domain part as its digital twin, which ideally accompanies the part throughout its lifetime. To ensure conformance with design intent, the actual part geometry and other performance indicators, such as mechanical, electrical, and thermal properties, are measured for quality control purposes. This measurement data is also added to the digital twin and, for tracking and forensic purposes, accompanies the physical part throughout its use cycle. The process used to produce the part, such as

the feed and speed values for machining, is yet another valuable data stream to be incorporated in the digital twin.

Industry 4.0 encompasses the collection, storage, and analysis of large manufacturing data streams to improve factory productivity and efficiency. Key concepts include (1) the Industrial Internet of Things, which includes the sensors and network that provide the data collection and connectivity capabilities; (2) cloud computing, which enables seamless access to the data and its subsequent analysis via the Internet and remote servers; and (3) the associated cybersecurity considerations for safeguarding manufacturing data from unauthorized use or modification. For example, when all the information relevant to a physical part (design, design intent, tolerances, performance specifications, manufacturing methods, tool paths, and testing procedures) is available digitally, it is vulnerable to cyberattack. Without pervasive, persistent data security, bad actors can steal the part and process outright, corrupt the files to damage the machine or workpiece, make small modifications to degrade performance, or insert malicious software.

1.1 The Big Picture

Discrete part production by machining remains an important manufacturing application. In commercial situations, the focus is naturally on producing accurate parts in the required time frame under conditions of maximized profit. Unfortunately, a number of factors can influence our ability to do so. Important contributors to process efficiency include:

- Workpiece loading/unloading from the machine.
- Fixturing, including clamping/unclamping the workpiece on the machine.
- Machining parameters, such as spindle speed, depth of cut, and feed rate.
- Path planning strategies.
- Tooling and holder selection.
- Tool wear.
- Tool changes.
- Coolant management.
- Chip evacuation.
- Tool and workpiece vibrations, including chatter and errors due to the cutting forces (we refer to the latter as surface location errors).
- Part measurement (on machine or post process).
- Machine accuracy, including geometric errors in the machine construction, thermally induced errors from heat sources associated with the machining process, and trajectory following errors caused by controller and machine structural dynamics.

We will focus our attention on process parameter selection to enable high material removal rates without introducing significant part errors due to cutting forces and the resulting dynamic tool deflections. Increasing our process dynamics understanding in order to “play the game better” is the intent of this book. We will also consider tool

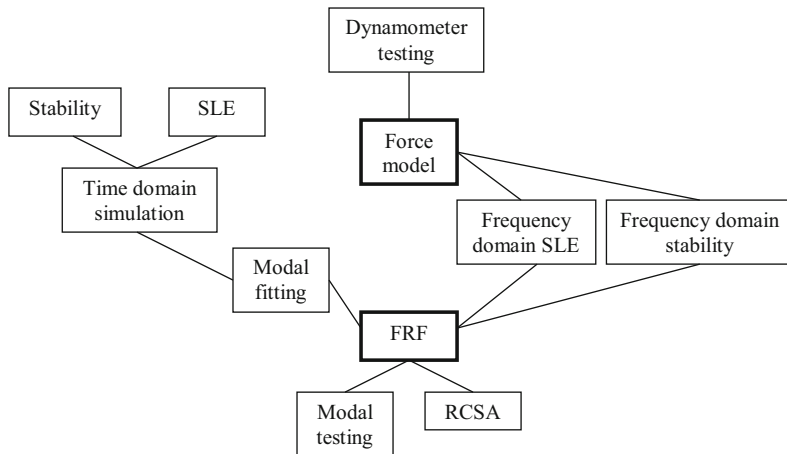


Fig. 1.1 Focus areas for study of machining dynamics. The critical frequency response function, FRF, and force model are indicated by the boxes with heavy solid lines

wear limitations, but to a lesser extent. The remaining issues, while important, are outside the scope of this text. Figure 1.1 displays an overview of our focus areas.

There are two critical items upon which our modeling efforts are based: the frequency response function, FRF, and the force model. These are identified in the central portion of the figure (boxes with heavy solid lines). In milling, for example, we require knowledge of the tool-holder-spindle-machine FRF as reflected at the tool point. We can obtain the necessary assembly dynamics through modal testing techniques or by a combination of testing and modeling using the receptance coupling substructure analysis, RCSA, approach. For the force model, the required coefficients can be determined from cutting tests carried out on a force dynamometer. Given the tool point FRF and force model, we can choose either (1) a time domain simulation strategy to predict stability and surface location errors, SLE; or (2) a frequency domain approach to stability and SLE predictions. For time domain simulation, an additional step of modal fitting is required to obtain modal parameters that describe the system FRF. We detail each of these topics in Chaps. 2 through 7. Tool wear is addressed in Chap. 8.



In a Nutshell

The frequency response function describes the motion of the point of interest to an exciting force. The motion that results from the force matches the frequency of the exciting force but varies in size based on the size of the force (magnitude) and the timing of the peak motion compared to the peak force (phase). The force model describes how the cutting forces are related to the geometric and material properties in the cutting zone.

1.2 A Brief Review

We cannot hope to capture all the significant contributions to machining science that have been previously reported in the literature, and we are wary of accidental omissions. However, we would like to provide a brief review of the foundational work that has led to our modern understanding of machining process dynamics. Clearly, with the process descriptions and models provided in this text, we are “dwarfs standing on the shoulders of giants (*nanos gigantium humeris insidentes*)”.¹

A primary building block for the study of machining is Taylor’s *On the Art of Cutting Metals* [2]. This paper established an empirical basis for the relationships between cutting parameters and process performance; contemporary research efforts still rely on variations of Taylor’s tool life model, for example. Later, Merchant’s work provided a mechanics-based understanding of cutting forces, as well as the corresponding stresses and strains during material removal [3]. Within the broad view of machining encompassed by these and other early efforts, researchers have subsequently studied such basic aspects of machining as chip geometry, shear stresses, friction, and cutting temperatures [4]. While we provide an introduction to these issues in Chap. 8, our focus is the process dynamics (Chaps. 2 through 7). The contributions of chip formation to turning and milling behavior are also indirectly included through the force models, which effectively treat this complex behavior using “process coefficients” that relate cutting force levels to the uncut chip area [5].

While advances in computer simulation of machining processes continue, the foundation for much of this work can be traced to papers by Tlusty, Tobias, and Merritt [6–9], which, in turn, followed earlier work by Arnold [10] and others. Based on these efforts, an understanding of the regeneration of surface waviness during material removal as the primary mechanism for self-excited vibrations (or chatter) in machining was established. When combined with the effects of forced vibrations during stable cutting, we have the basis for exploring the role of machining dynamics in discrete part production. Comprehensive reviews of subsequent modeling and experimental efforts have been compiled and presented in the literature. We refer the reader to [4, 11–17], for example.

1.3 Road Map

Figure 1.2 shows a modified version of Fig. 1.1, where we have now identified the relevant sections that detail these focus areas. The FRF is defined in Sects. 2.2 through 2.4. Its measurement is outlined in Sects. 2.5 through 2.7, while its prediction using the RCSA method is detailed in Sect. 7.6. The cutting force model is described in Sect. 3.1 for turning and Sects. 4.1 and 4.7 for milling. Experimental methods for

¹This quote is attributed to the twelfth-century philosopher Bernard of Chartres (*Bernardus Carnotensis*) [1].

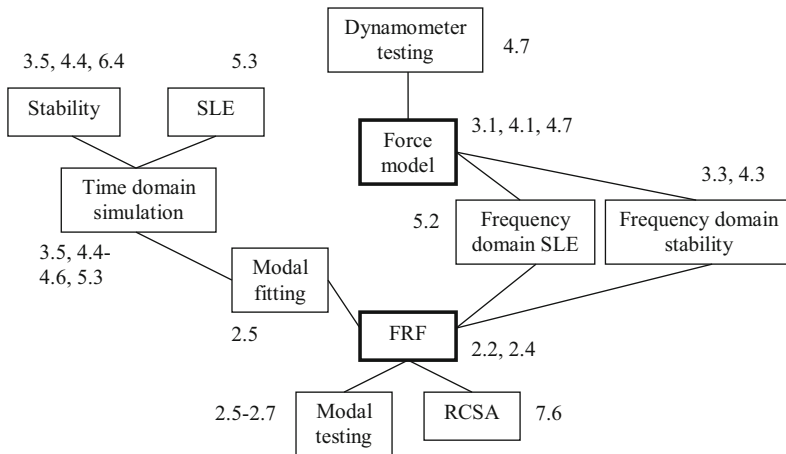


Fig. 1.2 A road map for the text is shown; section numbers are identified for each focus area

identifying force model coefficients in milling are covered in Sect. 4.7 as well. Time domain simulations are provided in Sect. 3.5 (turning), Sects. 4.4 through 4.6 (milling circular tool path), and Sect. 5.3 (milling cycloidal tool path). The necessary modal fitting step for determining the modal mass, damping, and stiffness coefficients used in the time domain simulation equations of motion is reviewed in Sect. 2.5. Application of time domain simulation to turning stability is shown in Sect. 3.5. Surface location error prediction is included in Sect. 5.3. Frequency domain techniques for stability analysis are described in Sect. 3.3 for turning and Sect. 4.3 for milling (two methods are included). The frequency domain analysis for milling surface location error is provided in Sect. 5.2.

While the content of this book is mathematical by its nature, it is possible to gain an understanding of the basic concepts and some ability to apply them without a detailed understanding of the mathematical formalities. Throughout the text, there are number of explanations/analogies labeled *For Instance* or *In a Nutshell* which attempt to convey the essence of the topic to the non-mathematical reader.

References

1. Retrieved April, 2018, from http://en.wikipedia.org/wiki/Standing_on_the_shoulders_of_giants.
2. Taylor, F. W. (1906). On the art of cutting metals. *Transactions of the ASME*, 28, 31–248.
3. Merchant, M. E. (1950). Metal cutting research—Theory and practice, machining—Theory and practice. *Am Soc Met*, 9, 5–44.
4. Komanduri, R. (1993). Machining and grinding: A historical review of the classical papers. *Applied Mechanics Reviews*, 46(3), 80–132.

5. Koenigsberger, F., & Sabberwal, A. (1961). An investigation into the cutting force pulsations during milling operations. *International Journal of Machine Tool Design and Research*, 1, 15–33.
6. Tlusty, J., & Polacek, M. (1957). *Besipiele der behandlung der selbsterregten Schwingung der Werkzeugmaschinen, FoKoMa*. Munchen: Hanser Verlag.
7. Tobias, S. A., & Fishwick, W. (1958). Theory of regenerative machine tool chatter. *The Engineer, London*, 258.
8. Tlusty, J., & Polaceck, M. (1963). The stability of machine tools against self-excited vibrations in machining. *International Research in Production Engineering*, 1, 465–474.
9. Merrit, H. (1965). Theory of self-excited machine tool chatter. *Journal of Engineering for Industry*, 87(4), 447–454.
10. Arnold, R. (1946). The mechanism of tool vibration in the cutting of steel. *Proceedings of the Institution of Mechanical Engineers*, 54, 261–284.
11. Tlusty, J. (1978). Analysis of the state of research in cutting dynamics. *Annals of the CIRP*, 27(2), 583–589.
12. Smith, S., & Tlusty, J. (1991). An overview of modeling and simulation of the milling process. *Journal of Engineering for Industry*, 113(2), 169–175.
13. Smith, S., & Tlusty, J. (1993). Efficient simulation programs for chatter in milling. *Annals of the CIRP*, 42(1), 463–466.
14. Ehmann, K., Kapoor, S., DeVor, R., & Lazoglu, I. (1997). Machining process modeling: A review. *Journal of Manufacturing Science and Engineering*, 119(4B), 655–663.
15. Smith, S., & Tlusty, J. (1997). Current trends in high-speed machining. *Journal of Manufacturing Science and Engineering*, 119(4B), 664–666.
16. Merchant, M. E. (1998). An interpretive look at twentieth century research on modeling of machining. *Machining Science and Technology*, 2(2), 157–163.
17. Altintas, Y., & Weck, M. (2004). Chatter stability of metal cutting and grinding. *Annals of the CIRP*, 53(2), 619–642.

Chapter 2

Modal Analysis



All these primary impulses, not easily described in words, are the springs of man's actions.

—Albert Einstein

As described in Chap. 1, a critical step in improving machining productivity through a consideration of the process dynamics is identifying the tool point frequency response function. In this chapter, we will briefly review the fundamentals of single and two degree of freedom free and forced vibrations, and, in so doing, we will establish notation conventions for a description of modal analysis. Naturally, this review will not replace the information provided in a mechanical vibrations textbook, such as [1–3], and some of the subtleties of a comprehensive treatment will not be included. However, it will provide us with the basis we need to describe techniques for frequency response function measurement and model development.

After this brief review, the remaining purposes of the chapter are to:

- Provide the background necessary to interpret measured frequency response functions.
- Detail a modal fitting technique.
- Describe the experimental procedures and equipment used to measure tool point frequency response functions.

In all discussions, we will assume linear vibrations. While nonlinearities can certainly be observed in physical systems, this idealization is generally acceptable in practice.



In a Nutshell

Vibrating systems exhibit an interplay between the inertial forces, the damping forces, and the spring forces. In a linear system, the inertial forces are proportional to acceleration through the constant mass; the viscous damping forces are proportional to velocity through the constant damping coefficient; and the spring forces are proportional to displacement through the

spring constant, although it is possible to design springs that stiffen as they are compressed, for example, to produce nonlinear behavior.

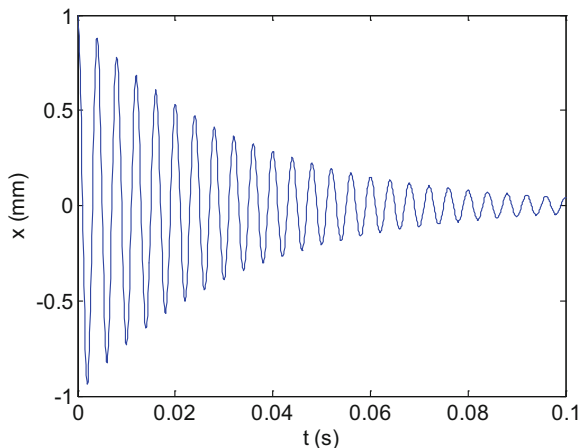
2.1 Single Degree of Freedom Free Vibration

Our structure of interest is a cutting tool of some geometry (single or multiple cutting edges) connected to either a tool post/turret and lathe or a tool-holder, spindle, and milling machine. Both of these cases can be represented as combined bodies that possess both mass and elasticity or the ability to deform without permanently changing shape. The vibration of bodies that exhibit these characteristics can be divided into three main categories: free, forced, and self-excited vibrations.

2.1.1 Free Vibration

Free vibration occurs in the absence of a long-term, external excitation force. It is the result of some initial conditions imposed on the system, such as a displacement from the system's equilibrium position, for example. Free vibration produces motion in one or more of the system's natural frequencies, and, because all physical structures exhibit some form of damping (or energy dissipation), it is seen as a decaying oscillation with a relatively short duration; see Fig. 2.1. Familiar acoustic examples include plucking a guitar string or striking a piano string.

Fig. 2.1 Damped free vibration example





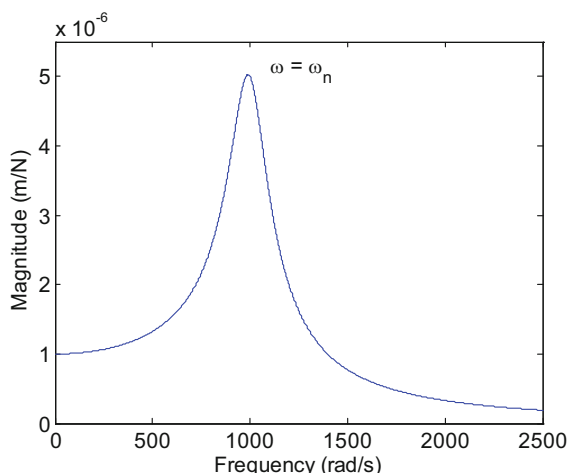
In a Nutshell

Free vibration occurs at the “natural frequency,” which is the square root of the stiffness divided by the mass (in appropriate units). You can observe this relationship in the guitar string analogy. The high pitch (high frequency) strings are thin (low mass) and under high tension (high stiffness). The low pitch (low frequency) strings are thick (high mass) with low tension (low stiffness). In fact, the low-pitch strings often have another string wrapped around them to add mass. Guitar tuning is achieved by adjusting the tension (stiffness) in each string individually until the correct pitch is obtained. All mechanical systems have components with mass, and all mechanical systems have components with stiffness (they deflect under load). So, all mechanical systems exhibit one or more natural frequencies.

2.1.2 *Forced Vibration*

Forced vibration takes place when a continuous, external periodic excitation produces a response with the same frequency as the forcing function (after the decay of initial transients). While free vibration is often represented in the time domain, forced vibration is typically analyzed in the frequency domain. This emphasizes the magnitude and phase dependence on frequency and enables the convenient identification of natural frequencies. A typical source of forced vibration in mechanical systems is rotating imbalance. In forced vibration, large vibrations occur when the forcing frequency, ω , is near a system natural frequency, ω_n , as shown in Fig. 2.2. This condition is referred to as resonance and is generally avoided. However, we'll see in Chaps. 3 and 4 that operating under resonant conditions can

Fig. 2.2 Example of forced vibration magnitude



actually improve the stability of cutting processes. While counter intuitive, the mechanism that leads to this behavior (overcutting of the previously machined surface) makes physical sense. We'll also discuss the impact of forced vibrations on machining accuracy in Chap. 5. In this case, we'll see that operating near resonance for lowly damped structures can lead to significant errors in the workpiece geometry, although the process remains stable.



In a Nutshell

Forced vibration occurs at the exciting force frequency. Forced vibration persists as long as the exciting force is present.

2.1.3 Self-Excited Vibration

In self-excited vibration, a steady input force is present, as in the case of forced vibration. However, this input is modulated into vibration at or near one of the system's natural frequencies, as with free vibration. The physical mechanisms that provide this modulation are varied. Common examples of self-excited vibration include playing a violin, aeroelastic flutter in airplane wings, feedback in a public address (microphone–amplifier–speaker) system, and chatter in machining. Naturally, our focus is on the latter in Chaps. 3 and 4.



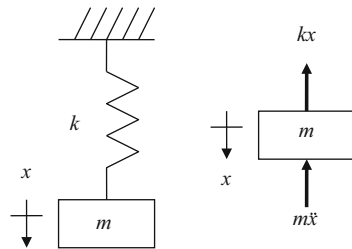
In a Nutshell

Self-excited vibration selects its own frequency depending on the physical mechanism that causes it.

2.1.4 Lumped Parameter Model: No Damping

Let's begin our discussion of single degree of freedom free vibration with a simple, lumped parameter model. In this model, all the mass is assumed to be concentrated at the coordinate location, and the spring that provides the oscillating restoring force is massless. The model is composed of a mass, m , attached to a linear spring, k , that provides a force proportional to its displacement from the mass's static equilibrium position. Because the rigid mass is only allowed to move vertically, a single time-dependent coordinate, x , is sufficient to describe its motion. In a physical sense, this means that knowledge of the motion of a single coordinate is adequate to completely describe the motion of a single degree of freedom system. See Fig. 2.3, which includes the free-body diagram. Summing the spring and inertial forces in the vertical direction yields the model's equation of motion:

Fig. 2.3 Single degree of freedom, undamped lumped parameter model (left); free-body diagram (right)



$$m\ddot{x} + kx = 0. \quad (2.1)$$

By assuming a harmonic solution of the form $x = Xe^{st}$, where X is a complex coefficient, $s = i\omega$, and ω is the frequency (in rad/s), we can express the velocity as the first time derivative of the displacement, $\dot{x} = sXe^{st} = i\omega Xe^{st}$, and the acceleration as the second time derivative, $\ddot{x} = s^2Xe^{st} = -\omega^2Xe^{st}$ (note that $i = \sqrt{-1}$ and $i^2 = -1$). Substitution into Eq. 2.1 gives:

$$Xe^{st}(ms^2 + k) = 0. \quad (2.2)$$



In a Nutshell

This technique for solving linear ordinary differential equations provides all solutions. Obviously, it is possible for the system to not vibrate at all. Even though we call that solution “trivial,” this approach finds it mathematically.

In Eq. 2.2, either Xe^{st} or $(ms^2 + k)$ is zero. If the first term is zero, this means that no motion has occurred, and it is described as the trivial solution. We are interested in the case that the second term is equal to zero. This is referred to as the characteristic equation for the system:

$$ms^2 + k = 0. \quad (2.3)$$

Solving for the complex variable s gives the two roots $s = \pm\sqrt{-\frac{k}{m}} = \pm i\sqrt{\frac{k}{m}}$. The vibrating frequency $\sqrt{\frac{k}{m}} = \omega_n$ is the natural frequency for the single degree of freedom system. Typical SI units for k and m are N/m and kg, respectively, which gives units of rad/s for ω_n . Alternately, the natural frequency may be expressed in units of Hz (cycles/s). In this case, we'll use the notation $f_n = \frac{\omega_n}{2\pi}$. The unit conversion occurs because there are 2π radians per oscillation cycle.

The total solution to Eq. 2.1 is the sum of the contributions from each of the two roots:

$$x = X_1 e^{i\omega_n t} + X_2 e^{-i\omega_n t}. \quad (2.4)$$

The complex coefficients, X_1 and X_2 , can be determined from the initial displacement, x_0 , and velocity, \dot{x}_0 , of the single degree of freedom system. Evaluating Eq. 2.4 at $t = 0$ gives:

$$x_0 = X_1 + X_2. \quad (2.5)$$

The first time derivative of Eq. 2.4 is:

$$\dot{x} = i\omega_n X_1 e^{i\omega_n t} - i\omega_n X_2 e^{-i\omega_n t}. \quad (2.6)$$

At $t = 0$, Eq. 2.6 becomes:

$$\dot{x}_0 = i\omega_n X_1 - i\omega_n X_2. \quad (2.7)$$

Using the linear combination approach, Eqs. 2.5 and 2.7 can be combined to determine the complex conjugate coefficients X_1 and X_2 :

$$X_1 = \frac{-i\dot{x}_0 + \omega_n x_0}{2\omega_n} \text{ and} \quad (2.8)$$

$$X_2 = \frac{i\dot{x}_0 + \omega_n x_0}{2\omega_n}. \quad (2.9)$$

These coefficients can then be substituted in Eq. 2.4 to determine the time-dependent displacement of the mass due to the imposed initial conditions. Alternately, the mass motion can be expressed in exponential form. To use this notation, we first need to identify the real (Re) and imaginary (Im) parts of the complex coefficients:

$$\text{Re}(X_1) = \frac{x_0}{2} \quad \text{Im}(X_1) = \frac{-\dot{x}_0}{2\omega_n}, \quad (2.10)$$

$$\text{Re}(X_2) = \frac{x_0}{2} \quad \text{Im}(X_2) = \frac{\dot{x}_0}{2\omega_n}. \quad (2.11)$$

These real and imaginary parts can then be used to write the coefficients in exponential form:

$$\begin{aligned} X_1 &= A e^{i\beta} = \sqrt{\text{Re}(X_1)^2 + \text{Im}(X_1)^2} \exp\left(i \cdot \tan^{-1}\left(\frac{\text{Im}(X_1)}{\text{Re}(X_1)}\right)\right), \\ X_1 &= \sqrt{\left(\frac{x_0}{2}\right)^2 + \left(\frac{-\dot{x}_0}{2\omega_n}\right)^2} \exp\left(i \cdot \tan^{-1}\left(\frac{\frac{-\dot{x}_0}{2\omega_n}}{\frac{x_0}{2}}\right)\right), \\ X_1 &= \sqrt{\frac{x_0^2 \omega_n^2 + \dot{x}_0^2}{4\omega_n^2}} \exp\left(i \cdot \tan^{-1}\left(-\frac{\dot{x}_0}{x_0 \omega_n}\right)\right), \end{aligned} \quad (2.12)$$

where the magnitude is $A = \sqrt{\frac{x_0^2\omega_n^2 + \dot{x}_0^2}{4\omega_n^2}}$ and the phase is $\beta = \tan^{-1}\left(-\frac{\dot{x}_0}{x_0\omega_n}\right)$. Similarly, $X_2 = Ae^{i\beta}$ (same magnitude, but negative phase) because it is the complex conjugate of X_1 . We can then rewrite the total solution from Eq. 2.4 in the form:

$$x = Ae^{i\beta}e^{i\omega_n t} + Ae^{-i\beta}e^{-i\omega_n t} = A\left(e^{i(\omega_n t + \beta)} + e^{-i(\omega_n t + \beta)}\right). \quad (2.13)$$

Finally, by applying the Euler identity $e^{i\theta} + e^{-i\theta} = 2 \cos(\theta)$, Eq. 2.13 can be rewritten as:

$$x = 2A \cos(\omega_n t + \beta). \quad (2.14)$$



In a Nutshell

If we know the mass and stiffness, and we know the initial conditions that started the vibration, then it is possible to describe the motion of the system at any time.

While Eq. 2.14 emphasizes the oscillatory nature of the mass motion and the dependence of the magnitude and phase on the initial conditions, we must also include damping in our analysis in order to model physical systems. Damping refers to the “leakage” of the input energy into the vibrating system. In other words, not all of the input energy serves to cause motion. Some of it is dissipated in other ways. A comprehensive model of damping is complicated and not particularly well suited for incorporation into our simple mathematical description of single degree of freedom free vibration. Therefore, one of three mathematically simple, but effective, damping models are typically applied.

2.1.5 Viscous Damping

A common assertion is that the retarding damping force is proportional to the mass velocity. You may have experienced this phenomenon if you’ve attempted to force a body through a fluid, such as pulling your hand through water or sticking your hand out the window of a moving vehicle. You probably observed that increasing the speed of your hand relative to the fluid raised the resistance proportionally. If we write the damping force as:

$$f = c\dot{x} \quad (2.15)$$

and substitute the velocity expression $\dot{x} = sXe^{st} = i\omega Xe^{st}$, we see that viscous damping is frequency dependent. When sketching models of lumped parameter systems, the damping element is often illustrated as a fluid dashpot (similar to a

car's shock absorber) when the viscous damping model is applied. Typical SI units for c are N s/m.



For Instance

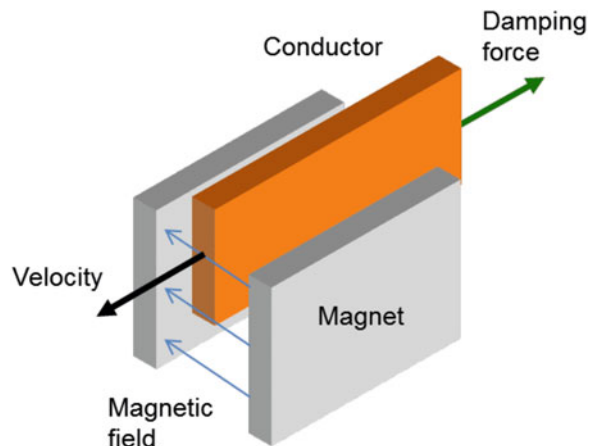
In a car, the body provides the mass, the suspension spring provides the stiffness, and the shock absorber provides the damping. Inside the shock absorber is a plate with holes that moves through a fluid and produces a force proportional to the velocity of the motion.

Eddy current damping provides another interesting physical realization of viscous damping. An eddy current damper dissipates energy when a conductor moves inside a magnetic field. The relative motion induces an eddy current in the conductor which, in turn, produces heat. The velocity-dependent damping force can be described analytically. Figure 2.4 displays the motion of a conductor¹ relative to a magnet (or magnet pair) with the motion perpendicular to the magnet pole direction. The vector quantity eddy current density, \mathbf{J} , depends on the conductivity, σ , and the cross product of the velocity, \mathbf{v} , and magnetic field, \mathbf{B} ; see Eq. 2.17. The eddy current force is then calculated as the volume integral of the product of the eddy current density and the magnetic field; see Eq. 2.18. Mathematically, the two cross products yield a damping force which acts in the direction opposite to the velocity.

$$\mathbf{J} = \sigma(\mathbf{v} \times \mathbf{B})\mathbf{n} \quad (2.16)$$

$$\mathbf{F} = \int_V (\mathbf{J} \times \mathbf{B}) dV \quad (2.17)$$

Fig. 2.4 Schematic of an eddy current damper



¹The conductor is a conductive, nonmagnetic material. Aluminum and copper are common choices.

The damping force magnitude, F , is described by Eq. 2.18, where δ is the conductor thickness, B is the magnetic field strength, S is the magnet surface area, α_1 incorporates surface charge effects, α_2 describes end effects from the finite dimension conductor, and v is the velocity magnitude [4]. The surface charge effects term, α_1 , is calculated using Eq. 2.19, where $2a$ is the height of the magnet area and $2b$ is the width.

$$F = (\sigma\delta B^2 S(\alpha_1 + \alpha_2))v = cv \quad (2.18)$$

$$\alpha_1 = 1 - \frac{1}{2\pi} \left[4 \tan^{-1} \left(\frac{b}{a} \right) + \frac{b}{a} \ln \left(1 + \frac{a^2}{b^2} \right) - \frac{a}{b} \ln \left(1 + \frac{b^2}{a^2} \right) \right] \quad (2.19)$$

The end effects term for the conductor, α_2 , is determined using Eq. 2.20, where I_1 and I_2 are defined by Eqs. 2.21 and 2.22. In these equations, $2H$ is the height of the conductor, $h = ba^{-1}$, and $w = Ha^{-1}$.

$$\alpha_2 = -\frac{1}{2\pi}(I_1 + I_2) \quad (2.20)$$

$$\begin{aligned} I_1 = & 4w \tan^{-1} \left(\frac{h}{w} \right) - 4(1-w) \tan^{-1} \left(\frac{h}{1-w} \right) + \frac{w^2}{h} \ln(w^2) \\ & - \frac{1}{h} (w^2 - h^2) \ln(w^2 + h^2) - \frac{1}{h} (1-w)^2 \ln(1-w)^2 \\ & + \frac{1}{h} ((1-w)^2 - h^2) \ln((1-w)^2 + h^2) \end{aligned} \quad (2.21)$$

$$\begin{aligned} I_2 = & 4w \tan^{-1} \left(\frac{h}{w} \right) - 4(1+w) \tan^{-1} \left(\frac{h}{1+w} \right) + \frac{w^2}{h} \ln(w^2) \\ & - \frac{1}{h} (w^2 - h^2) \ln(w^2 + h^2) - \frac{1}{h} (1+w)^2 \ln(1+w)^2 \\ & + \frac{1}{h} ((1+w)^2 - h^2) \ln((1+w)^2 + h^2) \end{aligned} \quad (2.22)$$

As shown in Eq. 2.18, the eddy current damping force can be rewritten as the product of a viscous damping coefficient, c , and the velocity magnitude. This viscous damping coefficient enables model-based damping prediction.

The eddy current damper concept displayed in Fig. 2.4 is shown embedded inside an aluminum, parallelogram leaf-type flexure in Fig. 2.5. The copper conductor is attached to the aluminum flexure platform, and two permanent magnet sets are attached to the aluminum flexure base, one on each side of the conductor. The arrangement of the eight square permanent magnets is shown in Fig. 2.6. This eddy current damped flexure provides a convenient platform for milling dynamics testing; its design and construction is described in [5].

Fig. 2.5 Flexure with embedded eddy current damper

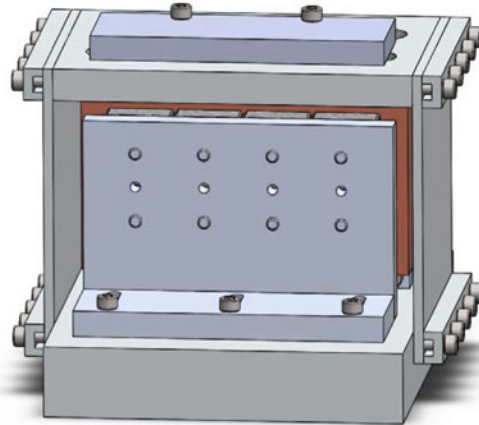


Fig. 2.6 Permanent magnet mount. The magnets face the conductor with one mount on each side

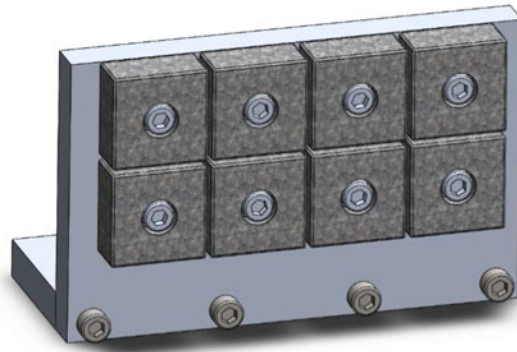
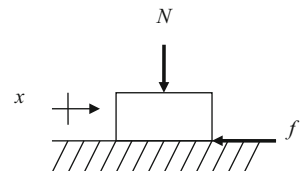


Fig. 2.7 Coulomb damping occurs due to dry sliding friction between the two surfaces. The normal and friction forces are shown



2.1.6 Coulomb Damping

Another effective damping model is Coulomb damping or dry sliding friction. Here, energy is dissipated due to relative motion between two contacting surfaces. The force magnitude depends on the sliding (kinetic) friction coefficient, μ , and the normal force, N , between the two bodies. See Fig. 2.7. Because the friction force

always opposes the direction of motion, the resulting equation of motion is nonlinear. A piecewise definition of the Coulomb damping force is [6]:

$$f = \begin{cases} -\mu N & \dot{x} > 0 \\ 0 & \dot{x} = 0 \\ \mu N & \dot{x} < 0 \end{cases}. \quad (2.23)$$

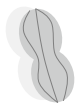


For Instance

Coulomb damping accounts for the energy dissipation by friction between two objects. It converts the kinetic energy from a rotating wheel into heat during braking in a car, for example. The key point regarding Coulomb damping in vibrations is that the Coulomb damping force always opposes the motion like viscous damping, but instead of being proportional to velocity, it is proportional to normal force.

2.1.7 Solid Damping

Even in the absence of an external fluid medium or sliding friction against another surface, the motion of a freely oscillating body decays over time. This is due to energy dissipation internal to the body (perhaps a good mental picture is molecules sliding relative to each other within the body itself during periodic motion and elastic deformation). The energy dissipation during a cycle of motion for this solid or structural damping is taken to be proportional to the square of the vibration magnitude. Using the concept of equivalent viscous damping, solid damping is often incorporated with stiffness to arrive at a complex stiffness term in the differential equation of motion [7]. We implement this approach in Sect. 7.4 when describing beam models for use in receptance coupling analyses. We use receptance coupling to predict the frequency response of tool-holder-spindle-machine assemblies in Sect. 7.6.



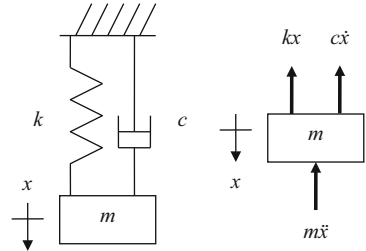
In a Nutshell

While there are certainly several kinds of damping, it is mathematically simpler and sufficiently accurate to consider the damping as viscous.

2.1.8 Lumped Parameter Model: Viscous Damping

For the remainder of this chapter, we will use viscous damping to describe energy dissipation in the lumped parameter models. The equation of motion for free vibration of the single degree of freedom spring-mass-damper (Fig. 2.8) can then be written as:

Fig. 2.8 Single degree of freedom, damped lumped parameter model (left); free-body diagram (right)



$$m\ddot{x} + cx + kx = 0. \quad (2.24)$$

Again assuming the harmonic solution $x = Xe^{st}$, we obtain the characteristic equation:

$$ms^2 + cs + k = 0, \quad (2.25)$$

which can be rewritten as:

$$s^2 + \frac{c}{m}s + \frac{k}{m} = 0. \quad (2.26)$$

This equation is quadratic in s^2 and has the two roots:

$$s_{1,2} = -\frac{c}{2m} \pm \sqrt{\left(\frac{c}{2m}\right)^2 - \frac{k}{m}}. \quad (2.27)$$

The vibratory behavior of the spring-mass-damper depends on the term under the radical in Eq. 2.27. If $\left(\frac{c}{2m}\right)^2 - \frac{k}{m} < 0$, the system is underdamped and vibratory. If $\left(\frac{c}{2m}\right)^2 - \frac{k}{m} = 0$, the system is said to be critically damped, and, if $\left(\frac{c}{2m}\right)^2 - \frac{k}{m} > 0$, then the system is overdamped. For these two cases, no vibration occurs. Because the damping is generally low in tool-holder combinations for lathes and milling machines, we will consider only the underdamped option in our analyses. For underdamped systems, Eq. 2.27 can be rewritten as:

$$s_{1,2} = -\zeta\omega_n \pm i\omega_d, \quad (2.28)$$

where we've introduced the dimensionless damping ratio, $\zeta = \frac{c}{2\sqrt{km}}$, and damped natural frequency, $\omega_d = \omega_n \sqrt{1 - \zeta^2}$. Under the viscous damping assumption, we see that the free-vibrating frequency is reduced in the presence of damping. However, for typical tool-holder systems, the damping is low enough that the frequency change is negligible. Using the two roots in Eq. 2.28, the total solution for the free motion of the single degree of freedom spring-mass-damper is:

$$x = X_1 e^{(-\zeta\omega_n + i\omega_d)t} + X_2 e^{(-\zeta\omega_n - i\omega_d)t} = e^{-\zeta\omega_n t} (X_1 e^{i\omega_d t} + X_2 e^{-i\omega_d t}). \quad (2.29)$$

Like the undamped case, the complex coefficients can be determined from the initial conditions. Taking the time derivative of Eq. 2.29; substituting the initial displacement, x_0 , and velocity, \dot{x}_0 ; and solving for X_1 and X_2 give the complex conjugate pair:

$$X_1 = \frac{x_0}{2} - i\frac{\dot{x}_0 + \zeta\omega_n x_0}{2\omega_d} \quad \text{and} \quad X_2 = \frac{x_0}{2} + i\frac{\dot{x}_0 + \zeta\omega_n x_0}{2\omega_d}. \quad (2.30)$$

Using these coefficients, the exponential form can again be developed in a similar way to Eq. 2.12 by substituting for the real and imaginary parts. For example, $\text{Re}(X_1) = \frac{x_0}{2}$ and $\text{Im}(X_1) = -\frac{\dot{x}_0 + \zeta\omega_n x_0}{2\omega_d}$ for the coefficient X_1 . Note that these terms simplify to Eq. 2.10 for the undamped case if ζ is set equal to zero.



In a Nutshell

Free vibration of a single degree of freedom system with viscous damping consists of two parts: a sinusoidal motion at the damped natural frequency and a decaying exponential envelope that bounds it. More damping means that the exponential envelope converges to zero more quickly.

2.2 Single Degree of Freedom Forced Vibration

We will again consider the spring-mass-damper model shown in Fig. 2.5. However, a harmonic external force is now applied to the mass. The force is shown as $fe^{i\omega t}$ in Fig. 2.9 but may be more properly considered as $\frac{f}{2}(e^{i\omega t} + e^{-i\omega t})$ so that the force is always real valued. This is illustrated in the real-imaginary (or complex) plane as two counter-rotating vectors with magnitude $\frac{f}{2}$ and phase $\pm\omega t$ whose sum is always a scalar value oscillating from f to $-f$ with the forcing frequency ω (Fig. 2.10).

$$m\ddot{x} + c\dot{x} + kx = fe^{i\omega t} \quad (2.31)$$

Fig. 2.9 Single degree of freedom, lumped parameter model (damped with force)

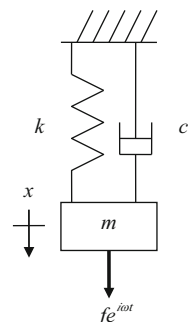
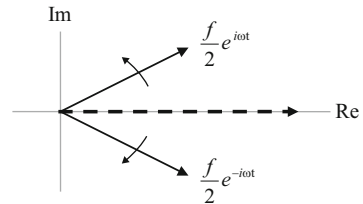


Fig. 2.10 Real valued force shown as sum of counter-rotating vectors



In a Nutshell

The external force exciting a forced vibration is assumed to be sinusoidal. In fact, any external excitation force can be thought of as a sum of sinusoidal forces (see the Fourier transform described in Sect. 4.3), so the method is generic to all kinds of external forces.

Although the total solution to Eq. 2.31 includes both the homogeneous (transient) and particular (steady-state) components, we have already described the damped transient response in the previous section. We will therefore consider only the steady-state solution here. Because the motion response has the same frequency as the forcing function, we can assume a solution of the form $x = Xe^{iot}$. The velocity and acceleration can then be written as $\dot{x} = i\omega Xe^{iot}$ and $\ddot{x} = -\omega^2 Xe^{iot}$. Substituting in Eq. 2.31 gives:

$$(-\omega^2 m + i\omega c + k)Xe^{iot} = f e^{iot}. \quad (2.32)$$

Rewriting Eq. 2.32 gives the complex-valued frequency response function. We will use this description of Eq. 2.33, rather than transfer function, because we can only consider positive frequencies and a single-system configuration (damping and natural frequency) when we perform measurements. The term transfer function refers to the theoretical situation where all frequencies ($-\infty$ to $+\infty$) and $\zeta\omega_n$ combinations are included.

$$\frac{X}{F} = \frac{1}{-m\omega^2 + i\omega c + k} \quad (2.33)$$

There are two primary ways to represent the complex function shown in Eq. 2.33. The first is to separate the function into its magnitude and phase components, and the second is to express the function using its real and imaginary parts. The frequency-dependent magnitude and phase are written as:

$$\left| \frac{X}{F} \right| = \frac{1}{k} \sqrt{\frac{1}{\left(1 - \left(\frac{\omega}{\omega_n}\right)^2\right)^2} + \left(2\zeta\frac{\omega}{\omega_n}\right)^2} \text{ and} \quad (2.34)$$

$$\Phi = \tan^{-1} \left(\frac{\text{Im} \left(\frac{X}{F} \right)}{\text{Re} \left(\frac{X}{F} \right)} \right) = \tan^{-1} \left(\frac{-2\zeta\frac{\omega}{\omega_n}}{1 - \left(\frac{\omega}{\omega_n} \right)^2} \right). \quad (2.35)$$



In a Nutshell

The magnitude and phase parts of the frequency response function emphasize key features of forced vibration: (1) the forced vibration occurs at the frequency of the exciting force; and (2) the size of the motion compared to the force (the magnitude) and the time delay between when the force reaches its maximum and the displacement reaches its maximum (the phase) depend on the frequency of the exciting force and the natural frequency of the system.

When the exciting frequency is low in comparison to the natural frequency, the motion is small and nearly in phase with the force (the force and the displacement reach their peaks at the same time). As the frequency of excitation increases, the size of the motion gets larger, and the peak of the displacement begins to happen later than the peak of the force. When the excitation force is very close to the natural frequency, then the displacement is as large as possible, and it is zero when the force is maximum (90 deg out of phase). Further increases in the frequency of the excitation force cause the size of the displacement to be reduced. At very high excitation frequencies, the size of the displacement is very small, and the displacement reaches its maximum when the force reaches its minimum (180 deg out of phase).

Because Eqs. 2.34 and 2.35 are somewhat cumbersome, it is common to replace the frequency ratio $\frac{\omega}{\omega_n}$ with another variable, such as r . We will also adopt this convention. The real and imaginary parts of the frequency response function, or FRF, are provided in Eqs. 2.36 and 2.37.

$$\text{Re}\left(\frac{X}{F}\right) = \frac{1}{k} \left(\frac{1 - r^2}{(1 - r^2)^2 + (2\zeta r)^2} \right) \quad (2.36)$$

$$\text{Im}\left(\frac{X}{F}\right) = \frac{1}{k} \left(\frac{-2\zeta r}{(1 - r^2)^2 + (2\zeta r)^2} \right) \quad (2.37)$$



In a Nutshell

“Real” and “Imaginary” are not terms that imply “exists” or “does not exist.” Rather, they are mathematical terms relating to the solution procedure. It may be more intuitive to think of these terms in the following way.

As we mentioned previously, we can consider the input force to be sinusoidal (sine or cosine). The resulting displacement is therefore also sinusoidal with the same frequency. If the input is a cosine force, then the “real part” of the resulting motion is the part that is also a cosine. The “imaginary part” of the resulting motion

is the part that is a sine. The combination of the motion's cosine and sine parts describes both the size (magnitude) of the resulting motion and the phase shift relative to the force.

Example 2.1 FRF for Single Degree of Freedom System Let's consider a single degree of freedom spring-mass-damper system with a mass of 1 kg, a spring constant of 1×10^6 N/m, and a viscous damping coefficient of 200 N s/m. In order to apply Eqs. 2.34 through 2.37, we must calculate the (undamped) natural frequency and damping ratio.

$$\omega_n = \sqrt{\frac{k}{m}} = \sqrt{\frac{1 \times 10^6}{1}} = 1000 \text{ rad/s}$$

$$\zeta = \frac{c}{2\sqrt{km}} = \frac{200}{2\sqrt{1 \times 10^6 \cdot 1}} = 0.1$$

Figure 2.11 shows the magnitude and phase as a function of the frequency ratio, r . Although a logarithmic magnitude axis (i.e., a semilog plot) is often shown in the literature, we will use a linear convention for plots in this text unless specified otherwise. The real and imaginary parts are provided in Fig. 2.12. Note that the zero frequency (DC) value for both the real part and magnitude is $\frac{1}{k} = 1 \times 10^{-6}$ m/N. This represents the real valued static deflection of the spring (away from its equilibrium position) under a unit force. We can also see that the magnitude at resonance ($r = 1$ or $\omega = \omega_n$) is significantly larger than the DC deflection. This magnitude is $\frac{1}{2\zeta} = 5 \times 10^{-6}$ m/N.

Fig. 2.11 Magnitude and phase for single degree of freedom system

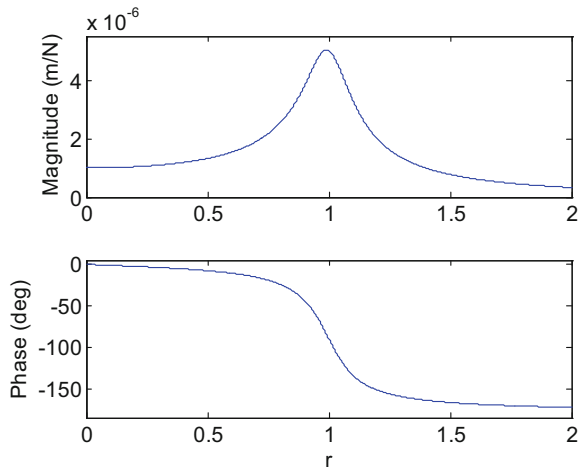
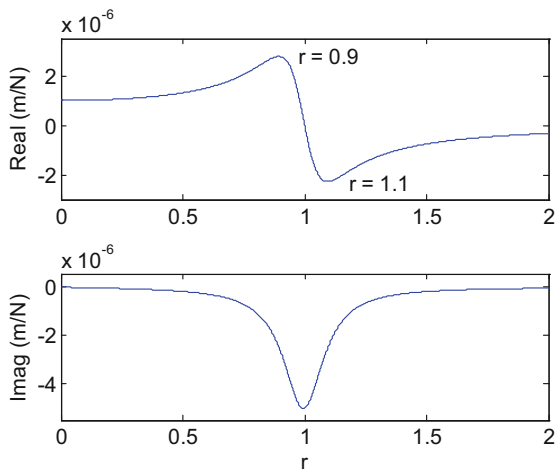


Fig. 2.12 Real and imaginary parts for single degree of freedom system



In a Nutshell

The logarithmic scale is often used to display information covering a broad range in a single graph. The sound pressure levels in acoustics vary over a huge range from a whisper to jet engine noise, for example.

The mathematics of acoustics and mechanical vibrations are similar, and, for this reason, many textbooks use the logarithmic scales from acoustics to show similar concepts in mechanical vibrations. In our case, focused on mechanical vibrations, the range of the signals is not so large, and the linear scale is more intuitive for most people, so we will use it almost exclusively.

The maximum value of the real part occurs at $r = \sqrt{1 - 2\zeta}$, which we will approximate as $r = 1 - \zeta = 0.9$ (this approximation is valid for small ζ values when ζ^2 is negligible; in this case the error is only 0.6%). The minimum real part occurs at $r = \sqrt{1 + 2\zeta}$, approximated as $r = 1 + \zeta = 1.1$. The difference in the real value between these maximum and minimum points is the same as the magnitude peak value $\frac{1}{2k\zeta} = 5 \times 10^{-6}$ m/N. The imaginary minimum is seen at resonance with a value of $\frac{-1}{2k\zeta} = -5 \times 10^{-6}$ m/N.

In addition to the frequency dependent representations of the FRF shown in Figs. 2.11 and 2.12, the Argand diagram can also be selected. In this case, the real part is graphed versus the imaginary part (i.e., the complex plane), and the same information identified in the previous paragraphs is compactly represented. As we traverse the “circle” clockwise from $r = 0$, where the real part is $\frac{1}{k} = 1 \times 10^{-6}$ m/N and the imaginary part is zero, we sequentially encounter the $r = 1 - \zeta = 0.9$ point where the real part is maximum, the $r = 1$ point where the real part is zero and the imaginary part is most negative, and the $r = 1 + \zeta = 1.1$ point where the real part is most negative, and, finally, we approach the $r = \infty$ frequency ratio where both the real and imaginary parts are zero.

Fig. 2.13 Argand diagram, for example, single degree of freedom system

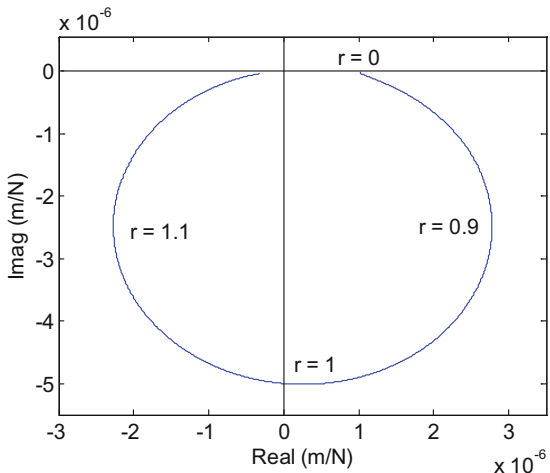
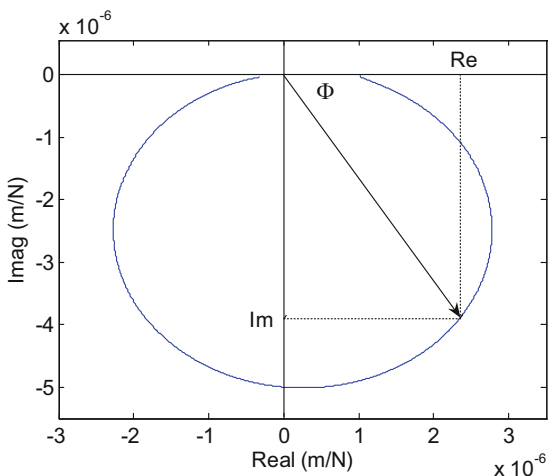


Fig. 2.14 Vector representation of FRF in the complex plane



Using a vector representation for $\frac{X}{F}$, the magnitude is identified as the length of the vector which extends from the origin to any point (i.e., a desired r value) on our “circle.” The phase lag between the displacement and force is the angle between the vector and the positive real axis. The real and imaginary parts are simply the projections of the vector on the real and imaginary axes. The MATLAB® program used to produce Figs. 2.12 through 2.14 for this example is provided with the textbook as p_2_1_1.m.

**In a Nutshell**

You can think of vibration as a vector (arrow) rotating in a plane (like a hand on a clock) in the counter-clockwise direction. The length of the vector is the size of the vibration. The speed of rotation is the frequency of the vibration. The projection of the tip of the rotating vector onto the horizontal axis is the real part, while the projection on the vertical axis is the imaginary part. Both the exciting force and the resulting displacement in a forced vibration can be represented this way. They are vectors that rotate together (have the same frequency), although they may have different lengths and the vibration vector will lag the force vector by some amount (i.e., they point to different times on the clock).

The Argand, or phase plane, representation summarizes the relationship between the force and the displacement. You can imagine that a picture has been taken when the force vector is horizontal (completely real). The curve on the Argand diagram represents the places where the tip of the resulting displacement vector can be found (as a function of frequency). When the frequency is low, the displacement vector is just below force vector. It is small in size and reaches its maximum at a time only shortly after the force. At resonance (where the exciting frequency is equal to the natural frequency), the displacement vector is large and is located 90 deg behind the force vector. When the excitation frequency is high, the displacement vector is again small and is 180 deg behind the force (it points in the opposite direction).

Of course few vibrating systems can be represented by a single coordinate. We extend the analysis to include a second coordinate in Sect. 2.3.

2.3 Two Degree of Freedom Free Vibration

We will again use the lumped parameter spring-mass-damper model as the basis for our discussion, but we will now include a second degree of freedom by adding a second spring-mass-damper to the first in a “chain-type” configuration; see Fig. 2.15. Using the free body diagrams for the top and bottom masses, where inertial forces are shown in addition to the spring and viscous damper forces, the two equations of motion can be written by equating the sum of the forces in the vertical direction to zero. The equation of motion for the top mass is:

$$m_1\ddot{x}_1 + (c_1 + c_2)\dot{x}_1 + (k_1 + k_2)x_1 - c_2\dot{x}_2 - k_2x_2 = 0 \quad (2.38)$$

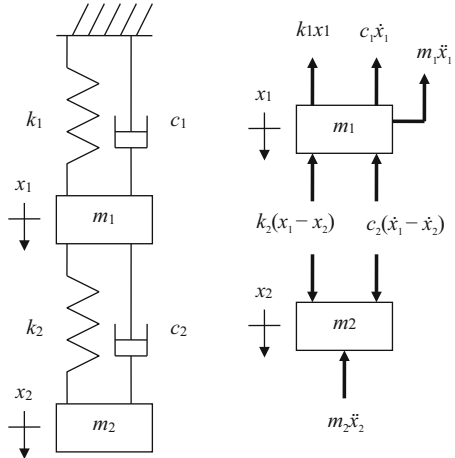
and the equation of motion for the bottom mass is:

$$m_2\ddot{x}_2 - c_2\dot{x}_1 - k_2x_1 + c_2\dot{x}_2 + k_2x_2 = 0. \quad (2.39)$$

**In a Nutshell**

A single degree of freedom system has one equation of motion. A two degree of freedom system has two equations of motion.

Fig. 2.15 Two degree of freedom, damped lumped parameter model (left); free body diagram (right)



The difference we may observe between the single and two degree of freedom situations is that, for the two degree of freedom case, the equations of motion are coupled; they both contain the displacements x_1 and x_2 and velocities \dot{x}_1 and \dot{x}_2 . This complicates the system solution and provides the motivation for modal analysis, which enables us to uncouple these two equations through a coordinate transformation and then use our single degree of freedom solution techniques. Before describing this approach, however, let's continue with our discussion of the chain-type two degree of freedom model.

The equations of motion are compactly expressed using a matrix formulation:

$$\begin{bmatrix} m_1 & 0 \\ 0 & m_2 \end{bmatrix} \begin{Bmatrix} \ddot{x}_1 \\ \ddot{x}_2 \end{Bmatrix} + \begin{bmatrix} c_1 + c_2 & -c_2 \\ -c_2 & c_2 \end{bmatrix} \begin{Bmatrix} \dot{x}_1 \\ \dot{x}_2 \end{Bmatrix} + \begin{bmatrix} k_1 + k_2 & -k_2 \\ -k_2 & k_2 \end{bmatrix} \begin{Bmatrix} x_1 \\ x_2 \end{Bmatrix} = \begin{Bmatrix} 0 \\ 0 \end{Bmatrix}. \quad (2.40)$$

The coupling is seen to occur in the symmetric damping and stiffness matrices for this chain-type model due to the nonzero off-diagonal terms in the matrix positions (1,2) and (2,1). If we represent the mass and stiffness matrices as $[M]$ and $[K]$, neglect damping for now, and assume a harmonic solution of the form $x = Xe^{st}$, we can write:

$$([M]s^2 + [K])\{X\}e^{st} = \{0\}. \quad (2.41)$$

Similar to Eq. 2.2, there are two possibilities for the product in Eq. 2.41. If $\{X\} = \{0\}$, we obtain the trivial solution. We are therefore interested in the case when $([M]s^2 + [K]) = \{0\}$. From linear algebra [8], we know that for this matrix of equations to have a nontrivial solution, the determinant must be equal to zero. This represents the characteristic equation for our system, where the $|x|$ notation indicates the determinant, not the absolute value.

$$|[M]s^2 + [K]| = 0. \quad (2.42)$$

The determinant of a two row, two column (2×2) matrix can be calculated by finding the difference between the products of the on-diagonal (row 1, column 1 and row 2, column 2) terms and the off-diagonal terms (1,2 and 2,1). This is expressed generically as:

$$\begin{vmatrix} as^2 + b & cs^2 + d \\ cs^2 + d & es^2 + f \end{vmatrix} = 0 \text{ or} \quad (2.43)$$

$$(as^2 + b)(es^2 + f) - (cs^2 + d)^2 = 0. \quad (2.44)$$

This equation is quadratic in s^2 , i.e., $gs^4 + hs^2 + m = 0$, and we can find the roots, s_1^2 and s_2^2 , using the quadratic equation. These two roots are the eigenvalues for the two degree of freedom system. The natural frequencies are calculated as:

$$s_1^2 = -\omega_{n1}^2 \quad \text{and} \quad s_2^2 = -\omega_{n2}^2, \quad (2.45)$$

where, by convention, $\omega_{n1} < \omega_{n2}$.



In a Nutshell

As you might guess, a single degree of freedom system has a single natural frequency (the frequency at which the system would “like” to vibrate), and a two degree of freedom system has two natural frequencies.

Interestingly, vibration in either of the two degree of freedom system’s natural frequencies is associated with a characteristic deformation pattern. That pattern is called a mode shape. Mathematically, it is referred to as an eigenvector, a German term that indicates that the natural frequencies (eigenvalues) and corresponding mode shapes (eigenvectors) are fundamental properties of the system.

To find the eigenvectors, or mode shapes, we substitute s_1^2 and s_2^2 into the equation of motion for the top or bottom mass (either will give the same solution because we imposed linear dependence between the two equations when we set the determinant equal to zero in Eq. 2.42). The equation of motion for the top mass corresponds to the top row in Eq. 2.46; recall that we are ignoring damping for now. See Eq. 2.47.

$$\begin{bmatrix} m_1s^2 + k_1 + k_2 & -k_2 \\ -k_2 & m_2s^2 + k_2 \end{bmatrix} \begin{Bmatrix} X_1 \\ X_2 \end{Bmatrix} = \begin{Bmatrix} 0 \\ 0 \end{Bmatrix} \quad (2.46)$$

$$(m_1s^2 + k_1 + k_2)X_1 - k_2X_2 = 0 \quad (2.47)$$

Because the two mode shapes represent the relative magnitude and direction of vibration between the two coordinates in the two degree of freedom system, we want

to calculate either the ratio $\frac{X_1}{X_2}$ or $\frac{X_2}{X_1}$. We can choose to normalize the eigenvector to either coordinate x_1 or x_2 . In most situations, the coordinate of interest or location of force application is selected. For example, we will normalize to the tool point for our studies of machining process dynamics. For the chain-type model, if we wish to normalize to coordinate x_1 , we require the ratios $\frac{X_1}{X_1} = 1$ and $\frac{X_2}{X_1}$. Using Eq. 2.47, we find that $\frac{X_2}{X_1} = \frac{m_1 s^2 + k_1 + k_2}{k_2}$ and the first mode shape is:

$$\psi_1 = \begin{Bmatrix} \frac{X_1}{X_1} \\ \frac{X_2}{X_1} \end{Bmatrix} = \begin{Bmatrix} 1 \\ \frac{m_1 s_1^2 + k_1 + k_2}{k_2} \end{Bmatrix}. \quad (2.48)$$

The second mode shape is determined by substitution of s_2^2 in place of s_1^2 :

$$\psi_2 = \begin{Bmatrix} \frac{X_1}{X_1} \\ \frac{X_2}{X_1} \end{Bmatrix} = \begin{Bmatrix} 1 \\ \frac{m_1 s_2^2 + k_1 + k_2}{k_2} \end{Bmatrix}. \quad (2.49)$$

The first mode shape corresponds to vibration in the first natural frequency ω_{n1} , while the second mode shape is associated with vibration at ω_{n2} . In general, the system will vibrate in a linear combination of both mode shapes/natural frequencies, depending on the initial conditions. If we've followed the convention of $\omega_{n1} < \omega_{n2}$ and normalized to the x_1 coordinate, we'll find that the first mode shape will take the form $\psi_1 = \begin{Bmatrix} 1 \\ a > 0 \end{Bmatrix}$, where a is a real number, which indicates that the two masses are vibrating exactly in phase with one another (i.e., they reach their maximum and minimum displacements at the same instants in time). We'll also see that the second mode shape will take the form $\psi_2 = \begin{Bmatrix} 1 \\ a < 0 \end{Bmatrix}$, which means that the mass motions are exactly out of phase with one another (i.e., when one mass reaches its maximum displacement, the other is at its minimum displacement).



In a Nutshell

Mode shapes only show relative size. A mode shape could show, for example, that when vibrating at the first natural frequency, the motion of coordinate 1 is twice as large as the motion of coordinate 2. This mode shape could be represented as $\psi_1 = \begin{Bmatrix} 1 \\ 0.5 \end{Bmatrix}$, $\psi_1 = \begin{Bmatrix} 2 \\ 1 \end{Bmatrix}$, or $\psi_1 = \begin{Bmatrix} 40,000 \\ 20,000 \end{Bmatrix}$. All of these representations are equivalent; they convey the characteristic deformation pattern. The “size” of the motion depends on the initial conditions, but the mode shapes do not.

Example 2.2 Free Vibration Using Complex Coefficients In this example we will calculate the time response of the system in Fig. 2.15 when the mass values are $m_1 = 1 \text{ kg}$ and $m_2 = 0.5 \text{ kg}$, the stiffness values are $k_1 = 1 \times 10^7 \text{ N/m}$ and $k_2 = 2 \times 10^7 \text{ N/m}$, the initial displacement of x_1 is $x_{0,1} = 1 \text{ mm}$ and the initial displacement of x_2 is $x_{0,2} = -1 \text{ mm}$, and the initial velocities are zero. The equations of motion in matrix form are:

$$\begin{bmatrix} 1 & 0 \\ 0 & 0.5 \end{bmatrix} \begin{Bmatrix} \ddot{x}_1 \\ \ddot{x}_2 \end{Bmatrix} + \begin{bmatrix} 1 \times 10^7 + 2 \times 10^7 & -2 \times 10^7 \\ -2 \times 10^7 & 2 \times 10^7 \end{bmatrix} \begin{Bmatrix} x_1 \\ x_2 \end{Bmatrix} = \begin{Bmatrix} 0 \\ 0 \end{Bmatrix}.$$

The characteristic equation is:

$$\begin{vmatrix} 1s^2 + 3 \times 10^7 & -2 \times 10^7 \\ -2 \times 10^7 & 0.5s^2 + 2 \times 10^7 \end{vmatrix} = 0, \text{ or } 0.5s^4 + 3.5 \times 10^7 s^2 + 2 \times 10^{14} = 0.$$

This equation yields the two roots $s_1^2 = -6.277 \times 10^6 \text{ (rad/s)}^2$ and $s_2^2 = -6.372 \times 10^7 \text{ (rad/s)}^2$, which give the natural frequencies $\omega_{n1} = \sqrt{-s_1^2} = 2505 \text{ rad/s}$ and $\omega_{n2} = \sqrt{-s_2^2} = 7983 \text{ rad/s}$. Expressed in units of Hz, these natural frequencies are $f_{n1} = \frac{\omega_{n1}}{2\pi} = 398.8 \text{ Hz}$ and $f_{n2} = \frac{\omega_{n2}}{2\pi} = 1271 \text{ Hz}$.

Let's normalize the mode shapes to x_2 and arbitrarily select the equation of motion for the top mass to calculate the ratio $\frac{X_1}{X_2} = \frac{2 \times 10^7}{1s^2 + 3 \times 10^7}$. We obtain the first mode shape, which corresponds to vibration in ω_{n1} , by substituting s_1^2 in this ratio:

$$\psi_1 = \begin{Bmatrix} \frac{X_1}{X_2} \\ \frac{X_2}{X_2} \end{Bmatrix} = \begin{Bmatrix} \frac{2 \times 10^7}{-6.277 \times 10^6 + 3 \times 10^7} \\ 1 \end{Bmatrix} = \begin{Bmatrix} 0.8431 \\ 1 \end{Bmatrix}.$$

See Fig. 2.16, where the relative deflection amplitudes between coordinates 1 and 2 are identified. The second mode shape, which corresponds to vibration in ω_{n2} , is:

Fig. 2.16 Mode shape
1 normalized to coordinate 2

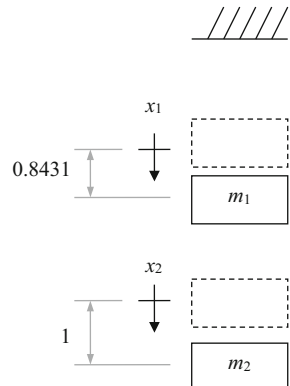
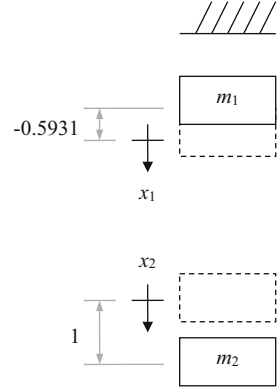


Fig. 2.17 Mode shape
2 normalized to coordinate 2



$$\psi_2 = \begin{Bmatrix} \frac{X_1}{X_2} \\ \frac{X_2}{X_2} \end{Bmatrix} = \begin{Bmatrix} \frac{2 \times 10^7}{-6.372 \times 10^7 + 3 \times 10^7} \\ 1 \end{Bmatrix} = \begin{Bmatrix} -0.5931 \\ 1 \end{Bmatrix}.$$

See Fig. 2.17, where the deflections are now in opposite directions (out of phase). Similar to Eq. 2.4, we can generically write the time domain solution for the x_1 and x_2 vibrations as:

$$\begin{aligned} x_1 &= X_{11} e^{i2505t} + X_{11}^* e^{-i2505t} + X_{12} e^{i7983t} + X_{12}^* e^{-i7983t} \quad \text{and} \\ x_2 &= X_{21} e^{i2505t} + X_{21}^* e^{-i2505t} + X_{22} e^{i7983t} + X_{22}^* e^{-i7983t}. \end{aligned}$$

Here, X_{ij} and X_{ij}^* represent a complex conjugate pair, where the subscript i indicates the coordinate number and the subscript j denotes the natural frequency number. This solution suggests the general case that the total vibration is a linear combination of vibration in each of the two modes. The first time derivatives are:

$$\begin{aligned} \dot{x}_1 &= i2505(X_{11} e^{i2505t} - X_{11}^* e^{-i2505t}) + i7983(X_{12} e^{i7983t} - X_{12}^* e^{-i7983t}) \quad \text{and} \\ \dot{x}_2 &= i2505(X_{21} e^{i2505t} - X_{21}^* e^{-i2505t}) + i7983(X_{22} e^{i7983t} - X_{22}^* e^{-i7983t}). \end{aligned}$$

Substitution of the initial conditions leads to a system of four equations with eight unknowns.

$$\begin{aligned} x_{0,1} &= 1 = X_{11} + X_{11}^* + X_{12} + X_{12}^* \\ x_{0,2} &= -1 = X_{21} + X_{21}^* + X_{22} + X_{22}^* \\ \dot{x}_{0,1} &= 0 = i2505(X_{11} - X_{11}^*) + i7983(X_{12} - X_{12}^*) \\ \dot{x}_{0,2} &= 0 = i2505(X_{21} - X_{21}^*) + i7983(X_{22} - X_{22}^*) \end{aligned}$$

However, we can apply the mode shape relationships to reduce this to a system of four equations with four unknowns. Using the same definitions for the X_{ij} subscripts,

we can write $\frac{X_{11}}{X_{21}} = 0.8431$ and $\frac{X_{11}}{X_{21}} = -0.5931$. After substitution and rewriting in matrix form, we obtain:

$$\begin{bmatrix} 0.8431 & 0.8431 & -0.5931 & -0.5931 \\ 1 & 1 & 1 & 1 \\ i2112 & -i2112 & i4734 & -i4734 \\ i2505 & -i2505 & i7983 & -i7983 \end{bmatrix} \begin{Bmatrix} X_{21} \\ X_{21}^* \\ X_{22} \\ X_{22}^* \end{Bmatrix} = \begin{Bmatrix} 1 \\ -1 \\ 0 \\ 0 \end{Bmatrix} \text{ or } [A]\{X\} = \{b\}.$$

We can determine the coefficients by inverting $[A]$ and premultiplying $\{b\}$ by this result, $\{X\} = [A]^{-1}\{b\}$. This can be accomplished in MATLAB® using the `inv` function. At the command prompt (`>>`), first define the 4×4 $[A]$ matrix and 4×1 $\{b\}$ vector, and then compute $\{X\}$:

```
>> A = [0.8431 0.8431 -0.5931 -0.5931; 1 1 1 1; 1i*2112 -1i*2112
1i*4734 -1i*4734; 1i*2505 -1i*2505 1i*7983 -1i*7983];
>> b = [1 -1 0 0]';
>> X = inv(A)*b
```

The result is
$$\begin{Bmatrix} X_{21} \\ X_{21}^* \\ X_{22} \\ X_{22}^* \end{Bmatrix} = \begin{Bmatrix} 0.1417 \\ 0.1417 \\ -0.6417 \\ -0.6417 \end{Bmatrix}$$
. Using these values and the mode shape

relationships to obtain the remaining four coefficients, we can substitute in the original x_1 and x_2 expressions to determine the time-dependent free vibration for our example system.

$$x_1 = 0.1194e^{i2505t} + 0.1194e^{-i2505t} + 0.3805e^{i7983t} + 0.3805e^{-i7983t}$$

$$x_2 = 0.1417e^{i2505t} + 0.1417e^{-i2505t} - 0.6417e^{i7983t} - 0.6417e^{-i7983t}$$

Further, we can use the Euler identity $e^{i\theta} + e^{-i\theta} = 2 \cos(\theta)$ to rewrite x_1 and x_2 as a sum of cosines. It is seen that the final motion of each mass is a linear combination of vibration in the two natural frequencies.

$$x_1 = 0.2388 \cos(2505t) + 0.7610 \cos(7983t)$$

$$x_2 = 0.2834 \cos(2505t) + 1.283 \cos(7983t)$$



In a Nutshell

The prior mathematic procedure is long, but the concept is this: the free vibration of a two degree of freedom system happens at the first natural frequency, at the second natural frequency, or a linear combination of the two at the same time. The final behavior depends on the initial conditions. No other

frequencies of motion are possible for the two degree of freedom system in free vibration.

A potential problem with this approach is that, for additional degrees of freedom, the size of the matrix varies with the square of the number of coordinates. For example, we inverted a $2^2 \times 2^2$, or 4×4 , complex matrix for our two degree of freedom system. For a three degree of freedom model, it would be necessary to invert a $3^2 \times 3^2$, or 9×9 , complex matrix, and so on. While computational capabilities continually increase, modal analysis offers an alternative to this approach. The fundamental idea behind modal analysis is that a coordinate transformation is applied to convert from the model, or local, coordinate system into a modal coordinate system. While these modal coordinates do not have physical significance, they lead to uncoupled equations of motion because the off-diagonal terms in the mass and stiffness matrices are zero. The coordinate transformation is a diagonalization process and relies upon the orthogonality of the eigenvectors (see Appendix). Let's rework Example 2.2 to demonstrate the modal analysis approach.



In a Nutshell

There are many possible choices of coordinates. For example, we used the motion of each mass relative to ground. An equally valid choice would be to use the motion of one mass relative to ground and the motion of the other mass relative to the first mass. Perhaps it is possible that there is a more favorable choice of coordinates—one that would make the math easier. Surprisingly, there is. It is always possible to choose a set of coordinates so that the equations of motion are uncoupled. For a two degree of freedom system, it means that it is possible to choose coordinates so that there are two separate single degree of freedom equations of motion. These special coordinates are called modal coordinates.

Example 2.3 Free Vibration by Modal Analysis The first step in the modal analysis approach is typically to find the eigensolution (natural frequencies and mode shapes). However, we have already completed this step in the previous example. Our next task is to define the modal matrix, $[P]$. It is a square matrix whose columns are composed of the mode shapes, $[P] = [\psi_1 \ \psi_2] = \begin{bmatrix} 0.8431 & -0.5931 \\ 1 & 1 \end{bmatrix}$, where we've continued with the decision to normalize to coordinate x_2 for illustrative purposes. As noted, the orthogonality conditions for eigenvectors enable us to diagonalize the mass and stiffness matrices (i.e., make the off-diagonal terms zero) and, therefore, uncouple the two equations of motion. The new mass and stiffness matrices in modal coordinates (identified by the q subscripts) are determined by premultiplying the mass and stiffness matrices in local coordinates by the transpose of the modal matrix and postmultiplying this product by the modal matrix.

$$\begin{aligned}
 [M_q] &= [P]^T [M] [P] = \begin{bmatrix} 0.8431 & 1 \\ -0.5931 & 1 \end{bmatrix} \begin{bmatrix} 1 & 0 \\ 0 & 0.5 \end{bmatrix} \begin{bmatrix} 0.8431 & -0.5931 \\ 1 & 1 \end{bmatrix} \\
 &= \begin{bmatrix} 1.211 & 0 \\ 0 & 0.8518 \end{bmatrix} \text{kg} \\
 [K_q] &= [P]^T [K] [P] \\
 &= \begin{bmatrix} 0.8431 & 1 \\ -0.5931 & 1 \end{bmatrix} \begin{bmatrix} 3 \times 10^7 & -2 \times 10^7 \\ -2 \times 10^7 & 2 \times 10^7 \end{bmatrix} \begin{bmatrix} 0.8431 & -0.5931 \\ 1 & 1 \end{bmatrix} \\
 &= \begin{bmatrix} 7.601 \times 10^6 & 0 \\ 0 & 5.4282 \times 10^7 \end{bmatrix} \text{N/m}
 \end{aligned}$$

These computations can be performed in MATLAB® by first defining $[P]$, $[M]$, and $[K]$, then typing the following commands:

```
>> Mq = P'*M*P;
>> Kq = P'*K*P;
```

Adding the semicolon to the ends of these commands suppresses the echo feature where the answer is displayed as soon as the “Enter” button is pressed. To see the results, either omit the semicolon or follow the first command with `>>Mq` which will display the most recent value of the variable `Mq`. Do not be alarmed if the off-diagonal terms are not identically zero in the modal mass and stiffness matrices. This is due to roundoff error in our modal matrix entries. Carrying more significant digits will drive the off-diagonal terms closer to zero.

The two equations of motion can now be written in modal coordinates q_1 and q_2 using the matrix formulation: $[M_q]\{\ddot{q}\} + [K_q]\{q\} = \{0\}$. We see that the two equations are uncoupled and may be treated as separate single degree of freedom systems.

$$\begin{aligned}
 1.211\ddot{q}_1 + 7.601 \times 10^6 q_1 &= 0 \\
 0.8518\ddot{q}_2 + 5.4282 \times 10^7 q_2 &= 0
 \end{aligned}$$

To use the solution techniques we developed in Sect. 2.1, we also need the initial conditions to be expressed in modal coordinates. Because the relationship between local and modal coordinates is $\{x\} = [P]\{q\}$, we can write $\{q\} = [P]^{-1}\{x\}$. To invert our 2×2 modal matrix, we switch the on-diagonal terms, change the sign of the off-diagonal terms, and divide each term by the scalar determinant, $|P| = P(1, 1)P(2, 2) - P(1, 2)P(2, 1)$.

$$[P]^{-1} = \frac{\begin{bmatrix} 1 & 0.5931 \\ -1 & 0.8431 \end{bmatrix}}{0.8431 \cdot 1 - (-0.5931) \cdot 1} = \begin{bmatrix} 0.6963 & 0.4130 \\ -0.6963 & 0.5870 \end{bmatrix}$$

We can then calculate the initial displacements $\{q_0\} = [P]^{-1}\{x_0\} = \begin{Bmatrix} 0.2833 \\ -1.283 \end{Bmatrix}$ mm and velocities $\{\dot{q}_0\} = [P]^{-1}\{\dot{x}_0\} = \begin{Bmatrix} 0 \\ 0 \end{Bmatrix}$ in modal coordinates. These calculations may be carried out in MATLAB® by typing the following commands:

```
>> P = [0.8431 -0.5931; 1 1];
>> x0 = [1 -1]';
>> q0 = inv(P)*x0
>> dx0 = [0 0]';
>> dq0 = inv(P)*dx0
```

We introduce here another general form for the solution of undamped free vibration given the initial displacement and velocity (in addition to the information provided in Sect. 2.1). The resulting displacement can be written as $x = \frac{\dot{x}_0}{\omega_n} \sin(\omega_n t) + x_0 \cos(\omega_n t)$. Using this form, the modal displacements are $q_1 = 0 \sin(2505t) + 0.2833 \cos(2505t)$, which represents motion in the first natural frequency, and $q_2 = 0 \sin(7983t) - 1.283 \cos(7983t)$, which describes motion in the second natural frequency. To obtain the motion in local coordinates, we must perform the coordinate transformation $\{x\} = [P]\{q\} = \begin{bmatrix} 0.8431 & -0.5931 \\ 1 & 1 \end{bmatrix} \begin{Bmatrix} q_1 \\ q_2 \end{Bmatrix}$, which provides the relationships:

$$\begin{aligned} x_1 &= 0.8431q_1 - 0.5931q_2 \quad \text{and} \\ x_2 &= q_1 + q_2. \end{aligned}$$

It should be emphasized that the x_2 vibration is determined simply by summing the modal displacements, q_1 and q_2 . This is a direct outcome of normalizing our mode shapes to x_2 and is an important result for us. We will take advantage of the fact that the local response can be written as a sum of the modal contributions when we perform our modal fitting of measured FRFs. Also, we see that the x_1 motion is a linear combination of q_1 and q_2 , where each modal response is scaled by the corresponding mode shape. Substitution of our q_1 and q_2 values into the previous equations for x_1 and x_2 yields the same result we obtained using the technique shown in Example 2.2, but the modal analysis approach did not require the inversion of the $2^2 \times 2^2$ complex matrix.

$$x_1 = 0.2388 \cos(2505t) + 0.7610 \cos(7983t)$$

$$x_2 = 0.2833 \cos(2505t) + 1.283 \cos(7983t)$$



In a Nutshell

All free vibration of a two degree of freedom systems can be thought of, in the general case, as a linear combination of motion in the two modes. Each mode has a natural frequency and a corresponding mode shape.

The resulting combination depends on the initial conditions. In Sects. 2.5 and 2.6, we discuss the measurement/determination of the modes that characterize the way a complicated system would “like” to vibrate.

The final consideration in this section is solution of the two degree of freedom free vibration problem in the presence of damping. We've already stated that every physical system dissipates energy, so our analysis should incorporate the viscous damping matrix shown in Eq. 2.40. However, this complicates the eigensolution. At this point, we need to introduce the concept of proportional damping. Physically, proportional damping means that all the coordinates pass through their equilibrium (zero) positions at the same instant for each mode shape. For the low damping observed in the tool-holder assemblies we will be considering, this assumption is realistic. For very high damping values, however, it is less reasonable because there may be significant phase differences between the motions of individual coordinates. Mathematically, proportional damping requires that the damping matrix can be written as a linear combination of the mass and stiffness matrices: $[C] = \alpha[M] + \beta[K]$, where α and β are real numbers.



In a Nutshell

Many kinds of damping are possible. There is great mathematical advantage in assuming that the damping is proportional and we often assume that it is, even if it is not.

Provided the proportional damping requirement is satisfied, then damping may be neglected in the eigensolution, and the modal analysis procedure follows the steps provided in Example 2.3. The only modifications are that we must calculate the modal damping matrix $[C_q] = [P]^T[C][P]$, and the general solution to the uncoupled modal equations of motion $[M_q]\{\ddot{q}\} + [C_q]\{\dot{q}\} + [K_q]\{q\} = \{0\}$ is different. For the underdamped case, we can write $q = e^{-\zeta\omega_n t} \left(\frac{\dot{q}_0 + \zeta\omega_n q_0}{\omega_d} \sin(\omega_d t) + q_0 \cos(\omega_d t) \right)$. Otherwise, the solution proceeds as before.

2.4 Two Degree of Freedom Forced Vibration

We will use the two degree of freedom lumped parameter spring-mass-damper model shown in Fig. 2.15 but will impose external harmonic forces at coordinates x_1 and x_2 for the general case. However, because our analysis is limited to linear systems, we can apply the principle of superposition to consider the forces separately and then sum the individual contributions. For demonstration purposes, we will consider only the $f_2 e^{i\omega t}$ force applied to coordinate x_2 . The equations of motion in matrix form for this system are:

$$\begin{aligned} & \begin{bmatrix} m_1 & 0 \\ 0 & m_2 \end{bmatrix} \begin{Bmatrix} \ddot{x}_1 \\ \ddot{x}_2 \end{Bmatrix} + \begin{bmatrix} c_1 + c_2 & -c_2 \\ -c_2 & c_2 \end{bmatrix} \begin{Bmatrix} \dot{x}_1 \\ \dot{x}_2 \end{Bmatrix} + \begin{bmatrix} k_1 + k_2 & -k_2 \\ -k_2 & k_2 \end{bmatrix} \begin{Bmatrix} x_1 \\ x_2 \end{Bmatrix} \\ & = \begin{Bmatrix} 0 \\ f_2 \end{Bmatrix}. \end{aligned} \quad (2.50)$$

By assuming solutions of the form $x_{1,2} = X_{1,2} e^{i\omega t}$ and substituting in Eq. 2.50, we obtain:

$$(-\omega^2 [M] + i\omega [C] + [K]) \{X\} e^{i\omega t} = \{F\} e^{i\omega t}. \quad (2.51)$$

We have two methods that we can use to determine the steady-state forced vibration response for this system. The first is modal analysis, which requires proportional damping, and the second is complex matrix inversion, which places no restrictions on the nature of the system damping. Let's begin with modal analysis.

2.4.1 Modal Analysis

Our first step in the modal analysis approach is to write the system equations of motion in local coordinates as shown in Eq. 2.50; we continue to consider the f_2 case in this discussion. Provided proportional damping exists (i.e., $[C] = \alpha[M] + \beta[K]$ is true), then we can ignore damping to find the eigensolution. Note that this solution is also independent of the external force(s). We find the eigenvalues (natural frequencies) and eigenvectors (modes shapes) using Eq. 2.41 ($[M]s^2 + [K]\{X\}e^{st} = \{0\}$). The eigenvalues are determined from the roots of Eq. 2.42 $|[M]s^2 + [K]| = 0$. The natural frequencies are computed from $s_j^2 = -\omega_{nj}^2$, $j = 1$ to 2 (the number of degrees of freedom). We can then use either of the equations of motion to find the 2×1 mode shapes for the two degree of freedom system:

$$\psi_1 = \begin{Bmatrix} \frac{X_1}{X_2}(s_1^2) \\ 1 \end{Bmatrix} \quad \text{and} \quad \psi_2 = \begin{Bmatrix} \frac{X_1}{X_2}(s_2^2) \\ 1 \end{Bmatrix}, \quad (2.52)$$

where we have normalized to the location of the force application (coordinate x_2). Using the mode shapes, we assemble the 2×2 modal matrix $[P] = [\psi_1 \ \psi_2]$. We can then use the modal matrix to transform into modal coordinates (and uncouple the equations of motion). The diagonal modal mass, damping, and stiffness matrices are $[M_q] = [P]^T [M] [P] = \begin{bmatrix} m_{q1} & 0 \\ 0 & m_{q2} \end{bmatrix}$, $[C_q] = [P]^T [C] [P] = \begin{bmatrix} c_{q1} & 0 \\ 0 & c_{q2} \end{bmatrix}$, and $[K_q] = [P]^T [K] [P] = \begin{bmatrix} k_{q1} & 0 \\ 0 & k_{q2} \end{bmatrix}$, respectively. We must also transform the local force vector into modal coordinates:

$$\{R\} = \begin{Bmatrix} R_1 \\ R_2 \end{Bmatrix} = [P]^T \{F\} = \begin{bmatrix} \frac{X_1}{X_2}(s_1^2) & 1 \\ \frac{X_1}{X_2}(s_2^2) & 1 \end{bmatrix} \begin{Bmatrix} 0 \\ f_2 \end{Bmatrix} = \begin{bmatrix} p_1 & 1 \\ p_2 & 1 \end{bmatrix} \begin{Bmatrix} 0 \\ f_2 \end{Bmatrix} = \begin{Bmatrix} f_2 \\ f_2 \end{Bmatrix}. \quad (2.53)$$

The modal equations of motion are:

$$\begin{aligned} m_{q1}\ddot{q}_1 + c_{q1}\dot{q}_1 + k_{q1}q_1 &= R_1, \\ m_{q2}\ddot{q}_2 + c_{q2}\dot{q}_2 + k_{q2}q_2 &= R_2 \end{aligned} \quad (2.54)$$

and the corresponding complex FRFs (steady-state responses in the frequency domain) are:

$$\frac{Q_1}{R_1} = \frac{1}{k_{q1}} \left(\frac{(1 - r_1^2) - i(2\zeta_{q1}r_1)}{(1 - r_1^2)^2 + (2\zeta_{q1}r_1)^2} \right) \quad \text{and} \quad \frac{Q_2}{R_2} = \frac{1}{k_{q2}} \left(\frac{(1 - r_2^2) - i(2\zeta_{q2}r_2)}{(1 - r_2^2)^2 + (2\zeta_{q2}r_2)^2} \right), \quad (2.55)$$

where $r_{1,2} = \frac{\omega}{\omega_{n1,2}}$ and $\zeta_{q1,2} = \frac{c_{q1,2}}{2\sqrt{k_{q1,2}m_{q1,2}}}$. We transform into local coordinates using.

$$\{X\} = \begin{Bmatrix} X_1 \\ X_2 \end{Bmatrix} = [P]\{Q\} = \begin{bmatrix} p_1 & p_2 \\ 1 & 1 \end{bmatrix} \begin{Bmatrix} Q_1 \\ Q_2 \end{Bmatrix} \quad \text{so that } X_1 = p_1Q_1 + p_2Q_2 \text{ and}$$

$X_2 = Q_1 + Q_2$. Dividing each of these equations by F_2 gives the cross and direct FRFs for the f_2 force application, respectively. The cross FRF, which indicates that the force and measurement coordinates are not coincident, is:

$$\frac{X_1}{F_2} = \frac{p_1Q_1 + p_2Q_2}{F_2} = p_1 \frac{Q_1}{F_2} + p_2 \frac{Q_2}{F_2} = p_1 \frac{Q_1}{R_1} + p_2 \frac{Q_2}{R_2}, \quad (2.56)$$

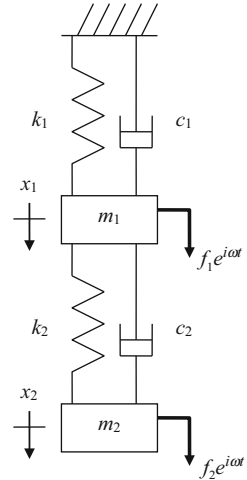
where we see that the cross FRF is the sum of the modal FRFs scaled by the mode shapes (remember that $R_1 = R_2 = F_2$ from Eq. 2.53). The direct FRF, which denotes that the measurement is performed at the force input location, is:

$$\frac{X_2}{F_2} = \frac{Q_1 + Q_2}{F_2} = \frac{Q_1}{F_2} + \frac{Q_2}{F_2} = \frac{Q_1}{R_1} + \frac{Q_2}{R_2}. \quad (2.57)$$

We observe the important result that the direct FRF is simply the sum of the modal contributions. This is important for our subsequent analyses. Measurement of the frequency response functions on a physical system enable extraction of the model parameters and visualization of the natural frequencies and mode shapes.

Example 2.4 Forced Vibration by Modal Analysis Consider the chain-type, lumped parameter two degree of freedom system shown in Fig. 2.18. For the upper spring-mass-damper, the local coordinate constants are $k_1 = 4 \times 10^5$ N/m, $c_1 = 80$ N s/m, and $m_1 = 2$ kg. For the lower spring-mass-damper, the local coordinate constants are

Fig. 2.18 Two degree of freedom, lumped parameter system (damped with force)



$k_2 = 6 \times 10^5$ N/m, $c_2 = 120$ N s/m, and $m_2 = 1$ kg. A harmonic force $f_2 = 100e^{i\omega t}$ N is applied to the lower mass (at coordinate x_2); we will not consider any force applied to the upper mass, although this force could be considered separately and the result added to the solution of the analysis we will perform here. The local mass, damping, and stiffness matrices are $M = \begin{bmatrix} 2 & 0 \\ 0 & 1 \end{bmatrix}$ kg, $C = \begin{bmatrix} 200 & -120 \\ -120 & 120 \end{bmatrix}$ N s/m, and $K = \begin{bmatrix} 1 \times 10^6 & -6 \times 10^5 \\ -6 \times 10^5 & 6 \times 10^5 \end{bmatrix}$ N/m, respectively. To use modal analysis, we must verify that proportional damping exists. For $\alpha = 0$ and $\beta = \frac{1}{5000}$, we see that the relationship $[C] = \alpha[M] + \beta[K]$ is satisfied. We can therefore determine the eigenvalues using:

$$\begin{vmatrix} 2s^2 + 1 \times 10^6 & -6 \times 10^5 \\ -6 \times 10^5 & s^2 + 6 \times 10^5 \end{vmatrix} = 0.$$

The two roots of the determinant are $s_1^2 = -1,22,799.81$ (rad/s)² and $s_2^2 = -9,77,200.19$ (rad/s)², which give the natural frequencies $\omega_{n1} = 350.43$ rad/s and $\omega_{n2} = 988.53$ rad/s ($\omega_{n1} < \omega_{n2}$). To determine the roots using MATLAB®, we first write the characteristic equation: $(2s^2 + 1 \times 10^6)(s^2 + 6 \times 10^5) - (-6 \times 10^5)^2 = 0$, or after simplifying $2s^4 + 2.2 \times 10^6 s^2 + 2.4 \times 10^{11} = 0$. Because this equation is quadratic in s^2 , we can find the roots s_1^2 and s_2^2 using the `roots` function.

```
>> roots([2 2.2e6 2.4e11])
```

For the eigenvectors (mode shapes), we normalize to the location of the force application, coordinate x_2 . Using the equation of motion for the top mass (arbitrarily selected), we obtain the required ratio $\frac{x_1}{x_2} = \frac{6 \times 10^5}{2s^2 + 1 \times 10^6}$. Substitution of $s_1^2 = -1,22,799.81$ (rad/s)² and $s_2^2 = -9,77,200.19$ (rad/s)² into Eq. 2.52 gives the two

mode shapes $\psi_1 = \begin{Bmatrix} 0.7953 \\ 1 \end{Bmatrix}$ and $\psi_2 = \begin{Bmatrix} -0.6287 \\ 1 \end{Bmatrix}$, respectively. We can now construct the modal matrix $[P] = [\psi_1 \ \psi_2] = \begin{bmatrix} 0.7953 & -0.6287 \\ 1 & 1 \end{bmatrix}$ and transform the local mass, stiffness, and damping matrices into modal coordinates:

$$\begin{aligned}[M_q] &= [P]^T [M] [P] = \begin{bmatrix} 2.265 & 0 \\ 0 & 1.790 \end{bmatrix} \text{kg}, \\ [K_q] &= [P]^T [K] [P] = \begin{bmatrix} 2.782 \times 10^5 & 0 \\ 0 & 1.750 \times 10^6 \end{bmatrix} \text{N/m, and} \\ [C_q] &= [P]^T [C] [P] = \begin{bmatrix} 55.63 & 0 \\ 0 & 349.9 \end{bmatrix} \text{Ns/m.} \end{aligned}$$

A simple check at this point is to recalculate the natural frequencies using the modal parameters. The results should match the eigenvalue solution. Here, we see that $\omega_{n1} = \sqrt{\frac{k_{q1}}{m_{q1}}} = \sqrt{\frac{2.782 \times 10^5}{2.265}} = 350.46 \text{ rad/s}$ and $\omega_{n2} = \sqrt{\frac{k_{q2}}{m_{q2}}} = \sqrt{\frac{1.750 \times 10^6}{1.790}} = 988.76 \text{ rad/s}$, where the differences are due to roundoff error but the results are essentially the same. We can also determine the modal damping ratios:

$$\begin{aligned}\zeta_{q1} &= \frac{c_{q1}}{2\sqrt{k_{q1}m_{q1}}} = \frac{55.63}{2\sqrt{2.782 \times 10^5 \cdot 2.265}} = 0.035 \text{ (3.5% damping)} \quad \text{and} \\ \zeta_{q2} &= \frac{c_{q2}}{2\sqrt{k_{q2}m_{q2}}} = \frac{349.9}{2\sqrt{1.750 \times 10^6 \cdot 1.790}} = 0.099 \text{ (9.9% damping).}\end{aligned}$$

To write our uncoupled equations of motion in modal coordinates, we also need the modal force vector, which we obtain by substitution into Eq. 2.53.

$$\{R\} = \begin{bmatrix} 0.7953 & 1 \\ -0.6287 & 1 \end{bmatrix} \begin{Bmatrix} 0 \\ 100 \end{Bmatrix} = \begin{Bmatrix} 100 \\ 100 \end{Bmatrix} \text{N}$$

$$2.265\ddot{q}_1 + 55.63\dot{q}_1 + 2.782 \times 10^5 q_1 = 100$$

$$1.790\ddot{q}_2 + 349.9\dot{q}_2 + 1.750 \times 10^6 q_2 = 100$$

The FRFs for the single degree of freedom modal systems are:

$$\begin{aligned}\frac{Q_1}{R_1} &= \frac{1}{2.782 \times 10^5} \left(\frac{(1 - r_1^2) - i(0.070r_1)}{(1 - r_1^2)^2 + (0.070r_1)^2} \right) \\ \text{and } \frac{Q_2}{R_2} &= \frac{1}{1.750 \times 10^6} \left(\frac{(1 - r_2^2) - i(0.198r_2)}{(1 - r_2^2)^2 + (0.198r_2)^2} \right),\end{aligned}$$

where $r_1 = \frac{\omega}{350.43}$ and $r_2 = \frac{\omega}{988.53}$. The direct and cross FRFs are then $\frac{X_2}{F_2} = \frac{Q_1}{R_1} + \frac{Q_2}{R_2}$ and $\frac{X_1}{F_2} = 0.7953 \frac{Q_1}{R_1} - 0.6287 \frac{Q_2}{R_2}$, respectively. See Figs. 2.19 and 2.20. Because motion in

Fig. 2.19 The real and imaginary parts of the direct FRF are determined from the sum of the modal contributions

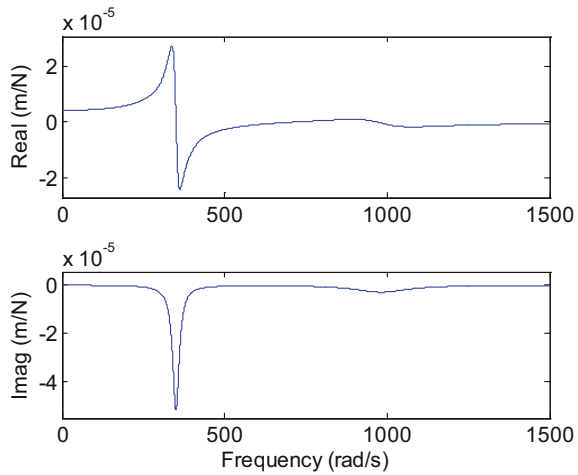
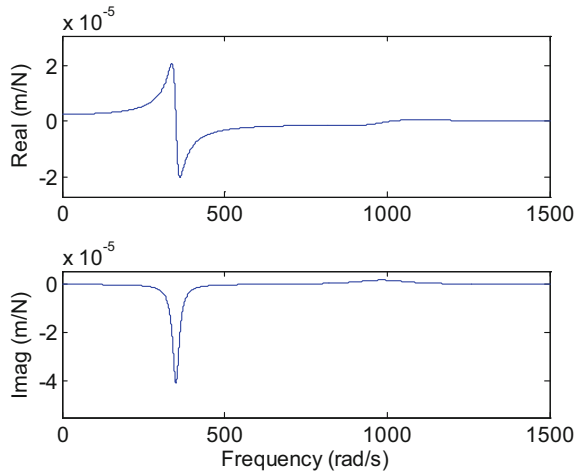


Fig. 2.20 The real and imaginary parts of the cross FRF are obtained by scaling the two modes by the corresponding mode shape and summing the results



the second mode shape, corresponding to $\omega_{n2} = 988.53$ rad/s, exhibits a 180 deg phase shift between the two coordinates (i.e., they are out of phase), the second mode is “inverted” in the cross FRF plot. The MATLAB® program used to produce these figures is provided with the textbook as p_2_4_1.m.

2.4.2 Complex Matrix Inversion

Our final task of this section is to describe an alternative to modal analysis, referred to as complex matrix inversion. This approach does not require proportional damping, but does include the inversion of a 2×2 frequency dependent, complex

matrix for the two degree of freedom system we are considering here. We'll first write Eq. 2.51 in the form $[A]\{X\} = \{F\}$, where $[A] = \begin{bmatrix} a_{11} & a_{12} \\ a_{21} & a_{22} \end{bmatrix} = (-\omega^2[M] + i\omega[C] + [K])$. The two degree of freedom system has four FRFs that we'd like to determine. First, we have the direct and cross FRFs, $\frac{X_2}{F_2}$ and $\frac{X_1}{F_2}$, due to the force application at coordinate x_2 that we previously determined using modal analysis. Second, we have the direct and cross FRFs, $\frac{X_1}{F_1}$ and $\frac{X_2}{F_1}$, due to the force application at coordinate x_1 . We did not explicitly show the modal solution to this case in Sect. 2.4, but the only differences are that we would normalize the mode shapes to x_1 and the FRFs would then be computed from $\frac{X_1}{F_1} = \frac{Q_1}{R_1} + \frac{Q_2}{R_2}$ and $\frac{X_2}{F_1} = p_1 \frac{Q_1}{R_1} + p_2 \frac{Q_2}{R_2}$, where $P = \begin{bmatrix} 1 & 1 \\ p_1 & p_2 \end{bmatrix}$ would be used to determine the modal mass, stiffness, and damping matrices.

Rewriting $[A]\{X\} = \{F\}$ as $\{X\}\{F\}^{-1} = [A]^{-1}$ provides all four FRFs. They are ordered as:

$$\begin{Bmatrix} \frac{X_1}{F_1} & \frac{X_1}{F_2} \\ \frac{X_2}{F_1} & \frac{X_2}{F_2} \end{Bmatrix} = \begin{bmatrix} b_{11} & b_{12} \\ b_{21} & b_{22} \end{bmatrix},$$

where we've used the b_{ij} notation to indicate the individual terms in the inverted $[A]$ matrix. In our analysis, $[A]$ is symmetric. Therefore, $b_{12} = b_{21}$ and $\frac{X_1}{F_2} = \frac{X_2}{F_1}$. This condition is referred to as reciprocity. Physically, it means that we get the same result if we (1) excite the system at coordinate x_2 and measure the response at x_1 , as if we (2) excite the system at coordinate x_1 and measure the response at x_2 .

For the two degree of freedom system, we can directly write the individual terms in $[A]^{-1}$ as:

$$\begin{aligned} [A]^{-1} &= \frac{\begin{bmatrix} a_{22} & -a_{12} \\ -a_{21} & a_{11} \end{bmatrix}}{a_{11} \cdot a_{22} - a_{12} \cdot a_{21}} \\ &= \frac{\begin{bmatrix} -\omega^2 m_2 + i\omega c_2 + k_2 & i\omega c_2 + k_2 \\ i\omega c_2 + k_2 & -\omega^2 m_1 + i\omega(c_1 + c_2) + k_1 + k_2 \end{bmatrix}}{a_{11} \cdot a_{22} - a_{12} \cdot a_{21}}. \end{aligned}$$

For example, $\frac{X_1}{F_1} = b_{11} = \frac{-\omega^2 m_2 + i\omega c_2 + k_2}{a_{11} \cdot a_{22} - a_{12} \cdot a_{21}}$. Note that this complex expression is a function of the forcing frequency ω , so it must be evaluated over the desired frequency range in order to produce plots equivalent to those obtained for the modal analysis example.



In a Nutshell

Complex matrix inversion is a mathematical technique that is used when it is certain that the damping is not proportional.

2.5 System Identification

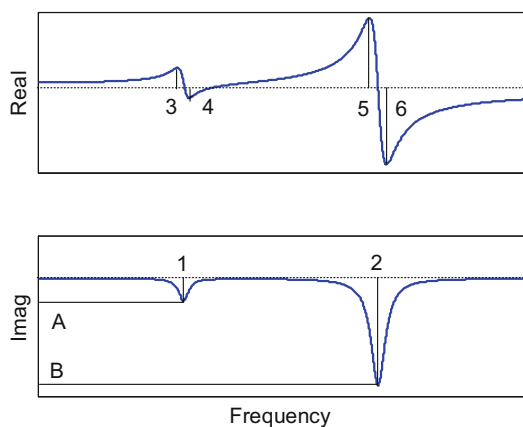
The previous section describes the modal analysis steps required to obtain the direct and cross FRFs in local coordinates given a system model (we treated the chain-type, lumped parameter case, but other model geometries could be considered as well). This approach required that the mass, damping, and stiffness matrices be known. However, this is not the case for arbitrary tool-holder assemblies. Our actual task is typically to measure the FRFs for the system of interest and then define a model by performing a modal fit to the measured data.

2.5.1 Modal Fitting

Our fitting approach will be a “peak-picking” method where we use the real and imaginary parts of the system FRFs to identify the modal parameters. This approach works well provided the system modes are not closely spaced. However, even if two modeled modes are relatively close in frequency, we can still obtain a reasonable modal fit as we’ll see in Example 2.5. For additional information on modal testing, see [1, 9].

To demonstrate the fitting steps, consider the direct FRF shown in Fig. 2.21. This FRF clearly has two modes within the measurement bandwidth. To determine the modal parameters which populate the 2×2 modal matrices, we must identify three frequencies and one peak value for each mode. [Note that we have automatically assumed proportional damping in using this approach. Additionally, if there were three dominant modes we wished to model, we would obtain 3×3 modal matrices and so on.] The frequencies labeled 1 and 2 along the horizontal frequency axis in the imaginary part of the direct FRF (Fig. 2.21) correspond to the minimum imaginary peaks and provide the two natural frequencies, ω_{n1} and ω_{n2} , respectively.

Fig. 2.21 Two degree of freedom direct FRF with the frequencies and amplitudes required for peak picking identified



The difference between frequencies 4 and 3, labeled along the frequency axis of the real part of the direct FRF, is used to determine the modal damping ratio for the first mode, ζ_{q1} :

$$\begin{aligned}\omega_4 - \omega_3 &= \omega_{n1}(1 + \zeta_{q1}) - \omega_{n1}(1 - \zeta_{q1}) = 2\zeta_{q1}\omega_{n1} \quad \text{or} \quad \zeta_{q1} \\ &= \frac{\omega_4 - \omega_3}{2\omega_{n1}}.\end{aligned}\quad (2.58)$$

Similarly, the difference between frequencies 6 and 5 is used to determine ζ_{q2} :

$$\zeta_{q2} = \frac{\omega_6 - \omega_5}{2\omega_{n2}}. \quad (2.59)$$

The (negative) peak value, A , identified along the vertical axis of the imaginary part of the direct FRF is next used to find the modal stiffness value, k_{q1} :

$$A = \frac{-1}{2k_{q1}\zeta_{q1}} \quad \text{or} \quad k_{q1} = \frac{-1}{2\zeta_{q1}A}. \quad (2.60)$$

Similarly, the peak value B is used to determine k_{q2} :

$$k_{q2} = \frac{-1}{2\zeta_{q2}B}. \quad (2.61)$$

At this point, we can directly populate the modal stiffness matrix $[K_q] = \begin{bmatrix} k_{q1} & 0 \\ 0 & k_{q2} \end{bmatrix}$. However, we must calculate the modal mass and damping values from the additional information we've obtained. We determine the modal masses using the natural frequencies and modal stiffness values:

$$\omega_{n1} = \sqrt{\frac{k_{q1}}{m_{q1}}} \quad \text{or} \quad m_{q1} = \frac{k_{q1}}{\omega_{n1}^2} \quad \text{and} \quad m_{q2} = \frac{k_{q2}}{\omega_{n2}^2}. \quad (2.62)$$

The modal damping coefficients are computed using the modal damping ratios, stiffness values, and masses:

$$\zeta_{q1} = \frac{c_{q1}}{2\sqrt{k_{q1}m_{q1}}} \quad \text{or} \quad c_{q1} = 2\zeta_{q1}\sqrt{k_{q1}m_{q1}} \quad \text{and} \quad c_{q2} = 2\zeta_{q2}\sqrt{k_{q2}m_{q2}}. \quad (2.63)$$

We can now write the remaining modal matrices $[M_q] = \begin{bmatrix} m_{q1} & 0 \\ 0 & m_{q2} \end{bmatrix}$ and $[C_q] = \begin{bmatrix} c_{q1} & 0 \\ 0 & c_{q2} \end{bmatrix}$. Identification of the modal matrices provides sufficient information for us to complete the time domain turning and milling simulations we develop in Chaps. 3 and 4. However, to complete this discussion, we will detail the steps necessary to define a chain-type, lumped parameter model based on measured FRFs. Before continuing with the model definition, let's complete an example of peak picking to determine the modal matrices.



In a Nutshell

Measured frequency response functions contain the information necessary to construct a mathematical model of the system in question.

Example 2.5 Peak-Picking Modal Fit Figure 2.22 shows an example FRF that could be obtained from a tool point measurement. Our task is to perform a modal fit to identify the modal mass, damping, and stiffness matrices. The first step is to decide how many modes we wish to fit. A visual inspection of the FRF shows that a three mode fit is appropriate. The three natural frequencies are identified by locating the three minimum peaks of the imaginary part and recording the associated frequencies. These are identified as {499, 761, and 849} Hz in Fig. 2.23. We determine the modal

Fig. 2.22 Example tool point FRF for peak-picking exercise

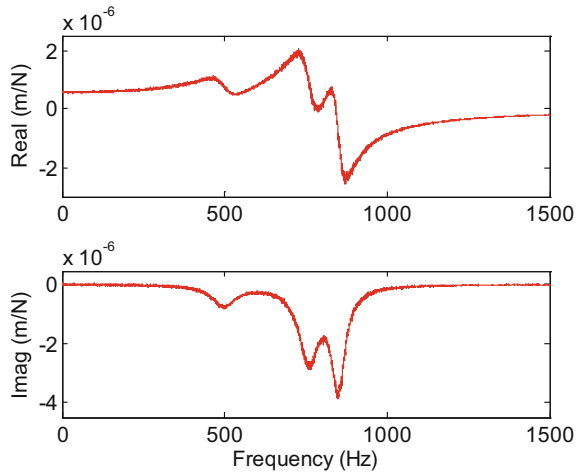
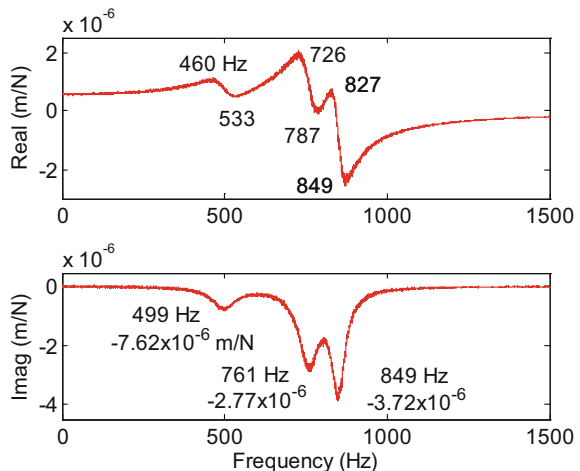


Fig. 2.23 Three degree of freedom peak-picking example with required frequencies and amplitudes identified



damping ratios using the frequencies of the local maximum and minimum values of the real part according to Eq. 2.58. These are shown as 460 Hz and 533 Hz for mode 1, 726 Hz and 787 Hz for mode 2, and 827 Hz and 873 Hz for mode 3. The modal damping ratios are then:

$$\zeta_{q1} = \frac{533 - 460}{2 \cdot 499} = 0.073, \quad \zeta_{q2} = \frac{787 - 726}{2 \cdot 761} = 0.040, \quad \text{and} \quad \zeta_{q3} = \frac{873 - 827}{2 \cdot 849} \\ = 0.027.$$

The imaginary part negative peak values for each mode are also listed in Fig. 2.23. The modal stiffness values are calculated using Eq. 2.60.

$$k_{q1} = \frac{-1}{2 \cdot 0.073 \cdot (-7.62 \times 10^{-7})} = 8.99 \times 10^6 \text{ N/m}$$

$$k_{q2} = \frac{-1}{2 \cdot 0.040 \cdot (-2.77 \times 10^{-6})} = 4.51 \times 10^6 \text{ N/m}$$

$$k_{q3} = \frac{-1}{2 \cdot 0.027 \cdot (-3.72 \times 10^{-6})} = 4.98 \times 10^6 \text{ N/m}$$

We find the modal masses using Eq. 2.62. We must be sure to pay special attention to units for these calculations; note that we have switched from frequency units of Hz to rad/s by multiplying by 2π and the stiffness values are expressed in N/m.

$$m_{q1} = \frac{8.99 \times 10^6}{(499 \cdot 2\pi)^2} = 0.914 \text{ kg} \quad m_{q2} = \frac{4.51 \times 10^6}{(761 \cdot 2\pi)^2} = 0.197 \text{ kg}$$

$$m_{q3} = \frac{4.98 \times 10^6}{(849 \cdot 2\pi)^2} = 0.175 \text{ kg}$$

Finally, the modal damping coefficients are determined using Eq. 2.63. Again, unit compatibility should be ensured. In the following calculations, stiffness and mass values are expressed in N/m and kg, respectively, to obtain damping coefficient units of N s/m.

$$c_{q1} = 2 \cdot 0.073 \sqrt{8.99 \times 10^6 \cdot 0.914} = 419 \text{ Ns/m}$$

$$c_{q2} = 2 \cdot 0.040 \sqrt{4.51 \times 10^6 \cdot 0.197} = 75.4 \text{ Ns/m}$$

$$c_{q3} = 2 \cdot 0.027 \sqrt{4.98 \times 10^6 \cdot 0.175} = 50.4 \text{ Ns/m}$$

The 3×3 modal matrices can now be written as:

$$\begin{aligned} [M_q] &= \begin{bmatrix} 0.914 & 0 & 0 \\ 0 & 0.197 & 0 \\ 0 & 0 & 0.175 \end{bmatrix} \text{ kg,} \\ [C_q] &= \begin{bmatrix} 419 & 0 & 0 \\ 0 & 75.4 & 0 \\ 0 & 0 & 50.4 \end{bmatrix} \text{ N s/m, and} \\ [K_q] &= \begin{bmatrix} 8.99 \times 10^6 & 0 & 0 \\ 0 & 4.51 \times 10^6 & 0 \\ 0 & 0 & 4.98 \times 10^6 \end{bmatrix} \text{ N/m.} \end{aligned}$$

The individual modal contributions may be described using Eq. 2.63:

$$\frac{Q_j}{R_j} = \frac{1}{k_{qj}} \left(\frac{(1 - r_j^2) - i(2\zeta_{qj}r_j)}{(1 - r_j^2)^2 + (2\zeta_{qj}r_j)^2} \right),$$

where $r_j = \frac{\omega}{\omega_{n,j}}$, $j = 1$ to 3. The individual modes are plotted, together with the original FRF, in Fig. 2.24. As we've discussed, however, the direct FRF in local (physical) coordinates is the sum of the modal contributions, so we may simply add the individual modal responses on a frequency-by-frequency basis to define our final fit. This result is shown in Fig. 2.25.

For this contrived example, the original modal parameters used to construct the “measured” FRF are known. Therefore, we can compare our modal approximation to the true values. These results are provided in Table 2.1. The MATLAB® program used to produce the example figures is provided with the textbook as p_2_5_1.m.

Fig. 2.24 Example tool point and three modal coordinate FRFs determined by peak-picking approach

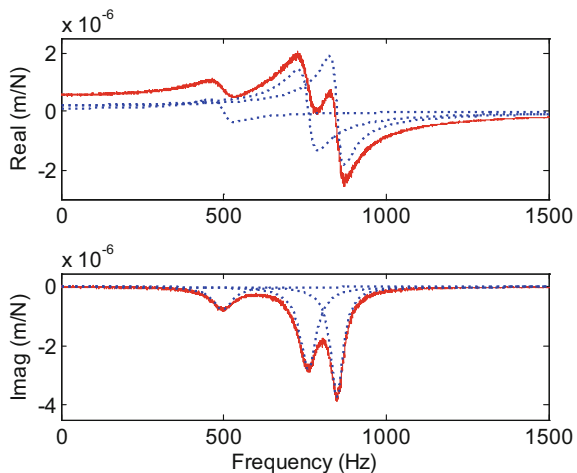


Fig. 2.25 Example tool point FRF with three degree of freedom modal fit obtained by peak picking

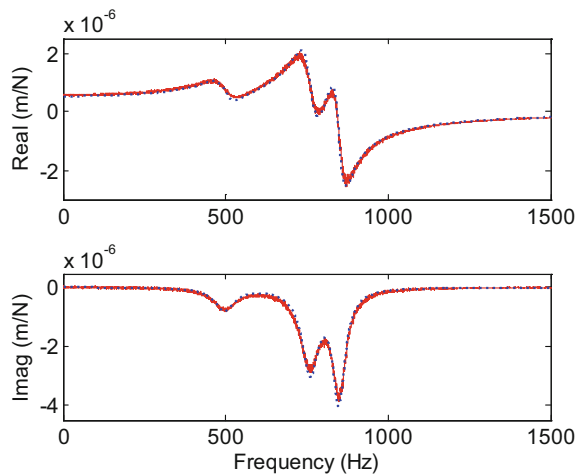


Table 2.1 True modal parameters and values obtained by peak-picking modal fit

	Mode 1		Mode 2		Mode 3	
	True	Fit	True	Fit	True	Fit
f_n (Hz)	500	499	760	761	850	849
ζ_q	0.090	0.073	0.050	0.040	0.030	0.027
k_q (N/m)	8.00×10^6	8.99×10^6	4.00×10^6	4.51×10^6	5.00×10^6	4.98×10^6



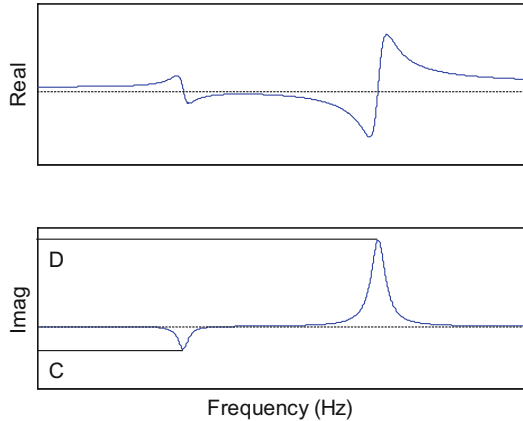
In a Nutshell

The errors between the true and fit parameters arise from limited resolution in the “measurement” and the simplifications used to create the fitting rules.

2.5.2 Model Definition

Once we have determined the modal matrices by peak picking, the next step in defining a model is to use the measured direct and cross FRFs to find the mode shapes and construct the modal matrix. We’ll again assume that the measured direct FRF, shown in Fig. 2.21, can be approximated with a two-mode fit. This means that our model will have two degrees of freedom. As we’ve seen, for a two degree of freedom model, the mode shapes are 2×1 vectors so that the square modal matrix has dimensions of 2×2 . Because the mode shapes have just two entries (one of which is 1), we only require one cross FRF to determine the second entry. As before, we can choose the coordinate to which we normalize our mode shapes for the model shown in Fig. 2.18. Let’s define the coordinate of interest as x_2 so that the form of the modal matrix is $[P] = \begin{bmatrix} p_1 & p_2 \\ 1 & 1 \end{bmatrix}$. We determine p_1 and p_2 using (1) the peak

Fig. 2.26 Two degree of freedom cross FRF with the amplitudes required for model development identified



imaginary part values denoted C , corresponding to the first mode with the natural frequency ω_{n1} , and D , the second mode with the natural frequency ω_{n2} , in the cross FRF² shown in Fig. 2.26, together with (2) the A and B values identified in Fig. 2.21.

$$\frac{C}{A} = \frac{\frac{-p_1}{2k_{q1}\zeta_{q1}}}{\frac{-1}{2k_{q1}\zeta_{q1}}} = p_1 \quad \text{and} \quad \frac{D}{B} = \frac{\frac{-p_2}{2k_{q2}\zeta_{q2}}}{\frac{-1}{2k_{q2}\zeta_{q2}}} = p_2 \quad (2.64)$$

We have used the ratio of the peak of the cross FRF to the direct FRF in each mode to determine the mode shapes because, as we discussed previously, the cross FRF can be expressed as the sum of the modal contributions with each mode scaled by the corresponding system mode shape. See Eq. 2.56. Once we have defined the modal matrix, we can determine the model parameters in local coordinates using the transformations (from modal to local coordinates) in Eqs. 2.65 through 2.67. The forms of $[M]$, $[C]$, and $[K]$ correspond to the preselected two degree of freedom chain-type, lumped parameter model.

$$[P]^{-T} [M_q] [P]^{-1} = [M] = \begin{bmatrix} m_1 & 0 \\ 0 & m_2 \end{bmatrix} \quad (2.65)$$

$$[P]^{-T} [C_q] [P]^{-1} = [C] = \begin{bmatrix} c_1 + c_2 & -c_2 \\ -c_2 & c_2 \end{bmatrix} \quad (2.66)$$

$$[P]^{-T} [K_q] [P]^{-1} = [K] = \begin{bmatrix} k_1 + k_2 & -k_2 \\ -k_2 & k_2 \end{bmatrix} \quad (2.67)$$

²We observe that the cross FRF in Fig. 2.26 looks very different than the direct FRF in Fig. 2.21; the higher frequency mode is “upside down” in Fig. 2.26. As we saw in Sect. 2.4, this is because the two modes are out of phase for the cross FRF, which results in the sign change.



In a Nutshell

The measured direct and cross frequency response functions provide a way to visualize the mode shape. The relative sizes (and signs) of peaks at the same frequency show the relative motion of the corresponding coordinates at that frequency.

As a final note regarding model definition, it should be emphasized that if the measured direct FRF has three modes that we wish to model, then the square modal matrix will have dimensions of 3×3 . To determine the modal matrix, we must measure, at minimum, two cross FRFs to give the two ratios required for the 3×1 mode shapes. Additional cross FRF measurements may be necessary to find measurement locations with good signal-to-noise ratio (i.e., away from system nodes or locations of zero vibration amplitude regardless of the force input level).

2.5.3 Modal Truncation

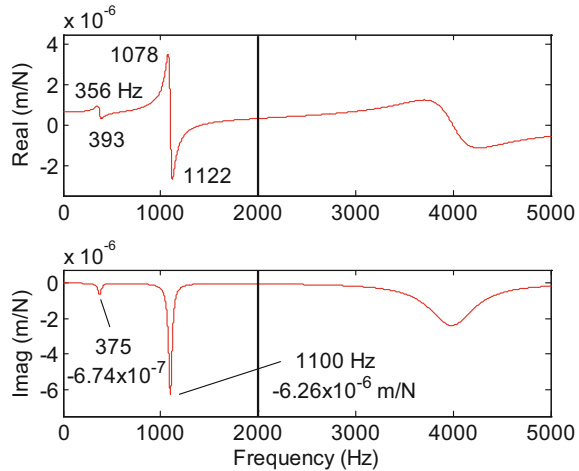
Prior to describing modal testing equipment, there is one remaining issue to highlight regarding modal fitting. Because FRF measurements always have a finite frequency range and elastic bodies possess an infinite number of degrees of freedom, there are necessarily modes that exist outside the measurement range. For tool point tests, we typically measure from zero to a few kHz (perhaps up to 10 kHz for a small mass impact hammer with a steel tip; see Sect. 2.6). For most machining applications, neglecting (or truncating) modes with natural frequencies of, for example, greater than 5 kHz in our modal fit is reasonable because they are not likely to be excited by the cutting force in any case. However, omitting these higher frequency modes during peak picking does affect the accuracy of the modal fit, particularly the real part of the FRF. Eqs. 2.36 and 2.37, which describe the real and imaginary parts of a single degree of freedom FRF, are reproduced here to demonstrate the effect.

$$\text{Re}\left(\frac{X}{F}\right) = \frac{1}{k} \left(\frac{1 - r^2}{(1 - r^2)^2 + (2\zeta r)^2} \right) \quad (2.68)$$

$$\text{Im}\left(\frac{X}{F}\right) = \frac{1}{k} \left(\frac{-2\zeta r}{(1 - r^2)^2 + (2\zeta r)^2} \right) \quad (2.69)$$

It is seen that when the frequency ratio $r = \frac{\omega}{\omega_n}$ is large, or the driving frequency ω is very high and outside the measurement range, the denominator within the right parenthetical terms in these two equations becomes very large, and the response approaches zero. This is seen at the right-hand side of Fig. 2.12, for example. However, as r approaches zero, the parenthetical term in the real part approaches one, and the parenthetical term in the imaginary part approaches zero. Therefore, the

Fig. 2.27 “Measured” direct FRF for Example 2.6. The peak-picking values are listed within the 2 kHz measurement bandwidth. A 5 kHz frequency range is provided to show the truncated 4000 Hz mode.



value of the real part approaches $\frac{1}{k}$ as r approaches zero.³ If there are modes beyond the measurement bandwidth, neglecting these terms and the associated $\frac{1}{k}$ contributions leads to errors in the vertical location of the modal fit’s real part. This is demonstrated in Example 2.6.

Example 2.6 High-Frequency Mode Truncation During Modal Fitting A “measured” FRF is provided in Fig. 2.27. We will presume that the measurement bandwidth was 2 kHz, although a 5 kHz frequency range is shown for demonstration purposes. Within the 2 kHz range, two modes are visible, and peak picking can be applied to determine the associated modal parameters. Using the values from the figure, the modal stiffness, mass, and damping matrix terms may be determined as shown in Example 2.5.

$$\zeta_{q1} = \frac{393 - 356}{2 \cdot 375} = 0.049 \quad \zeta_{q2} = \frac{1122 - 1078}{2 \cdot 1100} = 0.020$$

$$k_{q1} = \frac{-1}{2 \cdot 0.049 \cdot (-6.74 \times 10^{-7})} = 1.50 \times 10^7 \text{ N/m}$$

$$k_{q2} = \frac{-1}{2 \cdot 0.020 \cdot (-6.26 \times 10^{-6})} = 3.99 \times 10^6 \text{ N/m}$$

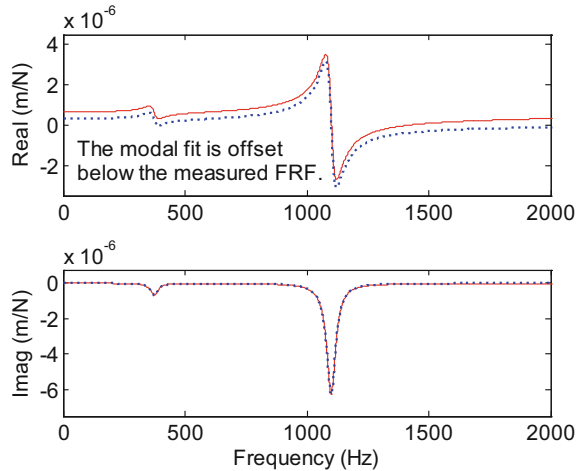
$$m_{q1} = \frac{1.50 \times 10^7}{(375 \cdot 2\pi)^2} = 2.70 \text{ kg} \quad m_{q2} = \frac{3.99 \times 10^6}{(1100 \cdot 2\pi)^2} = 0.084 \text{ kg}$$

$$c_{q1} = 2 \cdot 0.049 \sqrt{1.50 \times 10^7 \cdot 2.70} = 624 \text{ Ns/m}$$

$$c_{q2} = 2 \cdot 0.020 \sqrt{3.99 \times 10^6 \cdot 0.084} = 23.2 \text{ Ns/m}$$

³This $\frac{1}{k}$ term can be referred to as the DC compliance.

Fig. 2.28 Result of modal fitting. An offset in the real part of the fit (dotted line) is observed because the DC compliance of the 4000 Hz mode is not included



The fit to the measured direct FRF is determined by summing the two contributions in modal coordinates according to:

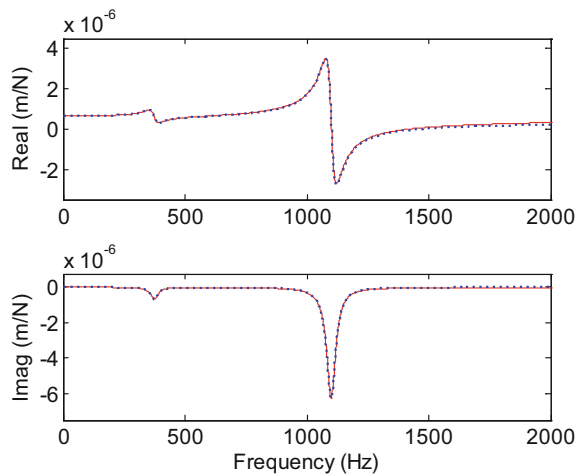
$$\frac{X}{F} = \frac{Q_1}{R_1} + \frac{Q_2}{R_2} = \frac{1}{k_{q1}} \left(\frac{(1 - r_1^2) - i(2\zeta_{q1}r_1)}{(1 - r_1^2)^2 + (2\zeta_{q1}r_1)^2} \right) + \frac{1}{k_{q2}} \left(\frac{(1 - r_2^2) - i(2\zeta_{q2}r_2)}{(1 - r_2^2)^2 + (2\zeta_{q2}r_2)^2} \right),$$

where $r_1 = \frac{f}{375}$ and $r_2 = \frac{f}{1100}$ and f is given in Hz. It is seen in Fig. 2.28 that, although the shape of the two modes within the 2 kHz bandwidth are correctly identified, there is a noticeable offset in the real part of the fit. It appears too stiff (i.e., it is located below the measured FRF) because the DC compliance due to the 4000 Hz mode has not been considered. Because this mode is outside the measurement frequency range, it is not possible to fit the mode and determine the appropriate modal parameters. However, given the visible offset in Fig. 2.28, the combined contributions of truncated modes can be included by adding an effective DC compliance term to the fit. Specifically, for this example, the fit could be rewritten as:

$$\frac{X}{F} = \frac{1}{k} + \frac{Q_1}{R_1} + \frac{Q_2}{R_2},$$

where the $\frac{Q_j}{R_j}$ terms ($j = 1, 2$) are obtained through peak picking as described previously and the $\frac{1}{k}$ value is selected to move the fit to a vertical overlap with the measured FRF. If a value of $k = 3 \times 10^6$ N/m is applied here, the fit is improved, and the result shown in Fig. 2.29 is obtained. Note that this stiffness value is equal to the modal stiffness of the 4000 Hz mode shown in Fig. 2.27 (for completeness, the modal damping ratio for this mode is 0.07). The MATLAB® program used to produce the Example 2.6 figures is provided with the textbook as p_2_6_1.m.

Fig. 2.29 Result of modal fitting with the addition of a DC compliance to correct for the truncated mode



In a Nutshell

A measured frequency response function includes the effect of all modes. Some of the modes contributing to the measured FRF may be outside the range of frequencies measured. Nevertheless, they still influence the data in the measured frequency range.

2.6 Modal Testing Equipment

The basic hardware required to measure FRFs is:

- A mechanism for known force input across the desired frequency range.
- A transducer for vibration measurement, again with the required bandwidth.
- A dynamic signal analyzer to record the time domain force and vibration inputs and convert these into the desired FRF.

The dynamic signal analyzer includes input channels for the time domain force and vibration signals and computes the Fourier transform of these signals to convert them to the frequency domain. It then calculates the ratio of the frequency domain vibration signal to the frequency domain force signal; this ratio is the FRF. The form of the FRF depends on the vibration transducer type and can be expressed as:

- Receptance/compliance—the ratio of displacement to force (considered in the previous sections).
- Mobility—the ratio of velocity to force.
- Inertance/accelerance—the ratio of acceleration to force.

2.6.1 Force Input

Common types of force excitation include:

- Fixed frequency sine wave—The complex response is determined one frequency at a time with averaging occurring at each frequency over a short time interval. This is referred to as a sine-sweep test.
- Random signal—The frequency content of the random signal may be broadband (white noise) or truncated to a desired range (pink noise). Averaging over a fixed period of time is again applied.
- Impulse—A short duration impact is used to excite the structure. This approach enables a broad range of frequencies to be excited in a single, short test. Multiple tests are typically averaged in the frequency domain to improve coherence or the correlation between the force and vibration signals.



In a Nutshell

Hitting the structure with a hammer excites many frequencies at almost the same level at the same time. (Really!)

Common force input hardware includes:

- Shaker (similar to a speaker)—These systems include a harmonically driven armature and a base. The armature may be actuated along its axis by a magnetic coil or hydraulic force. The magnetic coil, or electrodynamic, configurations can provide excitation frequencies of tens of kHz with force levels from tens to thousands of N (increased force typically means a lower frequency range). Hydraulic shakers offer high force with the potential for a static preload but relatively lower-frequency ranges. In either case, the force is often applied to the structure of interest through a “stinger,” or a slender rod that supports axial tension and compression, but not bending or shear. A load cell is often incorporated in the setup to measure the input force. One consideration is that this load cell adds mass to the system under test, which can alter the FRF for low mass structures. Finally, the shaker must be isolated from the structure to prevent reaction forces due to the shaker motion from being transmitted through the shaker base to the structure.
- Impact hammer—An impact hammer incorporates a force transducer in a metal, plastic, or rubber tip to measure the force input during a hammer strike. Because the setup and measurement time is short, it is a popular choice for tool-holder testing (referred to as impact testing). Naturally, the energy input to the structure is a function of the hammer mass; therefore, many sizes are available. Also, the bandwidth of the force input depends on the mass and tip stiffness. Stiffer tips tend to excite a wider frequency range but also spread the input energy over this wider range. Softer tips concentrate the energy over a lower frequency range. Hard, plastic tips are a common choice for tool testing because they do not damage the cutting edge and generally provide sufficient excitation bandwidth.

2.6.2 Vibration Measurement

Vibration transducers are available in both noncontact and contact types. While noncontact transducers, such as capacitance probes and laser vibrometers, are preferred because they do not influence the system dynamics, contacting types, such as accelerometers, are more convenient to implement. As a compromise, low-mass accelerometers are often used for tool point FRF testing. For most tools, the addition of a few grams or less of accelerometer mass does not appreciably alter the response, and the accelerometer can be attached using wax and then removed without damaging the cutting tool. Because accelerometers produce a signal which is proportional to acceleration, the inertance FRF is obtained. However, to convert from inertance, or $\frac{A}{F}$, to receptance, $\frac{X}{F}$, we can use the relationship:

$$\frac{X}{F} = -\frac{1}{\omega^2} \cdot \frac{A}{F}, \quad (2.70)$$

which follows from the harmonic solution, $x = Xe^{i\omega t}$, and its second time derivative $\ddot{x} = -\omega^2 Xe^{i\omega t} = -\omega^2 x$. Equation 2.70 describes double numerical integration in the frequency domain.

As noted, in impact testing, an impulsive force is applied to a structure, and a linear transducer is used to measure the response. The transducer employs amplifying electronics to convert the change in displacement/velocity/acceleration to a proportional voltage which may then be sampled by a data acquisition (DAQ) system. Depending on its design, the amplifier can induce a time delay in the measurement signal, i.e., there is a small time delay between the input displacement/velocity/acceleration of the target and the output voltage from the amplifier. For example, analog low-pass filters used to attenuate high frequency noise are often incorporated in the amplifying electronics. These filters can introduce a time delay. These time delays lead to frequency dependent phase errors in the FRF. Furthermore, the digital DAQ system may introduce synchronization errors between the force and response signals, which again result in a phase error. In [10], a frequency domain approach is detailed to correct the FRF for the phase errors. We'll summarize it here.

Figure 2.30 depicts the effect of a time delay on the measurement signal. For a constant time delay, this yields a phase error that increases linearly with frequency. Figure 2.31 displays the actual, x_a , and measured, x_m , signals for a 50 ms time delay at three different oscillating frequencies, f , of {1, 2, and 3} Hz. The corresponding phase errors are {-18, -36, and -54} deg. The frequency dependent phase error is calculated using Eq. 2.71.

$$\Delta\phi(f) = \cos^{-1}\left(\frac{x_a x_m}{|x_a||x_m|}\right). \quad (2.71)$$

Using Eq. 2.71, the frequency dependent phase error can be calculated for any time delay between x_a and x_m . Figure 2.32 displays the linearly varying phase error

Fig. 2.30 Schematic representation of time delay, Δt , between actual and measured vibration signals

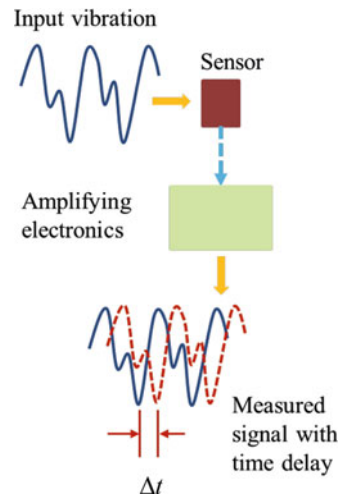
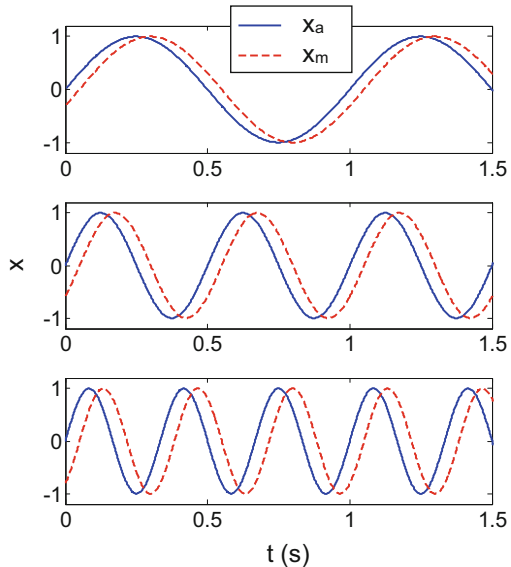


Fig. 2.31 Effect of 50 ms time delay on measured phase (dashed line). (Top) 1 Hz frequency gives a -18° deg phase lag. (Middle) 2 Hz frequency gives a -36° deg phase lag. (Bottom) 3 Hz frequency gives a -54° deg phase lag



for a range of time delays from 10 μ s to 90 μ s. The slope for each linear trend is listed in the legend. It is seen that a 50 μ s delay gives a slope of -18° deg/kHz and, therefore, a -90° deg phase error at 5000 Hz. This phase error distorts the measured FRF; for example, a -90° deg phase error switches the amplitudes of the real and imaginary parts and changes the sign of the imaginary part.

Given the frequency-dependent phase errors, the effect of the time delay can be removed from the measured FRF. The measured phase, ϕ_m , is corrected by subtracting the phase error, $\Delta\phi$, which is determined from the product of the

Fig. 2.32 Phase error for different time delays

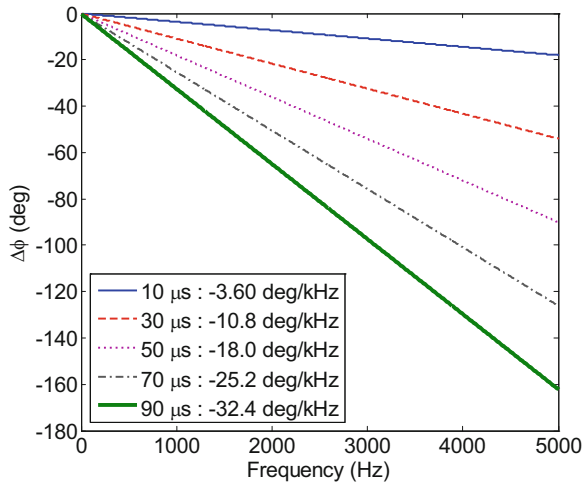
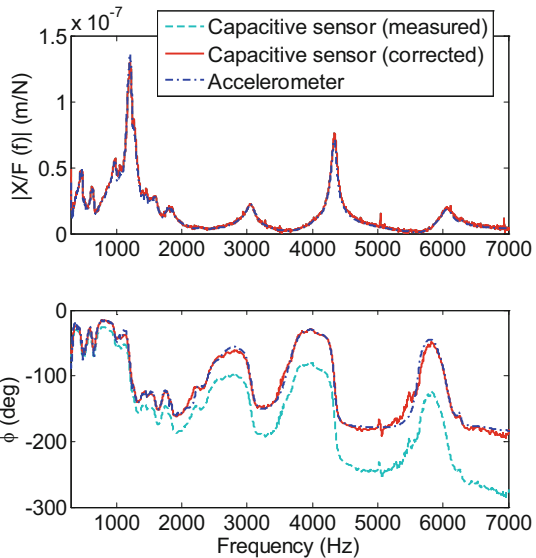


Fig. 2.33 Measured and corrected FRF comparison: magnitude (top) and phase (bottom)



slope, S (deg/Hz), of the linear time delay phase and the frequency, f (Hz). See Eq. 2.72, where $\phi_c(f)$ is the corrected phase.

$$\phi_c(f) = \phi_m - \Delta\phi = \phi_m - S \cdot f. \quad (2.72)$$

In the presence of a time delay induced phase error, the measured FRF is distorted. We see an example in Figs. 2.33 and 2.34. Measurements of the same structure (a tool mounted in the spindle of a computer numerically controlled milling machine) were performed using one impulse hammer and two transducers: a

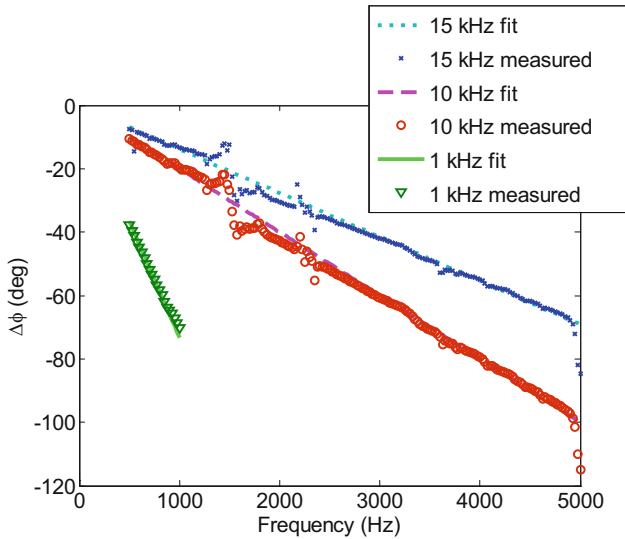
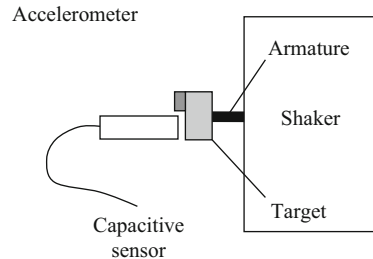


Fig. 2.34 Phase error between accelerometer and capacitive sensor at three low-pass filter settings for the capacitive sensor amplifying electronics

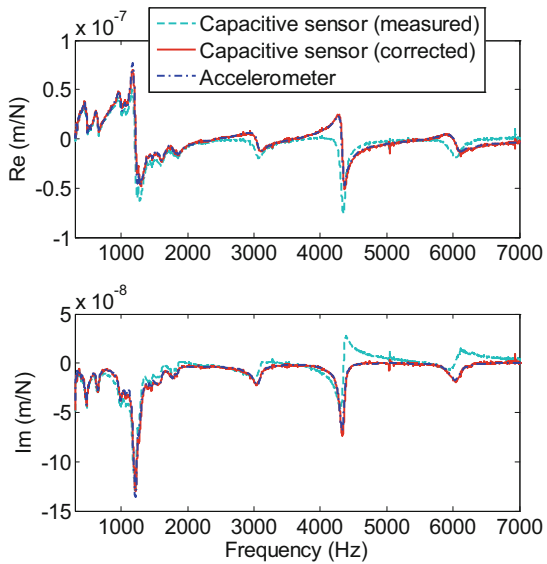
Fig. 2.35 Setup for phase difference measurement between accelerometer and capacitive sensor



piezoelectric accelerometer and a capacitive sensor. The magnitude and phase of the measured FRFs are displayed in Fig. 2.33. We see a linear trend in the capacitive sensor phase that is superimposed on the phase variation due to the structural dynamics. After correcting the phase using Eq. 2.72, where S is the slope of the phase difference between the two transducers (see Fig. 2.34), we observe that the frequency dependent phase between the two sensors agrees. The phase difference can be measured as shown in Fig. 2.35, where a shaker is used to excite the transducers simultaneously and their phase is compared at each selected oscillating frequency.

Given the correct phase, the measured real and imaginary parts must next be modified using Eqs. 2.73 and 2.74. The corrected results are presented in Fig. 2.36. Note the significant distortion in the capacitive sensor FRF for the modes near {3000, 4400, and 6000} Hz prior to correction.

Fig. 2.36 Measured and corrected FRF comparison: real (top) and imaginary (bottom)



$$\text{Re}\left(\frac{X}{F}(f)\right)_c = \left|\frac{X}{F}(f)\right| \cos(\phi_c(f)), \quad (2.73)$$

$$\text{Im}\left(\frac{X}{F}(f)\right)_c = \left|\frac{X}{F}(f)\right| \sin(\phi_c(f)). \quad (2.74)$$

2.7 Measurement Uncertainties

As with any measurement situation, a complete description of the FRF should include both the frequency dependent mean values of the real and imaginary parts, for instance, and the frequency dependent uncertainty in these values. A defensible uncertainty statement for FRF testing results requires a bivariate uncertainty analysis because the FRF is complex valued. In [11], an analysis is provided for tool point impact testing that considers statistical variations, uncertain calibration coefficients that convert the voltage to engineering units for the hammer and vibration transducer, misalignment between the intended and actual force/hammer direction during impact, and mass loading when using an accelerometer. The complex-valued FRF is expressed by its real and imaginary parts, which are potentially correlated, and this correlation is included in the bivariate analysis [12, 13]. An ellipsoid-shaped confidence region (at each frequency) is defined in the complex plane; the size and orientation of this region is determined from the individual input uncertainties. The scalar, total uncertainty is then determined using an eigenanalysis of the FRF covariance matrix [14]. While the full analysis is not reproduced here, we highlight some of its findings.

- For the endmill-holder-spindle assembly that was tested, the calibration coefficient uncertainties (as specified by the manufacturers) comprised >80% of the total uncertainty, which was approximately 2% of the mean tool point direct receptance.
- A small bias is introduced when the hammer force input direction is misaligned with the accelerometer axis. This cosine type bias can be compensated using [15]:

$$\text{FRF}_t = \frac{X}{F_t} = \frac{X}{F_t(1 - \frac{1}{2}u^2(\beta))} = \text{FRF}_m \left(1 - \frac{1}{2}u^2(\beta)\right)^{-1}, \quad (2.75)$$

where the t and m subscripts refer to “true” and “measured,” respectively, and $u(\beta)$ is the uncertainty in the misalignment angle, β . This uncertainty is typically a few degrees.

- Accelerometer mass loading of the measured structure also leads to a measurement bias. This bias can be compensated using [16]:

$$\text{FRF}_t = \frac{X_t}{F} = \frac{\text{FRF}_m}{1 + m_a\omega^2\text{FRF}_m}, \quad (2.76)$$

where m_a is the accelerometer mass, expressed in kg for compatibility with FRF units of m/N and frequency units of rad/s. An alternative compensation approach based on receptance coupling substructure analysis, or RCSA, is presented in Sect. 7.7.

Exercises

1. A harmonic motion has an amplitude of 0.2 cm and a period of 15 s.
 - (a) Determine the maximum velocity (m/s) and maximum acceleration (m/s^2) of the periodic motion.
 - (b) Assume that the motion expresses the free vibration of an undamped single degree of freedom system and that the motion was initiated with an initial displacement and no initial velocity. Express the motion (in units of meters) in each of the following four forms:
 1. $A \cos(\omega_n t + \Phi_c)$.
 2. $A \sin(\omega_n t + \Phi_s)$.
 3. $B \cos(\omega_n t) + C \sin(\omega_n t)$.
 4. $D e^{i(\omega_n t)} + E e^{-i(\omega_n t)}$.
2. A single degree of freedom lumped parameter system under free vibration can be modeled with the following mass, stiffness, and damping values: $m = 1 \text{ kg}$, $k = 4 \times 10^4 \text{ N/m}$, and $c = 10 \text{ N s/m}$.

- (a) Determine the natural frequency, f_n (Hz), and the damping ratio, ζ .
 (b) Given an initial displacement of 5 mm and an initial velocity of 0 mm/s, find an expression for the time response of the damped free vibration, $x(t)$, of the form:

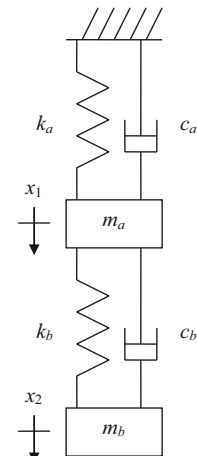
$$x(t) = e^{-\zeta \omega_n t} (A \sin(\omega_d t) + B \cos(\omega_d t)),$$

where $x(t)$ is expressed in meters. Plot the first 25 cycles of motion.

3. A single degree of freedom lumped parameter system has mass, stiffness, and damping values of 1.2 kg, 1×10^7 N/m, and 364.4 N s/m, respectively. Generate the following plots of the frequency response function:
- (a) Magnitude (m/N) versus frequency (Hz) and phase (deg) versus frequency (Hz).
 - (b) Real part (m/N) versus frequency (Hz) and imaginary part (m/N) versus frequency (Hz).
 - (c) Argand diagram, real part (m/N) versus imaginary part (m/N).
4. For the two degree of freedom, damped lumped parameter system shown in Fig. 2.37, complete parts (a) through (f).

$k_a = 2 \times 10^5$ N/m	$k_b = 5.5 \times 10^4$ N/m
$c_a = 60$ N s/m	$c_b = 16.5$ N s/m
$m_a = 2.5$ kg	$m_b = 1.2$ kg
$x_1(0) = 1$ mm	$x_2(0) = 0$ mm
$\dot{x}_1(0) = 0$ mm/s	$\dot{x}_2(0) = 0$ mm/s

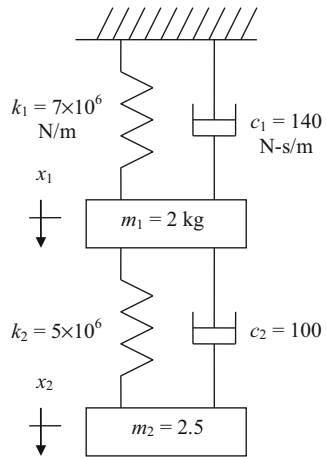
Fig. 2.37 Two degree of freedom, damped lumped parameter system



- (a) Obtain the equations of motion in matrix form and transform them into modal coordinates q_1 and q_2 . Normalize your eigenvectors to coordinate x_2 . Verify that proportional damping exists.
- (b) Determine the time responses $q_1(t)$ and $q_2(t)$ in mm. Express your solutions in the form: $q_{1,2}(t) = e^{-\zeta_{q1,2}\omega_{n1,2}t}(A \cos(\omega_{d1,2}t) + B \sin(\omega_{d1,2}t))$.
- (c) Transform the modal coordinate solutions, $q_1(t)$ and $q_2(t)$, back into local coordinates, $x_1(t)$ and $x_2(t)$.
- (d) Plot $x_1(t)$ and $x_2(t)$ (in mm) versus time (in seconds).
- (e) Determine the time responses $x_1(t)$ and $x_2(t)$ (in mm) if the initial velocities are zero and the initial displacements are $x_1(0) = 0.312$ mm and $x_2(0) = 1$ mm.
5. Assume that a harmonic force, $f_2 = f_0 e^{i\omega t}$, is applied to the lower mass (at coordinate x_2) in Fig. 2.37. Obtain the FRFs $\frac{Q_1}{R_1}$, $\frac{Q_2}{R_2}$, and $\frac{X_2}{F_2}$. Express them in equation form and then plot the real and imaginary parts (in m/N) versus frequency (in Hz).
6. For a single degree of freedom spring-mass-damper system under free vibration, determine the values for the mass, m (kg), viscous damping coefficient, c (N s/m), and spring constant, k (N/m), given the following information:
- The damping ratio is 0.1.
 - The undamped natural frequency is 100 Hz.
 - The initial displacement is 1 mm.
 - The initial velocity is 5 mm/s.
 - If the system was critically damped, the value of the damping coefficient would be 586.1 N s/m.
7. For a single degree of freedom spring-mass-damper system with $m = 2.5$ kg, $k = 6 \times 10^6$ N/m, and $c = 180$ N s/m, complete the following for the case of forced harmonic vibration:
- (a) Calculate the undamped natural frequency (in rad/s) and damping ratio.
 - (b) Sketch the imaginary part of the system FRF versus frequency. Identify the frequency (in Hz) and amplitude (in m/N) of the key features.
 - (c) Determine the value of the imaginary part of the vibration (in mm) for this system at a forcing frequency of 1500 rad/s if the harmonic force magnitude is 250 N.
8. Given the eigenvalues and eigenvectors for the two degree of freedom system shown in Fig. 2.38, determine the modal matrices m_q (kg), c_q (N s/m), and k_q (N/m).

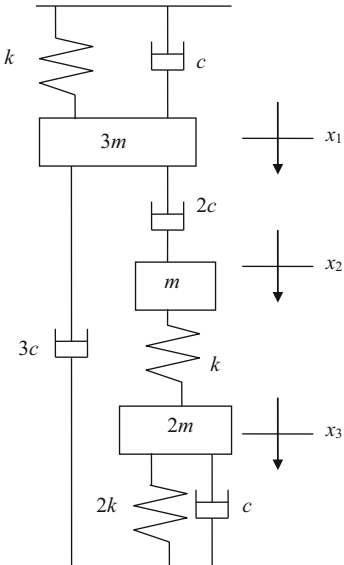
$$\begin{aligned}s_1^2 &= -1 \times 10^6 \text{ rad/s}^2 \\ s_2^2 &= -7 \times 10^6 \text{ rad/s}^2 \\ \psi_1 &= \begin{Bmatrix} 0.5 \\ 1 \end{Bmatrix} \quad \psi_2 = \begin{Bmatrix} -2.5 \\ 1 \end{Bmatrix}\end{aligned}$$

Fig. 2.38 Two degree of freedom spring-mass-damper system

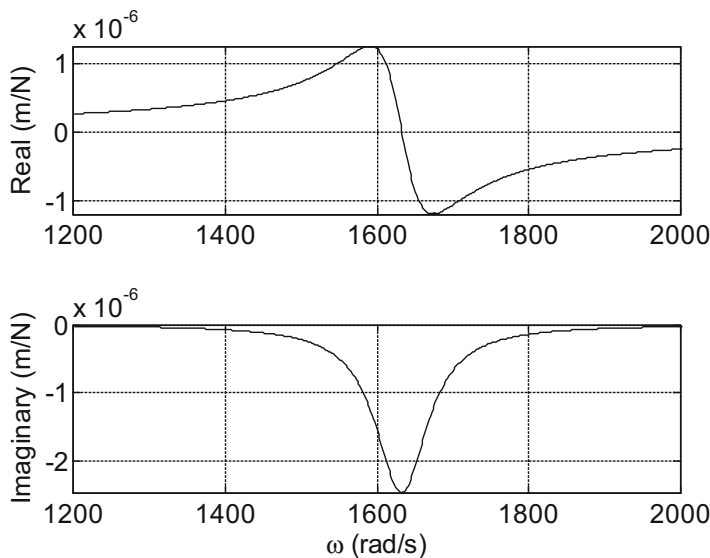
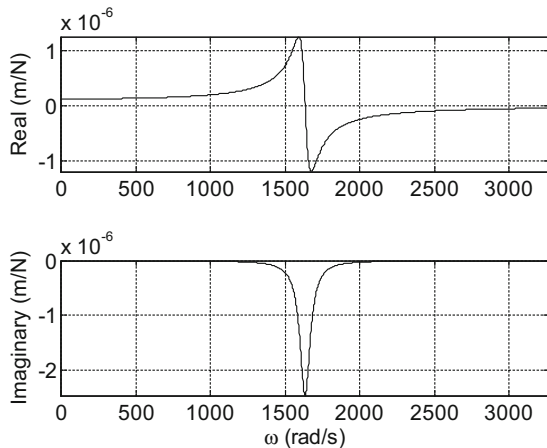


9. Determine the mass, damping, and stiffness matrices in local coordinates for the model shown in Fig. 2.39.

Fig. 2.39 Three degree of freedom spring-mass-damper model



10. For a single degree of freedom spring-mass-damper system subject to forced harmonic vibration, the measured FRF is displayed in Figs. 2.40 and 2.41. Using the peak picking method, determine m (in kg), k (in N/m), and c (in N s/m).

Fig. 2.40 Measured FRF**Fig. 2.41** Measured FRF (smaller frequency scale)

Appendix: Orthogonality of Eigenvectors

As described in Chap. 2, the orthogonality of eigenvectors with respect to the system mass and stiffness matrices is the basis for modal analysis. In general, we can say that two vectors are perpendicular if their scalar, or dot, product is zero. Consider the two vectors:

$$[U] = \begin{Bmatrix} u_{11} \\ u_{21} \end{Bmatrix} \quad \text{and} \quad [V] = \begin{Bmatrix} v_{11} \\ v_{21} \end{Bmatrix}. \quad (2.77)$$

Their dot product is:

$$[U] \cdot [V] = [U]^T [V] = \{u_{11} \ u_{21}\} \begin{Bmatrix} v_{11} \\ v_{21} \end{Bmatrix} = u_{11} \cdot v_{11} + u_{21} \cdot v_{21}. \quad (2.78)$$

This product is zero if the vectors are perpendicular. Orthogonality can be considered a generalization of the concept of perpendicularity.

From Chap. 2, we have seen that we can write the matrix form of the system equations of motion $([M]s^2 + [K])\{X\}e^{st} = \{0\}$ if we assume harmonic vibration. We used the characteristic equation, $|[M]s^2 + [K]| = 0$, to find the eigenvalues, s_1^2 and s_2^2 . We then substituted the eigenvalues into either of the linearly dependent equations of motion to find the eigenvectors, or mode shapes. Using $s_1^2 = -\omega_{n1}^2$, we can write:

$$(-[M]\omega_{n1}^2 + [K])\{\psi_1\} = \{0\}, \quad (2.79)$$

where ψ_1 is the corresponding mode shape. Equation 2.79 can be expanded to:

$$-\omega_{n1}^2[M]\{\psi_1\} + [K]\{\psi_1\} = \{0\}. \quad (2.80)$$

Premultiplying Eq. 2.80 by the transpose of the second mode shape ψ_2 , which corresponds to vibration at ω_{n2} , yields:

$$-\omega_{n1}^2\{\psi_2\}^T [M]\{\psi_1\} + \{\psi_2\}^T [K]\{\psi_1\} = 0. \quad (2.81)$$

Performing the transpose operation on Eq. 2.81 gives:

$$-\omega_{n1}^2\{\psi_1\}^T [M]\{\psi_2\} + \{\psi_1\}^T [K]\{\psi_2\} = 0, \quad (2.82)$$

where the transpose properties $([A][B])^T = [B]^T[A]^T$ and $([A]^T)^T = [A]$ (using matrices of appropriate dimensions) have been applied.

Completing the same operations using $s_2^2 = -\omega_{n2}^2$ gives:

$$-\omega_{n2}^2\{\psi_1\}^T [M]\{\psi_2\} + \{\psi_1\}^T [K]\{\psi_2\} = 0. \quad (2.83)$$

Taking the difference of Eqs. 2.82 and 2.83 yields:

$$(\omega_{n2}^2 - \omega_{n1}^2)\{\psi_1\}^T [M]\{\psi_2\} = 0. \quad (2.84)$$

Provided $\omega_{n2}^2 \neq \omega_{n1}^2$, then $\{\psi_1\}^T [M]\{\psi_2\} = 0$. Substituting this result into either Eq. 2.82 or Eq. 2.83 gives $\{\psi_1\}^T [K]\{\psi_2\} = 0$. Collecting these results, we obtain the orthogonality conditions shown in Eqs. 2.85 through 2.88.

$$\begin{aligned} \{\psi_1\}^T [M]\{\psi_2\} &= 0 \\ \{\psi_2\}^T [M]\{\psi_1\} &= 0 \end{aligned} \quad (2.85)$$

$$\begin{aligned}\{\psi_1\}^T[M]\{\psi_1\} &= m_{q1} & \text{(These products are not necessarily zero.)} \\ \{\psi_2\}^T[M]\{\psi_2\} &= m_{q2}\end{aligned}\quad (2.86)$$

$$\begin{aligned}\{\psi_1\}^T[K]\{\psi_2\} &= 0 \\ \{\psi_2\}^T[K]\{\psi_1\} &= 0\end{aligned}\quad (2.87)$$

$$\begin{aligned}\{\psi_1\}^T[K]\{\psi_1\} &= k_{q1} & \text{(These products are not necessarily zero.)} \\ \{\psi_2\}^T[K]\{\psi_2\} &= k_{q2}\end{aligned}\quad (2.88)$$

Using the modal matrix, $[P] = [\psi_1 \ \psi_2]$, and the orthogonality conditions we obtain the diagonalized modal mass and stiffness matrices:

$$[P]^T[M][P] = \begin{bmatrix} \{\psi_1\}^T[M]\{\psi_1\} & \{\psi_1\}^T[M]\{\psi_2\} \\ \{\psi_2\}^T[M]\{\psi_1\} & \{\psi_2\}^T[M]\{\psi_2\} \end{bmatrix} = \begin{bmatrix} m_{q1} & 0 \\ 0 & m_{q2} \end{bmatrix} = [M_q] \quad \text{and}$$

$$(2.89)$$

$$[P]^T[K][P] = \begin{bmatrix} \{\psi_1\}^T[K]\{\psi_1\} & \{\psi_1\}^T[K]\{\psi_2\} \\ \{\psi_2\}^T[K]\{\psi_1\} & \{\psi_2\}^T[K]\{\psi_2\} \end{bmatrix} = \begin{bmatrix} k_{q1} & 0 \\ 0 & k_{q2} \end{bmatrix} = [K_q]. \quad (2.90)$$

These diagonal modal mass and stiffness matrices uncouple the equations of motion and enable the solution of independent single degree of freedom systems in modal coordinates. The individual modal contributions can then be transformed back into local (physical) coordinates as discussed in Chap. 2.

References

1. Schmitz, T., & Smith, K. S. (2012). *Mechanical vibrations: Modeling and measurement*. New York, NY: Springer.
2. Thomson, W., & Dahleh, M. (1998). *Theory of vibration with application* (5th ed.). Upper Saddle River, NJ: Prentice Hall.
3. Weaver Jr., W., Timoshenko, S., & Young, D. (1990). *Vibration problems in engineering* (5th ed.). New York, NY: John Wiley and Sons.
4. Bae, J. S., Moon, K. K., & Inman, D. (2005). Vibration suppression of a cantilever beam using eddy current damper. *Journal of Sound and Vibration*, 284, 805–824.
5. Ransom, T., Honeycutt, A., & Schmitz, T. (2016). A new tunable dynamics platform for milling experiments. *Precision Engineering*, 44, 252–256.
6. Inman, D. (2001). *Engineering vibration* (2nd ed.). Upper Saddle River, NJ: Prentice Hall, Section 1.10.
7. Thomson, W., & Dahleh, M. (1998). *Theory of vibration with application* (5th ed.). Upper Saddle River, NJ: Prentice Hall, Section 3.9.
8. Leon, J. (1994). *Linear algebra with applications* (4th ed.). Englewood Cliffs, NJ: Prentice Hall, Section 5.6.

9. Ewins, D. (2000). *Modal testing: theory, practice, and application* (2nd ed.). London: Taylor & Francis.
10. Ganguly, V., & Schmitz, T. (2014). Phase correction for frequency response function measurements. *Precision Engineering*, 38, 409–413.
11. Kim, H., & Schmitz, T. (2007). Bivariate uncertainty analysis for impact testing. *Measurement Science and Technology*, 18, 3565–3571.
12. Jobson, J. (1992). *Applied multivariate data analysis*. New York, NY: Springer.
13. Ridler, N., & Salter, M. (2002). An approach to the treatment of uncertainty in complex S-parameter measurements. *Metrologia*, 39, 295–302.
14. Hall, B. (2004). On the propagation of uncertainty in complex-valued quantities. *Metrologia*, 41, 173–177.
15. International Standards Organization (ISO). (1993). *Guide to the expression of uncertainty in measurement* (Corrected and Reprinted 1995).
16. Ashory, M. (1999). *High quality modal testing methods*. Ph.D. Dissertation, Imperial College of Science, Technology, and Medicine, London.

Chapter 3

Turning Dynamics



Make everything as simple as possible, but not simpler.

—Albert Einstein

In Chap. 2, we discussed how to use modal analysis to describe the tool point dynamics for tool–holder combinations. In this chapter, we'll discuss regenerative chatter in turning and see how we can apply this understanding to develop analytical, frequency domain stability lobe diagrams that describe the limiting chip width (to avoid chatter) as a function of spindle speed. To complement this approximate analytical solution, we'll detail a time domain simulation for predicting cutting force and tool displacement during turning which will also enable us to determine stable and unstable cutting conditions. Finally, we'll explore modulated tool path turning, a method used to intentionally segment the long chips that are often encountered in continuous cutting operations such as turning, and process damping, which tends to increase turning stability at low cutting speeds.

3.1 Turning Description

Turning operations are generally carried out on a lathe where a workpiece is rotated in a spindle past a tool mounted on a two axis slide in order to give the desired shape to the axisymmetric part; see Fig. 3.1. The final shape can include both internal and external features. The lathe may be manual, where a machinist controls the slide positions during material removal, or computer numerically controlled (CNC). In this case, automatic control is used to command the slide positions to follow the path described by the part program. The part program is based on the desired workpiece dimensions and is typically developed using computer-aided design/computer-aided manufacturing (CAD/CAM) software.

During turning, a sharp cutting edge is used to remove material in the form of a chip. Many studies have been performed to better understand chip formation and the associated mechanics, but our focus is a broader view of the resulting cutting force and corresponding vibrations of the tool. Therefore, we will not focus so much on

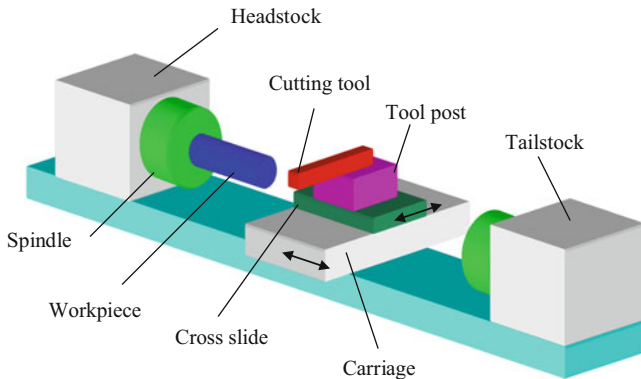


Fig. 3.1 Schematic of manual lathe. The workpiece is clamped in the rotating spindle but may also be supported at its free end using the tailstock. The cutting tool, which is clamped to the tool post, is moved relative to the workpiece by adjusting the positions of the carriage (axial direction) and cross slide (radial direction)

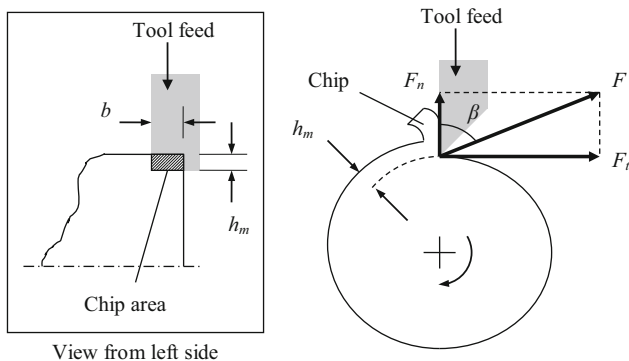


Fig. 3.2 Orthogonal cutting operation showing the cutting force with its normal and tangential components

the chip itself as on the corresponding system behavior. Texts that provide more information regarding metal cutting fundamentals, heat generation and heat transfer during cutting, and related technology include, for example, [1–4]. See also Chap. 8.

To begin, let's consider the tool and workpiece to be rigid and develop expressions for the cutting force, F . Figure 3.2 shows an “orthogonal cutting” operation, where only the normal, F_n , and tangential, F_t , components of the force are considered.



In a Nutshell

“Orthogonal cutting” means that in Fig. 3.2, the cutting edge is perpendicular to the flat end of the round workpiece. In the left of Fig. 3.2, the cutting edge appears as a straight line. On the right of Fig. 3.2, the cutting edge appears as a point (perpendicular to the plane of the page). On the right side of Fig. 3.2, all of the forces are in the plane of the page.

In general, the cutting force vector includes the third component along the workpiece rotation axis, but the orthogonal (planar) treatment is sufficient for us to describe the process dynamics. The figure also identifies (1) the mean chip thickness, h_m , or commanded feed per revolution for the facing operation pictured; and (2) the force angle, β , between F and F_n . The side view of this operation (inset in Fig. 3.2) shows the chip width, b . Together, the chip thickness and chip width define the area of material to be removed, $A = bh_m$. We approximate the cutting force as the product of this chip area and an empirical coefficient. This process-dependent coefficient is referred to as the specific (or per unit chip area) force, K_s , in [2] and depends on the workpiece material, tool geometry, and, to a lesser extent, the cutting speed (peripheral velocity of the rotating workpiece) and chip thickness.

$$F = K_s A = K_s b h_m. \quad (3.1)$$

The normal and tangential components, F_n and F_t , can be expressed using F and the force angle:

$$F_n = \cos(\beta)F = \cos(\beta)K_s b h_m = k_n b h_m \text{ and} \quad (3.2)$$

$$F_t = \sin(\beta)F = \sin(\beta)K_s b h_m = k_t b h_m, \quad (3.3)$$

where we've defined the cutting force coefficients, k_n and k_t , which incorporate both K_s and β . Although efforts continue to calculate these coefficients based on elastic and plastic material properties, a common approach used to characterize these process-dependent values is to prescribe known cutting conditions and measure the force components directly. If the tool is mounted on a cutting force dynamometer as shown in Fig. 3.3 and the b and h_m values are known, then the measured force component values can be used to determine the coefficients by rewriting Eqs. 3.2 and 3.3, $k_n = \frac{F_n}{b h_m}$ and $k_t = \frac{F_t}{b h_m}$. Typical units for k_n , k_t , and K_s are N/mm².

Selected K_s values are provided in [2, Tables 7.1 and 8.1]. These have been reproduced in Table 3.1, but should be considered to be representative values and not necessarily specific to a particular application.

Fig. 3.3 Force measurement during turning using a cutting force dynamometer. The tangential and normal cutting forces are measured as the x and y dynamometer force components

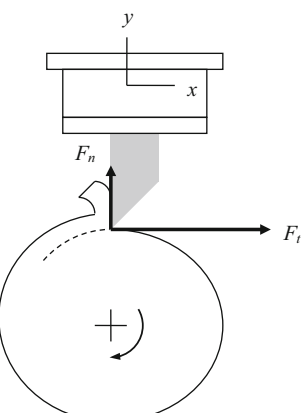
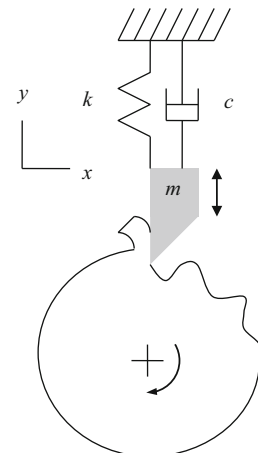


Table 3.1 Representative K_s values for selected workpiece materials [2]

Material	K_s (N/mm ²)	Material	K_s (N/mm ²)
Gray cast iron	1500	Ni-based Inconel X	3400
1020 carbon steel	2100	Ni-based Udimet 500	3500
1035 carbon steel	2300	Co-based L605	3500
1045 carbon steel	2600	Ti (6Al-4V)	2000
302 stainless steel	2700	Al 7075-T6	850
4140/5140 alloy steel	2800	Al 6061-T6	750

Fig. 3.4 Description of regenerative chatter in turning. Initial tool deflections are copied onto the workpiece surface and are encountered in subsequent revolutions. This varies the chip thickness and cutting force which, in turn, affects the resulting tool deflections



In a Nutshell

The force produced by the cutting operation is proportional to the frontal area of the chip through the coefficient K_s . Deriving K_s from first principles is quite difficult, and, in this way, it is similar to the elastic modulus, E . Tabulated values are approximate and often good enough. High-precision applications, on the other hand, may require careful measurement of the cut geometry and resulting forces using the intended tooling and workpiece materials.

3.2 Regenerative Chatter in Turning

If we remove the assumption of a rigid tool, then it is clear that the cutting force will cause deflections of the cutting tool. Because the tool has stiffness and mass, it can vibrate. If the tool is vibrating as it removes material, these vibrations are imprinted on the workpiece surface as a wavy profile. Figure 3.4 shows an exaggerated view, where the initial impact with the workpiece surface causes the tool to begin vibrating and the oscillations in the normal direction to be copied onto the workpiece. When the workpiece begins its second revolution, the vibrating tool encounters the wavy

surface produced during the first revolution. Therefore, the chip thickness at any instant depends both on the tool deflection at that time and the workpiece surface from the previous revolution. Vibration of the tool therefore leads to a variable chip thickness which, according to Eq. 3.1, will give a variable cutting force since the force is proportional to the chip thickness. The cutting force governs the current tool deflection, and, subsequently, the system exhibits feedback. In other words, the current behavior depends on previous behavior—the system has a “memory.”



In a Nutshell

Cutting produces a force that is proportional to the chip thickness and chip width. While the tool is stiff in comparison to objects in our everyday lives, it is not infinitely stiff. For this reason, varying cutting forces (from transients such as the initial contact of the tool with the workpiece) produce vibrations of the tool. The vibrating tool changes the chip thickness and leaves a wavy surface. Variable forces cause vibrations... vibrations cause wavy surfaces... wavy surfaces produce variable forces. The reality is that the cutting operation is only partially governed by the selected geometry. Dynamics, the response of a flexible system to varying forces, plays a strikingly powerful role.

From a modeling standpoint, this “regeneration of waviness” appears as a time delayed term in the chip thickness equation. Figure 3.5 shows an unwrapped view of the turning operation, where the surface on the left was produced in the previous revolution and the surface to the right of the tool (offset by the mean feed per revolution) was just cut away by the oscillating tool. We will consider only vibrations in the normal direction, y (positive direction out of the cut), which has the most direct influence on the chip thickness.

The time dependent, instantaneous chip thickness, $h(t)$, is determined using Eq. 3.4. It is seen that larger positive vibration during the previous revolution, $y(t - \tau)$, where τ is the time for one rotation, gives an increased chip thickness

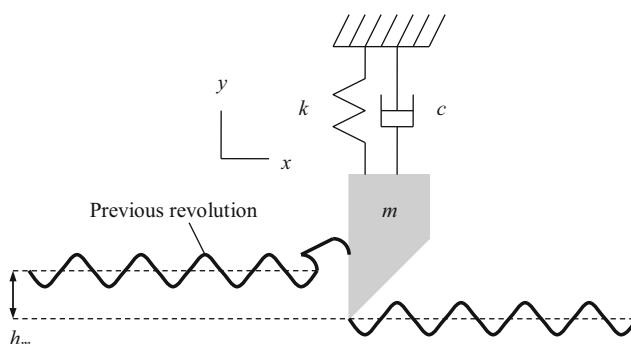


Fig. 3.5 Depiction of turning where the surface from the previous revolution, shown to the left of the tool, is removed by the vibrating cutter to produce a new wavy surface to the right of the tool

Fig. 3.6 The figure demonstrates the instantaneous chip thickness calculation. It depends on the mean feed per revolution, the current deflection, and the vibration during the previous revolution of the workpiece (to the left of the tool)

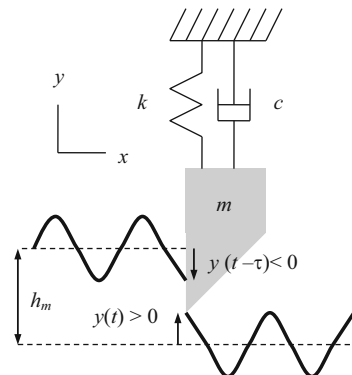
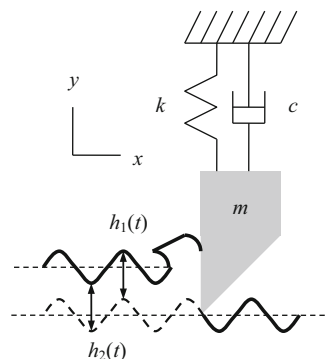


Fig. 3.7 The surface waviness between revolutions is in phase. Negligible chip thickness variation is obtained

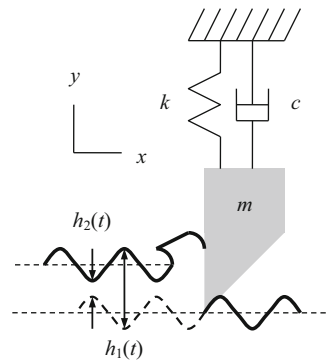


(i.e., less material was removed so the current chip is thicker). Larger positive current vibration, $y(t)$, on the other hand, yields a thinner chip. See Fig. 3.6.

$$h(t) = h_m + y(t - \tau) - y(t) \quad (3.4)$$

The relative phasing between the surface waviness from one pass to the next determines the level of force variation and whether the operation is stable or unstable (chatter occurs). Figures 3.7 and 3.8 show two possibilities. In Fig. 3.7, the wavy surfaces between two revolutions are in phase. Therefore, even though vibration is present during material removal, the chip thickness variation (vertical distance between the two curves) is negligible, and there is no appreciable force variation. This enables stable cutting at larger chip widths. Considering that the tool tends to vibrate at its natural frequency, it is intuitive that matching the workpiece rotating frequency (spindle speed) to the tool's natural frequency will lead to this preferred “in phase” situation. However, this is counterintuitive based on our traditional understanding of resonance where we avoid driving the system at its natural frequency. Figure 3.8 shows a less favorable phase relationship where there is significant variation in the chip thickness. This leads to unstable cutting at smaller chip widths than the previous case due to the force variations and subsequent tool deflections.

Fig. 3.8 Less favorable phase relationship between revolutions yields significant chip thickness variation



In a Nutshell

The cutting force is very sensitive to the revolution-to-revolution alignment of the current tool motion to the previous motion of the tool imprinted on the surface. A “good” alignment (in phase) results in negligible chip thickness variation. A “bad” alignment (180 deg out of phase) produces a strong chip thickness variation. The worst case occurs when significant variation in the chip thickness coincides with a large magnitude in the frequency response function. It turns out that the worst case is about 270 deg out of phase.

3.3 Stability Lobe Diagrams

Depending on the feedback system “gain,” or chip width b , and spindle speed, Ω , the turning operation will either be stable or exhibit chatter (unstable cutting), which causes large vibrations and forces and leads to poor surface finish and, potentially, tool/workpiece damage. In stable machining, the vibrations diminish from revolution to revolution. In unstable machining, the vibrations grow from revolution to revolution until limited in some way. Surprisingly, the vibrations may become large enough that the tool jumps out of the cut, losing contact with the workpiece. The vibrations in unstable cutting may be at least as large as the chip thickness, and it is not surprising that these large vibrations may result in damage to the machine, tool, and workpiece. The governing relationships for this behavior are provided in Eqs. 3.5 through 3.7 [2].

$$b_{\lim} = \frac{-1}{2K_s \cos(\beta) \operatorname{Re}[\text{FRF}]}, \quad (3.5)$$

$$\frac{f_c}{\Omega} = N + \frac{\varepsilon}{2\pi}, \quad (3.6)$$

$$\varepsilon = 2\pi - 2 \tan^{-1} \left(\frac{\operatorname{Re}[\text{FRF}]}{\operatorname{Im}[\text{FRF}]} \right). \quad (3.7)$$



For Instance

Chip width is the gain in turning operations in the same way as volume is the gain in public address (microphone-amplifier-speaker) systems. You may have experienced microphone “squeal” when the microphone was placed near the speaker. In this case, feedback occurs because sound from the speaker enters the microphone with a time delay. When the gain is too high, self-excited vibration occurs as the squeal frequency, which is analogous to the chatter frequency [5].

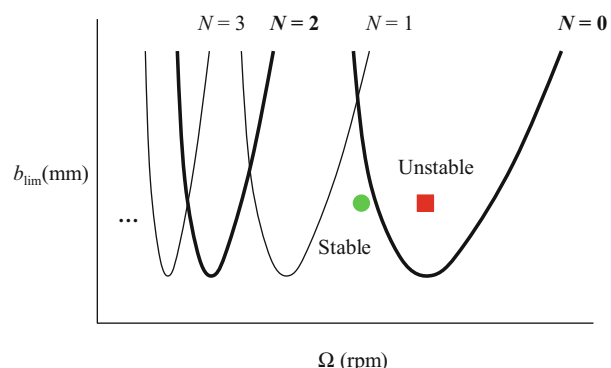
In these equations, b_{\lim} is the limiting chip width to avoid chatter, f_c is the chatter frequency (should it occur), N is the integer number of waves of vibration imprinted on the workpiece surface in one revolution, and $\frac{\epsilon}{2\pi}$ is any additional fraction of a wave, where ϵ is the phase (in rad) between current and previous tool vibrations. Note that for units consistency in Eq. 3.6, if f_c is expressed in Hz, then Ω must be specified in rev/s. Figure 3.9 shows an example stability lobe diagram where the Ω versus b_{\lim} family of curves ($N = 0, 1, 2, \dots$) separate the space into two regions. Any (Ω, b_{\lim}) pair that appears above the collective boundary indicates unstable behavior, while any pair below the boundary is presumed to be stable. We'll next discuss the foundation of the relationships, provided in Eqs. 3.5 through 3.7, that are applied to construct this diagram. We'll base this discussion on the normal force equation and the vector representation of tool deflections in the complex plane.



In a Nutshell

Whether we know it or not, whether we like it or not, every cutting operation has a picture like the one shown in Fig. 3.9. If we choose the cutting conditions at random, or at least without considering the applicable stability lobe diagram, then we sometimes choose stable cutting and sometimes not. Sometimes speeding up helps and other times it makes things worse. It appears to be random, and many machine shops struggle with this issue every day. If we have the diagram and choose the cutting conditions accordingly, then it is possible to avoid the unstable conditions (chatter) and increase productivity.

Fig. 3.9 Example stability lobe diagram. The stability boundary separates stable chip width-spindle speed combinations (below the boundary, marked as a circle) from unstable pairs (above, marked as a square)



Equation 3.4 shows that the instantaneous chip thickness depends on the commanded chip thickness, the normal direction vibration one revolution earlier, and the current vibration in the normal direction. If we substitute this $h(t)$ for h_m in the normal force expression provided in Eq. 3.2, we obtain:

$$F_n = k_n b h(t) = k_n b (h_m + y(t - \tau) - y(t)). \quad (3.8)$$

This force equation has both a constant part, $k_n b h_m$, and a variable part, $k_n b (y(t - \tau) - y(t))$. The constant part does not influence the stability of the linear system. We are therefore interested in the behavior of the variable part. To explore the value of b as a function of k_n and the tool vibrations, let's consider a unit value of the variable force, or $1 = k_n b (y(t - \tau) - y(t))$ from Eq. 3.8. This equation can be solved for b :

$$b = \frac{1}{k_n (y(t - \tau) - y(t))}. \quad (3.9)$$

Regarding the vibration levels from one revolution to the next in Eq. 3.9, we can state the following:

- If $y(t) > y(t - \tau)$, then the vibrations are growing from one revolution to the next and unstable behavior results.
- $y(t) = y(t - \tau)$ indicates the limit of stability—the vibration level is neither increasing or decreasing.
- If $y(t) < y(t - \tau)$, then the vibrations are decaying from one revolution to the next and stable behavior is achieved.

Let's draw the $\vec{y}(t)$ and $\vec{y}(t - \tau)$ vectors in the complex plane for the limiting case that $\vec{y}(t) = \vec{y}(t - \tau)$.¹ We will require that the following vector sum is satisfied:

$$\vec{y} + (\vec{y}(t - \tau) - \vec{y}) = \vec{y}(t - \tau). \quad (3.10)$$

It is also necessary that the difference $\vec{y}(t - \tau) - \vec{y}(t)$, which represents the variable part of the chip thickness, is real valued. In other words, the instantaneous chip thickness is a scalar quantity; it has no imaginary part. In the complex plane it must therefore be horizontal. Figure 3.10 shows the vectors $\vec{y}(t)$ and $\vec{y}(t - \tau)$ as well as the real valued difference $\vec{y}(t - \tau) - \vec{y}(t)$ for a single degree of freedom system. Note the similarity to Fig. 2.14. The real valued unit normal force and the phase between tool vibrations in subsequent revolutions, ϵ , are also shown. The geometry seen in this figure satisfies the following requirements: (1) the magnitude and phase of the tool deflections depend on the forcing frequency (spindle speed) and the tool's direct FRF as measured at the cutting edge; (2) the amplitudes for $\vec{y}(t)$

¹We represent $\vec{y}(t)$ and $\vec{y}(t - \tau)$ as vectors because they have both a magnitude and phase relative to the force, F_n . The force and both displacement vectors are displayed in Fig. 3.10.

Fig. 3.10 Vector representation of unit normal force and tool deflections (current and previous revolutions) for limit of stability

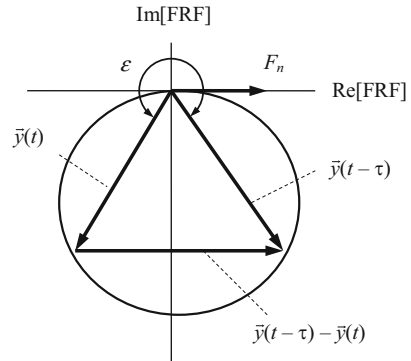
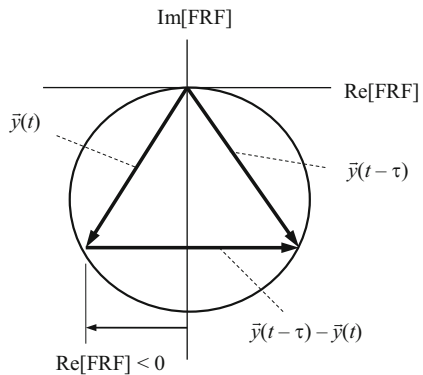


Fig. 3.11 Representing the length of the vector difference using the negative real part of the tool point FRF



and $\vec{y}(t - \tau)$ are equal (limit of stability); and (3) the difference $\vec{y}(t - \tau) - \vec{y}(t)$ is horizontal.

We can now rewrite Eq. 3.9 by substituting for $\vec{y}(t - \tau) - \vec{y}(t)$. Figure 3.11 shows that, due to the approximate symmetry, the length of the vector difference can be written as twice the negative real (Re) part of the tool's direct FRF. Equation 3.11 shows the new relationship, where the negative sign is included in order to obtain positive (limiting) chip width values. This equation matches Eq. 3.5, where k_n is substituted for the product $K_s \cos(\beta)$:

$$b_{\lim} = \frac{-1}{k_n(2\text{Re}[FRF])}. \quad (3.11)$$



In a Nutshell

It is the chip width (and not the chip thickness) that controls whether or not the cutting operation is stable. The real part of the frequency response function defines the limiting chip width. The higher the system's dynamic stiffness (more stiffness and more damping), the larger the chip width that can be obtained without chatter.

Fig. 3.12 Vector representation of $b_{\lim,\text{crit}}$ case ($f_c = f_n(1 + \zeta)$ and $\varepsilon = 270$ deg)

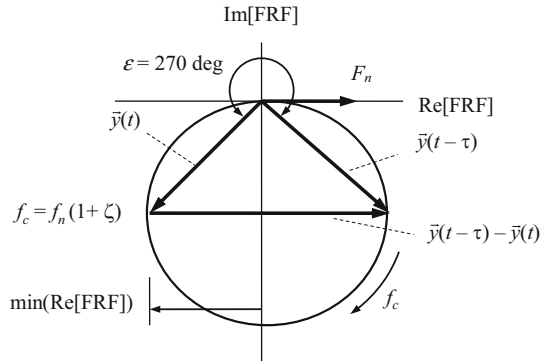
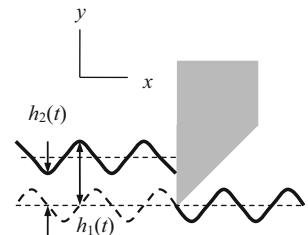


Fig. 3.13 Chip thickness variation for the $b_{\lim,\text{crit}}$ case when $\varepsilon = 270$ deg



Given Eq. 3.11, we can determine the smallest and largest potential values of b_{\lim} based on the range of magnitudes possible for the negative real part of the tool point FRF. The smallest value is obtained for the minimum, or most negative, value of Re [FRF], when the absolute value of the denominator is largest. We will refer to this minimum b_{\lim} value as the critical value, $b_{\lim,\text{crit}}$. See Eq. 3.12. The chatter frequency for this case (i.e., the $\min(\text{Re}[\text{FRF}])$) is $f_c = f_n(1 + \zeta)$ as shown in Fig. 2.13. The situation is pictured in Fig. 3.12. From the figure, we also see that ε is $\frac{3\pi}{2}$ rad or 270 deg. A representation of the time dependent tool deflections with this phase relationship is shown in Fig. 3.13. Again, the chip thickness variation is determined from the vertical distance between the two curves. It is interesting to note that the worst case (smallest chip width) is not obtained when $\varepsilon = 180$ deg or the vibrations from one revolution to the next are exactly out of phase.

$$b_{\lim,\text{crit}} = \frac{-1}{k_n(2 \cdot \min(\text{Re}[\text{FRF}]))} \quad (3.12)$$

The largest b_{\lim} value is obtained when $\varepsilon = 360$ deg. This is the “in phase” situation of negligible chip thickness variation. As seen in the complex plane representation given in Fig. 3.14, the real part of the tool point FRF is zero, and the chatter frequency is f_n . Substitution in Eq. 3.11 would suggest an infinite chip thickness, $b_{\lim} = \frac{-1}{k_n(2 \cdot 0)} = \infty$. However, we obtain finite b_{\lim} values for the left end of the $N = 0$ curve, even at a chatter frequency equal to f_n , because the adjacent stability curve with one more wave per revolution ($N = 1$) intersects the original curve and truncates it. See Fig. 3.15.

Fig. 3.14 Vector representation of largest b_{\lim} case with favorable phase relationship ($\epsilon = 360$ deg) between subsequent workpiece revolutions

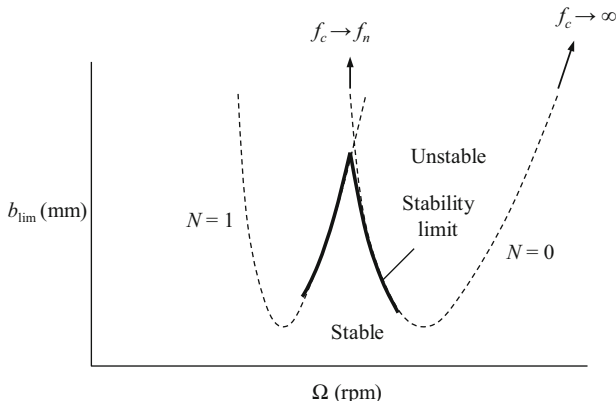
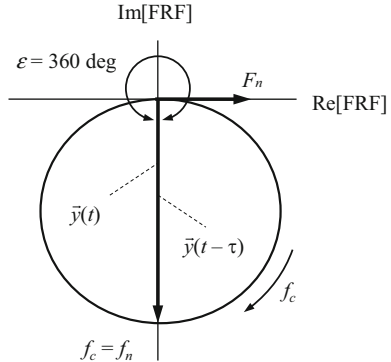


Fig. 3.15 Stability lobe diagram exhibiting truncation of $N = 0$ stability curve by $N = 1$ curve to obtain finite b_{\lim} values

We see a similar situation as the chatter frequency approaches infinity, $f_c \rightarrow \infty$. In this case (Fig. 3.16), even though the revolution to revolution phase relationship is unfavorable ($\epsilon \rightarrow 180$ deg, or exactly out of phase), the response amplitude approaches zero, $\text{Re}(\text{FRF}) \rightarrow 0$. Again, substitution in Eq. 3.11 would suggest an infinite chip thickness, $b_{\lim} = \frac{-1}{k_n(2 \cdot 0)} = \infty$. However, as seen in Fig. 3.15, the left side of the $N = 0$ curve serves to limit the right hand side of the $N = 1$ curve where $f_c \rightarrow \infty$.

We'll now see how each individual stability curve is actually a mapping of $\text{Re}[\text{FRF}]$ onto the (Ω, b_{\lim}) diagram. We'll first consider the $N = 0$ curve, which means that less than one wave is imprinted on the surface per revolution. We've already discussed the b_{\lim} values, so we'll now focus on the spindle speeds for the left end (labeled as 1 in Fig. 3.17), the minimum (2), and the right end (3). As we saw in Fig. 3.14, when the chatter frequency is equal to f_n , the $\epsilon = 360$ deg = 2π rad phase

Fig. 3.16 Vector representation of $\epsilon = 180$ deg phase relationship between subsequent workpiece revolutions ($f_c \rightarrow \infty$)

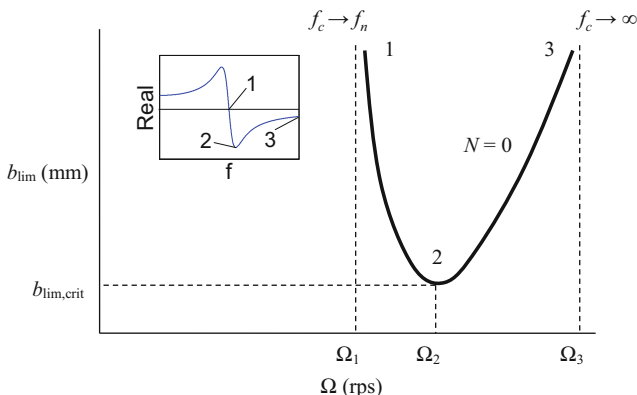
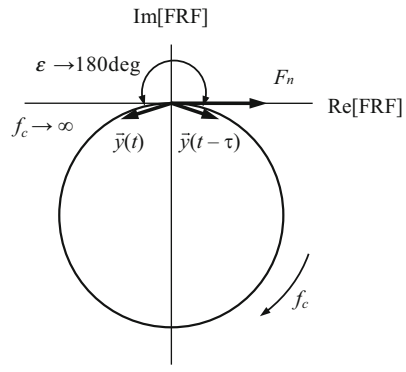


Fig. 3.17 Mapping of the real part of the tool point FRF onto the (Ω, b_{lim}) diagram for the $N = 0$ lobe. Spindle speeds provided in Eqs. 3.13 through 3.15

relationship is obtained, and $b_{\text{lim}} = \infty$ because the real part is zero. Point 1 therefore has a spindle speed of:

$$\Omega_1 = \frac{f_c}{N + \frac{\epsilon}{2\pi}} = \frac{f_n}{0 + \frac{2\pi}{2\pi}} = f_n \quad (3.13)$$

from Eq. 3.6. (Note that units of Hz for f_n gives equivalent units of rev/s, or rps, for spindle speed.) This corresponds to point 1 in the inset showing the real part of the tool point FRF.



In a Nutshell

The chip width can be very large without the occurrence of chatter if the spindle speed is set close to the natural frequency of the most flexible vibration mode. This surprising result comes from favorable alignment of the waviness from one revolution to the next at this speed.

Recall that we are only considering the negative portion of the real part so the applicable frequency range (for this single degree of freedom response) is f_n to ∞ . At point 2, which has the minimum chip width, $b_{\text{lim,crit}}$, we saw in Fig. 3.12 that the chatter frequency is $f_n(1 + \zeta)$ and $\epsilon = 270 \text{ deg} = \frac{3\pi}{2} \text{ rad}$. The corresponding spindle speed is:

$$\Omega_2 = \frac{f_n(1 + \zeta)}{0 + \frac{\frac{3\pi}{2}}{2\pi}} = \frac{4}{3} f_n(1 + \zeta). \quad (3.14)$$

At point 3 the chatter frequency approaches ∞ and ϵ approaches $180 \text{ deg} = \pi \text{ rad}$. The spindle speed is:

$$\Omega_3 = \frac{\infty}{0 + \frac{\pi}{2\pi}} = \infty. \quad (3.15)$$

Let's next consider the $N = 1$ stability curve (or lobe). In this case, there is at least one wave of vibration per revolution. See Fig. 3.18. Although the b_{lim} values are a function of the chatter frequency (via the tool point FRF), they do not depend on the lobe number, N . Therefore, these values do not change relative to the $N = 0$ calculations. Similarly, the ϵ values are independent of the lobe number and do not change. The spindle speed equation (Eq. 3.6), however, is a function of the lobe number. Using the same labeling convention for the left end, minimum, and right end points of Re[FRF], we obtain the three spindle speeds:

$$\Omega_1 = \frac{f_n}{1 + \frac{2\pi}{2\pi}} = \frac{f_n}{2}, \quad (3.16)$$

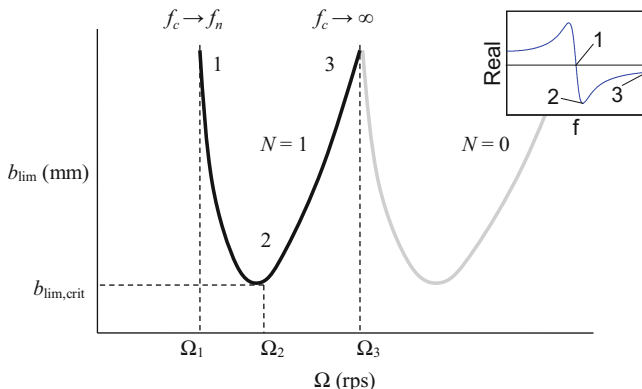


Fig. 3.18 Mapping of the real part of the tool point FRF onto the (Ω, b_{lim}) diagram for the $N = 1$ lobe. Spindle speeds provided in Eqs. 3.16 through 3.18

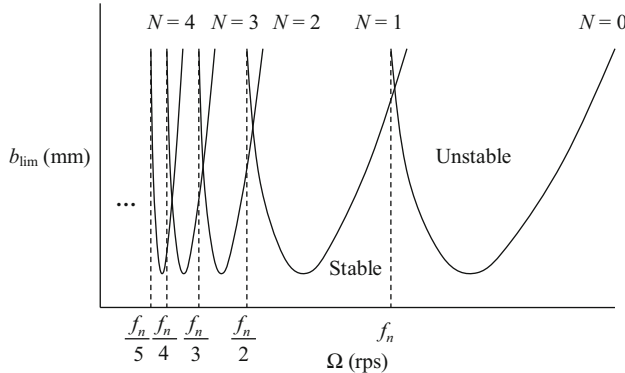


Fig. 3.19 Depiction of multiple stability lobes which, taken together, form the stability limit. It is seen that the peaks of the stable zone become less pronounced as N increases

$$\Omega_2 = \frac{f_n(1 + \zeta)}{1 + \frac{\frac{3\pi}{2}}{2\pi}} = \frac{4}{7}f_n(1 + \zeta), \text{ and} \quad (3.17)$$

$$\Omega_3 = \frac{\infty}{1 + \frac{\pi}{2\pi}} = \infty. \quad (3.18)$$

If we plot multiple lobes ($N = 0, 1, 2, \dots$), we obtain a result similar to Fig. 3.19. We see that all lobes exhibit the same minimum value, $b_{\lim,\text{crit}}$, and the peak values are located approximately at integer fractions of the tool point natural frequency. We can therefore write a “best speeds” equation which identifies these spindle speeds (in rev/min, or rpm). See Eq. 3.19, where f_n is expressed in Hz. As noted, any (Ω, b_{\lim}) pair located below the stability boundary leads to stable operation, while combinations above the boundary result in chatter.

$$\Omega_{\text{best}} = \frac{f_n \cdot 60}{N + 1} \text{ (rpm)} \quad (3.19)$$



In a Nutshell

We get the same favorable alignment of waviness at many different spindle speeds; these multiple speeds correspond to different numbers of integer waves of vibration imprinted on the workpiece surface per revolution. The increase in allowable chip width without chatter gets larger as the spindle speed gets higher (less waves of vibration per revolution). At lower speeds the lobes overlap to such an extent that the limiting chip width approaches a constant value.

Similarly, we can write a “worst speeds” equation that provides the spindle speeds where the $b_{\lim,\text{crit}}$ values are encountered; see Eq. 3.20. Equations 3.19 and

3.20 provide good approximations for dynamic systems that can be modeled as single degree of freedom. Multiple degree of freedom systems, on the other hand, are generally best described using the stability lobe diagram itself.

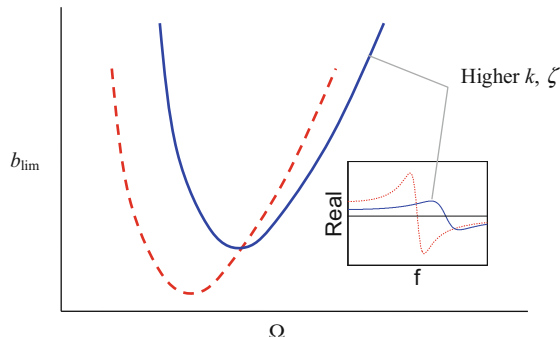
$$\Omega_{\text{worst}} = \frac{f_n(1 + \zeta) \cdot 60}{N + \frac{3}{4}} \text{ (rpm)} \quad (3.20)$$

Before discussing the concept of the “oriented FRF” introduced by Tlusty [2], let’s take a moment to explore which factors affect b_{lim} and the applicability of stability lobe diagrams to typical turning operations. From Eq. 3.5, we see that b_{lim} depends on K_s , β , and the negative real part of the tool point FRF, which we’ll describe using the stiffness, k , and damping ratio, ζ . (Again, we are assuming single degree of freedom dynamics.) As K_s and β decrease ($0 \leq \beta \leq 90$ deg), b_{lim} increases. Considering Table 3.1, we can see that, all other conditions being equal, we would obtain approximately a three times increase in the allowable chip width if we compared an aluminum alloy with a low alloy steel due to the corresponding K_s values. Considering only the Re[FRF], it becomes less negative as k and ζ are increased (Sect. 2.2). See the depiction in Fig. 3.20, where the increase in k yields not only a less negative real part but also an increase in the natural frequency. If the workpiece material/tool geometry is unchanged (so that K_s and β can be considered constant), this Re[FRF] change leads to an increase in b_{lim} , but also a shift in the stability lobes. Naturally this would need to be considered in implementation by a spindle speed adjustment.

Example 3.1 Best Spindle Speeds for a Single Degree of Freedom System Let’s consider a setup where the tool behaves like a single degree of freedom system with $f_n = 700$ Hz and corresponding k and ζ values determined from a curve fit to the direct FRF as measured at the tool point in the y direction. We can apply Eq. 3.19 to determine our “best” spindle speed for an increased limiting chip width. If we let $N = 0$ (this gives the right-most peak in the stability lobe diagram), we obtain:

$$\Omega_{\text{best}} = \frac{700 \cdot 60}{0 + 1} = 42,000 \text{ rpm.}$$

Fig. 3.20 Influence of changes in k and ζ on b_{lim}



The problem is that conventional lathe spindles don't turn this fast. Let's say the top spindle speed for a selected lathe is 3600 rpm. Which peak, and corresponding best spindle speed, must we then pick? We would require that:

$$\Omega_{\text{best}} = \frac{700 \cdot 60}{N + 1} \leq 3600 \text{ rpm.}$$

If we select $N = 11$ (i.e., the 12th peak counting from right to left in the diagram), the best spindle speed would be 3500 rpm and the maximum spindle speed constraint would be satisfied. However, as seen in Fig. 3.19, as N increases the relative improvement in b_{lim} afforded by the stability lobe peaks decreases dramatically. For $N = 11$, the improvement is generally negligible and $b_{\text{lim}} \approx b_{\text{lim,crit}}$. For this reason, stability lobe diagrams are typically more successfully implemented in high-speed milling, as opposed to traditional turning operations. The phenomenon known as process damping can be leveraged at low spindle speeds to increase the allowable chip width above $b_{\text{lim,crit}}$, however; see Sect. 3.7.

3.4 The Oriented FRF

Using the Tlusty model [2], Eq. 3.5 can be rewritten as:

$$b_{\text{lim}} = \frac{-1}{2K_s\mu\text{Re}[\text{FRF}]}, \quad (3.21)$$

where $\mu = \cos(\beta)$ is referred to as the “directional orientation factor” and the product of μ and $\text{Re}[\text{FRF}]$ is the real part of the “oriented FRF.” The concept is to first project the cutting force, F , into the direction of the system dynamics and, second, project this result into the surface normal, y . The projection into the surface normal is necessary because we are only considering the effects of tool vibrations in this sensitive direction. The two projection steps are required because it may be that the system dynamics are not known in the surface normal direction as we have assumed in our previous descriptions.

Consider, for example, an external turning operation where a square tool bar, whose sides are not aligned with x and y , is used to reduce the diameter of a workpiece; see Fig. 3.21. The impact tests described in Sect. 2.6 would naturally be performed along the tool bar faces (directions u_1 and u_2 in the figure), which would not provide FRFs in the y direction. Here μ would account for these misalignments as well as the force angle and, when combined with the measured FRFs, would provide the system dynamic stiffness in the direction of the surface normal. This is the oriented FRF.

Example 3.2 Single and Two Degree of Freedom Oriented FRF Let's consider an example single degree of freedom system where the vibration mode direction is not aligned with the surface normal as shown in Fig. 3.22. In order to calculate the

Fig. 3.21 Oriented FRF description using external turning operation

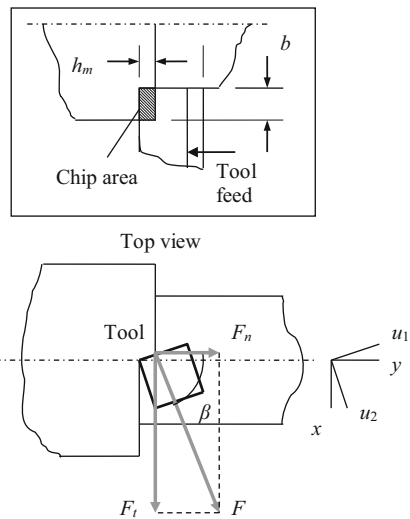
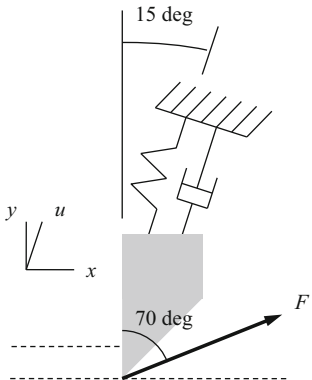


Fig. 3.22 Single degree of freedom system with vibration mode that is not aligned with the surface normal



directional orientation factor, the force projection onto the mode direction u is first determined:

$$F_u = F \cos(70 - 15) = F \cos(55).$$

This result is then projected onto the surface normal (y direction):

$$F_n = F_u \cos(15) = F \cos(55) \cos(15).$$

The directional orientation factor is then $\mu = \cos(55) \cos(15) = 0.55$ and the oriented FRF is the product of μ and the FRF measured in the u direction. Because μ is less than 1, the oriented FRF appears stiffer than the u direction FRF; see Fig. 3.23. Physically, this indicates that only a portion (55%) of the force/flexibility leads to vibration in the sensitive direction.

Fig. 3.23 $\text{Re}[\text{FRF}]$ in u direction compared to real part of oriented FRF

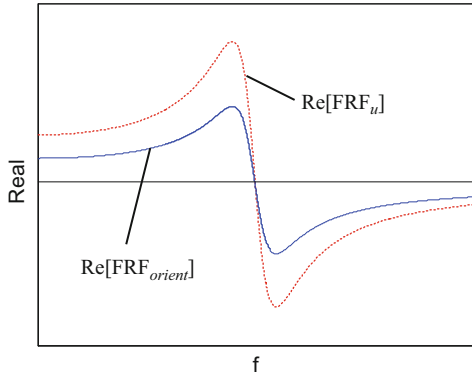
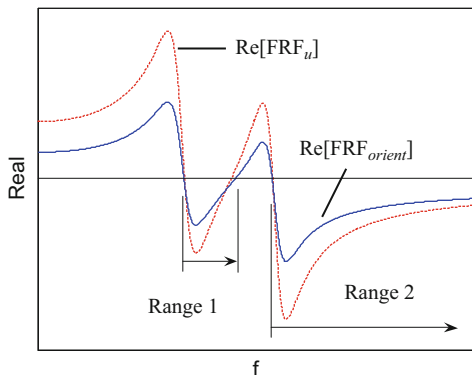


Fig. 3.24 $\text{Re}[\text{FRF}]$ in u direction compared to real part of oriented FRF for two degree of freedom system. Two valid chatter frequency ranges are seen



Next, consider the same u direction as shown in Fig. 3.22, but now with a second degree of freedom in this direction. The real part of an example two degree of freedom direct FRF at the tool point, as well as the oriented FRF real part, is shown in Fig. 3.24. As discussed in Sect. 3.3, the negative real part is used in the b_{\lim} calculation and defines the valid chatter frequency range. Figure 3.24 shows two valid chatter frequency ranges, unlike the previous single degree of freedom examples we've considered. This yields two stability boundary sections for each N value as shown in Example 3.3.

Example 3.3 Competing Lobes for Two Degree of Freedom Oriented FRF Consider the model shown in Fig. 3.25. A two degree of freedom system is aligned with the surface normal and the force angle is 70 deg. The directional orientation factor therefore only requires the projection of the force into the mode direction, $\mu = \cos(70)$. The modal parameters are $f_{n1} = 400$ Hz, $k_{q1} = 2 \times 10^7$ N/m, $\zeta_{q1} = 0.05$, $f_{n2} = 700$ Hz, $k_{q2} = 2.2 \times 10^7$ N/m, and $\zeta_{q2} = 0.05$. We will determine the stability behavior for this turning operation.

Fig. 3.25 Two degree of freedom model for turning stability evaluation

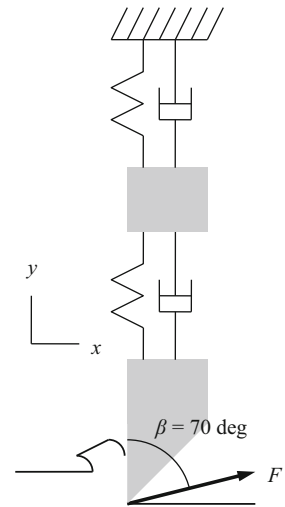
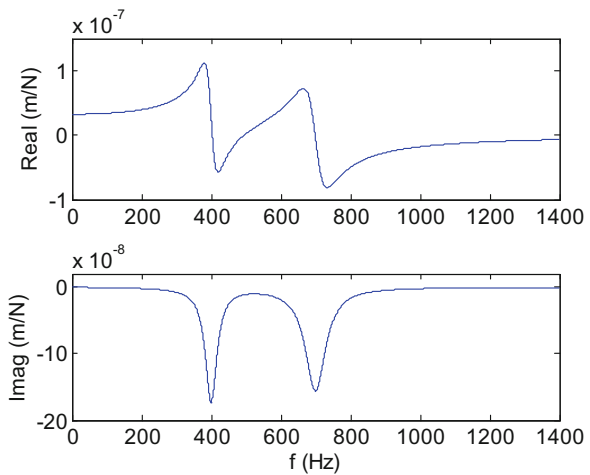


Fig. 3.26 Real and imaginary parts of the oriented FRF for the system in Example 3.3



The real and imaginary parts of the oriented FRF for this system are shown in Fig. 3.26. Two distinct modes with 400 Hz and 700 Hz natural frequencies are observed. As seen previously in Fig. 3.24, there are two valid chatter frequency ranges associated with this two mode system. They occur where the real part is less than zero and are pictured in the top panel of Fig. 3.27. In the bottom panel, the Ω and b_{\lim} values, which are both a function of the FRF and therefore the chatter frequency (as seen in Eqs. 3.1 through 3.3), are plotted against one another to define the stability limit ($K_s = 1500 \text{ N/mm}^2$). It is seen that a distinct lobe section is associated with each of the two chatter frequency ranges. Only the $N = 0$ pair is shown in this figure. However, it is the whole family of curves, $N = 0, 1, 2, \dots$, that defines the overall stability boundary. The $N = 0, 1$, and 2 lobes are shown in Fig. 3.28. Because

Fig. 3.27 (Top panel) Negative real part of oriented FRF. (Bottom panel) Corresponding $N = 0$ stability limit. The two lobe sections are present due to the two portions of the negative real part in the top panel

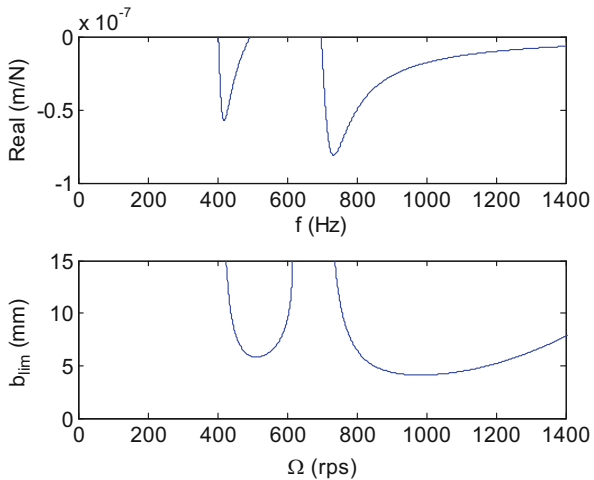
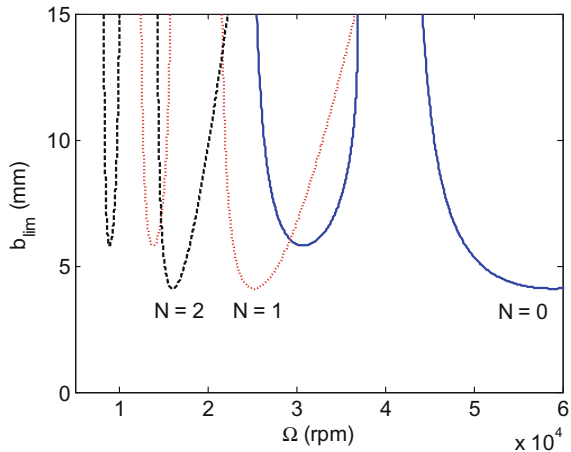


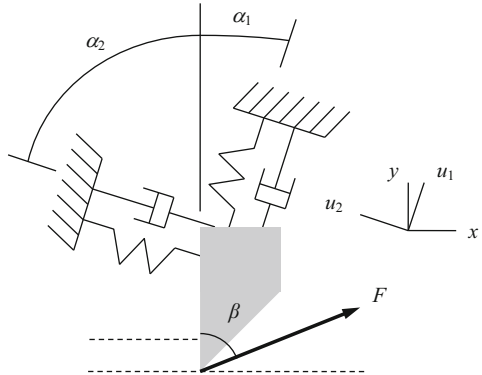
Fig. 3.28 Competing $N = 0, 1$, and 2 stability lobes for two degree of freedom system



these lobes can interfere with each other and limit the stable chip width, they may be considered as “competing lobes.” For example, it is seen that the right portion of the $N = 2$ lobe (corresponding to the 700 Hz mode) truncates the stable zone between the left (400 Hz mode) and right portions of the $N = 1$ lobe near 20,000 rpm. The MATLAB® program used to produce these figures is provided with the textbook as p_3_3_1.m.

As seen in Fig. 3.21, it is sometimes not sufficient to consider the system flexibility in one direction only. In this case, modes in both the u_1 and u_2 directions should be included in the stability evaluation described in the previous example. The model shown in Fig. 3.29 depicts a single degree of freedom aligned with both u_1 and u_2 , neither of which are coincident with y , the surface normal. The oriented FRF now depends on the contributions of both modes. We therefore calculate two directional orientation factors, each of which projects the force into the appropriate

Fig. 3.29 Turning model with a single degree of freedom in both the u_1 and u_2 directions



mode and then this result into the surface normal. Let's consider the u_1 mode. The first step is to project F into the u_1 direction:

$$F_{u_1} = F \cos (\beta - \alpha_1). \quad (3.22)$$

This result is then projected into the surface normal:

$$F_n = F_{u_1} \cos (\alpha_1) = F \cos (\beta - \alpha_1) \cos (\alpha_1). \quad (3.23)$$

The u_1 directional orientation factor is, therefore, $\mu_1 = \cos (\beta - \alpha_1) \cos (\alpha_1)$. Similarly, the steps in determining μ_2 are:

$$F_{u_2} = F \cos (\beta + \alpha_2) \quad \text{and} \quad (3.24)$$

$$F_n = F_{u_2} \cos (\alpha_2) = F \cos (\beta + \alpha_2) \cos (\alpha_2) \quad (3.25)$$

so that $\mu_2 = \cos (\beta + \alpha_2) \cos (\alpha_2)$. The oriented FRF is then calculated as a linear combination of the contributions of both modes/cutting force using these directional orientation factors. Note that this treatment is not limited to a single degree of freedom in either direction; it is generic to any number of degrees of freedom in the two perpendicular directions u_1 and u_2 .

$$\text{FRF}_{\text{orient}} = \mu_1 \text{FRF}_{u_1} + \mu_2 \text{FRF}_{u_2} \quad (3.26)$$



In a Nutshell

It is possible for a multiple degree of freedom system to chatter in any of its modes. The effect of each mode is determined by its dynamic characteristics, the alignment of the force with the direction of flexibility of the mode, and the ability of the deflection of the mode to imprint on the surface of the workpiece. These effects are combined in the “directional orientation factor.”

Example 3.4 Turning Model with Modes in Two Perpendicular Directions We'll next determine the stability for the model in Fig. 3.29 with the following parameters:

Fig. 3.30 Oriented FRF for Example 3.3. The two components of the oriented FRF are also shown

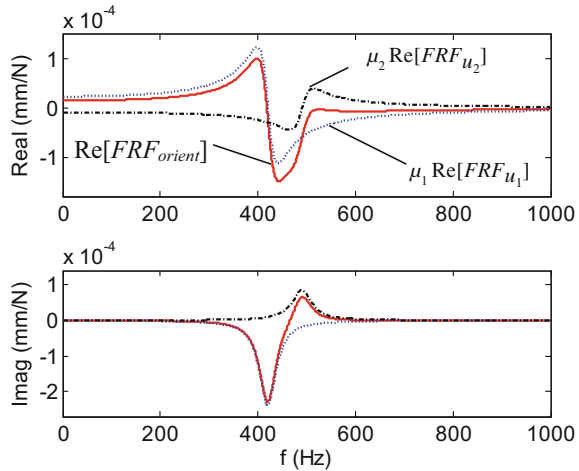


Table 3.2 Approximate best and worst spindle speeds for Example 3.3

N	Ω_{best} (rps)	Ω_{best} (rpm)	Ω_{worst} (rps)	Ω_{worst} (rpm)
0	418	25,080	591	35,460
1	209	12,540	253	15,180
2	139	8340	161	9665
3	105	6300	118	7088

$\alpha_1 = 30 \text{ deg}$, $\alpha_2 = 60 \text{ deg}$, $\beta = 70 \text{ deg}$, and $K_s = 2000 \text{ N/mm}^2$. The dynamics are defined by $f_{n1} = 421 \text{ Hz}$, $k_1 = 2.8 \times 10^7 \text{ N/m}$, and $\zeta_1 = 0.05$ for the u_1 direction and $f_{n2} = 491 \text{ Hz}$, $k_2 = 3.81 \times 10^7 \text{ N/m}$, and $\zeta_2 = 0.05$ for the u_2 direction. The directional orientation factors are calculated using Eqs. 3.22 through 3.25.

$$\mu_1 = \cos(\beta - \alpha_1) \cos(\alpha_1) = \cos(70 - 30) \cos(30) = 0.663$$

$$\mu_2 = \cos(\beta + \alpha_2) \cos(\alpha_2) = \cos(70 + 60) \cos(60) = -0.321$$

The oriented FRF, as well as its components $\mu_1 \text{FRF}_{u_1}$ and $\mu_2 \text{FRF}_{u_2}$, are shown in Fig. 3.30. It is seen that (1) the minimum real part of $\text{FRF}_{\text{orient}}$ occurs at 443 Hz with a value of $1.493 \times 10^{-4} \text{ mm/N}$; and (2) the real part crosses through zero amplitude at a frequency of 418 Hz (which corresponds to the natural frequency for a single degree of freedom system). Although this is not a single degree of freedom system, the real part of the oriented FRF bears some similarity to a single degree of freedom FRF real part. As an approximation, we can therefore calculate $b_{\text{lim,crit}}$ and the best and worst spindle speeds using the single degree of freedom equations presented in Sect. 3.3. The best and worst spindle speeds are summarized in Table 3.2.

$$b_{\text{lim,crit}} = \frac{-1}{2K_s \cdot \min(\text{Re}[\text{FRF}_{\text{orient}}])} = \frac{-1}{2 \cdot 2000 \cdot (-1.493 \times 10^{-4})} = 1.7 \text{ mm}$$

$$\Omega_{\text{best}} = \frac{418}{N+1} \text{ (rps)}$$

$$\Omega_{\text{worst}} = \frac{\frac{443}{3}}{N+1} \text{ (rps)}$$

Figure 3.31 shows one valid chatter frequency range associated with the oriented FRF. As before, it occurs where the real part is less than zero (top panel). In the bottom panel, the $N = 0$ Ω and b_{lim} values are plotted against one another to define the stability limit. It is seen that the best speed of 418 rps is a reasonable approximation of the actual behavior. Figure 3.32 shows the combined stability boundary

Fig. 3.31 (Top panel)
Negative real part of
oriented FRF for Example
3.4. (Bottom panel)
Corresponding $N = 0$
stability limit

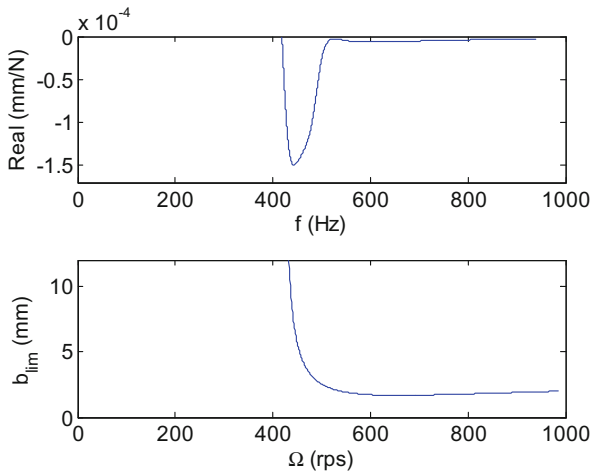
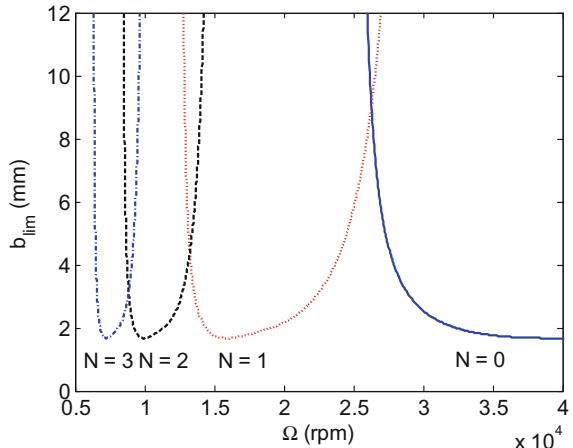


Fig. 3.32 Stability lobes for
Example 3.4 ($N = 0$ to 3)



for $N = 0$ to 3. The MATLAB[®] program used to produce these figures is provided with the textbook as p_3_4_1.m. Note that ϵ in Eq. 3.7 must now be calculated using $\text{FRF}_{\text{orient}}$.

3.5 Turning Time Domain Simulation

In this section, a time domain simulation is described that solves the turning equation of motion by numerical integration. This is in contrast to Tlusty's analytical, frequency domain solution detailed in the previous sections. The stability lobe diagram determined from the analytical solution gives a "global" picture of the stability behavior for a particular turning setup, but does not provide information regarding the cutting force or tool vibrations. On the other hand, time domain simulation gives "local" force and vibration levels for the selected cutting conditions, but not the same global view. The simulation proceeds as follows: (1) the instantaneous chip thickness is determined using the current and previous tool vibrations; (2) the cutting force is calculated; (3) the force is used to find the new displacement; and (4) the process is repeated in small time steps. The simulation model is the same as was presented in Fig. 3.29.

3.5.1 Chip Thickness Calculation

As shown in Eq. 3.4, the instantaneous chip thickness depends, at minimum, on the mean chip thickness (or feed per revolution), the current normal (y) direction vibration, and the vibration one revolution earlier, $h(t) = h_m + y(t - \tau) - y(t)$. We used Fig. 3.6 as an aid in visualizing this equation. In reality, the situation is a little more complicated because, depending on the vibration levels, the instantaneous chip thickness may depend on the current vibration and the vibration two revolutions earlier, for example. Consider the vibrations in two subsequent revolutions shown in Fig. 3.33. The current vibration state is defined by the tool position at three different times, t_1 , t_2 , and t_3 . The vibration one revolution earlier is represented by the solid, sinusoidal line and is offset from the current commanded mean chip thickness line by h_m . The vibration two revolutions earlier is shown as a dashed line and is offset by $2h_m$. The current surface is given by the heavy solid line. It is seen that the current surface depends on the previous revolution at certain times (including t_1 and t_2) and the vibration two revolutions earlier at other times (such as t_3). At t_1 , the chip thickness is determined in the traditional manner, $h_1 = h_m + y(t_1 - \tau) - y(t_1)$. At t_2 , the tool point is actually above the current surface. In other words, no cutting is taking place. Here, $y(t_2) > h_m + y(t_2 - \tau)$ so that $h_2 < 0$. Clearly, a negative chip thickness does not make physical sense, but this nonlinearity is conveniently incorporated in the simulation. At t_3 , the chip thickness is determined using

$h_3 = 2h_m + y(t_3 - 2\tau) - y(t_3)$. At this instant, we must consider the vibrations two revolutions prior.

The simulation is carried out in small time steps, dt . Because we are numerically integrating the system equation of motion to determine the tool vibrations, care must be exercised in selecting dt . If the value is too large, inaccurate results are obtained. As a rule of thumb, it is generally acceptable to set dt at least ten times smaller than the period corresponding to the highest natural frequency in the system's dynamic model.

Example 3.5 Numerical Integration Time Step Selection Consider a turning model with two natural frequencies, $f_{n1} = 800$ Hz and $f_{n2} = 1000$ Hz. The period of the higher natural frequency is:

$$\tau_2 = \frac{1}{f_{n2}} = 1 \times 10^{-3} \text{ s}$$

and the maximum dt value should be:

$$dt = \frac{\tau_2}{10} = 1 \times 10^{-4} \text{ s.}$$

Smaller dt values are naturally acceptable (e.g., dividing the time constant by 50 or 100), but there is a trade-off between improved numerical accuracy and execution time for the simulation. Once the time step is selected, the simulation time can be determined using:

$$t_n = n \cdot dt, \quad (3.27)$$

where n is the simulation counter ($n = 1, 2, \dots$). The number of time steps per spindle revolution, or *steps_rev*, is related to dt (in s) and the selected spindle speed, Ω (in rpm), as:

$$steps_rev = \frac{60}{dt \cdot \Omega}. \quad (3.28)$$

This value is critical because it enables us to keep track of the vibration state from one revolution to the next. At some discrete time t_n in the simulation, the behavior one revolution earlier ($t - \tau$ in a continuous sense) is $t_{n-steps_rev}$ (in a discrete sense). In practice, because *steps_rev* is used as part of the index for the simulation variables, only integer values are allowed. This is accomplished in MATLAB® using the *round* function. For example:

```
steps_rev = round(60/(dt*omega));
```

where *omega* represents the spindle speed in rpm. In simulation, the dependence of the actual surface on more than the most previous revolution can be incorporated by calculating the chip thickness according to:

$$h = y_{\min} - y_{n-1}, \quad (3.29)$$

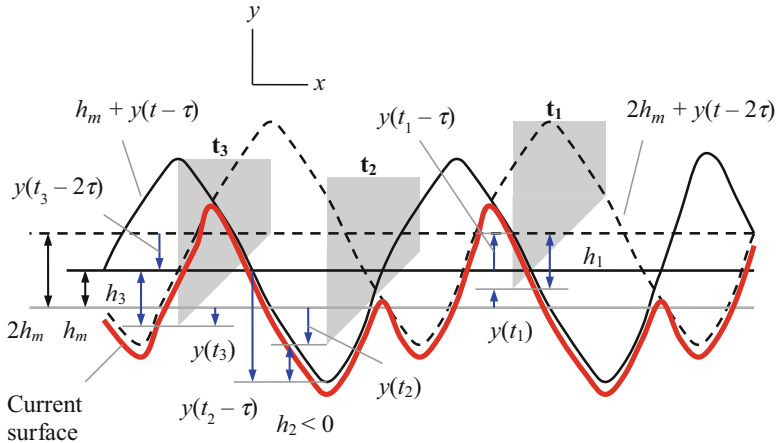


Fig. 3.33 Chip thickness determination at three different instants in time

where y_{\min} is the smallest value of $\{h_m + y_n - \text{steps_rev}, 2h_m + y_n - 2 \cdot \text{steps_rev}, \dots\}$ which, according to Fig. 3.33, defines the current workpiece surface. The index $(n - 1)$ on y in Eq. 3.29 is used because the vibration in the current time step (with index n) is only known after the force is determined and the equation of motion is solved.

3.5.2 Force Calculation

Once the chip thickness is computed using Eq. 3.29, the force in the current time step is determined using the selected chip width, b , and specific force:

$$F = K_s b h. \quad (3.30)$$

As described previously, it is possible that the calculated chip thickness will be negative if the current tool vibration is larger than the surface location (refer to Fig. 3.33 at t_2). In this case, no cutting is occurring. Therefore, the cutting force should be zero. We incorporate this nonlinearity by setting the force equal to zero if the result from Eq. 3.30 is less than zero (due to a negative chip thickness). Additionally, the surface is updated to reflect the actual location, y_{\min} , rather than the tool vibration: $y_{n-1} = y_{\min}$. Once the cutting force is known, it is resolved into the mode directions, u_1 and u_2 , as depicted in Fig. 3.29.

$$F_{u_1} = F \cos(\beta - \alpha_1) \quad \text{and} \quad F_{u_2} = F \cos(\beta + \alpha_2) \quad (3.31)$$

3.5.3 Displacement Calculation

Considering the single degree of freedom models shown in the u_1 and u_2 directions in Fig. 3.29, the corresponding equations of motion are:

$$m_1\ddot{u}_1 + c_1\dot{u}_1 + k_1u_1 = F_{u_1} \quad \text{and} \quad m_2\ddot{u}_2 + c_2\dot{u}_2 + k_2u_2 = F_{u_2}. \quad (3.32)$$

The mode direction accelerations in the current time step due to the two force components are determined by rewriting Eq. 3.32:

$$\ddot{u}_1 = \frac{F_{u_1} - c_1\dot{u}_1 + k_1u_1}{m_1} \quad \text{and} \quad \ddot{u}_2 = \frac{F_{u_2} - c_2\dot{u}_2 + k_2u_2}{m_2}, \quad (3.33)$$

where the velocities, \dot{u}_1 and \dot{u}_2 , and positions, u_1 and u_2 , from the previous time step are used (they are set equal to zero initially). The velocities and positions for the current time step are then determined by numerical (Euler) integration:

$$\dot{u}_1 = \dot{u}_1 + \ddot{u}_1 dt \quad \text{and} \quad \dot{u}_2 = \dot{u}_2 + \ddot{u}_2 dt, \quad (3.34)$$

$$u_1 = u_1 + \dot{u}_1 dt \quad \text{and} \quad u_2 = u_2 + \dot{u}_2 dt, \quad (3.35)$$

where the velocities on the right hand side of the equal signs in Eq. 3.34 are retained from the previous time step and used to update the current values. These current values are then applied to determine the current displacements in Eq. 3.35. Again, the displacements on the right hand side of Eq. 3.35 are those from the previous time step. Once u_1 and u_2 are known, they are projected into the normal (y) direction:

$$y_n = u_1 \cos(\alpha_1) + u_2 \cos(\alpha_2), \quad (3.36)$$

where the n subscript on y indicates the time step. Note that this value represents y_{n-1} in the next time step and is applied in Eq. 3.29 to calculate the updated chip thickness. The process of computing the force and resulting displacements is then repeated.

Example 3.6 Stability Evaluation by Time Domain Simulation Consider the turning model shown in Fig. 3.34. The dynamic constants are $m_1 = 1$ kg, $c_1 = 450$ N s/m, and $k_1 = 2 \times 10^7$ N/m for the u_1 direction and $m_2 = 1$ kg, $c_2 = 650$ N s/m, and $k_2 = 3 \times 10^7$ N/m for the u_2 direction. The other parameters are $\alpha_1 = 35$ deg, $\alpha_2 = 55$ deg, $\beta = 65$ deg, $h_m = 0.1$ mm, and $K_s = 2000$ N/mm². Prior to determining the time domain force and displacements using the simulation described in the previous paragraphs, let's calculate $b_{\lim,crit}$, the approximate best and worst speeds, and the stability lobe diagram for this model.

As seen in Example 3.4, the oriented FRF must be determined using the directional orientation factors prior to calculating $b_{\lim,crit}$. The directional orientation factors are:

Fig. 3.34 Model for turning time domain simulation in Example 3.6

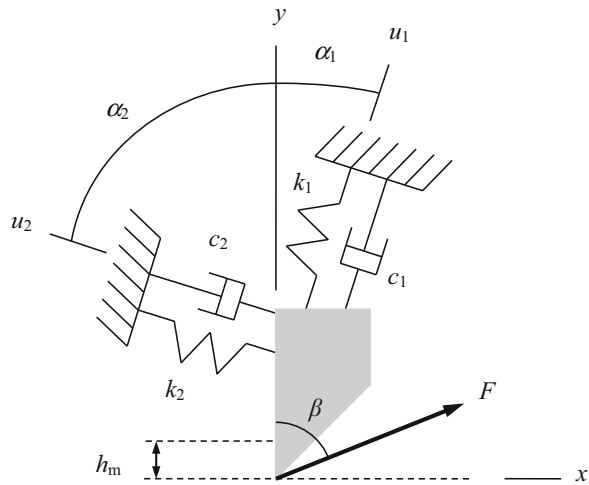
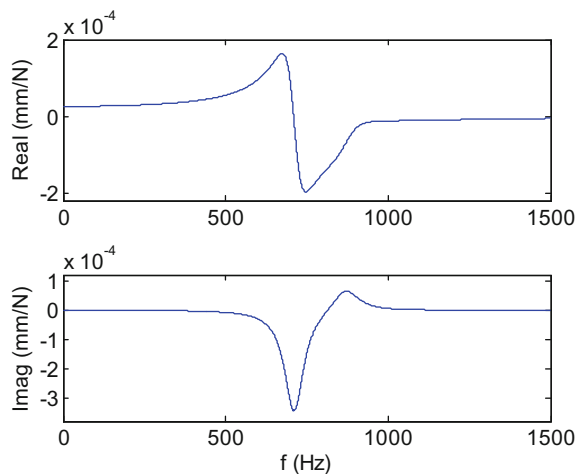


Fig. 3.35 Oriented FRF for Example 3.6



$$\mu_1 = \cos(\beta - \alpha_1) \cos(\alpha_1) = \cos(65 - 35) \cos(35) = 0.709 \quad \text{and}$$

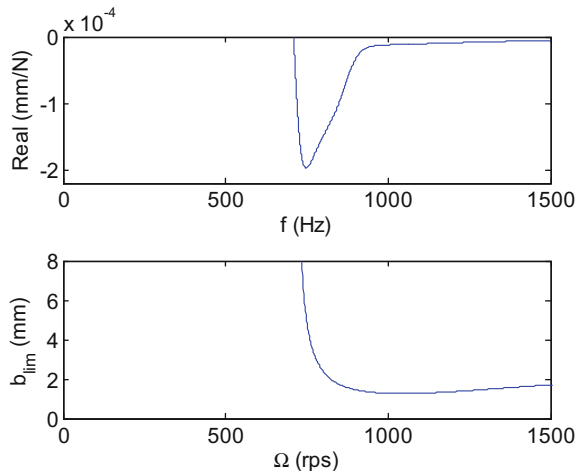
$$\mu_2 = \cos(\beta + \alpha_2) \cos(\alpha_2) = \cos(65 + 55) \cos(55) = -0.287.$$

The oriented FRF is displayed in Fig. 3.35. The minimum real part of occurs at 748 Hz with a value of $1.993 \times 10^{-4} \text{ mm/N}$ and the real part crosses through zero amplitude at a frequency of 709 Hz. Similar to Example 3.4, although this is not a single degree of freedom system, the real part of the oriented FRF resembles single degree of freedom system behavior. We can therefore approximate $b_{lim,crit}$ and the best and worst spindle speeds using the single degree of freedom equations presented in Sect. 3.3. The best and worst spindle speeds are summarized in Table 3.3.

Table 3.3 Approximate best and worst spindle speeds for Example 3.6

N	Ω_{best} (rps)	Ω_{best} (rpm)	Ω_{worst} (rps)	Ω_{worst} (rpm)
0	709	42,540	997	59,840
1	355	21,270	427	25,646
2	236	14,180	272	16,320
3	177	10,635	199	11,968
4	142	8508	157	9448

Fig. 3.36 (Top panel)
Negative real part of
oriented FRF for Example
3.6. (Bottom panel)
Corresponding $N = 0$
stability limit



$$b_{\text{lim,crit}} = \frac{-1}{2K_s \cdot \min(\text{Re}[\text{FRF}_{\text{orient}}])} = \frac{-1}{2 \cdot 2000 \cdot (-1.993 \times 10^{-4})} = 1.3 \text{ mm}$$

$$\Omega_{\text{best}} = \frac{709}{N+1} \text{ (rps)}$$

$$\Omega_{\text{worst}} = \frac{748}{N+\frac{3}{4}} \text{ (rps)}$$

The top panel of Fig. 3.36 shows a single valid chatter frequency range (real part <0) for the oriented FRF. In the bottom panel, it is observed that the best speed of 709 rps is an acceptable approximation of the actual behavior, although this is not a reasonable spindle speed (42,540 rpm) for typical turning applications. Figure 3.37 shows the combined stability boundary for $N = 0$ to 4. The MATLAB® programs used to produce these figures are provided with the textbook as p_3_6_1.m and p_3_6_2.m.

As discussed before, Fig. 3.37 provides a global view of the process stability, but does not provide local information, such as force and tool displacement, about particular operating parameter combinations. For example, the stability boundary would suggest that 44,490 rpm is a good operating speed for b values up to 6 mm [this spindle speed is somewhat higher than the simple approximation of 42,540 rpm provided in Table 3.3]. It also shows that the maximum allowable chip width at

Fig. 3.37 Stability lobes for Example 3.6 ($N = 0$ to 4)

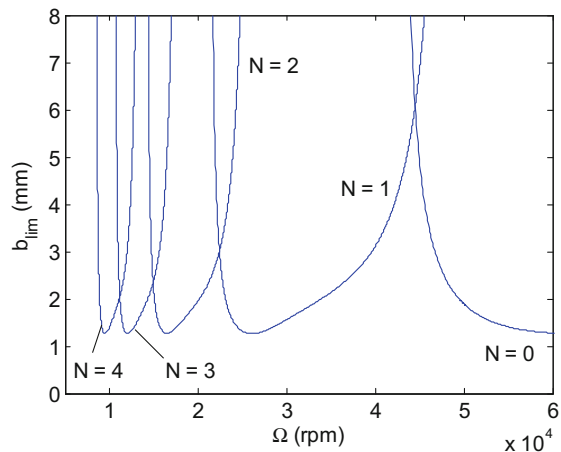
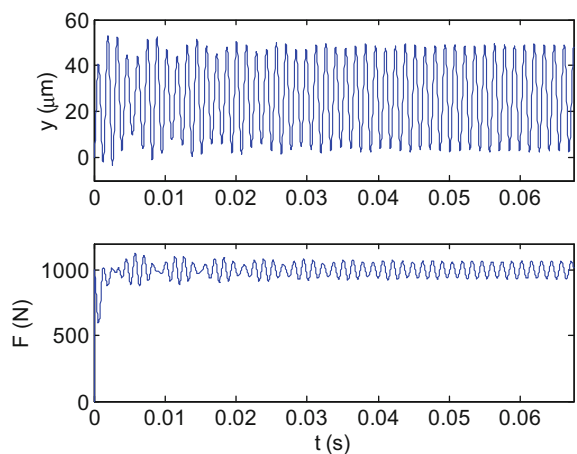


Fig. 3.38 Example 3.6 time domain force and displacement for $\Omega = 44,490$ rpm and $b = 5$ mm



26,140 rpm is slightly less than 1.3 mm. We will now use the time domain simulation to determine the force and tool displacement values near these stability thresholds. Figure 3.38 provides the results for $\Omega = 44,490$ rpm and $b = 5$ mm, where the total simulation time corresponds to 50 revolutions, $\frac{50}{44,490} = 0.067$ s. It is

seen that these conditions are actually near the stability limit since the force and displacement levels are neither growing nor diminishing. In this way, time domain simulation can be used to refine the analytical stability limit results. We can also check the simulation mean values against Eqs. 3.37 and 3.38. Equation 3.37 gives the mean cutting force, F_m , based on the commanded chip area and specific force. Equation 3.38 provides the mean normal direction displacement, y_m , where the sum of the $\frac{\mu}{k}$ ratios gives the static compliance of the oriented FRF. As expected, the simulation results in Fig. 3.38 agree with the analytical expressions in both cases. At

Fig. 3.39 Example 3.6 time domain force and displacement for $\Omega = 44,490$ rpm and $b = 6$ mm

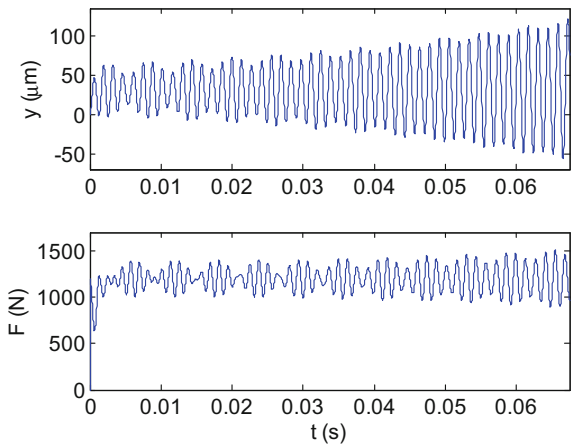
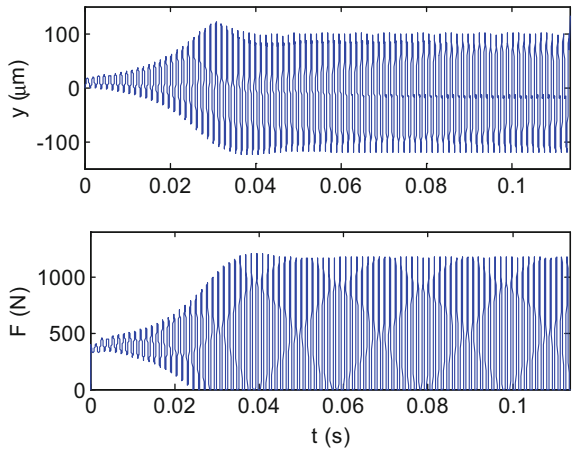


Fig. 3.40 Example 3.6 time domain force and displacement for $\Omega = 26,140$ rpm and $b = 2$ mm



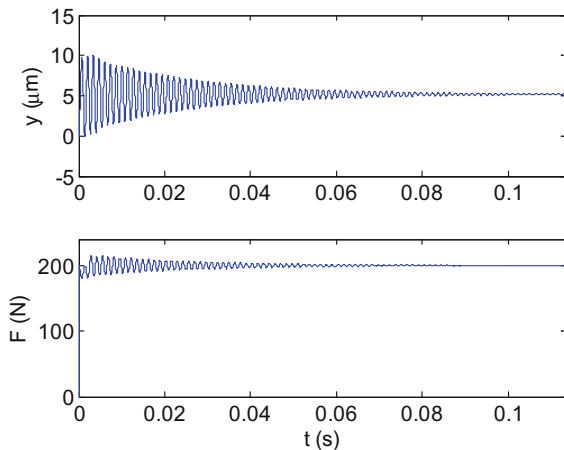
$\Omega = 44,490$ rpm and $b = 6$ mm, the cut is clearly unstable; the force and displacement values are growing significantly with time. See Fig. 3.39.

$$F_m = K_s b h_m = 2000 \cdot 5 \cdot 0.1 = 1000 \text{ N} \quad (3.37)$$

$$y_m = F_m \left(\frac{\mu_1}{k_1} + \frac{\mu_2}{k_2} \right) = 1000 \left(\frac{0.709}{2 \times 10^7} + \frac{-0.287}{3 \times 10^7} \right) = 2.6 \times 10^{-5} \text{ m} = 26 \text{ } \mu\text{m} \quad (3.38)$$

At the less favorable spindle speed of $\Omega = 26,140$ rpm, chatter is observed at $b = 2$ mm in Fig. 3.40. Not only are the force and displacement values growing with time, but the force nonlinearity is also observed (beginning at approximately $t = 0.025$ s) when the tool vibration grows large enough that there is no cutting intermittently and $F = 0$. The total simulated time for 50 revolutions is now

Fig. 3.41 Example 3.6 time domain force and displacement for $\Omega = 26,140$ rpm and $b = 1$ mm



$\frac{50}{\frac{26,140}{60}} = 0.115$ s. If the chip width is reduced to 1 mm, stable operation is obtained (Fig. 3.41). Here it is seen that the initial transient response quickly attenuates and the steady-state force and displacement are obtained. The MATLAB® program used to produce these figures is provided with the textbook as p_3_6_3.m.

$$F_m = K_s b h_m = 2000 \cdot 1 \cdot 0.1 = 200 \text{ N}$$

$$y_m = F_m \left(\frac{\mu_1}{k_1} + \frac{\mu_2}{k_2} \right) = 200 \left(\frac{0.709}{2 \times 10^7} + \frac{-0.287}{3 \times 10^7} \right) = 5 \times 10^{-6} \text{ m} = 5 \text{ } \mu\text{m}$$



In a Nutshell

Time domain simulation eliminates many of the simplifying assumptions required to obtain the global analytical solution. It explicitly includes nonlinearities, such as the tool losing contact with the workpiece. For that reason, time domain simulation is more accurate than the analytical solution. However, it provides information on a case-by-case basis only. That is, the cutting conditions for a single cut are selected, and the simulation is run. After that run, it is possible to determine if that particular cut is stable or not. Investigation of other cutting conditions requires additional runs of the simulation. Using time domain simulation to produce a stability lobe diagram requires many repeated executions, with conditions changed for each run.

3.5.4 Multiple Degree of Freedom Modeling

As a final point of consideration in this section, let's discuss how to extend the time domain simulation to include multiple degrees of freedom in the two mode

directions u_1 and u_2 . The important point to remember from Chap. 2 is that, provided we have measured the direct FRF at the location of interest (the tool point), the response can be expressed as a sum of the modal contributions. Therefore, once we have completed the curve fitting exercise to obtain the modal parameters (Sect. 2.5), we can treat each degree of freedom for both mode directions separately and determine the individual solutions using Euler integration as shown in Eqs. 3.33 through 3.35. After the displacements in each mode have been calculated, they are simply summed in each direction. For example, assume that two modes were identified and curve fitted using peak picking for the u_1 direction and three modes were selected for the u_2 direction. The modal parameters m_{q1,u_1} , c_{q1,u_1} , k_{q1,u_1} , m_{q2,u_1} , c_{q2,u_1} , and k_{q2,u_1} would be obtained for u_1 , while m_{q1,u_2} , c_{q1,u_2} , k_{q1,u_2} , m_{q2,u_2} , c_{q2,u_2} , k_{q2,u_2} , m_{q3,u_2} , c_{q3,u_2} , and k_{q3,u_2} would be obtained for u_2 . The modal accelerations in the u_1 direction would now include:

$$\ddot{u}_{1,q1} = \frac{F_{u_1} - c_{q1,u_1}\dot{u}_{1,q1} + k_{q1,u_1}u_{1,q1}}{m_{q1,u_1}} \quad \text{and} \quad \ddot{u}_{1,q2} = \frac{F_{u_1} - c_{q2,u_1}\dot{u}_{1,q2} + k_{q2,u_1}u_{1,q2}}{m_{q2,u_1}},$$

where the local u_1 direction force is used because the modal force vector is composed of identical local force values for each modeled mode (see Eq. 2.53). The modal coordinate velocities and positions would then be determined according to:

$$\begin{aligned} \dot{u}_{1,q1} &= \dot{u}_{1,q1} + \ddot{u}_{1,q1}dt & \text{and} \quad \dot{u}_{1,q2} &= \dot{u}_{1,q2} + \ddot{u}_{1,q2}dt & \text{and} \\ u_{1,q1} &= u_{1,q1} + \dot{u}_{1,q1}dt & \text{and} \quad u_{1,q2} &= u_{1,q2} + \dot{u}_{1,q2}dt. \end{aligned}$$

Finally, the u_1 local displacement would be calculated using $u_1 = u_{1,q1} + u_{1,q2}$. Similarly, the u_2 direction modal accelerations would be:

$$\ddot{u}_{2,q1} = \frac{F_{u_2} - c_{q1,u_2}\dot{u}_{2,q1} + k_{q1,u_2}u_{2,q1}}{m_{q1,u_2}}, \quad \ddot{u}_{2,q2} = \frac{F_{u_2} - c_{q2,u_2}\dot{u}_{2,q2} + k_{q2,u_2}u_{2,q2}}{m_{q2,u_2}}, \quad \text{and}$$

$$\ddot{u}_{2,q3} = \frac{F_{u_2} - c_{q3,u_2}\dot{u}_{2,q3} + k_{q3,u_2}u_{2,q3}}{m_{q3,u_2}}.$$

The modal coordinate velocities and positions in the u_2 direction would then be determined using:

$$\dot{u}_{2,q1} = \dot{u}_{2,q1} + \ddot{u}_{2,q1}dt, \quad \dot{u}_{2,q2} = \dot{u}_{2,q2} + \ddot{u}_{2,q2}dt, \quad \text{and} \quad \dot{u}_{2,q3} = \dot{u}_{2,q3} + \ddot{u}_{2,q3}dt,$$

$$u_{2,q1} = u_{2,q1} + \dot{u}_{2,q1}dt, \quad u_{2,q2} = u_{2,q2} + \dot{u}_{2,q2}dt, \quad \text{and} \quad u_{2,q3} = u_{2,q3} + \dot{u}_{2,q3}dt$$

and the u_2 local displacement would be calculated using $u_2 = u_{2,q1} + u_{2,q2} + u_{2,q3}$. As with the single degree of freedom case, all initial values of the modal velocities and displacements should be set equal to zero prior to simulation execution.



In a Nutshell

Modal analysis provides a convenient way to summarize the dynamic characteristics of complicated vibration systems. When applying time domain simulation, the compact modal data representation facilitates determination of the appropriate parameters for stable machining.

3.6 Modulated Tool Path Turning

In continuous cutting processes, such as turning, boring, and threading, once the cutting edge is engaged with the workpiece, it remains in contact at a specified feed rate until the cut concludes. This tends to produce a continuous chip that can wrap and collect near the cutting edge when machining ductile materials; see Fig. 3.42. The local buildup of this continuous chip can result in one or more of several undesirable outcomes, including workpiece scratching, tool damage, machinist injury, and increased cycle time to clear the chip(s) from the tool/workpiece.

Existing chip management strategies include the use of specialized rake face geometries (i.e., chip breakers) and high-pressure coolant directed at the rake face-chip interface to intentionally fracture the otherwise continuous chip. The performance of these strategies depends on the chip thickness, chip radius of curvature, and workpiece material [6], as well as the coolant pressure, direction, and location when high-pressure coolant is applied.

An alternative approach to these techniques is modulated tool path (MTP) turning, where discrete chips are formed through repeated interruption of the continuous chip formation by using the machine axes to superimpose low-frequency tool oscillations on the nominal tool feed motion. In this case, successful chip separation is based on the oscillation frequency relative to the spindle speed and the oscillation amplitude relative to the global feed per revolution.

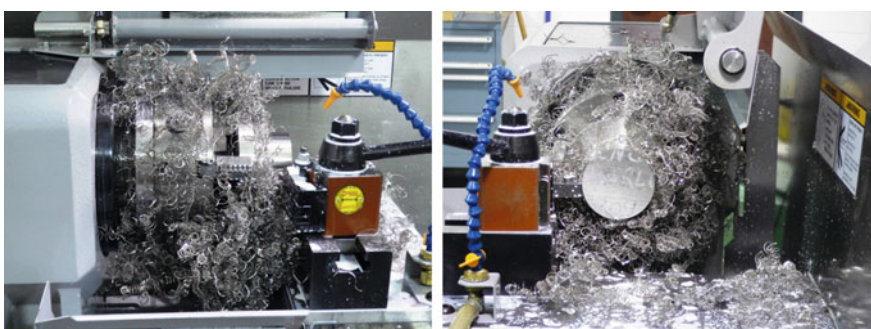


Fig. 3.42 Chip buildup observed in a turning operation



In a Nutshell

In modulated tool path turning, the CNC part program is written in such a way that the axes of the machine superimpose a vibration on the feed motion. This vibration is parallel to the generated surface and periodically enforces a separation of the tool from the chip. By selection of the superimposed vibration frequency and amplitude, the length of the broken chip can be programmed. The demands on the axis motion are surprisingly minimal.

Prior MTP research efforts have demonstrated its effectiveness for controlling broken chip length in both turning [7–10] and threading [11]. Additionally, an experimental setup used to measure feed motion, force, temperature, and chip formation data using both constant feed and MTP cutting conditions was described [12, 13]. In this section, we'll explore the stability of MTP turning. We'll establish stability using two approaches: (1) frequency domain analysis, where the frequency content of a process signal is analyzed to identify the chatter frequency magnitude (should it exist); and (2) a periodic sampling approach, where the synchronicity of the sampled signal is evaluated numerically. We'll demonstrate the two methods using force, acceleration, and velocity data in a tube turning (orthogonal cutting) setup.

As noted, MTP is a turning technique which produces discontinuous chips by superimposing oscillations in the tool feed direction to repeatedly interrupt the cutting process [10]. An exaggerated depiction of an MTP turning operation is displayed in Fig. 3.43. The broken chip length is dependent on two, user-defined MTP parameters: (1) the tool oscillation frequency relative to the spindle speed, or oscillations per revolution (*OPR*); and (2) the oscillation amplitude relative to the global feed per revolution, or the ratio of the amplitude to the feed rate (*RAF*).

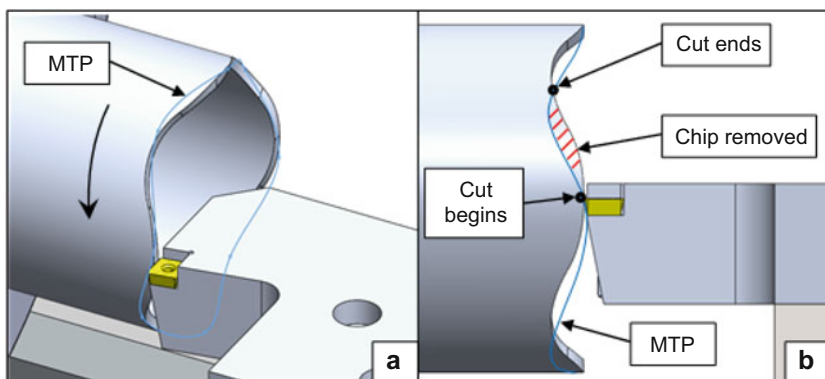


Fig. 3.43 (a) The tool feed motion is varied sinusoidally to produce a wavy surface in the feed direction. (b) By selecting appropriate *OPR* and *RAF* values, broken chips are periodically produced

The MTP parameters are defined as:

$$OPR = \frac{60f}{\Omega}, \quad (3.39)$$

$$RAF = \frac{A}{f_r}, \quad (3.40)$$

where f is the tool oscillation frequency (Hz) in the feed direction, Ω is the spindle speed (rpm), A is the tool oscillation amplitude, and f_r is the global feed per revolution for a traditional, constant feed turning operation. The time-dependent feed motion of the tool relative to the work, z_f , is then described using these two parameters.

$$z_f = \left(\frac{\Omega}{60} f_r \right) t + RAF \cdot f_r \sin \left(\frac{\Omega}{60} 2\pi \cdot OPR \cdot t \right) \quad (3.41)$$

Figure 3.44 displays the MTP feed motion for a spindle speed of 200 rpm, a feed of 0.1 mm/rev, and RAF and OPR values of 0.8 and 0.5, respectively. In the figure, the dashed line denotes the constant feed advance of the tool into the part, while the solid line shows the superposition of the MTP oscillation onto the constant feed. The vertical dashed lines identify each revolution; three revolutions are plotted.

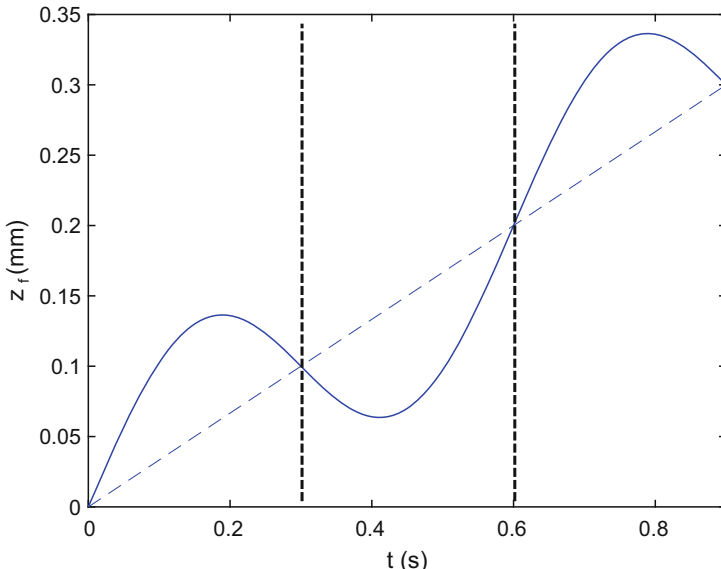


Fig. 3.44 MTP feed motion for three spindle revolutions. The spindle speed is 200 rpm, the feed per revolution is 0.1 mm/rev, and the RAF and OPR values are 0.8 and 0.5. The dashed positive slope line identifies the constant feed contribution to the motion (first term in Eq. 3.41), while the solid line shows its sum with the sinusoidal MTP contribution (second term). The vertical dotted lines denote each revolution

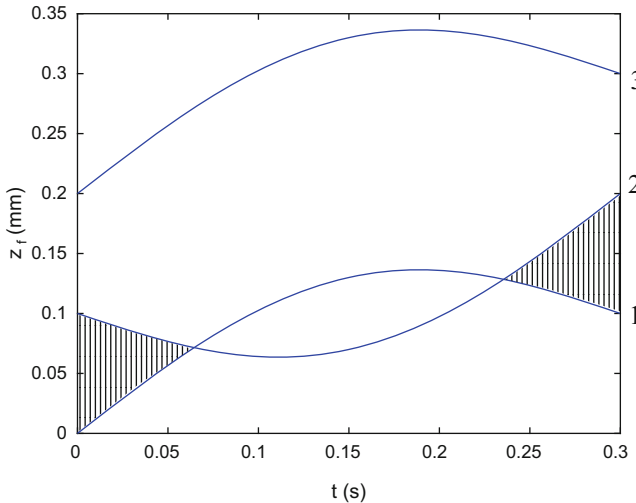


Fig. 3.45 Chip thickness calculation for revolution 2. The nonzero chip thickness zones are denoted by the hatched areas

The discontinuous nature of the chip formation is demonstrated using Fig. 3.45. In this figure, the Fig. 3.44 data is parsed by revolution. The revolution numbers are included on the right-hand side of the figure. The nominal chip thickness is the difference between the current tool position and the maximum value of all previous revolutions. Figure 3.45 shows the chip thickness for revolution 2 as the hatched areas. The chip thickness is zero when the revolution 2 oscillation dips below the revolution 1 oscillation. Note that the $+z_f$ direction is positive into the part, so “below” here means away from the part and no cutting occurs.

Figure 3.46 displays the chip thickness (hatched area) for revolution 3. Note that the instantaneous chip thickness is the difference between revolutions 3 and 1 for the time period between 0.0645 s and 0.2355 s and the difference between revolutions 3 and 2 for all other times. The corresponding chip thickness, h , for the two revolutions is shown in Fig. 3.47. The two revolutions are segmented by the vertical dashed line. Because the OPR is 0.5 for this example, the chip thickness profile in Fig. 3.47 repeats every two revolutions. MTP turning therefore exhibits periodic excitation, unlike traditional turning where the chip thickness and force are nominally constant.

3.6.1 Stability Analysis

In interrupted cutting operations, two types of system response may exist. These are forced vibrations and self-excited vibrations (chatter). In forced vibrations, the response occurs at the excitation frequency [14]. In milling, this is the tooth passing frequency, which is defined by the product of the spindle speed and number of teeth

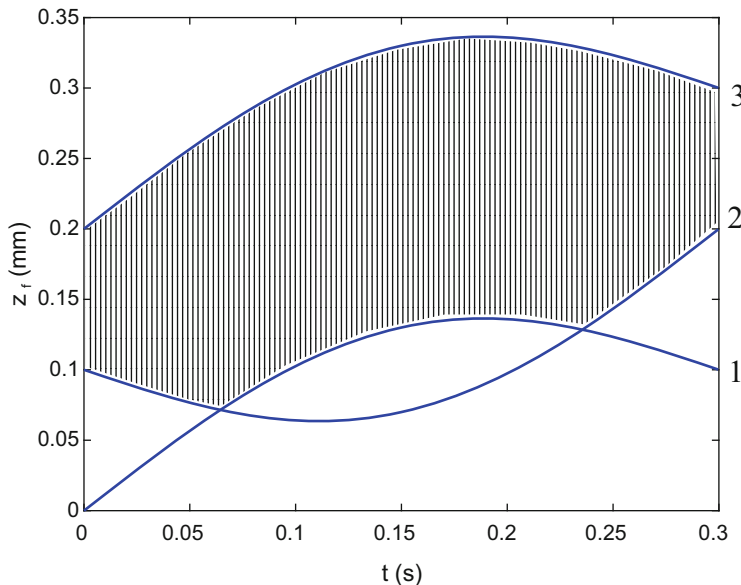


Fig. 3.46 Chip thickness calculation for revolution 3. The instantaneous chip thickness is the difference between the current MTP motion and the maximum of all prior revolutions at the same rotation angle

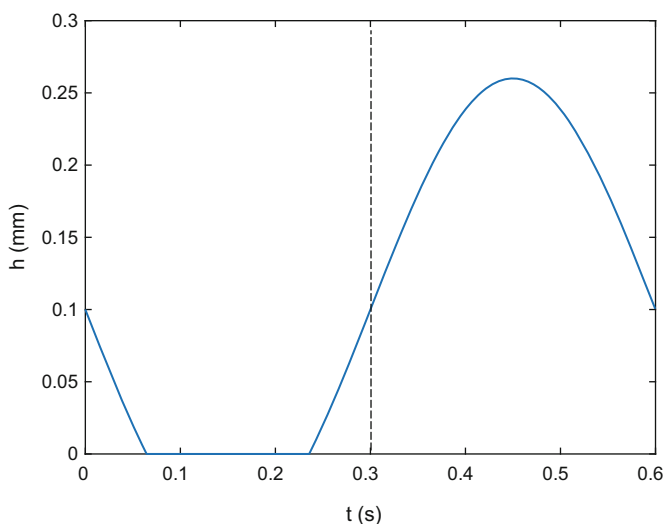


Fig. 3.47 Instantaneous chip thickness for revolutions 2 and 3. This chip thickness profile produces interrupted cutting and is periodic

on the rotating cutter. The tooth passing frequency describes the number of cutting-edge contacts with the work per unit time. For example, the tooth passing frequency for a spindle speed of 6000 rpm using a four-tooth endmill is $\frac{6000 \cdot 4}{60} = 400(4)/60 = 400$ Hz. In MTP, the excitation frequency is the product of the spindle speed and *OPR*. For a 600 rpm spindle speed and an *OPR* of 0.5, the excitation frequency is $\frac{6000 \cdot 4}{60} = 400(0.5)/60 = 5$ Hz. The practical limit on this excitation frequency is the bandwidth for the CNC lathe's axis motion control.

In self-excited vibration, on the other hand, the periodic forcing function is modulated by some physical mechanism into oscillation near the system's natural frequency that corresponds to the most flexible vibration mode. For machining operations, this physical mechanism is the feedback provided by the overcutting of the previous surface in the current pass. This yields a time delay because the current chip thickness depends on the commanded chip thickness, the current tool vibration state, and the tool's vibration state when leaving the previous surface.

Because the response frequencies differ between forced and self-excited vibrations, periodic sampling of machining signals at the forcing frequency enables stable (forced vibration) and unstable (self-excited vibration) behavior to be distinguished. When sampled at the forcing frequency, forced vibrations repeat. For self-excited vibration, on the other hand, the sampled points do not repeat because both the forcing frequency and the (generally) incommensurate² chatter frequency are present. To demonstrate the approach, let's consider an example for a selected dynamic system. The nominal specifications are $\Omega = 600$ rpm and $f_r = 0.17$ mm/rev. The chip thickness for *RAF* and *OPR* values of 1.0 and 0.5 is displayed in Fig. 3.48. The periodic sampling is shown as well (circles). Because the sampled points repeat, the cut exhibits forced vibration and is considered stable.

Figure 3.49 shows the results for *RAF* and *OPR* values of 1.0 and 0.25 (all other conditions identical). In this case, the sampled points do not repeat, and quasiperiodic behavior is observed. This behavior occurs because both the forcing frequency and the incommensurate chatter frequency are present; the self-excited response identifies the cut as unstable. Note that the sampling period is different than Fig. 3.48 because the *OPR* value was reduced. The smaller value yields a larger sampling period (lower forcing frequency).

The variation in the periodically sampled points due to self-excited vibration enables a numerical value to be assigned that indicates stable or unstable behavior. We define this MTP stability metric, M , to be:

$$M = \frac{\sum_{i=2}^N |x_s(i) - x_s(i-1)|}{N}, \quad (3.42)$$

²In other words, the ratio of the chatter frequency to forcing frequency cannot be expressed as a ratio of whole numbers.

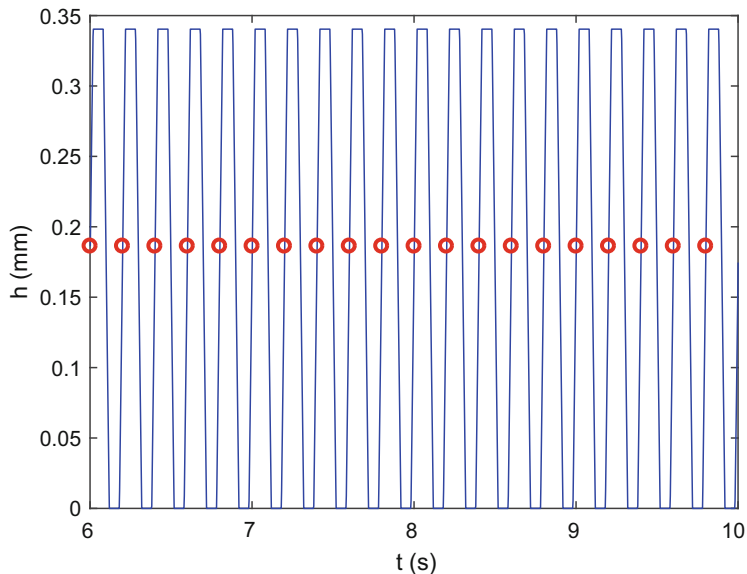


Fig. 3.48 Chip thickness variation for $RAF = 1.0$ and $OPR = 0.5$

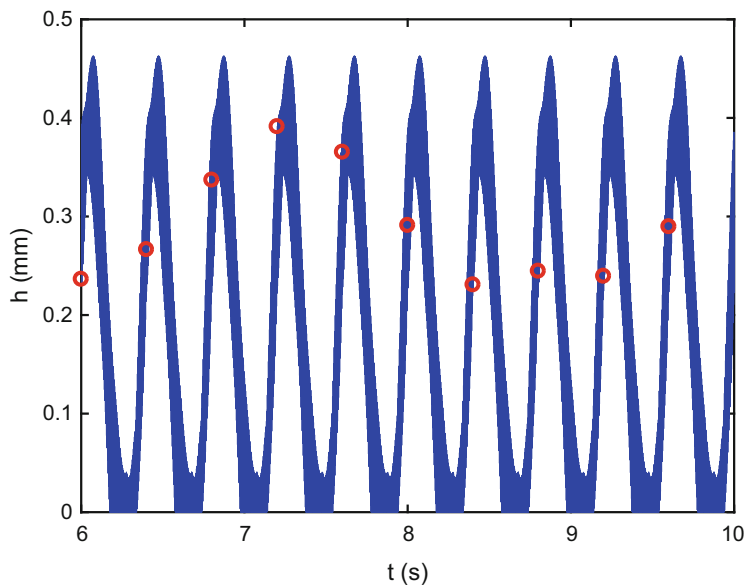


Fig. 3.49 Chip thickness variation for $RAF = 1.0$ and $OPR = 0.25$

where x_s is a vector of periodically sampled x values and N is the length of the x_s vector. The x values can be any process signal, including displacement, velocity, or acceleration of the tool or workpiece; cutting force; or sound [15]. With this stability metric, the absolute value of the differences in successive sampled points is summed and then normalized. For stable cuts (forced vibration), the sampled points repeat, so the M value is ideally zero. For unstable cuts, however, $M > 0$ [16, 17].



In a Nutshell

MTP can have a stabilizing effect on the turning operation because the interruption in the cut disturbs the regeneration mechanism responsible for chatter in the first place.

3.6.2 Experimental Demonstration

Let's examine this periodic sampling approach for MTP stability evaluation using experimental data.³ The testbed for the tube turning experiments was a CNC lathe. Tubular workpieces were machined from 6061-T6 aluminum. The outside diameter of the workpieces was 72 mm and the wall thickness was {1, 1.5, and 2} mm. Concentricity and cylindricity of the outside and inside diameters with the rotational axis of the lathe spindle were assured by performing a finishing cut prior to conducting the experiments. Carbide inserts with a zero rake angle, 7 deg relief angle, and a flat rake face were used. Orthogonal cutting (tube turning) was selected so that the cutting speed would not vary with a fixed spindle speed; see also Sect. 8.1. Experiments were conducted at a cutting speed of 206 m/min (911 rpm) with a nominal feed rate of 0.102 mm/rev. The commanded *OPR* and *RAF* values for all tests were 0.5 and 0.8, respectively. The tests were then repeated using a constant feed rate so that MTP performance could be compared to traditional turning. Stability of the cut was controlled by varying the tube wall thickness (i.e., the chip width) in both cases.

Dynamic cutting forces were measured using a three-axis dynamometer mounted to the lathe's cross slide. A notch-type flexure was mounted to the top of the three-axis dynamometer [18]. This flexure carried the carbide insert and acted as the cutting tool. This configuration provided a flexible response in the sensitive direction (z_f). A laser vibrometer was used to measure the feed (z_f) direction velocity of the cutting tool. An accelerometer was fixed to the free end of the tool to measure the tool acceleration in the thrust direction. A laser tachometer was used to determine the actual spindle speed for periodic sampling at the MTP forcing frequency. A photograph of the setup is provided in Fig. 3.50, and a schematic is provided in Fig. 3.51.

³T. Schmitz recognizes the significant contributions of R. Copenhaver and M. Rubeo to the experimental setup.

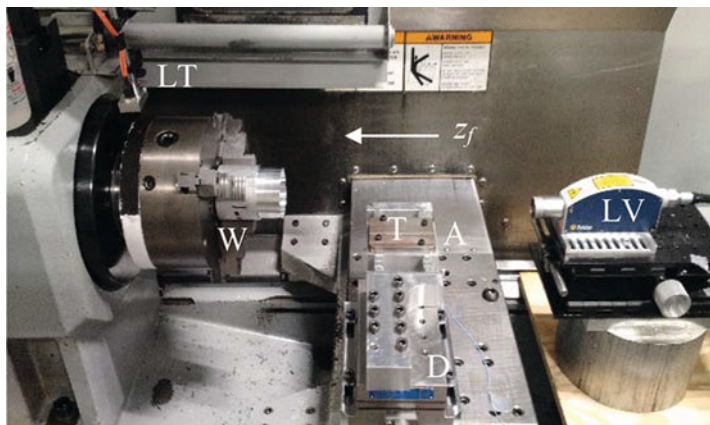


Fig. 3.50 Photograph of tube turning setup including workpiece (W), dynamometer (D), flexure-based cutting tool (T), laser tachometer (LT), accelerometer (A), and laser vibrometer (LV)

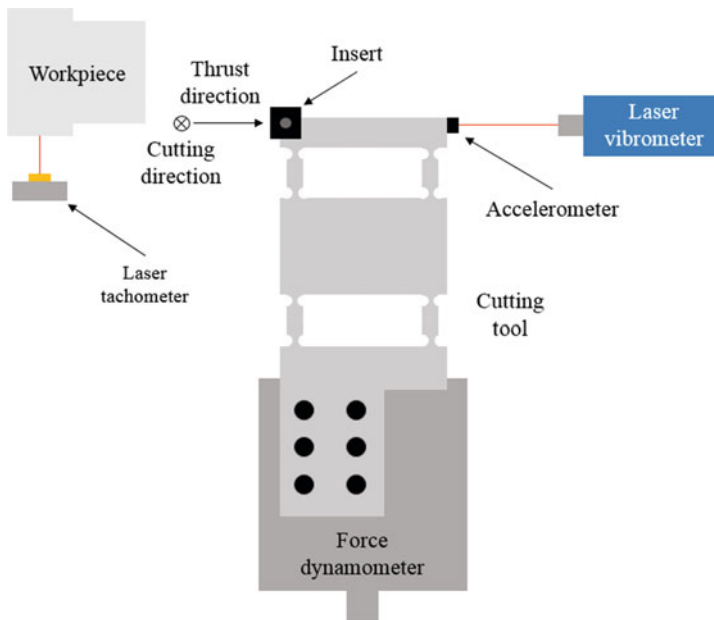


Fig. 3.51 Schematic of the experimental setup

The thrust direction is aligned with the spindle axis, while the cutting direction is tangent to the cut surface.

The FRF at the free end of the cutting tool was measured using impact testing. The real and imaginary parts of the thrust direction response are displayed in Fig. 3.52. Three primary vibration modes are observed at {298, 395, and 1464} Hz.

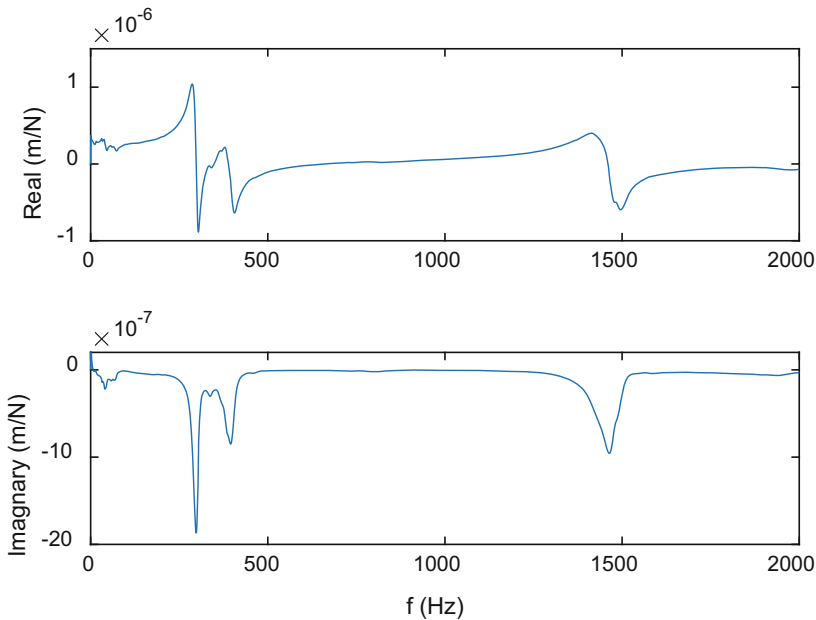


Fig. 3.52 Tool point FRF in the thrust direction

One approach for examining and quantifying unstable cutting is to convert the time domain data to the frequency domain using the Fast Fourier Transform (FFT) and then analyze the frequency content for a chatter frequency (i.e., content at a frequency other than the forcing frequency and its harmonics); see Sect. 6.1 for milling. As noted, a second approach is to use periodic sampling to determine the synchronicity of the MTP process signal with respect to the forcing frequency defined by the spindle speed and *OPR*. The two techniques were applied to MTP cutting test signals and compared. Results are presented for three chip widths (i.e., tube wall thicknesses), $b = \{1, 1.5, \text{ and } 2\}$ mm.

Let's review the FFT-based analyses first. For brevity, results are presented in Figs. 3.53 and 3.54 for thrust direction force only at 1 and 2 mm chip widths. Similar results were obtained for the acceleration and velocity signals. For the stable 1 mm chip width, the forcing frequency $(911(0.5)/60 = 7.6 \text{ Hz})$ appears, but no appreciable chatter frequency content is observed. For the unstable 2 mm chip width, a 406 Hz chatter frequency is seen (this corresponds to the 395 Hz cutting tool mode in Fig. 3.52).

Let's next consider the periodic sampling analyses. Results are again presented for thrust direction force at 1 mm and 2 mm chip widths. However, the signals are now sampled at the forcing frequency of 7.6 Hz. The samples are superimposed on the time domain signals as circles in Figs. 3.55 and 3.56. It is observed that the sampled points repeat for the 1 mm chip width, which indicates stable behavior. For the unstable 2 mm chip width, on the other hand, the points do not repeat.

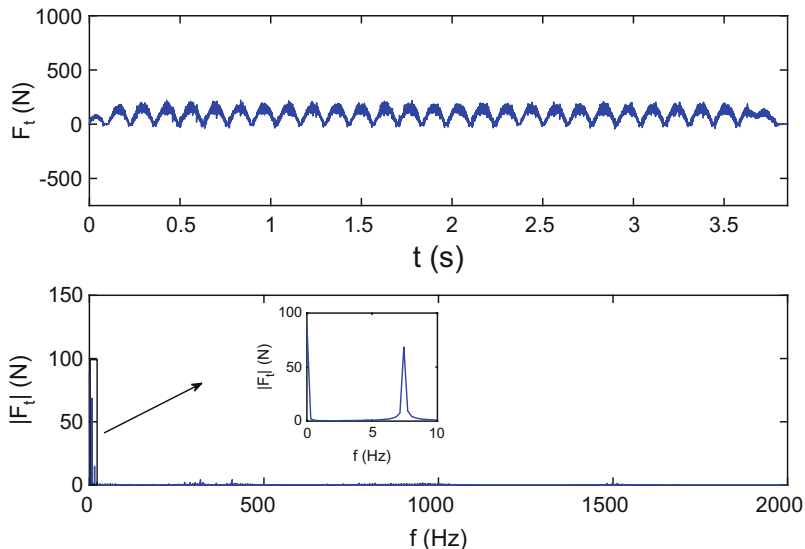


Fig. 3.53 (Top) Thrust direction force for 1 mm chip width. (Bottom) Frequency content

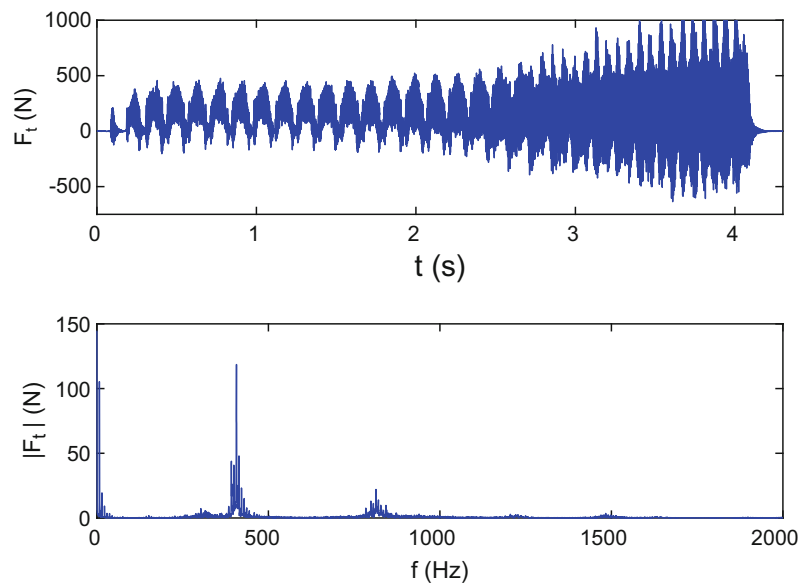


Fig. 3.54 (Top) Thrust direction force for 2 mm chip width. (Bottom) Frequency content

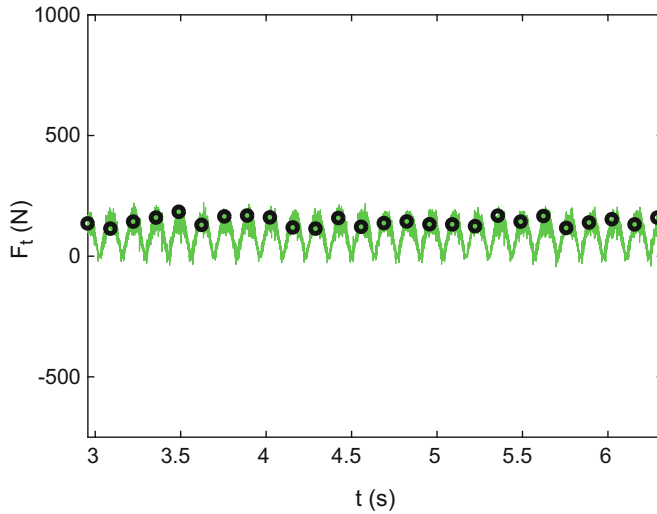


Fig. 3.55 Periodic sampling of the thrust direction force for 1 mm chip width. The time domain signal is represented by the solid line and the sampled points by the circles

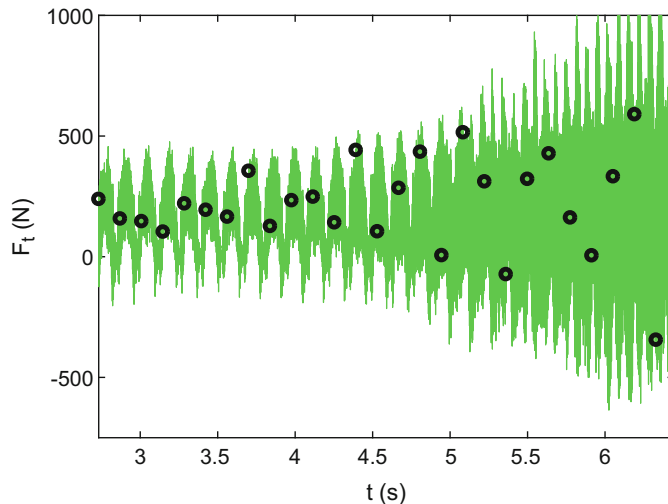


Fig. 3.56 Periodic sampling of the thrust direction force for 2 mm chip width

Let's now calculate the stability metric from Eq. 3.42 for all three process signals (force, acceleration, and velocity) at the three chip widths, $b = \{1, 1.5, \text{ and } 2\}$ mm. The results are summarized in Table 3.4. It is seen that the metric value, M , changes dramatically between stable ($b = 1$ mm and 1.5 mm) and unstable cutting conditions ($b = 2$ mm).

Table 3.4 Stability metric values for force, acceleration, and velocity signals from MTP cuts

Signal type	b (mm)	M
Force	1	18.1 N
Force	1.5	23.1 N
Force	2	109.0 N
Acceleration	1	137.3 m/s^2
Acceleration	1.5	141.6 m/s^2
Acceleration	2	272.0 m/s^2
Velocity	1	0.014 m/s
Velocity	1.5	0.014 m/s
Velocity	2	0.056 m/s

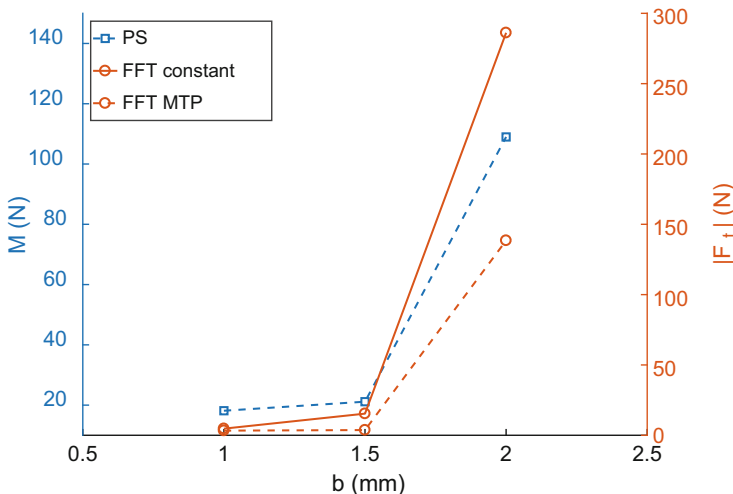


Fig. 3.57 Comparison of FFT (chatter frequency peak magnitude) and periodic sampling (metric value) results for thrust direction force

To conclude MTP stability study, let's compare the FFT and periodic sampling results for the MTP cuts. Additionally, we'll present results for constant feed rate machining trials (with all other conditions remaining the same) to compare the stability behavior between the constant feed and MTP cases. These results are presented in Figs. 3.57 through 3.59. We observe that the FFT and periodic sampling (PS) approaches demonstrate the same trends, i.e., the $b = 1$ mm and 1.5 mm cuts are stable with small values, while the $b = 2$ mm cut is unstable with a much larger value.

One interesting difference is that the constant feed cut with a chip width of 1.5 mm is only marginally stable as indicated by the elevated FFT amplitude at the chatter frequency for the acceleration and velocity signals. This identifies a potential difference in stability between constant feed and MTP cutting conditions. Note that no periodic sampling results are presented for the constant feed cut since there is no external forcing frequency in this case.

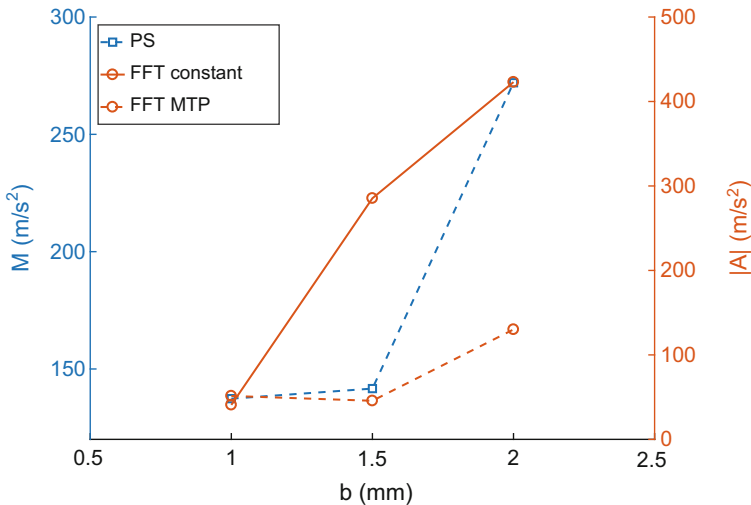


Fig. 3.58 Comparison of FFT (chatter frequency peak magnitude) and periodic sampling (metric value) results for thrust direction acceleration

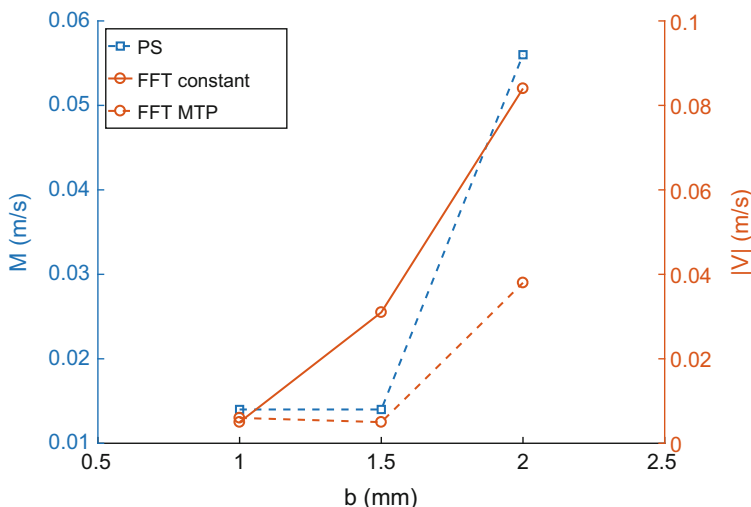


Fig. 3.59 Comparison of FFT (chatter frequency peak magnitude) and periodic sampling (metric value) results for thrust direction velocity

3.7 Process Damping

The analytical stability lobe diagram described in Sect. 3.3 offers an effective predictive capability for selecting stable spindle speed-chip width combinations. However, the increase in allowable chip width provided at spindle speeds near integer fractions of the system's dominant natural frequency is diminished

substantially at the low spindle speeds typically available for turning. For these low speeds, the stability lobes are closely spaced and $b_{\text{lim}} \approx b_{\text{lim,crit}}$. Fortunately, the process damping effect can serve to increase the chatter-free chip widths at these low speeds.⁴ This increased stability at low spindle speeds is particularly important for hard-to-machine materials that exhibit prohibitive tool wear at high cutting speeds (see Chap. 8).

Many researchers have investigated process damping in turning and milling operations. Early studies were carried out by Wallace and Andrew [19], Sisson and Kegg [20], Peters et al. [21], and Tlusty [22]. More recent efforts include:

- A plowing force model based on the interference between the tool and workpiece [23].
- The application of this plowing force model to milling operations [24–27].
- A mechanistic description of the contributions of shearing and plowing forces to process damping [28].
- A first-order Fourier transform representation of the interference between the tool and workpiece [29, 30].
- Numerical simulation of the nonlinear process damping stability model [31, 32].
- An experimental investigation of the nonlinear process damping stability model [33].
- Experimental identification of the process damping model [34, 35].

These studies described process damping as energy dissipation due to interference between the cutting tool clearance face and machined surface during relative vibrations between the tool and workpiece. It was shown that, given fixed system dynamics, the influence of process damping increases at low spindle speeds because the number of undulations on the machined surface between revolutions/teeth increases, which also increases the slope of the wavy surface. This, in turn, leads to increased interference and additional energy dissipation.

In this section, we describe an iterative, analytical stability analysis that incorporates the effects of process damping. The analytical stability limit is validated using time domain simulation.

3.7.1 Process Damping Description

As we discussed in Sect. 3.2, the variable component of the instantaneous cutting force may be written as:

$$F = K_s b(y(t - \tau) - y(t)), \quad (3.43)$$

where K_s is the specific cutting force, b is the chip width, $y(t - \tau)$ is the vibration amplitude in the surface normal direction from the previous revolution, and $y(t)$ is the

⁴T. Schmitz recognizes the significant contributions of C. Tyler to this section.

Fig. 3.60 The variable component of the cutting force, F , depends on the instantaneous chip thickness. The chip width is measured into the page; the mean chip thickness, h_m , is also identified

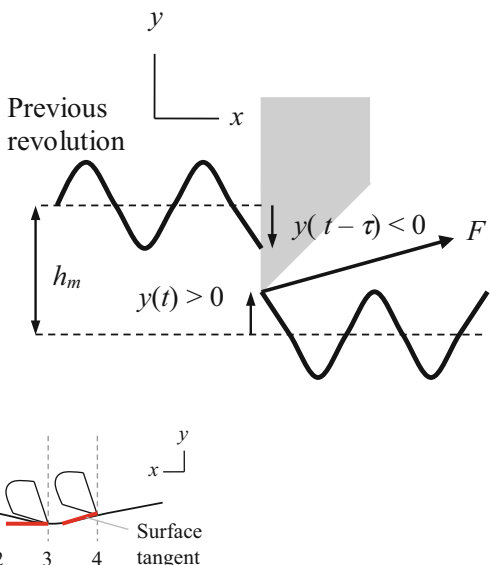


Fig. 3.61 Physical description of process damping. The clearance angle varies with the instantaneous surface tangent as the tool removes material on the sinusoidal surface

current vibration amplitude; see Fig. 3.60. The underlying assumption in Eq. 3.43 is that there is no phase shift between the variable force and chip thickness; this is indicated by the real values of K_s and b . However, for low cutting speeds, v , it has been shown that a phase shift can occur. This behavior is captured by the phenomenon referred to as process damping. Practically speaking, the effect of process damping is to enable significantly higher chip widths at low cutting speeds than our previous analytical stability analysis predicts.

To describe the physical mechanism for process damping, consider a tool moving on a sine wave while shearing away the chip [2]; see Fig. 3.61. Four locations are identified: (1) the clearance angle, γ , between the flank face of the tool and the work surface tangent is equal to the nominal relief angle for the tool; (2) γ is significantly decreased and can become negative (which leads to interference between the tool's relief face and surface); (3) γ is again equal to the nominal relief angle; and (4) γ is significantly larger than the nominal value.

At points 1 and 3 in Fig. 3.61, the clearance angle is equal to the nominal value, so there is no effect due to cutting on the sinusoidal path. However, at point 2 the clearance angle is small (or negative), and the thrust force in the surface normal direction, y , is increased. At point 4, on the other hand, the clearance angle is larger than the nominal, and the thrust force is decreased. Because the change in force caused by the sinusoidal path is 90 deg out of phase with the displacement and has the opposite sign from velocity, it is considered to be a viscous damping force (i.e., a force that is proportional to velocity). Given the preceding description, the process damping force, F_d , in the y direction can be expressed as a function of velocity, \dot{y} , chip width, cutting speed, and a constant C [35]. See Eq. 3.44.

$$F_d = -C \frac{b}{v} \dot{y} \quad (3.44)$$

As a final note regarding the sinusoidal path description in Fig. 3.61, the damping effect is larger for shorter vibration wavelengths, λ , because the slope of the sinusoidal surface increases and, subsequently, the variation in clearance angle increases. The wavelength equation, provided in Eq. 3.45, shows that lower cutting speeds or higher vibrating frequencies, f , gives shorter wavelengths and, subsequently, increased process damping.

$$\lambda = \frac{v}{f} \quad (3.45)$$



In a Nutshell

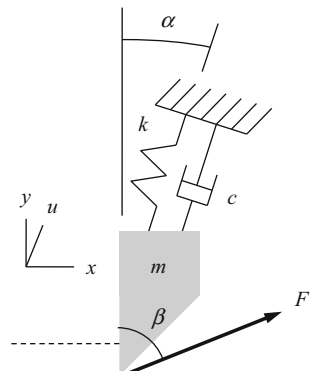
For a given chatter frequency (like the one that occurs at the bottom of a stability lobe), as the spindle speed gets slower, the wavelength of the vibration gets shorter. Eventually, the tool is too dull to reproduce the waviness and chatter stops. Interestingly, this correctly implies that worn tools are more resistant to chatter than sharp ones. Slowing the cutting operation enough will always stop chatter. Unfortunately, at low spindle speeds, there is often less power available.

3.7.2 Stability Algorithm

To describe the stability algorithm, let's consider the single degree of freedom turning model displayed in Fig. 3.62. As shown in Sects. 3.3 and 3.4, the limiting stable chip width, b_{lim} , for regenerative chatter is defined as:

$$b_{\text{lim}} = \frac{-1}{2K_s \text{Re}[\text{FRF}_{\text{orient}}]}, \quad (3.46)$$

Fig. 3.62 Single degree of freedom turning model



where $\text{FRF}_{\text{orient}}$ is the oriented frequency response function, $\text{FRF}_{\text{orient}} = \cos(\beta - \alpha) \cos(\alpha)\text{FRF}_u$. In this expression, β is the force angle relative to the surface normal, α is the angle between the u direction and the surface normal, and FRF_u is the frequency response function in the u direction. To relate the frequency-dependent b_{lim} vector to spindle speed, Ω , Eq. 3.47 is applied to define the relationship between Ω and the valid chatter frequencies, f_c (i.e., those frequencies where the real part of $\text{FRF}_{\text{orient}}$ is negative):

$$\frac{f_c}{\Omega} = N + \frac{\varepsilon}{2\pi}, \quad (3.47)$$

where $N = 0, 1, 2, \dots$ is the integer number of waves per revolution (i.e., the lobe number) and $\varepsilon = 2\pi - 2 \tan^{-1} \left(\frac{\text{Re}[\text{FRF}_{\text{orient}}]}{\text{Im}[\text{FRF}_{\text{orient}}]} \right)$ (rad) is the phase between the current vibration and the previous revolution.

To incorporate the process damping force (which acts in the y direction), we first project it into the u direction.

$$F_u = F_d \cos(\alpha) = -C \frac{b}{v} \dot{y} \cos(\alpha) = -\left(C \frac{b}{v} \cos(\alpha)\right) \dot{y} \quad (3.48)$$

The final form of Eq. 3.48 emphasizes that the u projection of the process damping force is effectively a viscous damping term. Therefore, the force can be incorporated in the traditional regenerative chatter stability analysis by modifying the structural damping in FRF_u . As shown in Fig. 3.62, the single degree of freedom, lumped parameter dynamic model can be described using the mass, m , viscous damping coefficient, c , and spring stiffness, k . In the absence of process damping, the equation of motion in the u direction is:

$$m\ddot{u} + c\dot{u} + ku = F \cos(\beta - \alpha). \quad (3.49)$$

The corresponding frequency response function in the u direction is:

$$G_u = \frac{U}{F \cos(\beta - \alpha)} = \frac{1}{-m\omega^2 + ic\omega + k}, \quad (3.50)$$

where ω is the excitation frequency (rad/s). When process damping is included, however, the equation of motion becomes:

$$m\ddot{u} + c\dot{u} + ku = F \cos(\beta - \alpha) - \left(C \frac{b}{v} \cos(\alpha)\right) \dot{y}. \quad (3.51)$$

Replacing \dot{y} in Eq. 3.51 with $\cos(\alpha)\dot{u}$ gives:

$$m\ddot{u} + c\dot{u} + ku = F \cos(\beta - \alpha) - \left(C \frac{b}{v} \cos^2(\alpha)\right) \dot{u}. \quad (3.52)$$

Rewriting Eq. 3.52 to combine the velocity terms yields:

$$m\ddot{u} + \left(c + \left(C \frac{b}{v} \cos^2(\alpha) \right) \right) \dot{u} + ku = F \cos(\beta - \alpha), \quad (3.53)$$

where the new viscous damping coefficient is $c_{\text{new}} = c + C \frac{b}{v} \cos^2(\alpha)$. Replacing the original damping coefficient, c , (from the structure dynamics only) with c_{new} enables process damping to be incorporated in the analytical stability model. The new frequency response function is:

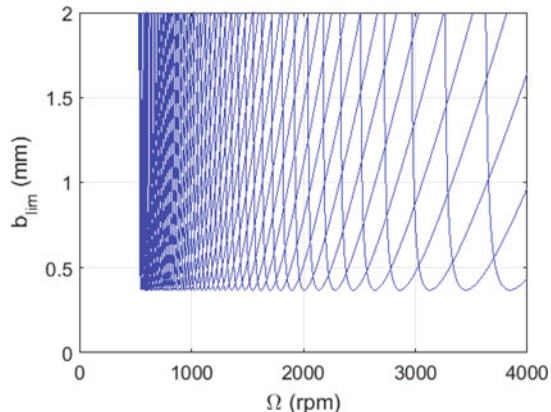
$$G_u = \frac{U}{F \cos(\beta - \alpha)} = \frac{1}{-m\omega^2 + ic_{\text{new}}\omega + k}. \quad (3.54)$$

However, the new damping value is a function of both the spindle speed-dependent limiting chip width and the cutting speed. The cutting speed (m/s) depends on the spindle speed (rpm) and workpiece diameter (m) according to $v = \frac{\pi d}{60} \Omega$. Therefore, the b and Ω vectors must be known in order to implement the new damping value. This leads to the converging nature of the stability analysis that incorporates process damping. We complete the following steps for each lobe number, or N value (see Eq. 3.47):

1. The analytical stability boundary is calculated with no process damping to identify initial b and Ω vectors.
2. These vectors are used to determine the corresponding c_{new} vector.
3. The stability analysis is repeated with the new damping value to determine updated b and Ω vectors.
4. The process is repeated until the stability boundary converges [36–42].

Example 3.7 Single Degree of Freedom Turning Stability Analysis with Process Damping To demonstrate the approach, let's consider the model in Fig. 3.62 with $\alpha = 0$, $k = 6.48 \times 10^6$ N/m, $m = 0.561$ kg, $c = 145$ N s/m, $K_s = 2927 \times 10^6$ N/m², $\beta = 61.79$ deg, and $d = 0.035$ m. The stability boundary with no process damping ($C = 0$) is displayed in Fig. 3.63 for $N = 0$ to 60. We observe that the limiting chip

Fig. 3.63 Stability diagram for single degree of freedom model from Fig. 3.62 with $\alpha = 0$, $k = 6.48 \times 10^6$ N/m, $m = 0.561$ kg, $c = 145$ N s/m, $K_s = 2927 \times 10^6$ N/m², $\beta = 61.79$ deg, $d = 0.035$ m, and $C = 0$



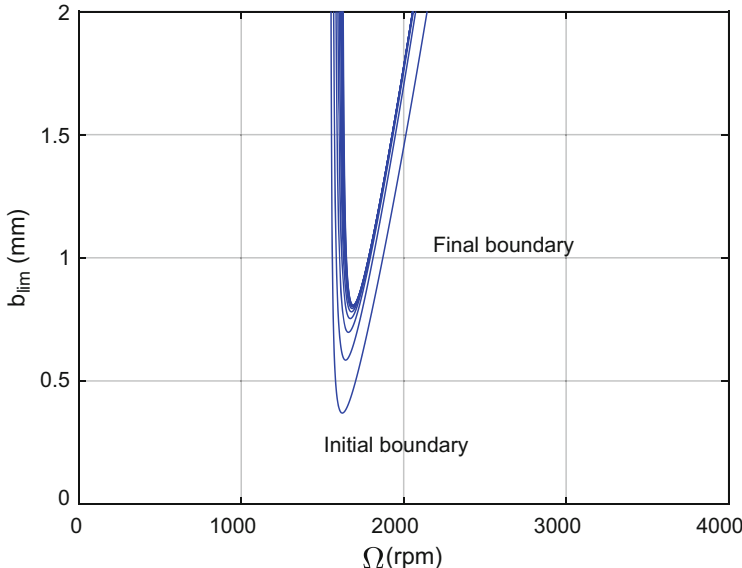


Fig. 3.64 Convergence demonstration ($N = 20$, 10 iterations) for single degree of freedom model from Fig. 3.62 with $\alpha = 0$, $k = 6.48 \times 10^6$ N/m, $m = 0.561$ kg, $c = 145$ N s/m, $K_s = 2927 \times 10^6$ N/m², $\beta = 61.79$ deg, $d = 0.035$ m, and $C = 6.11 \times 10^5$ N/m

width approaches the asymptotic stability limit of 0.37 mm for spindle speeds below 1000 rpm. The MATLAB® program used to produce this figure is provided with the textbook as p_3_7_1.m.

Results of the converging procedure with process damping for the $N = 20$ stability boundary are provided in Fig. 3.64. Converging behavior is observed for the 10 iterations as the lobes move up and slightly to the right. Although a convergence criterion, such as a threshold percent difference between subsequent minimum values, could be implemented, we will apply a practical selection of 20 iterations to ensure convergence. Figure 3.65 displays the new stability diagram for $N = 0$ to 60 with $C = 6.11 \times 10^5$ N/m. The MATLAB® programs used to produce these figures are provided with the textbook as p_3_7_2.m and p_3_7_3.m.

We'll next extend the process damping model to consider vibration modes in two orthogonal directions as shown in Fig. 3.66. The analysis procedure is similar, but there are now two new damping values to be calculated: $c_{\text{new},1} = c_1 + C_v^b \cos(\alpha_2)^2$ for the u_1 direction and $c_{\text{new},2} = c_2 + C_v^b \cos(\alpha_1)^2$ for the u_2 direction. We use these two damping values to update the FRF_{u_1} and FRF_{u_2} frequency response functions; see Eq. 3.54. The oriented frequency response function for this case is $\text{FRF}_{\text{orient}} = \cos(\beta - \alpha_1) \cos(\alpha_1) \text{FRF}_{u_1} + \cos(\beta + \alpha_2) \cos(\alpha_2) \text{FRF}_{u_2}$.

Example 3.8 Comparison with Time Domain Simulation Let's compare our analytical stability predictions to time domain simulation results. We'll update the turning

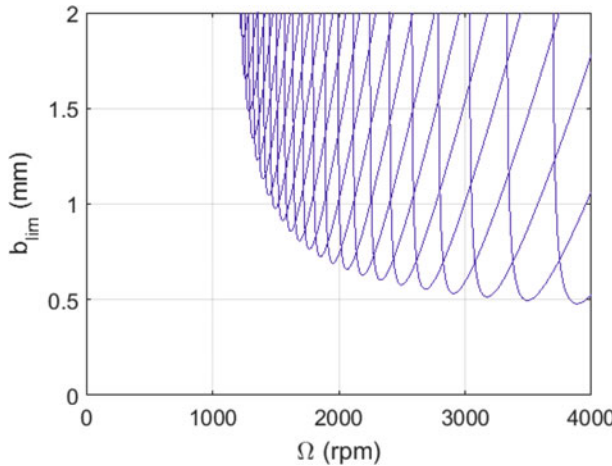
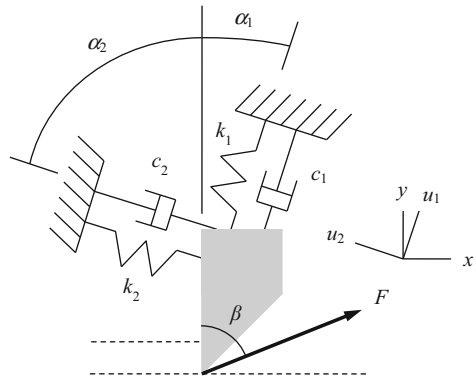


Fig. 3.65 Stability diagram for single degree of freedom model from Fig. 3.62 with $\alpha = 0$, $k = 6.48 \times 10^6$ N/m, $m = 0.561$ kg, $c = 145$ N s/m, $K_s = 2927 \times 10^6$ N/m², $\beta = 61.79$ deg, $d = 0.035$ m, and $C = 6.11 \times 10^5$ N/m

Fig. 3.66 Two degree of freedom turning model



time domain simulation from Sect. 3.5 to include process damping. Let's again consider the model in Fig. 3.62 with $\alpha = 0$, $k = 6.48 \times 10^6$ N/m, $m = 0.561$ kg, $c = 145$ N s/m, $K_s = 2927 \times 10^6$ N/m², $\beta = 61.79$ deg, and $d = 0.035$ m. We incorporate process damping by including the process damping force projection in the u direction as shown in Eq. 3.52.

$$F_u = F \cos(\beta - \alpha) - C * b / v * (\cos(\alpha))^2 * \text{vel}_u;$$

In this equation, F_u is the force in the u direction, and vel_u is the velocity in the u direction. This velocity is determined from the numerical integration. Figure 3.67 shows the simulation results for a spindle speed of 1000 rpm and chip width of 1 mm with $C = 0$ (no process damping). As predicted by Fig. 3.63, the cut is

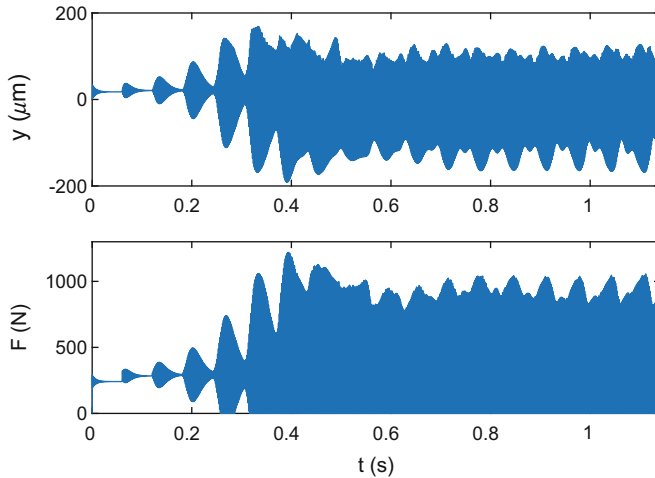


Fig. 3.67 Time domain simulation results for $\{\Omega, b\} = \{1000 \text{ rpm}, 1 \text{ mm}\}$ with $C = 0$

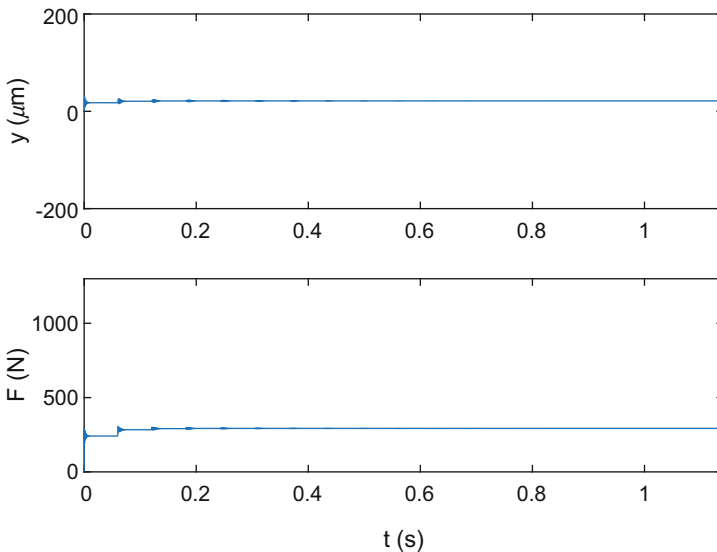


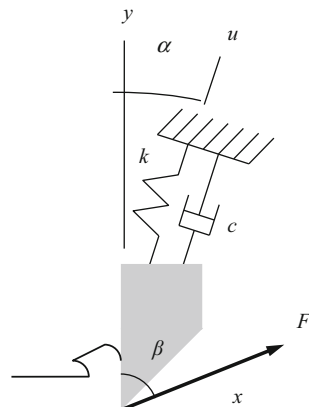
Fig. 3.68 Time domain simulation results for $\{\Omega, b\} = \{1000 \text{ rpm}, 1 \text{ mm}\}$ with $C = 6.11 \times 10^5 \text{ N/m}$. The vertical axis scales were selected to match Fig. 3.67

unstable because $b > b_{\lim}$ at 1000 rpm. With the inclusion of process damping, $C = 6.11 \times 10^5 \text{ N/m}$, however, the cut is now stable as displayed in Fig. 3.68. This supports Fig. 3.65, which shows that a $\{\Omega, b\}$ pair of $\{1000 \text{ rpm}, 1 \text{ mm}\}$ is in the process damping stable zone. The MATLAB® program used to produce these figures is p_3_8_1.m.

Exercises

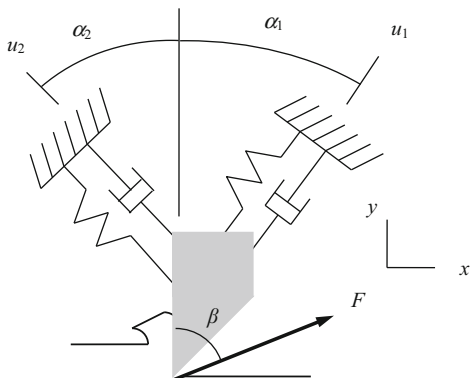
1. For the turning schematic shown in Fig. 3.69, complete parts (a) through (f). For the single degree of freedom dynamics, the mass is 2 kg, the damping ratio is 0.05, and the stiffness is 2×10^7 N/m. The u direction is oriented at an angle, α , of 35 deg relative to the surface normal, y . The force model parameters are $K_s = 1500$ N/mm² and $\beta = 70$ deg.

Fig. 3.69 Turning model with flexible tool



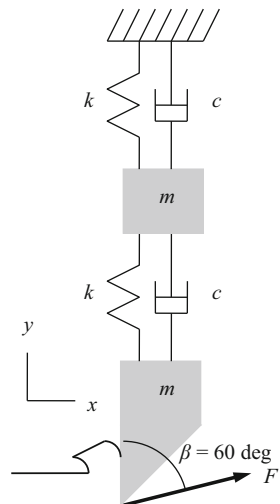
- (a) Calculate the directional orientation factor. Using this value, compute and plot the real and imaginary parts (in m/N) of the oriented frequency response function versus frequency (in Hz).
 - (b) Determine the minimum value of the real part of the oriented frequency response function and the corresponding chatter frequency. Calculate $b_{\lim, \text{crit}}$.
 - (c) Determine the spindle speed (in rpm) corresponding to the stability peak defined by the intersection of the $N = 0$ and $N = 1$ stability lobes.
 - (d) Find the spindle speed (in rpm) corresponding to the minimum stability limit for the $N = 0$ lobe.
 - (e) Determine the spindle speed (in rpm) corresponding to the stability peak defined by the intersection of the $N = 3$ and $N = 4$ stability lobes.
 - (f) Plot the first four stability lobes ($N = 0$ to 3) for this system. Use b_{\lim} units of mm and spindle speed units of rpm.
2. Using the turning schematic shown in Fig. 3.70, complete parts (a) through (d). For the u_1 direction, the mass is 10 kg, the damping is 170 N s/m, and the stiffness is 7×10^6 N/m. The u_1 direction is oriented at an angle, α_1 , of 60 deg relative to the surface normal, y . For the u_2 direction, the mass is 12 kg, the damping is 1700 N s/m, and the stiffness is 5×10^7 N/m. The u_2 direction is oriented at an angle, α_2 , of 30 deg relative to the y direction. The force model parameters are $K_s = 2000$ N/mm² and $\beta = 60$ deg.

Fig. 3.70 Turning model with a single degree of freedom in both the u_1 and u_2 directions



- Compute the directional orientation factors, μ_1 and μ_2 . Plot the real and imaginary parts (in m/N) of the oriented frequency response function versus frequency (in Hz).
 - Determine the minimum value of the real part of the oriented frequency response function and the corresponding chatter frequency. Calculate $b_{\text{lim,crit}}$.
 - Find the spindle speed (in rpm) corresponding to the minimum stability limit for the $N = 2$ lobe.
 - Plot the first five stability lobes ($N = 0$ to 4) for this system. Use b_{lim} units of mm and spindle speed units of rpm.
3. Considering the turning model shown in Fig. 3.71, determine the critical stability limit if $K_s = 750 \text{ N/mm}^2$. For both lumped parameter degrees of freedom, the mass is 1 kg, the stiffness is $7 \times 10^6 \text{ N/m}$, and the damping is 200 N s/m.

Fig. 3.71 Two degree of freedom turning model



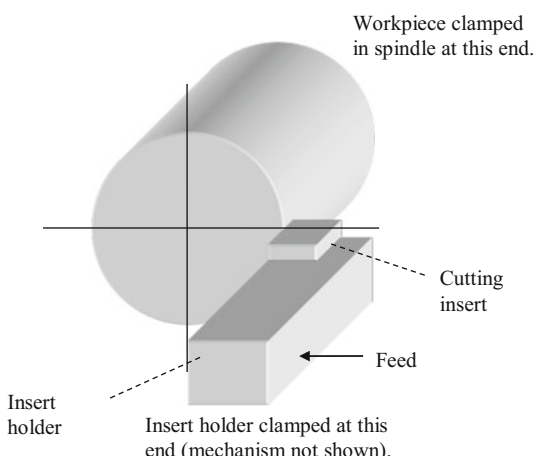
4. Complete time domain simulations for the turning model described in Exercise 2. Evaluate the following points for stable or unstable behavior. Use a mean chip thickness (feed per revolution) of 0.15 mm and carry out your simulations for 25 revolutions.

Ω (rpm)	b (mm)
2150	0.1
2150	0.5
2500	0.1
2500	0.5
2930	0.1
2930	0.5
3750	0.1
3750	0.5
4600	0.1
4600	0.5

- Superimpose your results on the stability lobe diagram from Exercise 2, part (d). Use a circle for stable operating points and an “x” for unstable points.
5. For the facing (turning) operation shown in Fig. 3.72, identify all items on the picture:

- The direction the spindle rotates
- The chip width, b
- The tangential, F_t , and normal, F_n , direction cutting force components that act on the insert/holder
- The resultant cutting force, F
- The force angle, β
- The surface normal direction (for chip thickness variations)

Fig. 3.72 Facing operation schematic



6. For the SDOF turning model shown in Fig. 3.73 with the following parameters, complete parts (a) through (c).

$$k = 2 \times 10^6 \text{ N/m}$$

$$m = 2 \text{ kg}$$

$$c = 120 \text{ N s/m}$$

$$\alpha = 20 \text{ deg}$$

$$\beta = 60 \text{ deg}$$

$$K_s = 750 \text{ N/mm}^2 \text{ (aluminum alloy)}$$

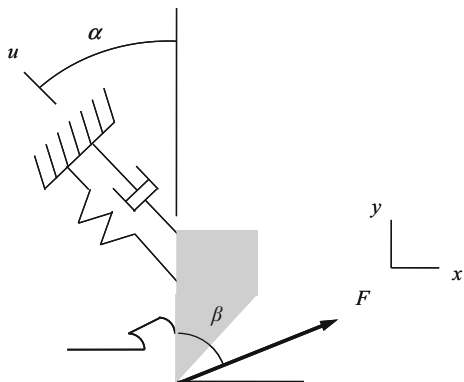
$$h_m = 0.2 \text{ mm/rev}$$

(a) Compute $b_{\lim, \text{crit}}$ (in mm).

(b) Compute the best spindle speed (in rpm) for the $N = 3$ stability lobe.

(c) Compute the approximate chatter frequency (in Hz) at the worst speed for the $N = 4$ stability lobe.

Fig. 3.73 Turning model with a single degree of freedom in the u direction



References

1. Trent, E., & Wright, P. (2000). *Metal cutting* (4th ed.). Boston, MA: Butterworth-Heinemann.
2. Tlusty, G. (2000). *Manufacturing equipment and processes*. Upper Saddle River, NJ: Prentice-Hall.
3. Altintas, Y. (2000). *Manufacturing automation: Metal cutting mechanics, machine tool vibrations, and CNC design*. Cambridge: Cambridge University Press.
4. Stephenson, D., & Agapiou, J. (1997). *Metal cutting theory and practice*. New York, NY: Marcel Dekker, Inc.
5. Schmitz, T. (2015). The microphone feedback analogy for chatter in machining. *Shock and Vibration, 2015*, 976819.
6. Zhang, Y. Z. (1980). Chip curl, chip breaking, and chip control of difficult-to-cut materials. *Annals of the CIRP, 29*(1), 79–83.
7. Adams, D. (2008) *Chip breaking in turning operations using CNC toolpaths*. MS thesis, UNC Charlotte, Charlotte, NC.
8. Assaid, T. S. (2010). *Generation, measurement, and assessment of modulated tool-path chip breaking in CNC turning processes*. MS thesis, UNC Charlotte, Charlotte, NC.

9. Tursky, D. (2010). *Chip breaking through oscillating CNC toolpaths and its effect on chip length, tool wear and machine dynamics*. MS thesis, UNC Charlotte, Charlotte, NC.
10. Berglind, L., & Zeigert, J. (2013). Chip breaking parameter selection for constant surface speed machining. In: *ASME 2013 international mechanical engineering congress and exposition. Vol. 2B: Advanced manufacturing*, San Diego, CA.
11. Berglind, L., & Zeigert, J. (2015). Modulated tool path (MTP) machining for threading applications. *Procedia Manufacturing*, 1, 546–555.
12. Copenhaver, R., Rubeo, M., Guzorek, S., Landge, S., Smith, K. S., Ziegert, J., & Schmitz, T. (2017). A fundamental investigation of modulated tool path turning mechanics. *Procedia Manufacturing*, 10, 159–170.
13. Rubeo, M., Copenhaver, R., Landge, S., & Schmitz, T. (2016). Experimental platform for in-process metrology during orthogonal turning, American Society for Precision Engineering Annual Meeting, October 23–28, Portland, OR.
14. Schmitz, T., & Smith, K. S. (2012). *Mechanical vibrations: Modeling and measurement*. New York, NY: Springer.
15. Delio, T., Tlusty, J., & Smith, S. (1992). Use of audio signals for chatter detection and control. *Journal of Engineering for Industry*, 114, 146–157.
16. Honeycutt, A., & Schmitz, T. (2016). A new metric for automated stability identification in time domain milling simulation. *Journal of Manufacturing Science and Engineering*, 138(7), 074501.
17. Honeycutt, A., & Schmitz, T. (2017). Milling stability interrogation by subharmonic sampling. *Journal of Manufacturing Science and Engineering*, 139(4), 041009.
18. Smith, S. T. (2000). *Flexures: elements of elastic mechanisms*. Boca Raton, FL: CRC Press.
19. Wallace, P. W., & Andrew, C. (1965). Machining forces: Some effects of tool vibration. *Journal of Mechanical Engineering Science*, 7, 152–162.
20. Sisson, T. R., & Kegg, R. L. (1969). An explanation of low-speed chatter effects. *Journal of Engineering for Industry*, 91, 951–958.
21. Peters, J., Vanherck, P., & Van Brussel, H. (1971). The measurement of the dynamic cutting coefficient. *Annals of the CIRP*, 21(2), 129–136.
22. Tlusty, J. (1978). Analysis of the state of research in cutting dynamics. *Annals of the CIRP*, 27 (2), 583–589.
23. Wu, D. W. (1989). A new approach of formulating the transfer function for dynamic cutting processes. *Journal of Engineering for Industry*, 111, 37–47.
24. Elbestawi, M. A., Ismail, F., Du, R., & Ullagaddi, B. C. (1994). Modelling machining dynamics damping in the tool-workpiece interface. *Journal of Engineering for Industry*, 116, 435–439.
25. Lee, B. Y., Trang, Y. S., & Ma, S. C. (1995). Modeling of the process damping force in chatter vibration. *International Journal of Machine Tools and Manufacture*, 35, 951–962.
26. Abraria, F., Elbestawi, M. A., & Spencea, A. D. (1998). On the dynamics of ball end milling: Modeling of cutting forces and stability analysis. *International Journal of Machine Tools and Manufacture*, 38, 215–237.
27. Ahmadi, K., & Ismail, F. (2010). Machining chatter in flank milling. *International Journal of Machine Tools and Manufacture*, 50, 75–85.
28. Huang, C. Y., & Wang, J. J. (2007). Mechanistic modeling of process damping in peripheral milling. *Journal of Manufacturing Science and Engineering*, 129, 12–20.
29. Chiou, Y. S., Chung, E. S., & Liang, S. Y. (1995). Analysis of tool wear effect on chatter stability in turning. *International Journal of Mechanical Sciences*, 37, 391–404.
30. Chiou, R. Y., & Liang, S. Y. (1998). Chatter stability of a slender cutting tool in turning with tool wear effect. *International Journal of Machine Tools and Manufacture*, 38, 315–327.
31. Chandiramani, N. K., & Pothala, T. (2006). Dynamics of 2-dof regenerative chatter during turning. *Journal of Sound and Vibration*, 290, 448–464.
32. Jemielniak, K., & Widota, A. (1989). Numerical simulation of non-linear chatter vibration in turning. *International Journal of Machine Tools and Manufacture*, 29, 239–247.

33. Ahmadi, K., & Ismail, F. (2010). Experimental investigation of process damping nonlinearity in machining chatter. *International Journal of Machine Tools and Manufacture*, 50, 1006–1014.
34. Budak, E., & Tunc, L. T. (2009). A new method for identification and modeling of process damping in machining. *Journal of Manufacturing Science and Engineering*, 131(051019), 1–10.
35. Altintas, Y., Eynian, M., & Onozuka, H. (2008). Identification of dynamic cutting force coefficients and chatter stability with process damping. *Annals of the CIRP*, 57(1), 371–374.
36. Tyler, C., & Schmitz, T. (2012). Process damping analytical stability analysis and validation. *Transactions of the NAMRI/SME*, 40, 37–47.
37. Tyler, C., & Schmitz, T. (2013). Analytical process damping stability prediction. *Journal of Manufacturing Processes*, 15, 69–76.
38. Tyler, C., Karandikar, J., & Schmitz, T. (2013). Process damping coefficient identification using Bayesian inference. *Transactions of the NAMRI/SME*, 41, 1–8.
39. Tyler, C., & Schmitz, T. (2014). Process damping milling model database. *Transactions of the NAMRI/SME*, 42, 1–10.
40. Tyler, C., Troutman, J., & Schmitz, T. (2015). Radial depth of cut stability lobe diagrams with process damping effects. *Precision Engineering*, 40, 318–324.
41. Tyler, C., Troutman, J., & Schmitz, T. (2016). A coupled dynamics, multiple degree of freedom process damping model, Part 1: Turning. *Precision Engineering*, 46, 65–72.
42. Tyler, C., Troutman, J., & Schmitz, T. (2016). A coupled dynamics, multiple degree of freedom process damping model, Part 2: Milling. *Precision Engineering*, 46, 73–80.

Chapter 4

Milling Dynamics



If we knew what it was we were doing, it would not be called research, would it?

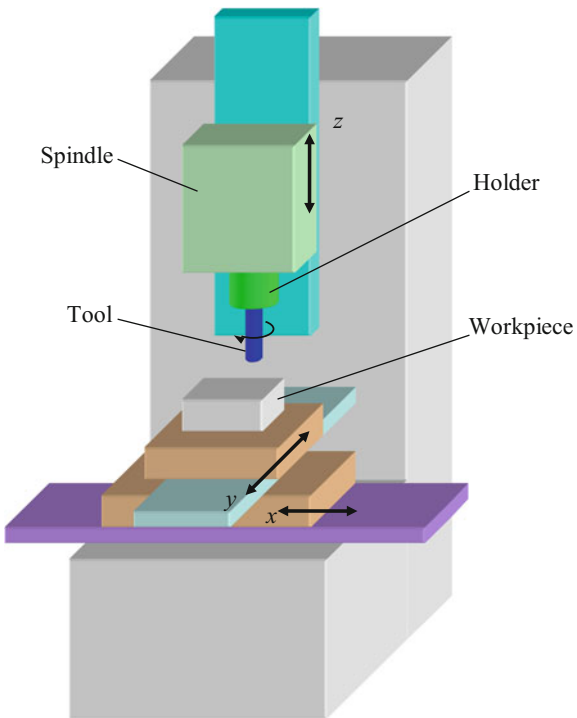
—Albert Einstein

In Chap. 3, we applied knowledge of the tool point dynamics from modal analysis (Chap. 2) to predict regenerative chatter in turning using stability lobe diagrams and time domain simulation. This chapter follows a similar format, but our focus is milling. We again develop force expressions, discuss surface regeneration, and present the relevant equations and examples for analytical, frequency domain stability lobe diagrams. This is followed by a description of time domain simulations that predict forces and displacements during milling for selected operating parameters, including a periodic sampling approach for automated stability identification. We continue with a description of the experimental determination of cutting force coefficients, which are required for both the analytical stability lobe diagrams and the numerical simulations. The chapter concludes with a description of process damping, which tends to increase milling stability at low cutting speeds.

4.1 Milling Description

In milling, a rotating tool with defined cutting edges is moved relative to a workpiece in order to remove material and obtain the desired workpiece geometry and dimensions. The tool is typically mounted in a holder which is attached to the spindle. The spindle provides the tool's rotational speed, torque, and power. Multiple axes are then used to manipulate the tool-holder-spindle relative to the workpiece. At minimum, three linear axes are generally arranged in a mutually perpendicular configuration; these linear motions are traditionally labeled x , y , and z with the latter indicating the tool axis. However, milling machines are also available with additional rotational axes to provide contouring capabilities for non-prismatic parts. In this case, the rotational degrees of freedom are typically labeled A , B , and C , which indicate rotations about the x , y , and z axes, respectively. As with lathes, milling

Fig. 4.1 Schematic of vertical spindle milling machine. The tool is clamped in a holder which is attached to the rotating spindle. The tool-holder-spindle is moved relative to the workpiece using the three orthogonal axes to remove material in the subtractive milling process



machines may be manual or computer numerically controlled. Figure 4.1 shows an example representation of a three axis milling machine. A vertical spindle configuration is shown, although horizontal spindle geometries are also available. The latter is often preferred in high-speed milling applications because the chips fall from the workpiece for later collection.

Cutting tools and holders are available in many varieties that are tailored to specific applications, such as peripheral, end, contour, and face milling. For analysis purposes, we will focus on peripheral and endmilling operations, although the concepts can be extended to other operations as well. Endmills may be loosely categorized according to their free-end geometry, including square, ball nose, and bull nose. Square endmills have a cylindrical shape with a small end radius so that the profile is rectangular. Ball nose endmills are hemispherical at their free end to enable contouring of internal cavities and external, three-dimensional non-prismatic features. Endmills with a bull nose geometry have larger end radii than square endmills, but are not fully hemispherical. Similar to ball nose endmills, they also enable contouring. See Fig. 4.2.

Endmills may have the cutting teeth ground directly into the body or may have replaceable inserts clamped to a cylinder. Typical materials for ground cutters include high-speed steel and sintered carbide, while inserted cutters traditionally use steel bodies with carbide or ceramic inserts. Coatings designed to improve tool life are also often applied in single or multiple layers; see Sect. 8.2. For either ground

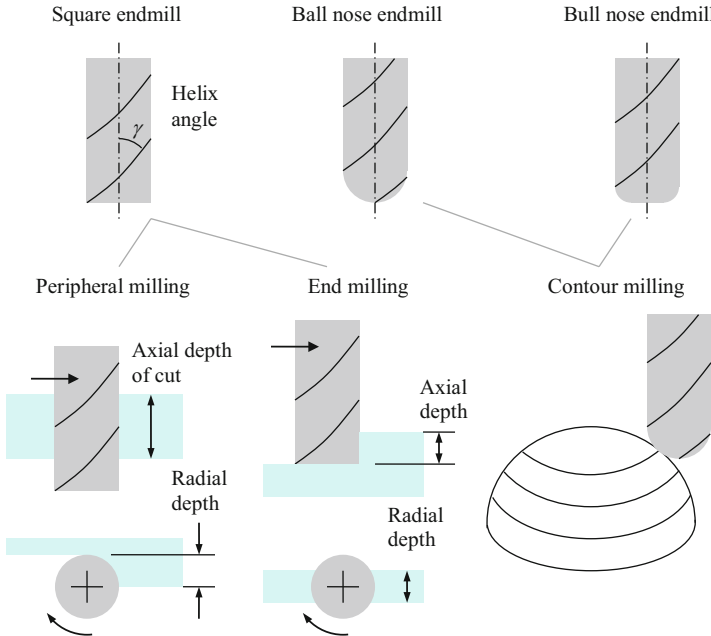


Fig. 4.2 Example milling applications and tool geometries

or solid body endmills, the cutting edge is not usually parallel to the tool's rotating axis (referred to as "straight" teeth). Rather, the edge is inclined so that the chip to be removed is spread over an increased length and the cutting edge pressure is reduced. For solid body cutters, the edge is typically ground with a helical profile around the tool periphery using a constant helix angle, γ . The chip width, \tilde{b} , is then related to the axial depth of cut, b , as:

$$\tilde{b} = \frac{b}{\cos(\gamma)}. \quad (4.1)$$

This will have implications for the surface location error calculations described in Chap. 5. However, for now we will neglect the cutting edge's helical shape and assume straight cutter teeth ($\tilde{b} = b$ for $\gamma = 0$). This simplification enables us to obtain some insight into the milling operation and is reasonable if the axial depth of cut is small. A second assumption that we will apply is referred to as the "circular tool path" approximation. The actual path followed by any point on the cutter's periphery as the tool rotates during translation is cycloidal in nature. However, because the linear advance is generally small relative to the product of the rotational speed and tool radius, the path may be approximated as a series of circles, each offset by the feed per tooth, f_t , so that the time dependent chip thickness can be expressed as:

$$h = f_t \sin(\phi), \quad (4.2)$$

Fig. 4.3 Cutter angle definition

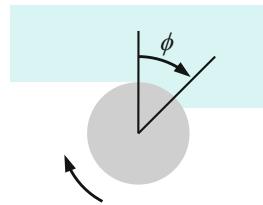
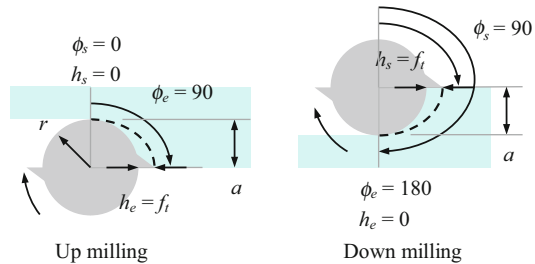


Fig. 4.4 Chip thickness variation for up and down milling ($a = r$)



where ϕ is the tool's rotational angle; see Fig. 4.3. The feed per tooth is described in terms of the linear feed, f , spindle speed, Ω , and number of teeth on the cutter, N_t , in Eq. 4.3. Typical units for these variables are mm/tooth for feed per tooth, rpm for spindle speed, mm/min for linear feed rate, and teeth/rev for number of teeth. An improved analytical model for chip thickness is provided in [1], but the circular tool path approximation offers sufficient accuracy for our purposes.

$$f_t = \frac{f}{\Omega N_t} \quad (4.3)$$

As Eq. 4.2 shows, the chip thickness in milling varies periodically, even in the absence of tool or workpiece vibrations. It is zero when $\phi = 0$ and 180 deg and maximum (equal to f_t) when $\phi = 90$ deg. Figure 4.4 shows this variation for both conventional, or up, and climb, or down, peripheral milling operations. Note that the chip thickness increases during up milling and decreases in down milling. In both cases, it is zero for $180 < \phi < 360$ deg because no cutting occurs between these angles. The entry, or start, angle for up milling is $\phi_s = 0$, while the exit angle, ϕ_e , depends on the radial depth of cut, a , and tool radius, r :

$$\phi_e = \cos^{-1}\left(\frac{r - a}{r}\right). \quad (4.4)$$

In down milling, the exit angle is $\phi_e = 180$ deg. Similar to up milling, the start angle is written as a function of the radial depth and tool radius. See Eq. 4.5 and Fig. 4.5.

$$\phi_s = 180 - \theta = 180 - \cos^{-1}\left(\frac{r - a}{r}\right) \text{ (deg)} \quad (4.5)$$

Fig. 4.5 Exit and start angle geometry for up and down milling

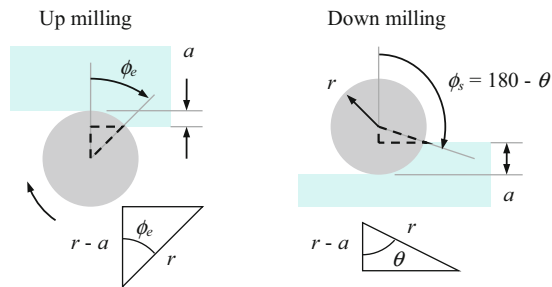
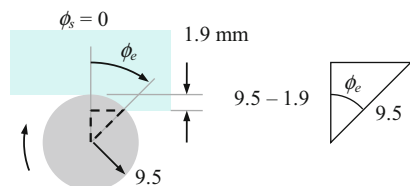


Fig. 4.6 Exit angle for 10% radial immersion up milling cut



In a Nutshell

Whereas in turning operations the chip thickness and chip width are fixed, this is not the case in milling. In a straight slotting cut, the chip thickness encountered by each tooth varies continuously as that tooth enters and exits the cut. In pocket milling, the radial depth of cut may also change. Finally, in sculptured surface milling, the axial depth of cut may vary as well. Even though the motion of the rotating tool with respect to the workpiece may be relatively simple to visualize, the exact conditions of the cutting edge engagement with the workpiece can be surprisingly complicated.

Example 4.1 Start and Exit Angles for Up Milling Consider the peripheral up milling cut shown in Fig. 4.6 where the radial depth of cut is 1.9 mm. For a 19 mm diameter (9.5 mm radius) cutter, we will refer to this as a 10% radial immersion cut. (Using this notation, a slotting cut with a radial depth of 19 mm would be described as 100% radial immersion for the 19 mm diameter cutter.) Because it is an up milling cut, the start angle is $\phi_s = 0$. The exit angle is:

$$\phi_e = \cos^{-1}\left(\frac{9.5 - 1.9}{9.5}\right) = \cos^{-1}(0.8) = 37 \text{ deg}$$

and the instantaneous chip thickness between the start and exit angles can be defined by Eq. 4.2.

As with turning, let's begin our discussion of cutting force by assuming a rigid tool and workpiece, that is, by considering the geometry alone. Unlike turning, however, the cutting force is not constant under these conditions. Rather, it is a function of the cutting angle. As we'll see, the cutting force expression is complicated by the chip thickness variation with cutter angle, the number of teeth

Fig. 4.7 Cutting force geometry for milling

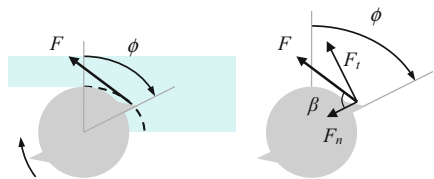
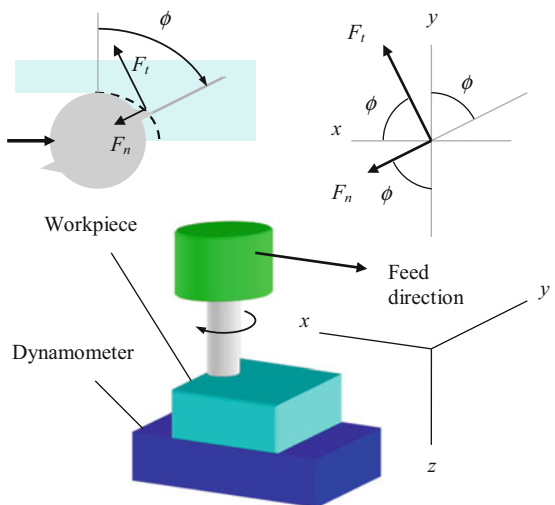


Fig. 4.8 Projection geometry for tangential and normal cutting force components into x and y directions



simultaneously engaged in the cut at any instant, and the projection of the cutting force into a nonrotating coordinate frame. Similar to Eqs. 3.1 through 3.3, we can express the cutting force on any cutting edge as a function of the chip area and specific force:

$$F = K_s A = K_s b h. \quad (4.6)$$

The normal and tangential components can be written using Eqs. 4.7 and 4.8, as demonstrated in Fig. 4.7:

$$F_n = \cos(\beta)F = \cos(\beta)K_s b h = k_n b h \quad \text{and} \quad (4.7)$$

$$F_t = \sin(\beta)F = \sin(\beta)K_s b h = k_t b h. \quad (4.8)$$

This figure shows the cutting force exerted on a single tooth, where the force is described in a coordinate frame that rotates with the tool. For measurement purposes, however, it is generally more convenient to express the force in a fixed frame. For example, the workpiece may be mounted on a cutting force dynamometer and the x, y, and z direction force components recorded during milling (Fig. 4.8). To describe these forces analytically, we must project the normal and tangential components into the x and y directions using the cutter angle ϕ . Based on our assumption of straight cutter teeth, we may neglect the z direction component.

$$F_x = F_t \cos(\phi) + F_n \sin(\phi) \quad (4.9)$$

$$F_y = F_t \sin(\phi) - F_n \cos(\phi) \quad (4.10)$$

We can now substitute for the tangential and normal force components in Eqs. 4.9 and 4.10. This yields:

$$F_x = k_t b f_t \sin(\phi) \cos(\phi) + k_n b f_t \sin(\phi) \sin(\phi) \text{ and} \quad (4.11)$$

$$F_y = k_t b f_t \sin(\phi) \sin(\phi) - k_n b f_t \sin(\phi) \cos(\phi), \quad (4.12)$$

where we have also replaced the instantaneous chip thickness with the expression provided in Eq. 4.2. These forces are clearly periodic with ϕ , but we must also consider the cut geometry in the final force calculations. See the following example.



In a Nutshell

As the tool rotates, the force on each tooth changes. In addition, the force orientation (direction) on that tooth varies during the tool rotation. Therefore, the forces generated by a single tooth, as seen by the workpiece or machine tool, vary periodically with the rotation of the tool. In addition, the total force changes as additional teeth enter or leave the cut.

Example 4.2 Cutting Forces for Rigid Tool and Workpiece Consider a 25% radial immersion peripheral up milling operation carried out using a tool with four teeth; see Fig. 4.9. The radial depth of cut is 25% of the cutter diameter or one half of its radius, $a = \frac{r}{2}$. Because it is an up milling operation, $\phi_s = 0$ and the exit angle is:

$$\phi_e = \cos^{-1}\left(\frac{r - \frac{r}{2}}{r}\right) = \cos^{-1}(0.5) = 60 \text{ deg.}$$

Therefore, each of the four teeth, equally spaced at 90 deg intervals around the periphery of the cutter, is engaged in the cut for only 60 deg. For this 60 deg range, the force components in the fixed x - y frame can be described using Eqs. 4.11 and 4.12. For the remaining 30 deg, the forces are zero. The x and y direction cutting

Fig. 4.9 25% radial immersion up milling geometry for Example 4.2

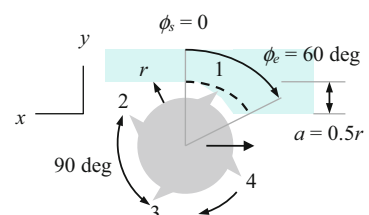


Fig. 4.10 25% radial immersion up milling cutting forces for Example 4.2

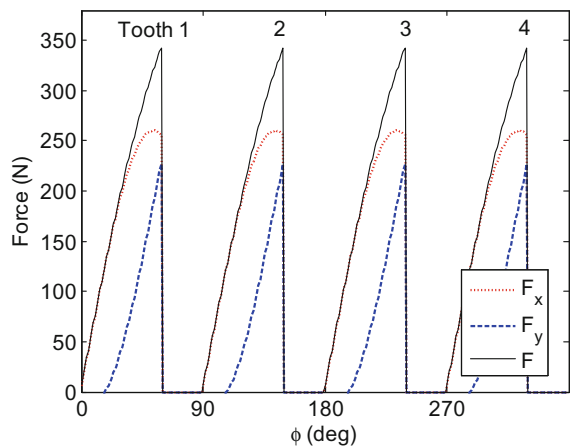
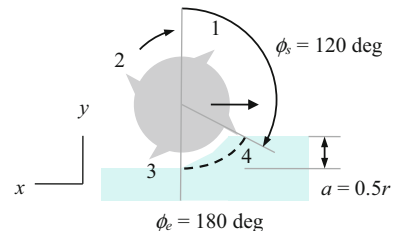


Fig. 4.11 25% radial immersion down milling geometry for Example 4.2



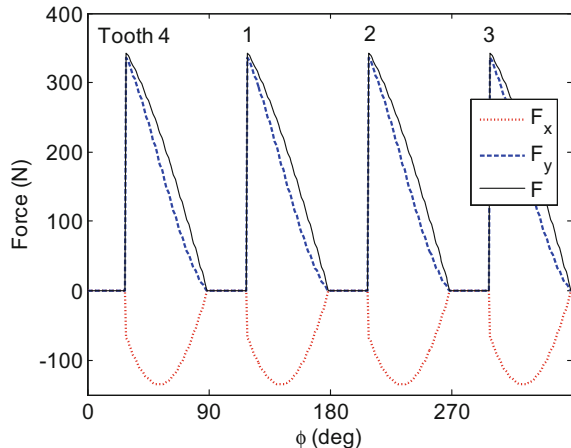
forces over one revolution are shown in Fig. 4.10, where the resultant force, $F = \sqrt{F_x^2 + F_y^2}$, is also included. For illustration purposes, the following parameters were selected: $k_t = 750 \text{ N/mm}^2$ and $k_n = 250 \text{ N/mm}^2$ (corresponds to $K_s = 791 \text{ N/mm}^2$ and $\beta = 71.6 \text{ deg}$ —these values would be reasonable for an aluminum alloy), $b = 5 \text{ mm}$, and $f_t = 0.1 \text{ mm/tooth}$. We see that tooth 1 is engaged between 0 deg and 60 deg (assuming a start angle of $\phi = 0$ when tooth 1 is vertical). Because the chip thickness increases as the cutter angle increases in up milling, the force levels grow. At 60 deg, the forces drop to zero until tooth 2 enters the cut at 90 deg. It is engaged until 150 deg (60 deg beyond 90 deg) when the force again drops to zero and so on for one full revolution (all four teeth). The MATLAB® program used to produce Fig. 4.10 is provided with the textbook as p_4_2_1.m. A detailed description of the code is given in Sect. 4.4.

For comparison purposes, Fig. 4.11 shows the geometry for a 25% radial immersion down milling cut and Fig. 4.12 displays the corresponding single revolution cutting force profile. All parameters remain the same, except that the starting angle is:

$$\phi_s = 180 - \cos^{-1}\left(\frac{r - \frac{L}{2}}{r}\right) = 180 - \cos^{-1}(0.5) = 120 \text{ deg}$$

and the exit angle is $\phi_e = 180 \text{ deg}$. It is observed that tooth 4 enters the cut first (again assuming a start angle of $\phi = 0$ when tooth 1 is vertical). This entry occurs

Fig. 4.12 25% radial immersion down milling cutting forces for Example 4.2



after a 30 deg delay where no cutting occurs (i.e., the 90 deg lead of tooth 4 relative to tooth 1 plus 30 deg gives the 120 deg cut starting angle). The maximum force level is encountered at 30 deg and then decreases with the chip thickness to an angle of 90 deg; this trend of force reduction as the final surface is being created explains why down milling is often selected for finishing passes when surface finish is most critical. After $\phi = 90$ deg is reached, the force is again zero until tooth 1 enters the cut at 120 deg and the cycle is repeated. Note that the x direction force is now negative (acting to the right). This is in direct contrast to the positive up milling x force seen in Fig. 4.10. The MATLAB® program used to produce Fig. 4.12 is provided with the textbook as p_4_2_2.m.

4.1.1 Tooth Passing Frequency

As a final point of emphasis for Example 4.2, let's discuss the frequency content of cutting force signals. As seen in Figs. 4.10 and 4.12, the forces during these partial immersion (up and down milling) cuts resemble trains of periodic impulses. To determine the resulting frequency spectrum, we first convert the abscissa to time (s), rather than tooth angle (deg). This conversion requires that the spindle speed, Ω , (rpm) is specified:

$$t = \frac{\phi \cdot 60}{\Omega \cdot 360} \quad (\text{s}). \quad (4.13)$$

Figures 4.13 (up milling) and 4.14 (down milling) show the resulting time vs. force plots for a spindle speed of 7500 rpm. It is seen that each tooth passage (90 deg angular interval for the cutter with four teeth) requires 0.002 s, or 2×10^{-3} s. The Fourier transform may now be applied to determine the frequency

Fig. 4.13 Time domain 25% radial immersion up milling cutting forces for Example 4.2

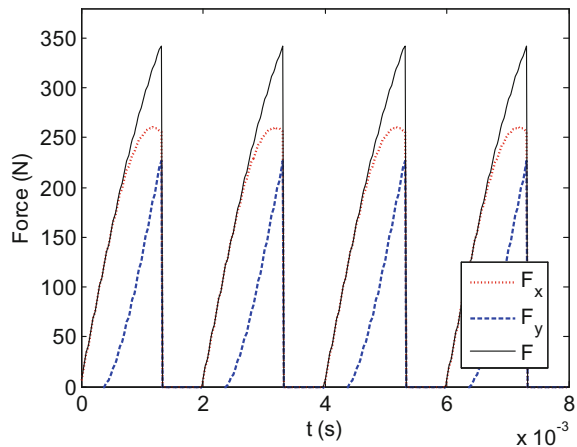
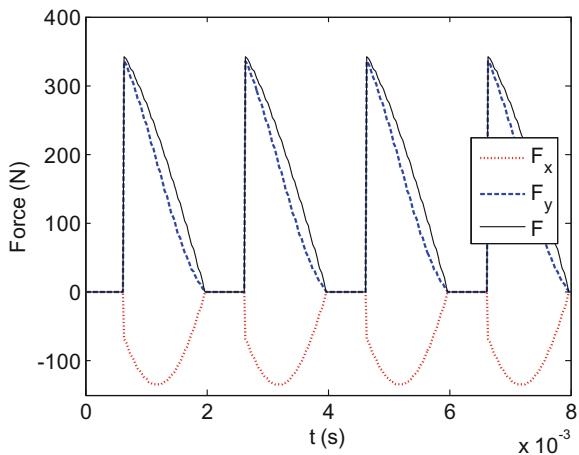


Fig. 4.14 Time domain 25% radial immersion down milling cutting forces for Example 4.2

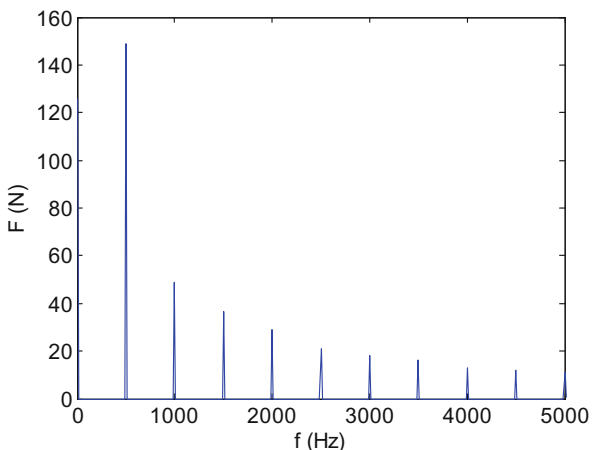


content. Because the time domain signal is a succession of impulse-like peaks, frequency content is observed not only at the tooth passing frequency:

$$f_{\text{tooth}} = \frac{\Omega \cdot N_t}{60} \text{ (Hz)}, \quad (4.14)$$

where the spindle speed is again expressed in rpm, but also at integer multiples of f_{tooth} . We refer to f_{tooth} as the fundamental tooth passing frequency or first harmonic, $2f_{\text{tooth}}$ as the second harmonic, and so on. The relative magnitudes of these harmonics depend on the “sharpness” of the force impulses; sharper peaks lead to increased magnitudes of higher order harmonics. Zero frequency, or DC, content is also typically observed. For example, the perfectly sinusoidal x direction force profile obtained for a two tooth cutter in a slotting cut exhibits content at only DC (because its average value is nonzero) and the fundamental tooth passing frequency

Fig. 4.15 25% radial immersion down milling frequency spectrum for resultant force in Example 4.2



(because it is a pure sinusoid and not impulsive in nature). Returning to Figs. 4.13 and 4.14, we saw that the tooth period was 0.002 s. This corresponds to a frequency of $\frac{1}{0.002} = 500$ Hz, which matches the result obtained from Eq. 4.14, $f_{\text{tooth}} = \frac{7500.4}{60} = 500$ Hz. The magnitude vs. frequency plot for the down milling resultant force, F , is shown in Fig. 4.15. As expected, peaks are observed at $\{500, 1000, 1500\}$ Hz, and higher order harmonics. This figure was generated using the MATLAB® program p_4_2_3.m included with the textbook. The MATLAB® function `fft` was implemented to compute the fast Fourier transform of the force data.



In a Nutshell

The cutting force varies with the angle of the cutting edge. By including the spindle speed, we see that the cutting force varies in time and that the forces generated by the teeth are an external excitation that cause forced vibration. Changing the spindle speed modifies the excitation frequency. Because the force is periodic, but not purely sinusoidal, it can be thought of as a combination of many sinusoidal forces, and these can be determined using the mathematical technique of the Fourier transform. The resulting plot shows the “frequency content” of the force. In many ways it is like looking at a graphic equalizer in a home stereo system¹ with the height of the peaks in the graph representing the force level at the corresponding frequency.

¹The “old” authors realize that graphic equalizer displays on stereos are not as common as they were in our teenage years. For that matter, they don’t call them “boom boxes” any more, do they? P.S. We are not **that** old!

4.1.2 Multiple Teeth in the Cut

A natural extension of the previous example is to consider cases where there are more teeth on the cutter or the radial immersion is increased. In these instances, it is possible for more than one tooth to be engaged in the cut at a given time. Further, it is possible to alternate between, for example, one tooth cutting over some interval and two teeth in another. This situation is illustrated in Fig. 4.16, where the radial immersion is 75% and the cutter again has four teeth. First, we notice that the cut includes both up ($0 \leq \phi \leq 90$ deg) and down ($90 < \phi \leq 120$ deg) milling portions. Next, we see that when $0 \leq \phi \leq 30$ deg, both teeth 4 and 1 are cutting (assume $\phi = 0$ when tooth 1 is vertical). However, when $30 < \phi \leq 90$ deg, only tooth 1 is engaged. For $90 < \phi \leq 120$ deg, two teeth (1 and 2) are again cutting simultaneously. As ϕ continues to increase, the cycle continues, and, unlike the previous example, the cutting force components never drop to zero. As seen in Fig. 4.17, during the intervals when two teeth are engaged simultaneously, the cutting forces are constant. This surprising result leads to constant cutting forces at all times for slotting operations with an even number of teeth, where $N_t > 2$. The MATLAB® program p_4_2_3.m can be modified to (1) produce Fig. 4.17 by selecting $\text{phie} = 120$; and (2) demonstrate the constant force for slotting with $N_t = 4, 6, 8, \dots$ by setting $\text{phis} = 0, \text{phie} = 180$, and N_t to the appropriate value. Because multiple teeth can

Fig. 4.16 75% radial immersion milling geometry

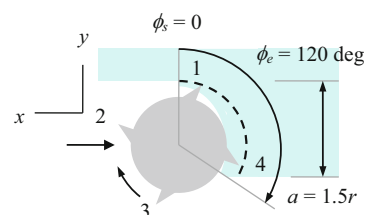
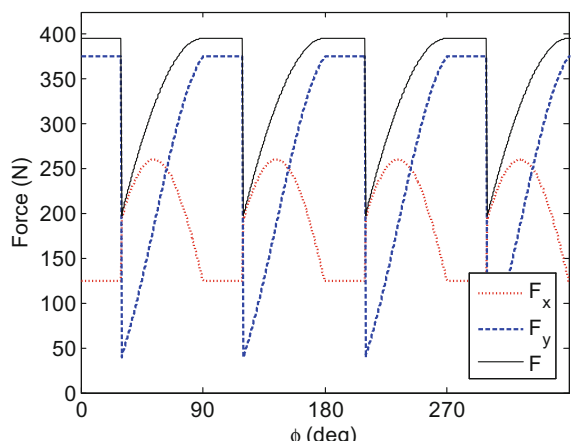


Fig. 4.17 75% radial immersion cutting forces



be cutting at any instant, the force expressions in Eqs. 4.11 and 4.12 should be updated to include the necessary summations:

$$F_x = \sum_{j=1}^{N_t} k_t b f_t \sin(\phi_j) \cos(\phi_j) + k_n b f_t \sin(\phi_j) \sin(\phi_j) \text{ and} \quad (4.15)$$

$$F_y = \sum_{j=1}^{N_t} k_t b f_t \sin(\phi_j) \sin(\phi_j) - k_n b f_t \sin(\phi_j) \cos(\phi_j), \quad (4.16)$$

where ϕ_j is the angle of each tooth on the cutter. For a cutter with four teeth, as shown in Fig. 4.9, for example, if the angle for tooth 1 is $\phi_1 = 40$ deg, then the remaining angles are $\phi_2 = 310$ deg, $\phi_3 = 220$ deg, and $\phi_4 = 130$ deg. In this case, each successive tooth angle is decremented by 90 deg (the tooth pitch for equally spaced teeth is equal to 360 deg divided by the number of teeth), where $0 \leq \phi_j < 360$. As we've seen, to calculate the final cutting force, we must also verify that the j th tooth in question is between ϕ_s and ϕ_e prior to summing its contribution to the overall force value. Otherwise, the tooth is not engaged in the cut and zero force is added to the summation at that instant.



For Instance

If the radial depth of cut is very small, there are long periods of time when no tooth is cutting at all. In this case, the cutting force looks like a series of very short impacts. If the radial depth of cut is larger, then the number of teeth cutting simultaneously may be constant or vary depending on the cut geometry and the tooth spacing.

Prior to beginning our discussion of regenerative chatter, let's identify four other important terms related to milling performance. The cutting speed, v , is the peripheral velocity of the cutter and is described by:

$$v = \frac{r\Omega \cdot 2\pi}{60} = \frac{d\Omega \cdot \pi}{60} \text{ (mm/s)}, \quad (4.17)$$

where Ω is given in rpm and the tool radius (or diameter) is stated in mm. This quantity is important because the cutting temperature generally increases with cutting speed. Since diffusive tool wear (typically characterized by diffusion of the tool material into the workpiece/chip) is temperature dependent, high temperatures at the tool-chip interface can lead to prohibitive wear and, therefore, place an upper bound on the allowable cutting speed. This, in turn, limits the top available spindle speed (for a given tool diameter) and can reduce the availability of the large stable zones observed to the right of stability lobe diagrams at higher spindle speeds. High temperatures are particularly problematic when the workpiece material exhibits low thermal conductivity. This causes the heat to remain at the tool-chip interface, rather than being conducted away into the workpiece, and accelerates diffusive wear. A well-known example is the difficulty in machining the titanium alloy 6Al-4V, with a thermal

conductivity value approximately 20 times less than 7075 aluminum, for instance, due to the associated excessive wear rates at high cutting speeds (see Chap. 8).

For any cut to be carried out, the spindle must possess the required torque to continue rotating the tool against the retarding tangential component of the cutting force. The instantaneous torque, T , is expressed as the sum of the products of the tool radius and tangential force for each tooth engaged in the cut. Similar to Eqs. 4.15 and 4.16, the torque can be written as:

$$T = \sum_{j=1}^{N_t} r \cdot F_{t,j} = r \sum_{j=1}^{N_t} F_{t,j} = r \sum_{j=1}^{N_t} k_t b f_t \sin(\phi_j) = r k_t b f_t \sum_{j=1}^{N_t} \sin(\phi_j), \quad (4.18)$$

where the same ϕ_j definition holds and typical units for torque are N m. For most spindles, the available torque is spindle speed dependent and is provided as a “torque curve” with the spindle specifications. Because the rotating spindle has inertia, it acts like a flywheel. For that reason it is often the average torque, rather than the instantaneous torque, that matters. The cutting operation can very briefly sustain a torque in excess of the torque curve (thereby slightly slowing the rotation of the spindle) if the average torque is sufficiently low.

Similar to torque, the available spindle power can limit the potential cut geometry (i.e., if the power is exceeded, the spindle will stall). The power is determined from the product of torque and rotational speed. If the spindle speed is expressed in rpm and torque in N m, the power in W is:

$$P = \frac{T\Omega \cdot 2\pi}{60}. \quad (4.19)$$

Again, the spindle power is a function of spindle speed and is expressed via a “power curve” supplied by the spindle manufacturer. Like torque, it is often the average power that counts. Interestingly, the average power is proportional to the average metal removal rate.

In order to reduce machining time and, subsequently, cost, it is often desired to increase the mean material removal rate, MRR, or average volume of material removed per unit time.

$$\text{MRR} = abf = abf_t N_t \Omega \quad (4.20)$$

4.2 Regenerative Chatter in Milling

If we remove the assumption of a rigid tool, then the cutting force could cause deflections of the tool.² Additionally, if the tool is vibrating as it removes material, we would expect these vibrations to be “imprinted” on the workpiece surface as a wavy profile just as we discussed for turning. The difference in milling is that the

²We will assume a rigid workpiece in our analysis.

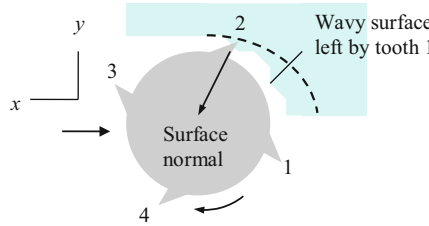
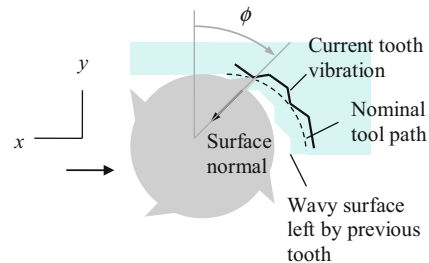


Fig. 4.18 Regeneration in milling. Cutter deflections during the passage of tooth 1 are copied onto the workpiece surface and are encountered by tooth 2. This varies the chip thickness and cutting force which, in turn, affects the resulting tool deflections

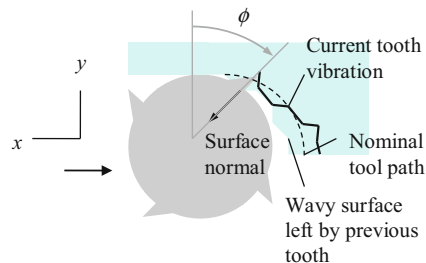
Fig. 4.19 Condition when the vibrations from one tooth to the next are in phase. This yields chip thickness variation that is seen for the cycloidal tool path only



time delayed surface regeneration step occurs from tooth to tooth, rather than from revolution to revolution as in turning. Figure 4.18 shows that the wavy surface left behind by tooth 1 is removed by tooth 2 and so on. This again provides a feedback mechanism because the instantaneous chip thickness depends on both the current vibration and the surface left by the previous tooth (one tooth period, or time from one tooth to the next, earlier). The variable chip thickness governs the cutting force which, in turn, affects subsequent tool vibrations. The result is the possibility for instability, or chatter, just as we saw with turning operations. We will again consider vibrations normal to the cut surface in order to determine the chip thickness. However, this normal direction (through the cutting edge toward the tool center) constantly varies as the cutter rotates; see Fig. 4.18.

Analogous to turning, the relative phasing between the surface waviness from one tooth to the next determines the level of force variation and, together with the chip width, whether the operation is stable or unstable. Figures 4.19 and 4.20 show two possibilities. In Fig. 4.19, the wavy surface and current vibration between two subsequent teeth are in phase. Therefore, even though the tool is vibrating during material removal, the chip thickness variation (along the instantaneous surface normal) is similar to what would be obtained from the cycloidal tool path alone. This tends to produce forced vibration only and stable cutting. Again, because the tool vibrates at its natural frequency (we'll assume a single degree of freedom system for now), it is intuitive that matching the tooth passing frequency to the tool's natural frequency will lead to this preferred "in phase" situation. We recognize, however, that driving the system at resonance does lead to larger vibration levels, although less

Fig. 4.20 Out-of-phase condition where the tool vibrations from one tooth to the next lead to significant chip thickness variation



than what would be obtained during chatter. We will explore this issue further in Chap. 5. Figure 4.20 shows a less favorable phase relationship where there is significant variation in the chip thickness (beyond the periodic variation due to the cycloidal tool path). This can lead to self-excited vibrations and unstable cutting, depending on the chip width, due to the force variations and subsequent tool deflections.



In a Nutshell

Although the geometry is more complicated, milling stability is conceptually similar to turning. The varying cutting force causes vibration of the tool, which generates a wavy surface. The wavy surface causes a variable chip thickness which, in turn, yields a variable cutting force. Depending on the cutting conditions and the alignment of the waves, the vibration can grow (chatter) or diminish (stable) with subsequent tooth passes.

As mentioned, the chip thickness is measured along the surface normal just as for turning, but the surface normal is a function of the cutter angle, ϕ . The projection of the instantaneous chip thickness along the surface normal under the circular tool path assumption is characterized by Eq. 4.2 in the absence of tool vibrations. However, if we now allow the tool to undergo vibrations in the x and y directions due to the application of the cutting force to the nonrigid tool, the chip thickness equation must be modified. First, we can project the x and y vibrations onto the surface normal, n , according to:

$$n = x \sin(\phi) - y \cos(\phi). \quad (4.21)$$

Note that the positive direction for n is out of the cut. Because ϕ varies with time, $\phi = \Omega(2\pi)\frac{180}{\pi}\frac{1}{60}t = 6\Omega t$ deg where Ω is given in rpm and t in s, the direction of n is also a function of time. Similar to the chip thickness in turning, Eq. 3.4, the instantaneous chip thickness for milling can then be written as:

$$h(t) = f_t \sin(\phi) + n(t - \tau) - n(t), \quad (4.22)$$

where $f_t \sin(\phi)$ replaces the “mean chip thickness” in Eq. 3.4 and τ is the tooth period in seconds. The $n(t - \tau)$ term represents the vibration contributions along the

Fig. 4.21 Geometry of instantaneous chip thickness calculation for milling

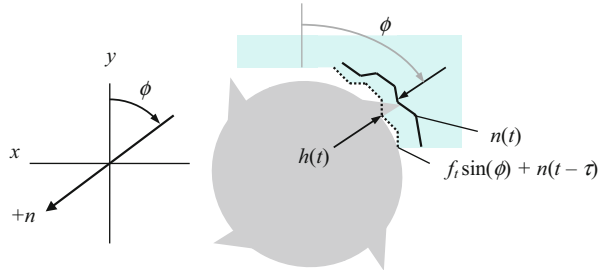
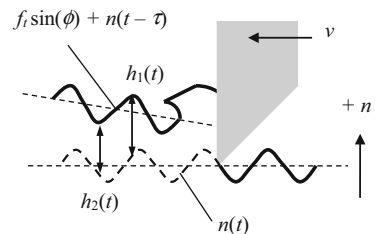


Fig. 4.22 Unwrapped view of milled surface for comparison to chip thickness variation in turning



surface normal by the previous tooth and $\tau = \frac{60}{\Omega N_t}$ (this is the reciprocal of Eq. 4.14), where Ω is again given in rpm. The geometry of Eq. 4.22 is shown in Fig. 4.21. As we saw in turning, larger (more positive) vibrations by the previous tooth increase the chip thickness because less material is removed than commanded. Larger vibrations by the current tooth lead to decreased chip thickness by the same logic. If the vibrations from one tooth to the next are equal, Eq. 4.22 reduces to Eq. 4.2. To complete our analogy to turning, let's "unwrap" the milled surface and show the current and previous vibrations along the "planar" instantaneous surface normal. We can observe the similarity of Fig. 4.22 for milling to Fig. 3.7 for turning. The inherent chip thickness variation due to the cycloidal tool path is schematically represented as a wedge (an up milling cut is presumed where the chip thickness grows as the cutter rotates). In Fig. 4.22, recall that v is the cutting speed; its direction is shown.

4.3 Stability Lobe Diagrams

4.3.1 Average Tooth Angle Approach

Tlusty modified his frequency domain turning stability analysis, presented in Sect. 3.3, to accommodate the milling process [2–4]. A primary obstacle to defining an analytical solution to milling stability (aside from the inherent time delay) is the time dependence of the cutting force direction. Tlusty solved this problem by assuming an "average" angle of the tooth in the cut and, therefore, an average force direction. This created an autonomous, or time invariant, system. He then

made use of directional orientation factors to first project this force into the x and y mode directions and, second, project these results onto the surface normal. Just as for turning, depending on the feedback system “gain,” represented by the chip width, b , and the spindle speed, Ω , the milling operation is either stable or it exhibits chatter. Let’s first discuss the required equations and then determine the directional orientation factors for various radial immersions.

$$b_{\lim} = \frac{-1}{2K_s \operatorname{Re}[\operatorname{FRF}_{\text{orient}}] N_t^*} \quad (4.23)$$

$$\frac{f_c}{\Omega N_t} = N + \frac{\epsilon}{2\pi} \quad (4.24)$$

$$\epsilon = 2\pi - 2 \tan^{-1} \left(\frac{\operatorname{Re}[\operatorname{FRF}_{\text{orient}}]}{\operatorname{Im}[\operatorname{FRF}_{\text{orient}}]} \right) \quad (4.25)$$

Due to the assumption of a fixed force direction, only minor modifications are necessary to adapt the turning stability equations to the milling case. In Eq. 4.23, a new variable, N_t^* , appears in the denominator. This represents the average number of teeth in the cut. As discussed in Sect. 4.1, it is possible for multiple teeth to be engaged simultaneously and, further, for the number of teeth in the cut to vary over one revolution. This average value is calculated by dividing the difference between the exit and starting angles by the angular tooth spacing (we’ll assume equal, or proportional, teeth spacing for now). See Eq. 4.26, where the start and exit angles are given in deg. We also see that Eq. 4.24 differs from Eq. 3.6 by a single term. Specifically, N_t appears in the denominator of the left hand side. Because the product ΩN_t represents the tooth passing frequency, the left hand side gives the ratio of the chatter frequency to the forcing frequency. (Units compatibility requires that Ω is given in rev/s if f_c is expressed in Hz.) This is analogous to Eq. 3.6, where the ratio is $\frac{f_c}{\Omega}$ because the forcing frequency is simply the rotating speed in turning.

$$N_t^* = \frac{\phi_e - \phi_s}{\frac{360}{N_t}} \quad (4.26)$$

The milling stability lobe diagram is generated by:

1. Determining the oriented FRF and identifying the valid chatter frequency range (s), i.e., where the real part is negative.
2. Solving for ϵ ; the phase between the current and previous tooth vibrations, over the valid frequency range(s).
3. Finding the average number of teeth in the cut for the selected radial immersion.
4. Calculating b_{\lim} over the valid frequency range(s).
5. Selecting an N value (integer number of waves between teeth) and calculating the associated spindle speeds over the valid frequency range(s).

6. Plotting Ω vs. b_{lim} (both are a function of the same frequency vector, so the first spindle speed value corresponds to the first limiting chip width and so on) for each N value ($N = 0, 1, 2, \dots$).

Just as with turning, any (Ω, b_{lim}) pair that appears above the collective boundary indicates unstable behavior, while any pair below the boundary indicates stable cutting. Notice that because the N value denotes the integer number of waves between teeth, rather than the integer number of waves per revolution as in turning, the expanded stable zones appear at much lower spindle speeds. For this reason, the use of the stability lobe diagram to find high performance stable zones in milling is a much more enticing prospect than it is in turning.

4.3.2 Oriented FRF

The oriented FRF is calculated by summing the products of the directional orientation factors and corresponding FRFs for the x and y directions; see Eq. 4.27. We'll show the directional orientation factor computations through examples.

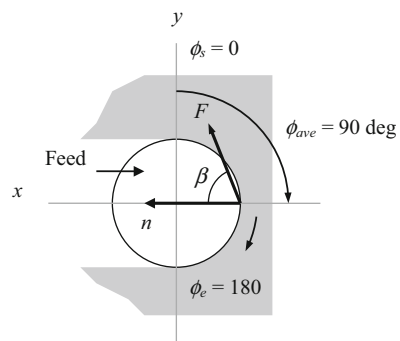
$$\text{FRF}_{\text{orient}} = \mu_x \text{FRF}_x + \mu_y \text{FRF}_y \quad (4.27)$$

Example 4.3 Directional Orientation Factors for Slotting For a 100% radial immersion (slotting) cut, the cut start angle is 0 deg and the exit angle is 180 deg (based on the circular tool path approximation). The average angle of a tooth in the cut is therefore:

$$\phi_{\text{ave}} = \frac{\phi_s + \phi_e}{2} = \frac{0 + 180}{2} = 90 \text{ deg.}$$

The surface normal is drawn at ϕ_{ave} with the positive direction out of the cut, and the cutting force, F , is oriented at the force angle, β (opposing the direction of rotation), with respect to the surface normal. Figure 4.23 shows this geometry.

Fig. 4.23 Geometry for determining directional orientation factors for slotting



Two steps are required to determine the x and y direction directional orientation factors. First, the force is projected onto the mode direction. Second, this result is projected onto the surface normal. These two steps are repeated once for each direction. For μ_x , projection onto the x direction gives $F_x = F \cos (\beta)$. The projection of this result onto the “average” surface normal is:

$$F_n = F_x \cos (0) = F \cos (\beta) \cos (0) = F \cos (\beta)$$

because the surface normal is parallel to the mode direction in this instance. The directional orientation factor is then $\mu_x = \cos (\beta)$. For μ_y , projection onto the y direction gives $F_y = F \cos (90 - \beta) = F \sin (\beta)$, where β is expressed in deg. The projection of this result onto the “average” surface normal is $F_n = F_y \cos (90) = F \sin (\beta) \cos (90) = 0$ because the surface normal is perpendicular to the mode direction in this instance. The directional orientation factor is then $\mu_y = 0$. According to Eq. 4.27, the oriented FRF is $\text{FRF}_{\text{orient}} = \cos (\beta)\text{FRF}_x + 0 \cdot \text{FRF}_y$, which suggests that compliance in the y direction has no influence on the milling stability.

Example 4.4 Directional Orientation Factors for Down Milling Consider the 50% radial immersion down milling cut pictured in Fig. 4.24. To find μ_x , we first project F onto the x direction to obtain $F_x = F \cos (45 + \beta)$, where β is given in deg. The projection of this result onto the average surface normal, which occurs at the angle

$$\phi_{\text{ave}} = \frac{90 + 180}{2} = 135 \text{ deg}, \text{ is:}$$

$$F_n = F_x \cos (45) = F \cos (45 + \beta) \cos (45).$$

For μ_y , projection onto the y direction gives $F_y = F \cos (\beta - 45)$. The projection of this result onto the average surface normal is $F_n = F_y \cos (45) = F \cos (\beta - 45) \cos (45)$. The directional orientation factors are $\mu_x = \cos (45 + \beta) \cos (45)$ and $\mu_y = \cos (\beta - 45) \cos (45)$.

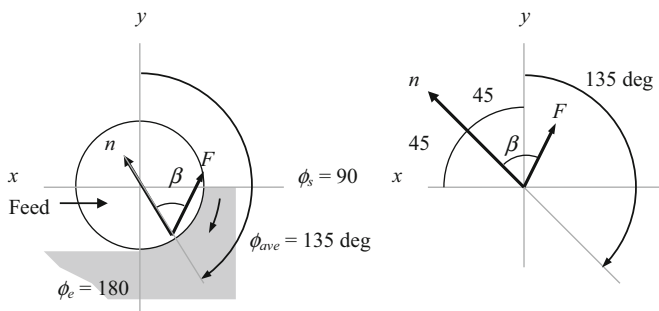
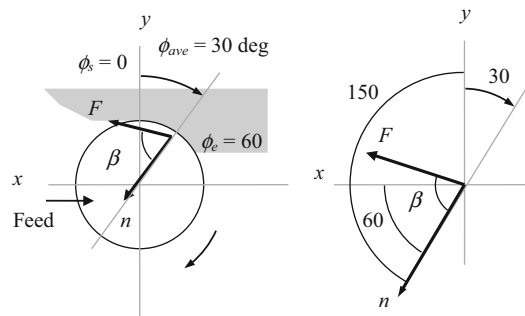


Fig. 4.24 Geometry for determining 50% radial immersion down milling directional orientation factors

Fig. 4.25 Geometry for determining 25% radial immersion up milling directional orientation factors



Example 4.5 Directional Orientation Factors for Up Milling. A 25% radial immersion up milling cut in depicted in Fig. 4.25. As shown in Eq. 4.4, the exit angle is $\phi_e = \cos^{-1}\left(\frac{r - \frac{r}{2}}{r}\right) = \cos^{-1}(0.5) = 60$ deg. The start angle for any up milling cut is zero. To find μ_x , we first project F onto the x direction to obtain $F_x = F \cos(\beta - 60)$, where β is given in deg. The projection of this result onto the average surface normal, which occurs at the angle $\phi_{ave} = \frac{0 + 60}{2} = 30$ deg, is $F_n = F_x \cos(60) = F \cos(\beta - 60) \cos(60)$. For μ_y , projection onto the y direction gives $F_y = F \cos(150 - \beta)$. The projection of this result onto the average surface normal is $F_n = F_y \cos(150) = F \cos(150 - \beta) \cos(150)$. The directional orientation factors are $\mu_x = \cos(\beta - 60) \cos(60)$ and $\mu_y = \cos(150 - \beta) \cos(150)$.

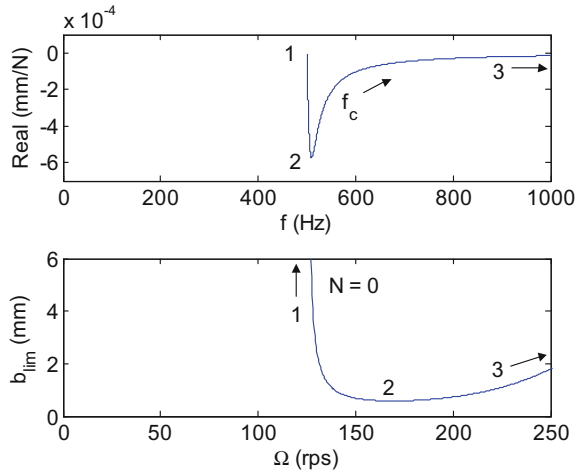
Let's now examine stability lobes for milling. We'll see that the stability limit is again a mapping of the real part of the oriented FRF onto the (Ω, b_{lim}) diagram. In the following slotting example, we'll demonstrate analytical calculations for the best and worst spindle speeds and $b_{lim,crit}$ and show the resulting stability lobes. We'll then complete an example for 20% radial immersion down milling.

Example 4.6 Slotting Stability Lobe Calculations For this example, the x and y direction dynamics are symmetric and can be described by $f_n = 500$ Hz, $k = 8 \times 10^6$ N/m = 8×10^3 N/mm, and $\zeta = 0.02$. As shown in Example 4.3, the directional orientation factors are $\mu_x = \cos(\beta)$ and $\mu_y = 0$ for slotting, and the oriented FRF is $FRF_{orient} = \cos(\beta)FRF_x$. We'll assume an aluminum alloy machined with a four tooth, 19 mm diameter square endmill that together exhibit a specific force of 750 N/mm² and a force angle of 68 deg.

For this single degree of freedom example, the best spindle speed is defined for a phase angle of $\epsilon = 2\pi$ rad = 360 deg (see Fig. 3.14) just as we observed for turning. The corresponding chatter frequency is $f_c = f_n$. Equation 4.24 shows that the best spindle speed for the $N = 0$ lobe is:

$$\Omega_1 = \frac{f_c}{N_t} \cdot \frac{1}{N + \frac{\epsilon}{2\pi}} = \frac{f_n}{4} \cdot \frac{1}{0 + \frac{2\pi}{2\pi}} = \frac{f_n}{4} = \frac{500}{4} = 125 \text{ rps}$$

Fig. 4.26 Mapping of the oriented FRF onto the (Ω, b_{lim}) diagram for Example 4.6



or $125(60) = 7500$ rpm. This provides a reasonable target spindle speed for milling. Note that for turning (with $N_t = 1$, effectively), the best spindle speed for $N = 0$ is 500 rps or 30,000 rpm. Also, the tooth passing frequency for this spindle speed is:

$$f_{\text{tooth}} = \frac{\Omega N_t}{60} = \frac{7500(4)}{60} = 500 \text{ Hz.}$$

Point 1, where f_{tooth} is set equal to f_n , is identified in Fig. 4.26. The theoretical limiting chip width for point 1 is:

$$b_1 = \frac{-1}{2K_s \text{Re}[\text{FRF}_{\text{orient}}] N_t^*} = \frac{-1}{2K_s(0) N_t^*} = \infty.$$

However, just as with turning, the $N = 1$ lobe truncates the $N = 0$ lobe and gives a finite chip width where they cross. The average number of teeth in the cut is $N_t^* = \frac{180 - 0}{\frac{360}{4}} = 2$ for this slotting example.

The worst spindle speed is obtained when ϵ is $\frac{3\pi}{2}$ rad or 270 deg (see Fig. 3.12). The chatter frequency for this case (i.e., the frequency for $\min(\text{Re}[\text{FRF}_{\text{orient}}])$ or $\min(\text{Re}[\mu_x \text{FRF}_x])$) is $f_c = f_n(1 + \zeta)$. Substitution in Eq. 4.24 gives:

$$\Omega_2 = \frac{f_c}{N_t N + \frac{1}{2\pi}} = \frac{f_n(1 + \zeta)}{4} \frac{1}{0 + \frac{\frac{3\pi}{2}}{2\pi}} = \frac{f_n(1 + \zeta)}{4} \frac{1}{0 + \frac{3}{4}} = \frac{500(1 + 0.02)}{3} = 170 \text{ rps}$$

or 10,200 rpm. Point 2 is also shown in Fig. 4.26. The corresponding minimum limiting chip width, $b_{\text{lim,crit}}$, is determined by rewriting Eq. 4.23,

$b_{\text{lim,crit}} = \frac{-1}{2K_s \min(\text{Re}[\mu_x \text{FRF}_x]) N_t^*}$. For a single degree of freedom system, the minimum real part can be approximated by:

$$\min(\text{Re}[\text{FRF}]) = \frac{-1}{4k\zeta(1+\zeta)}. \quad (4.28)$$

We can therefore write a simple expression for the point 2 chip width (in this single degree of freedom, slotting example):

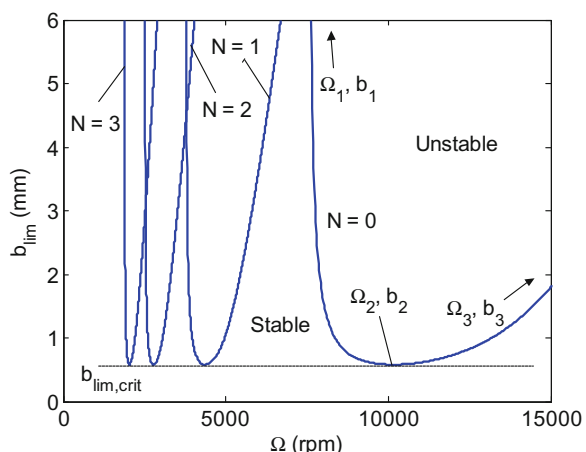
$$b_{\text{lim,crit}} = \frac{4k\zeta(1+\zeta)}{2K_s \mu_x N_t^*} = \frac{4 \cdot 8 \times 10^3 (0.02)(1+0.02)}{2(750) \cos(68)(2)} = 0.58 \text{ mm.}$$

Point 3, where $f_c \rightarrow \infty$, is similar to point 1 in Fig. 4.26. As shown previously in Fig. 3.16, even though the tooth-to-tooth phase relationship is unfavorable ($\varepsilon \rightarrow 180$ deg, or exactly out of phase), the response amplitude approaches zero, $\text{Re}(\text{FRF}) \rightarrow 0$, so the vibration level is small. Substitution in Eq. 4.23 yields an infinite chip thickness, $b_3 = \frac{-1}{2K_s(0)N_t^*} = \infty$. However, the left end of the $N = 0$ curve, where $f_c = 0$, serves to limit the right hand side of the $N = 1$ curve, where $f_c \rightarrow \infty$. Figure 4.27 shows the $N = 0$ to 3 lobes for this example. The MATLAB® program used to produce Fig. 4.27 is provided with the textbook as p_6_1.m.

To conclude this example, let's calculate the mean material removal rate if we selected (Ω_2, b_2) with a feed per tooth of 0.15 mm/tooth as the operating parameters. As shown in Eq. 4.20, the mean MRR for milling is computed from the product of the axial depth of cut, radial depth (equal to the tool diameter for slotting), feed per tooth, number of teeth, and spindle speed:

$$\text{MRR} = b_{\text{lim,crit}} df_t N_t \Omega_2 = 0.58(19)0.15(4)10,200 = 67,442 \text{ mm}^3/\text{min.}$$

Fig. 4.27 Stability lobe diagram for Example 4.6 ($N = 0$ to 3)



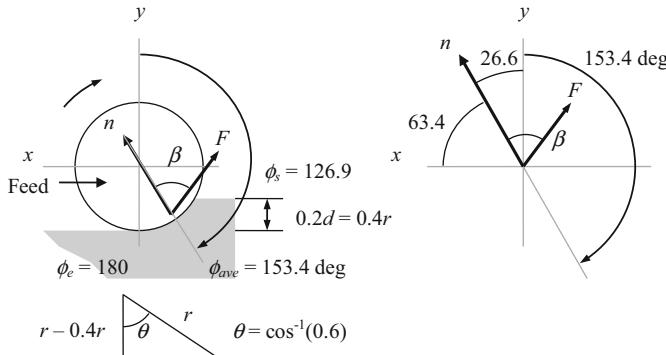


Fig. 4.28 Geometry for Example 4.7 20% radial immersion down milling cut

To visualize this removal rate, let's divide by 60×10^3 to determine the cubic centimeters per second, $MRR = 1.1240 \text{ cm}^3/\text{s}$. This means that the equivalent of approximately a $1 \text{ cm} \times 1 \text{ cm} \times 1 \text{ cm}$ cube of aluminum is removed each second under these conditions.

Example 4.7 20% Radial Immersion Down Milling Stability Lobe Calculations Figure 4.28 shows the geometry for a 20% radial immersion down milling cut. The start angle is $\phi_s = 180 - \cos^{-1}(0.6) = 126.9 \text{ deg}$, and the exit angle is $\phi_e = 180 \text{ deg}$. The average angle of a tooth in the cut is $\phi_{ave} = \frac{126.9 + 180}{2} = 153.4 \text{ deg}$. The x (feed) direction dynamics are given by $f_{nx} = 900 \text{ Hz}$, $k_x = 9 \times 10^6 \text{ N/m} = 9 \times 10^3 \text{ N/mm}$, and $\zeta_x = 0.02$. The y direction dynamics are $f_{ny} = 950 \text{ Hz}$, $k_y = 1 \times 10^7 \text{ N/m} = 1 \times 10^4 \text{ N/mm}$, and $\zeta_y = 0.01$. The workpiece material is a low-carbon steel alloy, and it is machined with a three tooth, 19 mm diameter square endmill. Together they give a specific force of $K_s = 2250 \text{ N/mm}^2$ and a force angle of $\beta = 75 \text{ deg}$.

As shown in Fig. 4.28, the directional orientation factor for the x direction is determined from the two projections:

$$F_x = F \cos(63.4 + \beta) \quad \text{and} \quad F_n = F_x \cos(63.4) = F \cos(63.4 + \beta) \cos(63.4),$$

where β is expressed in deg. Therefore, $\mu_x = \cos(63.4 + \beta) \cos(63.4) = -0.335$. For the y direction, the projections are:

$$F_y = F \cos(\beta - 26.6) \quad \text{and} \quad F_n = F_y \cos(26.6) = F \cos(\beta - 26.6) \cos(26.6)$$

and $\mu_y = \cos(\beta - 26.6) \cos(26.6) = 0.594$. Additionally, the average number of teeth in the cut is $N_t^* = \frac{180 - 126.9}{360} = 0.443$.

The oriented FRF is shown in Fig. 4.29. The unusual shape of the real and imaginary parts is due to the negative μ_x value. The minimum real part is observed

Fig. 4.29 Oriented FRF for Example 4.7

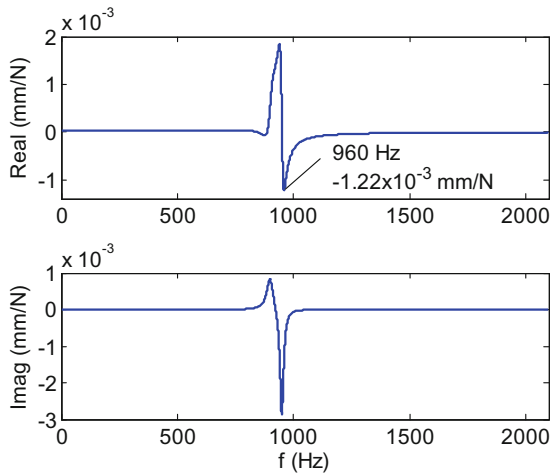
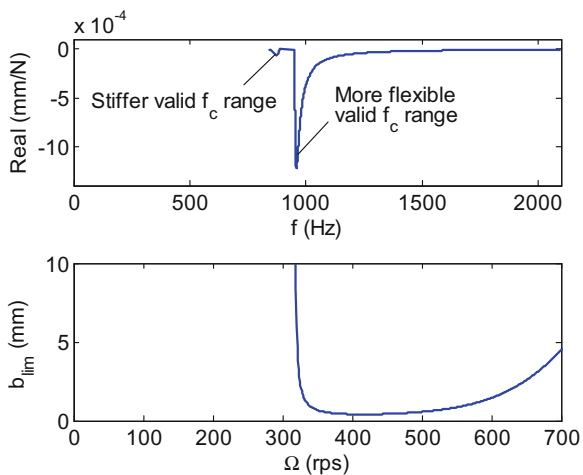


Fig. 4.30 (Top) Valid chatter frequency ranges for the real part of the oriented FRF. (Bottom) $N = 0$ stability lobe



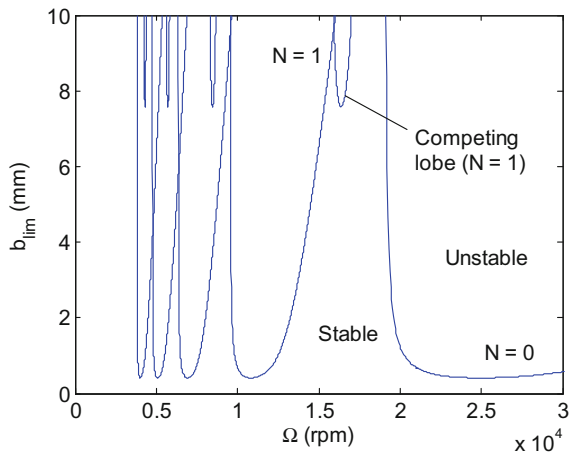
at 960 Hz with a value of $-1.22 \times 10^{-3} \text{ mm/N}$. The corresponding worst spindle speed (for the $N = 0$ lobe) and $b_{\text{lim},\text{crit}}$ are approximated by:

$$\Omega_{\text{worst}} = \frac{960}{3} \frac{1}{0 + \frac{\frac{3\pi}{2}}{2\pi}} = \frac{960}{3} \frac{4}{3} = 427 \text{ rps} = 25,600 \text{ rpm and}$$

$$b_{\text{lim},\text{crit}} = \frac{-1}{2 \cdot 2250 (-1.22 \times 10^{-3}) 0.443} = 0.41 \text{ mm.}$$

The real part of the oriented FRF for the valid chatter frequency ranges ($\text{Re}[\text{FRF}_{\text{orient}}] < 0$) and the corresponding $N = 0$ stability lobe are shown in Fig. 4.30. Two valid ranges are seen; the first, lower frequency range is much stiffer

Fig. 4.31 Example 4.7 stability lobe diagram ($N = 0$ to 4)



than the second. The “competing lobe” effect of this stiffer section is observed in Fig. 4.31, where the $N = 0$ to 4 lobes are plotted. In this case, the stability boundary is nearly completely established by the much more flexible section. The “best speeds” equation from Sect. 3.3 can also be updated for milling:

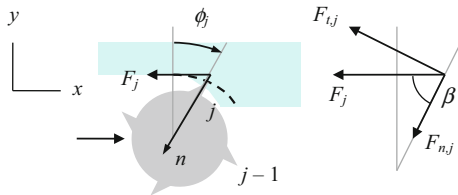
$$\Omega_{\text{best}} = \frac{f_n(60)}{(N+1)N_t} \text{ (rpm).} \quad (4.29)$$

If we choose f_n to be the zero crossing for the more flexible real part valid chatter frequency range (at 951 Hz from Figs. 4.29 and 4.30), then the associated best speeds are 19,020 rpm, 9510 rpm, 6340 rpm, and so on for the three-tooth endmill. These speeds match those seen in Fig. 4.31 for the right-hand side of the stable zones moving from right to left on the diagram. For example, 19,020 rpm corresponds to the stable gap created by the intersection of the $N = 0$ and $N = 1$ lobes. The MATLAB® program used to produce these figures is provided with the textbook as p_4_7_1.m.

4.3.3 Fourier Series Approach

In [5], Altintas and Budak use an alternate technique to transform the dynamic milling equations into a time invariant but radial immersion-dependent system. Similar to Tlusty, they approximate the time-dependent cutting forces by an average value but employ a different approach to identify this mean. Rather than using the average angle of the tooth in the cut, the time-varying coefficients of the dynamic milling equations, which depend on the angular orientation of the tool as it rotates through the cut, are expanded into a Fourier series, and then the series is truncated to include only the average component. We’ll first present a brief review of this approach and then rearrange the analytical stability equations into the form expected by the MATLAB® `eig` function.

Fig. 4.32 Notation for Fourier series stability analysis



The development of the time dependent cutting force equations closely follows the previous analysis. The primary difference is that the positive x direction is taken to be in the direction of the feed (following the convention in [5]); compare Fig. 4.32 (Fourier series) to Fig. 4.9 (average tooth angle). The projection of the x and y vibrations onto the surface normal (referred to as the radial direction in [5]) is now:

$$n = -x \sin(\phi) - y \cos(\phi) \quad (4.30)$$

and the instantaneous chip thickness equation for tooth j becomes:

$$h(\phi_j) = (f_t \sin(\phi_j) + n_{j-1} - n_j) \cdot g(\phi_j), \quad (4.31)$$

where the switching function, $g(\phi_j)$, is equal to one when the j th tooth is engaged in the cut (i.e., between the cut start and exit angles) and zero otherwise; see Eq. 4.32. Also, n_{j-1} indicates the normal direction vibration from the previous tooth and n_j the current tooth vibration.

$$g(\phi_j) = \begin{cases} 1, & \text{when } \phi_s \leq \phi_j \leq \phi_e \\ 0, & \text{when } \phi_j < \phi_s, \phi_j > \phi_e \end{cases} \quad (4.32)$$

If the variable x and y contributions are substituted into Eq. 4.31 and the nominal component $f_t \sin(\phi_j)$ is neglected (because we are interested in linear stability), the cutter angle dependent chip thickness in the normal direction may be written as shown in Eq. 4.33.

$$\begin{aligned} h(\phi_j) &= ((-x_{j-1} \sin(\phi_j) - y_{j-1} \cos(\phi_j)) - (-x_j \sin(\phi_j) - y_j \cos(\phi_j)))g(\phi_j) \\ h(\phi_j) &= ((x_j - x_{j-1}) \sin(\phi_j) + (y_j - y_{j-1}) \cos(\phi_j))g(\phi_j) \\ h(\phi_j) &= (\Delta x \sin(\phi_j) + \Delta y \cos(\phi_j))g(\phi_j) \end{aligned} \quad (4.33)$$

The tangential and normal (radial) force components are then written as a function of the chip thickness:

$$F_{t,j} = K_t b h(\phi_j) \quad \text{and} \quad F_{n,j} = K_n F_{t,j} = K_n K_t b h(\phi_j), \quad (4.34)$$

where K_t is equal to the previously defined tangential specific force k_t . The relationship between (K_t , K_n) and K_s is defined using Fig. 4.32:

$$F_j = K_s b h(\phi_j),$$

$$F_j = \sqrt{F_{t,j}^2 + F_{n,j}^2} = \sqrt{K_t^2 + K_n^2 K_t^2} b h(\phi_j) = K_t \sqrt{1 + K_n^2} b h(\phi_j) \quad (4.35)$$

so that $K_s = K_t \sqrt{1 + K_n^2}$. Also, $\tan(\beta) = \frac{F_{t,j}}{F_{n,j}} = \frac{K_t b h(\phi_j)}{K_n K_t b h(\phi_j)} = \frac{1}{K_n}$. The projections of the tangential and normal force components onto the fixed (x and y) coordinate frame are:

$$F_{x,j} = -F_{t,j} \cos(\phi_j) - F_{n,j} \sin(\phi_j) \quad \text{and} \quad F_{y,j} = F_{t,j} \sin(\phi_j) - F_{n,j} \cos(\phi_j). \quad (4.36)$$

Substitution into the $F_{x,j}$ component gives Eq. 4.37.

$$F_{x,j} = \begin{pmatrix} -(K_t b (\Delta x \sin(\phi_j) + \Delta y \cos(\phi_j)) g(\phi_j)) \cos(\phi_j) \\ -(K_n K_t b (\Delta x \sin(\phi_j) + \Delta y \cos(\phi_j)) g(\phi_j)) \sin(\phi_j) \end{pmatrix}$$

$$F_{x,j} = -K_t b g(\phi_j) \begin{pmatrix} (\Delta x \sin(\phi_j) + \Delta y \cos(\phi_j)) \cos(\phi_j) \\ + K_n (\Delta x \sin(\phi_j) + \Delta y \cos(\phi_j)) \sin(\phi_j) \end{pmatrix} \quad (4.37)$$

$$F_{x,j} = -K_t b g(\phi_j) \begin{pmatrix} \Delta x (\sin(\phi_j) \cos(\phi_j) + K_n \sin^2(\phi_j)) \\ + \Delta y (\cos^2(\phi_j) + K_n \sin(\phi_j) \cos(\phi_j)) \end{pmatrix}$$

Similarly, the $F_{y,j}$ component is expressed as shown in Eq. 4.38.

$$F_{y,j} = \begin{pmatrix} (K_t b (\Delta x \sin(\phi_j) + \Delta y \cos(\phi_j)) g(\phi_j)) \sin(\phi_j) \\ -(K_n K_t b (\Delta x \sin(\phi_j) + \Delta y \cos(\phi_j)) g(\phi_j)) \cos(\phi_j) \end{pmatrix}$$

$$F_{y,j} = K_t b g(\phi_j) \begin{pmatrix} (\Delta x \sin(\phi_j) + \Delta y \cos(\phi_j)) \sin(\phi_j) \\ - K_n (\Delta x \sin(\phi_j) + \Delta y \cos(\phi_j)) \cos(\phi_j) \end{pmatrix} \quad (4.38)$$

$$F_{y,j} = K_t b g(\phi_j) \begin{pmatrix} \Delta x (\sin^2(\phi_j) - K_n \cos(\phi_j) \sin(\phi_j)) \\ + \Delta y (\cos(\phi_j) \sin(\phi_j) - K_n \cos^2(\phi_j)) \end{pmatrix}$$

Substituting the trigonometric identities $\sin(\phi) \cos(\phi) = \frac{\sin(2\phi)}{2}$, $\sin^2(\phi) = 1 - \cos^2(\phi)$, and $\cos^2(\phi) = \frac{1 + \cos(2\phi)}{2}$ into Eqs. 4.37 and 4.38 yields:

$$F_{x,j} = -\frac{1}{2} K_t b g(\phi_j) \begin{pmatrix} \Delta x (\sin(2\phi_j) + K_n (1 - \cos(2\phi_j))) \\ + \Delta y (1 + \cos(2\phi_j) + K_n \sin(2\phi_j)) \end{pmatrix} \quad \text{and} \quad (4.39)$$

$$F_{y,j} = \frac{1}{2} K_t b g(\phi_j) \begin{pmatrix} \Delta x((1 - \cos(2\phi_j)) - K_n \sin(2\phi_j)) \\ + \Delta y(\sin(2\phi_j) - K_n(1 + \cos(2\phi_j))) \end{pmatrix}. \quad (4.40)$$

The force expressions are completed by including the summation over all teeth so that the contributions of (potentially) multiple teeth in the cut are considered.

$$F_x = \sum_{j=1}^{N_t} F_{x,j} \quad \text{and} \quad F_y = \sum_{j=1}^{N_t} F_{y,j} \quad (4.41)$$

The x and y direction force expressions are now arranged in matrix form to obtain:

$$\begin{pmatrix} F_x \\ F_y \end{pmatrix} = \frac{1}{2} b K_t \begin{bmatrix} a_{xx} & a_{xy} \\ a_{yx} & a_{yy} \end{bmatrix} \begin{pmatrix} \Delta x \\ \Delta y \end{pmatrix} = \frac{1}{2} b K_t [A](\Delta), \quad (4.42)$$

where the individual A matrix entries, referred to in [5] as the “time varying directional dynamic force coefficients,” are:

$$\begin{aligned} a_{xx} &= \sum_{j=1}^{N_t} -g(\phi_j)(\sin(2\phi_j) + K_n(1 - \cos(2\phi_j))), \\ a_{xy} &= \sum_{j=1}^{N_t} -g(\phi_j)(1 + \cos(2\phi_j) + K_n \sin(2\phi_j)), \\ a_{yx} &= \sum_{j=1}^{N_t} g(\phi_j)((1 - \cos(2\phi_j)) - K_n \sin(2\phi_j)), \quad \text{and} \\ a_{yy} &= \sum_{j=1}^{N_t} g(\phi_j)(\sin(2\phi_j) - K_n(1 + \cos(2\phi_j))). \end{aligned}$$

Here we note that, because these expressions are periodic with the tooth pitch, $\phi_p = \frac{2\pi}{N_t}$ (rad), they are also periodic in time over the tooth period, $\tau = \frac{60}{\Omega N_t}$ (s), where Ω is expressed in rpm. Therefore, although the A matrix is written as a function of ϕ in Eq. 4.42, it is equivalently a function of time, $t = \frac{\phi}{\Omega} \frac{60}{2\pi}$ (s), where Ω is given in rpm and ϕ in rad. In order to remove the time dependence of the A matrix, now written explicitly as $[A(t)]$, it is first expanded into a Fourier series:

$$[A(t)] = \sum_{r=-\infty}^{\infty} [A_r] e^{ir\omega_{tooth}t}, \quad (4.43)$$

where $\omega_{tooth} = 2\pi \cdot f_{tooth}$ (rad/s) and the Fourier coefficients are $[A_r] = \frac{1}{N_t \tau} \int_0^{N_t \tau} [A(t)] e^{-ir\omega_{tooth}t} dt$, and then only the $r = 0$ term is retained. Although $[A(t)]$

is best represented using multiple harmonics of ω_{tooth} , setting $r = 0$ leads to the desired time invariance because the exponential term becomes unity ($e^0 = 1$). The trade-off is that the accuracy degrades as the radial immersion is reduced (the same is true for the average tooth angle approximation). This is particularly true when the radial immersion is only a few percent and the cutting force becomes more “impulse-like” [6–9]. Equation 4.44 shows the $r = 0$ coefficient, $[A_0]$, written explicitly as a function of ϕ (as in Eq. 4.42). By modifying the integration limits to be ϕ_s and ϕ_e (all angles in rad), the switching function is effectively removed since it is equal to one within these limits and zero otherwise.

$$[A_0] = \frac{1}{2\pi} \int_0^{2\pi} [A(\phi)] d\phi = \frac{1}{2\pi} \int_{\phi_s}^{\phi_e} [A(\phi)] d\phi = \frac{N_t}{2\pi} \begin{bmatrix} \alpha_{xx} & \alpha_{xy} \\ \alpha_{yx} & \alpha_{yy} \end{bmatrix} \quad (4.44)$$

The individual α terms, similar to the directional orientation factors defined in the average tooth angle approach, are provided in Eq. 4.45, where the integrals must be evaluated between ϕ_s and ϕ_e to obtain the final scalar values. Note that the N_t term is introduced in the final Eq. 4.44 expression due to the summations ($\sum_{j=1}^{N_t} \dots$) in the a terms from Eq. 4.42.

$$\begin{aligned} \alpha_{xx} &= \frac{1}{2} (\cos(2\phi) - 2K_n\phi + K_n \sin(2\phi)) \Big|_{\phi_s}^{\phi_e} \\ \alpha_{xy} &= \frac{1}{2} (-\sin(2\phi) - 2\phi + K_n \cos(2\phi)) \Big|_{\phi_s}^{\phi_e} \\ \alpha_{yx} &= \frac{1}{2} (-\sin(2\phi) + 2\phi + K_n \cos(2\phi)) \Big|_{\phi_s}^{\phi_e} \\ \alpha_{yy} &= \frac{1}{2} (-\cos(2\phi) - 2K_n\phi - K_n \sin(2\phi)) \Big|_{\phi_s}^{\phi_e} \end{aligned} \quad (4.45)$$

The stability analysis begins by equating the frequency domain vibrations in the x and y directions (the j subscripts indicate the current tooth) with the product of the frequency response function matrix and the frequency domain representation of the cutting forces.

$$\begin{pmatrix} X_j \\ Y_j \end{pmatrix} = \begin{bmatrix} \text{FRF}_{xx} & \text{FRF}_{xy} \\ \text{FRF}_{yx} & \text{FRF}_{yy} \end{bmatrix} \begin{pmatrix} F_x \\ F_y \end{pmatrix} e^{i\omega_c t} = \begin{bmatrix} \text{FRF}_{xx} & 0 \\ 0 & \text{FRF}_{yy} \end{bmatrix} \begin{pmatrix} F_x \\ F_y \end{pmatrix} e^{i\omega_c t} \quad (4.46)$$

In Eq. 4.46, the cross FRFs (FRF_{xy} , representing measurement in the x direction with excitation in the y direction, and FRF_{yx}) are set equal to zero because the x and y directions are orthogonal and zero cross talk between the two directions is assumed. Also, the ω_c notation indicates chatter frequencies (rad/s). The vibrations one tooth period earlier (denoted by the $j - 1$ subscripts) are similarly written as:

$$\begin{pmatrix} X_{j-1} \\ Y_{j-1} \end{pmatrix} = \begin{pmatrix} X_j \\ Y_j \end{pmatrix} e^{-i\omega_c \tau} = \begin{bmatrix} \text{FRF}_{xx} & 0 \\ 0 & \text{FRF}_{yy} \end{bmatrix} \begin{pmatrix} F_x \\ F_y \end{pmatrix} e^{i\omega_c t} e^{-i\omega_c \tau}, \quad (4.47)$$

where $e^{-i\omega_c \tau}$ represents the delay of one tooth period. Taking the difference between Eqs. 4.46 and 4.47 gives:

$$\begin{pmatrix} X_j \\ Y_j \end{pmatrix} - \begin{pmatrix} X_{j-1} \\ Y_{j-1} \end{pmatrix} = (1 - e^{-i\omega_c \tau}) \begin{bmatrix} \text{FRF}_{xx} & 0 \\ 0 & \text{FRF}_{yy} \end{bmatrix} \begin{pmatrix} F_x \\ F_y \end{pmatrix} e^{i\omega_c t}. \quad (4.48)$$

The left hand side of Eq. 4.48 can be written as $\begin{pmatrix} X_j \\ Y_j \end{pmatrix} - \begin{pmatrix} X_{j-1} \\ Y_{j-1} \end{pmatrix} = \begin{pmatrix} \Delta X \\ \Delta Y \end{pmatrix}$, which enables substitution into the frequency domain representation of Eq. 4.42, the “dynamic milling equation” according to [5].

$$\begin{pmatrix} F_x \\ F_y \end{pmatrix} e^{i\omega_c t} = \frac{1}{2} b K_t [A_0] (1 - e^{i\omega_c \tau}) \begin{bmatrix} \text{FRF}_{xx} & 0 \\ 0 & \text{FRF}_{yy} \end{bmatrix} \begin{pmatrix} F_x \\ F_y \end{pmatrix} e^{i\omega_c t} \quad (4.49)$$

Rearranging Eq. 4.49 gives $\begin{pmatrix} F_x \\ F_y \end{pmatrix} e^{i\omega_c t} \left([I] - \frac{1}{2} b K_t (1 - e^{i\omega_c \tau}) [A_0] \begin{bmatrix} \text{FRF}_{xx} & 0 \\ 0 & \text{FRF}_{yy} \end{bmatrix} \right) = 0$, which has a nontrivial solution only if:

$$\det \left([I] - \frac{1}{2} b K_t (1 - e^{i\omega_c \tau}) [A_0] \begin{bmatrix} \text{FRF}_{xx} & 0 \\ 0 & \text{FRF}_{yy} \end{bmatrix} \right) = 0, \quad (4.50)$$

where $[I] = \begin{bmatrix} 1 & 0 \\ 0 & 1 \end{bmatrix}$ is the 2×2 identity matrix. This is the characteristic equation of the closed loop dynamic milling system [5]. The product $[A_0][\text{FRF}]$ from Eq. 4.50 is analogous to the oriented FRF from the average tooth angle approach. Expanding gives Eq. 4.51.

$$\begin{aligned} [A_0][\text{FRF}] &= \frac{N_t}{2\pi} \begin{bmatrix} \alpha_{xx} & \alpha_{xy} \\ \alpha_{yx} & \alpha_{yy} \end{bmatrix} \begin{bmatrix} \text{FRF}_{xx} & 0 \\ 0 & \text{FRF}_{yy} \end{bmatrix} = \\ &\frac{N_t}{2\pi} \begin{bmatrix} \alpha_{xx}\text{FRF}_{xx} & \alpha_{xy}\text{FRF}_{yy} \\ \alpha_{yx}\text{FRF}_{xx} & \alpha_{yy}\text{FRF}_{yy} \end{bmatrix} = \frac{N_t}{2\pi} [\text{FRF}_{\text{or}}]. \end{aligned} \quad (4.51)$$

A new variable, Λ , is now defined as:

$$\Lambda = \frac{N_t}{2\pi} \left(-\frac{1}{2} b K_t (1 - e^{-i\omega_c \tau}) \right) = -\frac{N_t}{4\pi} b K_t (1 - e^{-i\omega_c \tau}) \quad (4.52)$$

so that the characteristic equation can be rewritten as shown in Eq. 4.53, which includes the new oriented FRF, FRF_{or} , from Eq. 4.51.

$$\det([I] + \Lambda[\text{FRF}_{\text{or}}]) = 0 \quad (4.53)$$

Computing the determinant, $\det \begin{bmatrix} 1 + \Lambda\alpha_{xx}\text{FRF}_{xx} & \Lambda\alpha_{xy}\text{FRF}_{yy} \\ \Lambda\alpha_{yx}\text{FRF}_{xx} & 1 + \Lambda\alpha_{yy}\text{FRF}_{yy} \end{bmatrix} = 0$, gives an expression which is quadratic in Λ .

$$(1 + \Lambda\alpha_{xx}\text{FRF}_{xx})(1 + \Lambda\alpha_{yy}\text{FRF}_{yy}) - \Lambda^2(\alpha_{xy}\text{FRF}_{yy})(\alpha_{yx}\text{FRF}_{xx}) = 0$$

$$\Lambda^2(\alpha_{xx}\alpha_{yy}\text{FRF}_{xx}\text{FRF}_{yy} - \alpha_{xy}\alpha_{yx}\text{FRF}_{xx}\text{FRF}_{yy}) + \Lambda(\alpha_{xx}\text{FRF}_{xx} + \alpha_{yy}\text{FRF}_{yy}) + 1 = 0$$

This frequency dependent equation is rewritten as $a_0\Lambda^2 + a_1\Lambda + 1 = 0$, where $a_0 = \text{FRF}_{xx}\text{FRF}_{yy}(\alpha_{xx}\alpha_{yy} - \alpha_{xy}\alpha_{yx})$ and $a_1 = \alpha_{xx}\text{FRF}_{xx} + \alpha_{yy}\text{FRF}_{yy}$. The two roots are the system eigenvalues, Λ_1 and Λ_2 . These complex eigenvalues can be determined using the quadratic equation:

$$\Lambda_{1,2} = \frac{-a_1 \pm \sqrt{a_1^2 - 4a_0}}{2a_0} = -\frac{1}{2a_0} \left(a_1 \mp \sqrt{a_1^2 - 4a_0} \right).$$

Note that these eigenvalues are a function of ω_c due to the dependence on the x and y direction FRFs. At each potential chatter frequency, the minimum b_{lim} value (from the two available eigenvalues) is selected to establish the limiting chip width. The relationship between b_{lim} and Ω is detailed next.

Equation 4.52 is now rewritten by recognizing the complex nature of the eigenvalues, $\Lambda = \Lambda_{\text{Re}} + i\Lambda_{\text{Im}}$, and substituting the Euler identity $e^{-i\omega_c\tau} = \cos(\omega_c\tau) - i\sin(\omega_c\tau)$:

$$\Lambda_{\text{Re}} + i\Lambda_{\text{Im}} = -\frac{N_t}{4\pi} b K_t (1 - \cos(\omega_c\tau) + i\sin(\omega_c\tau)). \quad (4.54)$$

Equation 4.54 is solved for b to obtain the limiting chip width, b_{lim} :

$$b_{\text{lim}} = -(\Lambda_{\text{Re}} + i\Lambda_{\text{Im}}) \frac{4\pi}{N_t K_t} \frac{1}{(1 - \cos(\omega_c\tau) + i\sin(\omega_c\tau))}. \quad (4.55)$$

Rationalizing Eq. 4.55 gives Eq. 4.56.

$$\begin{aligned} b_{\text{lim}} &= -(\Lambda_{\text{Re}} + i\Lambda_{\text{Im}}) \frac{4\pi}{N_t K_t} \frac{(1 - \cos(\omega_c\tau) - i\sin(\omega_c\tau))}{((1 - \cos(\omega_c\tau))^2 + (\sin(\omega_c\tau))^2)} \\ b_{\text{lim}} &= -\frac{4\pi}{N_t K_t} \frac{(\Lambda_{\text{Re}} + i\Lambda_{\text{Im}})(1 - \cos(\omega_c\tau) - i\sin(\omega_c\tau))}{(2 - 2\cos(\omega_c\tau))} \\ b_{\text{lim}} &= -\frac{2\pi}{N_t K_t} \left(\begin{array}{l} \left(\frac{(\Lambda_{\text{Re}}(1 - \cos(\omega_c\tau)) + \Lambda_{\text{Im}}\sin(\omega_c\tau))}{(1 - \cos(\omega_c\tau))} + \right. \\ \left. i \frac{(\Lambda_{\text{Im}}(1 - \cos(\omega_c\tau)) - \Lambda_{\text{Re}}\sin(\omega_c\tau))}{(1 - \cos(\omega_c\tau))} \right) \end{array} \right) \end{aligned} \quad (4.56)$$

Next, it is recognized that, because b_{lim} must be real valued, the imaginary part of the final expression in Eq. 4.56 must be equal to zero, giving $\Lambda_{\text{Im}}(1 - \cos(\omega_c \tau)) - \Lambda_{\text{Re}} \sin(\omega_c \tau) = 0$. From this statement, the new variable κ is defined.

$$\kappa = \frac{\Lambda_{\text{Im}}}{\Lambda_{\text{Re}}} = \frac{\sin(\omega_c \tau)}{1 - \cos(\omega_c \tau)}. \quad (4.57)$$

Equation 4.56 is now rewritten to obtain the final, frequency-dependent expression for the stability limit.

$$\begin{aligned} b_{\text{lim}} &= -\frac{2\pi}{N_t K_t} \left(\frac{(\Lambda_{\text{Re}}(1 - \cos(\omega_c \tau)) + \Lambda_{\text{Im}} \sin(\omega_c \tau))}{(1 - \cos(\omega_c \tau))} \right) \\ b_{\text{lim}} &= -\frac{2\pi}{N_t K_t} \left(\Lambda_{\text{Re}} + \frac{\Lambda_{\text{Im}} \sin(\omega_c \tau)}{(1 - \cos(\omega_c \tau))} \right) \\ b_{\text{lim}} &= -\frac{2\pi}{N_t K_t} \Lambda_{\text{Re}} \left(1 + \frac{\Lambda_{\text{Im}}}{\Lambda_{\text{Re}}} \frac{\sin(\omega_c \tau)}{(1 - \cos(\omega_c \tau))} \right) = -\frac{2\pi}{N_t K_t} \Lambda_{\text{Re}} (1 + \kappa^2) \end{aligned} \quad (4.58)$$

The corresponding frequency dependent spindle speeds are determined by first writing the phase shift in the surface undulations between subsequent tooth passages (similar to the average tooth angle derivation), $\epsilon = \pi - 2\psi$ (rad), where $\psi = \tan^{-1}(\kappa)$ (rad). The tooth passing periods are next expressed as $\tau = \frac{1}{\omega_c}(\epsilon + j \cdot 2\pi)$ (s), where $j = 0, 1, 2, \dots$ refers to the integer number of waves between teeth. Incrementing j leads to the individual lobes; it serves in the same capacity as N in Eq. 4.24. Finally, the spindle speeds are obtained from:

$$\Omega = \frac{60}{N_t \tau} \text{ (rpm)}. \quad (4.59)$$

Because our computing platform of choice is MATLAB®, we will rewrite the eigenvalue problem as stated in Eq. 4.53, $\det([I] + \Lambda[\text{FRF}_{\text{or}}]) = 0$, in the more traditional format required by the `eig` function. This formulation is $\det([\text{FRF}_{\text{or}}] - \lambda[I]) = 0$, where the new eigenvalue expression is $\lambda = \frac{4\pi}{N_t} \frac{1}{bK_t(1 - e^{-j\omega_c \tau})}$. The corresponding revised stability limit is:

$$\tilde{b}_{\text{lim}} = \frac{2\pi}{N_t K_t (\lambda_{\text{Re}}^2 + \lambda_{\text{Im}}^2)} \lambda_{\text{Re}} (1 + \tilde{\kappa}^2), \quad (4.60)$$

where $\tilde{\kappa} = \frac{\lambda_{\text{Im}}}{\lambda_{\text{Re}}}$. The derivation that leads to Eq. 4.60 is included in Appendix. The two complex eigenvalues, λ_1 and λ_2 , are determined using the MATLAB® function call `eig(FRF_or)` in p_4_8_1.m, where `FRF_or` is the oriented FRF defined in Eq. 4.51. The spindle speed equations are also modified to be $\tilde{\psi} = \tan^{-1}(\tilde{\kappa})$ (rad), $\tilde{\epsilon} = \pi - 2\tilde{\psi}$ (rad), $\tilde{\tau} = \frac{1}{\omega_c}(\tilde{\epsilon} + j(2\pi))$ (s), and

$$\tilde{\Omega} = \frac{60}{N_t \tilde{\tau}} \text{ (rpm).} \quad (4.61)$$

The stability lobe diagram is obtained by plotting $\tilde{\Omega}$ versus the two \tilde{b}_{lim} values for each chatter frequency (the minimum at each spindle speed is selected to define the stability boundary). Note that in this analysis, the valid chatter frequencies are not limited to those corresponding to negative real values of the oriented FRF. Instead, the full frequency range of FRF_{or} is applied.



In a Nutshell

There are two related, but slightly different, methods for dealing with the varying orientation of the cutting force as the teeth pass through the cutting zone. Both approaches are simplifications of reality and have cutting conditions and machine dynamic characteristics where they predict experimental results more or less accurately. Conceptually, the milling stability lobe diagram is similar to the turning stability lobe diagram. The biggest stable zone occurs where the tooth passing frequency matches the dominant natural frequency and other stable zones occur at integer fractions of that best speed.

Example 4.8 Comparison with Example 4.7 Stability Results In this example, the conditions are the same as for Example 4.7. Specifically, a 20% radial immersion down milling cut with a start angle of $\phi_s = 126.9$ deg and exit angle of $\phi_e = 180$ deg is analyzed. The x (feed) direction dynamics are $f_{nx} = 900$ Hz, $k_x = 9 \times 10^6$ N/m, and $\zeta_x = 0.02$. The y direction dynamics are $f_{ny} = 950$ Hz, $k_y = 1 \times 10^7$ N/m, and $\zeta_y = 0.01$. The workpiece material is a low-carbon steel alloy, and it is machined with a three tooth, 19 mm diameter square endmill. For a specific force value of $K_s = 2250$ N/mm² and a force angle of $\beta = 75$ deg, the corresponding cutting force coefficients are $K_n = \frac{1}{\tan(\beta)} = 0.268$ and $K_t = \frac{K_s}{\sqrt{1 + K_n^2}} = 2173$ N/mm².

Based on the selected start and exit angles and K_n value, the α values from Eq. 4.45 required to calculate FRF_{or} are $\alpha_{xx} = 0.5198$, $\alpha_{xy} = -1.2356$, $\alpha_{yx} = 0.6180$, and $\alpha_{yy} = -1.0165$. The stability lobe diagram obtained from the Fourier series analysis is provided in Fig. 4.33. Two limits are seen; the dotted line is obtained from λ_1 and the solid line from λ_2 . It is observed that the composite stability limit (defined collectively from the minimum of the λ_1 and λ_2 b_{lim} values at each spindle speed) is very similar to the average tooth angle limit shown in Fig. 4.31. For example, $b_{\text{lim, crit}} = 0.50$ mm from Fig. 4.33 compares favorably with the 0.41 mm value from Fig. 4.31, and the stability boundary peaks and troughs occur at the same spindle speeds. As noted previously, the MATLAB® program used to produce Fig. 4.33 is provided with the textbook as p_4_8_1.m.

Example 4.9 Comparison with Example 4.6 Stability Results In contrast to the close agreement between the two approaches seen in Example 4.6, the methods diverge somewhat in the case of slotting. Although the best speeds agree, the allowable chip widths differ. As in Example 4.6, the symmetric x and y direction dynamics are

Fig. 4.33 Example 4.8 stability lobe diagram ($j = 0$ to 4)

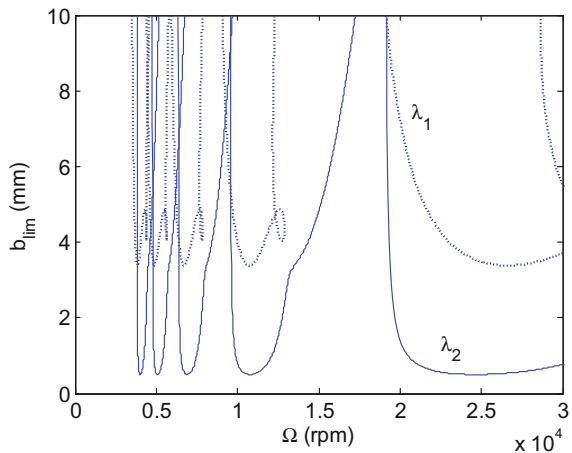
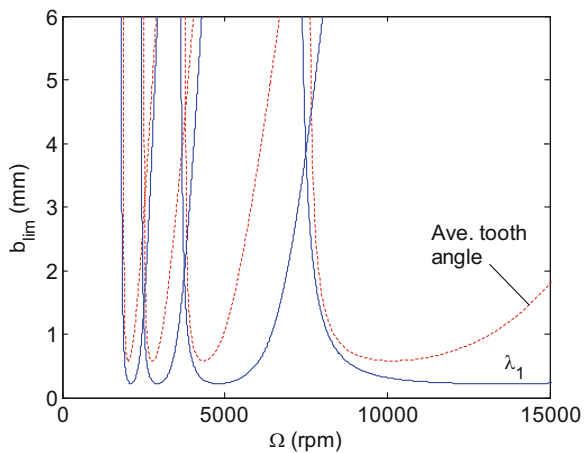


Fig. 4.34 Example 4.9 stability lobe diagram ($j = 0$ to 3). The solid line shows the Fourier series stability boundary, while the dotted line gives the average tooth angle result ($N = 0$ to 3)



$f_n = 500$ Hz, $k = 8 \times 10^6$ N/m, and $\zeta = 0.02$. An aluminum alloy is machined with a four tooth square endmill and the cutting force coefficients are $K_t = 695$ N/mm² and $K_n = 0.404$, corresponding to $K_s = 750$ N/mm² and $\beta = 68$ deg. For $\phi_s = 0$ and $\phi_e = 180$ deg, the α values are $\alpha_{xx} = -1.2693$, $\alpha_{xy} = -3.1416$, $\alpha_{yx} = 3.1416$, and $\alpha_{yy} = -1.2693$. The Fourier series approach stability limit is shown as the solid line in Fig. 4.34. Only the λ_1 boundary is seen at the selected scale (the λ_2 boundary occurs at higher chip widths in this case). For comparison convenience, the result from the average tooth angle approach (previously shown in Fig. 4.27) is also included as the dotted line. In this case, the $b_{\text{lim},\text{crit}}$ values are 0.22 mm (Fourier series) and 0.58 mm (average tooth angle). Additionally, the stable zone (beneath the stability boundary) has a smaller area for the Fourier series calculations. We will explore this disagreement further in Sect. 4.4. The MATLAB® program used to produce Fig. 4.34 is included as p_4_9_1.m with the textbook.

4.4 Milling Time Domain Simulation with Straight Teeth

In this section, a time domain simulation for the milling problem is detailed. It is based on the “Regenerative Force, Dynamic Deflection Model” described by Smith and Tlusty [4]. As with the turning analysis in Chap. 3, the analytical stability lobe diagrams detailed in Sect. 4.3 provide a “global” picture of the stability behavior, but do not provide information regarding the “local” cutting force or tool vibrations. The time domain simulation, on the other hand, gives this “local” force and vibration information for the selected cutting conditions. The simulation again applies numerical integration to solve the time-delayed differential equations of motion and includes the nonlinearity that occurs if the tooth leaves the cut. Assumptions include straight cutter teeth, the circular tool path, and a square endmill geometry. Similar to turning, the simulation proceeds as follows:

1. The instantaneous chip thickness is determined using the vibration of the current and previous teeth at the selected tooth angle.
2. The cutting force is calculated.
3. The force is used to find the new displacements.
4. The tooth angle is incremented and the process is repeated.

The simulation model geometry is the same as was presented in Fig. 4.8. We use modal parameters to describe the dynamics of the nonrigid tool in the x and y directions, where multiple degrees of freedom in each direction can be accommodated as described in Sect. 3.5.



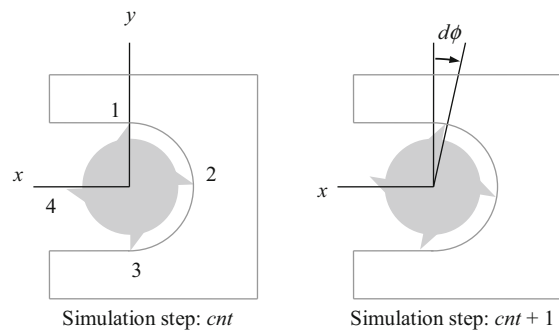
In a Nutshell

Nothing is a better representation of reality than reality (actual cutting). However, milling simulation removes many of the simplifying assumptions required by the analytical derivations. As in turning, time domain simulation provides detailed information about a specific case but loses the global information provided by the analytical solutions. The production of a stability lobe diagram requires many executions of the simulation.

4.4.1 Chip Thickness Calculation

The instantaneous chip thickness depends on the nominal, tooth angle-dependent chip thickness (Eq. 4.2), the current normal direction vibration, and the vibration of the previous tooth at the same angle. As described in Sect. 4.2, the chip thickness can be expressed as $h(t) = f_t \sin(\phi) + n(t - \tau) - n(t)$, where τ is the tooth period, $\tau = \frac{60}{\Omega N_t}$ (s), and Ω is given in rpm. The vibrations in the direction of the surface normal for the current tooth depend on the x and y vibrations as well as the tooth angle, according to $n = x \sin(\phi) - y \cos(\phi)$. Figure 4.22 presented an “unwrapped”

Fig. 4.35 Cutter rotation by $d\phi$ from one simulation step to the next (a slotting cut is depicted)



view of the milled surface that demonstrates the regeneration mechanism in the chip thickness equation. Note that the positive *x* direction again opposes the feed direction. For this simulation, we will neglect the possibility that the current surface may depend on more than the prior and current tooth vibrations (as shown for turning in Fig. 3.33). Also, because we have assumed straight teeth, we will ignore vibrations in the *z* direction.

As discussed in the stability lobe development, the milling equations may be equivalently considered to be a function of time or angle. For the simulation, our strategy is to divide the angle of the cut into a discrete number of steps. At each small time step, dt , we increment the cutter angle by the corresponding small angle, $d\phi$. This approach enables convenient computation of the chip thickness for each simulation step because: (1) we have predefined the possible teeth orientations; and (2) we can store the surface created by the previous tooth at each angle. The cutter rotation by the $d\phi$ increment is depicted in Fig. 4.35, where the size of the increment depends on the selection of the number of steps per revolution (`steps_rev` in `p_4_10_1.m` with the textbook), specifically, $d\phi = 360/\text{steps_rev}$ (deg). The corresponding time step is $dt = [60/\text{steps_rev}(\Omega)]$ (s), where Ω is the spindle speed in rpm. (Note that the teeth number labeling convention differs from that shown in Sects. 4.1 and 4.2. Previously, the teeth were numbered according to their order of entry into the cut for convenience of description, while they are now labeled according to increasing angle in a clockwise manner for “bookkeeping” purposes within the simulation.) A vector of angles is defined to represent the potential orientations of the teeth as the cutter is rotated through one revolution of the circular tool path, $\phi = [0, d\phi, 2d\phi, 3d\phi, \dots, (\text{steps_rev} - 1)d\phi]$. The locations of the teeth within the cut are then defined by referencing entries in this vector (`phi` in `p_4_10_1.m`). For equal teeth spacing, this means that the teeth are located every $\text{steps_rev}/N_t$. A vector of tooth orientations that indicates particular entries in the ϕ vector, not actual angles, is then defined as: $\text{teeth} = [1, (\text{steps_rev}/N_t) + 1, 2\text{steps_rev}/N_t + 1, \dots, (N_t - 1)\text{steps_rev}/N_t + 1]$. Incrementing the teeth angles by $d\phi$ is then a simple matter of adding one to each entry in the `teeth` vector. Finally, individual tooth angles can be identified by the MATLAB® statement: `phi(teeth(cnt))`, where `cnt` indicates the tooth in question. Therefore, a requirement for using the $\text{steps_rev}/N_t$ ratio to indicate locations within the ϕ vector is that it is an

integer greater than zero (necessary for MATLAB® indices). This is explored in Example 4.10.

Example 4.10 Simulation Tooth Angle Definition We'll consider the case where 650 steps per revolution has been selected for a cutter with four teeth. The spindle speed is 10,000 rpm. Our first requirement is that $steps_rev/N_t$ is an integer so that the ϕ vector can be referenced using the $teeth$ entries. In this case, $steps_rev/N_t = \frac{650}{4} = 162.5$ steps/tooth. To correct the non-integer situation, the MATLAB® function `round` can be implemented to determine the nearest integer ratio:

```
temp = round(steps_rev/Nt);
steps_rev = temp*Nt;
```

as shown in `p_4_10_1.m`. The result is that the new ratio, saved to the `temp` variable, is 163, and the updated number of steps per revolution is 652. The angular increment is $d\phi = \frac{360}{652} = 0.5521$ deg and the time increment for numerical integration is $dt = \frac{60}{652 \cdot 10,000} = 9.2025 \times 10^{-6}$ s. The vector of possible tooth angles (in MATLAB® syntax) is $\phi = [0 \ 0.5521 \ 1.1043 \ 1.6564 \dots 359.4479]$ deg, and the $teeth$ vector can be initially described by `teeth = [1 164 327 490]`. For this cutter orientation, tooth 1 is positioned at $\phi(teeth(1)) = \phi(1) = 0$. Similarly, the angles for teeth 2 through 4 are $\phi(teeth(2)) = \phi(164) = 90$ deg, $\phi(teeth(3)) = \phi(327) = 180$ deg, and $\phi(teeth(4)) = \phi(490) = 270$ deg, respectively. In the next time increment, 9.2025×10^{-6} s later, the $teeth$ vector values are each incremented by one to be `teeth = [2 165 328 491]`. The teeth angles are $\phi(teeth(1)) = \phi(2) = 0.5521$ deg, $\phi(teeth(2)) = \phi(165) = 90.5521$ deg, $\phi(teeth(3)) = \phi(328) = 180.5521$ deg, and $\phi(teeth(4)) = \phi(491) = 270.5521$ deg.

The next step in determining the (discrete) chip thickness at each simulation step is to address the $n(t - \tau)$ and $n(t)$ terms in the continuous $h(t) = f_t \sin(\phi) + n(t - \tau) - n(t)$ chip thickness equation. The $n(t)$ term is simply the current normal direction vibration level determined using:

```
n = (x*sin(phi(teeth(cnt3))*pi/180) - y*cos(phi(teeth(cnt3))
*pi/180));
```

in `p_4_10_1.m`, where `x` and `y` are the current `x` and `y` direction vibrations, the `sin` and `cos` functions require arguments in rad, and `cnt3` is a simulation index that counts through the individual teeth to sum the force contributions. To accommodate the $n(t - \tau)$ term, the normal direction vibration for the previous tooth at the current angular orientation is required. To organize these values, a new variable `surf` is defined. Values in this vector are indexed in the same way as `phi` (according to entries in the `teeth` vector), i.e., `surf(teeth(cnt3))`. The `surf` entries are updated after the current chip thickness calculation so that each time the value is

queried at a particular orientation, the entry for that tooth angle is referencing the result from the last time a tooth was positioned at the current angle. There are two scenarios for updating the `surf` value. First, if the current tooth is cutting (it is between ϕ_s and ϕ_e and the tangential cutting force is greater than or equal to zero), then the value is set to the current vibration using:

```
surf(teeth(cnt3)) = n;
```

in p_4_10_1.m. Recall that this value will not be referenced until the next tooth is at the current angle. Second, if the current tooth is bounded by the start and exit angles, but the tangential force is less than zero, then the tooth has vibrated out of the cut and the updating command is:

```
surf(teeth(cnt3)) = surf(teeth(cnt3)) + ft*sin(phi(teeth(cnt3))
*pi/180);
```

so that the previous value is appended by the nominal feed per tooth that was not removed. If the current angle is not bounded by the cut, then no updating is necessary. Finally, the instantaneous chip thickness equation is:

```
h = ft*sin(phi(teeth(cnt3))*pi/180) + surf(teeth(cnt3)) - n;
```

in p_4_10_1.m.

4.4.2 Force Calculation

Once the chip thickness is computed, the tangential component of the force in the current time step is determined using Eq. 4.8, where the chip width, b , is equal to the axial depth of cut for straight teeth. As with turning, the calculated chip thickness is negative if the current tool vibration in the normal direction is larger than the surface location (equal to the sum of the nominal chip thickness, $f_t \sin \phi$, and the vibration of the previous tooth at the same angle). The tangential cutting force is set to zero in this situation that no cutting is occurring. The normal force is then computed, and these results are projected into the x and y directions as shown in Eqs. 4.11 and 4.12.

4.4.3 Displacement Calculation

Considering a single degree of freedom in the x and y directions, the equations of motion are:

$$m_x \ddot{x} + c_x \dot{x} + k_x x = F_{x_1} \quad \text{and} \quad m_y \ddot{y} + c_y \dot{y} + k_y y = F_{y_1}. \quad (4.62)$$

Rewriting Eq. 4.62 yields expressions for the x and y direction accelerations in the current time step:

$$\ddot{x} = \frac{F_x - c_x \dot{x} + k_x x}{m_x} \quad \text{and} \quad \ddot{y} = \frac{F_y - c_y \dot{y} + k_y y}{m_y}, \quad (4.63)$$

where the velocities, \dot{x} and \dot{y} , and positions, x and y , from the previous time step are used (initial values are zero to begin the simulation). The new velocities and positions are then determined by numerical (Euler) integration:

$$\dot{x} = \dot{x} + \ddot{x}(dt) \quad \dot{y} = \dot{y} + \ddot{y}(dt), \quad (4.64)$$

$$x = x + \dot{x}(dt) \quad y = y + \dot{y}(dt), \quad (4.65)$$

where the velocities on the right hand side of the equal signs in Eq. 4.64 are retained from the previous time step. The new velocities are then applied to determine the new displacements in Eq. 4.65. Again, the displacements on the right-hand side of Eq. 4.65 are those from the previous time step. As mentioned previously, multiple degrees of freedom in each direction can be accommodated by summing the individual modal contributions as described in Sect. 3.5. Again, considering the dynamic characteristics of the machine in a modal sense facilitates the computation.

4.4.4 Simulation Summary and Implementation

The milling simulation provided in p_4_10_1.m completes three basic activities at each time step. First, the cutter is rotated by $d\phi$ by adding one to each entry in the *teeth* vector. Second, within a `for` loop (indexed by *cnt*) that sums over all the cutter teeth, it is first verified that the tooth in question is bounded by the start and exit cut angles. If so, the chip thickness is determined and the cutting force is calculated (including the nonlinearity if a tooth leaves the cut due to excessive vibration). If not, the force is set to zero. Third, the displacement is determined by numerical integration. To exercise the simulation, comparisons between the stability limits described in Example 4.9 and the simulated forces and displacements are made in Example 4.11.

Example 4.11 Comparison with Example 4.9 Using Time Domain Simulation To review, the x and y direction dynamics are symmetric with $f_n = 500$ Hz, $k = 8 \times 10^6$ N/m, and $\zeta = 0.02$. An aluminum alloy is machined with a four tooth square endmill, and the cutting force coefficients are $k_t = 695$ N/mm² and $k_n = 281$ N/mm², corresponding to $K_s = 750$ N/mm² and $\beta = 68$ deg. For the slotting cut, $\phi_s = 0$ and $\phi_e = 180$ deg. Additionally, there are 652 steps per revolution, the feed per tooth is 0.15 mm/tooth, and 20 revolutions are simulated, where the number of revolutions (*rev*) is related to the total number of simulation steps (*steps*) by $rev = \frac{steps(dt)\Omega}{60}$. Four different cases are considered: (1) $\Omega = 7500$ rpm and $b = 3$ mm; (2) $\Omega = 7500$ rpm

Fig. 4.36 Operating points for comparison between analytical stability boundaries from Example 4.9 and time domain simulation. (1) $\Omega = 7500$ rpm and $b = 3$ mm; (2) $\Omega = 7500$ rpm and $b = 5$ mm; (3) $\Omega = 5000$ rpm and $b = 0.1$ mm; and (4) $\Omega = 5000$ rpm and $b = 0.5$ mm

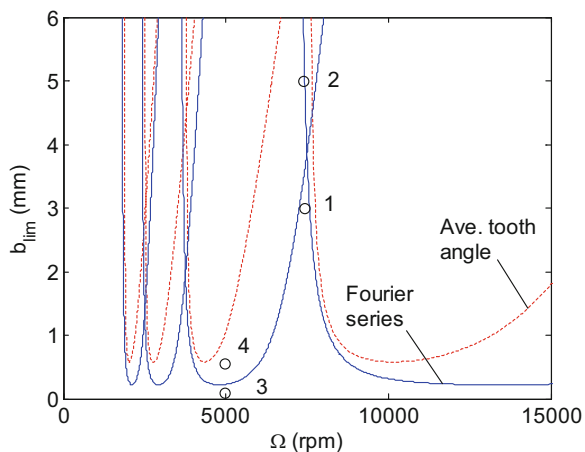
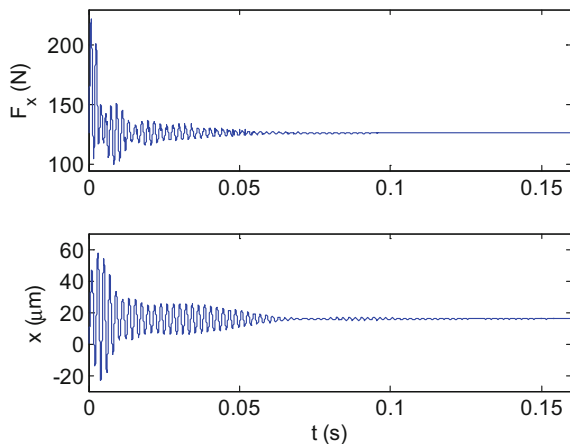


Fig. 4.37 Example 4.11 stable case 1 ($\Omega = 7500$ rpm and $b = 3$ mm) simulation results for x direction force (top) and displacement (bottom)



and $b = 5$ mm; (3) $\Omega = 5000$ rpm and $b = 0.1$ mm; and (4) $\Omega = 5000$ rpm and $b = 0.5$ mm. These operating points are identified in Fig. 4.36, which includes the average tooth angle and Fourier series stability limits.

According to the two analytical approaches, cases 1 and 3 should provide stable operating conditions. The time domain simulation corroborates these predictions. Figures 4.37 and 4.38 show the x and y direction forces and displacements, respectively, for case 1. It is seen that, once the initial transients attenuate after approximately 0.07 s, the expected constant force for a four tooth cutter in a slotting cut is obtained. Similar results are observed for case 3 in Figs. 4.39 and 4.40.

For cases 2 and 4, however, the Fourier series approach predicts that the cuts will be unstable, while the average tooth angle approximation shows these should be stable conditions. Figures 4.41 and 4.42 display the x and y direction results for case 2. Chatter is observed with the forces and displacement increasing over time. Additionally, Fig. 4.43 shows the resultant force and nonlinearity when the force

Fig. 4.38 Example 4.11 stable case 1 ($\Omega = 7500$ rpm and $b = 3$ mm) simulation results for y direction force (top) and displacement (bottom)

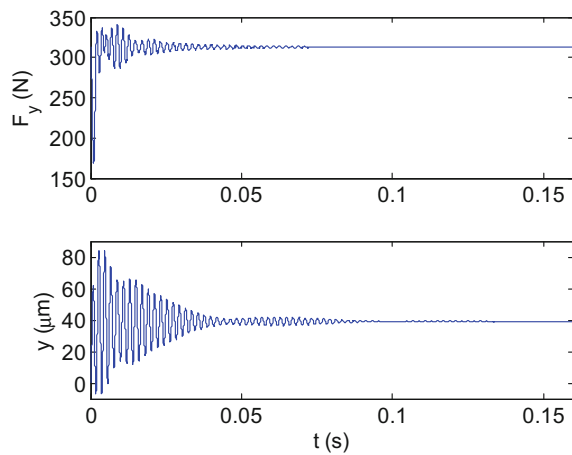


Fig. 4.39 Example 4.11 stable case 3 ($\Omega = 5000$ rpm and $b = 0.1$ mm) simulation results for x direction force (top) and displacement (bottom)

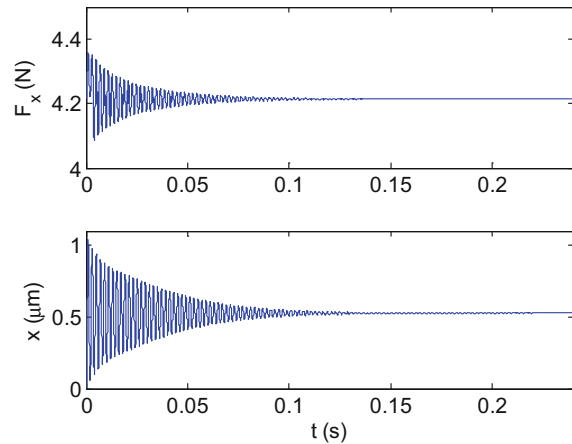


Fig. 4.40 Example 4.11 stable case 3 ($\Omega = 5000$ rpm and $b = 0.1$ mm) simulation results for y direction force (top) and displacement (bottom)

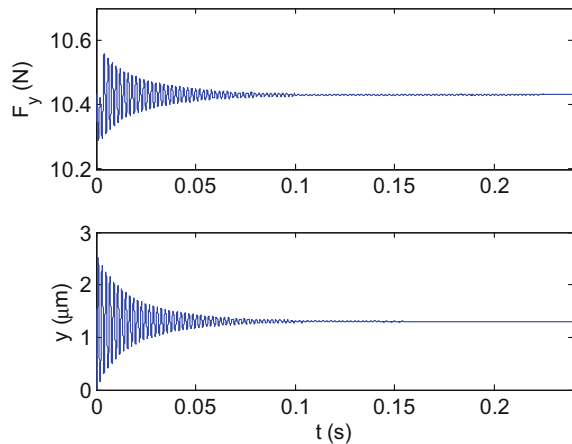


Fig. 4.41 Example 4.11
unstable case
2 ($\Omega = 7500$ rpm and
 $b = 5$ mm) simulation
results for x direction force
(top) and displacement
(bottom)

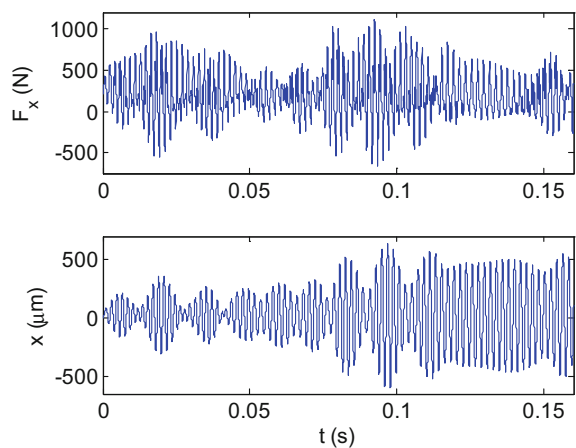


Fig. 4.42 Example 4.11
unstable case
2 ($\Omega = 7500$ rpm and
 $b = 5$ mm) simulation
results for y direction force
(top) and displacement
(bottom)

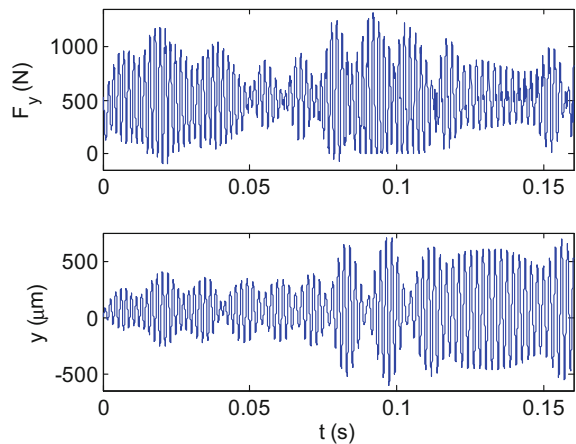


Fig. 4.43 Example 4.11
unstable case
2 ($\Omega = 7500$ rpm and
 $b = 5$ mm) simulation
results for resultant force

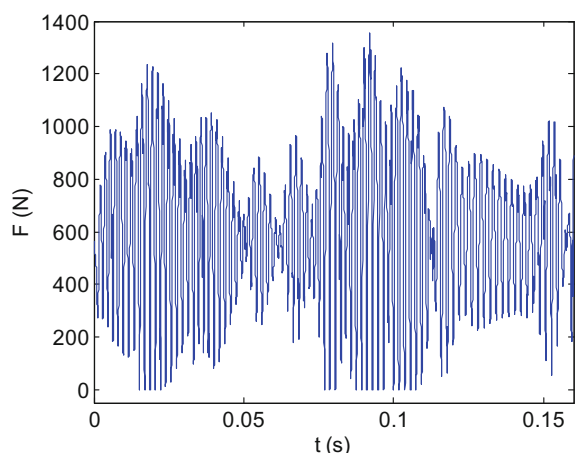


Fig. 4.44 Example 4.11
unstable case
4 ($\Omega = 5000$ rpm and
 $b = 0.5$ mm) simulation
results for x direction force
(top) and displacement
(bottom)

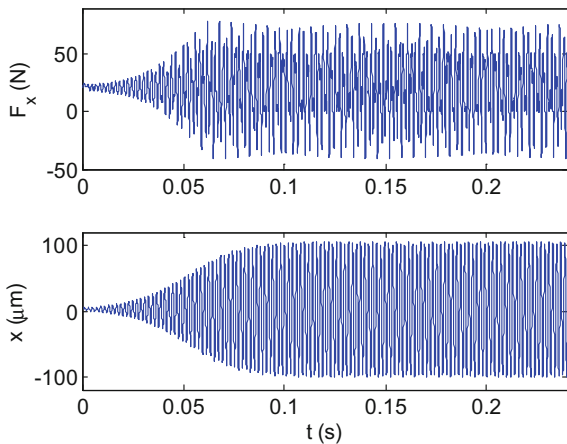
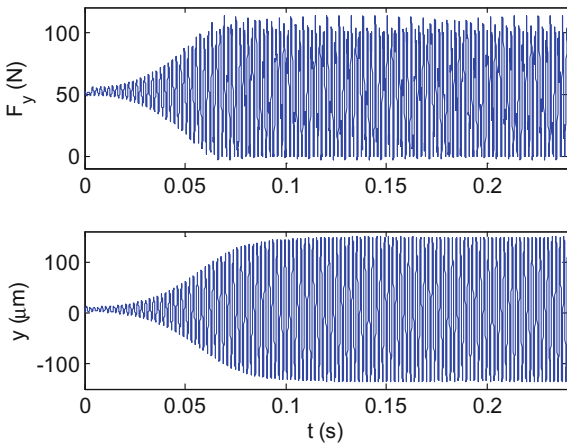


Fig. 4.45 Example 4.11
unstable case
4 ($\Omega = 5000$ rpm and
 $b = 0.5$ mm) simulation
results for y direction force
(top) and displacement
(bottom)



drops to zero as the tooth vibrates out of the cut (e.g., in the vicinity of 0.1 s). Similar results are seen for case 4 in Figs. 4.44 through 4.46. Here the vibration and force levels grow quickly until the nonlinearity is reached and then the levels persist. The disagreement between the average tooth angle stability boundary and time domain simulation for cases 2 and 4 is due to the orthogonality between the average surface normal and y direction in slotting. This causes the directional orientation factor for the y direction, μ_y , to be zero (see Example 4.6) and the contribution of the dynamics in the y direction to be neglected. The simulation used to produce Figs. 4.37 through 4.46 is included as p_4_10_1.m with the textbook.

Example 4.12 Comparison with Example 4.8 Using Time Domain Simulation The milling conditions are 20% radial immersion down milling cut with a start angle of $\phi_s = 126.9$ deg and exit angle of $\phi_e = 180$ deg. The x direction dynamics are

Fig. 4.46 Example 4.11
unstable case
4 ($\Omega = 5000$ rpm and
 $b = 0.5$ mm) simulation
results for resultant force

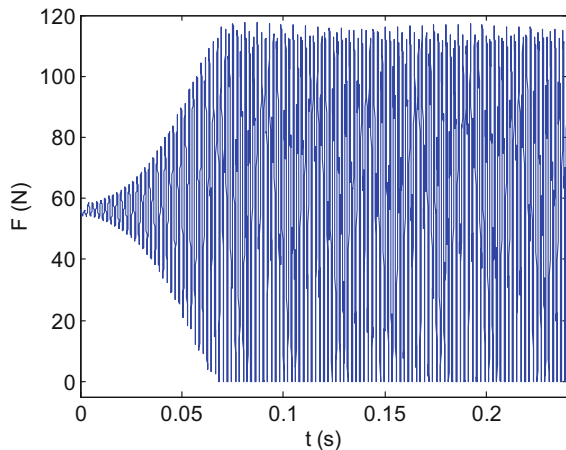
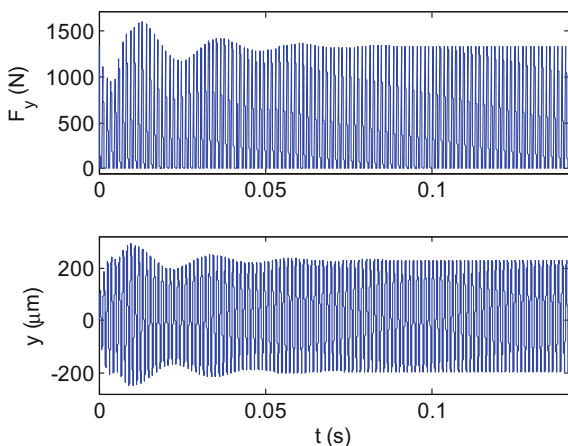


Fig. 4.47 Example 4.12
stable case
1 ($\Omega = 17,000$ rpm and
 $b = 4$ mm) simulation
results for y direction force
(top) and displacement
(bottom)



$f_{nx} = 900$ Hz, $k_x = 9 \times 10^6$ N/m, and $\zeta_x = 0.02$. The y direction dynamics are $f_{ny} = 950$ Hz, $k_y = 1 \times 10^7$ N/m, and $\zeta_y = 0.01$. The workpiece material is a low carbon steel alloy and it is machined with a three tooth, 19 mm diameter square endmill and feed per tooth of 0.2 mm/tooth. For a specific force value of $K_s = 2250$ N/mm² and a force angle of $\beta = 75$ deg, the corresponding cutting force coefficients are $k_t = 2173$ N/mm² and $k_n = 582$ N/mm². The number of steps per revolution is 801 and 40 revolutions are simulated.

Based on the analytical stability lobe results in Figs. 4.31 and 4.33, let's select two (Ω, b) combinations for numerical simulation. Case 1 with $\Omega = 17,000$ rpm and $b = 4$ mm should be stable according to the stability lobes. Case 2 with $\Omega = 13,000$ rpm and $b = 4$ mm should be unstable. Figure 4.47 displays the y direction force and vibration for case 1. It takes approximately half of the first 40 revolutions for the transients to attenuate, but the final result is stable cutting. The force and vibrations results between 0.13 s and 0.14 s are displayed in Fig. 4.48.

Fig. 4.48 Portion of results from Fig. 4.47 between 0.13 s and 0.14 s

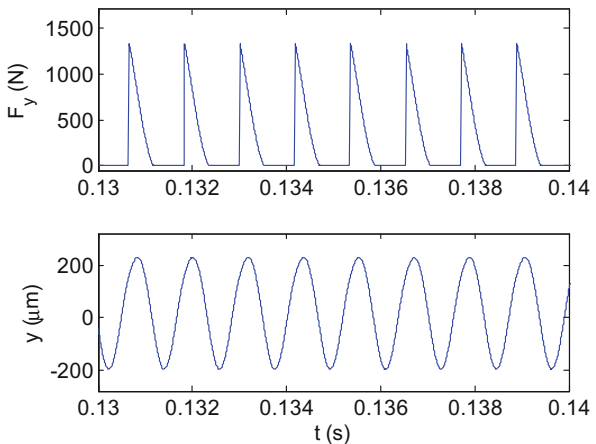
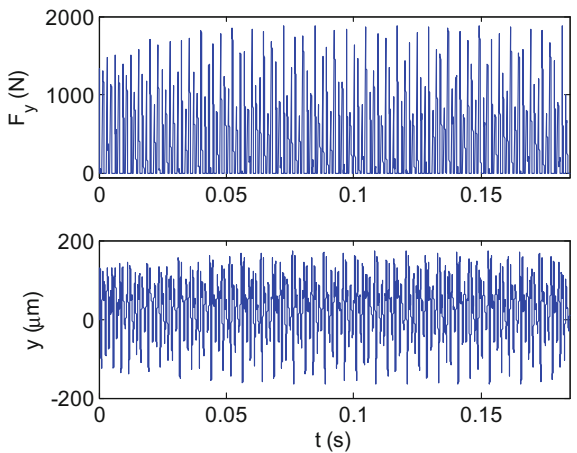


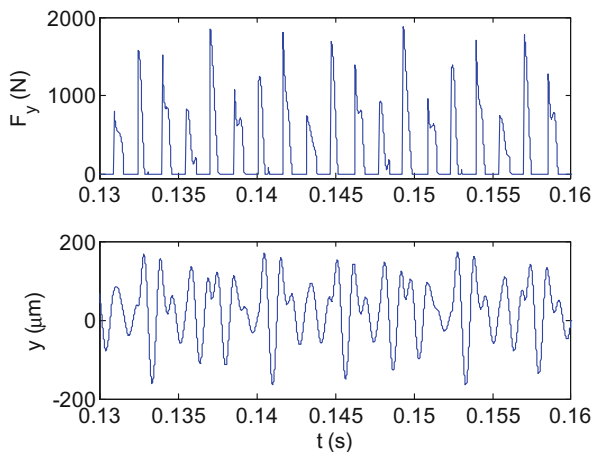
Fig. 4.49 Example 4.12 unstable case 2 ($\Omega = 13,000$ rpm and $b = 4$ mm) simulation results for y direction force (top) and displacement (bottom)



We see the expected force profile for the down milling cut. Note that only one tooth is engaged at any time so the force drops to zero during the delay between one tooth leaving the cut and the next tooth entering the cut (we refer to this as interrupted cutting). Also, the force is largest at the cut entry when the chip thickness is at its maximum value for down milling and drops to zero as the chip thickness decreases to zero, according to $f_t \sin(\phi)$, at the cut exit. The resulting tool vibrations are sinusoidal in nature.

The y direction force and vibration for case 2 are provided in Fig. 4.49. The behavior differs substantially from Figs. 4.48 and 4.49. For the previous stable cut (case 1), the vibration exhibited only a forced vibration response to the cutting force. For the unstable case 2, the vibration now occurs at both the chatter frequency (near the tool's natural frequency) and the forcing frequencies (the tooth passing frequency and its harmonics as demonstrated in Fig. 4.15). We will examine the

Fig. 4.50 Portion of results from Fig. 4.49 between 0.13 s and 0.16 s



frequency content of stable and unstable milling signals further in Chap. 6. Figure 4.50 shows the portion of the force and vibration between 0.13 s and 0.16 s. The behavior is clearly different than the stable case shown in Fig. 4.48. The simulation used to produce the figures for this example is included as p_4_12_1.m with the textbook.

4.4.5 Periodic Sampling

In this section, we will establish a metric that automatically differentiates between stable and unstable behavior for our milling time domain simulation. The approach is based on periodic sampling of the output signals and is similar to the strategy used for modulated tool path (MTP) turning in Sect. 3.6. We apply periodic sampling to establish the synchronicity of the response (e.g., displacement, velocity, or acceleration) with the excitation (tooth passage). For stable cutting conditions, only forced vibration is present and the sampled point repeats for each tooth passage. For unstable cutting, on the other hand, the response does not repeat. Further, the distribution of the sampled points identifies the type of instability: secondary Hopf or period- n bifurcations. Additional information on these instability types is provided in Sect. 6.4. For now, we will simply stipulate that the sampled points either repeat (stable forced vibration) or they do not (unstable behavior).

An alternative to the analytical stability lobe diagrams that we detailed in Sect. 4.3 is a stability map. To construct this stability map, time domain simulations may be completed over the desired grid of spindle speed and axial depth values. A primary challenge for time domain simulation, however, is automatically identifying stable or unstable behavior. To address this difficulty, we will define a stability criterion based on once-per-tooth sampled signals available from our time domain simulation.

The metric builds on the approach in [10–12], where the standard deviation of the periodically sampled milling audio signal was calculated. This work recognized that the distribution in sampled stable signals is small, while it is large for sampled unstable signals. The stability metric we will implement is:

$$M = \frac{\sum_{i=2}^N |x_s(i) - x_s(i-1)|}{N}, \quad (4.66)$$

where x_s is a vector of periodically sampled x values and N is the length of the x_s vector. The x values can be any process signal, including displacement, velocity, or acceleration of the tool or workpiece; cutting force; or sound [13]. With this stability metric, the absolute value of the differences in successive sampled points is summed and then normalized. For stable cuts (forced vibration), the sampled points repeat, so the M value is nominally zero. For unstable cuts, however, $M > 0$ [14, 15].

Example 4.13 Demonstration of Time Domain Simulation Stability Metric To demonstrate the metric, let's return to Example 4.12. We'll use the same cutting conditions and system dynamics but now periodically sample the cutting force and displacement signals. Since the forcing frequency is defined by each tooth passage, we will sample at the tooth passing frequency, $f_{\text{tooth}} = \frac{N_t}{60}$ (Hz). To accomplish this periodic sampling, we update our time domain simulation; see p_4_13_1.m included with the textbook. First, we need to ensure an integer number of simulation steps per tooth.

```
wnmax = max([wnx wny]);
fnmax = wnmax/2/pi;
DT = 1/(50*fnmax); % integration time step, s
steps_rev = 60/(omega*DT); % steps per revolution
steps_tooth = steps_rev/Nt; % steps per tooth
steps_tooth = round(steps_tooth); % set steps_tooth as an integer
steps_rev = steps_tooth*Nt;
dt = 60/(steps_rev*omega); % reset dt, s
```

Second, we wish to consider the signal after the initial transients have attenuated, sample the time dependent x and y displacement (or position) and force signals, and then calculate the associated M values. We accomplish these three tasks using the following code. Here we have truncated the output signals to remove the first 67% and, subsequently, the initial transients.³

```
% Remove initial transients
start = round(length(time)*0.67);
time = time(start:length(time));
```

³The selection of 67% was arbitrary. It caused the first point to not coincide with the cut entry so that the variation in the sampled force could be clearly observed.

```

xpos = xpos(start:length(xpos));
ypos = ypos(start:length(ypos));
Forcex = Forcex(start:length(Forcex));
Forcey = Forcey(start:length(Forcey));

% Complete periodic sampling
time_s = time(1:steps_tooth:length(time));
xpos_s = xpos(1:steps_tooth:length(xpos));
ypos_s = ypos(1:steps_tooth:length(ypos));
Forcex_s = Forcex(1:steps_tooth:length(Forcex));
Forcey_s = Forcey(1:steps_tooth:length(Forcey));

% Calculate metric values
metricxpos = sum(abs(diff(xpos_s*1e6)))/length(xpos_s) %micrometers
metricypos = sum(abs(diff(ypos_s*1e6)))/length(ypos_s)

```

The results are displayed in Figs. 4.51 and 4.52. Figure 4.51 shows the results for the stable case ($\Omega = 17,000$ rpm and $b = 4$ mm). We observe that the periodically sampled points repeat. The M value for the y displacement is 0.06 μm (close to zero). Figure 4.52 presents the results for the unstable case ($\Omega = 13,000$ rpm and $b = 4$ mm). The periodically sampled points do not repeat and the corresponding M value for the y displacement is now 45.56 μm ; this represents a greater than 750 \times increase over the stable case.

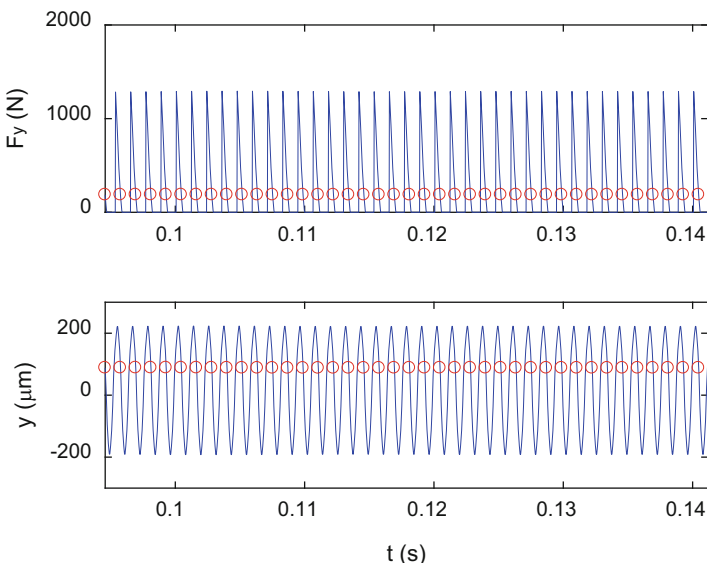


Fig. 4.51 Simulation (line) and sampling (circles) results for the stable case ($\Omega = 17,000$ rpm and $b = 4$ mm)

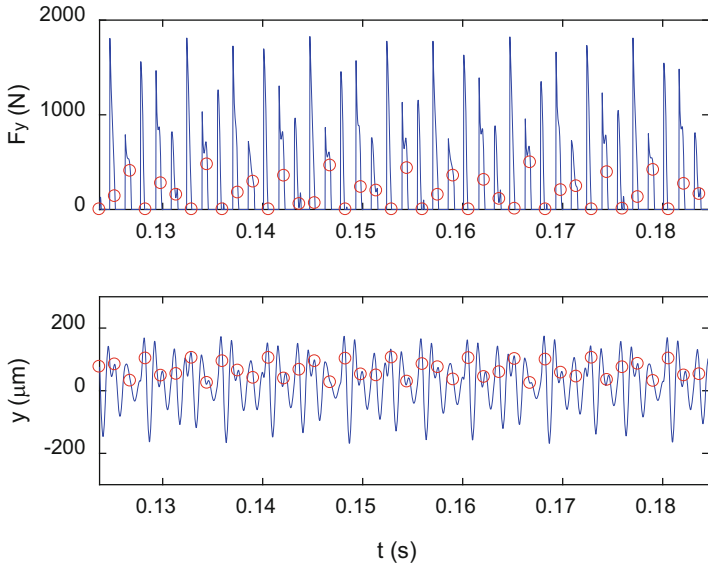


Fig. 4.52 Simulation (line) and sampling (circles) results for the unstable case ($\Omega = 13,000$ rpm and $b = 4$ mm)

4.5 Milling Time Domain Simulation with Helical Teeth

While the simulation described in Sect. 4.4 is capable of predicting forces and displacements in milling, the assumption of straight cutter teeth is rarely applicable in practice. As discussed in Sect. 4.1, the cutting edges are typically inclined at the helix angle, γ , so that the chip to be removed is spread over an increased length and the cutting edge pressure is reduced. The result of the helical cutting edge geometry is that the full length of the cutting edge does not enter (or exit) the cut at the same instant. Instead, there is an increasing delay of the cut entry (and exit) when moving from the free end of the cutter toward the spindle. The situation is depicted in Fig. 4.53 for the helical square endmill geometry considered in this section.

We can visualize the angular delay, χ , of the helical cutting edge, which increases with distance from the cutter free end, by “unrolling” the periphery of the cylindrical endmill as described in [16]. The helical teeth now appear as straight lines and angles, ϕ (in rad), become distances, $r\phi$, where r is the endmill radius. Note that the velocity of every point on the tooth edge is the cutting speed, v (Eq. 4.17), with a direction perpendicular to the z axis. The unrolled view of the endmill pictured in Fig. 4.53 is presented in Fig. 4.54. The delay distance, $r\chi$, is zero at $z = 0$ (endmill free end) because we have referenced the cutter rotation angle, ϕ , to this axial location. However, at $z = -b$ the delay distance is now:

$$r\chi = b \tan(\gamma). \quad (4.67)$$

Fig. 4.53 The helical endmill geometry causes the cutting edge to enter and exit the cut at later instants in time when moving from its free end toward the spindle

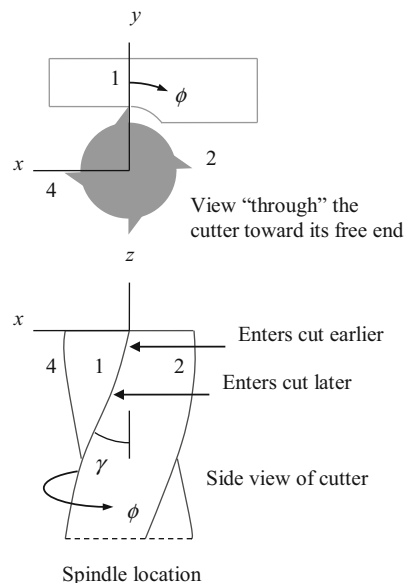
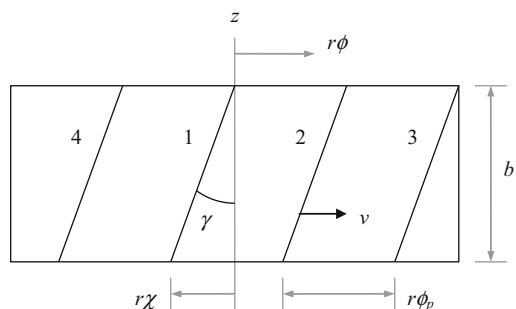


Fig. 4.54 Unrolled view of helical endmill geometry. The helical teeth appear as straight lines and angles are seen as distances



In order to discretize this relationship and retain the $d\phi$ angular increments in our time domain simulation, we section the tool into a number of slices (or disks) perpendicular to the z axis. Each slice is treated as an individual straight tooth endmill, where the thickness of each slice is a small fraction, db , of the axial depth of cut, b . This approximation is shown in Fig. 4.55. Note that each slice incorporates the distance delay $r\chi = db \tan(\gamma)$ relative to the prior slice (nearer the cutter free end), which becomes the angular delay between slices of:

$$\chi = \frac{db \tan(\gamma)}{r} = \frac{2db \tan(\gamma)}{d} \text{ (rad)} \quad (4.68)$$

for the rotating endmill. In Eq. 4.68, d is the endmill diameter. In order to ensure that the angles for each axial slice match the phi vector entries in the time domain simulation, we require that the delay angle between slices is $\chi = d\phi$. This places a

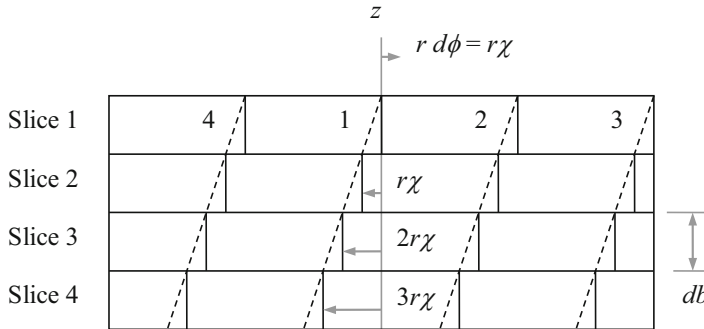


Fig. 4.55 Discretized version of unrolled helical endmill geometry. The axial depth is sectioned into multiple slices with thickness db . Each slice is treated as a straight tooth cutter with the delay distance $r\chi = r d\phi$ relative to the adjacent slice nearer the free end of the endmill

constraint on the db value. By substituting $d\phi$ for χ in Eq. 4.68 and rearranging, we see that we must select it such that:

$$db = \frac{d \cdot d\phi}{2 \tan(\gamma)}. \quad (4.69)$$

The integer number of axial slices for the simulation is then determined using the MATLAB® expression: `steps_axial = round(b/db)`. Naturally, the accuracy is improved if $db \ll b$, which requires that $d\phi$ is small (i.e., the `steps_rev` value is high).

The primary modifications to the time domain simulation described in Sect. 4.4 are that (1) an additional `for` loop is added to count through the individual axial slices (`cnt4` in `p_4_14_1.m` included with the textbook); and (2) the `surf` vector is now replaced by an array, where each row in the array includes the `surf` information for a single axial slice. This array is also named `surf` in `p_4_14_1.m`. It is organized similar to Fig. 4.55, where the first row, `surf(1, 1:steps_rev)`, contains the data for the axial slice nearest the free end of the cutter ($z = 0$) and there are `steps_axial` total rows. Within the `cnt4` loop, the angle of the current axial slice, `phia`, is determined by decrementing the angle for the tooth in question, referenced to the free end of the cutter and indexed by `cnt3` in the next outer `for` loop, by `phi_counter = teeth(cnt3) - (cnt4-1)`. Because we selected `db` using Eq. 4.69 to ensure that the angular delay corresponds to `dphi` between slices, the current axial slice angle is then `phia = phi(phi_counter)`.

A secondary modification in `p_4_14_1.m`, relative to `p_4_10_1.m` and `p_4_12_1.m`, is that a vector notation for the modal parameters, velocities, and displacements is added. This new format enables the convenient inclusion of multiple modes in the models of the system dynamics for the x and y directions. For each mode in the x direction, for example, a separate numerical integration is completed to update the modal velocity, `dp(cnt5)`, and displacement, `p(cnt5)`, where `cnt5` is the mode number index. Because the response in local (physical)

coordinates is the sum of the modal contributions, the individual modal displacements are simply added to obtain the x direction displacement. The y direction approach is the same, except the modal velocities and displacement are contained in the dq and q vectors, respectively. Strictly speaking, due to the helical geometry, we should also consider the axial (z direction) forces and potential deflections. However, for most endmilling applications, the z direction dynamic stiffness is much higher than the x or y direction stiffness values, so it is common to consider the z direction to be rigid.

Finally, because these simulations tend to take longer than the straight tooth cases, a progress bar has been added (for the impatient among us). The MATLAB® function `waitbar` was used to accomplish this task.⁴



In a Nutshell

Because the teeth are helical, the portion of each tooth that is engaged in the cut varies as the tool rotates. The changing deflection of the tool is imprinted on the machined surface parallel to the tools' axis of rotation.

It is difficult to include this complexity in the analytical formulations but relatively straightforward to include in the time domain simulation. For this and many other reasons, time domain simulation is a better representation of the cutting process that either of the analytical formulations described earlier. As with all of engineering, however, there is an inherent trade-off to be made. In this case, it is that increased accuracy is computationally more intensive.

Example 4.14 Comparison of Forces Between Straight and Helical Teeth In this example, we compare the cutting forces produced by straight and helical teeth with all other conditions being equal. We model a 30% radial immersion up milling cut with a zero start angle and exit angle of 66.4 deg. There are two identical modes in both the x and y directions. These are expressed in modal coordinates as $f_{n1} = 800$ Hz, $k_{q1} = 2 \times 10^7$ N/m, and $\zeta_{q1} = 0.05$ and $f_{n2} = 1000$ Hz, $k_{q2} = 1.5 \times 10^7$ N/m, and $\zeta_{q2} = 0.03$. The FRF in local coordinates for these modal parameters is displayed in Fig. 4.56. The workpiece material is an aluminum alloy, and it is machined with a four tooth, 19 mm diameter square endmill using a feed per tooth of 0.15 mm/tooth. For a specific force value of $K_s = 600$ N/mm² and force angle of $\beta = 60$ deg, the corresponding cutting force coefficients are $k_t = 520$ N/mm² and $k_n = 300$ N/mm² or, equivalently, $K_t = 520$ N/mm² and $K_n = 0.577$.

We wish to consider stable cutting conditions for the time domain force simulations. To aid in the selection of stable (Ω , b) combinations, we first generate the stability lobe diagrams using the average tooth angle and Fourier series approaches. The directional orientation factors for the average tooth angle approach are $\mu_x = \cos(\beta - 56.8) \cos(56.8)$ and $\mu_y = \cos(146.8 - \beta) \cos(146.8)$ as described in Example 4.5, where the average tooth angle in the cut is now 33.2 deg. The stability lobe diagrams for the two analytical methods are shown in

⁴Author T. Schmitz recognizes B. Mann for recommending this function.

Fig. 4.56 Two mode FRF for Example 4.14 (x and y direction responses are equal)

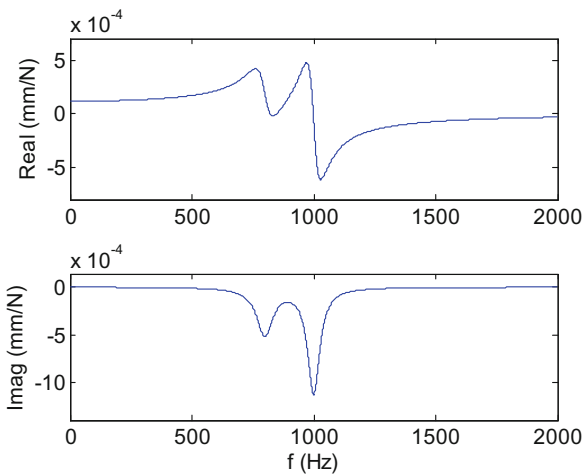
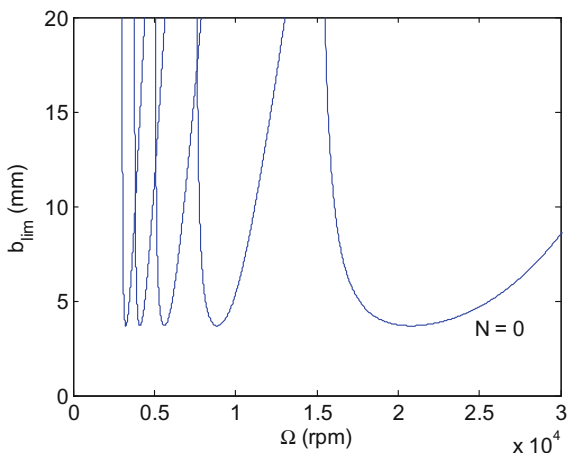


Fig. 4.57 Stability lobe diagram for Example 4.14 using average tooth angle approach ($N = 0$ to 4)



Figs. 4.57 and 4.58. We observe that the stability limits are similar and a preferred speed is near 15,000 rpm. This agrees with the best spindle speed selection rule given in Eq. 4.29 even though this is a two degree of freedom system. The MATLAB® program p_4_14_2.m (available with the textbook) was used to generate these two figures.

$$\Omega_{\text{best}} = \frac{f_n(60)}{(N+1)N_t} = \frac{1000(60)}{(0+1)4} = 15,000 \text{ rpm}$$

For the time domain simulations, let's choose the number of steps per revolution to be 800 and the number of revolutions to be 30. The spindle speed is 15,000 rpm and two axial depths of cut are considered. Figures 4.59 and 4.60 show the resultant cutting forces (in the x - y plane) for a small time portion of the simulation result with

Fig. 4.58 Stability lobe diagram for Ex. 4.14 using Fourier series approach ($j = 0$ to 4)

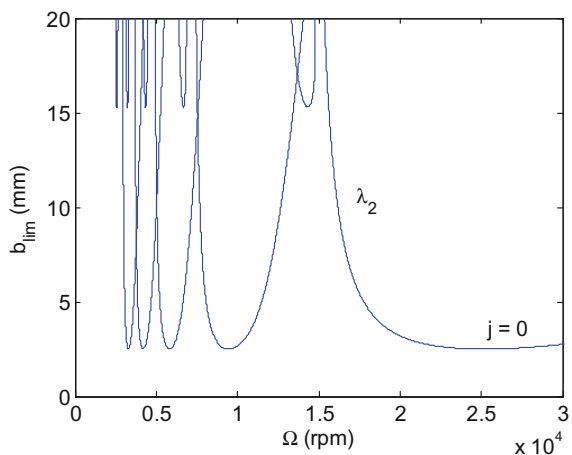


Fig. 4.59 Resultant cutting force versus time for zero helix angle endmill with $\Omega = 15,000$ rpm and $b = 5$ mm

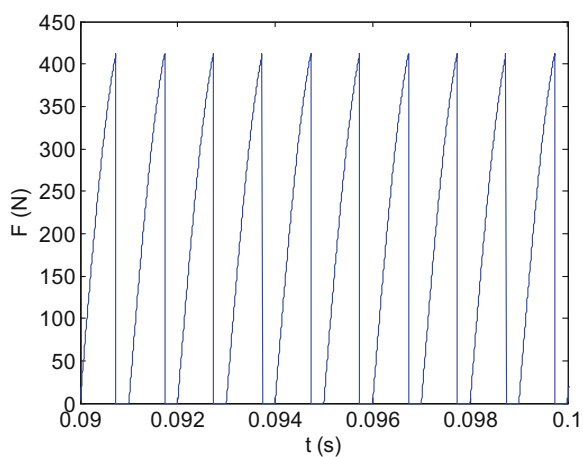
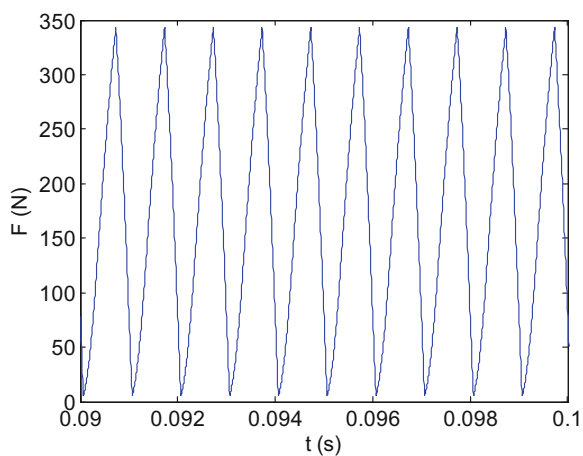


Fig. 4.60 Resultant cutting force versus time for 45 deg helix angle endmill with $\Omega = 15,000$ rpm and $b = 5$ mm



$b = 5$ mm and helix angles of zero and 45 deg, respectively. A comparison of the two figures shows clear differences. First, the maximum cutter force is lower for the helical teeth endmill. Second, the force grows to its maximum value and then abruptly drops to zero at the cut exit angle for the straight tooth endmill. For the helical teeth cutter, on the other hand, the force grows and then decreases in a more saw tooth pattern and does not quite reach zero. We can understand this behavior using Eq. 4.68 and Fig. 4.54. The lag angle between the free end of the cutter and the helical edge at $b = 5$ mm is $\chi = \frac{2b \tan(\gamma)}{d} = \frac{2(5) \tan(45)}{19} = 30.2$ deg. This means that the cutter rotates 30.2 deg between the time that the free end of the helical tooth enters the cut (assume that $\phi = 0$ here) and the time that the helical edge at $b = 5$ mm is engaged. At $\phi = 66.4$ deg, the free end cutting edge begins to exit the cut, but the helical portion nearer the spindle remains engaged. The force therefore does not drop immediately to zero. In fact, it does not drop to zero at all because, by the time the $b = 5$ mm helical portion exits the cut (30.2 deg later), the next tooth has entered the cut (i.e., $30.2 + 66.4 = 96.6$ deg is greater than the tooth pitch of 90 deg).

As noted in [16, Example 9.12], this “wrapping” behavior of the helical cutting edge can be exploited to achieve a constant cutting force at particular axial depths of cut. These b values are obtained when the lag angle is equal to the pitch angle. In this case, the same cutting edge length is engaged regardless of the cutter angle or radial depth of cut. The situation is depicted in Fig. 4.61, where the left gray box covers the cutting edge length for tooth 1. At a later instant in time, the right gray box represents the same lag distance for the helical endmill. Although tooth 1 is no longer engaged, we see that the same cutting edge length is covered, but it is now made up of portions of teeth 2 and 3. This constant cutting edge length leads to the same force value for the two instants. The b value at which this behavior is observed is determined by rewriting Eq. 4.69 to be $b = \frac{d\phi_p}{2 \tan(\gamma)}$. For this example (45 deg helix with four teeth), the axial depth for constant cutting force is:

Fig. 4.61 When the lag angle is equal to the pitch angle, the same length of cutting edge is engaged regardless of the cutter angle (as shown by the two gray boxes). The force is constant for this axial depth

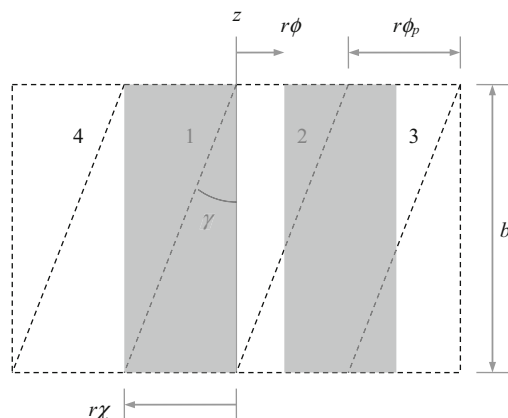


Fig. 4.62 Resultant cutting force versus time for zero helix angle endmill with $\Omega = 15,000$ rpm and $b = 14.9$ mm

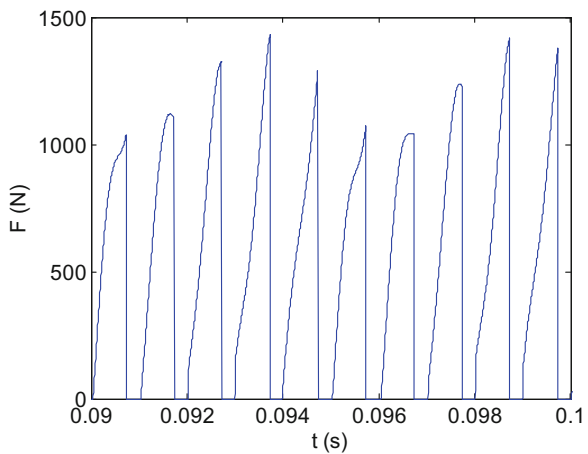
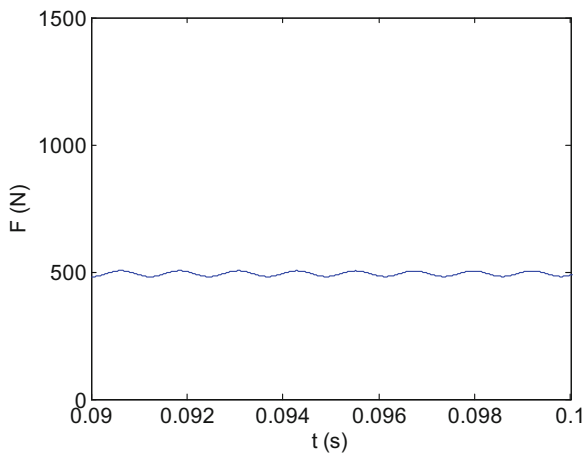


Fig. 4.63 Resultant cutting force versus time for 45 deg helix angle endmill with $\Omega = 15,000$ rpm and $b = 14.9$ mm



$$b = \frac{d\phi_p}{2 \tan(\gamma)} = \frac{19(90) \frac{\pi}{180}}{2 \tan(45)} = 14.9 \text{ mm.}$$

Multiples of this axial depth will yield the same constant force behavior provided the cutting conditions remain stable (and sufficient flute length is available), although this is unlikely for typical tool-workpiece combinations.

Figures 4.62 and 4.63 show the resultant forces for $\Omega = 15,000$ rpm and $b = 14.9$ mm with helix angles of zero and 45 deg, respectively. It is seen that the cut is bordering on instability in Fig. 4.62; the force is disturbed from its nominal values by regeneration. In Fig. 4.63, however, the force is nearly constant with a small oscillation that is retained from the initial transients. Note that the same force scale is used on both plots. Clearly, the maximum force is much lower for the helical cutter. Figures 4.60 through 4.63 were produced using program p_4_14_1.m.

4.6 Ball Milling Time Domain Simulation with Helical Teeth

In this section we extend the helical teeth milling simulation for square endmills from Sect. 4.5 to incorporate the spherical geometry of ball endmills. The circular tool path assumption is again applied. Additionally, the tool is sectioned into slices along its axis, as before, and the tool axis is perpendicular to the feed direction (in practice, the ball endmill axis is often inclined with respect to the feed direction to avoid cutting with the zero velocity point at the ball apex, but we will not treat this case). The ball endmilling simulation geometry and variables are displayed in Fig. 4.64, where we now compute the z direction force component although we maintain our assumption of rigid z direction dynamics. As shown, the width of the axial slices along the tool axis is dz . This value is again selected to ensure that the instantaneous cutter angle is coincident with one of the predefined ϕ angles as in Sect. 4.5. See Eq. 4.70, where γ is the global helix angle (the local helix on the spherical end varies with the z location as described in [17]).

$$dz = \frac{d(d\phi)}{2 \tan(\gamma)} \quad (4.70)$$

The new variable, κ' , is identified in Fig. 4.64 (the prime is used to differentiate it from the variable κ used in the Fourier series stability analysis). This represents the angle between the tool axis and the ball surface normal for the current axial slice and is calculated using Eq. 4.71, where j is the axial slice in question (cnt4 in

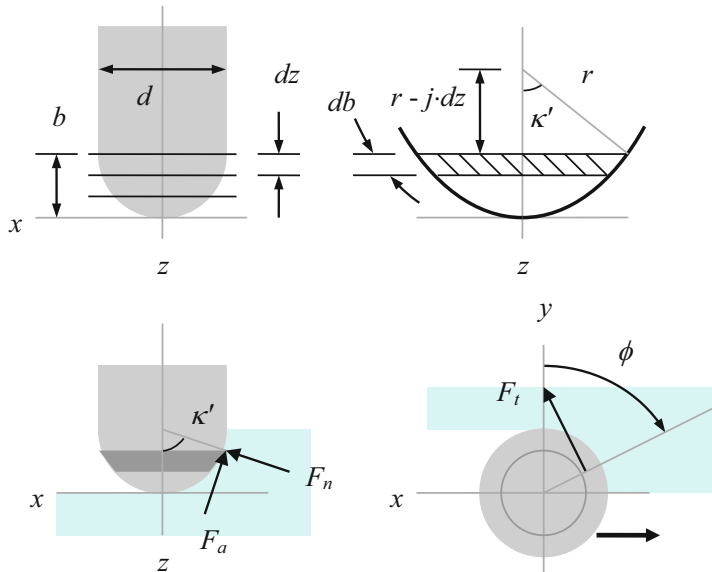


Fig. 4.64 Ball endmilling simulation geometry. The normal force component, F_n , is oriented along the ball surface normal

`p_4_15_1.m`) and r is the radius. It is used to first project the chip thickness from the x - y plane onto the tool surface normal direction and, second, project the tangential, normal, and axial force components onto the x - y - z coordinate directions (together with the tooth angle) [17].

$$\kappa' = \cos^{-1} \left(1 - \frac{j(dz)}{r} \right) = \cos^{-1} \left(1 - \frac{2j(dz)}{d} \right) \quad (4.71)$$

As with the helical square endmill simulation, the instantaneous chip thickness in the x - y plane is determined from the (1) nominal chip thickness, which depends on the feed per tooth and angle of the current tooth for the selected slice, phia ; (2) vibrations in the x and y directions from the previous tooth, collected in the `surf` array (defined in the same way as described in Sect. 4.5); and (3) the x and y vibrations of the current tooth projected in the radial direction (i.e., the direction from the current tooth toward the tool axis in the x - y plane—this was the normal direction, n , for the helical square endmill simulation `p_4_14_1.m`). However, the x - y plane thickness must then be projected onto the ball surface normal direction using κ' (`kappa_p`). The relevant lines from the MATLAB® program `p_4_15_1.m` are provided here.

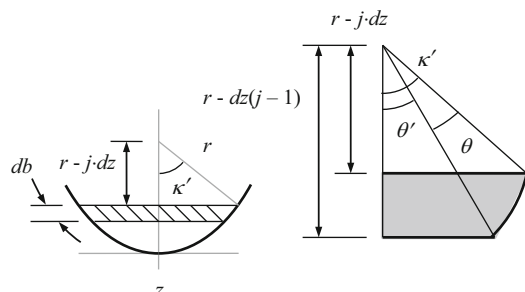
```
n = x*sin(phi*a*pi/180) - y*cos(phi*a*pi/180);
h=(ft*sin(phi*a*pi/180)+surf(cnt4, phi_counter)-n)*sin(kappa_p);
```

In addition to calculating the chip thickness, the chip width for each slice, db , must also be determined. While this was simply the width of each axial slice for the square endmill geometry, it is now the arc length of the current slice when cutting with the ball surface. The situation is depicted in Fig. 4.65, where the arc length is the product of the radius and the angle θ . See Eq. 4.72. The angle θ is, in turn, the difference between κ' and θ' , $\theta = \kappa' - \theta'$. The angle θ' is defined in Eq. 4.73.

$$db = r\theta \quad (4.72)$$

$$\theta' = \cos^{-1} \left(\frac{r - dz(j-1)}{r} \right) = \cos^{-1} \left(1 - \frac{dz(j-1)}{r} \right) = \cos^{-1} \left(1 - \frac{2dz(j-1)}{d} \right) \quad (4.73)$$

Fig. 4.65 Geometry for chip width, db , calculation when cutting on ball surface



Once the chip thickness and width are determined, the cutting force components in the tangential, normal, and axial directions are determined for each axial slice. See Eqs. 4.74 through 4.76 (referring to the F_a component as axial is actually something of a misnomer since it is directed along the tool axis only when κ' is 90 deg). Notice that a new cutting force coefficient, k_a , is defined in Eq. 4.76. It fills the same role as k_t and k_n , to relate the force to chip area, and is expressed in units of N/mm², or equivalent.

$$F_t = k_t hdb \quad (4.74)$$

$$F_n = k_n hdb \quad (4.75)$$

$$F_a = k_a hdb \quad (4.76)$$

As shown in Fig. 4.64, the projection of these components on the x - y - z fixed coordinate frame depends on both the instantaneous cutter angle, ϕ , and the ball surface normal direction, κ' , for the selected tooth and slice. The force relationships are provided in matrix form in Eq. 4.77, where ϕ_a is the tooth angle phia from the MATLAB® program p_4_15_1.m.

$$\begin{Bmatrix} F_x \\ F_y \\ F_z \end{Bmatrix} = \begin{bmatrix} \cos(\phi_a) & \sin(\phi_a) \sin(\kappa') & -\sin(\phi_a) \cos(\kappa') \\ \sin(\phi_a) & -\cos(\phi_a) \sin(\kappa') & \cos(\phi_a) \cos(\kappa') \\ 0 & -\cos(\kappa') & -\sin(\kappa') \end{bmatrix} \begin{Bmatrix} F_t \\ F_n \\ F_a \end{Bmatrix} \quad (4.77)$$

The only remaining issue that must be addressed in the simulation is treating the case where the commanded axial depth is greater than the ball radius. In this situation κ' is set to 90 deg and Eq. 4.77 collapses to Eq. 4.78. The x and y force projections are now identical to the helical square endmill simulation, and the z component is equal to the axial force (with the appropriate sign convention applied).

$$\begin{Bmatrix} F_x \\ F_y \\ F_z \end{Bmatrix} = \begin{bmatrix} \cos(\phi_a) & \sin(\phi_a) & 0 \\ \sin(\phi_a) & -\cos(\phi_a) & 0 \\ 0 & 0 & -1 \end{bmatrix} \begin{Bmatrix} F_t \\ F_n \\ F_a \end{Bmatrix} \quad (4.78)$$

Example 4.15 Comparison of Forces Between Square and Ball Endmills Here we compare the cutting forces produced by helical square and ball endmills. As in Example 4.14, we consider a 30% radial immersion up milling cut with a zero start angle and exit angle of 66.4 deg with an axial depth of 5 mm (which is less than the tools' radii of 9.5 mm). The dynamic responses in the two directions are the same as was previously presented. The workpiece material is an aluminum alloy, and it is assumed that the cutting force coefficients are the same for both four tooth endmills. For a specific force value of $K_s = 600$ N/mm² and force angle of $\beta = 60$ deg, the corresponding cutting force coefficients are $k_t = 520$ N/mm² and $k_n = 300$ N/mm², and the axial coefficient, k_a , is taken to be equal to k_n . The feed per tooth is 0.15 mm/tooth.

Fig. 4.66 Comparison of x direction cutting force for ball (solid line) and square (dotted line) helical endmills

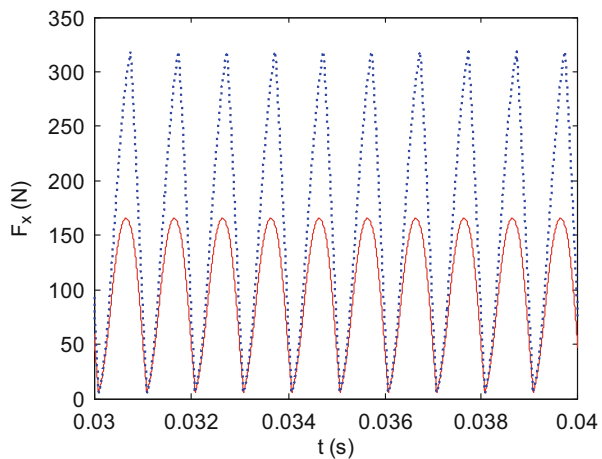
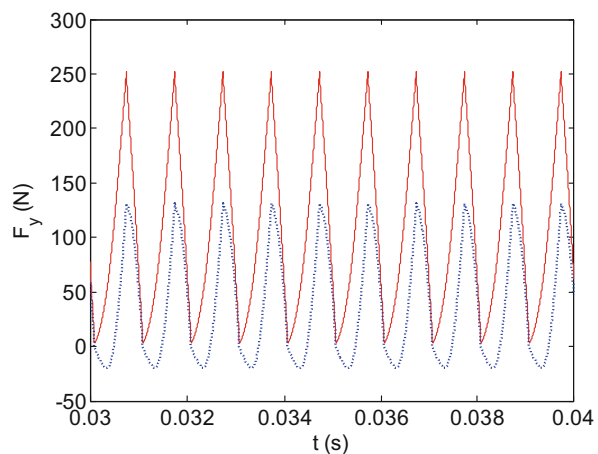
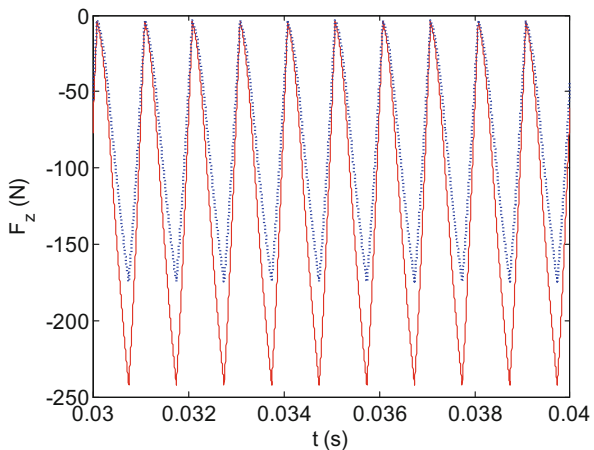


Fig. 4.67 Comparison of y direction cutting force for ball (solid line) and square (dotted line) helical endmills



For the simulations, let's use 1200 steps per revolution and complete 10 full revolutions. Results for the cutting forces in the x , y , and z directions under these conditions are displayed in Figs. 4.66 through 4.68, respectively (the time span includes data that follows the attenuation of the initial transients). Differences are observed in all three directions. This is due to the variation in the ball surface normal angle and the corresponding projections of the normal and axial components according to Eq. 4.77. Naturally, the resultant force, $F = \sqrt{F_x^2 + F_y^2 + F_z^2}$, is the same for both endmills. The MATLAB® programs p_4_15_1.m (helical ball endmilling) and p_4_15_2.m (helical square endmilling) may be used to obtain Figs. 4.66 through 4.68.

Fig. 4.68 Comparison of z direction cutting force for ball (solid line) and square (dotted line) helical endmills



4.7 Experimental Cutting Force Coefficients

To conclude this chapter, let's discuss experimental determination of the cutting force coefficients for the milling force model (a square endmill geometry is again presumed). As shown in Fig. 4.8, these tests are carried out by prescribing a known feed per tooth and axial depth and measuring the x (feed), y , and z (axial) direction cutting force components in the dynamometer's fixed coordinate frame. Prior to detailing the numerical and experimental techniques used to obtain the coefficient values, however, let's revisit the force model and corresponding coefficients.

4.7.1 Updated Force Model

Equations 4.6 through 4.10 and 4.34 are all based on the assumption that the resultant cutting force, F in Fig. 4.7, is directly proportional to the chip thickness (and axial depth) and independent of other operating parameters. Although this is a reasonable assumption for the development of stability lobe diagrams used to guide the selection of preferred spindle speeds, comparison with measured cutting forces can show discrepancies with this approximation. First, because the cutting edge radius is nonzero, as the chip thickness is reduced to values near the edge radius, there is increased rubbing⁵ between the cutting edge and work surface which leads to a larger cutting force than the $F = K_s b h$ model would predict. With respect to chip formation in orthogonal cutting (Sect. 3.1), the rake angle, or inclination of the cutting edge relative to the surface normal, depends on both the chip thickness and

⁵Plowing (alternately ploughing), or plastic deformation without material removal, can also occur for significant interference between the tool relief surface and workpiece.

edge radius in this case and can become negative if the ratio is unity or smaller, although the tool may have been designed with a positive rake angle at the macroscopic level. This rubbing phenomenon can be incorporated in the force model by adding a constant, or DC, force component that scales with the axial depth only, such that the force is nonzero even as the chip thickness approaches zero. This is referred to as the “edge effect” in [18] or, alternately, the threshold value. Additionally, the force may not linearly increase with chip thickness, but could follow a power law such as $F = K_s b h^c$, where c is a positive constant less than one [16]. Second, due to the variation in strain rate, temperature, and subsequent chip formation behavior, decreases in cutting force can be observed for higher cutting speeds [19]. This imposes a spindle speed dependence on the cutting force coefficients. Both of these issues (rubbing effect and cutting speed dependence) highlight the notion that these coefficients should not be considered material properties of the workpiece but rather as approximate descriptions of the process behavior which depend on the tool-workpiece combination and, to a lesser extent, the operating conditions. Additional investigations of cutting force modeling may be reviewed in [20–30].

In order to improve the accuracy of the cutting force model without introducing significant complexity, let’s augment Eqs. 4.7 and 4.8 to incorporate edge effects. Equations 4.79 and 4.80 now each include two coefficients: one is associated with “cutting” (or shearing) and includes the chip thickness dependence; and the other is the “rubbing” (or plowing) term, which is independent of chip thickness (denoted by the “e” subscript extension that indicates an edge effect). We note that the DC rubbing terms, $k_{ne}b$ and $k_{te}b$, would be neglected in our analytical linear stability analyses anyway, so this does not invalidate our previous stability lobe diagram derivations. We have also added the axial force term in Eq. 4.81, which was neglected in our straight tooth analysis.

$$F_n = k_nbh + k_{ne}b \quad (4.79)$$

$$F_t = k_tbh + k_{te}b \quad (4.80)$$

$$F_a = k_abh + k_{ae}b \quad (4.81)$$

We determine the six coefficients via linear regression using the average cutting forces measured by the dynamometer over a range of feed per tooth values. Projection of the normal and tangential components into the x , y , and z directions for the square endmill geometry, as shown in Fig. 4.8, gives Eqs. 4.82 through 4.84.

$$F_x = k_lbf_t \sin(\phi) \cos(\phi) + k_{te}b \cos(\phi) + k_nb f_t \sin^2(\phi) + k_{ne}b \sin(\phi) \quad (4.82)$$

$$F_y = k_lbf_t \sin^2(\phi) + k_{te}b \sin(\phi) - k_nb f_t \sin(\phi) \cos(\phi) - k_{ne}b \cos(\phi) \quad (4.83)$$

$$F_z = -k_abf_t \sin(\phi) - k_{ae}b \quad (4.84)$$

If we apply the double angle identities $\sin(\phi)\cos(\phi) = \frac{\sin(2\phi)}{2}$ and $\sin^2(\phi) = \frac{1 - \cos(2\phi)}{2}$, we obtain Eqs. 4.85 and 4.86. The z direction force equation is unchanged.

$$F_x = k_t b f_t \frac{\sin(2\phi)}{2} + k_{te} b \cos(\phi) + k_n b f_t \frac{(1 - \cos(2\phi))}{2} + k_{ne} b \sin(\phi) \quad (4.85)$$

$$F_y = k_t b f_t \frac{(1 - \cos(2\phi))}{2} + k_{te} b \sin(\phi) - k_n b f_t \frac{\sin(2\phi)}{2} - k_{ne} b \cos(\phi) \quad (4.86)$$

To determine the mean cutting force per revolution, we must first augment the previous equations with the summation that accounts for all teeth on the cutter and the switching function that is nonzero only when the tooth angle is bounded by the cut start and exit angles.

$$F_x = \sum_{j=1}^{N_t} \left(k_t b f_t \frac{\sin(2\phi_j)}{2} + k_{te} b \cos(\phi_j) + k_n b f_t \frac{(1 - \cos(2\phi_j))}{2} + k_{ne} b \sin(\phi_j) \right) \times g(\phi_j) \quad (4.87)$$

$$F_y = \sum_{j=1}^{N_t} \left(k_t b f_t \frac{(1 - \cos(2\phi_j))}{2} + k_{te} b \sin(\phi_j) - k_n b f_t \frac{\sin(2\phi_j)}{2} - k_{ne} b \cos(\phi_j) \right) \times g(\phi_j) \quad (4.88)$$

$$F_z = \sum_{j=1}^{N_t} (-k_a b f_t \sin(\phi_j) - k_{ae} b) g(\phi_j) \quad (4.89)$$

The mean force per revolution in the x direction, for example, is then determined by $\bar{F}_x = \frac{1}{2\pi} \int_{\phi_s}^{\phi_e} F_x d\phi$. Because the integration limits are set between the start and exit angles, the switching function is always equal to one and is effectively removed from the integral. Also, the summation is incorporated by the multiplication of the integral by N_t as shown in Eq. 4.90. This equation is rewritten in Eq. 4.91.

$$\bar{F}_x = \frac{N_t}{2\pi} \int_{\phi_s}^{\phi_e} \left(k_t b f_t \frac{\sin(2\phi)}{2} + k_{te} b \cos(\phi) + k_n b f_t \frac{(1 - \cos(2\phi))}{2} + k_{ne} b \sin(\phi) \right) d\phi \quad (4.90)$$

$$\bar{F}_x = \frac{N_t b}{4\pi} \int_{\phi_s}^{\phi_e} (k_t f_t \sin(2\phi) + 2k_{te} \cos(\phi) + k_n f_t - k_n f_t \cos(2\phi) + 2k_{ne} \sin(\phi)) d\phi \quad (4.91)$$

By application of $\int \sin(ax)dx = -\frac{1}{a} \cos(ax)$ and $\int \cos(ax)dx = \frac{1}{a} \sin(ax)$, the integral in Eq. 4.91 is determined to be:

$$\bar{F}_x = \frac{N_t b}{4\pi} \left[-\frac{k_t}{2} f_t \cos(2\phi) + 2k_{te} \sin(\phi) + k_n f_t \phi - \frac{k_n}{2} f_t \sin(2\phi) - 2k_{ne} \cos(\phi) \right]_{\phi_s}^{\phi_e}, \quad (4.92)$$

which can be rewritten as shown in Eq. 4.93.

$$\bar{F}_x = \left[\frac{N_t b f_t}{8\pi} (-k_t \cos(2\phi) + k_n (2\phi - \sin(2\phi))) + \frac{N_t b}{2\pi} (k_{te} \sin(\phi) - k_{ne} \cos(\phi)) \right]_{\phi_s}^{\phi_e} \quad (4.93)$$

Similarly, the y and z direction mean cutting forces per revolution are:

$$\bar{F}_y = \left[\frac{N_t b f_t}{8\pi} (k_t (2\phi - \sin(2\phi)) + k_n \cos(2\phi)) - \frac{N_t b}{2\pi} (k_{te} \cos(\phi) + k_{ne} \sin(\phi)) \right]_{\phi_s}^{\phi_e} \quad (4.94)$$

and

$$\bar{F}_z = \left[\frac{N_t b}{2\pi} (k_a f_t \cos(\phi) - k_{ae} \phi) \right]_{\phi_s}^{\phi_e}. \quad (4.95)$$

If we select 100% radial immersion (slotting) for the cutting tests, then $\phi_s = 0$ and $\phi_e = 180$ deg and Eqs. 4.93 through 4.95 simplify to:

$$\bar{F}_x = \frac{N_t b k_n}{4} f_t + \frac{N_t b k_{ne}}{\pi}, \quad (4.96)$$

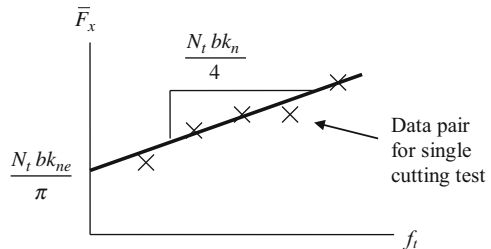
$$\bar{F}_y = \frac{N_t b k_t}{4} f_t + \frac{N_t b k_{te}}{\pi}, \text{ and} \quad (4.97)$$

$$\bar{F}_z = -\frac{N_t b k_a}{\pi} f_t - \frac{N_t b k_{ae}}{2}. \quad (4.98)$$

4.7.2 Linear Regression

Given these expressions, we complete linear regressions (over chip thickness) to determine the six unknown cutting force coefficients k_n , k_{ne} , k_t , k_{te} , k_a , and k_{ae} from measured (mean) force values. Note that the first term on the right hand side of the average force expressions in Eqs. 4.96 through 4.98 is a function of the feed per tooth, while the second term is not. These equations therefore match the (linear)

Fig. 4.69 Graph of Eq. 4.96, which relates the feed per tooth to the x direction mean force per revolution for slotting



slope-intercept form if f_t is the independent variable and the mean force is the dependent variable. In the x direction, for example, the slope is $\frac{N_t b k_n}{4}$ and the intercept is $\frac{N_t b k_{n_e}}{\pi}$. See Fig. 4.69.

The form of the linear regression for the x direction is $\bar{F}_{x,i} = a_{0x} + a_{1x}f_{t,i} + E_i$, where $(f_{t,i}, \bar{F}_{x,i})$ are the data pairs, a_{0x} is the intercept, a_{1x} is the slope, and E_i is the error between the measured \bar{F}_x values and the line $a_{0x} + a_{1x}f_t$. For $n > 2$ data pairs, the slope and intercept are determined by minimizing the sum of the errors squared [31].

$$\sum_{i=1}^n E_i^2 = \sum_{i=1}^n (\bar{F}_{x,i} - a_{0x} - a_{1x}f_{t,i})^2$$

The slope and intercept expressions obtained from this minimization are provided in Eqs. 4.99 and 4.100.

$$a_{1x} = \frac{n \sum_{i=1}^n f_{t,i} \bar{F}_{x,i} - \sum_{i=1}^n f_{t,i} \sum_{i=1}^n \bar{F}_{x,i}}{n \sum_{i=1}^n f_{t,i}^2 - \left(\sum_{i=1}^n f_{t,i} \right)^2}, \quad (4.99)$$

$$a_{0x} = \frac{1}{n} \sum_{i=1}^n \bar{F}_{x,i} - a_{1x} \frac{1}{n} \sum_{i=1}^n f_{t,i}. \quad (4.100)$$

To determine the quality of the linear fit to the data, we can calculate the coefficient of determination, r^2 , where r is the correlation coefficient. The r^2 value describes how well the original uncertainty is explained by the linear model. For example, if $r^2 = 0.95$, then the line captures 95% of the data behavior. (There are exceptions where a high r^2 value does not guarantee a successful fit, but a visual analysis of the data and line is sufficient to identify these situations [31].) See Eq. 4.101, which is again specific to the x direction.

$$r_x^2 = \frac{\sum_{i=1}^n \left(\bar{F}_{x,i} - \frac{1}{n} \sum_{i=1}^n \bar{F}_{x,i} \right)^2 - \sum_{i=1}^n E_i^2}{\sum_{i=1}^n \left(\bar{F}_{x,i} - \frac{1}{n} \sum_{i=1}^n \bar{F}_{x,i} \right)^2} \quad (4.101)$$

Once the slope and intercept values are determined from the linear regressions for the x , y , and z direction mean force data (for slotting conditions), the cutting force coefficients are determined from Eqs. 4.102 through 4.104. In these expressions, the first a subscript denotes slope (1) or intercept (0), while the second subscript indicates the measurement direction (x , y , or z) as shown in Eqs. 4.99 and 4.100.

$$k_n = \frac{4a_{1x}}{N_t b} \quad k_{ne} = \frac{\pi \cdot a_{0x}}{N_t b} \quad (4.102)$$

$$k_t = \frac{4a_{1y}}{N_t b} \quad k_{te} = \frac{\pi \cdot a_{0y}}{N_t b}, \quad (4.103)$$

$$k_a = -\frac{\pi \cdot a_{1z}}{N_t b} \quad k_{ae} = -\frac{2a_{0z}}{N_t b}. \quad (4.104)$$

Example 4.16 Determination of Cutting Force Coefficients To demonstrate the linear regression procedure for obtaining cutting force coefficient values from a particular tool-workpiece material pair, the MATLAB® program p_4_16_1.m is included with the textbook. In this program, the cutting forces are first generated for the following conditions: $k_n = 190 \text{ N/mm}^2$, $k_{ne} = 5 \text{ N/mm}$, $k_t = 710 \text{ N/mm}^2$, $k_{te} = 4 \text{ N/mm}$, $k_a = 95 \text{ N/mm}^2$, and $k_{ae} = 2 \text{ N/mm}$; $b = 5 \text{ mm}$, $f_t = \{0.05, 0.1, 0.15, 0.2, \text{ and } 0.25\} \text{ mm/tooth}$, $\Omega = 5000 \text{ rpm}$, $\phi_s = 0$, and $\phi_e = 180 \text{ deg}$; and $N_t = 2$, $\beta = 30 \text{ deg}$, and $d = 19 \text{ mm}$ for the square endmill. Figure 4.70 shows the forces for a single cutter revolution and feed per tooth of 0.25 mm, where (mean zero) Gaussian noise has been added. The mean forces for the x , y , and z directions are 136.1 N, 458.5 N, and -86.4 N, respectively. After the forces are generated and the mean values computed, the linear regression is completed to determine the slopes

Fig. 4.70 Simulated cutting forces for linear regression demonstration in Ex. 4.16. The feed per tooth for the slotting cut is 0.25 mm/tooth

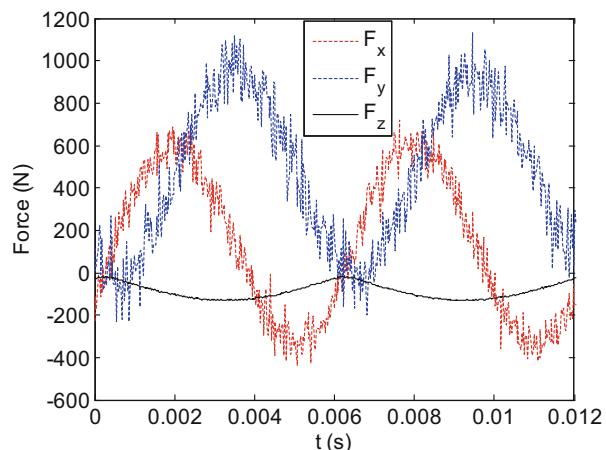
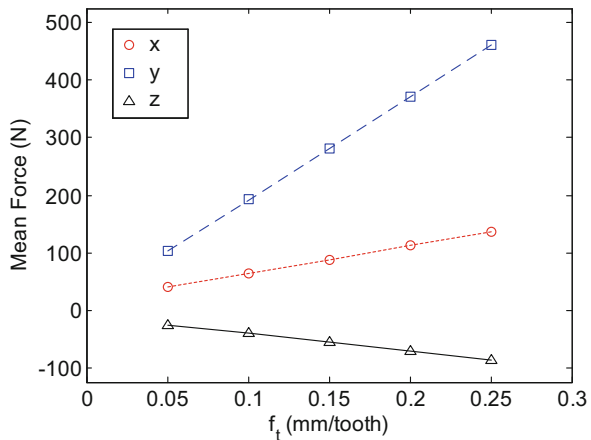


Fig. 4.71 Linear regression results for simulated forces in Example 4.16



and intercepts for the x , y , and z directions; see Fig. 4.71. They are then used, together with the preselected N_t and b values, to determine the six cutting force coefficients as shown in Eqs. 4.102 through 4.104. Finally, the coefficients of determination are calculated.

4.7.3 Nonlinear Optimization

Alternately, the cutting force coefficients may be determined using an instantaneous force, nonlinear optimization method which solves a nonlinear, least-squares curve fitting problem and takes into account the user-defined lower and upper bounds on the decision variables, including the six force coefficients and flute-to-flute runout (see Sect. 6.2).⁶ One option for the optimization routine is to use a trust-region-reflective least-squares algorithm, which equates cutting forces simulated in the time domain with measured cutting forces at each discrete time step [32].

As described in Sects. 4.4 through 4.6 and 5.3, the time domain simulation calculates the cutting forces at each small time step, dt . At each time step, the instantaneous chip thickness is computed, the cutting force is calculated, the tooth angle, ϕ , is incremented by a small angle, $d\phi$, which depends on the spindle speed and the time step, and the process is repeated for one complete revolution of the cutting tool. Because the instantaneous force, nonlinear optimization method is capable of solving nonlinear curve fitting problems, the mechanistic force model may be modified to include a nonlinear dependence on chip thickness (see Sects. 4.7.1 and 8.1).

The tangential, F_t , normal, F_n , and axial, F_a , cutting force components may be calculated according to the mechanistic force model defined in Eqs. 4.79 through 4.81.

⁶T. Schmitz recognizes the significant contributions of M. Rubeo to the nonlinear optimization analysis.

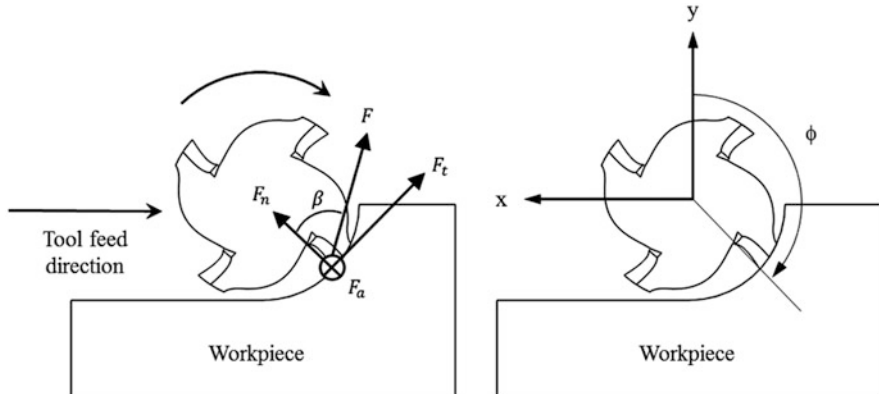


Fig. 4.72 Relationship between rotating and fixed force coordinate frames

In order to represent the simulated forces in the fixed coordinate frame of the measured cutting forces, a coordinate transformation is performed:

$$\begin{Bmatrix} F_x \\ F_y \\ F_z \end{Bmatrix}_{\text{simulated}} = \begin{bmatrix} \cos & \sin & 0 \\ \sin & -\cos & 0 \\ 0 & 0 & 1 \end{bmatrix} \begin{Bmatrix} F_t \\ F_n \\ F_a \end{Bmatrix}_{\text{simulated}}, \quad (4.105)$$

where ϕ is the instantaneous cutter rotation angle; see Fig. 4.72. We may define the objective function as:

$$f_i(k) = \begin{Bmatrix} F_x \\ F_y \\ F_z \end{Bmatrix}_i^{\text{simulated}} - \begin{Bmatrix} F_x \\ F_y \\ F_z \end{Bmatrix}_i^{\text{measured}}, \quad (4.106)$$

where k is the vector of decision variables, which includes the six cutting force coefficients and the flute-to-flute runout of the cutting tool, and $f_i(k)$ is the difference between the x , y , and z components of the instantaneous simulated and measured cutting forces at the i th time step.

Because the time step between each simulated instantaneous cutting force must coincide with the measured cutting forces, the size of the resulting system of equations depends on the sampling frequency of the measurement and the number of cutting tool revolutions (i.e., number of time steps) included in the optimization. The nonlinear, least-squares curve fitting problem takes the form:

$$\min_k \|f(k)\|_2^2 = \min_k (f_1(k)^2 + f_2(k)^2 + \dots + f_n(k)^2), \quad (4.107)$$

where n is the number of time steps. The curve fitting problem is solved using a trust-region-reflective algorithm, which is based on an interior-reflective Newton

approach that is well suited for solving nonlinear optimization problems where the decision variables are bounded by upper and/or lower limits [33]. Experimental results, including the dependence of the cutting force coefficients on feed per tooth, spindle speed, milling configuration, and radial immersion, are presented in [32].

One advantage of the nonlinear optimization approach is that, unlike the linear regression technique, only a single cut is required to identify the cutting force coefficients. This can be an important consideration when the tool wear rate is high (e.g., in hard-to-machine alloys). As the tool wears, the cutting force tends to grow which, in turn, affects the force coefficients. See Chap. 8 for additional information on tool wear.

4.7.4 Experimental Techniques

The required forces are typically measured using a table top cutting force dynamometer. The dynamometer is mounted to the machine table and aligned with the feed direction. Important considerations for force measurement include the force signal magnitudes and frequency content. As with any digital data collection, the range of the x , y , and z direction data acquisition channels should be selected so that adequate resolution is achieved. To set the maximum and minimum signal levels prior to machining, the simulation provided in p_4_16_1.m, for example, may be used with assumed coefficient values for the tool-workpiece material pair. Table 3.1 can be useful in estimating the cutting force coefficients.

Regarding frequency content, a dynamometer is also a dynamic system and therefore has its own associated frequency response. Naturally, if the cutting force has frequency content near a natural frequency of the dynamometer, then this content will be artificially amplified and the force data will be corrupted by the dynamometer dynamic response. The tooth passing frequency, defined in Eq. 4.14, provides a lower bound on the desired dynamometer bandwidth (i.e., the location of the first natural frequency for the dynamometer-workpiece combination). However, as shown in Fig. 4.15, multiple harmonics of the tooth passing frequency may be present, depending on the number of teeth and radial immersion. To determine the frequency response for a particular dynamometer-workpiece setup, impact testing can be applied. (It is necessary to include the mounted workpiece because it effectively mass loads the dynamometer and reduces its natural frequencies.) The impact hammer is used to excite the dynamometer in the x , y , and z directions, and the corresponding force output is measured. The frequency domain ratio of the output to input force can then be calculated and analyzed. To avoid data corruption by the dynamometer, the tooth passing frequency can be set such that there is no appreciable content at or beyond the first natural frequency of the dynamometer-workpiece combination. However, because decreases in cutting forces can be observed for higher cutting speeds [19], it may be preferable to test in the anticipated spindle speed range. In this case, one option is to filter the measured force using the inverse of the dynamometer force-to-input force frequency response. See, for

example, the method proposed in [32]. An inverse filtering approach for a spindle-based torque dynamometer is also described in [34].

As a final note, it should of course be ensured that the cutting tests are stable. As described in the previous sections, the tool point frequency response function in the x and y directions should be measured and used as input, together with assumed cutting force coefficients, to one or both of the analytical stability lobe algorithms in order to estimate a stable axial depth of cut for the selected radial depth (slotting in Eqs. 4.102 through 4.104), number of cutter teeth, and spindle speed.



In a Nutshell

Is it worth the extra effort to get the most accurate cutting force coefficients? The answer is—sometimes! It depends on your purpose. Even with a very crude force model, the dynamic behavior of the milling operation will be generally correctly captured. The good and bad speeds will be generally correct. However, the accuracy of the location of the stability boundary directly depends on the accuracy of the cutting force coefficients, just as it depends directly on the accuracy of the FRF measurement. The more accurately we want to know the boundary, the more accurately we need to know the data. Accurate knowledge of the cutting force coefficients introduces significant complexity.

Of course, what constitutes “significant complexity” is in the eye of the beholder. Most of the information about stable and unstable cutting conditions can be correctly deduced using the approximation that the cutting force is proportional to the frontal area of the chip through a single cutting force coefficient. Increasing the accuracy of the prediction requires increasing the complexity of the model and the amount of required information. Knowing where to draw the line in order to obtain an answer that is good enough is the essence of engineering. Different readers will have varying objectives and will draw that line in different places.

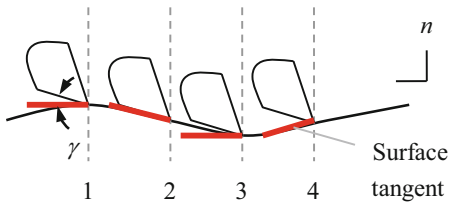
4.8 Process Damping

We presented an introduction to process damping for turning in Sect. 3.7. We provide a brief review here and then demonstrate how we can use the same approach to include process damping in milling.

4.8.1 Process Damping Description

To describe the physical mechanism for process damping, consider a tool moving on a sine wave while shearing away the chip [16]; see Fig. 4.73. Four locations are identified: (1) the clearance angle, γ , between the flank face of the tool and the work surface tangent is equal to the nominal relief angle for the tool; (2) γ is significantly decreased and can become negative (which leads to interference between the tool’s

Fig. 4.73 Physical description of process damping. The clearance angle varies with the instantaneous surface tangent as the tool removes material on the sinusoidal surface



relief face and surface); (3) γ is again equal to the nominal relief angle; and (4) γ is significantly larger than the nominal value.

At points 1 and 3 in Fig. 4.73, the clearance angle is equal to the nominal value, so there is no effect due to cutting on the sinusoidal path. However, at point 2 the clearance angle is small (or negative), and the thrust force in the surface normal direction, n , is increased. At point 4, on the other hand, the clearance angle is larger than the nominal, and the thrust force is decreased. Because the change in force caused by the sinusoidal path is 90 deg out of phase with the displacement and has the opposite sign from velocity, it is considered to be a viscous damping force (i.e., a force that is proportional to velocity). Given the preceding description, the process damping force, F_d , in the surface normal direction can be expressed as a function of velocity, \dot{n} , chip width, cutting speed, and a constant C [35]. See Eq. 4.108.

$$F_d = -C \frac{b}{v} \dot{n} \quad (4.108)$$

4.8.2 Stability Algorithm

Let's incorporate process damping in the average tooth angle approach from Sect. 4.3.1. As shown, the limiting stable chip width, b_{lim} , for regenerative chatter is defined as:

$$b_{\text{lim}} = \frac{-1}{2K_s \text{Re}[\text{FRF}_{\text{orient}}] N_t^*}, \quad (4.109)$$

where $\text{FRF}_{\text{orient}}$ is the oriented frequency response function and N_t^* is the average number of teeth engaged in the cut based on the radial immersion (Eq. 4.26). To relate the frequency dependent b_{lim} vector to spindle speed, Ω , Eq. 4.109 is applied to define the relationship between Ω and the valid chatter frequencies, f_c (i.e., those frequencies where the real part of $\text{FRF}_{\text{orient}}$ is negative):

$$\frac{f_c}{\Omega N_t} = N + \frac{\epsilon}{2\pi}, \quad (4.110)$$

where N_t is the number of teeth on the rotating cutter, $N = 0, 1, 2, \dots$ is the integer number of waves per revolution (i.e., the lobe number), and $\epsilon = 2\pi - 2 \tan^{-1} \left(\frac{\text{Re}[\text{FRF}_{\text{orient}}]}{\text{Im}[\text{FRF}_{\text{orient}}]} \right)$ (rad) is the phase between the current vibration and the previous tooth.

4.8.2.1 Up Milling

We include the process damping force in Eq. 4.108, where the surface normal direction depends on the average tooth angle orientation, ϕ_{ave} , as shown in Fig. 4.74. The projection of the process damping force from the n direction onto the x direction is:

$$F_x = F_d \cos(90 - \phi_{ave}) = -\left(C \frac{b}{v} \cos(90 - \phi_{ave})\right) \dot{n}. \quad (4.111)$$

Substituting $\dot{n} = \cos(90 - \phi_{ave}) \dot{x}$ in Eq. 4.111 gives:

$$F_x = -\left(C \frac{b}{v} \cos^2(90 - \phi_{ave})\right) \dot{x}. \quad (4.112)$$

The new damping in the converging stability calculation for the x direction FRF, $\text{FRF}_{x,x}$, is therefore:

$$c_{\text{new},x} = c_x + C \frac{b}{v} \cos^2(90 - \phi_{ave}). \quad (4.113)$$

The corresponding new y direction damping is:

$$c_{\text{new},y} = c_y + C \frac{b}{v} \cos^2(180 - \phi_{ave}). \quad (4.114)$$

The oriented FRF for this case is $\text{FRF}_{\text{orient}} = \mu_x \text{FRF}_x + \mu_y \text{FRF}_y$, where $\mu_x = \cos(\beta - (90 - \phi_{ave})) \cos(90 - \phi_{ave})$ and $\mu_y = \cos((180 - \phi_{ave}) - \beta) \cos(180 - \phi_{ave})$.

Fig. 4.74 Geometry for up milling using the average tooth angle stability analysis (a 25% radial immersion cut is shown for illustrative purposes)

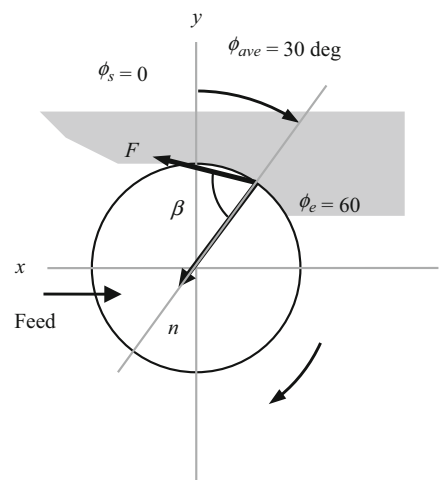
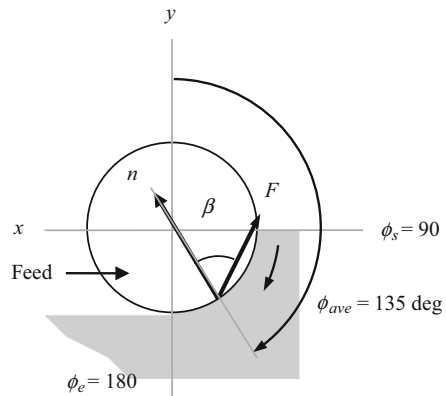


Fig. 4.75 Model for down milling (a 50% radial immersion cut is shown)



4.8.2.2 Down Milling

The geometry for the down milling case is shown in Fig. 4.75. Using the same approach as described for the up milling case, the x and y direction damping values are provided in Eqs. 4.115 and 4.116.

$$c_{\text{new},x} = c_x + C \frac{b}{v} \cos^2(\phi_{ave} - 90) \quad (4.115)$$

$$c_{\text{new},y} = c_y + C \frac{b}{v} \cos^2(180 - \phi_{ave}) \quad (4.116)$$

The oriented FRF is $\text{FRF}_{\text{orient}} = \mu_x \text{FRF}_x + \mu_y \text{FRF}_y$, where $\mu_x = \cos(\beta + (\phi_{ave} - 90)) \cos(\phi_{ave} - 90)$ and $\mu_y = \cos(\beta - (180 - \phi_{ave})) \cos(180 - \phi_{ave})$.

Due to the nature of the cosine projections in both the process damping force and directional orientation factors, the up and down milling expressions give identical answers for the same ϕ_{ave} value. For simplicity, we'll use the up milling equations in the MATLAB® programs for our analytical and time domain solutions.

As with the turning analysis, the new damping value is a function of both the spindle speed dependent limiting chip width and the cutting speed. The cutting speed (m/s) depends on the spindle speed (rpm) and tool diameter, d , (m) according to $v = \frac{\pi d}{60}$. Therefore, the b and Ω vectors must be known in order to implement the new damping value. This leads to the converging nature of the stability analysis that incorporates process damping. We complete the following steps for each lobe number, or N value (see Eq. 4.110):

1. The analytical stability boundary is calculated with no process damping to identify initial b and Ω vectors.
2. These vectors are used to determine the corresponding c_{new} vector.
3. The stability analysis is repeated with the new damping value to determine updated b and Ω vectors.
4. The process is repeated until the stability boundary converges [36–42].

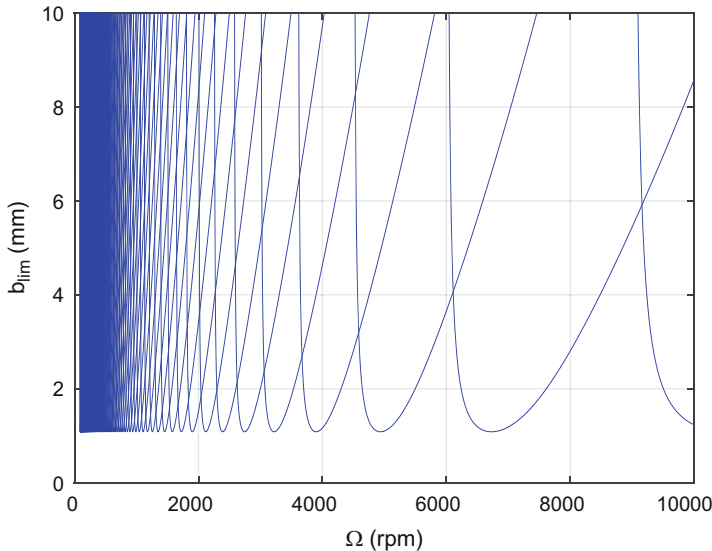


Fig. 4.76 Stability diagram for 50% radial immersion up milling operation with $k = 9 \times 10^6$ N/m, $f_n = 900$ Hz, $\zeta = 0.03$, $K_s = 2000 \times 10^6$ N/m 2 , $\beta = 70$ deg, $d = 0.019$ m, and $C = 0$

Example 4.17 Milling Stability Analysis with Process Damping To demonstrate the approach, let's consider the model in Fig. 4.74 with symmetric dynamics $k = 9 \times 10^6$ N/m, $f_n = 900$ Hz, and $\zeta = 0.03$ for a 50% radial immersion up milling operation ($\phi_s = 0$, $\phi_e = 90$ deg, and $\phi_{\text{ave}} = 45$ deg). The force model is $K_s = 2000 \times 10^6$ N/m 2 and $\beta = 70$ deg for a 19 mm diameter cutter with three teeth. The stability boundary with no process damping ($C = 0$) is displayed in Fig. 4.76 for $N = 0$ to 200. We observe that the limiting chip width approaches the asymptotic stability limit of 1.08 mm for spindle speeds below 500 rpm. The MATLAB® program used to produce this figure is provided with the textbook as p_4_17_1.m.

Figure 4.77 displays the new stability diagram for $N = 1$ to 200 with $C = 2 \times 10^4$ N/m. In the low spindle speed range (approximately less than 150 rpm depending on the axial depth of cut), the stable process damping zone is now observed. The MATLAB® program used to produce this figure is p_4_17_2.m

Example 4.18 Comparison with Time Domain Simulation Let's compare our analytical stability predictions to time domain simulation results. To do this, we'll need to update the milling time domain simulation from Sect. 4.5 to include process damping. Let's again consider the model in Fig. 4.74 with symmetric dynamics $k = 9 \times 10^6$ N/m, $f_n = 900$ Hz, and $\zeta = 0.03$ for a 50% radial immersion up milling operation ($\phi_s = 0$, $\phi_e = 90$ deg, and $\phi_{\text{ave}} = 45$ deg). The force model is $K_s = 2000 \times 10^6$ N/m 2 and $\beta = 70$ deg for a 19 mm diameter cutter with three teeth. We incorporate process damping ($C = 2 \times 10^4$ N/m) by including the process damping force in the surface normal, n , direction. This requires that we add a

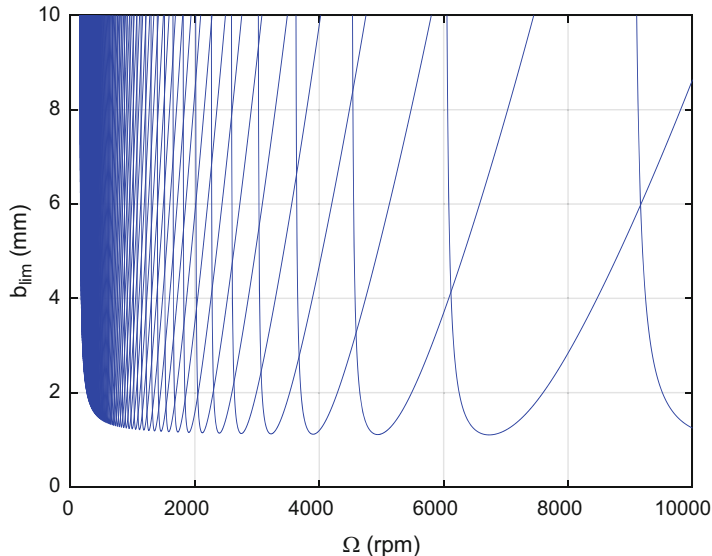


Fig. 4.77 Stability diagram for 50% radial immersion up milling operation with $k = 9 \times 10^6$ N/m, $f_n = 900$ Hz, $\zeta = 0.03$, $K_s = 2000 \times 10^6$ N/m², $\beta = 70$ deg, $d = 0.019$ m, and $C = 2 \times 10^4$ N/m

calculation for the velocity, \dot{n} , in the n direction. It is a projection of the velocities in the x and y directions, \dot{x} and \dot{y} , determined from the numerical integration.

$$n_dot = x_dot * \sin(\phiia * \pi / 180) - y_dot * \cos(\phiia * \pi / 180);$$

The updated force expression in the normal direction now includes the process damping contribution.

$$Fn = kn * db * h - C * db / v * n_dot;$$

Figure 4.78 shows the feed, x , direction simulation results for a spindle speed of 9000 rpm and an axial depth of 3 mm. As predicted by the stability lobe diagrams in Figs. 4.76 and 4.77, the cut is stable because $b < b_{lim}$ at this spindle speed. In contrast, the result is unstable at 7500 rpm as displayed in Fig. 4.79. For this spindle speed range, there is no significant contribution by process damping so the diagrams in Figs. 4.76 and 4.77 are similar.

We'll now compare simulation results with and without process damping in the low spindle speed range. Let's select a spindle speed of 250 rpm, again at an axial depth of 3 mm. The simulation results without process damping ($C = 0$) are displayed in Fig. 4.80. The cut is clearly unstable. Process damping is included in Fig. 4.81 ($C = 2 \times 10^4$ N/m), and stable operation is now observed. The MATLAB® program used to produce these figures is p_4_18_1.m.

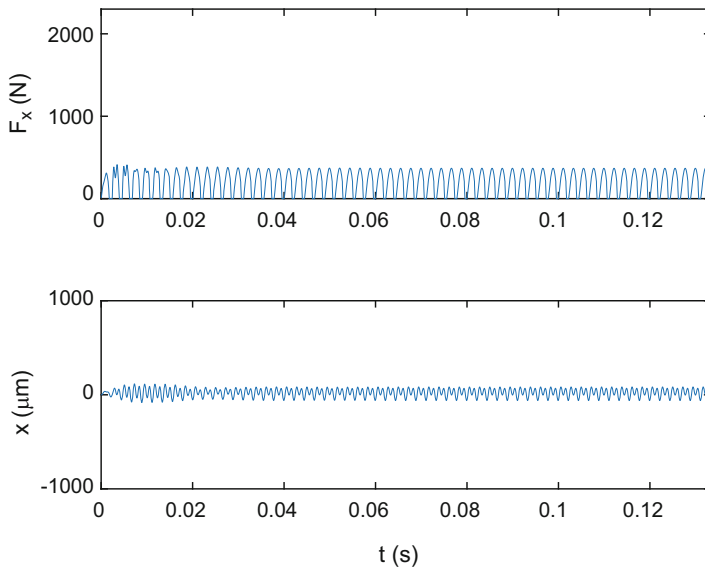


Fig. 4.78 Stable time domain simulation results for $\{\Omega, b\} = \{9000 \text{ rpm}, 3 \text{ mm}\}$ with $C = 2 \times 10^4 \text{ N/m}$

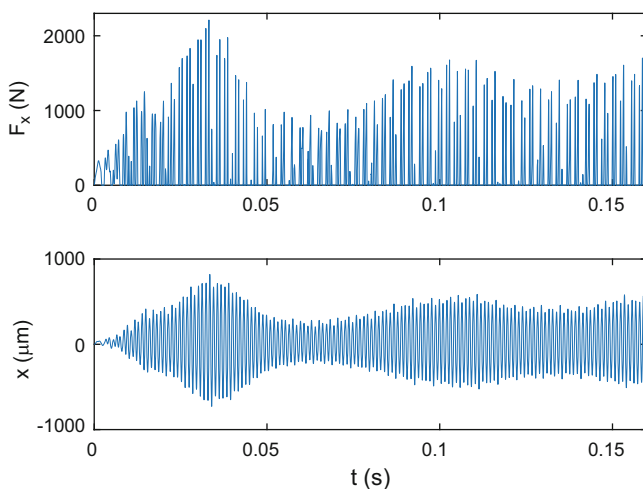


Fig. 4.79 Unstable time domain simulation results for $\{\Omega, b\} = \{7500 \text{ rpm}, 3 \text{ mm}\}$ with $C = 2 \times 10^4 \text{ N/m}$

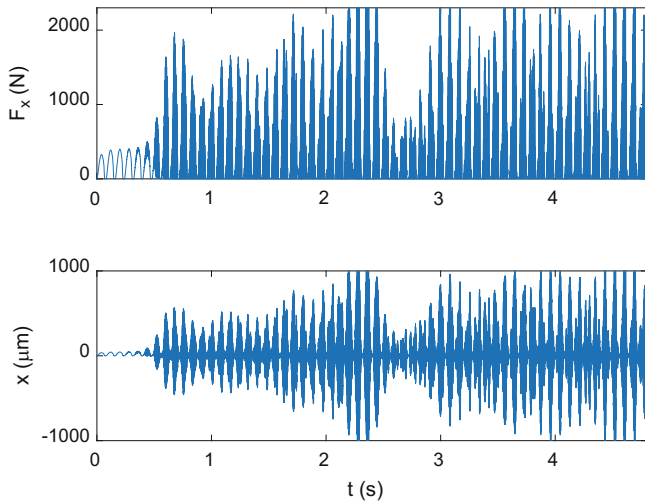


Fig. 4.80 Unstable time domain simulation results for $\{\Omega, b\} = \{250 \text{ rpm}, 3 \text{ mm}\}$ with $C = 0$

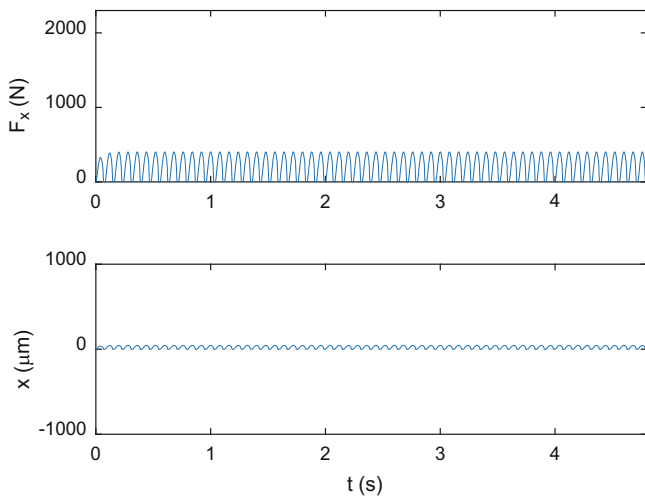
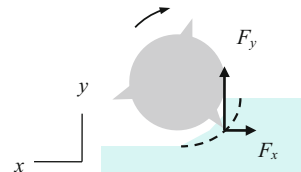


Fig. 4.81 Stable time domain simulation results for $\{\Omega, b\} = \{250 \text{ rpm}, 3 \text{ mm}\}$ with $C = 2 \times 10^4 \text{ N/m}$

Exercises

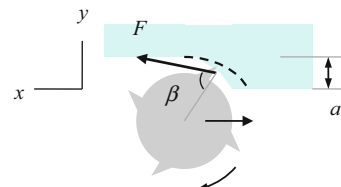
1. Compute the start and exit angles for the following milling cases.
 - (a) Up milling, 30% radial immersion
 - (b) Down milling, 40% radial immersion
2. Determine the tooth passing frequency for a cutter with three teeth rotating at 10,000 rpm.
3. Calculate the maximum y direction force for a 40% radial immersion down milling cut carried out using a three tooth end mill; see Fig. 4.82. The material-tool combination gives: $k_t = 720 \text{ N/mm}^2$ and $k_n = 200 \text{ N/mm}^2$ (aluminum alloy). Also, $b = 2.5 \text{ mm}$ and $f_t = 0.2 \text{ mm/tooth}$. Assume a rigid cutting tool and workpiece.

Fig. 4.82 Down milling force geometry



4. For the average tooth angle milling stability analysis, complete parts (a) through (d). A 35% radial immersion up milling cut is to be performed using a square end mill with four teeth and the force angle, β , is 68 deg. See Fig. 4.83.

Fig. 4.83 35% radial immersion up milling geometry



- (a) Determine the average angle of a tooth in the cut.
- (b) Calculate the directional orientation factors.
- (c) Compute the oriented frequency response function and identify the valid chatter frequency range(s) in Hz. The x direction dynamics are given by: $f_{nx} = 1000 \text{ Hz}$, $k_x = 7 \times 10^6 \text{ N/m}$, and $\zeta_x = 0.03$ and the y direction dynamics are: $f_{ny} = 1200 \text{ Hz}$, $k_y = 6 \times 10^7 \text{ N/m}$, and $\zeta_y = 0.04$. You may assume that these single degree of freedom parameters were obtained from a modal fit to frequency responses measured in the x and y directions with bandwidths of 0–2500 Hz.
- (d) Plot the first five stability lobes, $N = 0$ to 4. The workpiece material is 1020 carbon steel; see Table 3.1.

5. For the cut described in Exercise 4, use the Fourier approach to obtain the stability lobe diagram ($j = 0$ to 4).
6. Calculate the lowest axial depth for which a constant cutting force is obtained independent of the selected radial depth of cut. The helical square end mill has a diameter of 10 mm, six teeth, and a 42 deg helix angle.
7. For a particular milling application, the spindle speed is 6000 rpm. The x and y direction cutting forces are shown in Fig. 4.84. The coordinate system is defined in Fig. 4.85. Only one tooth is engaged in the cut at any time and the cut is stable. The cutter teeth are straight.

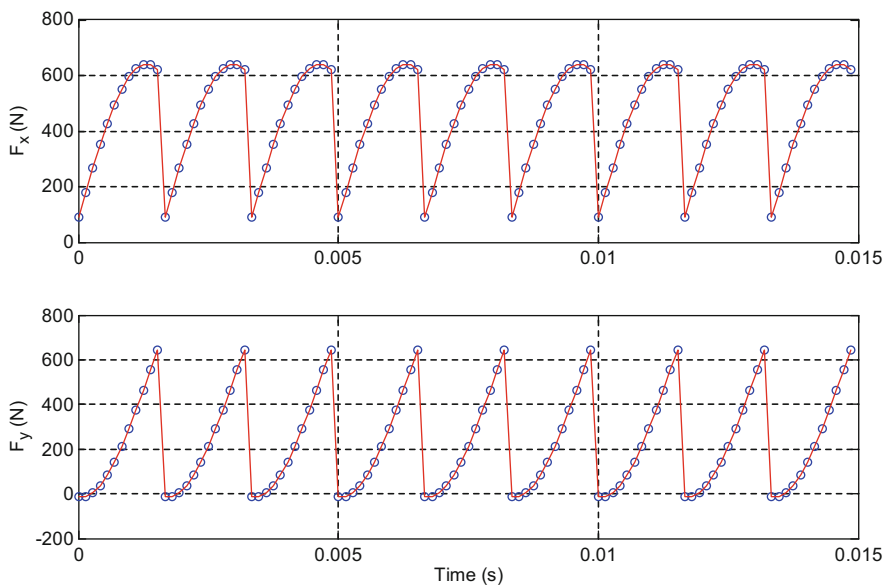
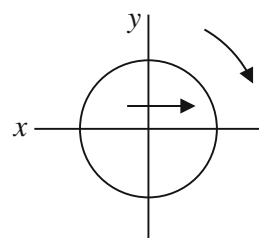


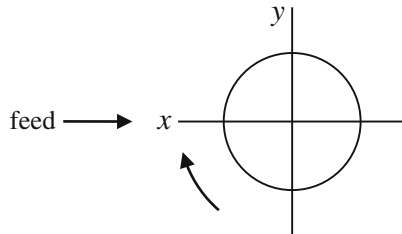
Fig. 4.84 Time domain forces in the x and y directions

Fig. 4.85 Coordinate system for forces



- (a) Is this cut up or down milling?
- (b) How many teeth are on the milling cutter?
- (c) If the Fourier transform for either cutting force signal (x or y direction) were computed, at what frequencies (in Hz) would peaks be expected?

- (d) Determine k_t and k_n , where the tangential and normal force components are expressed as: $F_t = k_t b h$ and $F_n = k_n b h$, where $b = 5 \text{ mm}$, $f_t = 0.2 \text{ mm/tooth}$, and the circular tool path approximation may be applied.
8. An endmill with four teeth is being used in a cut with an entry (starting) angle of 15 deg and an exit angle of 75 deg.
- Determine the average number of teeth in the cut (average tooth angle approach).
 - What is the average angle of the surface normal for a tooth engaged in the cut (average tooth angle approach)? Sketch the cut and identify the surface normal and angle on your sketch.



- (c) If $\beta = 60 \text{ deg}$ (average tooth angle approach), determine the directional orientation factors.

Appendix: Reformulation of Fourier Series Eigenvalue Problem

In Sect. 4.3.3, we detailed the truncated Fourier series approach to obtaining the analytical stability limit for milling [5]. The dynamic milling equation (Eq. 4.49) was presented as:

$$\begin{pmatrix} F_x \\ F_y \end{pmatrix} e^{i\omega_c t} = \frac{1}{2} b K_t [A_0] (1 - e^{i\omega_c \tau}) \begin{bmatrix} \text{FRF}_{xx} & 0 \\ 0 & \text{FRF}_{yy} \end{bmatrix} \begin{pmatrix} F_x \\ F_y \end{pmatrix} e^{i\omega_c t}, \quad (4.117)$$

which is true if $\begin{pmatrix} F_x \\ F_y \end{pmatrix} e^{i\omega_c t} = \begin{bmatrix} 1 & 0 \\ 0 & 1 \end{bmatrix} \begin{pmatrix} F_x \\ F_y \end{pmatrix} e^{i\omega_c t} = [I] \begin{pmatrix} F_x \\ F_y \end{pmatrix} e^{i\omega_c t}$. This enables us to write $\frac{1}{2} b K_t [A_0] (1 - e^{i\omega_c \tau}) \begin{bmatrix} \text{FRF}_{xx} & 0 \\ 0 & \text{FRF}_{yy} \end{bmatrix} = [I]$ or $\frac{N_t}{4\pi} b K_t (1 - e^{-i\omega_c \tau}) [\text{FRF}_{\text{or}}] = [I]$. The eigenvalue problem was then posed in [5] as:

$$\det([I] + \Lambda [\text{FRF}_{\text{or}}]) = 0, \quad (4.118)$$

where $\Lambda = -\frac{N_t}{4\pi} b K_t (1 - e^{-i\omega_c \tau})$ gives the eigenvalues. To apply the MATLAB® `eig` function, we must restate the eigenvalue problem as $\det([\text{FRF}_{\text{or}}] - \lambda[I]) = 0$. The new complex eigenvalues are therefore $\lambda = \lambda_{\text{Re}} + i\lambda_{\text{Im}} = \frac{4\pi}{N_t b K_t (1 - e^{-i\omega_c \tau})}$. We determine the corresponding stability limit by solving this expression for b , rationalizing the result, and then substituting for $e^{-i\omega_c \tau}$ using the Euler identity $e^{-i\omega_c \tau} = \cos(\omega_c \tau) - i \sin(\omega_c \tau)$.

$$\begin{aligned}\tilde{b}_{\text{lim}} &= \frac{4\pi}{N_t K_t (\lambda_{\text{Re}} + i\lambda_{\text{Im}})(1 - e^{-i\omega_c \tau})} \\ \tilde{b}_{\text{lim}} &= \frac{4\pi(\lambda_{\text{Re}} - i\lambda_{\text{Im}})}{N_t K_t (\lambda_{\text{Re}} + i\lambda_{\text{Im}})(\lambda_{\text{Re}} - i\lambda_{\text{Im}})(1 - e^{-i\omega_c \tau})} \\ \tilde{b}_{\text{lim}} &= \frac{4\pi(\lambda_{\text{Re}} - i\lambda_{\text{Im}})}{N_t K_t (\lambda_{\text{Re}}^2 + \lambda_{\text{Im}}^2)(1 - \cos(\omega_c \tau) + i \sin(\omega_c \tau))}\end{aligned}\quad (4.119)$$

After the Euler identity substitution, we again rationalize to obtain Eq. 4.120.

$$\begin{aligned}\tilde{b}_{\text{lim}} &= \frac{4\pi}{N_t K_t (\lambda_{\text{Re}}^2 + \lambda_{\text{Im}}^2)} \frac{(\lambda_{\text{Re}} - i\lambda_{\text{Im}})(1 + \cos(\omega_c \tau) - i \sin(\omega_c \tau))}{(1 - \cos(\omega_c \tau) + i \sin(\omega_c \tau))(1 - \cos(\omega_c \tau) - i \sin(\omega_c \tau))} \\ \tilde{b}_{\text{lim}} &= \frac{4\pi}{N_t K_t (\lambda_{\text{Re}}^2 + \lambda_{\text{Im}}^2)} \frac{(\lambda_{\text{Re}} - i\lambda_{\text{Im}})(1 + \cos(\omega_c \tau) - i \sin(\omega_c \tau))}{(2 - 2 \cos(\omega_c \tau))} \\ \tilde{b}_{\text{lim}} &= \frac{2\pi}{N_t K_t (\lambda_{\text{Re}}^2 + \lambda_{\text{Im}}^2)} \frac{\left((\lambda_{\text{Re}}(1 - \cos(\omega_c \tau)) + \lambda_{\text{Im}} \sin(\omega_c \tau)) \right.}{\left. + i(\lambda_{\text{Im}}(1 - \cos(\omega_c \tau)) - \lambda_{\text{Re}} \sin(\omega_c \tau)) \right)}{(1 - \cos(\omega_c \tau))}\end{aligned}\quad (4.120)$$

Because \tilde{b}_{lim} must be real valued, the imaginary part from the parenthetical portion of the numerator in the final line in Eq. 4.120 must be equal to zero:

$$\lambda_{\text{Im}}(1 - \cos(\omega_c \tau)) - \lambda_{\text{Re}} \sin(\omega_c \tau) = 0. \quad (4.121)$$

This gives $\frac{\lambda_{\text{Im}}}{\lambda_{\text{Re}}} = \frac{\sin(\omega_c \tau)}{1 - \cos(\omega_c \tau)} = \tilde{\kappa}$. Substitution in Eq. 4.120 yields Eq. 4.122.

$$\begin{aligned}\tilde{b}_{\text{lim}} &= \frac{2\pi}{N_t K_t (\lambda_{\text{Re}}^2 + \lambda_{\text{Im}}^2)} \left(\frac{\lambda_{\text{Re}}(1 - \cos(\omega_c \tau))}{(1 - \cos(\omega_c \tau))} + \frac{\lambda_{\text{Im}} \sin(\omega_c \tau)}{(1 - \cos(\omega_c \tau))} \right) \\ \tilde{b}_{\text{lim}} &= \frac{2\pi}{N_t K_t (\lambda_{\text{Re}}^2 + \lambda_{\text{Im}}^2)} (\lambda_{\text{Re}} + \lambda_{\text{Im}} \tilde{\kappa}) \\ \tilde{b}_{\text{lim}} &= \frac{2\pi}{N_t K_t (\lambda_{\text{Re}}^2 + \lambda_{\text{Im}}^2)} \lambda_{\text{Re}} \left(1 + \frac{\lambda_{\text{Im}}}{\lambda_{\text{Re}}} \tilde{\kappa} \right) = \frac{2\pi}{N_t K_t (\lambda_{\text{Re}}^2 + \lambda_{\text{Im}}^2)} \lambda_{\text{Re}} (1 + \tilde{\kappa}^2)\end{aligned}\quad (4.122)$$

References

1. Kumanchik, L., & Schmitz, T. (2007). Improved analytical chip thickness model for milling. *Precision Engineering*, 31, 317–324.
2. Tlusty, J., Zaton, W., & Ismail, F. (1983). Stability lobes in milling. *Annals of the CIRP*, 32(1), 309–313.
3. Smith, S., & Tlusty, J. (1990). Update on high-speed milling dynamics. *Journal of Engineering for Industry*, 112, 142–149.
4. Smith, S., & Tlusty, J. (1991). An overview of modeling and simulation of the milling process. *Journal of Engineering for Industry*, 113, 169–175.
5. Altintas, Y., & Budak, E. (1995). Analytical prediction of stability lobes in milling. *Annals of the CIRP*, 44(1), 357–362.
6. Davies, M., Pratt, J., Dutterer, B., & Burns, T. (2000). The stability of low radial immersion milling. *Annals of the CIRP*, 49(1), 37–40.
7. Davies, M., Pratt, J., Dutterer, B., & Burns, T. (2002). Stability prediction for low radial immersion milling. *Journal of Manufacturing Science and Engineering*, 124(2), 217–225.
8. Bayly, P., Mann, B., Schmitz, T., Peters, D., Stépàn, G., & Insperger, T. (2002). Effects of radial immersion and cutting direction on chatter instability in endmilling. In *Proceedings of ASME International Mechanical Engineering Conference and Exposition, IMECE2002-34116*, New Orleans, LA (on CD).
9. Mann, B., Bayly, P., Davies, M., & Halley, J. (2004). Limit cycles, bifurcations, and accuracy of the milling process. *Journal of Sound and Vibration*, 227, 31–48.
10. Schmitz, T., Davies, M., Medicus, K., & Snyder, J. (2001). Improving high-speed machining material removal rates by rapid dynamic analysis. *Annals of the CIRP*, 50(1), 263–268.
11. Schmitz, T., Medicus, K., & Dutterer, B. (2002). Exploring once-per-revolution audio signal variance as a chatter indicator. *Machining Science and Technology*, 6(2), 215–233.
12. Schmitz, T. (2003). Chatter recognition by a statistical evaluation of the synchronously sampled audio signal. *Journal of Sound and Vibration*, 262(3), 721–730.
13. Delio, T., Tlusty, J., & Smith, S. (1992). Use of audio signals for chatter detection and control. *Journal of Engineering for Industry*, 114, 146–157.
14. Honeycutt, A., & Schmitz, T. (2016). A new metric for automated stability identification in time domain milling simulation. *Journal of Manufacturing Science and Engineering*, 138(7), 074501.
15. Honeycutt, A., & Schmitz, T. (2017). Milling stability interrogation by subharmonic sampling. *Journal of Manufacturing Science and Engineering*, 139(4), 041009.
16. Tlusty, G. (2000). *Manufacturing equipment and processes*. Upper Saddle River, NJ: Prentice-Hall, Section 9.5.4.
17. Altintas, Y., & Lee, P. (1996). A general mechanics and dynamics model for helical end mills. *Annals of the CIRP*, 45(1), 59–64.
18. Altintas, Y. (2000). *Manufacturing automation: metal cutting mechanics, machine tool vibrations, and CNC design*. Cambridge: Cambridge University Press, Sect. 2.8.1.
19. Duncan, G. S. (2006). *Milling dynamics prediction and uncertainty analysis using receptance coupling substructure analysis*. Ph.D. Dissertation, University of Florida.
20. Koenigsberger, F., & Sabberwal, A. (1961). An investigation into the cutting force pulsations during milling operations. *International Journal of Machine Tool Design and Research*, 1, 15–33.
21. Tlusty, J., & MacNeil, P. (1975). Dynamics of cutting forces in end milling. *Annals of the CIRP*, 24(1), 21–25.
22. Kline, W., DeVor, R., & Lindberg, J. (1982). The prediction of cutting forces in end milling with applications to cornering cuts. *International Journal of Machine Tool Design and Research*, 22, 7–22.
23. Fu, H., DeVor, R., & Kapoor, S. (1984). A mechanistic model for the prediction of the force system in face milling operations. *Journal of Engineering for Industry*, 111, 27–36.

24. Yellowley, I. (1985). Observations of the mean values of forces, torque and specific power in the peripheral milling process. *International Journal of Machine Tool Design and Research*, 25, 337–346.
25. Amarego, E., & Whitfield, R. (1985). Computer based modeling of popular machining operations for forces and power prediction. *Annals of the CIRP*, 34, 65–69.
26. Wang, J.-J., Liang, S., & Book, W. (1994). Convolution analysis of cutting force pulsation. *Journal of Engineering for Industry*, 116, 17–25.
27. Endres, W., DeVor, R., & Kapoor, S. (1995). A dual-mechanism approach to the prediction of machining forces, Part 1: Model development. *Journal of Engineering for Industry*, 117, 526–533.
28. Budak, E., Altintas, Y., & Amarego, E. (1998). Prediction of milling force coefficients from orthogonal cutting data. *Journal of Manufacturing Science and Engineering*, 120, 216–224.
29. Jayaram, S., Kapoor, S., & DeVor, R. (2001). Estimation of the specific cutting pressures for mechanistic cutting force models. *International Journal of Machine Tools and Manufacture*, 41, 265–281.
30. Wang, J.-J., & Zheng, C. (2002). An analytical force model with shearing and ploughing mechanisms for end milling. *International Journal of Machine Tools and Manufacture*, 42, 761–771.
31. Chapra, S., & Canale, R. (1985). *Numerical methods for engineers*. New York, NY: McGraw-Hill Book Co., Section 10.1.
32. Rubeo, M., & Schmitz, T. (2016). Mechanistic force model coefficients: a comparison of linear regression and nonlinear optimization. *Precision Engineering*, 45, 311–321.
33. Coleman, T. F., & Li, Y. (1994). On the convergence of interior-reflective newton methods for nonlinear minimization subject to bounds. *Mathematical Programming*, 67, 189–224.
34. Smith, D., Smith, S., & Tlusty, J. (1998). High performance milling torque sensor. *Journal of Manufacturing Science and Engineering*, 120(3), 504–514.
35. Altintas, Y., Eynian, M., & Onozuka, H. (2008). Identification of dynamic cutting force coefficients and chatter stability with process damping. *Annals of the CIRP*, 57(1), 371–374.
36. Tyler, C., & Schmitz, T. (2012). Process damping analytical stability analysis and validation. *Transactions of the NAMRI/SME*, 40, 1–8.
37. Tyler, C., & Schmitz, T. (2013). Analytical process damping stability prediction. *Journal of Manufacturing Processes*, 15, 69–76.
38. Tyler, C., Karandikar, J., & Schmitz, T. (2013). Process damping coefficient identification using bayesian inference. *Transactions of the NAMRI/SME*, 41, 1–8.
39. Tyler, C., & Schmitz, T. (2014). Process damping milling model database. *Transactions of the NAMRI/SME*, 42, 1–8.
40. Tyler, C., Troutman, J., & Schmitz, T. (2015). Radial depth of cut stability lobe diagrams with process damping effects. *Precision Engineering*, 40, 318–324.
41. Tyler, C., Troutman, J., & Schmitz, T. (2016). A coupled dynamics, multiple degree of freedom process damping model, Part 1: Turning. *Precision Engineering*, 46, 65–72.
42. Tyler, C., Troutman, J., & Schmitz, T. (2016). A coupled dynamics, multiple degree of freedom process damping model, Part 2: Milling. *Precision Engineering*, 46, 73–80.

Chapter 5

Surface Location Error in Milling



*No amount of experimentation can ever prove me right;
a single experiment can prove me wrong.*

—Albert Einstein

In Chapter 4 we described analytical approaches for predicting milling stability. We showed stability lobe diagrams that identify stable and unstable combinations of spindle speed and axial depth of cut in a graphical format. We also developed time domain simulations that predict forces and displacements for straight and helical teeth square endmills and helical teeth ball endmills. These simulations could also be employed to determine stability. In this chapter, we presume that stable cutting conditions have been selected, and we investigate the influence of forced vibrations on part geometric accuracy. We refer to part errors that occur due to forced vibrations as surface location errors and again apply both analytical frequency domain and time domain approaches to their prediction.

5.1 Surface Location Error

As we've seen, the process dynamics can impose significant limitations on milling efficiency due to chatter, or self-excited vibrations that lead to large forces, displacements, and poor surface quality. However, productivity can also be limited by forced vibrations which cause surface location error, or workpiece geometric inaccuracies that result from dynamic displacements of the tool during stable milling [1–14]. Other limiting factors include, for example, machine tool quasi-static positioning errors, thermal errors, contouring errors, and tool wear [15], but we do not address these here. Tool wear is discussed on Chap. 8.



For Instance

Positioning errors may occur because the axes are not perpendicular to each other or because the linear axis ball screws are not perfect. Thermal errors may occur because the machine tool is located in an uncontrolled thermal environment and the machine and workpiece have different coefficients of thermal expansion. In addition, the cutting process and various machine components act as heat sources, and the machine and workpiece experience uneven localized heating, which causes thermal deformation. Even with “warm-up” procedures, most machine tools never reach a thermal steady state. Contouring errors occur due to the inability of the control system to position the cutting point on the tool exactly where we wish. In servo control, there must be a position error (i.e., the “following error”) to generate an axis motion. If the following errors differ between axes, then the tool does not follow the desired path.

A visual explanation of the surface location error phenomenon is provided in Fig. 5.1. Even under stable cutting conditions, the tool experiences forced/synchronous vibrations which depend on the system frequency response function (FRF) and excitation frequency (or tooth passing frequency; see Eq. 4.14), as well as other process parameters, including the radial and axial depths of cut, feed per tooth, and force model coefficients (although the actual cutting force doesn't inherently obey our selected force model, we do require a model with corresponding coefficients for simulation purposes). In Fig. 5.1a, we conveniently assume that the tool vibration follows a sinusoidal profile in the feed direction while peripheral milling a square shape. The position of the tool in its periodic vibration cycle as it exits the down milling cut determines the actual location of the machined surface¹. In Fig. 5.1b, due to the selected tooth passing frequency, the surface is undercut, i.e., less material is removed than commanded. In this case, the tool vibration is away from the intended surface at each instant that a tooth is exiting the cut (only these cutter angles are shown and the lateral scale is greatly exaggerated). Figure 5.1c represents the overcut condition where more material is removed than commanded. Now the tool vibration is toward the intended surface when the tool is exiting the cut. Analogous representations could be provided for up milling, except we are interested in the tool location as it enters the cut.

The source of the surface location error behavior is the variation of the machine-spindle-holder-tool, and potentially, the workpiece-fixture FRF magnitude and phase with forcing frequency (e.g., as shown in Fig. 2.11). Due to the change in phase with tooth passing frequency (spindle speed), the time lag between the force and vibration varies. Therefore, the location of the cutter in its vibration cycle when leaving the surface depends on the selected spindle speed. The dependence of surface location error on the phase lag between the forcing function and displacement causes significant variation near the natural frequency (considering a single

¹This also explains why a vibrating tool can leave a smooth surface. Because the tool vibration is synchronous with rotation, the tool is in the same position each time it creates the new surface.

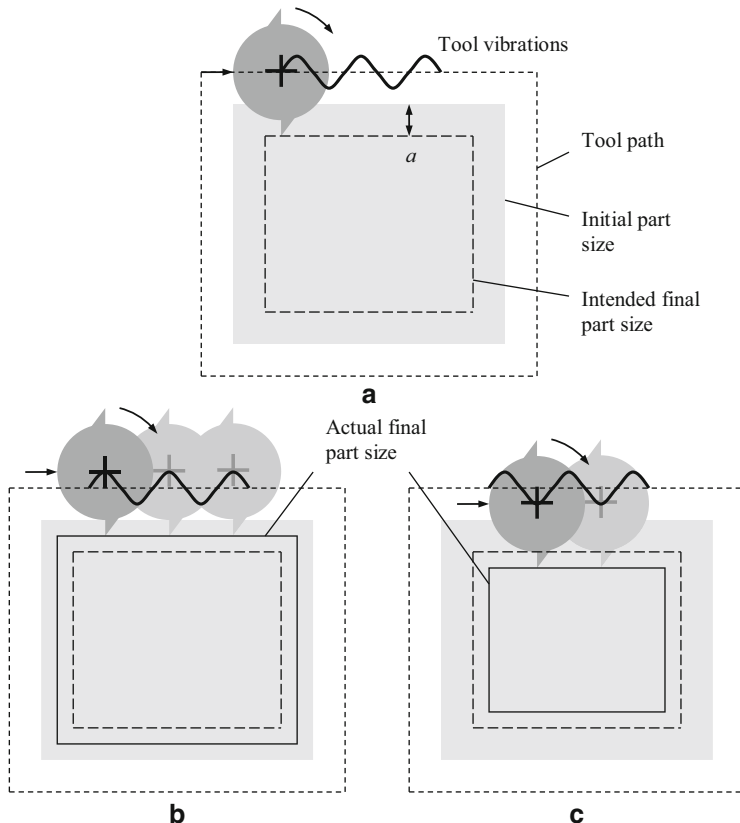


Fig. 5.1 Demonstration of surface location error. (a) Intended down milling cut geometry. (b) Undercut example. (c) Overcut example

degree of freedom system for simplicity) because for the lowly damped tool point FRFs typically observed in practice, the phase changes rapidly in this frequency range. To explore this behavior, we first describe a frequency domain solution for surface location error and then demonstrate the spindle speed dependence with numerical examples.



In a Nutshell

The concept of surface location error may be surprising to some readers.

In CNC programming packages, the tool is modeled as a cylinder (or perhaps a cylinder with a spherical end), the workpiece is modeled as a prismatic solid, and the workpiece is created by the relative motion of the cylinder with respect to the solid. However, the tool is not a cylinder. It is a collection of cutting edges that rotate together.

It is obvious to many that the tool and workpiece are not rigid. This is certainly one of the reasons for making a roughing pass followed by a finishing pass. This

intuition reveals the static surface location error. However, actual surface generation is more complicated than a static deflection. The variable cutting force, even in stable machining, causes the tool to vibrate. The surface location is controlled by the position of the tool in its cycle of vibration at the time that a tooth is in a position to generate the final surface. The tool may exhibit large vibrations yet still produce an accurately located surface. Under other conditions, these large vibrations may produce significant errors in the surface location.

By analogy, we might imagine that the vibrating tool is like a swing on a playground. The surface generation is like the moment of contact between the pusher and the swing. The pusher can stand far behind the swing and push as the swing reaches its peak displacement (poorly located surface) or the pusher may stand to the side and push the swing as it passes through its equilibrium position (perfectly located surface).

Of course, the cutting operation is more complicated. Naturally, the surface location error is spindle speed dependent. The spindle speed sets the frequency of the force exciting the vibration and, therefore, defines the resulting displacement according to the frequency response function. In addition, if the cutter teeth are helical, then different levels of the surface are generated at different instants in time. The surface location error along a line parallel to the tool's rotation axis, therefore, varies from the tip of the tool to the full axial depth of cut.

5.2 Frequency Domain Solution

In Chap. 4 we described the average tooth angle [16] and Fourier series [17] approaches to stability behavior prediction in milling. Both were frequency domain methods that relied on knowledge of the FRF and force model coefficients. To complement these analytical tools, we now describe a frequency domain solution to surface location error [18]. Together, these provide a comprehensive picture of the role of milling dynamics in process productivity.

In order to determine surface location error using a frequency domain (or steady-state) approach, we make two basic assertions. First, although vibrations of the cutter occur in both the x and y directions, the y direction vibrations dominate the final surface location for an x direction feed. Second, regeneration can be neglected in stable machining. Based on these assumptions, the concept is to:

1. Express the y direction cutting force in the frequency domain, $F_y(\omega)$, using a Fourier series.
2. Determine the frequency domain y displacement, $Y(\omega)$, by multiplying $F_y(\omega)$ by the machine-spindle-holder-tool direct FRF (measured or modeled at the tool point) in the y direction, $\frac{Y(\omega)}{F_y(\omega)}$.
3. Inverse Fourier transform this result and sample at the cut entry (up milling) or exit (down milling) to find the surface location error.

Note that, unlike time domain simulation, the tool point FRF can be used directly without the requirement for a modal fit in this approach.

5.2.1 Fourier Force Model

If we apply the cutting force model provided in Eq. 5.1, which relates the tangential, F_t , and normal, F_n , cutting force components to the axial depth of cut, b , and chip thickness, h , $F_y(\phi)$ can be expressed as shown in Eq. 5.2. In this equation, the summations account for all possible teeth within the cut, a circular tool path is assumed, f_t is the feed per tooth, and $g(\phi_i)$ is the switching function previously defined in Eq. 4.32. Also, the angle of each tooth, i (N_t total), at any instant in time is $\phi_i = \omega t + \frac{2\pi}{N_t}(i - 1)$ (rad), where ω is the spindle rotating frequency (in rad/s).

$$\begin{aligned} F_t(\phi) &= k_t b h(\phi) + k_{te} b \\ F_n(\phi) &= k_n b h(\phi) + k_{ne} b \end{aligned} \quad (5.1)$$

$$F_y(\phi) = -b \left[\begin{array}{l} \frac{-k_t f_t}{2} \sum_{i=1}^{N_t} g(\phi_i) (1 - \cos(2\phi_i)) + \frac{k_n f_t}{2} \sum_{i=1}^{N_t} g(\phi_i) \sin(2\phi_i) \\ -k_{te} \sum_{i=1}^{N_t} g(\phi_i) \sin(\phi_i) + k_{ne} \sum_{i=1}^{N_t} g(\phi_i) \cos(\phi_i) \end{array} \right]. \quad (5.2)$$

The equivalent Fourier series for the y direction cutting force can be written once the Fourier coefficients, a_n and b_n , are determined.

$$F_y(\phi) = \sum_{i=1}^{N_t} \left(a_0 + \sum_{n=1}^{\infty} (a_n \cos(n\phi_i) + b_n \sin(n\phi_i)) \right)$$

The a_0 term, for example, can be found using Eq. 5.3, where the integral for a full revolution of the selected tooth may be divided into three parts. The three subsequent integrals are delineated by ϕ_1 , which represents the cut entry angle in down milling or cut exit angle in up milling, and π rad, which defines the maximum angle that a tooth can be engaged in the cut (if ϕ is defined positive in a clockwise sense from the positive y axis). See Fig. 5.2. Considering a down milling cut, for example, only the middle of the three integrals in Eq. 5.3 is nonzero due to the switching function embedded in $F_y(\phi)$. Performing the relevant integration for down milling yields Eq. 5.4. For up milling, only the first integral in Eq. 5.3 is nonzero, and the integration limits become zero to ϕ_1 in Eq. 5.4.

$$a_0 = \frac{1}{2\pi} \int_0^{2\pi} F_y(\phi) d\phi = \frac{1}{2\pi} \left[\int_0^{\phi_1} F_y(\phi) d\phi + \int_{\phi_1}^{\pi} F_y(\phi) d\phi + \int_{\pi}^{2\pi} F_y(\phi) d\phi \right] \quad (5.3)$$

$$a_0 = -\frac{b N_t}{2\pi} \left[-\frac{k_t f_t \phi}{2} + \frac{k_t f_t}{4} \sin 2\phi - \frac{k_n f_t}{4} \cos 2\phi + k_{te} \cos \phi + k_{ne} \sin \phi \right]_{\phi_1}^{\pi} \quad (5.4)$$

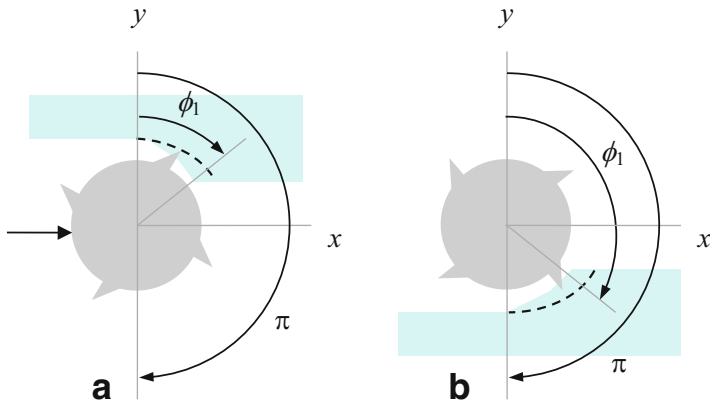


Fig. 5.2 Angles for Fourier series integrals. (a) Up milling. (b) Down milling

The a_n coefficients are computed using Eq. 5.5 and the b_n coefficients using Eq. 5.6. Again, the integrals can be partitioned using ϕ_1 and π as shown in Eq. 5.3. Closed-form equations for $n = 3, 4, 5, \dots$ coefficients are determined by observing the recursive patterns after integration. See Appendix.

$$a_n = \frac{1}{\pi} \int_0^{2\pi} F_y(\phi) \cos(n\phi) d\phi \quad (5.5)$$

$$b_n = \frac{1}{\pi} \int_0^{2\pi} F_y(\phi) \sin(n\phi) d\phi \quad (5.6)$$

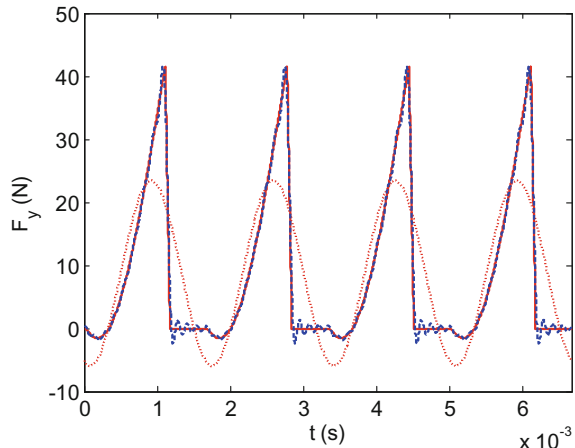
To accurately represent milling forces, however, it is also necessary to account for the influence of the teeth helix angle, γ . This can be accomplished by sectioning the tool into A axial slices. Each slice is assumed to have a zero helix angle, and the slices are rotated relative to one another by the angle $\chi = \frac{2db \tan(\gamma)}{d}$ (rad), where db is the slice height and d is the cutter diameter (see Fig. 4.55). The Fourier series is now written as:

$$F_y(\phi) = \sum_{j=1}^A \sum_{i=1}^{N_t} \left(a_0 + \sum_{n=1}^{\infty} (a_n \cos(n\phi_i) + b_n \sin(n\phi_i)) \right),$$

where $\phi_i = \omega t + \frac{2\pi}{N_t}(i-1) - \chi(j-1)$. Naturally, a larger number of slices improves the force fidelity.

Example 5.1 Fourier Series Force Dependence on Number of Coefficients As expected, the accuracy of the Fourier series force depends on the number, n , of coefficients included in the series. Figure 5.3 shows a comparison of the y direction

Fig. 5.3 Force reconstruction using time domain (solid line) and Fourier series (dotted line, $n = 5$; dashed line, $n = 50$). Additional coefficients increase the force fidelity



force determined by time domain simulation and its Fourier series for $n = 5$ and $n = 50$. The cutting conditions are up milling, 25% radial immersion, $N_t = 4$, $d = 19$ mm, $\gamma = 30$ deg, $b = 1$ mm, $f_t = 0.1$ mm/tooth, $k_t = 700$ N/mm², $k_n = 210$ N/mm², $k_{te} = k_{ne} = 0$ N/mm, and $\omega = 300\pi$ rad/s (i.e., the spindle speed, Ω , is 9000 rev/min, or rpm). Figure 5.3 was generated using the MATLAB® program p_5_1_1.m included with the textbook. The MATLAB® function eval, used to evaluate strings, was implemented to enable an arbitrary number of Fourier coefficients to be computed without requiring significant reprogramming.

5.2.2 Frequency Domain Surface Location Error

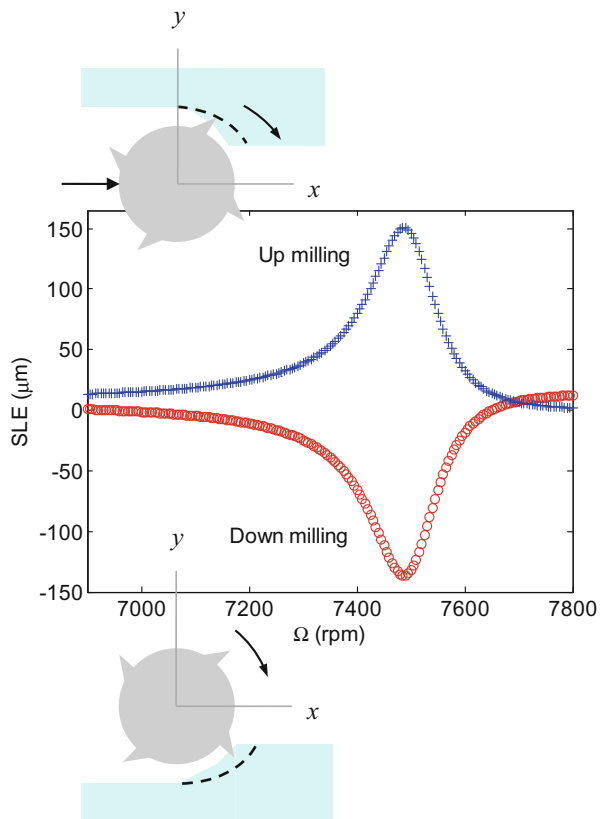
The four steps for frequency domain surface location error prediction, namely:

- Using a Fourier series to determine $F_y(t)$ and applying the discrete Fourier transform to obtain $F_y(\omega)$
- Calculating the frequency domain y displacement using $Y(\omega) = \frac{Y(\omega)}{F_y(\omega)} F_y(\omega)$, where $\frac{Y(\omega)}{F_y(\omega)}$ is the y direction machine-spindle-holder-tool direct FRF (at the tool point)
- Inverse Fourier transforming $Y(\omega)$ to obtain $y(t)$
- Sampling it at the cut entry (for up milling) or exit (for down milling)

are carried out in p_5_2_1.m. The function, p_5_2_2.m, called from within p_5_2_1.m, actually completes the individual surface location error computations.

Example 5.2 Frequency Domain Surface Location Error Calculations To compare the surface location error (SLE) in up and down milling, simulations were completed for the following conditions: 50% radial immersion (up and down milling) at spindle speeds from 6900 rpm to 7800 rpm, $N_t = 4$, $\gamma = 30$ deg, $d = 12.7$ mm diameter,

Fig. 5.4 Surface location error (SLE) for Example 5.2.
Both up and down milling lead to an overcut condition



$f_t = 0.1$ mm/tooth, $b = 1$ mm, $k_t = 700$ N/mm 2 , $k_n = 210$ N/mm 2 , $k_{tc} = k_{ne} = 0$ N/mm, symmetric structural dynamics with a stiffness of 1×10^7 N/m, 1% damping (i.e., a damping ratio, ζ , of 0.01), and 500 Hz natural frequency. The results are displayed in Fig. 5.4, where 50 terms were used in the Fourier series force model. It is seen that the surface location error yields an overcut surface in both instances. For up milling, the positive SLE means that the cutter is radially deeper into the cut than commanded when creating the final surface. Similarly, for down milling, the negative SLE indicates that the cutter is farther into the cut than desired.

Because the frequency domain surface location error simulation neglects regeneration, stable conditions are predicted in all instances (i.e., only forced vibrations are considered). Therefore, these calculations must be accompanied by the appropriate stability lobe diagram to select stable machining parameters. The Fourier series approach stability lobe diagram corresponding to the selected up milling scenario is provided in Fig. 5.5. The stability lobe diagram for 50% radial immersion down milling is nearly identical and is not shown. The test range for the surface location error simulations is indicated by the solid line. It is verified that the selected cutting conditions for Fig. 5.4 are in the stable zone. Figure 5.5 was generated using the MATLAB® program p_5_2_3.m.

Fig. 5.5 Stability lobe diagram for Example 5.2 (50% radial immersion up milling). Two test ranges are also identified: (solid line) 6900 rpm to 7800 rpm at 1 mm axial depth and (dotted line rectangle) 6900 rpm to 7700 rpm with axial depths from 0.5 mm to 5 mm

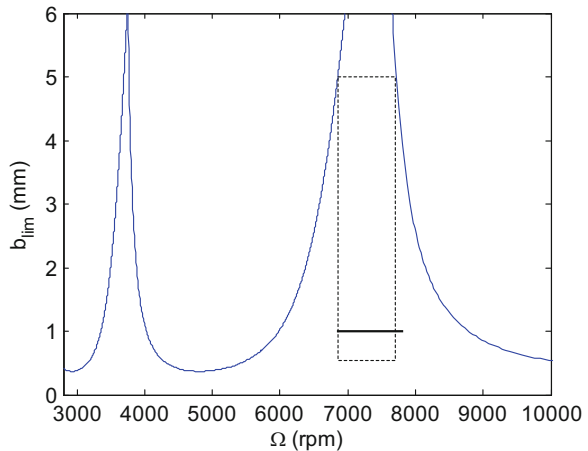
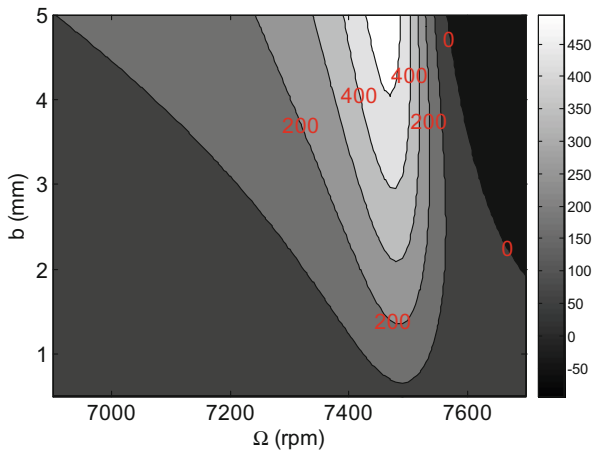


Fig. 5.6 Surface location error contours for rectangular stable zone identified in Fig. 5.5. High sensitivity of the error to spindle speed is observed near 7500 rpm, the traditional best speed for increased chatter-free axial depth of cut

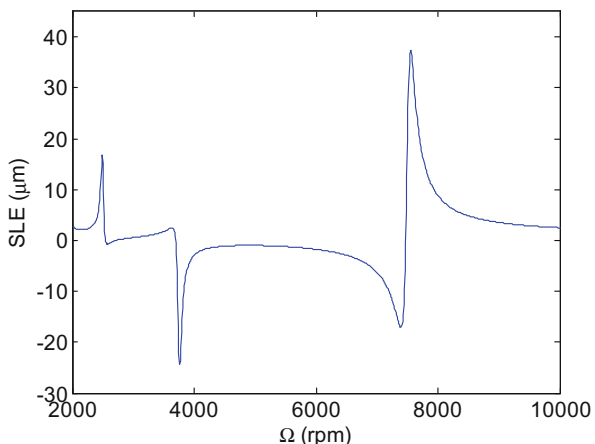


To compare surface location error trends over a broader range, calculations were completed using the same system under 50% radial immersion up milling for spindle speeds from 6900 rpm to 7700 rpm and axial depths from 0.5 mm to 5 mm. See the dotted rectangle in Fig. 5.5. The surface location error contours (lines of constant error) are provided in Fig. 5.6, where 50 terms were again used for the Fourier series force. An interesting aspect of this figure is the high sensitivity of surface location error to spindle speeds near 7500 rpm. Using Eq. 4.29, we see that the best speeds for increasing axial depth of cut without chatter are:

$$\Omega_{\text{best}} = \frac{f_n \cdot 60}{(N+1) \cdot N_t} = \frac{500 \cdot 60}{(N+1) \cdot 4} = \frac{7500}{(N+1)}.$$

For the rightmost ($N = 0$) lobe highlighted by the rectangular simulation range in Fig. 5.5, the best speed is therefore in the high slope surface location error range. This high slope indicates that small errors in our knowledge of the system dynamics

Fig. 5.7 Variation in surface location error from 2000 rpm to 10,000 rpm for the system described in Example 5.2. The up milling radial immersion is 25% and the axial depth is 0.75 mm. The behavior is periodic with error sensitivity near the best speeds identified in Eq. 4.29



or spindle speed could lead to significant changes in the predicted error and affect our ability to compensate by tool path adjustments, for example. We also see that the error tends to increase with axial depth. This result is expected given that the force magnitude and, consequently, the vibration level scales with axial depth. While these results do not preclude the use of the best speed equation to select a preferred spindle speed, it does demonstrate that combining consideration of surface location error with stability may lead to a slightly different spindle speed choice to balance the two requirements. This is explored further at the end of this section. Figure 5.6 was generated using the MATLAB® program p_5_2_4.m.

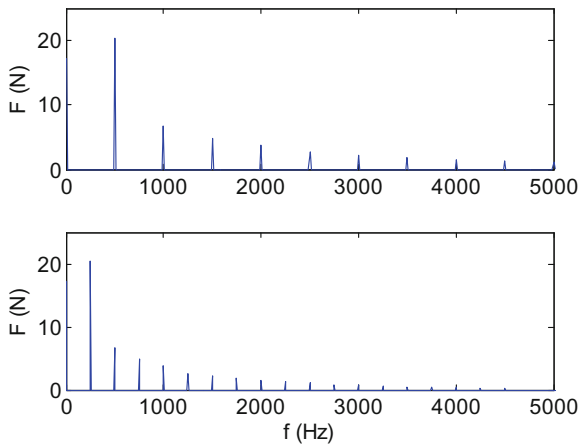
A natural question to ask is if this same variation in surface location error also occurs in higher N value stability lobes. To answer this question, let's complete simulations for the spindle speed range from 2000 rpm to 10,000 rpm. This span encompasses the first three best speeds ($N = 0, 1$, and 2) at $\{7500, 3750$, and $2500\}$ rpm. Using a 25% radial immersion to raise the critical stability limit (the depth at which the cut is stable for all spindle speeds) and enable an axial depth of 0.75 mm, but maintaining consistency in all other conditions with respect to Fig. 5.6, produces the error variation displayed in Fig. 5.7 (p_5_2_5.m). We see that the surface location error shows sensitivity to spindle speed at each of the best speeds.



In a Nutshell

It can be seen that over broad segments of the spindle speed range, the surface location error is quite small. However, there are also narrow bands in which the surface location error is large or changes rapidly from large negative to large positive values, for example. Unfortunately, these sections of extreme speed sensitivity are located within the stable zones of the stability lobe diagram. It is for this reason that the combined ability to choose stable cutting parameters as well as predict the surface location error is so important.

Fig. 5.8 Force spectrum for 7500 rpm (top) and 3750 rpm (bottom)



As noted in Sect. 5.1, it is the change in phase with frequency that varies the time lag between the force and vibration and causes the surface location error dependence on spindle speed. Further, the variation in phase with tooth passing frequency (0 to -180 deg for a single degree of freedom system) is strongest near the natural frequency. The repetitive behavior observed in Fig. 5.7 occurs as increasing harmonics of the fundamental tooth passing frequency excite the system resonance. Figure 5.8 shows the spectra of the y direction cutting force for 7500 rpm and 3750 rpm (p_5_2_6.m). At 7500 rpm (top), the first harmonic, or fundamental peak, is coincident with the 500 Hz natural frequency. At 3750 rpm, (bottom) the first harmonic occurs at 250 Hz, but the second harmonic now matches the natural frequency. Similarly, the third harmonic excites resonance at 2500 rpm (not shown). The surface location error magnitude decreases with each increasing N value because the energy in the subsequent harmonics reduces. Figure 5.9 is included to demonstrate this phenomenon pictorially.

As a final activity before considering the effect of the helix angle on surface location error, let's investigate the influence of radial depth of cut. We'll use the same dynamic system with a spindle speed range of 6900 rpm to 7800 rpm and vary the radial engagement for down milling from 50% to 20% in decrements of 10%. The corresponding starting angles are $\{90, 101.5, 113.6, \text{ and } 126.9\}$ deg, respectively, as calculated using Eq. 4.5, and the exit angle is always 180 deg for down milling based on the circular tool path approximation. Let's select an axial depth below the 50% radial immersion critical stability limit. We can see from Fig. 5.5 that $b = 0.35$ mm ensures stable conditions for any spindle speed, so we'll apply that value (although Fig. 5.5 is for up milling, the stability limit is similar for down milling at the same radial immersion in this case). The results, which were obtained using p_5_2_7.m, are provided in Fig. 5.10. We see that the transition from overcutting (negative error for down milling) to undercutting (positive error for down milling) near the $N = 0$ best spindle speed shifts to the left as the radial immersion is reduced. Also, the shape of the error profile changes, and the peak-to-peak magnitude decreases. The latter occurs because the force level reduces with smaller radial depth of cut.

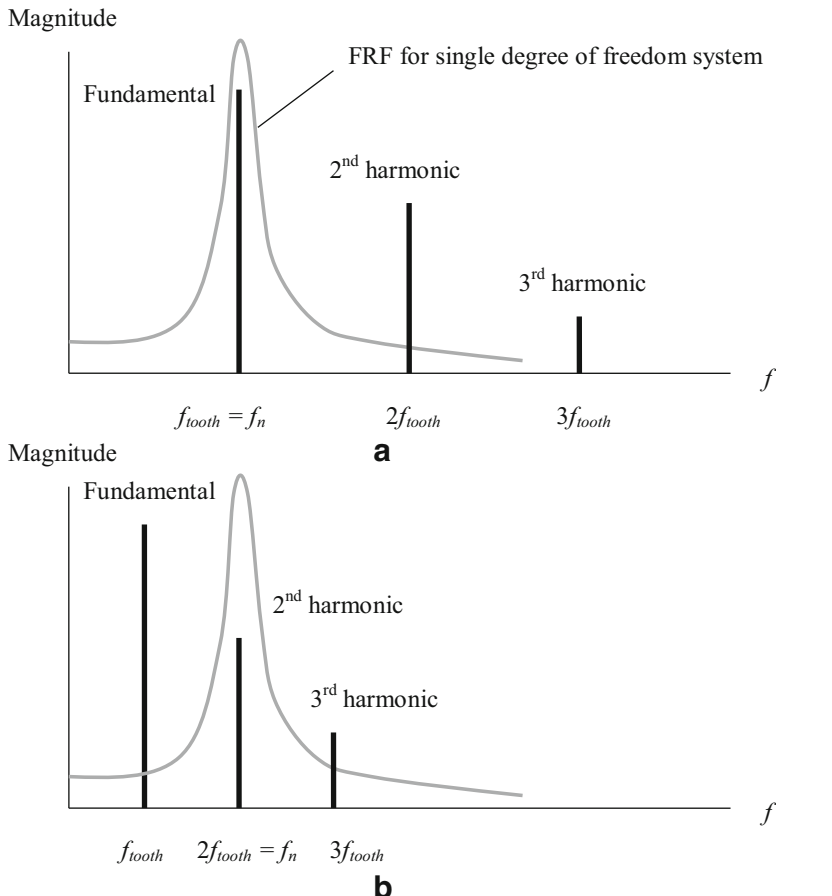
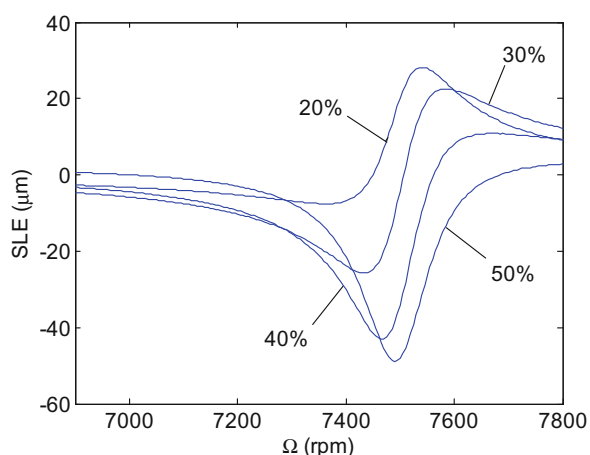


Fig. 5.9 Description of periodic surface location error variation. (a) The tooth passing frequency is coincident with the natural frequency (resonant forced vibrations) for the $N = 0$ best spindle speed. (b) The second harmonic is located at resonance for the $N = 1$ best spindle speed

Fig. 5.10 Variation in surface location error with radial depth of cut. The four curves represent percent radial immersion cases of 50% to 20% down milling with a constant axial depth of 0.35 mm. The system dynamics are the same as were defined in Example 5.2



5.2.3 Variation in Surface Location Error with Axial Location

As discussed in Sect. 4.5, the effect of the helical cutting edge geometry is that the full length of the cutting edge does not enter (or exit) the cut at the same instant. The edge nearest the free end of the tool enters first, and there is an increasing delay of the cut entry (and exit) for points on the edge that are farther from the free end (toward the spindle). The helical square endmill geometry considered here is shown in Fig. 5.11.

Due to the entry delay for up milling and exit delay for down milling, the surface location error varies with axial location (z direction) along the helical cutting edge length. Effectively, this occurs because the surface location is determined by the time dependent y vibration, but all points along the surface (in the z direction) are not generated simultaneously. Relative to the free end of the cutter, the angular delay along the tool axis is $\chi = \frac{2|z|\tan(\gamma)}{d}$ (rad), where $|z|$ is the absolute value of the distance from the end. The corresponding time delay is $\frac{\chi}{\Omega/2\pi}$ (s), where Ω is the spindle speed in rpm. The surface along the cutter axis (from the free end toward the spindle) is therefore produced at progressively later points in time, while the cutter vibration state varies continuously. This leads to a periodic variation in the surface location error with the z value, as shown in [14].

We can use the MATLAB® program p_5_2_8.m to investigate this behavior. Similar to the time domain simulations in Sects. 4.5 and 4.6, the tool is discretized into axial slices. The angular delay with z location is handled by changing the times at which the $y(t)$ vector is sampled to determine surface location error. For axial slices not at the tool point, the time vector is sampled later than the cut entry (up milling) or exit (down milling) by $dX * (cnt-1) / (\Omega/60*2*pi)$, where $cnt = 1, 2, 3\dots$ is the index of the current axial slice (equal to 1 at the tool point), the delay angle per slice is $dX = 2*db*\tan(\gamma/\pi/180)/d$

Fig. 5.11 The helical endmill geometry causes the cutting edge to enter and exit the cut at later instants in time when moving from its free end toward the spindle (the feed direction is to the left for this figure)

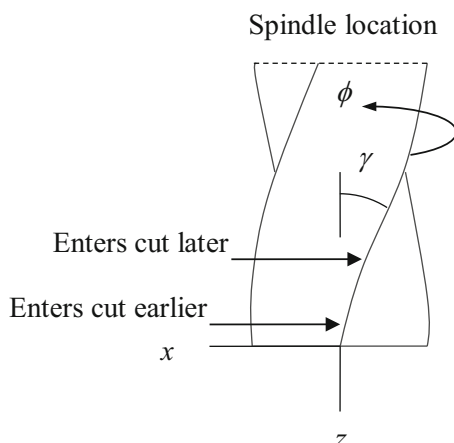


Fig. 5.12 Surface location error variation with axial location for $b = 12$ mm, $\Omega = 7500$ rpm, and $\gamma = 30$ deg (helix angle). The $|z| = 0$ position corresponds to the tool's free end (see Fig. 5.11)

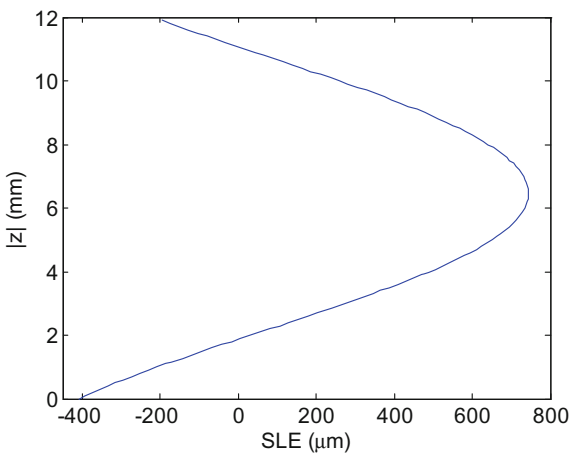
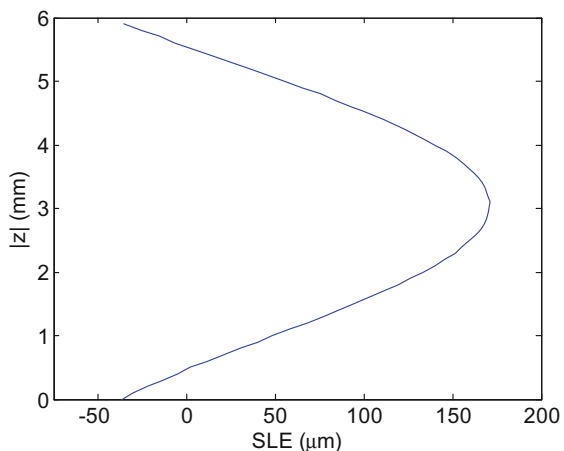
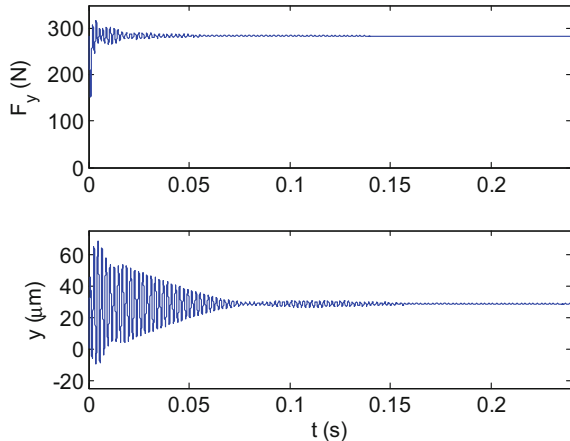


Fig. 5.13 Surface location error variation with axial location for $b = 6$ mm, $\Omega = 3750$ rpm, and $\gamma = 30$ deg



(rad), db is the slice width in the z direction, gamma is the helix angle (deg), and d is the tool diameter. Figure 5.12 shows the results for 50% radial immersion up milling with the same specifications provided previously. The spindle speed is 7500 rpm, and the axial depth of cut is 12 mm; the stability of this cut was verified using p_5_2_3.m. Clearly, the surface location error is strongly dependent on the axial location for this example, where the $|z| = 0$ location corresponds to the tool's free end and the orientation is the same as shown in Fig. 5.11. We should state explicitly here that all previous figures reported results for the error only at the free end of the cutting tool. For comparison purposes, p_5_2_8.m was used to calculate the surface location error for $b = 6$ mm at 3750 rpm, the $N = 1$ best speed from Fig. 5.5. This result is provided in Fig. 5.13. We see that the general profile is maintained relative to Fig. 5.12, although the error magnitude is decreased (the smaller axial depth gives smaller force and deflection) and the spatial period (in z) is reduced.

Fig. 5.14 Constant y direction cutting force and displacement when $b = 10.0$ mm for a helix angle of 45 deg on the four-tooth, 12.7 mm diameter endmill



Let's explore what happens to surface location error and its axial variation if we select the axial depth for constant cutting force, as described in Sect. 4.5. For the selected tool, the constant cutting force axial depth is:

$$b = \frac{d(\phi_p)}{2 \tan(\gamma)} = \frac{12.7(90)\frac{\pi}{180}}{2 \tan(30)} = 17.3 \text{ mm.}$$

Unfortunately, this axial depth is unstable for the given FRF and force model, even at the $N = 0$ best speed of 7500 rpm. If the helix angle is increased to 45 deg, however, the constant force depth becomes 10.0 mm, which is stable at 7500 rpm. In this case, the constant force eliminates the surface location error variation with axial depth due to the time invariance of the vibration, i.e., constant force yields constant deflection (after the initial transients have decayed), so the time at which the cutter enters or exits the cut does not change the error. We must realize that the resulting surface location error still is not zero, even for the constant force condition. The error is simply determined from the ratio of the force to the stiffness, where $k = 1 \times 10^7$ N/m for this example. The MATLAB® program p_5_2_9.m was used to generate Fig. 5.14, which displays the y direction force, $F_y = 284$ N at steady state, and corresponding deflection, $y = \frac{284}{1 \times 10^7} = 2.8 \times 10^{-5}$ m = 28 μm . For the selected up milling 50% radial immersion cut, this gives an overcut surface. However, the error is small relative to the 12 mm axial depth, nonconstant force results shown in Fig. 5.12.



In a Nutshell

The helix of the tool allows the surface location error to vary along the axis of an endmill because the surface of interest is generated at different points in the rotation, which means different moments in time, which means different points in the vibration cycle. For this reason, a perfectly ground, exactly centered, and correctly balanced endmill that is rotating in a spindle with no error motions may still produce a non-straight sidewall during peripheral milling. The error along the wall that is parallel to the axis of the tool is a record of the tool's

dynamic displacement as it rotates because different levels of the wall (bottom to top) are created at successive instants in time during the tool's rotation. It seems strange to many users, as the error can appear as a line in the direction of tool motion. Sometimes users even suspect that this line is caused by a damaged tool.

5.2.4 Combining Stability and Surface Location Error in a Single Diagram

As a final activity in this section, let's combine the stability and surface location error data in a single diagram. We'll consider the following conditions: 50% radial immersion up milling at spindle speeds from 2800 rpm to 10,000 rpm, $N_t = 4$, $\gamma = 30$ deg, $d = 12.7$ mm diameter, $f_t = 0.1$ mm/tooth, b = 0.4 to 5 mm (for the surface location error calculations), $k_t = 700$ N/mm², $k_n = 210$ N/mm², $k_{te} = k_{ne} = 0$ N/mm, and symmetric structural dynamics with a stiffness of 1×10^7 N/m, 1% damping, and 500 Hz natural frequency. The results are displayed in Fig. 5.15, where 15 terms were used in the Fourier series force model.² The MATLAB® program p_5_2_10.m

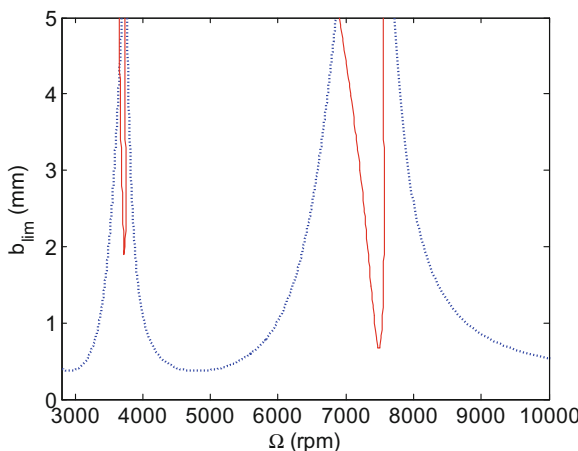


Fig. 5.15 Stability (dotted line) and surface location error (solid line) information combined in a single diagram. The solid contour lines identify the (spindle speed, axial depth) combinations where the error level is 100 μm . The simulation parameters are 50% radial immersion up milling, $N_t = 4$, $\gamma = 30$ deg, $d = 12.7$ mm diameter, $f_t = 0.1$ mm/tooth, $k_t = 700$ N/mm², $k_n = 210$ N/mm², $k_{te} = k_{ne} = 0$ N/mm, and symmetric structural dynamics with a stiffness of 1×10^7 N/m, 1% damping, and 500 Hz natural frequency

²In general, it is not necessary to use a large number of terms to represent the force. It is usually only necessary that the first few harmonics be characterized since higher-order harmonics often have little impact on the system behavior.

was executed to generate the figure, which displays the stability boundary (dotted line) in addition to surface location error contours (solid lines) at a constant error level of 100 µm; note that the surface location error was calculated at the free end of the tool for this example. The error level is larger within the contours similar to Fig. 5.6. This “super” diagram shows that a portion of the stable zone (inside the error contours) is inaccessible if the user desires the surface location error to be less than 100 µm. The information provided in Fig. 5.15 could be used at the process planning stage, for example, to select machining conditions that satisfy both stability and accuracy requirements.

5.3 Cycloidal Tool Path Time Domain Simulation

Similar to Sects. 4.4 and 4.5, we now detail a time domain milling simulation based on the “regenerative force, dynamic deflection model” described by Smith and Tlusty [6]. The simulation includes the contribution of the tool vibrations to the instantaneous chip thickness and provides predictions for both force and deflection in the x (feed) and y directions. Vibrations along the tool axis, or z direction, are not considered. We also model the cycloidal motion of the cutter teeth, rather than assuming a circular tool path. Other instances of cycloidal tool path simulations from the literature are provided in [19–21], for example. Our approach [12] is similar in nature to that described in [21].

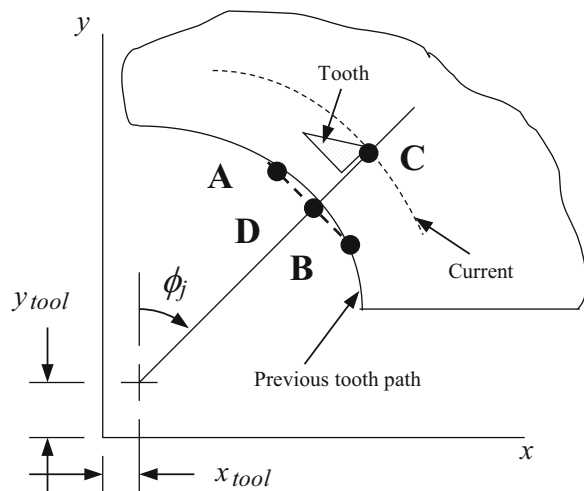
We begin the milling simulation by first defining the cutting parameters, including spindle speed, Ω , feed per tooth, f_t , radial and axial depths of cut, a and b , respectively, and the number of teeth, N_t . We then describe the system dynamics using the modal mass, m , damping, c , and stiffness, k , values for any number of modes in the x (feed) and y directions. As detailed in Sect. 2.5, these values are typically obtained from impact tests followed by a modal fitting procedure, such as the peak-picking method.

We determine the forces and deflections by numerical integration over small steps in time, $dt = \frac{60}{SR(\Omega)}$ (s), where SR is the number of steps per cutter revolution and Ω is expressed in rpm. In each time step, we rotate the cutter by an angle, $d\phi = \frac{360}{SR}$ (deg). We then calculate the current nominal coordinates of each tooth on the cutter (Cx_j , Cy_j) according to Eq. 5.7, where r is the cutter radius, ϕ_j is the tooth angle, j is the tooth number which varies from 1 to N_t , $df = \frac{N_t f_t}{SR}$ is the incremental feed during the time step dt , and x_{tool} and y_{tool} are the tool center coordinates determined in the previous time step (set equal to zero initially).

$$\begin{aligned} Cx_j &= r \sin \phi_j + df + x_{\text{tool}} \\ Cy_j &= r \cos \phi_j + y_{\text{tool}} \end{aligned} \quad (5.7)$$

In order to calculate the instantaneous chip thickness at each time step, we compare the (Cx_j , Cy_j) coordinates of the current tooth (i.e., point C in Fig. 5.16)

Fig. 5.16 Determination of instantaneous chip thickness by linear interpolation for cycloidal tool path



to the surface coordinates recorded during the prior tooth passage at the same angular orientation. However, because we are not applying the circular tool path assumption, it is not required that a data point exist at this angle from the prior pass. Therefore, we must complete a search to determine the two points from the previous tooth passage which bound this angle; we refer to these points as **A** and **B** in Fig. 5.16. We then carry out linear interpolation between points **A** and **B** to determine point **D**, which lies on the line between point **C** and the cutter origin [22]. The coordinates of point **D** (Dx_j, Dy_j) are given in Eq. 5.8:

$$Dx_j = \frac{\tan(\phi_j)Ax_jC^* - \tan(\phi_j)Ay_j + \tan(\phi_j)Cy_j - Cx_j}{\tan(\phi_j)C^* - 1}, \quad (5.8)$$

$$Dy_j = Ay_j - Ax_jC^* + Dx_jC^*,$$

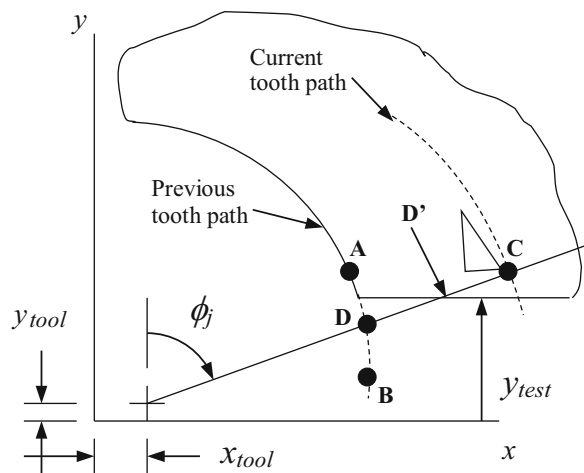
where $C^* = \frac{Ay_j - By_j}{Ax_j - Bx_j}$. We include the nonlinearity that is exhibited when the vibration amplitude is large enough that a tooth leaves the cut by setting the chip thickness, h_j , equal to zero if:

$$\sqrt{(Cx_j - x_{\text{tool}})^2 + (Cy_j - y_{\text{tool}})^2} < \sqrt{(Dx_j - x_{\text{tool}})^2 + (Dy_j - y_{\text{tool}})^2}. \quad (5.9)$$

We must also query two other conditions for the chip thickness calculation. First, we must determine if the current tooth is bounded by the specified radial immersion. Second, we must verify that the chip thickness has not been reduced during cut entry for down milling or cut exit for up milling. The chip thickness reduction that occurs at the cut exit for up milling, for example, is exhibited in Fig. 5.17.

To determine if the current tooth is bounded by the selected radial depth of cut (i.e., engaged in the cut), we use the value y_{test} , which gives the y direction

Fig. 5.17 Reduced instantaneous chip thickness at cut exit in up milling



coordinate of the desired surface as shown in Fig. 5.17. For up milling with less than or equal to 50% radial immersion, cutting occurs if Cy_j is greater than y_{test} . This situation is depicted in Fig. 5.17. If the up milling radial immersion is greater than 50%, then Dy_j must be greater than y_{test} if cutting is to occur (note that y_{test} is negative in this case). For down milling, Cy_j must be less than y_{test} if the radial immersion is less than or equal to 50% and cutting is to take place (y_{test} is again negative). If the radial immersion is greater than 50%, it is required that Dy_j be less than y_{test} if cutting is to occur. In each case, provided the chip thickness is not reduced at the cut exit (up milling) or entry (down milling), as shown in Fig. 5.17, and the tooth has not vibrated out of the cut (Eq. 5.9), then h_j is calculated according to Eq. 5.10:

$$h_j = \sqrt{(Cx_j - Dx_j)^2 + (Cy_j - Dy_j)^2}. \quad (5.10)$$

To check if the chip thickness reduction condition is met, we again compare the tooth coordinates to y_{test} . The thickness reduction occurs if the following circumstances are satisfied:

1. Up milling, less than or equal to 50% radial immersion: Dy_j is less than y_{test} .
2. Up milling, greater than 50% radial immersion: Cy_j is less than y_{test} .
3. Down milling, less than or equal to 50% radial immersion: Dy_j is greater than y_{test} .
4. Down milling, greater than 50% radial immersion: Cy_j is greater than y_{test} .

In these cases, we can no longer use Eq. 5.10 to compute the instantaneous chip thickness. Rather, we must consider point \mathbf{D}' identified in Fig. 5.17. The coordinates of this point (Dx'_j , Dy'_j) are provided in Eq. 5.11.

$$\begin{aligned} Dx'_j &= (y_{test} - y_{tool}) \tan \phi_j + x_{test} \\ Dy'_j &= y_{test} \end{aligned} \quad (5.11)$$

Under these conditions, we calculate the chip thickness using Eq. 5.12 for up or down milling with less than or equal to 50% radial immersion or Eq. 5.13 for greater than 50% radial immersion.

$$h_j = \sqrt{\left(Cx_j - Dx'_j\right)^2 + \left(Cy_j - Dy'_j\right)^2} \quad (5.12)$$

$$h_j = \sqrt{\left(Dx'_j - Dx_j\right)^2 + \left(Dy'_j - Dy_j\right)^2} \quad (5.13)$$

In any case that the computed chip thickness is greater than zero, we calculate the tangential and normal force components, $F_{t,j}$ and $F_{n,j}$, respectively, for tooth j according to Eq. 5.14, where we have included the edge effects described in Sect. 4.7:

$$\begin{aligned} F_{t,j} &= k_t b h_j + k_{te}, \\ F_{n,j} &= k_n b h_j + k_{ne}, \end{aligned} \quad (5.14)$$

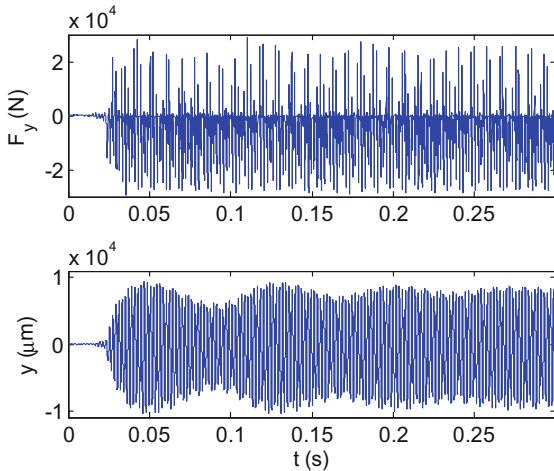
where k_t and k_n are the force model cutting (shearing) coefficients and k_{te} and k_{ne} are the edge (rubbing/plowing) coefficients. Next, we project the forces $F_{t,j}$ and $F_{n,j}$ onto the x and y directions using Eq. 5.15. We then sum the x and y direction forces over all teeth engaged in the cut at the given instant in time, $F_x = \sum_{j=1}^{N_t} F_{x,j}$ and $F_y = \sum_{j=1}^{N_t} F_{y,j}$.

We use these force values to determine the instantaneous displacements x_{tool} and y_{tool} for the next time step by numerical integration of the modal equations of motion with the appropriate modal parameters. If multiple vibration modes are included, we sum the displacement contributions from each mode to determine the total displacement. Provided the modal parameters were determined from a direct FRF measurement (or model), we use the same forces for each vibration mode as shown in Sect. 3.5.

$$\begin{aligned} F_{x,j} &= -F_{t,j} \cos(\phi_j) - F_{n,j} \sin(\phi_j) \\ F_{y,j} &= F_{t,j} \sin(\phi_j) - F_{n,j} \cos(\phi_j) \end{aligned} \quad (5.15)$$

In the case of a helical cutting edge, we segment the tool into multiple slices along its axis, each of which is treated as having a zero helix angle. We sum the forces for all slices to determine the total normal and tangential cutting force components for that particular simulation time step (and cutter angular orientation). We then apply Eq. 5.15 to project the forces onto the x and y directions, sum the forces over all the teeth engaged in the cut, and complete the numerical integration. The difference, $\Delta\phi$ (deg), between the tooth angle, ϕ_j , for tooth j on slice k and the angle for the same tooth j on slice $k + 1$ (located farther away from the tool tip by a distance b/SA) is provided in Eq. 5.16, where γ is the helix angle, SA is the number of axial slices, and d is the cutter diameter.

Fig. 5.18 Example 5.3
 y direction force (top) and
displacement (bottom)
versus time results. Unstable
behavior for $\Omega = 6000$ rpm
and $b = 4$ mm is observed



$$\Delta\phi = \frac{2b \tan(\gamma)}{\text{SA}(d)} \frac{180}{\pi} \quad (5.16)$$

Example 5.3 Comparison of Time Domain Simulation Results to Example 5.2 In order to demonstrate the capabilities of the cycloidal tool path time domain simulation (p_5_3_1.m) described in the previous paragraphs, let's compare results with those obtained from the frequency domain analysis in Example 5.2. We'll use the same specifications: 50% radial immersion up milling, $N_t = 4$, $\gamma = 30$ deg, $d = 12.7$ mm diameter, $f_t = 0.1$ mm/tooth, $k_t = 700$ N/mm 2 , $k_n = 210$ N/mm 2 , $k_{te} = k_{ne} = 0$ N/mm, and symmetric structural dynamics with a stiffness of 1×10^7 N/m, 1% damping, and 500 Hz natural frequency. The stability lobe diagram for this situation is provided in Fig. 5.5. As a first step, we will verify the stability behavior at $\Omega = 6000$ rpm and 7500 rpm for an axial depth of 4 mm. Figure 5.18 displays the y direction force and displacement for 6000 rpm. As expected, the cut is strongly unstable. Figure 5.19 shows the stable result for 7500 rpm.

In addition to the time plots, we can also use the simulation to display the x versus y tool path. Figure 5.20 presents the results for the $\Omega = 7500$ rpm 50% radial immersion up milling cut with $b = 4$ mm at the tool point, i.e., the axial slice nearest the free end of the tool. Only the portion of the tool path where the teeth enter the material (i.e., the “top” of the tool for the up milling case) is included. The tool center is nominally located at $y = 0$, while the x position varies with the time dependent feed. We can see that the top of the path is initially at the tool radius of 6.35 mm (near $x = 0$). After the entry transients, the y displacement approaches 6.77 mm at the path apex where the machined surface is located. This indicates an overcut condition because more material is removed than commanded for the up milling cut. Note that the material to be cut away is located above the tool in Fig. 5.20. Other axial slices can also be selected using the `plot_depth` variable in p_5_3_1.m, where a value of one designates the slice at the tool point and larger integer values (up to `steps_axial`) specify slices nearer the spindle face.

Fig. 5.19 Example 5.3
 y direction force (top) and
displacement (bottom)
versus time results. Stable
behavior for $\Omega = 7500$ rpm
and $b = 4$ mm is seen

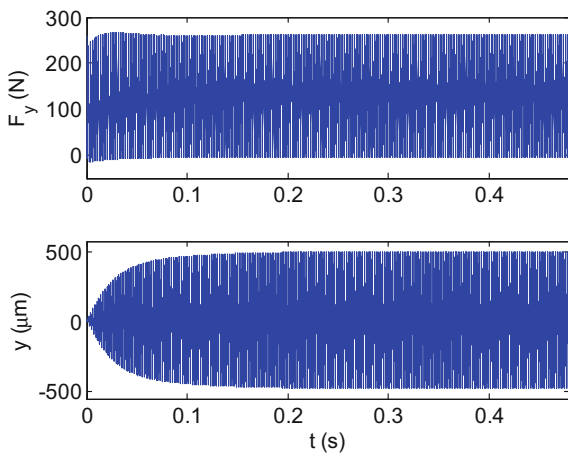
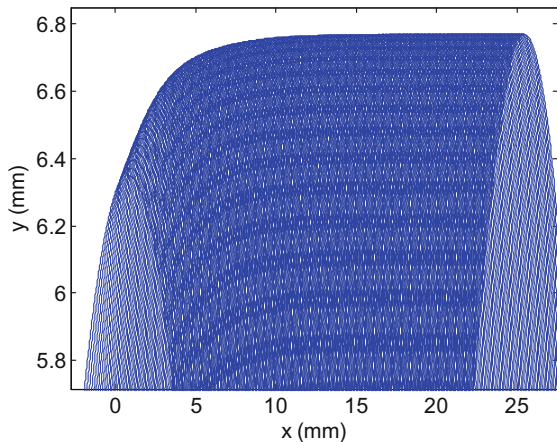
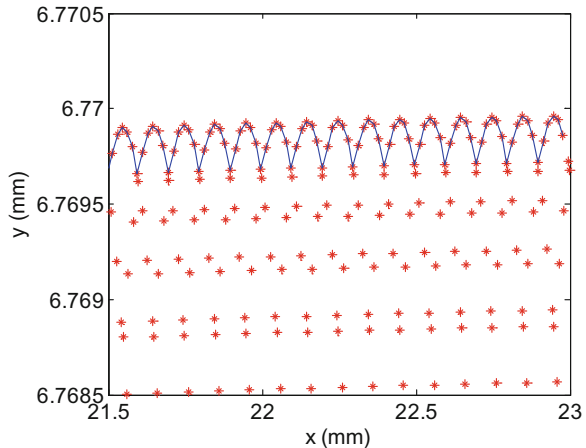


Fig. 5.20 Tool path for
 $\Omega = 7500$ rpm 50% radial
immersion up milling cut
with $b = 4$ mm. The x versus
 y teeth coordinates are
shown for the axial slice
nearest the free end of the
cutter



The benefit of this figure is that it can be used to isolate the machined surface. Using a trimming algorithm to identify only the extreme points on the tool path, which define the machined surface geometry, the surface location error and roughness average, R_a [23], are determined to be 420 and 0.2 μm , respectively, from Fig. 5.20. The discrete roughness average equation is provided in Eq. 5.17, where n is the number of points that define the machined surface. Figure 5.21 displays the individual points and surface (solid line that connects the points) for the selected axial slice (`plot_depth = 1`). The small slope in the line indicates that steady state has not quite been reached. However, the (overcut) surface location error value of 420 μm agrees with the tool point frequency domain solution results previously reported in Fig. 5.6 (read the contour value at the coordinates $\Omega = 7500$ rpm and $b = 4$ mm to verify this statement). The surface location error is determined by comparing the y coordinate of the mean of this line to the tool radius (the commanded surface location). For the up milling case shown, if the line is positioned

Fig. 5.21 The machined surface geometry is defined by isolating the extreme points from the tool path. The surface location error is determined by comparing the mean of this line to the tool radius (the commanded surface location). For the up milling case shown, if the line is positioned above the tool radius, more material is removed than commanded, and an overcut surface is obtained



above the tool radius, more material is removed than commanded, and an overcut surface is obtained. The trimming algorithm used to identify the machined surface at the selected axial slice proceeds by:

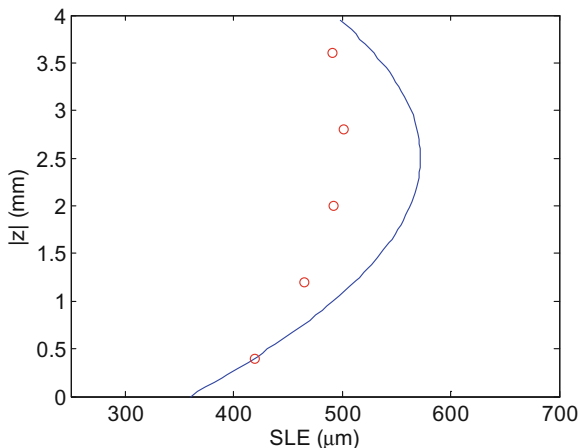
- Arranging all points on the tool path in ascending x (feed direction) values
- Selecting a point and comparing its y value to the y values of the next two points
- Keeping the higher point from the next two points for up milling and lower point for down milling
- Incrementing to the next point and repeating the comparison process
- Repeating the entire exercise multiple times to “bubble up” (up milling) or “trickle down” (down milling) to the final surface.

Although this is not a particularly elegant solution, it is effective. We do not have a defined stopping condition for the procedure, but experience has shown that 50 to 100 iterations are generally adequate.

$$Ra = \frac{\sum_{i=1}^n |y_i - \bar{y}|}{n} \quad (5.17)$$

Once the surface location error has been determined for all axial slices, the change in error with axial depth can be interrogated as shown in Sect. 5.2; see Figs. 5.12 and 5.13. The time domain simulation results (circles) are superimposed on the frequency domain solution (line) in Fig. 5.22 for the conditions described in Example 5.3. For the time domain solution, five axial slices were used so that $db = 4/5 = 0.8$ mm. The points are placed at the midpoint of each slice in the figure, i.e., $\{0.4, 1.2, 2, 2.8, \text{ and } 3.6\}$ mm. The MATLAB® program p_5_3_2.m was used to generate the frequency domain results in Fig. 5.22. The time domain results were obtained from p_5_3_1.m by sequentially plotting and trimming the tool path for $\text{plot_depth} = 1, 2, \dots, 5$.

Fig. 5.22 Variation in surface location error with axial location. The circles represent the time domain result for each axial slice; they are located at the midpoint of each of the five slices. The line displays the frequency domain solution



In a Nutshell

As with stability, the use of time domain simulation to predict surface location error eliminates many of the simplifying assumptions. The tool path may be modeled as a cycloid instead of a circle. Unequal teeth spacing may be applied (see Sect. 6.3). The surface produced by an unstable cut may be predicted. For the analytical solution, these features are difficult to incorporate. For time domain simulation, on the other hand, they are relatively easy to include.

Exercises

- Determine the value of the mean y direction cutting force for the following cuts using Eq. 5.3. The aluminum alloy-four tooth cutter combination gives: $k_t = 790 \text{ N/mm}^2$ and $k_n = 190 \text{ N/mm}^2$, $k_{te} = 8 \text{ N/mm}$, and $k_{ne} = 4 \text{ N/mm}$. Also, $b = 5 \text{ mm}$ and $f_t = 0.15 \text{ mm/tooth}$. Assume a rigid cutting tool and workpiece.
 - Up milling, 30% radial immersion
 - Down milling, 40% radial immersion
- Plot the y direction force over one cutter revolution for: down milling, 50% radial immersion, $N_t = 2$, $d = 19 \text{ mm}$, $\gamma = 30 \text{ deg}$, $b = 2 \text{ mm}$, $f_t = 0.2 \text{ mm/tooth}$, $k_t = 730 \text{ N/mm}^2$, $k_n = 205 \text{ N/mm}^2$, $k_{te} = k_{ne} = 0 \text{ N/mm}$, and $\Omega = 10,000 \text{ rpm}$. Use the Fourier series approach and show results for both five and 25 terms.
- Calculate the surface location error for the following conditions: 25% radial immersion down milling, spindle speeds from 11,000 rpm to 13,000 rpm, $N_t = 4$, $\gamma = 30 \text{ deg}$, $d = 12.7 \text{ mm}$ diameter, $f_t = 0.15 \text{ mm/tooth}$, $b = 2 \text{ mm}$, $k_t = 700 \text{ N/mm}^2$, $k_n = 210 \text{ N/mm}^2$, $k_{te} = k_{ne} = 2 \text{ N/mm}$, and symmetric structural dynamics with a stiffness of $8 \times 10^6 \text{ N/m}$, $\zeta = 0.02$, and 800 Hz natural frequency. For the

Fourier computations, use 15 terms, five axial steps, and a spindle speed resolution of 20 rpm. At a spindle speed of 12,140 rpm is the surface overcut or undercut?

4. Using time domain simulation, determine the surface location error at the free end of the cutter for the same conditions described in Exercise 3. Use a spindle speed equal to the best speed calculated from Eq. 4.29 for the $N = 0$ (rightmost) lobe. Carry out your simulation for 40 revolutions with 500 steps per tooth.
5. Plot the y direction force over one cutter revolution for: up milling, 50% radial immersion, $N_t = 4$, $d = 12.7$ mm, $\gamma = 30$ deg, $b = 2$ mm, $f_t = 0.1$ mm/tooth, $k_t = 700$ N/mm², $k_n = 200$ N/mm², $k_{te} = k_{ne} = 0$ N/mm, and $\Omega = 12,000$ rpm. Use the Fourier series approach and show results for both five and 25 terms. Compare these results to the y direction force for straight teeth with all other parameters identical.

Appendix: Fourier Force Series Coefficients

The Fourier coefficients, a_n and b_n , for the y direction force series:

$$F_y(\phi) = \sum_{j=1}^A \sum_{i=1}^{N_t} \left(a_0 + \sum_{n=1}^{\infty} (a_n \cos(n\phi_i) + b_n \sin(n\phi_i)) \right),$$

where $\phi_i = \omega t + \frac{2\pi}{N_t}(i-1) - \chi(j-1)$, are provided here [18]. The terms in Eqs. 5.18 through 5.23 were determined using Eqs. 5.5 and 5.6. The integration limits for down milling (ϕ_1 to π) are shown. For up milling, the limits are modified to be zero to ϕ_1 .

$$a_1 = -\frac{bN_t}{\pi} \left[k_t c \left(-\frac{1}{4} \sin \phi + \frac{1}{12} \sin 3\phi \right) + k_n c \left(-\frac{1}{4} \cos \phi - \frac{1}{12} \cos 3\phi \right) + k_{te} \left(\frac{1}{4} \cos 2\phi \right) + k_{ne} \left(\frac{1}{2} \phi + \frac{1}{4} \sin 2\phi \right) \right]_{\phi_1}^{\pi} \quad (5.18)$$

$$a_2 = -\frac{bN_t}{\pi} \left[k_t c \left(\frac{1}{4} \phi - \frac{1}{4} \sin 2\phi + \frac{1}{16} \sin 4\phi \right) + k_n c \left(-\frac{1}{16} \cos 4\phi \right) + k_{te} \left(-\frac{1}{2} \cos \phi + \frac{1}{6} \cos 3\phi \right) + k_{ne} \left(\frac{1}{2} \sin \phi + \frac{1}{6} \sin 3\phi \right) \right]_{\phi_1}^{\pi} \quad (5.19)$$

$$a_n = -\frac{bN_t}{\pi} \left[\begin{array}{l} k_t c \left(-\frac{1}{2n} \sin n\phi + \frac{1}{4(n-2)} \sin(n-2)\phi + \frac{1}{4(n+2)} \sin(n+2)\phi \right) \\ + k_n c \left(\frac{1}{4(n-2)} \cos(n-2)\phi - \frac{1}{4(n+2)} \cos(n+2)\phi \right) \\ + k_{te} \left(-\frac{1}{2(n-1)} \cos(n-1)\phi + \frac{1}{2(n+1)} \cos(n+1)\phi \right) \\ + k_{ne} \left(\frac{1}{2(n-1)} \sin(n-1)\phi + \frac{1}{2(n+1)} \sin(n+1)\phi \right) \end{array} \right]_{\phi_1}^{\pi}, \quad n = 3, 4, \dots \quad (5.20)$$

$$b_1 = -\frac{bN_t}{\pi} \left[\begin{array}{l} k_t c \left(\frac{3}{4} \cos \phi - \frac{1}{12} \cos 3\phi \right) + k_n c \left(\frac{1}{4} \sin \phi - \frac{1}{12} \sin 3\phi \right) \\ + k_{te} \left(-\frac{1}{2} \phi + \frac{1}{4} \sin 2\phi \right) + k_{ne} \left(-\frac{1}{4} \cos 2\phi \right) \end{array} \right]_{\phi_1}^{\pi} \quad (5.21)$$

$$b_2 = -\frac{bN_t}{\pi} \left[\begin{array}{l} k_t c \left(\frac{1}{4} \cos 2\phi - \frac{1}{16} \cos 4\phi \right) + k_n c \left(\frac{1}{4} \phi - \frac{1}{16} \sin 4\phi \right) \\ + k_{te} \left(-\frac{1}{2} \sin \phi + \frac{1}{6} \sin 3\phi \right) + k_{ne} \left(-\frac{1}{2} \cos \phi - \frac{1}{6} \cos 3\phi \right) \end{array} \right]_{\phi_1}^{\pi} \quad (5.22)$$

$$b_n = -\frac{bN_t}{\pi} \left[\begin{array}{l} k_t c \left(\frac{1}{2n} \cos n\phi - \frac{1}{4(n-2)} \cos(n-2)\phi - \frac{1}{4(n+2)} \cos(n+2)\phi \right) \\ + k_n c \left(\frac{1}{4(n-2)} \sin(n-2)\phi - \frac{1}{4(n+2)} \sin(n+2)\phi \right) \\ + k_{te} c \left(-\frac{1}{2(n-1)} \sin(n-1)\phi + \frac{1}{2(n+1)} \sin(n+1)\phi \right) \\ + k_{ne} c \left(-\frac{1}{2(n-1)} \cos(n-1)\phi - \frac{1}{2(n+1)} \cos(n+1)\phi \right) \end{array} \right]_{\phi_1}^{\pi}, \quad n = 3, 4, \dots \quad (5.23)$$

References

1. Kline, W., DeVor, R., & Shareef, I. (1982). The prediction of surface accuracy in end milling. *Journal of Engineering for Industry*, 104, 272–278.
2. Kline, W., DeVor, R., & Lindberg, J. (1982). The prediction of cutting forces in end milling with application to cornering cuts. *International Journal of Machine Tool Design Research*, 22, 7–22.

3. Tlusty, J. (1985). Effect of end milling deflections on accuracy. In R. I. King (Ed.), *Handbook of high speed machining technology* (pp. 140–153). New York: Chapman and Hall.
4. Sutherland, J., & DeVor, R. (1986). An improved method for cutting force and surface error prediction in flexible end milling systems. *Journal of Engineering for Industry*, 108, 269–279.
5. Montgomery, D., & Altintas, Y. (1991). Mechanism of cutting force and surface generation in dynamic milling. *Journal of Engineering for Industry*, 113(2), 160–168.
6. Smith, S., & Tlusty, J. (1991). An overview of modeling and simulation of the milling process. *Journal of Engineering for Industry*, 113(2), 169–175.
7. Altintas, Y., Montgomery, D., & Budak, E. (1992). Dynamic peripheral milling of flexible structures. *Journal of Engineering for Industry*, 114(2), 137–145.
8. Tarng, Y., Liao, C., & Li, H. (1994). A mechanistic model for prediction of the dynamics of cutting forces in helical end milling. *International Journal of Modeling and Simulation*, 14(2), 92–97.
9. Schmitz, T., & Ziegert, J. (1999). Examination of surface location error due to phasing of cutter vibrations. *Precision Engineering*, 23(1), 51–62.
10. Altintas, Y. (2000). *Manufacturing automation*. Cambridge, UK: Cambridge University Press.
11. Mann, B., Bayly, P., Davies, M., & Halley, J. (2004). Limit cycles, bifurcations, and accuracy of the milling process. *Journal of Sound and Vibration*, 277, 31–48.
12. Schmitz, T., Couey, J., Marsh, E., Mauntler, N., & Hughes, D. (2007). Runout effects in milling: Surface finish, surface location error, and stability. *International Journal of Machine Tools and Manufacture*, 47, 841–851.
13. Yun, W.-S., Ko, J., Cho, D.-W., & Ehmann, K. (2002). Development of a virtual machining system, Part 2: Prediction and analysis of a machined surface error. *International Journal of Machine Tools and Manufacture*, 42, 1607–1615.
14. Tlusty, G. (2000). *Manufacturing equipment and processes*. Upper Saddle River, NJ: Prentice-Hall Section 9.5.5, Fig. 9.50.
15. Schmitz, T., Ziegert, J., Canning, J. S., & Zapata, R. (2007). Case study: A comparison of error sources in high-speed milling. *Precision Engineering*, 32, 126–133.
16. Tlusty, J., Zaton, W., & Ismail, F. (1983). Stability lobes in milling. *Annals of the CIRP*, 32(1), 309–313.
17. Altintas, Y., & Budak, E. (1995). Analytical prediction of stability lobes in milling. *Annals of the CIRP*, 44(1), 357–362.
18. Schmitz, T., & Mann, B. (2006). Closed form solutions for surface location error in milling. *International Journal of Machine Tools and Manufacture*, 46, 1369–1377.
19. Ikua, B. W., Tanaka, H., Obata, F., & Sakamoto, S. (2001). Prediction of cutting forces and machining error in ball end milling of curved surfaces—I. Theoretical analysis. *Precision Engineering*, 25(4), 266–273.
20. Ranganath, S., Narayanan, K., & Sutherland, J. (1999). The role of flank face interference in improving the accuracy of dynamic force predictions in peripheral milling. *Journal of Manufacturing Science and Engineering*, 121, 593–599.
21. Campomanes, M. L., & Altintas, Y. (2003). An improved time domain simulation for dynamic milling at small radial immersions. *Journal of Manufacturing Science and Engineering*, 125, 416–422.
22. Chau, W.-M. (1992). *Accuracy of milling operations based on dynamic models and simulation*. M.S. Thesis, University of Florida.
23. American Society of Mechanical Engineers. (2003). ASME B46.1-2002, Surface Texture (Surface Roughness, Waviness, and Lay), New York, NY.

Chapter 6

Special Topics in Milling



If the facts don't fit the theory, change the facts.

—Albert Einstein

In Chaps. 4 and 5, we analyzed the milling process for both stability and surface location error through frequency and time domain approaches. Using frequency domain analyses, we (1) generated stability lobe diagrams that identify stable and unstable combinations of spindle speed and axial depth of cut; and (2) completed surface location error predictions over the same parameter space. We developed time domain simulations for the circular tool path approximation that predict forces and displacements for square and ball endmills, including the effects of helical teeth geometries. We next extended the square endmill time domain simulation to incorporate the actual cycloidal tool path and investigated both stability and surface location error for various cutting conditions. Finally, we compared stability and surface location error solutions between the frequency and time domain analyses. In this chapter, we continue our investigation of milling by exploring the frequency content of stable and unstable milling signals and enhancing our time domain simulations to include runout of the cutter teeth and variable teeth spacing. We then discuss low radial immersion milling and the corresponding stability behavior. We conclude the chapter with some comments regarding stability boundary uncertainty evaluation for the frequency domain analyses.

6.1 Frequency Content of Milling Signals

Let's return to the average tooth angle analysis for milling stability from Sect. 4.3 [1]. The relationships used to determine the spindle speed dependent axial depth of cut limit, b_{\lim} , are repeated in Eqs. 6.1 through 6.3.

$$b_{\lim} = \frac{-1}{2K_s \operatorname{Re}[\operatorname{FRF}_{\text{orient}}] N_t^*} \quad (6.1)$$

$$\frac{f_c}{\Omega N_t} = N + \frac{\epsilon}{2\pi} \quad (6.2)$$

$$\epsilon = 2\pi - 2 \tan^{-1} \left(\frac{\text{Re}[\text{FRF}_{\text{orient}}]}{\text{Im}[\text{FRF}_{\text{orient}}]} \right) \quad (6.3)$$

As a reminder, we restate the variable definitions here:

- K_s , specific force—process dependent coefficient that relates the resultant cutting force to the uncut chip area.
- $\text{FRF}_{\text{orient}}$, oriented frequency response function— x and y direction frequency response functions, or FRFs, “weighted” by the direction orientation factors, which are determined from the two step projection of the cutting force (due to a tooth located at the average between the start and exit angles) first onto the x and y directions and then onto the average surface normal.
- N_t^* , average number of teeth in the cut—it is possible for multiple teeth to be engaged simultaneously and for the number of teeth in the cut to vary during a single revolution; the average value $N_t^* = \frac{\phi_e - \phi_s}{\frac{360}{N_t}}$ captures this behavior, where ϕ_e and ϕ_s are the exit and start angles (deg), respectively, and N_t is the number of teeth on the cutter.
- f_c , chatter frequency (Hz)—frequency at which self-excited vibrations will occur if the stability limit is exceeded.
- Ω , spindle speed (rev/s)—the rotating frequency of the spindle for milling.
- N , lobe number— $N = 0, 1, 2, \dots$ indexed from right to left (higher to lower spindle speeds) in a stability lobe diagram.
- ϵ , phase between the current and previous tooth vibrations (rad)—varies between π rad (180 deg) and 2π rad (360 deg), where $\epsilon = 3\pi/2$ rad (270 deg) is the least favorable value.

We use Eqs. 6.1 through 6.3 to generate milling stability lobe diagrams for the average tooth angle approach by:

1. Determining the oriented FRF and identifying the valid chatter frequency range(s), i.e., where the real part of $\text{FRF}_{\text{orient}}$ is negative.
2. Solving for ϵ over the valid frequency range(s).
3. Finding the average number of teeth in the cut for the selected radial immersion.
4. Calculating b_{lim} over the valid frequency range(s).
5. Selecting an $N = 0, 1, 2, \dots$ value (representing N waves of vibration between teeth) and calculating the associated spindle speeds over the valid frequency range(s).
6. Plotting Ω vs. b_{lim} for each N value. As we discussed previously, any (Ω, b) pair leads to stable or unstable behavior depending on whether it appears above or below the stability boundary, respectively.

In our discussions of both stability and surface location error, we showed spectra of the cutting force signals which included content not only at the tooth passing

frequency but also at multiple harmonics due to the “impulse train” nature of typical milling force profiles. The notable constant force exceptions are (1) slotting with an even number of teeth, where $N_t > 2$; and (2) particular axial depths of cut for helical square endmills which are determined from $b = \frac{d(\phi_p)}{2\tan(\gamma)}$, where d is the cutter diameter, $\phi_p = \frac{2\pi}{N_t}$ (rad) is the pitch angle, and γ is the helix angle. We expressed the tooth passing frequency as a function of the spindle speed (rpm) and number of teeth, $f_{\text{tooth}} = \frac{\Omega N_t}{60}$ (Hz). We can expect, then, that during stable cutting conditions we should observe content at f_{tooth} and integer multiples of this value.

“What about unstable cuts?”, we may ask. We’ve already shown in Sect. 4.3, through our description of the average tooth angle approach, that each stability lobe can be described as a mapping of the oriented FRF onto the (Ω, b_{\lim}) parameter space. See Fig. 4.26, for example, where the chatter frequency is scanned through its potential values to obtain the stability limit for each N value. We know, therefore, that the chatter frequency (should chatter occur) is not a fixed value. It depends on the spindle speed and occurs within the valid chatter frequency range from $\text{FRF}_{\text{orient}}$. We also found that increased axial depths of cut were available at the “best speeds” of $\Omega_{\text{best}} = \frac{60f_n}{(N+1)N_t}$ (rpm), where f_n is expressed in Hz, although multiple vibration modes can lead to competing lobes and more complicated stability lobe diagrams. The purpose of this best speed equation is to match the tooth passing frequency to the system natural frequency so that the tooth-to-tooth surface undulations are in phase, i.e., $\epsilon = 360$ deg, and the force variation due to chip thickness modulation is minimized. Given this circumstantial information, we can expect that unstable cuts will exhibit content not only at f_{tooth} and its harmonics but also some chatter frequency.



For Instance

Stable cuts sound different from those that chatter. Stable cuts generate sound at the tooth passing frequency, runout frequency (see Sect. 6.2), and multiples of these. For that reason, stable cuts sound “clean”; they produce “pure” tones. Unstable cuts, however, also emit sound at the chatter frequency, which is generally not a multiple of the tooth passing or runout frequencies. For this reason, unstable cuts sound “harsh” or “raspy.” They exhibit a mixture of frequencies that are not harmonically related. Machinists are familiar with this phenomenon and can usually tell if a cut sounds bad or good, not just loud or quiet.

To explore the frequency content of milling signals in more detail, as well as how we might capitalize on this information, let’s update the average tooth angle MATLAB® code we developed previously. In p_6_1_1.m, we’ll add new figures to show the chatter and tooth passing frequencies, as well as the phase between surface undulations from one tooth to the next, as a function of spindle speed. We’ll then see how we can use the chatter frequency for an unstable (Ω, b_{\lim}) combination to select a

Fig. 6.1 50% radial immersion up milling model for Example 6.1

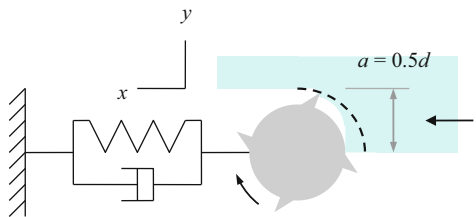
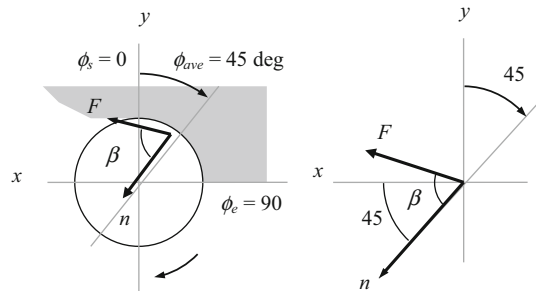


Fig. 6.2 Geometry for determining 50% radial immersion up milling directional orientation factor, μ_x



new spindle speed and converge on the preferred $\varepsilon = 360$ deg phase relationship [2, 3] in Example 6.1.

Example 6.1 Selecting New Spindle Speeds Using the Chatter Frequency For simplicity, we'll consider the single degree of freedom model shown in Fig. 6.1. A single mode in the x (feed) direction is identified with $f_n = 800$ Hz, $k = 5 \times 10^6$ N/m, and $\zeta = 0.01$. We'll assume the y direction is rigid. The cutter has four teeth, and the tool-material pair yields a specific force of $K_s = 2000$ N/mm² and force angle of $\beta = 72$ deg for the 50% radial immersion up milling cut.

Our first task is to determine the directional orientation factor, μ_x . As detailed in Sect. 6.4.3, two steps are required to calculate this value. First, the force is projected onto the x direction. Second, this result is projected onto the average surface normal. As shown in Fig. 6.2, projection of the force onto the x direction gives $F_x = F \cos (\beta - 45)$. The projection of this result onto the average surface normal is $F_n = F_x \cos (45) = F \cos (\beta - 45) \cos (45)$. Using Eq. 4.27, we obtain $\text{FRF}_{\text{orient}} = \mu_x \text{FRF}_x = \cos (\beta - 45) \cos (45) \text{FRF}_x$. This result is displayed in Fig. 6.3 for the selected x direction dynamics. Figure 6.4 shows the valid chatter frequency range ($\text{Re}[\text{FRF}_{\text{orient}}] < 0$) for the oriented FRF (top) and corresponding $N = 0$ stability limit versus spindle speed in rev/s (bottom). Note the $\frac{1}{N_t}$ relationship between frequency and spindle speed from the top to bottom subplots. This mapping supports both the best speeds equation $\Omega_{\text{best}} = \frac{f_n}{(N+1)N_t} = \frac{800}{(0+1)^4} = 200$ rev/s and the worst speeds equation $\Omega_{\text{worst}} = \frac{f_n}{N_t} \frac{1}{N+2\pi} = \frac{f_n(1+\zeta)}{4} \frac{1}{\frac{3\pi}{2\pi}} = \frac{800(1+0.01)}{4} \frac{1}{0+\frac{3}{4}} = 269.3$ rev/s since

Fig. 6.3 Oriented frequency response function for Example 6.1

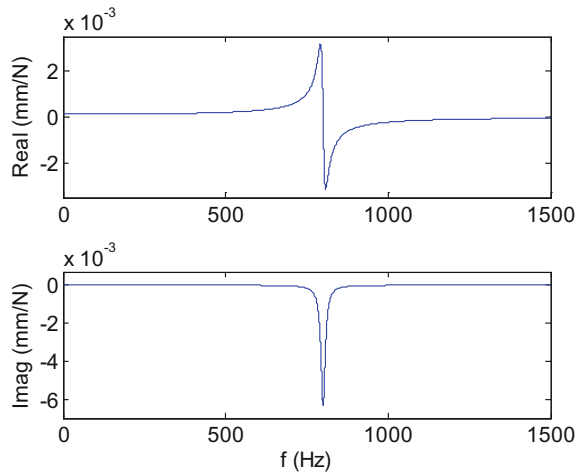
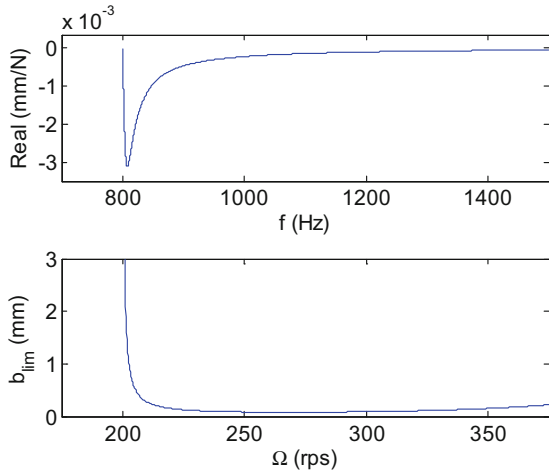


Fig. 6.4 Valid chatter frequency range for oriented FRF (top). Corresponding (Ω, b_{lim}) parameter space for $N = 0$ mapping (bottom)



increased axial depths are obtained near 200 rev/s and the minimum allowable depth, equal to the critical stability limit, occurs at 269.3 rev/s.

In Fig. 6.5, we have included the $N = 0$ to 4 stability lobes and converted the spindle speed to rpm in the top subplot. The bottom subplot shows the potential chatter frequencies (solid lines) and harmonics of the tooth passing frequency (dotted) as a function of spindle speed. The latter naturally grow linearly with spindle speed. The rightmost dotted line represents f_{tooth} , while subsequent dotted lines moving from right to left indicate increasing harmonics of $2f_{tooth}$ to $5f_{tooth}$. For this single degree of freedom case, the valid chatter frequencies begin at $f_n = 800$ Hz and then increase with spindle speed. This reiterates the behavior observed in Fig. 6.4, which shows the mapping from chatter frequency to spindle speed between the top and bottom subplots. Figure 6.5 also identifies selected points at 10,000 rpm. We'll discuss these next.

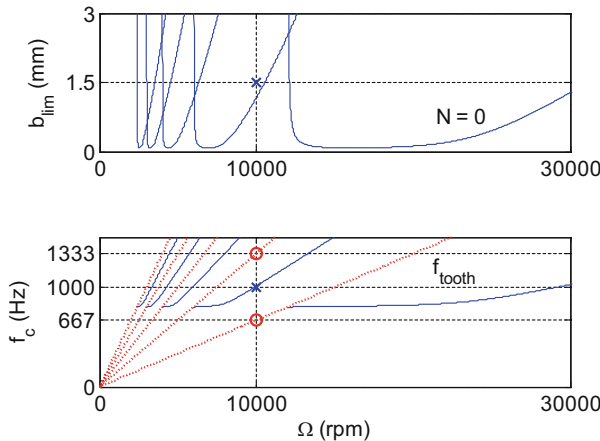


Fig. 6.5 (Top) Stability lobes for $N = 0$ to 4; the selected cutting condition of (10,000 rpm, 1.5 mm) is indicated by the “ \times ”. (Bottom) The tooth passing frequencies (dotted lines) and chatter frequencies (solid) are shown as a function of spindle speed. The tooth passing frequency content at 667 Hz and 1333 Hz is identified by the circles, while the chatter frequency at 1000 Hz is located by the “ \times ”

Let's assume a cut was attempted at $\Omega = 10,000$ rpm, $b = 1.5$ mm (suppose that we did not know if the cut would be stable or unstable). This cut is identified by the “ \times ” at $\Omega = 10,000$ rpm and $b = 1.5$ mm in the top subplot. We would expect frequency content at $f_{\text{tooth}} = \frac{\Omega N_t}{60} = \frac{10,000(4)}{60} = 667$ Hz, $2f_{\text{tooth}} = 2 \frac{10,000(4)}{60} = 1333$ Hz, and so on, if the cut was stable, since only forced vibrations would be present. Circles in the bottom subplot indicate these frequencies within the plot's vertical limits. However, because the operating point (10,000 rpm, 1.5 mm) is located in the unstable zone of the stability lobe diagram (top of Fig. 6.5), content will also be observed at 1000 Hz due to the self-excited vibration. This point is marked with an “ \times ” on the chatter frequency line in the bottom subplot. Note that this relationship between chatter frequency and spindle speed is defined in Eq. 6.2.

Returning to the best speed equation, its purpose is to match the tooth passing frequency to the chatter frequency in order to drive the operating condition toward a tooth-to-tooth undulation phase relationship of $\varepsilon = 360$ deg. Given the chatter frequency of 1000 Hz identified in the bottom subplot of Fig. 6.5, we should select a new spindle speed of:

$$\Omega = \frac{60f_c}{(N+1)N_t} = \frac{60(1000)}{(0+1)4} = 15,000 \text{ rpm}$$

for the $N = 0$ lobe and:

$$\Omega = \frac{60f_c}{(N+1)N_t} = \frac{60(1000)}{(1+1)4} = 7500 \text{ rpm}$$

Fig. 6.6 (Top) A first spindle speed regulation scenario gives new speeds at 7500 rpm and 15,000 rpm ($N = 1$ and 0 lobes, respectively) based on the 1000 Hz chatter frequency from Fig. 6.5. (Bottom) The new cutting conditions are also unstable and yield chatter frequencies of 818 Hz ($N = 1$) and 806 Hz ($N = 0$)

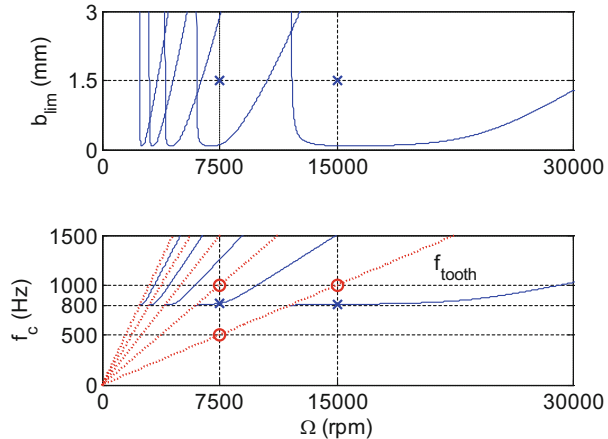
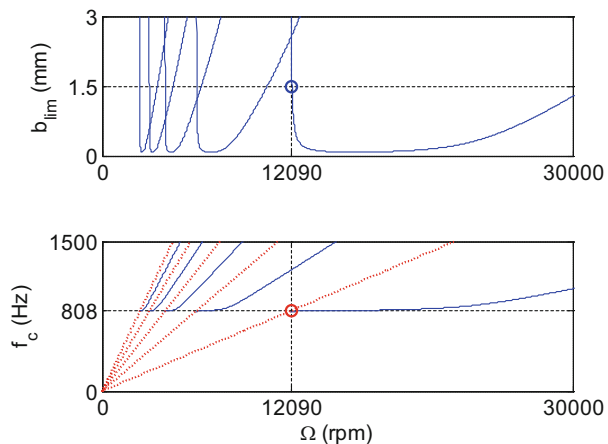


Fig. 6.7 (Top) Based on the 806 Hz chatter frequency at (15,000 rpm, 1.5 mm) from Fig. 6.6, the new spindle speed is 12,090 rpm. The new cut is identified by a circle and is stable. (Bottom) Because the cut is stable, the milling signal only includes content at $f_{\text{tooth}} = 806$ Hz (indicated by the circle) and integer harmonics, which occur outside the axis limits



for the $N = 1$ lobe. The tooth passing frequency for 15,000 rpm is $f_{\text{tooth}} = \frac{15,000(4)}{60} = 1000$ Hz, as expected. Similarly, the tooth passing frequency for 7500 rpm is $f_{\text{tooth}} = \frac{7500(4)}{60} = 500$ Hz, and the second harmonic is 1000 Hz. The points are shown as the circles in the bottom subplot of Fig. 6.6. However, because the cuts at (15,000 rpm, 1.5 mm) for the $N = 0$ lobe and (7500 rpm, 1.5 mm) for the $N = 1$ lobe are again unstable—see the top subplot of Fig. 6.6—we will observe content at the corresponding chatter frequencies. These are 818 Hz and 806 Hz for the $N = 0$ and 1 lobe spindle speed adjustments, respectively. Each of these points is marked by an “ \times ” in the bottom subplot of Fig. 6.6. If we make a second spindle speed adjustment for the $N = 0$ lobe, for example, the new value is $\Omega = \frac{60(806)}{(0+1)^4} = 12,090$ rpm. Figure 6.7 shows this final regulation into the stable zone. On the other hand, the $N = 1$ lobe would yield a new spindle speed of $\Omega = \frac{60(818)}{(1+1)^4} = 6135$ rpm. Although this selection corresponds to the gap between

Fig. 6.8 (Top) Stability lobes for $N = 0$ to 4; the selected cutting condition of (10,000 rpm, 1.5 mm) is indicated by the “ \times ”. (Bottom) The tooth-to-tooth undulation phase is shown as a function of spindle speed. The 185 deg phase for the unstable cut is identified by the “ \times ”

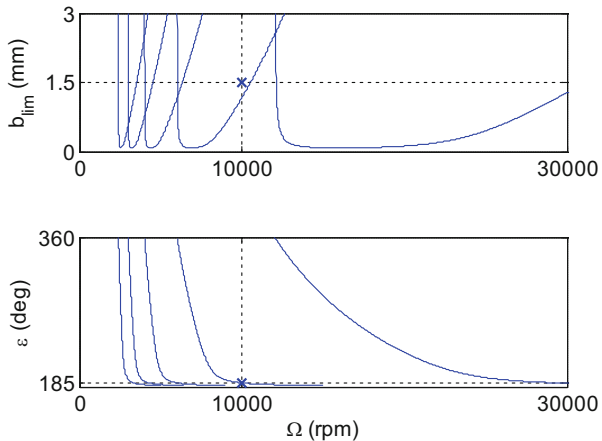
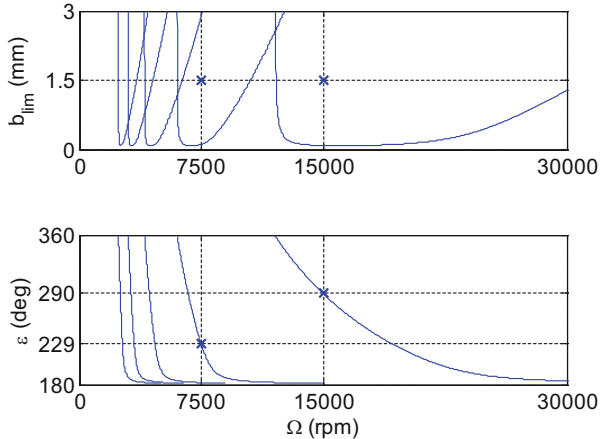


Fig. 6.9 (Top) The first spindle speed regulation gives new values at 7500 rpm and 15,000 rpm ($N = 1$ and 0 lobes, respectively) based on the 1000 Hz chatter frequency from Fig. 6.5. (Bottom) The new cutting conditions are also unstable and yield ε values of 229 deg ($N = 1$ lobe) and 290 deg ($N = 0$)

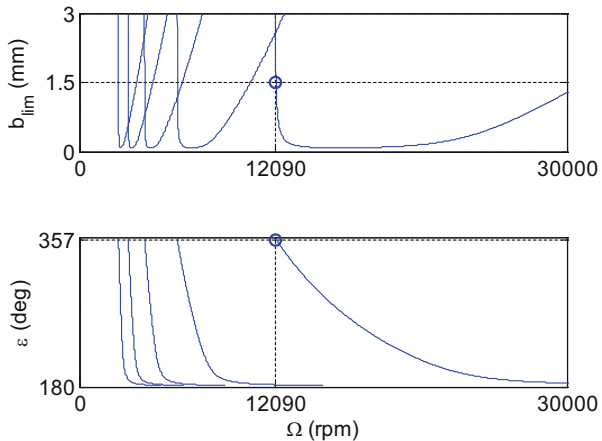


the $N = 1$ and 2 lobes, the axial depth (gain) is still too high and the cut would again be unstable.

As we noted previously, we use the best speeds equation to converge on the $\varepsilon = 360$ deg phase relationship. Let’s repeat the previous analysis but show the spindle speed versus ε relationship for the two regulations. Figure 6.8 displays the (Ω, b_{\lim}) parameter space (top), as well as the (Ω, ε) relationship (bottom), again for the $N = 0$ to 4 lobes. We see that the tooth-to-tooth undulation phase relationship is initially 185 deg, or nearly directly out of phase, for the (10,000 rpm, 1.5 mm) cutting condition.

As shown in Fig. 6.6, the first adjustment based on the 1000 Hz chatter frequency leads to new spindle speeds of 15,000 rpm ($N = 0$ lobe) or 7500 rpm ($N = 1$). The corresponding (Ω, ε) diagram is provided in Fig. 6.9 (bottom). We see that the phase relationship between subsequent tooth passages is $\varepsilon = 229$ deg for $\Omega = 7500$ rpm and 290 for 15,000 rpm. Both speeds are unstable (top). For the second spindle speed

Fig. 6.10 (Top) For the 806 Hz chatter frequency observed in Fig. 6.6 for (15,000 rpm, 1.5 mm), the new spindle speed is 12,090 rpm. The stable cut is identified by the circle. (Bottom) The ϵ value is 357 deg for the stable cut



adjustment ($N = 0$ lobe), however, the $\Omega = \frac{60(806)}{(0+1)^4} = 12,090$ rpm speed gives stable cutting conditions. The corresponding ϵ value is 357 deg, very near the “best” tooth-to-tooth undulation phase relationship of 360 deg. This case is shown in Fig. 6.10.

To conclude this example, let’s describe potential sources of the required chatter frequency information, which we can use to converge on preferred spindle speeds for improvements in stable axial depths of cut. Essentially, any signal that is derived from the milling process is acceptable. However, the most common choices include force, displacement, acceleration, and the audio signal emitted by the cutting process [3] due to acceptable signal-to-noise ratios in most instances.

The cutting force is a natural option since it directly communicates not only the tooth passing frequency and harmonics but also the chatter frequency for unstable conditions. The challenge, however, is obtaining this signal. Mounting a tabletop dynamometer between the workpiece and pallet/tombstone on the milling center is possible, but inherent drawbacks are:

1. The dynamometer influences the system dynamic response.
2. The dynamometer has a limited bandwidth so that content at higher frequencies may be corrupted by the dynamometer response (see Sect. 4.7).
3. The cost is significant for commercially available cutting force dynamometers/amplifiers.
4. This approach is not well suited to industrial applications.

The information could also be obtained from the torque signal emitted by a spindle-based torque dynamometer [4]. However, the same difficulties apply.

The tool displacement signal can be used, but the tool-workpiece interface is notoriously difficult to instrument. Displacement can be recorded on the tool shank, but noncontact sensors will generally be affected by coolant, for example, and this approach is again not particularly well suited to shop floor conditions. Accelerometers can be placed in convenient locations, such as within the spindle housing. Care must be exercised, however, to ensure that mechanical filtering of the acceleration

signal does not obscure the required information. The use of a microphone to record the cutting process audio signal offers a good compromise and has been implemented in a control system to sense and correct unstable cutting conditions using the techniques described in the previous paragraphs [5].

A natural challenge, regardless of the transduction scheme, is setting a threshold on what magnitude of spurious frequency content (not at the tooth passing frequency or harmonics) constitutes chatter. This threshold selection remains largely experience-based, although some efforts have been made toward automating the process of chatter identification. See [6–9], for example, which apply the statistical distribution in the periodically sampled (once-per-revolution or once-per-tooth) signal. The fundamental concept is that stable milling signals will repeat with the once-per-revolution/tooth sampling because the vibration is synchronous with the force. For self-excited vibrations, on the other hand, vibration occurs at the system natural frequency (corresponding to the most flexible mode) which is incommensurate¹ with the forcing frequency in general. When the unstable milling signal is sampled at once-per-revolution/tooth, therefore, it will not repeat [10]. The statistical variation in the unstable (and asynchronous) sampled signal will be larger than for the stable sampled signal.



In a Nutshell

It is surprising that, given the complexity of milling (including the tooth passing frequency content and system dynamics), there exists such a simple strategy for directing unstable cuts into stable zones. You do not have to understand the physics or the math, unless you want to understand why the strategy works. We provide the basic steps in the strategy here:

- 1) *Record the frequency content of the cutting signal. A microphone works well, but other signals are possible. The authors have used a variety of microphones, accelerometers, and dynamometers. It is even possible to record the sound remotely using a smartphone.*
- 2) *Ignore any frequency components caused by the teeth passing. They can be removed with a filter or literally ignored. It is important to know the actual spindle speed accurately. It often differs from the commanded spindle speed a little due to the load caused by the cutting or due to the digitization of the spindle speed command. The spindle speed can be measured or inferred from the runout frequency and harmonics.*
- 3) *If there is a significant frequency peak remaining, then that is the chatter frequency. This is the “chatter detector” part of the strategy. The hard part of this step, of course, is to define what “significant” means. Typically, we record the signal without cutting and set the threshold just above that level.*
- 4) *Choose a new spindle speed so that the tooth passing frequency or a multiple of the tooth passing frequency is equal to the detected chatter frequency.*

¹In other words, the ratio of the natural frequency to forcing frequency cannot be expressed as a ratio of whole numbers [63].

That is it! This approach identifies a stable speed if one is available at the selected axial and radial depths of cut. It sometimes takes a few iterations, but not many. There are a few more details to consider; read on.

Example 6.2 Selecting New Spindle Speeds in the Presence of Competing Lobes To continue with our study of milling frequency content in the presence of chatter, let's consider a slightly more complicated dynamic system with two modes modeled in both the x and y directions. The symmetric modal dynamics are described by $f_{n1} = 800$ Hz, $k_1 = 5 \times 10^6$ N/m, and $\zeta_1 = 0.01$ (first mode) and $f_{n2} = 900$ Hz, $k_2 = 9 \times 10^6$ N/m, and $\zeta_2 = 0.02$ (second mode). We'll consider the 25% radial immersion up milling cut depicted in Fig. 6.11, which is completed using a four tooth cutter in a tool-material pair that exhibits a specific force of $K_s = 700$ N/mm² and force angle of $\beta = 66$ deg (Fig. 6.12).

The exit angle is calculated using Eq. 4.4:

$$\phi_e = \cos^{-1}\left(\frac{r - \frac{r}{2}}{r}\right) = \cos^{-1}(0.5) = 60 \text{ deg}$$

and the start angle for the up milling cut is zero. To find μ_x , we first project F onto the x direction to obtain $F_x = F \cos(\beta - 60)$, where β is given in deg. The projection of this result onto the average surface normal, which occurs at the angle $\phi_{ave} = \frac{0+60}{2} = 30$ deg, is $F_n = F_x \cos(60) = F \cos(\beta - 60) \cos(60)$. For μ_y , projection onto the y direction gives $F_y = F \cos(150 - \beta)$. The projection of this result onto the average surface normal is $F_n = F_y \cos(150) = F \cos(150 - \beta) \cos(150)$. The directional orientation factors are therefore $\mu_x = \cos(\beta - 60) \cos(60)$ and $\mu_y = \cos(150 - \beta) \cos(150)$.

This oriented FRF is shown in Fig. 6.13 for the symmetric two mode dynamics. The top subplot in Fig. 6.14 displays the negative real part of $\text{FRF}_{\text{orient}}$ so that the two valid chatter frequency ranges may be identified, while the bottom subplot provides the $N = 0$ stability limit versus spindle speed in rev/s (bottom). The two sections correspond to the two chatter frequency ranges, and the overall stability limit is the

Fig. 6.11 25% radial immersion up milling model for Example 6.2

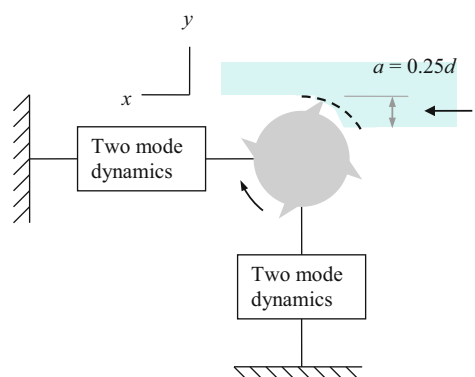


Fig. 6.12 Geometry for determining 25% radial immersion up milling directional orientation factors

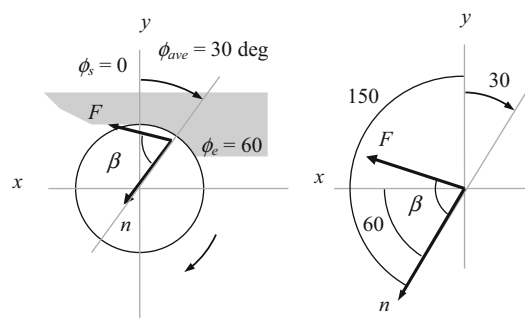


Fig. 6.13 Oriented frequency response function for Example 6.2

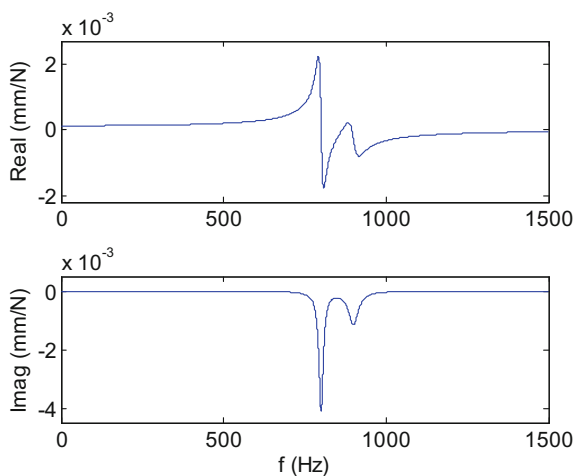


Fig. 6.14 Valid chatter frequency range for oriented FRF (top). Corresponding (Ω , b_{lim}) parameter space for $N = 0$ mapping (bottom). Competing lobes are seen due to the two valid chatter frequency ranges

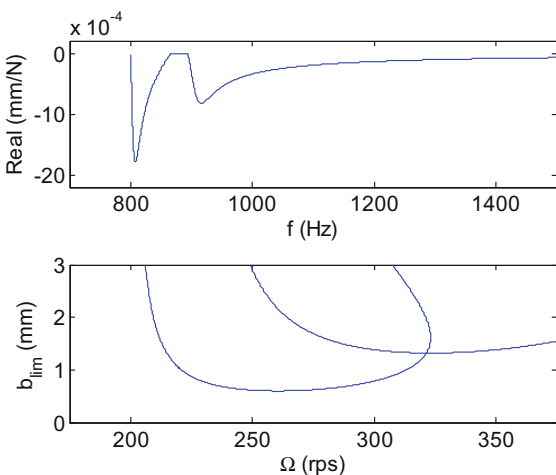
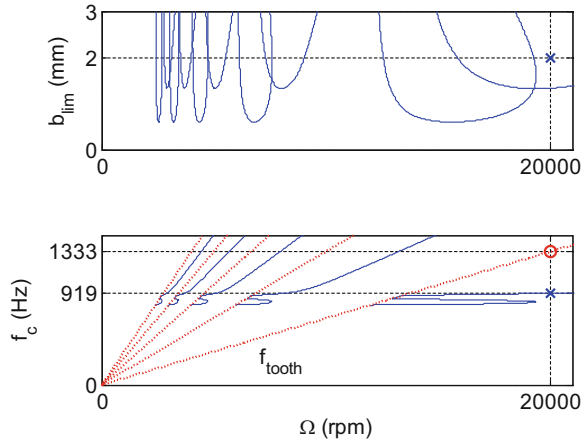


Fig. 6.15 (Top) Stability lobes for $N = 0$ to 4; the selected cutting condition of (20,000 rpm, 2 mm) is indicated by the “ \times .” (Bottom) The tooth passing frequency content at 1333 Hz is identified by the circle, while the chatter frequency at 919 Hz is marked by the “ \times ”



lowest point from the pair at each spindle speed where they overlap. You may recall that this situation is referred to as “competing” lobes, as described in Sect. 4.3.

If the cutting conditions are initially selected to be 20,000 rpm (let’s say this is the maximum available spindle speed) with an axial depth of 2 mm, chatter would be observed. Similar to the previous example, however, we know that if we can obtain the chatter frequency from an appropriate transducer, then we can use this information to select a new spindle speed. In Fig. 6.15, the unstable cutting conditions are identified by an “ \times ” in the top subplot. In the bottom subplot, we see that the chatter frequency for 20,000 rpm is 919 Hz; we also know that the tooth passing frequency is $f_{\text{tooth}} = \frac{20,000(4)}{60} = 1333$ Hz. These frequencies are marked with an “ \times ” and circle, respectively. Similar to the competing lobes, the chatter frequency curve for each N value has two distinct sections. Because the stability limit for the second section of the $N = 0$ lobe is exceeded in this instance, the chatter frequency also occurs on the second section of the chatter frequency curve for $N = 0$.

Based on our previous discussions, we know that the Fourier transform of the time domain milling signal for the unstable cut will contain content at f_c , as well as f_{tooth} and its harmonics. The corresponding phase relationship for surface undulations between subsequent teeth is provided in Fig. 6.16. From the bottom subplot, we see that $\epsilon = 248$ deg for the initial, unstable milling conditions. Further, this value is obtained from the second section of the undulation phase curve for $N = 0$.

Based on the 919 Hz chatter frequency from Fig. 6.15, the new spindle speed for $N = 0$ is $\Omega = \frac{60(919)}{(0+1)^4} = 13,785$ rpm. The updated operating condition is shown in the top subplot of Fig. 6.17, where we see that the cut is again unstable. We also observe that this initial regulation moved the spindle speed to the left of the second competing lobe because chatter occurred in this section from the first cutting condition. The corresponding chatter frequency is 804 Hz. As seen in the bottom subplot, this chatter frequency is obtained from the lower portion of the first section of the curve because the stability limit imposed by the first competing lobe is exceeded to the left

Fig. 6.16 (Top) Stability lobes for $N = 0$ to 4; the unstable cutting condition of (20,000 rpm, 2 mm) is indicated by the “ \times .” (Bottom) The tooth-to-tooth undulation phase of 248 deg for the unstable cut is identified by the “ \times ”

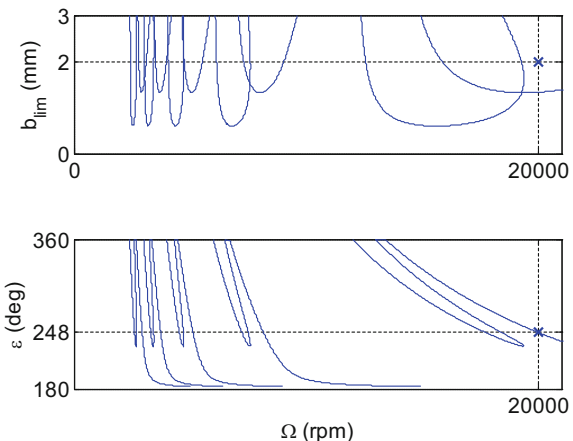
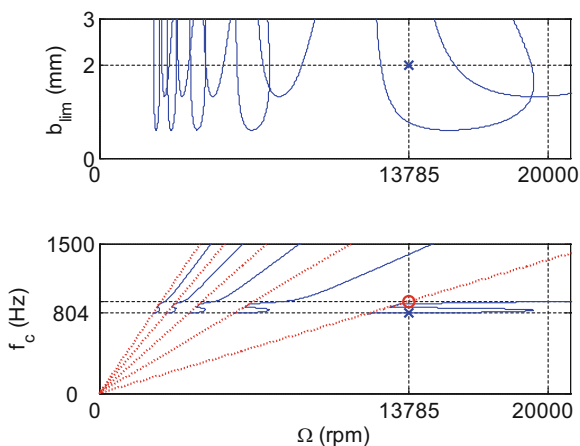


Fig. 6.17 (Top) The first spindle speed regulation gives a new speed at 13,785 rpm ($N = 0$) based on the 919 Hz chatter frequency from Fig. 6.15. The new cutting condition is also unstable. (Bottom) The new cutting condition is also unstable and gives a chatter frequency of 804 Hz ($N = 1$); this value is located by the “ \times .” The tooth passing frequency at 919 Hz is identified with a circle



of the reversal in speed direction at 19,384 rpm. The undulation phase is determined from Fig. 6.18. We see that $\epsilon = 315$ deg and the value is again obtained from the first section of the undulation phase curve following the same logic as for the chatter frequency.

A second regulation to $\Omega = \frac{60(804)}{(0+1)^4} = 12,060$ rpm provides a stable cutting condition, however. The new spindle speed is located to the left of the first competing lobe for $N = 0$, where increases in the stable axial depth may be obtained. The new operating point and corresponding tooth passing frequency (804 Hz) are shown in Fig. 6.19. The undulation phase is displayed in Fig. 6.20 (358 deg). Figures 6.13 through 6.20 were obtained using p_6_2_1.m, which is included with the textbook.

Example 6.3 Sound Content of Stable and Unstable Milling Signals In this section, we've highlighted the fact that the frequency content of milling signals changes

Fig. 6.18 (Top) The first spindle speed regulation gives a new speed at 13,785 rpm ($N = 0$). This new condition is again unstable. (Bottom) The undulation phase is 315 deg for the new unstable cutting condition (13,785 rpm, 2 mm)

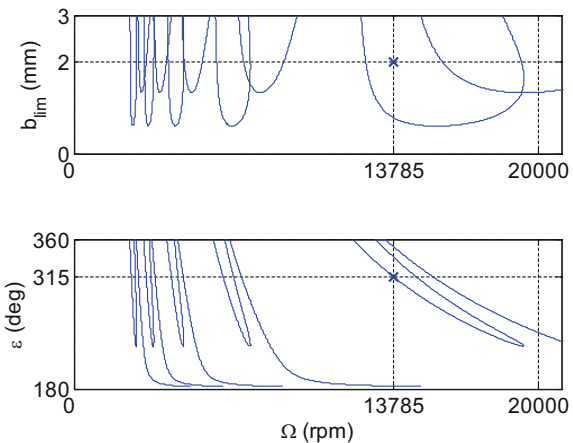


Fig. 6.19 (Top) The second spindle speed regulation gives a new stable speed of 12,060 rpm ($N = 0$) based on the 804 Hz chatter frequency from Fig. 6.17. (Bottom) The tooth passing frequency for the stable cut is 804 Hz (circle)

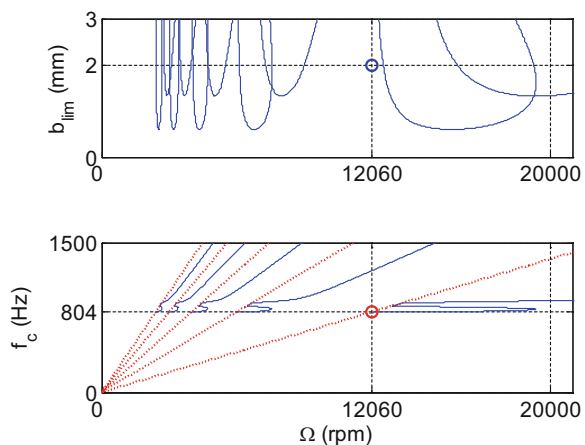
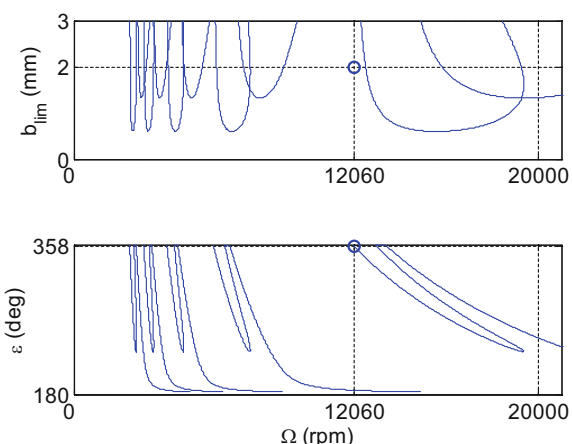


Fig. 6.20 (Top) The second spindle speed regulation provides a new stable speed of 12,060 rpm ($N = 0$). (Bottom) The undulation phase is 358 deg for the stable cutting condition (12,060 rpm, 2 mm)



when the axial depth stability limit is exceeded at a selected spindle speed (i.e., the chatter frequency appears). Let's now update our time domain simulation from Example 4.14 (p_14_1.m) to enable us to physically hear the difference between stable and unstable cuts. We add the following code to obtain p_6_3_1.m:

```
fs = 1/dt;
F = F/max(F);
sound(F, fs)
```

This implements the MATLAB® sound function, which requires two inputs: the signal to play (we've selected the resultant cutting force, F) and the sampling frequency, fs (Hz). Because the function input signal is assumed to have values between -1 and 1 , we normalized the force by its maximum value. To hear the difference between stable and unstable cuts, execute the code for an axial depth of 10 mm at two different spindle speeds: 15,000 rpm (stable) and 10,000 rpm (unstable). You may try other combinations using Figs. 4.57 and 4.58 to guide your selections. Make sure your speakers are connected and the volume is up when completing this exercise.

6.2 Runout

One complication that we did not address in the previous section is that content other than the tooth passing frequency, its harmonics, and the chatter frequency may be present in the milling signal spectrum (i.e., the magnitude of the Fourier transformed time domain signal). Even in the absence of external noise sources, such as pumps on the machine tool and other equipment on the shop floor, for example, runout (or eccentricity) leads to content in the milling signal which is synchronous with spindle speed. Here we include the following possibilities under the generic heading of runout:

- Axis of rotation errors of the spindle, including radial excursions of the spindle centerline during rotation [11–13].
- An offset between the holder centerline and spindle axis of rotation.
- An offset between the tool centerline and holder centerline.
- Radii variation between cutter teeth due to imperfect grinding for a solid tool or errors in the cutting edge placement for inserted cutters.



In a Nutshell

Runout is almost always present whether we like it or not. It is nearly impossible to completely eliminate all possible sources of runout.

For demonstration purposes, let's focus on variation in the teeth radii as shown in Fig. 6.21. Naturally, the associated variation in chip thickness due to the “big tooth”

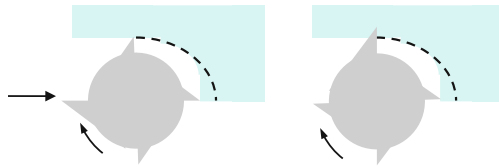
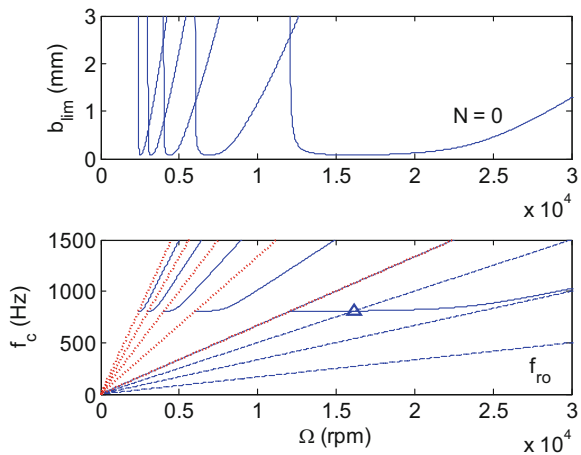


Fig. 6.21 Example of runout from a deviation in the radius from tooth to tooth in a solid endmill. (Left) A tooth with the nominal radius is entering the up milling cut where the chip thickness is zero according to the circular tool path approximation. (Right) The “big tooth” has a nonzero chip thickness for the same cutter angle

Fig. 6.22 An intersection between the third runout harmonic and the chatter frequency curve is seen at 808 Hz (marked by the triangle). This impedes our ability to identify potential chatter frequencies in the milling signal spectrum



is synchronous with spindle rotation. This generates frequency content at the runout frequency, $f_{\text{ro}} = \frac{\Omega}{60} = \frac{f_{\text{tooth}}}{N_t}$ (Hz), where Ω is expressed in rpm and f_{tooth} in Hz. We also observe content at the higher harmonics $2f_{\text{ro}}, 3f_{\text{ro}}, \dots$ in general.

Example 6.4 Frequency Content in the Presence of Runout If we return to Example 6.1 and plot the chatter frequency, tooth passing frequency and harmonics, and runout frequency with its first few harmonics (using p_6_4_1.m), we see that the third runout harmonic, $3f_{\text{ro}}$, intersects the chatter frequency curve (solid line). We also observe that $4f_{\text{ro}}$ (dot-dashed line) exactly overlaps f_{tooth} (dotted line). The latter is expected because $N_t = 4$. According to Fig. 6.22 (bottom subplot), we cannot discern between a potential chatter frequency and the third runout harmonic at 808 Hz, as indicated by the triangle. This is an important issue because one strategy to aid in isolating the chatter frequency for unstable cuts is applying a comb filter, i.e., a frequency domain filter that passes all content except at selected equally spaced frequencies, to reject the tooth passing frequency and its harmonics [3, 4]. The same technique cannot be applied to remove runout content if it coincides with possible chatter frequencies [14].

Let's use Eq. 6.2 to determine when this intersection between the chatter frequency and runout harmonics may occur. Restating this equation, we have $\frac{f_c}{\Omega N_t} = N + \frac{\epsilon}{2\pi}$. We also have the relationship $Nf_{ro} = n\Omega$, where $n = 1, 2, 3, \dots$ and Ω is expressed in rev/s in both instances. We are looking for instances when the chatter frequency is equal to a runout harmonic, or $f_c = Nf_{ro} = n\Omega$. Substituting for f_c from Eq. 6.2 and solving for n , we obtain:

$$n = N_t \left(N + \frac{\epsilon}{2\pi} \right). \quad (6.4)$$

Because $\pi < \epsilon < 2\pi$ rad (e.g., see Fig. 3.10), only particular integer n values yield acceptable ϵ values for a selected number of teeth and lobe number. We'll explore this in Example 6.5.

Example 6.5 Identifying Intersections Between Runout Harmonics and Chatter Frequencies Consider a four tooth cutter that exhibits runout. For the $N = 0$ lobe, we have $n = 4(\frac{\epsilon}{2\pi})$ from Eq. 6.4. If $n = 1$, we obtain $\epsilon = \frac{\pi}{2}$; therefore, no intersection is possible because this is not an acceptable ϵ value. For $n = 2$, we find that $\epsilon = \pi$. However, because $\epsilon \rightarrow \pi$ only as $f_c \rightarrow \infty$, this asymptotic approach is not practically important. For $n = 3$, on the other hand, $\epsilon = \frac{3\pi}{2}$, and an intersection is possible as shown in Fig. 6.22. We also know from Sect. 4.3 that this is the least favorable tooth-to-tooth undulation phase relationship (for a single degree of freedom system).



In a Nutshell

Bad luck! If we are ignoring multiples of the runout frequency, we might miss a real chatter frequency that corresponds to the worst case. The good news is that it is hard to make this happen unless we try. That is, the intersection is very precise.

Note that if we know ϵ and f_c , then we can calculate the corresponding spindle speed for a selected lobe number by rearranging Eq. 6.2. Specifically, we compute:

$$\Omega = \frac{f_c}{(N + \frac{\epsilon}{2\pi})N_t} = \frac{808}{\left(0 + \frac{\frac{3\pi}{2}}{2\pi}\right)4} = 269.3 \text{ rev/s} = 16,160 \text{ rpm.}$$

When $n = 4$, we have an overlap with f_{tooth} , and intersection is only possible for $\epsilon = 2\pi$, which represents the most favorable undulation phase.

Runout in milling affects the instantaneous chip thickness as demonstrated in Fig. 6.21. Therefore, the force is also influenced and, subsequently, the vibration. Well-known outcomes include premature cutting edge failure and increased machined surface roughness. We can investigate these effects using updated versions of our time domain simulations.

6.2.1 Simulation Modification

Incorporating the effects of runout in the cutter teeth, as depicted in Fig. 6.21, is straightforward. We'll first consider the circular tool path time domain simulation for helical square endmills introduced in Sect. 4.5. Including runout requires that we modify the chip thickness, h , calculation to be:

$$h = ft * \sin(\phiia * \pi / 180) + surf(cnt4, phi_counter) - n + RO(cnt3);$$

where ft is the feed per tooth, ϕia is the tooth angle for the current tooth and axial slice, $surf$ is the array that contains the surface position for the previous tooth at each axial slice, n is the current vibration along the instantaneous surface normal direction, and RO is the vector that contains the tooth-to-tooth runout values. To establish a convention for the simulation and match general measurement procedures, we'll normalize the RO vector entries to the largest tooth radii (i.e., we'll set the dial indicator to zero at the largest tooth and measure the deviation in radii, if any, for the other teeth). This means that one RO entry will be zero and all other values will be zero (for no runout) or less than zero if runout is present. Naturally, the number of entries in this vector is N_t .

In addition to changing the chip thickness calculation, the $surf$ array updating must include the runout effect. Specifically, we use the following line when the computed chip thickness is greater than zero (i.e., the current tooth is cutting):

$$surf(cnt4, phi_counter) = n - RO(cnt3);$$

This approach neglects variation in runout along the tool axis, which is clearly possible for actual cutters. To include axial dependence, the RO vector could be redefined as an array with a column for each tooth and a row for each axial slice, for example. We leave this activity as an exercise. As an example of the effect of runout, let's show the force profile for the helical endmill described in Example 4.14 together with the force variation in the presence of tooth-to-tooth runout.

Example 6.6 Comparison of Forces With and Without Runout In this example, we compare the cutting forces produced by helical endmills with and without runout. We'll consider a 30% radial immersion up milling cut (zero start angle and 66.4 deg exit angle). There are two identical modes in both the x and y directions. The modal parameters are $f_{n1} = 800$ Hz, $k_{q1} = 2 \times 10^7$ N/m, and $\zeta_{q1} = 0.05$ and $f_{n2} = 1000$ Hz, $k_{q2} = 1.5 \times 10^7$ N/m, and $\zeta_{q2} = 0.03$. The workpiece material is an aluminum alloy, and it is machined with a four tooth, 19 mm diameter, 45 deg helix square endmill using a feed per tooth of 0.15 mm/tooth. The cutting force coefficients are $k_t = 520$ N/mm² and $k_n = 300$ N/mm². The corresponding stability diagram is shown in Fig. 4.57. The resultant cutting force for an axial depth of 5 mm at a spindle speed of 15,000 rpm with no runout is shown as the dotted line in Fig. 6.23. The force with runout, $RO = [0 \ -10 \ 0 \ -15]$ μm , is shown as the solid line. At $t = 0.0977$ s, the runout force is smaller by 25.5 N (7.4% decrease from the nominal

Fig. 6.23 Comparison of the resultant cutting force without runout (dotted line) and with runout (solid line) for the circular tool path simulation

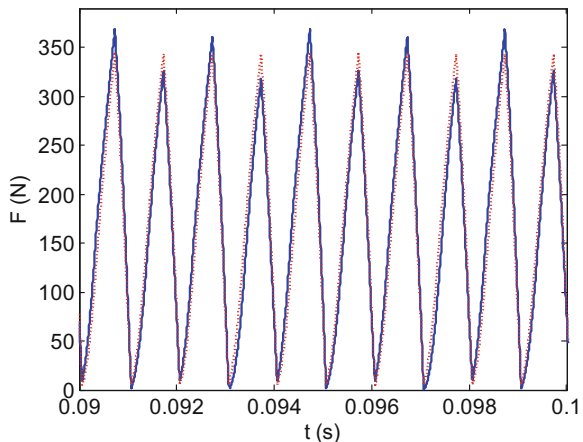
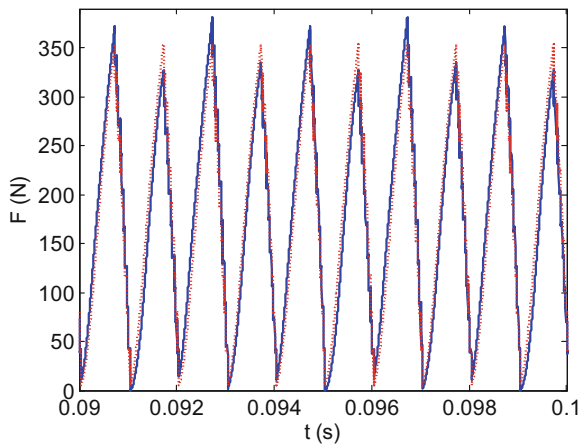


Fig. 6.24 Comparison of the resultant cutting force without runout (dotted line) and with runout (solid line) for the cycloidal simulation



force). At $t = 0.0947$ s, the runout force is larger by 25.1 N (7.3% increase). This behavior matches the “big-little” teeth profile described by the selected runout values. Figure 6.23 was produced using the MATLAB® program p_6_6_1.m.

Let’s now consider the cycloidal tool path simulation. We define the tooth dependent runout values in vector form, again using the same convention (normalized to a maximum value of zero). The only other changes to the program described in Sect. 5.3 are updating the radius with the runout values, $r = d/2 + RO$, and indexing r by the appropriate N_t counter each time it appears [15].

Example 6.7 Comparison of Cycloidal and Circular Tool Path Results In this example, we compare the cutting forces for the cycloidal tool path simulation (p_6_7_1.m) to those observed in Example 6.6. The conditions are identical. The results with and without runout, $RO = [0 -10 0 -15]$ μm , are shown in Fig. 6.24. We see that the force levels are similar to those seen in Fig. 6.23. Perhaps more

Fig. 6.25 Machined surface profile for Example 6.7 with no runout. The “*” symbols indicate the simulated cutting-edge locations. The surface is shown by the solid line; it is defined using the “bubble up” algorithm described in Sect. 5.3. Note that the remaining material is located above the line for the up milling cut

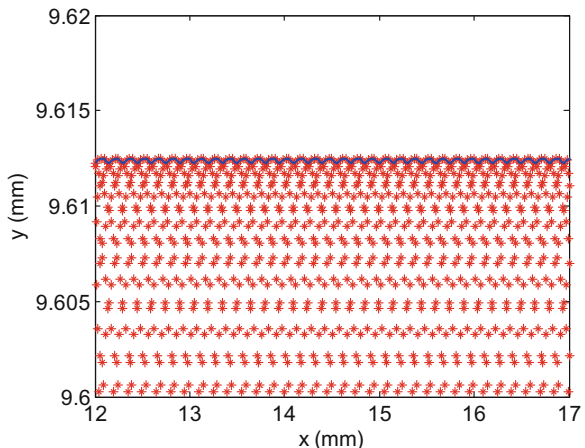
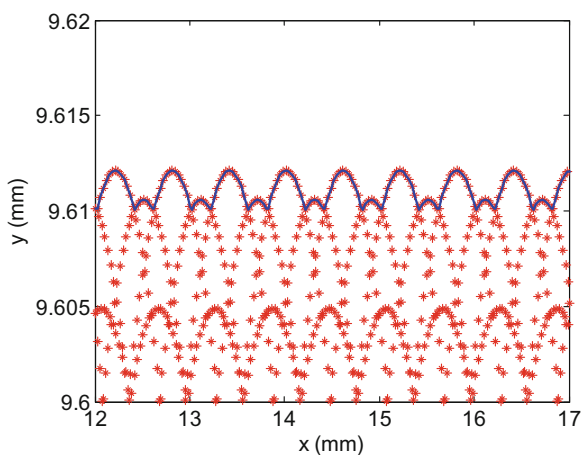


Fig. 6.26 Machined surface profile for Example 6.7 with runout. The roughness average is approximately eight times higher than the surface in Fig. 6.25



interesting, however, is a comparison of the machined surface profiles predicted by the cycloidal simulation. Figure 6.25 shows the surface without runout; the corresponding roughness average is $0.08 \mu\text{m}$. When including runout, the roughness average increases to $0.66 \mu\text{m}$ (greater than eight times larger) as seen in Fig. 6.26. Note that the surface location error at the tool’s free end is essentially unaffected: $87.4 \mu\text{m}$ overcut without runout and $86.1 \mu\text{m}$ when including runout effects. Additional information regarding the influence of runout on machining behavior can be found in [15–34]. In [15], for example, the influences of runout, feed per tooth, and teeth spacing on surface roughness, surface location error, and stability are explored.

6.3 Variable Teeth Spacing

In all our previous stability analyses, we have assumed that the teeth are equally spaced around the cutter periphery (i.e., constant teeth pitch). It is of course also possible to place the teeth with unequal, or nonproportional, spacing. Several researchers have implemented variable teeth spacing to interrupt regeneration of surface waviness (caused by tool vibrations) and, therefore, modify stability behavior [35–43]. Although we could argue that determining the stability lobe diagram and using it to select cutting parameters are a valid approach, the use of variable teeth spacing can be applied in situations where it is inconvenient to adjust the spindle speed, such as a transfer line, or the larger stable lobes available at higher spindle speeds are inaccessible due to significant tool wear at the corresponding spindle (and cutting) speeds. In these cases, changing the teeth spacing can yield stable zones where they would not otherwise exist. Varying the helix angle from tooth to tooth has also been implemented to reduce chatter [44], but we will focus on variable teeth spacing here.



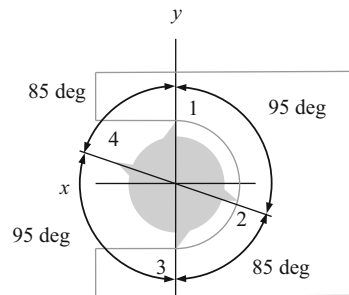
In a Nutshell

Because nonproportional tooth spacing disturbs regeneration of waviness, it can improve milling stability. Not all spacing selections increase stability, however, and whether or not there is improvement depends on the system dynamics, tooth spacing, and spindle speed. In addition, stability improvement by this technique generally requires an accompanying feed reduction. Why? Constant spindle speed with nonproportional tooth spacing produces a nonconstant feed per tooth. Because the maximum permissible chip load is a function of the cutting edge strength, the maximum feed for a tool with nonproportionally spaced teeth is controlled by the tooth with the largest preceding angle. One tooth takes the largest chip load, and all other teeth are essentially underused. We have to set the feed based on the most loaded tooth, and this is a reduction from the feed that would be possible if the teeth were all used equally. The required feed reduction must be recovered through an increased axial depth of cut to simply break even in terms of the material removal rate.

6.3.1 Simulation Updating

As described in Sect. 4.3, there is a periodic time delay between teeth engagements due to the (typically) uniform teeth spacing. Changing the teeth spacing, therefore, varies this time delay and interrupts the surface regeneration periodicity. We can explore this through minor modifications to our time domain simulations. First, let's consider the circular tool path code. The first modification is to directly define the angles of the individual teeth starting from tooth 1 located at an initial angle of zero. The teeth are ordered by increasing clockwise angles as described in Sect. 4.4 and

Fig. 6.27 Variable teeth spacing example with four teeth at angles {0 95 180 275} deg



shown in Fig. 6.27. Teeth angles of {0 95 180 275} deg are depicted, where teeth 2 and 4 have been advanced by 5 deg relative to their uniform spacing angles of 90 deg. To describe the teeth spacing, a new vector is defined in p_6_8_1.m.

```
tooth_angle = [0 95 180 275] ;
```

Due to the variable teeth angles, the feed per tooth also changes from one tooth to the next. This is handled using the following code, where `ft_mean` is the mean feed per tooth value (m/tooth) and `theta` is the angle between teeth (deg); it is defined using the MATLAB® `diff` function.

```
ft_mean = 0.15e-3;
theta = diff([tooth_angle 360]);
for cnt = 1:Nt
    ft(cnt) = (ft_mean*theta(cnt)*Nt)/360;
end
```

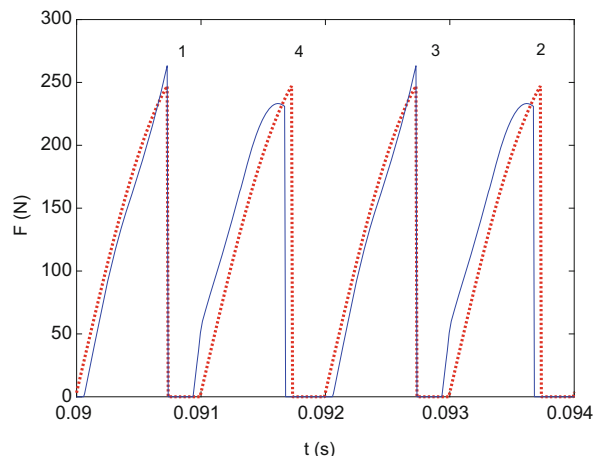
Based on these modifications, two additional changes are made. First, the `teeth` vector, which is used to index the appropriate `phi` entry, is redefined using the following `for` loop. The `round` function is necessary because the teeth entries must be integer values.

```
for cnt = 1:Nt
    teeth(cnt) = round(tooth_angle(cnt)/dphi) + 1;
end
```

Finally, each time the feed per tooth appears, it must now be indexed using the tooth (`Nt`) counter: `ft(cnt)`. Note that the runout vector entries, `RO`, must now correspond to the appropriate entries in `tooth_angle`.

Example 6.8 Comparison of Uniform and Variable Teeth Spacing Forces Let's compare the cutting forces produced by endmills with uniform and variable teeth spacing. We'll consider the same 30% radial immersion up milling cut (zero start angle and 66.4 deg exit angle) as in the previous section. Again, there are two identical modes in the `x` and `y` directions with modal parameters: $f_{n1} = 800$ Hz, $k_{q1} = 2 \times 10^7$ N/m, and $\zeta_{q1} = 0.05$ and $f_{n2} = 1000$ Hz, $k_{q2} = 1.5 \times 10^7$ N/m, and

Fig. 6.28 Resultant cutting force for uniform (dotted line) and variable (solid line) teeth spacing with angles $\{0\ 95\ 180\ 275\}$ deg. The helix angle is zero, the axial depth of cut is 3 mm, and the spindle speed is 15,000 rpm for the 30% radial immersion up milling cut. The teeth numbers are also identified (as depicted in Fig. 6.27)



$\zeta_{q2} = 0.03$. The workpiece material is an aluminum alloy machined with a four tooth, 19 mm diameter square endmill using a feed per tooth of 0.15 mm/tooth. The cutting force coefficients are $k_t = 520 \text{ N/mm}^2$ and $k_n = 300 \text{ N/mm}^2$. We'll consider tools with zero helix angles (straight teeth) and tooth angles of $\{0\ 90\ 180\ 270\}$ deg and $\{0\ 95\ 180\ 275\}$ deg.

Figure 6.28 shows the resultant forces for an axial depth of 3 mm at 15,000 rpm. The figure is produced using p_6_8_1.m, where the teeth numbers are marked according to the convention shown in Fig. 6.27. Both cuts are clearly stable; however, we see that the time between one tooth's exit and the next tooth's entry (where the force is zero) varies periodically with the variable teeth spacing. As we'd expect, the time is smaller for the decreased spacing between teeth 1 and 4 and, similarly, teeth 3 and 2.

Next let's explore the global stability behavior of the variable teeth spacing tool relative to the uniform teeth spacing tool. We obtain the stability lobe diagram for the latter using p_6_8_2.m; see Fig. 6.29. To establish a baseline for the comparison of the time domain and frequency domain solutions, let's select a grid of points and complete time domain simulations using p_6_8_1.m. For each $\{\Omega, b\}$ combination, we determine stability from the corresponding force and displacement profiles. The stable cuts are marked with a circle in Fig. 6.29 and the unstable cuts with an “ \times .” Good agreement is observed.

Implementing the variable teeth spacing $\{0\ 95\ 180\ 275\}$ deg yields the results provided in Fig. 6.30. Again, the variable teeth spacing stability is compared to the frequency domain uniform teeth spacing solution. A significant increase in the allowable axial depth of cut is observed in the region near 4000 rpm. Although we would not expect the same behavior for different system dynamics, this example does demonstrate the potential gains made available by selection of appropriate tooth angles.

Fig. 6.29 Stability limits for uniform teeth spacing cutter. The frequency domain solution for the same tool geometry is identified by the solid line. Using the circular tool path time domain simulation, stable results are identified by circles and unstable results by “ \times ” symbols

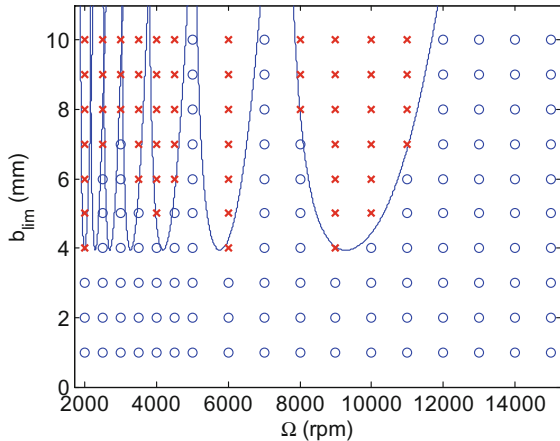
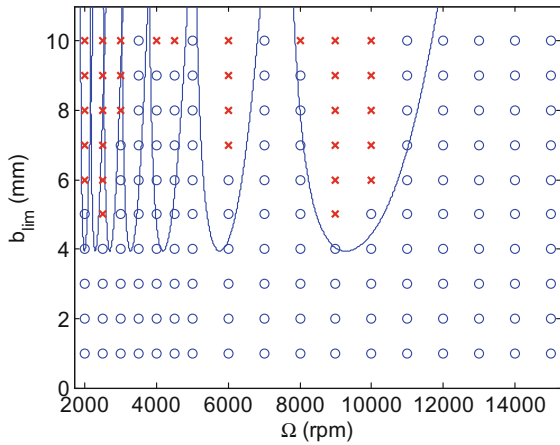


Fig. 6.30 Stability limits for variable teeth spacing, {0 95 180 275} deg, cutter. The frequency domain solution for the uniform teeth spacing cutter is again identified by the solid line. Using the circular tool path time domain simulation for the variable teeth spacing cutter, stable results are identified by circles and unstable results by “ \times ” symbols. Improved stability is seen near 4000 rpm



In a similar manner, we can model variable teeth spacing in the cycloidal tool path time domain milling simulation by specifying the appropriate teeth angles in the vector `teeth`. This vector serves the same function as `tooth_angle` in the circular tool path simulation. See the MATLAB® program `p_6_7_1.m` included with the textbook.

6.4 Period- n Bifurcations

In 1998, Davies et al. reported that “undesirable vibrations observed in partial immersion cuts seem inconsistent with existing theory” [10]. Using a Poincaré sectioning technique (once-per-revolution sampling) combined with capacitive measurements of the tool shank displacements in the x (feed) and y directions during

cutting, they found that some unstable low radial immersion cuts gave discrete clusters of once-per-revolution sampled points when plotted in the x - y plane, while others presented elliptical distributions. They subsequently showed that this behavior was the manifestation of two different types of instability [45, 46]. Traditional quasiperiodic chatter, also referred to as secondary Hopf bifurcation,² leads to the elliptical distribution of periodically sampled points. The second instability type, encountered during low radial immersions, is a period-2, or flip, bifurcation. It reveals itself as two tightly grouped clusters of sampled points as opposed to a single group of points for the synchronous vibrations that occur during stable cutting with forced vibrations only. Subsequent modeling efforts are described in [47–53] and include temporal finite element analysis, time domain simulation, a multifrequency analytical solution, and the semi-discretization approach. These techniques give improved accuracy for the predicted stability limit over the average tooth angle and frequency domain approaches (Chap. 4) in very low radial immersion (less than 10%) cases. However, they do not offer the convenient closed-form expressions for the stability boundary.



In a Nutshell

The cutting force in low radial immersion milling resembles a series of impacts. In between impacts, the tool experiences free vibration. The new cutting force depends on where the tool is in its decaying free vibration cycle (during the noncontact portion of the rotation) when the tooth next encounters the previous surface. The result is the formation of additional stable areas near what was previously the worst case for stability.

Example 6.9 Low Radial Immersion Stability We can use time domain simulation to explore the secondary Hopf and period-2 bifurcations. By modifying the cycloidal tool path code to include once-per-tooth sampling (see Sect. 4.4), we can observe the two instabilities in x (feed direction) versus y displacement plots [10]. We'll use single degree of freedom, symmetric dynamics ($f_n = 720$ Hz, $k = 4.1 \times 10^5$ N/m, and $\zeta = 0.009$) for a 5% radial immersion up milling cut (zero start angle and 25.8 deg exit angle). The workpiece material is an aluminum alloy machined with a single tooth, 45 degree helix, 8 mm diameter square endmill using a feed per tooth of 0.1 mm/tooth. The cutting force coefficients are $k_t = 644$ N/mm² and $k_n = 238$ N/mm². These conditions mimic those reported in [53] to enable convenient comparison. The code added in p_6_9_1.m to enable once-per-tooth sampling follows, where $xpos$ and $ypos$ are the tool displacements in the x and y directions, respectively, $steps_tooth$ is the number of simulation steps per tooth passage, and $xsamp1e$ and $ysamp1e$ are the sampling results.

```
xsamp1e = xpos(1:steps_tooth:length(xpos)) ;
ysamp1e = ypos(1:steps_tooth:length(ypos)) ;
```

²In the analysis of dynamic systems, a bifurcation represents the sudden appearance of a qualitatively different solution for a nonlinear system as some parameter is varied [64].

Fig. 6.31 The frequency domain solution stability limit (solid line) is compared to time domain simulation results for the $j = 0$ lobe. For the time domain simulations, stable cuts are represented by circles and unstable cuts by “ \times ” symbols (secondary Hopf) and triangles (period-2)

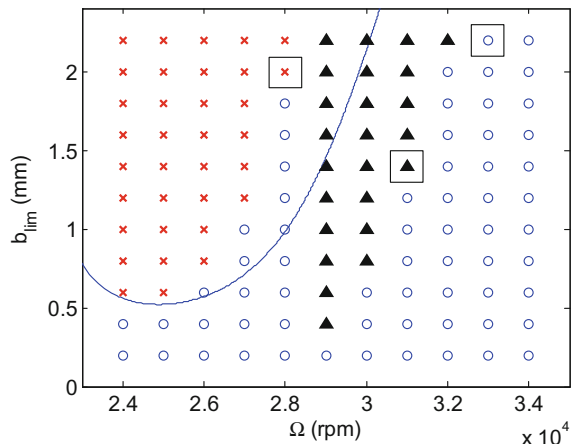


Fig. 6.32 Time history for the x (feed) and y direction displacements obtained from the {28,000 rpm, 2 mm} cut in Fig. 6.31. The once-per-tooth sampled data (“+” symbols) demonstrate quasiperiodic, secondary Hopf instability

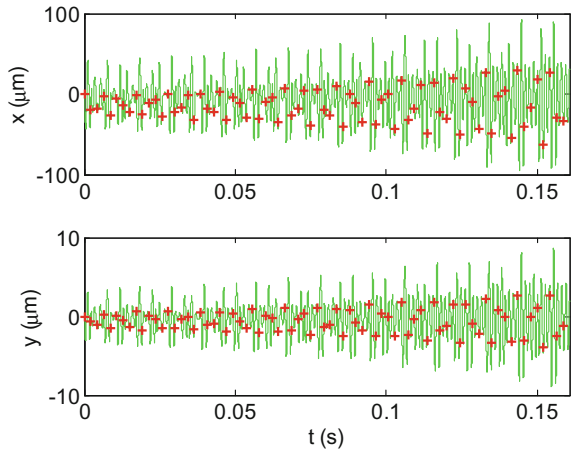


Figure 6.31 shows the stability limit obtained using the frequency domain solution (Sect. 4.3) as a solid line; see p_6_9_2.m. The region shown corresponds to the left side of the $j = 0$ (rightmost) lobe. The results of time domain simulations are identified by circles (stable), “ \times ” symbols (secondary Hopf bifurcation), and triangles (period-2 bifurcation). A narrowband of increased stability is seen between 27,000 rpm and 28,000 rpm. This is accompanied by the spindle speed range from 29,000 rpm and 32,000 rpm which exhibits period-2 bifurcation behavior. Three points are selected for further study. The {28,000 rpm, 2 mm} point demonstrates the traditional secondary Hopf instability; see Fig. 6.32 for the time history and Fig. 6.33 for the x versus y plot. As discussed previously, the once-per-tooth sampled data appears as an elliptical distribution for secondary Hopf instability. Conversely, Figs. 6.34 and 6.35 show the period-2 bifurcation for the {31,000 rpm, 1.4 mm} operating parameters. The synchronously sampled data now occur in two clusters after the

Fig. 6.33 Plot of x versus y direction displacements obtained from the {28,000 rpm, 2 mm} cut. The elliptical distribution of the once-per-tooth sampled data (“+” symbols) indicates secondary Hopf instability

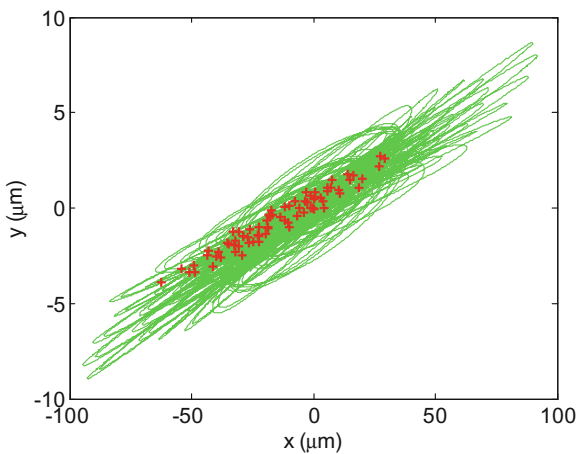


Fig. 6.34 Time history for the x (feed) and y direction displacements obtained from the {31,000 rpm, 1.4 mm} cut. The once-per-tooth sampled data (“+” symbols) demonstrate a period-2 bifurcation

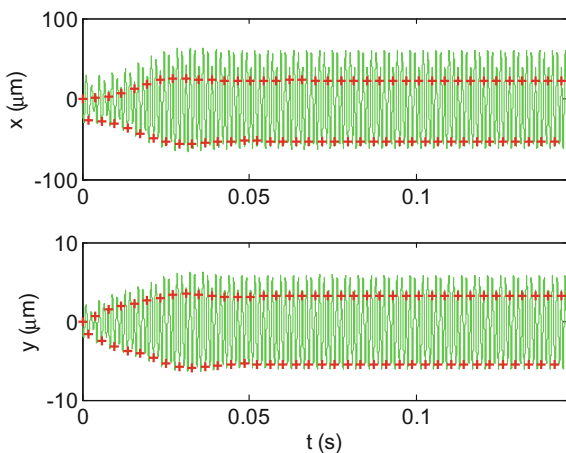


Fig. 6.35 Plot of x versus y direction displacements obtained from the {31,000 rpm, 1.4 mm} cut. The two clusters of once-per-tooth sampled data (“+” symbols) identify a period-2 instability

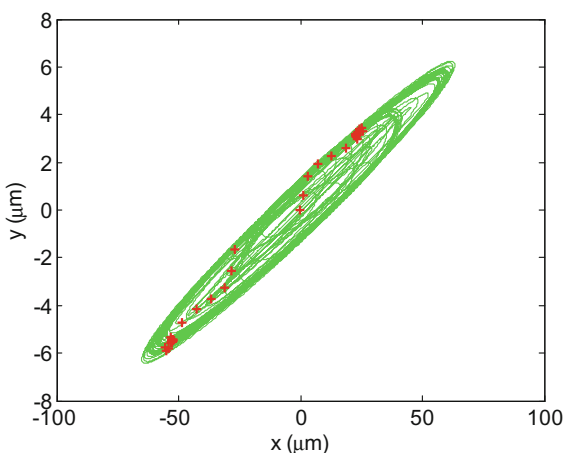


Fig. 6.36 Time history for the x (feed) and y direction displacements obtained from the {33,000 rpm, 2.2 mm} cut. The once-per-tooth sampled data (“+” symbols) demonstrate stable behavior

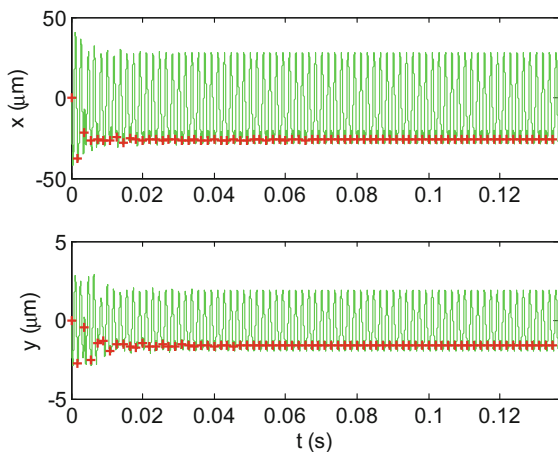
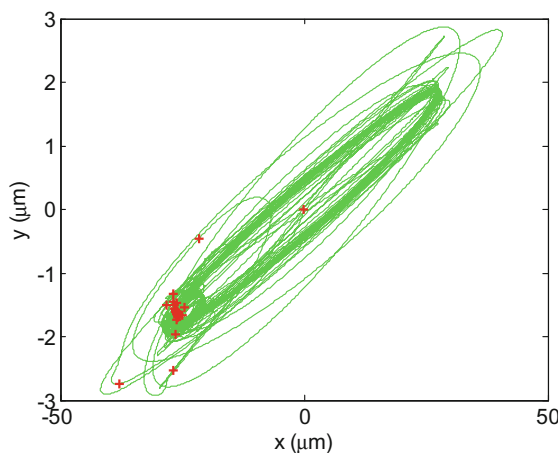


Fig. 6.37 Plot of x versus y direction displacements obtained from the {33,000 rpm, 2.2 mm} cut. The single cluster of once-per-tooth sampled data (“+” symbols) indicates stable operation



initial transients attenuate in the x vs. y plot (Fig. 6.35). A stable cut is represented by the {33,000 rpm, 2.2 mm} spindle speed, axial depth of cut pair. As expected, Figs. 6.36 and 6.37 display repetitive behavior from one tooth passage to the next (forced vibration only).



In a Nutshell

For those concerned with detailed process modeling, the exact nature of the milling instability (secondary Hopf or period-2 bifurcation) is extremely interesting. For practical machining applications, we just need to consider the radial depth of cut. As long as the radial depth is high, then the stability lobe algorithms described in Sect. 4.3 are valid. When the radial depth of cut is low, additional stable zones appear that “split” the higher radial depth stability lobes.

In the remainder of this section, we'll detail Poincaré maps, bifurcation diagrams, and stability maps. These are advanced tools that enable us to further explore milling behavior under both stable and unstable conditions.

6.4.1 *Poincaré Maps*

Poincaré maps may be developed using both experiments and simulations. For experiments, the displacement and velocity of the flexible tool (or workpiece) are recorded and then sampled once-per-tooth period. In simulation, the displacement and velocity are predicted, but the same sampling strategy is applied. By plotting the displacement versus velocity, the phase space trajectory can be observed in both cases. The once-per-tooth period samples are then superimposed and used to interrogate the milling process behavior. For stable cuts, the motion is periodic with the tooth period, so the sampled points repeat, and a single grouping of points is observed. When secondary Hopf instability occurs, the motion is quasiperiodic with tool rotation because the chatter frequency is (generally) incommensurate with the tooth passing frequency. In this case, the once-per-tooth sampled points do not repeat, and they form an elliptical distribution. For period-2 instability, the motion repeats only once every other cycle (i.e., it is a subharmonic of the forcing frequency). In this case, the once-per-tooth sampled points alternate between two solutions. For period- n ($n = 3, 4, \dots$) instability, the sampled points appear at n distinct locations in the Poincaré map.

6.4.2 *Bifurcation Diagrams*

In milling bifurcation diagrams, the once-per-tooth sampled displacement (vertical axis) or other process signal is plotted against the axial depth of cut (horizontal axis), a critical process control parameter. The transition in stability behavior from stable (at low axial depths) to period- n or secondary Hopf instability (at higher axial depths) is then directly observed. This diagram represents the information from multiple Poincaré maps over a range of axial depths, all at a single spindle speed. A stable cut appears as a single point (i.e., the sampled points repeat when only forced vibration is present). A period-2 bifurcation, on the other hand, appears as a pair of points offset from each other in the vertical direction. This represents the two collections of once-per-tooth sampled points from the Poincaré map. A secondary Hopf bifurcation is seen as a vertical distribution of points; this represents the range of once-per-tooth sampled displacements from the elliptical distribution of points in the Poincaré map.



For Instance

Interested readers can find a lot of interesting overlap between the literature on chatter in metal cutting and the mathematical literature on chaotic systems.

6.4.3 Stability Maps

Stability maps identify the limiting axial depth of cut (vertical axis) as a function of spindle speed (horizontal axis). Traditionally, this limit is represented as a single contour which separates stable (forced vibration only) from unstable (secondary Hopf or period- n) parameter combinations. This map provides a global view of the stability behavior, but does not identify the type of instability. Because a bifurcation diagram presents the stability behavior as a function of axial depth, but only at one spindle speed, it can be considered as a high-fidelity vertical slice of a stability map. Conversely, a stability map can be interpreted as a series of bifurcation diagrams where a binary switching function is used to categorize the behavior represented by the vertical distribution of once-per-tooth sampled points as either stable or unstable. The metric defined in Eq. 4.66 can serve as this switching function; it is small (close to zero) for stable behavior and large for unstable conditions.

Example 6.10 Experimental Investigation of Milling Bifurcation Behavior In this example, comparisons are made between time domain simulation predictions and milling experiments for multiple setups; various period- n bifurcations are presented.³ A single degree of freedom (SDOF) flexure was used to define the system dynamics, where the SDOF flexure was much less stiff than the cutting tool [48]. The flexure setup also simplified the measurement instrumentation; see Sect. 2.1.4. The flexure motions were measured using a capacitance probe, laser vibrometer, and low-mass accelerometer. To enable once-per-tooth sampling of the vibration signals, a laser tachometer was used. A section of reflective tape was attached to the tool-holder, and the corresponding (digital) tachometer signal was used to perform the periodic sampling [54, 55].

The cutting tool was a 19.1 mm diameter, single flute carbide square endmill (30 deg helix angle). Modal impact testing verified that the cutting tool dynamic stiffness (1055 Hz natural frequency, 0.045 viscous damping ratio, and 4.2×10^7 N/m stiffness) was much higher than the SDOF flexure. Cutting tests were completed using the Fig. 6.38 setup. The measured flexure dynamics and cutting conditions are listed in Table 6.1. Each cut of the 6061-T6 aluminum workpiece was performed using a feed per tooth of 0.10 mm/tooth. The aluminum alloy cutting force coefficients were $k_t = 792 \times 10^6$ N/m², $k_n = 352 \times 10^6$ N/m², $k_{te} = 26 \times 10^3$ N/m, and $k_{ne} = 28 \times 10^3$ N/m.

³T. Schmitz recognizes the significant contributions of A. Honeycutt to this experimental study.

Fig. 6.38 Milling experimental setup with laser vibrometer (LV), piezoelectric accelerometer (PA), laser tachometer (LT), and capacitance probe (CP)

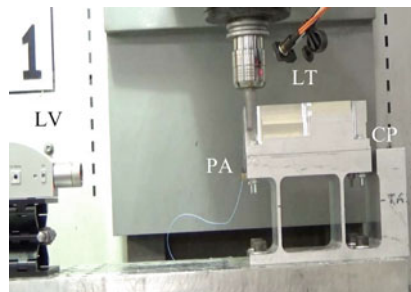


Table 6.1 Cutting conditions and flexure dynamics for experiments

Period- <i>n</i>	Cutting conditions			SDOF flexure dynamics		
	Spindle speed (rpm)	Axial depth, <i>b</i> (mm)	Radial depth (mm)	Stiffness (N/m)	Natural frequency (Hz)	Viscous damping ratio (%)
2	3486	2.0	1.0	9.0×10^5	83.0	2.00
3	3800	4.5	5.0	5.6×10^6	163.0	1.08
8	3310	15.0	2.0	2.1×10^6	130.1	1.47

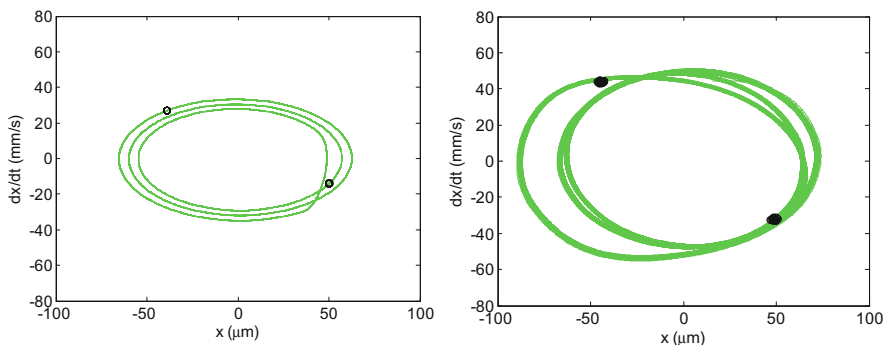


Fig. 6.39 Poincaré map for period-2 bifurcation. (Left) simulation, (right) experiment

Results for period-2, period-3, and period-8 bifurcations are displayed in Figs. 6.39 through 6.41. In each figure, the left plot shows the simulated behavior and the right plot shows the experimental result, where the cut entry and exit transients were removed before plotting. Good agreement is observed in each case.

A bifurcation diagram for a spindle speed of 3800 rpm and radial depth of 5 mm was predicted by simulation, and then cuts were performed from 1 mm to 7 mm axial depths in 0.5 mm steps. The capacitance probe displacement signal was sampled using the laser tachometer to construct an experimental bifurcation diagram; Fig. 6.42 provides the comparison between prediction and experiment. For this axial depth of cut range, period-3 bifurcations were observed (see the period-3 entry from Table 6.1 for the flexure dynamics).

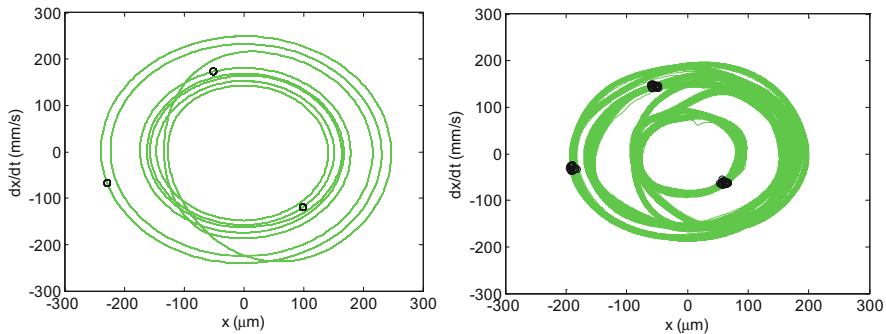


Fig. 6.40 Poincaré map for period-3 bifurcation. (Left) simulation, (right) experiment

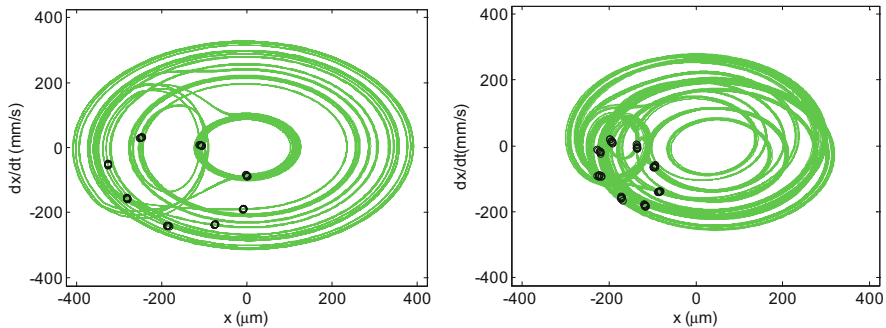


Fig. 6.41 Poincaré map for period-8 bifurcation. (Left) simulation, (right) experiment

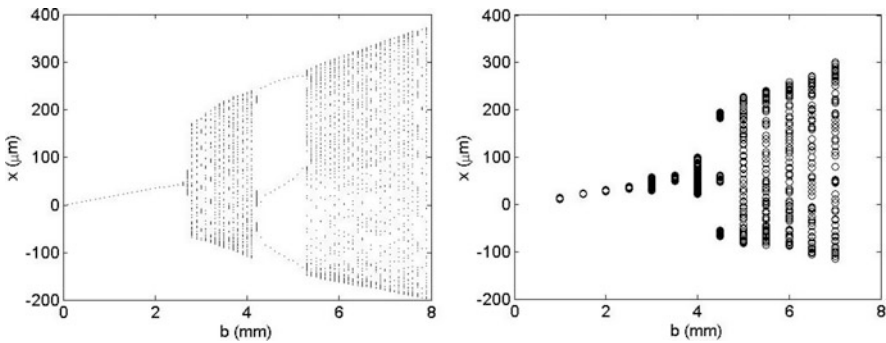


Fig. 6.42 Bifurcation diagram for 3800 rpm and 5 mm radial depth of cut. (Left) simulation, (right) experiment

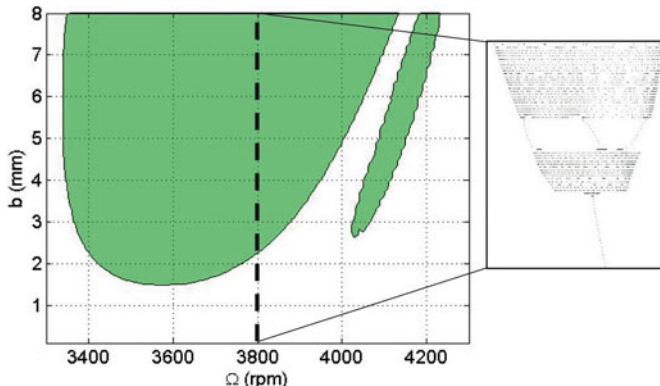


Fig. 6.43 Simulated stability map for period-3 experimental setup from Table 6.1 ($M = 1 \mu\text{m}$ contour). The transition from stable to unstable behavior occurs at approximately 2.6 mm for a spindle speed of 3800 rpm. The inset shows the bifurcation diagram progression at 3800 rpm from stable to quasiperiodic instability to period-3 and back to quasiperiodic behavior

A simulated stability map for the same axial depth of cut range as Fig. 6.42, but spindle speeds from 3300 rpm to 4300 rpm, is displayed in Fig. 6.43 (the same dynamics were again used). The diagram was constructed by completing time domain simulations over a grid with a spindle speed resolution of 10 rpm and an axial depth resolution of 0.1 mm. The initial transients were removed, and the M value for each simulation was calculated (see Eq. 4.66). An arbitrarily small value of 1 μm was selected to differentiate between stable and unstable parameter combinations; this contour is shown in Fig. 6.43 and identifies the stability limit. The transition from stable to unstable behavior at 3800 rpm observed in Fig. 6.42 is replicated. However, the transition from secondary Hopf to period-3 to secondary Hopf seen in the bifurcation diagram is not detailed in the stability map. To address this limitation, a subharmonic sampling approach used to automatically distinguish between the various bifurcation types in stability maps produced from time domain simulations is detailed in [56].

6.5 Uncertainty Propagation

In the stability lobe diagrams we've displayed so far, the stability boundary has been represented by a single line. This indicates step-like behavior, where the cut is stable below the line and unstable above. If the inputs were perfectly known and the theory exactly captured the physical behavior, then this step behavior could be true (although in practice, even experienced machinists could disagree over whether a particular cut was stable or unstable near the stability limit). However, no measured quantity, such as the cutting force coefficients or tool point frequency response function, is perfectly known. Instead, there are uncertainties associated with these

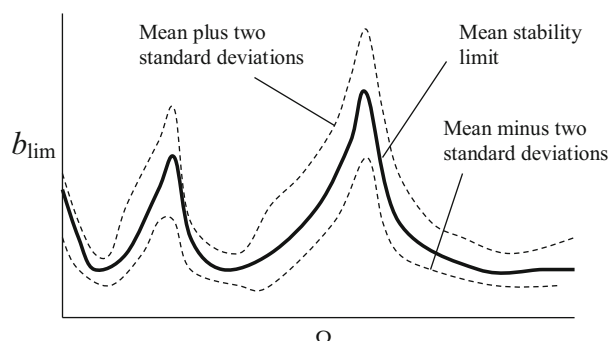
inputs. Additionally, the analytical stability algorithms incorporate approximations that limit their accuracy.

As stated in the National Institute of Standards and Technology (NIST) Technical Note 1297 [57], “the result of a measurement is only an approximation or estimate of the value of the specific quantity in question, that is, the measurand, and thus the result is complete only when accompanied by a quantitative statement of its uncertainty.” The inclusion of a defensible uncertainty statement enables the user to determine his/her confidence in the measurement and its usefulness in decision making. This concept can be extended to simulation results based on measured input quantities. Again, the user requires some indication of the reliability of the analysis output to gage its usefulness.

Guidelines for evaluating the uncertainty in measurement results are described in [57–60], for example. Often the measurand is not observed directly but is expressed as a mathematical function of multiple input quantities. In this case, the fundamental steps in uncertainty estimation are to define the measurand, identify the input uncertainty contributors and their distributions, and propagate the uncertainties through the measurand using either analytical (Taylor series expansion) or sampling (such as Monte Carlo or Latin hypercube) approaches.

Identification of the uncertainty in the stability limit for both the average tooth angle [1] and frequency domain [61] solutions is described in [62]. In this work, Monte Carlo simulation was applied to propagate uncertainties in the measured tool point FRF, cutting force coefficients (determined using the method outlined in Sect. 4.7), and radial depth of cut through the two approaches. In Monte Carlo simulation, random samples from the input variable distributions are selected and the output is computed over many iterations. The mean and standard deviation in the output are then reported. For the stability analyses, this requires that a new diagram is computed in each of the iterations. It is then necessary to identify the stability limit distribution at each spindle speed within the range of interest. The uncertainty is therefore spindle speed dependent and forms an envelope around the mean stability boundary as depicted in Fig. 6.44. To interpret the uncertainty region shown in the figure, we can state that it represents the axial depths, at the corresponding spindle speeds, where the cuts can either be stable or unstable. Above the upper bound, cuts

Fig. 6.44 Representation of two standard deviation uncertainty limits superimposed on the mean stability boundary determined from Monte Carlo simulation [62]



are expected to be unstable, while cuts should be stable below the lower bound (with 95% confidence due to the selection of $+/-$ two standard deviations about the mean). Naturally, we could apply the same approach to determining the uncertainty in surface location error predictions using the frequency domain technique described in Sect. 5.2.



In a Nutshell

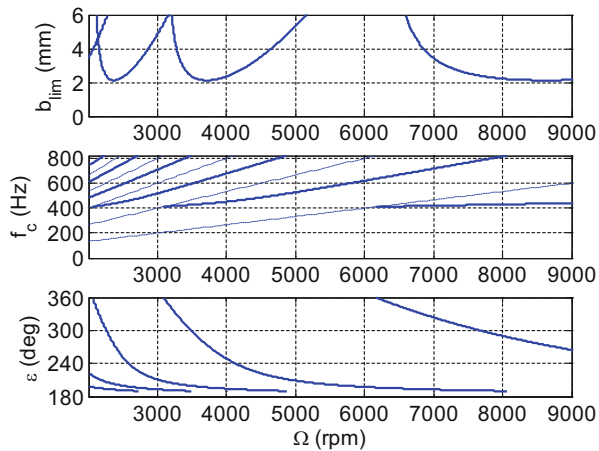
Uncertainties in the input data are part of the reason that simplified expressions for cutting forces and stability lobes are widely applied. It does not make much sense to attempt to model the location of the stability boundary with great accuracy when the force model coefficients, cutting geometry, and system dynamics are only approximately known. Certainly there is an incentive (as in all of engineering) to strive for improved accuracy in models, but it is also sensible to avoid implementing models that are more complicated than the uncertainties in the required inputs warrant.

Exercises

1. For parts (a) through (d), indicate the action of an automatic spindle speed regulation system for chatter avoidance in milling. The chatter avoidance system operates by: (1) sampling the sound signal produced by the cutting process using a microphone; (2) computing the Fourier transform of the microphone signal; and (3) analyzing the spectrum content. Based on the spectrum content, a new spindle speed is recommended if chatter is sensed.
 - (a) The cutter has eight teeth, the spindle speed is 3000 rpm, and the frequency spectrum shows a large peak at 400 Hz. The maximum available spindle speed is 7500 rpm.
 - (b) The cutter has six teeth, the spindle speed is 4200 rpm, and the frequency spectrum shows a large peak at 380 Hz. The maximum available spindle speed is 5000 rpm.
 - (c) The cutter has four teeth, the spindle speed is 10,000 rpm, and the frequency spectrum shows a large peak at 820 Hz. The maximum available spindle speed is 10,000 rpm.
 - (d) The cutter has four teeth, the spindle speed is 30,000 rpm, and the frequency spectrum shows a large peak at 1520 Hz. The maximum available spindle speed is 30,000 rpm. The spindle speed is regulated once and the spectrum of the second cut shows a large peak at 2280 Hz.
2. Calculate the ϵ value(s) in radians which correspond to coincidence(s) between the runout harmonics and chatter frequencies for the $N = 0$ lobe when using a cutter with three teeth.

3. Chatter was observed for milling at 7000 rpm with a 4 mm axial depth of cut. The helical square end mill had four teeth. Using the diagrams provided in Fig. 6.45, describe the automatic spindle speed regulation step(s) required to arrive at a stable cut. List the chatter frequency(s) encountered, the spindle speed(s) selected, and the corresponding ε value(s).

Fig. 6.45 Stability, chatter frequency, and undulation phase diagrams



4. Consider a 30% radial immersion up milling cut. The tool dynamics are described by two identical modes in both the x and y directions (assume the workpiece is rigid). The modal parameters are: $f_{n1} = 800$ Hz, $k_{q1} = 2 \times 10^7$ N/m, and $\zeta_{q1} = 0.05$; and $f_{n2} = 1000$ Hz, $k_{q2} = 1.5 \times 10^7$ N/m, and $\zeta_{q2} = 0.03$. The workpiece material is an aluminum alloy and it is machined with a four tooth, 12.7 mm diameter, 30 deg helix square endmill using a feed per tooth of 0.2 mm/tooth. The variable teeth spacing for this cutter is $\text{teeth} = [0 \ 95 \ 180 \ 275]$ deg. The cutting force coefficients are $k_t = 520$ N/mm², $k_n = 300$ N/mm², and $k_{te} = k_{ne} = 0$. The axial depth of cut is 5 mm and the spindle speed is 15,000 rpm. Determine the roughness average (in μm) for runout values of $RO = [0 \ 0 \ -20 \ 0]$ μm using the cycloidal tool path time domain simulation. Compare this value to the roughness average with zero runout.
5. For a particular milling system, the diagrams in Fig. 6.46 are provided.
- How many teeth are on the milling cutter?
 - A cut is commanded with an axial depth of 7 mm at a spindle speed of 10,000 rpm. If the cut is stable, provide the phase and spectral content. If the cut is unstable, describe the spindle speed regulation(s) to obtain a stable cut. For each regulation (until stable conditions are achieved), list the phase and spectral content. Mark the relevant points on each of the three diagrams in Fig. 6.46.

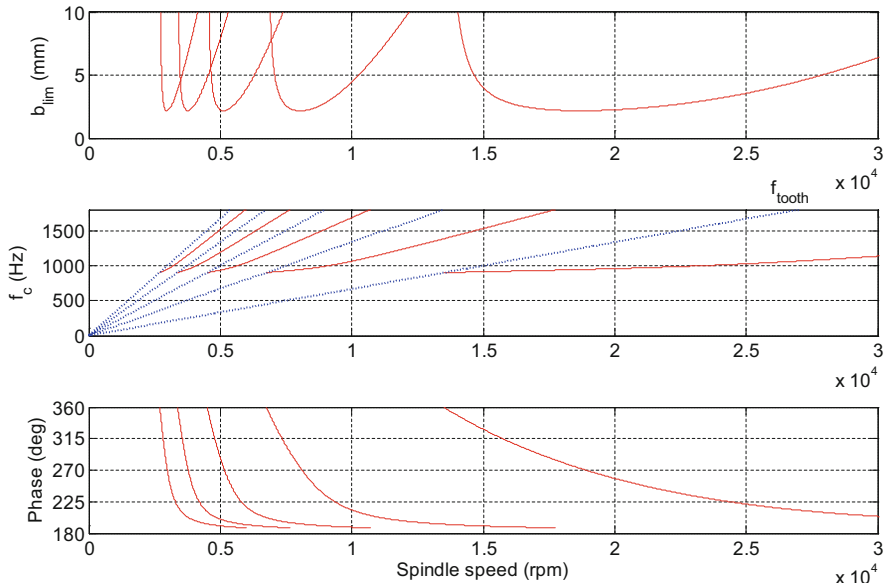


Fig. 6.46 Stability, chatter frequency, and undulation phase diagrams

References

1. Tlusty, J., Zaton, W., & Ismail, F. (1983). Stability lobes in milling. *Annals of the CIRP*, 32(1), 309–313.
2. Smith, S., & Tlusty, J. (1992). Stabilizing chatter by automatic spindle speed regulation. *Annals of the CIRP*, 41(1), 433–436.
3. Delio, T., Tlusty, J., & Smith, S. (1992). Use of audio signals for chatter detection and control. *Journal of Engineering for Industry*, 114, 146–157.
4. Smith, D., Smith, S., & Tlusty, J. (1998). High performance milling torque sensor. *Journal of Manufacturing Science and Engineering*, 120(3), 504–514.
5. Smith, S., & Delio, T. (1992). Sensor-based chatter detection and avoidance by spindle speed selection. *Journal of Dynamic Systems, Measurement, and Control*, 114(3), 486–492.
6. Schmitz, T., Davies, M., Medicus, K., & Snyder, J. (2001). Improving high-speed machining material removal rates by rapid dynamic analysis. *Annals of the CIRP*, 50(1), 263–268.
7. Schmitz, T., Medicus, K., & Dutterer, B. (2002). Exploring once-per-revolution audio signal variance as a chatter indicator. *Machining Science and Technology*, 6(2), 215–233.
8. Schmitz, T. (2003). Chatter recognition by a statistical evaluation of the synchronously sampled audio signal. *Journal of Sound and Vibration*, 262(3), 721–730.
9. Cheng, C.-H., Duncan, G. S., & Schmitz, T. (2007). Rotating tool point frequency response prediction using RCSA. *Machining Science and Technology*, 11(3), 433–446.
10. Davies, M., Dutterer, B., Pratt, J., & Schaut, A. (1998). On the dynamics of high-speed milling with long, slender endmills. *Annals of the CIRP*, 47(1), 55–60.
11. Tlusty, J. (1959). Systems and methods of machine tool testing. *Microtechnic*, 13, 162–178.
12. Bryan, J., Clouser, R., & Holland, B. (1967). Spindle accuracy. *American Machinist*, 612, 149–164.
13. American National Standards Institute. (1985). *ANSI/ASME B89.3.4M, axes of rotation: methods for specifying and testing*. New York: American Society of Mechanical Engineers.

14. Smith, S., & Winfough, W. R. (1994). The effect of runout filtering on the identification of chatter in the audio spectrum of milling. *Transactions of the NAMRI/SME*, 22, 173–178.
15. Schmitz, T., Couey, J., Marsh, E., Mauntler, N., & Hughes, D. (2007). Runout effects in milling: surface finish, surface location error, and stability. *International Journal of Machine Tools and Manufacture*, 47, 841–851.
16. Kline, W., & DeVor, R. (1983). The effect of runout on cutting geometry and forces in end milling. *International Journal of Machine Tool Design and Research*, 23(2–3), 123–140.
17. Armarego, E., & Deshpande, N. (1991). Computerized end milling force predictions with cutting models allowing eccentricity and cutter deflections. *Annals of the CIRP*, 40(1), 25–29.
18. Altintas, Y., & Chan, P. (1992). In-process detection and suppression of chatter in milling. *International Journal of Machine Tools and Manufacture*, 32(3), 329–347.
19. Liang, S., & Wang, J. (1994). Milling force convolution modeling for identification of cutter axis offset. *International Journal of Machine Tools and Manufacture*, 34(8), 1177–1190.
20. Feng, H.-Y., & Menq, C.-H. (1994). The prediction of cutting forces in the ball-end milling process—I. Model formulation and model building procedure. *International Journal of Machine Tools and Manufacture*, 34(5), 697–710.
21. Feng, H.-Y., & Menq, C.-H. (1994). The prediction of cutting forces in the ball-end milling process—II. Cut geometry analysis and model verification. *International Journal of Machine Tools and Manufacture*, 34(5), 711–719.
22. Yan, D., El-Wardany, T., & Elbestawi, M. (1995). A multi-sensor strategy for tool failure detection in milling. *International Journal of Machine Tools and Manufacture*, 35(3), 383–398.
23. Stevens, A., & Liang, S. (1995). Runout rejection in end milling through two-dimensional repetitive force control. *Mechatronics*, 5(1), 1–13.
24. Hekman, K., & Liang, S. (1997). In-process monitoring of end milling cutter runout. *Mechatronics*, 7(1), 1–10.
25. Baek, D., Ko, T., & Kim, H. (1997). A dynamic surface roughness model for face milling. *Precision Engineering*, 20(3), 171–178.
26. Zheng, H., Li, X., Wong, Y., & Nee, A. (1999). Theoretical modeling and simulation of cutting forces in face milling with cutter runout. *International Journal of Machine Tools and Manufacture*, 39(12), 2003–2018.
27. Yun, W.-S., & Cho, D.-W. (2001). Accurate 3-D cutting force prediction using cutting condition independent coefficients in end milling. *International Journal of Machine Tools and Manufacture*, 41(4), 463–478.
28. Baek, D., Ko, T., & Kim, H. (2001). Optimization of feedrate in a face milling operation using a surface roughness model. *International Journal of Machine Tools and Manufacture*, 41(3), 451–462.
29. Mezentsev, O., Zhu, R., DeVor, R., Kapoor, S., & Kline, W. (2002). Use of radial forces for fault detection in tapping. *International Journal of Machine Tools and Manufacture*, 42(4), 479–488.
30. Ko, J., Yun, W.-S., Cho, D.-W., & Ehmann, K. F. (2002). Development of a virtual machining system, Part 1: Approximation of the size effect for cutting force prediction. *International Journal of Machine Tools and Manufacture*, 42(15), 1595–1605.
31. Ranganath, S., & Sutherland, J. (2002). An improved method for cutter runout modeling in the peripheral milling process. *Machining Science and Technology*, 6(1), 1–20.
32. Wang, J.-J., & Zheng, C. (2003). Identification of cutter offset in end milling without a prior knowledge of cutting coefficients. *International Journal of Machine Tools and Manufacture*, 43 (7), 687–697.
33. Lazoglu, I. (2003). Sculpture surface machining: a generalized model of ball-end milling force system. *International Journal of Machine Tools and Manufacture*, 43(5), 453–462.
34. Atabay, F., Lazoglu, I., & Altintas, Y. (2003). Mechanics of boring processes—Part II. Multi-insert boring heads. *International Journal of Machine Tools and Manufacture*, 43(5), 477–484.
35. Slavicek, J. (1965). The effect of irregular tooth pitch on stability of milling. In *Proceedings of the sixth machine tool design and research conference* (pp. 15–22). London: Pergamon Press

36. Vanherck, P. (1967). Increasing milling machine productivity by use of cutter with non-constant edge pitch. In *Proceedings of the 8th machine tool design and research conference* (pp. 947–960).
37. Doolan, P., Phadke, M. S., & Wu, S. (1975). Computer design of vibration free face milling cutters. *Journal of Engineering for Industry*, 97B(3), 925–930.
38. Doolan, P., Burney, F., & Wu, S. (1976). Computer design of a multi-purpose minimum vibration face milling cutter. *international journal of machine tool design and Research*, 16 (3), 187–192.
39. Tlusty, J., Ismail, F., & Zaton, W. (1983). Use of special milling cutters against chatter. *Transactions of the NAMRI/SME*, 11, 408–415.
40. Shirase, K., & Altintas, Y. (1995). Cutting force and dimensional surface error generation in peripheral milling with variable pitch helical end mills. *International Journal of Machine Tools and Manufacture*, 36(5), 567–584.
41. Choudhury, S., & Mathew, J. (1995). Investigations of the effect of non-uniform insert pitch on vibration during face milling. *International Journal of Machine Tools and Manufacture*, 35 (10), 1435–1444.
42. Altintas, Y., Engin, S., & Budak, E. (1999). Analytical stability prediction and design of variable pitch cutters. *Journal of Manufacturing Science and Engineering*, 121, 173–178.
43. Budak, E. (2003). An analytical design method for milling cutters with nonconstant pitch to increase stability, Part 1: Theory, Part 2: Application. *Journal of Manufacturing Science and Engineering*, 123, 29–38.
44. Stone, B. (1970). The effect on the chatter behavior of cutters with different helix angles on adjacent teeth. In *Proceedings of the 11th international machine tool design and research conference* (pp. 169–180).
45. Davies, M., Pratt, J., Dutterer, B., & Burns, T. (2000). The stability of low radial immersion milling. *Annals of the CIRP*, 49(1), 37–40.
46. Davies, M., Pratt, J., Dutterer, B., & Burns, T. (2002). Stability prediction for low radial immersion milling. *Journal of Manufacturing Science and Engineering*, 124(2), 217–225.
47. Insperger, T., Mann, B., Stépàn, G., & Bayly, P. (2003). Stability of up-milling and down-milling, Part 1: Alternative analytical methods. *International Journal of Machine Tools and Manufacture*, 43(1), 25–34.
48. Mann, B., Insperger, T., Bayly, P., & Stépàn, G. (2003). Stability of up-milling and down-milling, Part 2: Experimental verification. *International Journal of Machine Tools and Manufacture*, 43(1), 35–40.
49. Campomanes, M., & Altintas, Y. (2003). An improved time domain simulation for dynamic milling at small radial immersions. *Journal of Manufacturing Science and Engineering*, 125(3), 416–422.
50. Merdol, S., & Altintas, Y. (2004). Multi frequency solution of chatter stability for low immersion milling. *Journal of Manufacturing Science and Engineering*, 126(3), 459–466.
51. Bayly, P., Halley, J., Mann, B., & Davies, M. (2004). Stability of interrupted cutting by temporal finite element analysis. *Journal of Manufacturing Science and Engineering*, 125(2), 220–225.
52. Mann, B., Bayly, P., Davies, M., & Halley, J. (2004). Limit cycles, bifurcations, and accuracy of the milling process. *Journal of Sound and Vibration*, 277(1–2), 31–48.
53. Govekar, E., Gradišek, J., Kalveram, M., Insperger, T., Weinert, K., Stépàn, G., & Grabec, I. (2005). On stability and dynamics of milling at small radial immersion. *Annals of the CIRP*, 54(1), 357–362.
54. Honeycutt, A., & Schmitz, T. (2016). A numerical and experimental investigation of period-n bifurcations in milling. *Journal of Manufacturing Science and Engineering*, 139(1), 011003.
55. Honeycutt, A., & Schmitz, T. (2016). Experimental validation of period-n bifurcations in milling. *Procedia Manufacturing*, 5, 362–374.
56. Honeycutt, A., & Schmitz, T. (2017). Milling stability interrogation by subharmonic sampling. *Journal of Manufacturing Science and Engineering*, 139(4), 041009.

57. Taylor, B., & Kuyatt, C. (1994). *Guidelines for evaluating and expressing the uncertainty of NIST measurement results*. NIST Technical Note 1297 1994 Edition.
58. International Standards Organization (ISO). (1993). *Guide to the expression of uncertainty in measurement* (Corrected and Reprinted 1995).
59. American National Standards Institute. (1997). ANSI/NCSL Z540-2-1997, US Guide to the Expression of Uncertainty in Measurement.
60. Bevington, P., & Robinson, D. (1992). *Data reduction and error analysis for the physical sciences* (2nd ed.). Boston, MA: WCB/McGraw-Hill.
61. Altintas, Y., & Budak, E. (1995). Analytical prediction of stability lobes in milling. *Annals of the CIRP*, 44(1), 357–362.
62. Duncan, G. S., Kurdi, M., Schmitz, T., & Snyder, J. (2006). Uncertainty propagation for selected analytical milling stability limit analyses. *Transactions of the NAMRI/SME*, 34, 17–24.
63. Weisstein, E. “*Incommensurate*” from MathWorld—A Wolfram Web Resource. Retrieved May, 2008, from <http://mathworld.wolfram.com/Incommensurate.html>
64. Weisstein, E. “*Bifurcation*” from MathWorld—A Wolfram Web Resource. Retrieved May, 2008, from <http://mathworld.wolfram.com/Bifurcation.html>

Chapter 7

Tool Point Dynamics Prediction



The secret to creativity is knowing how to hide your sources.

—Albert Einstein

In Chaps. 4 through 6, we analyzed several aspects of milling with the ultimate goal of enabling a priori stability and surface location error predictions in order to improve productivity. We described frequency domain solutions that offer closed-form expressions for both stability (Chap. 4) and surface location error (Chap. 5). The primary inputs to these analyses are the force model coefficients and tool point frequency response function, or FRF. In this chapter, we apply the receptance coupling technique to prediction of the tool point response in order to complement the frequency domain process models detailed previously.¹ To support this effort, we include a brief review of Euler-Bernoulli beam theory and provide closed form solutions for the direct and cross receptances (FRFs) under free-free and clamped-free boundary conditions. We also review a receptance coupling approach for compensating the effects of accelerometer-cable mass on measured FRFs in order to increase accuracy. Finally, we apply the receptance coupling technique to model variations in thin rib dynamics during machining.

¹If the tool point FRF is known, the modal fitting procedure described in Sect. 2.5 can be applied to identify the modal parameters required for time domain simulation as well.

7.1 Motivation

While impact testing (Sect. 2.6) provides a convenient approach to obtaining the tool-holder-spindle-machine² FRF (typically measured at the tool point), it requires a separate set of measurements for each assembly. For example, if there are 25 tools in a machine tool's magazine, then a minimum of 50 measurements are required (one each for the x and y directions, assuming the axial compliance in the z direction is negligible). Further, if the tool insertion length is modified due to new requirements or inadequate control during tooling setup, the measurements must be repeated for that tool-holder combination. This requirement for multiple measurements certainly does not preclude the application of the process analyses we've discussed in production environments. However, the required time and cost for impact testing do pose an obstacle to convenient implementation at the shop floor level.



In a Nutshell

Although FRF measurements provide us with essential information, they are specific to the setup. The tool-holder-spindle-machine FRF changes strongly with tool length and diameter, for example. Unfortunately, modern CNC systems encourage poor setup repeatability by including tool length offset correction. Although this may enable you to put the tool point at the correct geometric location, it also leads to almost certain variability in day-to-day machining performance due to the change in assembly dynamics.

While no predictive approach replaces actual data, the requirement for a separate measurement of every conceivable setup can lead to a substantial number of measurements. In this chapter we describe a new method that eliminates the need to measure each tool-holder in a particular spindle. By combining measurements of a simple artifact inserted in the spindle in question with models of tools and holders, we can perform off-line FRF predictions for a range of tools.

7.2 Basic Receptance Coupling

Rather than considering the tool-holder-spindle-machine combination as a single assembly, we can view it as being composed of three separate entities, specifically the tool, the holder, and the spindle machine. Of these three, the tool and holder are convenient to model because they are not structurally complicated. The spindle machine, on the other hand, is much more challenging. Spindle dynamics modeling, often completed using finite element analysis, requires detailed knowledge of the mechanical design, bearing stiffness values (which depend on the assembly

²The workpiece can also be the source of significant dynamic compliance. However, we will limit our discussions to situations where the workpiece can be assumed to be rigid relative to the tool-holder-spindle-machine assembly.

tolerances), and damping levels.³ For commercial machining centers, the spindle design is often proprietary or unavailable to the end user and the bearing stiffness values are difficult to obtain. Also, the first principle estimates of the spindle damping remain an active research area. Comparable problems are encountered in modeling the machine dynamics, particularly obtaining the damping values, which often depend on multiple energy dissipation mechanisms and locations. Even more problematic, different lengths and diameters of tools may activate these mechanisms by differing amounts (especially within the spindle).



For Instance

A short, large diameter tool may be very stiff and emphasize the spindle modes in the assembly FRF. The primary damping source in this case would be the spindle bearings and interface between the spindle and motor rotor. If the tool is long and slender, by contrast, the spindle may appear nearly rigid (but not always!).⁴ This tool geometry would generally emphasize the damping in the tool-tool-holder-spindle interfaces with relatively less energy dissipated by the spindle bearings.

This leads us to a scenario where we can consider modeling those components that lend themselves to this activity (the tool and holder) and measuring the difficult-to-model component (the spindle-machine).⁵ Additionally, rather than describing the modeled and measured parts, or substructures, using modal parameters, for example, it is sensible to develop substructure FRFs since the assembly FRF is a primary input for the analytical milling process analyses. A convenient approach for joining these substructure FRFs to obtain the assembly response is receptance coupling [1, 2] or receptance coupling substructure analysis (RCSA) as referenced in recent literature [3–12]. Prior to detailing RCSA for tool point FRF prediction, let's examine receptance coupling solutions for some simple dynamic systems.

7.2.1 Two Component Rigid Coupling

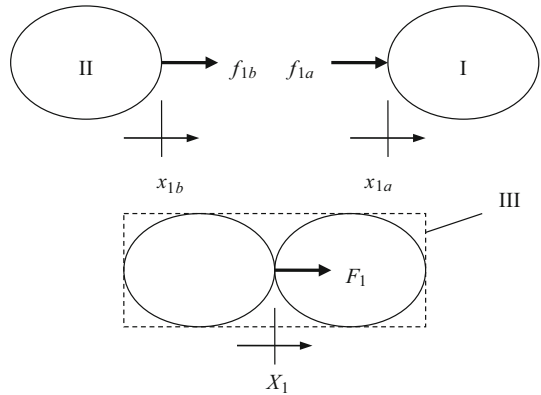
As shown in Fig. 7.1, two components, I and II, are to be rigidly coupled to form assembly III. The coupling coordinates are x_{1a} and x_{1b} for the two substructures I and II, respectively. The corresponding assembly coordinate, X_1 , is located at the same physical location as x_{1a} and x_{1b} after they are joined. An attractive aspect of receptance coupling is that the component FRFs are only required at the coupling locations and any point where the assembly response is to be predicted [13–15].

³T. Schmitz acknowledges conversations with N. Arakere regarding dynamic modeling of rotating systems.

⁴See Example 7.4.

⁵T. Schmitz recognizes discussions with J. Pratt in forming this observation.

Fig. 7.1 Rigid coupling of components I and II to form assembly III. The force F_1 is applied to the assembly in order to determine H_{11}



Therefore, the direct (see Sect. 2.4) assembly response, $H_{11}(\omega) = \frac{X_1}{F_1}$, due to a harmonic force applied at coordinate X_1 can be fully described using the direct component receptances $h_{1a1a}(\omega) = \frac{x_{1a}}{f_{1a}}$ and $h_{1b1b}(\omega) = \frac{x_{1b}}{f_{1b}}$ obtained from harmonic forces applied at x_{1a} and x_{1b} , respectively. Note that we've used upper case variables to designate assembly terms and lower case variables to identify component terms.

To determine the assembly response, we must first state the compatibility condition, $x_{1b} - x_{1a} = 0$, which represents the rigid coupling between component coordinates x_{1a} and x_{1b} . We can therefore write $x_{1b} = x_{1a} = X_1$ due to our decision to locate assembly coordinate X_1 at the (rigid) coupling point. We must also define the equilibrium condition, $f_{1a} + f_{1b} = F_1$, which equates the internal (component) and external (assembly) forces. Let's substitute for the displacements in the compatibility equation.

$$x_{1b} - x_{1a} = 0$$

$$h_{1b1b}f_{1b} - h_{1a1a}f_{1a} = 0$$

We next use the equilibrium condition, rewritten as $f_{1a} = F_1 - f_{1b}$, to eliminate f_{1a} . Rearranging enables us to solve for f_{1b} .

$$\begin{aligned} h_{1b1b}f_{1b} - h_{1a1a}F_1 + h_{1a1a}f_{1b} &= 0 \\ (h_{1a1a} + h_{1b1b})f_{1b} &= h_{1a1a}F_1 \\ f_{1b} &= (h_{1a1a} + h_{1b1b})^{-1}h_{1a1a}F_1 \end{aligned}$$

Now that we have f_{1b} , we can again use the equilibrium condition to determine f_{1a} .

$$\begin{aligned} f_{1a} &= F_1 - f_{1b} \\ f_{1a} &= \left(1 - (h_{1a1a} + h_{1b1b})^{-1}h_{1a1a}\right)F_1 \end{aligned}$$

We solve for H_{11} as shown in Eq. 7.1. This equation gives the direct assembly response at the coupling coordinate, X_1 , as a function of the component receptances.

These frequency dependent, complex valued receptances may have any number of modes. There are no restrictions on the relationship between the number of modes and coordinates as with modal analysis (i.e., we saw in Sect. 2.4 that the number of modeled modes and coordinates must be equal to obtain square matrices when using modal techniques).

$$H_{11} = \frac{X_1}{F_1} = \frac{x_{1a}}{F_1} = \frac{h_{1a1a}f_{1a}}{F_1} = h_{1a1a} - h_{1a1a}(h_{1a1a} + h_{1b1b})^{-1}h_{1a1a} \quad (7.1)$$



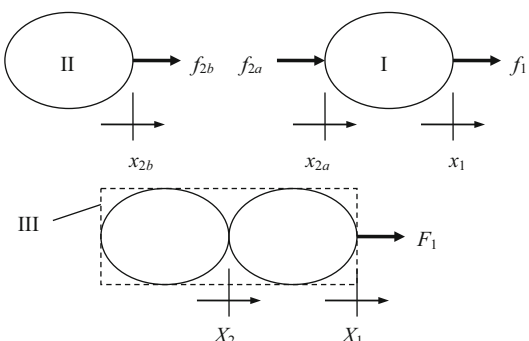
In a Nutshell

The spindle-machine FRF is difficult to model from first principles or material properties, primarily due to damping and nonlinearities. We accept this fact and determine the spindle-machine FRF by measurement.

As we've discussed, the FRF shows the real and imaginary parts of the frequency dependent motion at a selected coordinate in response to a force. The tool and holder, on the other hand, are easier to manage. They can be modeled using beam theory with reasonable accuracy. The measured and modeled FRFs are then connected at the appropriate coordinate and this is the essence of receptance coupling. Using this approach, the FRF of the assembled structure can be predicted at any coordinate on the modeled portion of the assembly.

Similarly, we can predict the assembly response at another coordinate, not coincident with the coupling point, by defining the component receptance at the desired location. Consider Fig. 7.2, where the direct assembly response at X_1 is again desired, but this location is now at another point on component I. We again assume x_1 and X_1 are collocated before and after coupling. The new coupling coordinates at the rigid coupling point are x_{2a} and x_{2b} . The component receptances corresponding to Fig. 7.2 are $h_{11} = \frac{x_1}{f_1}$ and $h_{2a2a} = \frac{x_{2a}}{f_{2a}}$ for I and $h_{2b2b} = \frac{x_{2b}}{f_{2b}}$ for II. The compatibility condition for the rigid coupling is $x_{2b} - x_{2a} = 0$ and we can therefore write $x_{2a} = x_{2b} = X_2$. Also, $x_1 = X_1$. The equilibrium conditions are $f_{2a} + f_{2b} = 0$ and $f_1 = F_1$.

Fig. 7.2 Example showing rigid coupling of components I and II to form assembly III. The force F_1 is applied to the assembly in order to determine H_{11} and H_{21}



To determine $H_{11} = \frac{x_1}{F_1}$, we'll first write the component displacements. For I, we now have two forces acting on the body, so the displacements are:

$$x_1 = h_{11}f_1 + h_{12a}f_{2a} \quad \text{and} \quad x_{2a} = h_{2a1}f_1 + h_{2a2a}f_{2a}. \quad (7.2)$$

For II, we have $x_{2b} = h_{2b2b}f_{2b}$. Substitution into the compatibility condition gives:

$$h_{2b2b}f_{2b} - h_{2a1}f_1 - h_{2a2a}f_{2a} = 0. \quad (7.3)$$

We apply the equilibrium conditions to replace f_1 and eliminate f_{2a} ($f_{2a} = -f_{2b}$).

$$h_{2b2b}f_{2b} - h_{2a1}F_1 + h_{2a2a}f_{2b} = 0 \quad (7.4)$$

This enables us to group terms and solve for f_{2b} . Specifically, we have that $f_{2b} = (h_{2a2a} + h_{2b2b})^{-1}h_{2a1}F_1$. Therefore, we can also write $f_{2a} = -(h_{2a2a} + h_{2b2b})^{-1}h_{2a1}F_1$. Substitution of this force value into the H_{11} expression gives us the desired result; see Eq. 7.5. Again, the assembly response is written as a function of the component direct (h_{11} , h_{2a2a} , and h_{2b2b}) and cross (h_{12a} and h_{2a1}) receptances.

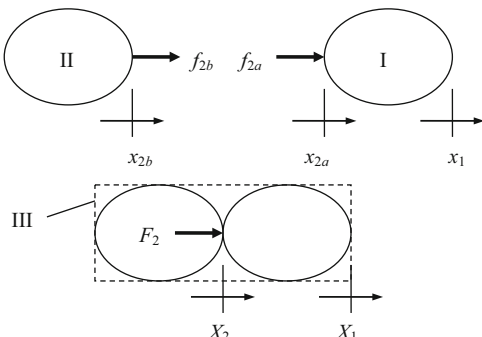
$$\begin{aligned} H_{11} &= \frac{X_1}{F_1} = \frac{x_1}{F_1} = \frac{h_{11}f_1 + h_{12a}f_{2a}}{F_1} = \frac{h_{11}f_1 - h_{12a}(h_{2a2a} + h_{2b2b})^{-1}h_{2a1}F_1}{F_1} \\ H_{11} &= \frac{h_{11}F_1 - h_{12a}(h_{2a2a} + h_{2b2b})^{-1}h_{2a1}F_1}{F_1} = h_{11} - h_{12a}(h_{2a2a} + h_{2b2b})^{-1}h_{2a1} \end{aligned} \quad (7.5)$$

We can also use f_{2a} to determine the cross receptance H_{21} . See Eq. 7.6.

$$\begin{aligned} H_{21} &= \frac{X_2}{F_1} = \frac{x_{2a}}{F_1} = \frac{h_{2a1}f_1 + h_{2a2a}f_{2a}}{F_1} = \frac{h_{2a1}f_1 - h_{2a2a}(h_{2a2a} + h_{2b2b})^{-1}h_{2a1}F_1}{F_1}, \\ H_{21} &= \frac{h_{2a1}F_1 - h_{2a2a}(h_{2a2a} + h_{2b2b})^{-1}h_{2a1}F_1}{F_1} = h_{2a1} - h_{2a2a}(h_{2a2a} + h_{2b2b})^{-1}h_{2a1}. \end{aligned} \quad (7.6)$$

In an analogous way, we can find the direct and cross receptances, H_{22} and H_{12} , respectively, due to a force applied at X_2 . See Fig. 7.3. The component receptances

Fig. 7.3 Example showing rigid coupling of components I and II to form assembly III. The force F_2 is applied to the assembly in order to determine H_{22} and H_{12}



are again $h_{11} = \frac{x_1}{f_1}$ and $h_{2a2a} = \frac{x_{2a}}{f_{2a}}$ for I and $h_{2b2b} = \frac{x_{2b}}{f_{2b}}$ for II. The compatibility condition for the rigid coupling remains as $x_{2b} - x_{2a} = 0$. However, the equilibrium condition is $f_{2a} + f_{2b} = F_2$.

To determine $H_{22} = \frac{X_2}{F_2}$, we begin by writing the component displacements. For I, the displacements are:

$$x_1 = h_{12a}f_{2a} \quad \text{and} \quad x_{2a} = h_{2a2a}f_{2a}. \quad (7.7)$$

For II, we have $x_{2b} = h_{2b2b}f_{2b}$. Substitution in the compatibility condition gives:

$$h_{2b2b}f_{2b} - h_{2a2a}f_{2a} = 0. \quad (7.8)$$

We apply the equilibrium condition, $f_{2a} = F_2 - f_{2b}$, to eliminate f_{2a} in Eq. 7.8.

$$h_{2b2b}f_{2b} - h_{2a2a}F_2 + h_{2a2a}f_{2b} = 0 \quad (7.9)$$

This enables us to group terms and solve for f_{2b} . We find that $f_{2b} = (h_{2a2a} + h_{2b2b})^{-1}h_{2a2a}F_2$. Again using the equilibrium condition, we can write $f_{2a} = (1 - (h_{2a2a} + h_{2b2b})^{-1}h_{2a2a})F_2$. Equation 7.10 gives the desired H_{22} expression.

$$\begin{aligned} H_{22} &= \frac{X_2}{F_2} = \frac{x_{2a}}{F_2} = \frac{h_{2a2a}f_{2a}}{F_2} = \frac{h_{2a2a}\left(1 - (h_{2a2a} + h_{2b2b})^{-1}h_{2a2a}\right)F_2}{F_2} \\ H_{22} &= \frac{h_{2a2a}F_2 - h_{2a2a}(h_{2a2a} + h_{2b2b})^{-1}h_{2a2a}F_2}{F_2} = h_{2a2a} \\ &\quad - h_{2a2a}(h_{2a2a} + h_{2b2b})^{-1}h_{2a2a} \end{aligned} \quad (7.10)$$

We use f_{2a} to find the cross receptance H_{12} as well. See Eq. 7.11.

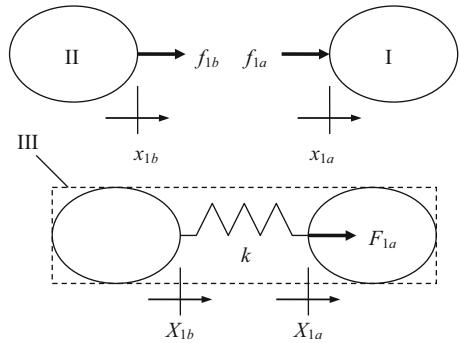
$$\begin{aligned} H_{12} &= \frac{X_1}{F_2} = \frac{x_1}{F_2} = \frac{h_{12a}f_{2a}}{F_2} = \frac{h_{12a}\left(1 - (h_{2a2a} + h_{2b2b})^{-1}h_{2a2a}\right)F_2}{F_2} \\ H_{12} &= h_{12a} - h_{12a}(h_{2a2a} + h_{2b2b})^{-1}h_{2a2a} \end{aligned} \quad (7.11)$$

7.2.2 Two Component Flexible Coupling

Let's continue with the system shown in Fig. 7.1, but now couple the two components through a linear spring, described by the constant k . This is displayed in Fig. 7.4. The component receptances are $h_{1a1a} = \frac{x_{1a}}{f_{1a}}$ and $h_{1b1b} = \frac{x_{1b}}{f_{1b}}$ and the equilibrium condition is $f_{1a} + f_{1b} = F_{1a}$. These are analogous to the rigid coupling case. However, the compatibility condition now becomes:

$$k(x_{1b} - x_{1a}) = -f_{1b}. \quad (7.12)$$

Fig. 7.4 Flexible coupling of components I and II to form assembly III. The force F_{1a} is applied to the assembly in order to determine H_{1a1a} and H_{1b1a}



Because the component and assembly coordinates are coincident, we have that $x_{2a} = X_{2a}$ and $x_{2b} = X_{2b}$. To determine $H_{1a1a} = \frac{X_{1a}}{F_{1a}}$, let's first substitute the component displacements in the compatibility condition. See Eq. 7.13.

$$k(h_{1b1b}f_{1b} - h_{1a1a}f_{1a}) = -f_{1b} \quad (7.13)$$

Using the equilibrium condition, $f_{1a} = F_{1a} - f_{1b}$, we can eliminate f_{1a} to obtain the equation for f_{1b} .

$$\begin{aligned} k(h_{1b1b}f_{1b} - h_{1a1a}F_{1a} + h_{1a1a}f_{1b}) &= -f_{1b} \\ kh_{1b1b}f_{1b} - kh_{1a1a}F_{1a} + kh_{1a1a}f_{1b} &= -f_{1b} \\ \left(h_{1a1a} + h_{1b1b} + \frac{1}{k} \right) f_{1b} &= h_{1a1a}F_{1a} \\ f_{1b} &= \left(h_{1a1a} + h_{1b1b} + \frac{1}{k} \right)^{-1} h_{1a1a}F_{1a} \end{aligned}$$

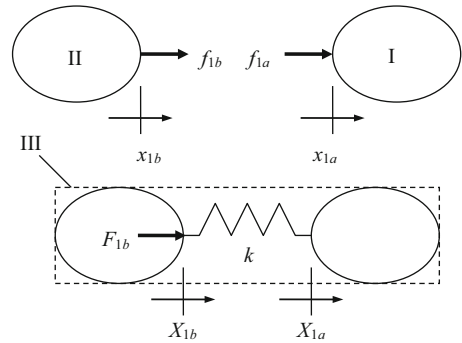
Using f_{1b} and the equilibrium condition, we find that $f_{1a} = (1 - (h_{1a1a} + h_{1b1b} + \frac{1}{k})^{-1} h_{1a1a})F_{1a}$. Substitution then yields the direct assembly receptance H_{1a1a} as shown in Eq. 7.14. We can see that this equation simplifies to Eq. 7.1 as k approaches infinity (rigid connection).

$$\begin{aligned} H_{1a1a} &= \frac{X_{1a}}{F_{1a}} = \frac{x_{1a}}{F_{1a}} = \frac{h_{1a1a}f_{1a}}{F_{1a}} = \frac{h_{1a1a}\left(1 - (h_{1a1a} + h_{1b1b} + \frac{1}{k})^{-1} h_{1a1a}\right)F_{1a}}{F_{1a}} \\ H_{1a1a} &= h_{1a1a} - h_{1a1a}\left(h_{1a1a} + h_{1b1b} + \frac{1}{k} \right)^{-1} h_{1a1a} \end{aligned} \quad (7.14)$$

The cross receptance due to the force F_{1a} is provided in Eq. 7.15.

$$\begin{aligned} H_{1b1a} &= \frac{X_{1b}}{F_{1a}} = \frac{x_{1b}}{F_{1a}} = \frac{h_{1b1b}f_{1b}}{F_{1a}} = \frac{h_{1b1b}(h_{1a1a} + h_{1b1b} + \frac{1}{k})^{-1} h_{1a1a}F_{1a}}{F_{1a}} \\ H_{1b1a} &= h_{1b1b}\left(h_{1a1a} + h_{1b1b} + \frac{1}{k} \right)^{-1} h_{1a1a} \end{aligned} \quad (7.15)$$

Fig. 7.5 Flexible coupling of components I and II to form assembly III. The force F_{1b} is applied to the assembly in order to determine H_{1b1b} and H_{1a1b}



As shown in Fig. 7.5, we can alternately apply the assembly force to coordinate X_{1b} . The component receptances and displacements are unchanged, but the equilibrium condition is $f_{1a} + f_{1b} = F_{1b}$. Similarly, we modify the compatibility condition to be:

$$k(x_{1a} - x_{1b}) = -f_{1a}. \quad (7.16)$$

Substitution for the component displacements and f_{1b} (from the equilibrium condition) yields the expression for f_{1a} :

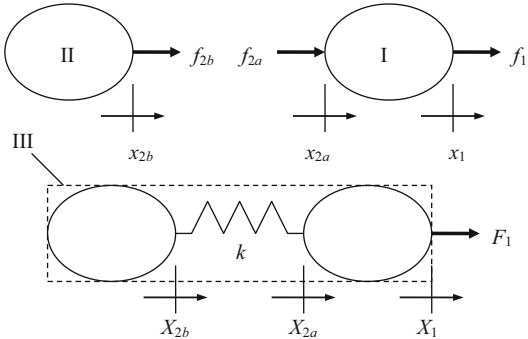
$$\begin{aligned} k(h_{1a1a}f_{1a} - h_{1b1b}F_{1b} + h_{1b1b}f_{1a}) &= -f_{1a} \\ kh_{1a1a}f_{1a} - kh_{1b1b}F_{1b} + kh_{1b1b}f_{1a} &= -f_{1a} \\ \left(h_{1a1a} + h_{1b1b} + \frac{1}{k}\right)f_{1a} &= h_{1b1b}F_{1b} \\ f_{1a} &= \left(h_{1a1a} + h_{1b1b} + \frac{1}{k}\right)^{-1}h_{1b1b}F_{1b} \end{aligned}$$

Again applying the equilibrium condition, $f_{1b} = F_{1b} - f_{1a}$, we obtain $f_{1b} = \left(1 - \left(h_{1a1a} + h_{1b1b} + \frac{1}{k}\right)^{-1}h_{1b1b}\right)F_{1b}$. Substitution then gives the assembly direct and cross receptances due to F_{1b} .

$$\begin{aligned} H_{1b1b} &= \frac{X_{1b}}{F_{1b}} = \frac{x_{1b}}{F_{1b}} = \frac{h_{1b1b}f_{1b}}{F_{1b}} = \frac{h_{1b1b}\left(1 - \left(h_{1a1a} + h_{1b1b} + \frac{1}{k}\right)^{-1}h_{1b1b}\right)F_{1b}}{F_{1b}} \\ H_{1b1b} &= h_{1b1b} - h_{1b1b}\left(h_{1a1a} + h_{1b1b} + \frac{1}{k}\right)^{-1}h_{1b1b} \end{aligned} \quad (7.17)$$

$$\begin{aligned} H_{1a1b} &= \frac{X_{1a}}{F_{1b}} = \frac{x_{1a}}{F_{1b}} = \frac{h_{1a1a}f_{1a}}{F_{1b}} = \frac{h_{1a1a}(h_{1a1a} + h_{1b1b} + \frac{1}{k})^{-1}h_{1b1b}F_{1b}}{F_{1b}} \\ H_{1a1b} &= h_{1a1a}\left(h_{1a1a} + h_{1b1b} + \frac{1}{k}\right)^{-1}h_{1b1b} \end{aligned} \quad (7.18)$$

Fig. 7.6 Flexible coupling of components I and II to form assembly III. The force F_1 is applied to the assembly in order to determine H_{11} , H_{2a1} , and H_{2b1}



Similar to the rigid connection example depicted in Fig. 7.2, we can again add another coordinate, not located at the coupling location, and apply the external force at that point. See Fig. 7.6. The component displacements are again $x_1 = h_{11}f_1 + h_{12a}f_{2a}$ and $x_{2a} = h_{2a1}f_1 + h_{2a2a}f_{2a}$ for substructure I and $x_{2b} = h_{2b2b}f_{2b}$ for substructure II. The equilibrium conditions are $f_{2a} + f_{2b} = 0$ and $f_1 = F_1$. The compatibility condition is:

$$k(x_{2b} - x_{2a}) = -f_{2b}. \quad (7.19)$$

As before, the component and assembly coordinates are coincident, so we have that $x_1 = X_1$, $x_{2a} = X_{2a}$, and $x_{2b} = X_{2b}$. To determine $H_{11} = \frac{x_1}{F_1}$, let's first substitute the component displacements in the compatibility condition. See Eq. 7.20.

$$k(h_{2b2b}f_{2b} - h_{2a1}f_1 - h_{2a2a}f_{2a}) = -f_{2b} \quad (7.20)$$

Using the equilibrium conditions, we can eliminate f_{2a} and replace f_1 with F_1 to obtain the equation for f_{2b} .

$$\begin{aligned} k(h_{2b2b}f_{2a} - h_{2a1}F_1 + h_{2a2a}f_{2b}) &= -f_{2b} \\ kh_{2b2b}f_{2b} - kh_{2a1}F_1 + kh_{2a2a}f_{2b} &= -f_{2b} \\ \left(h_{2a2a} + h_{2b2b} + \frac{1}{k} \right) f_{2b} &= h_{2a1}F_1 \\ f_{2b} &= \left(h_{2a2a} + h_{2b2b} + \frac{1}{k} \right)^{-1} h_{2a1}F_1 \end{aligned}$$

Applying the equilibrium condition $f_{2a} = -f_{2b}$, we obtain:

$$f_{2a} = -\left(h_{2a2a} + h_{2b2b} + \frac{1}{k} \right)^{-1} h_{2a1}F_1.$$

This enables us to write the direct and cross receptances as shown in Eqs. 7.21 and 7.22, respectively. We note that these equations simplify to the rigid coupling results provided in Eqs. 7.5 and 7.6 as k approaches infinity. The assembly cross receptance at coordinate X_{2b} is given by Eq. 7.23.

$$\begin{aligned}
H_{11} &= \frac{X_1}{F_1} = \frac{x_1}{F_1} = \frac{h_{11}f_1 + h_{12a}f_{2a}}{F_1} = \frac{h_{11}f_1 - h_{12a}(h_{2a2a} + h_{2b2b} + \frac{1}{k})^{-1}h_{2a1}F_1}{F_1} \\
H_{11} &= \frac{h_{11}F_1 - h_{12a}(h_{2a2a} + h_{2b2b} + \frac{1}{k})^{-1}h_{2a1}F_1}{F_1} = h_{11} - h_{12a}\left(h_{2a2a} + h_{2b2b} + \frac{1}{k}\right)^{-1}h_{2a1}
\end{aligned} \tag{7.21}$$

$$\begin{aligned}
H_{2a1} &= \frac{X_{2a}}{F_1} = \frac{x_{2a}}{F_1} = \frac{h_{2a1}f_1 + h_{2a2a}f_{2a}}{F_1} = \frac{h_{2a1}F_1 - h_{2a2a}(h_{2a2a} + h_{2b2b} + \frac{1}{k})^{-1}h_{2a1}F_1}{F_1} \\
H_{2a1} &= h_{2a1} - h_{2a2a}\left(h_{2a2a} + h_{2b2b} + \frac{1}{k}\right)^{-1}h_{2a1}
\end{aligned} \tag{7.22}$$

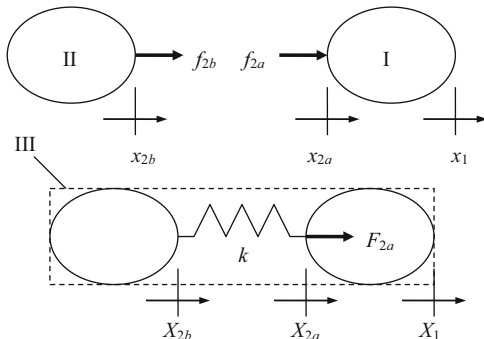
$$\begin{aligned}
H_{2b1} &= \frac{X_{2b}}{F_1} = \frac{x_{2b}}{F_1} = \frac{h_{2b2b}f_{2b}}{F_1} = \frac{h_{2b2b}(h_{2a2a} + h_{2b2b} + \frac{1}{k})^{-1}h_{2a1}F_1}{F_1} \\
H_{2b1} &= h_{2b2b}\left(h_{2a2a} + h_{2b2b} + \frac{1}{k}\right)^{-1}h_{2a1}
\end{aligned} \tag{7.23}$$

Let's now apply the external force, F_{2a} , to coordinate X_{2a} as shown in Fig. 7.7 in order to determine the assembly receptances H_{2a2a} , H_{2b2a} , and H_{12a} . The component displacements are $x_1 = h_{12a}f_{2a}$ and $x_{2a} = h_{2a2a}f_{2a}$ for substructure I and $x_{2b} = h_{2b2b}f_{2b}$ for substructure II. The equilibrium condition is $f_{2a} + f_{2b} = F_{2a}$ and the compatibility condition is:

$$k(x_{2b} - x_{2a}) = -f_{2b}. \tag{7.24}$$

We first determine the force f_{2b} by substituting the component displacements in Eq. 7.24 and replacing f_{2a} with $F_{2a} - f_{2b}$.

Fig. 7.7 Flexible coupling of components I and II to form assembly III. The force F_{2a} is applied to the assembly in order to determine H_{2a2a} , H_{2b2a} , and H_{12a}



$$\begin{aligned}
k(h_{2b2b}f_{2b} - h_{2a2a}F_{2a} + h_{2a2a}f_{2b}) &= -f_{2b} \\
kh_{2b2b}f_{2b} - kh_{2a2a}F_{2a} + kh_{2a2a}f_{2b} &= -f_{2b} \\
\left(h_{2a2a} + h_{2b2b} + \frac{1}{k} \right) f_{2b} &= h_{2a2a}F_{2a} \\
f_{2b} &= \left(h_{2a2a} + h_{2b2b} + \frac{1}{k} \right)^{-1} h_{2a2a}F_{2a}
\end{aligned}$$

Again using the equilibrium condition, we find the equation for f_{2a} .

$$f_{2a} = F_{2a} - f_{2b} = \left(1 - \left(h_{2a2a} + h_{2b2b} + \frac{1}{k} \right)^{-1} h_{2a2a} \right) F_{2a}$$

The direct and cross receptances for this situation (depicted in Fig. 7.7) are provided in Eqs. 7.25 through 7.27.

$$\begin{aligned}
H_{2a2a} &= \frac{X_{2a}}{F_{2a}} = \frac{x_{2a}}{F_{2a}} = \frac{h_{2a2a}f_{2a}}{F_{2a}} = \frac{h_{2a2a} \left(1 - \left(h_{2a2a} + h_{2b2b} + \frac{1}{k} \right)^{-1} h_{2a2a} \right) F_{2a}}{F_{2a}} \\
H_{2a2a} &= h_{2a2a} - h_{2a2a} \left(h_{2a2a} + h_{2b2b} + \frac{1}{k} \right)^{-1} h_{2a2a}
\end{aligned} \tag{7.25}$$

$$\begin{aligned}
H_{2b2a} &= \frac{X_{2b}}{F_{2a}} = \frac{x_{2b}}{F_{2a}} = \frac{h_{2b2b}f_{2b}}{F_{2b}} = \frac{h_{2b2b} \left(h_{2a2a} + h_{2b2b} + \frac{1}{k} \right)^{-1} h_{2a2a}F_{2a}}{F_{2a}} \\
H_{2b2a} &= h_{2b2b} \left(h_{2a2a} + h_{2b2b} + \frac{1}{k} \right)^{-1} h_{2a2a}
\end{aligned} \tag{7.26}$$

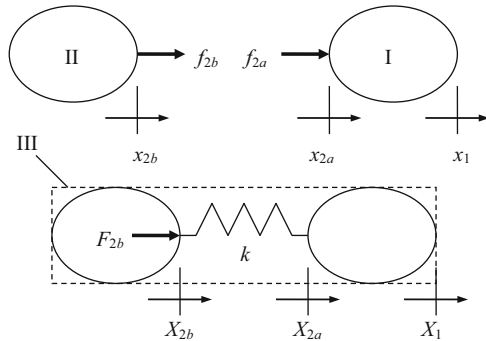
$$\begin{aligned}
H_{12a} &= \frac{X_1}{F_{2a}} = \frac{x_1}{F_{2a}} = \frac{h_{12a}f_{2a}}{F_{2a}} = \frac{h_{12a} \left(1 - \left(h_{2a2a} + h_{2b2b} + \frac{1}{k} \right)^{-1} h_{2a2a} \right) F_{2a}}{F_{2a}} \\
H_{12a} &= h_{12a} - h_{12a} \left(h_{2a2a} + h_{2b2b} + \frac{1}{k} \right)^{-1} h_{2a2a}
\end{aligned} \tag{7.27}$$

Our final scenario for the two component flexible coupling is shown in Fig. 7.8. Here, we apply the external force F_{2b} to coordinate X_{2b} to obtain the direct and cross assembly receptances H_{2b2b} , H_{2a2b} , and H_{12b} . The component displacements are the same as the previous case: $x_1 = h_{12a}f_{2a}$ and $x_{2a} = h_{2a2a}f_{2a}$ for substructure I and $x_{2b} = h_{2b2b}f_{2b}$ for substructure II. However, the equilibrium condition is modified to be $f_{2a} + f_{2b} = F_{2b}$ and the compatibility condition is rewritten as:

$$k(x_{2a} - x_{2b}) = -f_{2a}. \tag{7.28}$$

We find f_{2a} by substituting the component displacements in Eq. 7.28 and replacing f_{2b} with $F_{2a} - f_{2a}$.

Fig. 7.8 Flexible coupling of components I and II to form assembly III. The force F_{2b} is applied to the assembly in order to determine H_{2b2b} , H_{2a2b} , and H_{12b}



$$k(h_{2a2a}f_{2a} - h_{2b2b}F_{2b} + h_{2b2b}f_{2a}) = -f_{2a}$$

$$kh_{2a2a}f_{2a} - kh_{2b2b}F_{2b} + kh_{2b2b}f_{2a} = -f_{2a}$$

$$\left(h_{2a2a} + h_{2b2b} + \frac{1}{k} \right) f_{2a} = h_{2b2b}F_{2b}$$

$$f_{2a} = \left(h_{2a2a} + h_{2b2b} + \frac{1}{k} \right)^{-1} h_{2b2b}F_{2b}$$

Again using the equilibrium condition, we find the equation for f_{2b} .

$$f_{2b} = F_{2b} - f_{2a} = \left(1 - \left(h_{2a2a} + h_{2b2b} + \frac{1}{k} \right)^{-1} h_{2b2b} \right) F_{2b}$$

The direct and cross receptances for the case shown in Fig. 7.8 are given in Eqs. 7.29 through 7.31.

$$H_{2b2b} = \frac{X_{2b}}{F_{2b}} = \frac{x_{2b}}{F_{2b}} = \frac{h_{2b2b}f_{2b}}{F_{2b}} = \frac{h_{2b2b} \left(1 - \left(h_{2a2a} + h_{2b2b} + \frac{1}{k} \right)^{-1} h_{2b2b} \right) F_{2b}}{F_{2b}}$$

$$H_{2b2b} = h_{2b2b} - h_{2b2b} \left(h_{2a2a} + h_{2b2b} + \frac{1}{k} \right)^{-1} h_{2b2b}$$
(7.29)

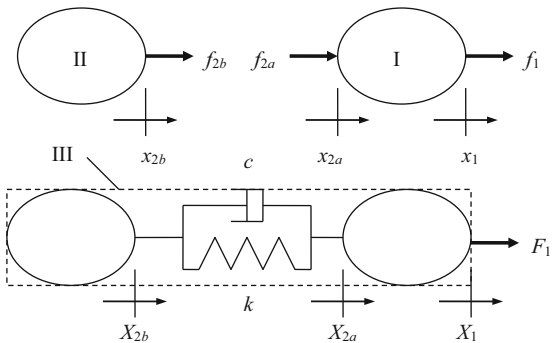
$$H_{2a2b} = \frac{X_{2a}}{F_{2b}} = \frac{x_{2a}}{F_{2b}} = \frac{h_{2a2a}f_{2a}}{F_{2b}} = \frac{h_{2a2a} \left(h_{2a2a} + h_{2b2b} + \frac{1}{k} \right)^{-1} h_{2b2b}F_{2b}}{F_{2b}}$$
(7.30)

$$H_{2a2b} = h_{2a2a} \left(h_{2a2a} + h_{2b2b} + \frac{1}{k} \right)^{-1} h_{2b2b}$$

$$H_{12b} = \frac{X_1}{F_{2b}} = \frac{x_1}{F_{2b}} = \frac{h_{12a}f_{2a}}{F_{2a}} = \frac{h_{12a} \left(h_{2a2a} + h_{2b2b} + \frac{1}{k} \right)^{-1} h_{2b2b}F_{2b}}{F_{2b}}$$
(7.31)

$$H_{12b} = h_{12a} \left(h_{2a2a} + h_{2b2b} + \frac{1}{k} \right)^{-1} h_{2b2b}$$

Fig. 7.9 Viscously damped, flexible coupling of components I and II to form assembly III. As with the two component flexible coupling case, the force F_1 is applied to the assembly in order to determine H_{11} , H_{2a1} , and H_{2b1}



7.2.3 Two Component Flexible, Damped Coupling⁶

As we discussed in Sect. 2.1, damping is always present in mechanical systems. Therefore, as a final step in our receptance coupling of bodies I and II to form assembly III, we can expand the model in Fig. 7.6 to include viscous damping at the coupling interface. See Fig. 7.9.



In a Nutshell

We recognize that the interface between the tool and holder, as with any common interface, is not rigid. Small relative motions between these bodies can produce damping.

The expressions for the component displacements and equilibrium conditions remain unchanged relative to the flexible coupling derivation when we add damping. However, the compatibility condition is now:

$$k(x_{2b} - x_{2a}) + i\omega c(x_{2b} - x_{2a}) = -f_{2b}, \quad (7.32)$$

where we have assumed harmonic motion so that the velocity dependent damping forces can be express in the form $i\omega cx$. Equation 7.32 can be rewritten as:

$$(k + i\omega c)(x_{2b} - x_{2a}) = -f_{2b}. \quad (7.33)$$

If we substitute the complex, frequency dependent variable k' for $(k + i\omega c)$, then we see that the compatibility equation takes the same form as shown in Eq. 7.19 and we can simply replace k in Eq. 7.21 with k' to obtain Eq. 7.34 [5]. This defines the direct FRF at coordinate X_1 on assembly III in Fig. 7.9. The same substitution can be made in the other assembly receptances derived for the two component flexible coupling in order to obtain the two component flexible, damped coupling results.

⁶T. Schmitz acknowledges collaboration with T. Burns in developing the damping analysis.

Table 7.1 Direct and cross receptances for two component coupling

C-type	Substructure coordinates		Receptances		Fig.	Eq.
	I	II	R-type			
R	x_{1a}	x_{1b}	D	$H_{11} = h_{1a1a} - h_{1a1a}(h_{1a1a} + h_{1b1b})^{-1}h_{1a1a}$	7.1	7.1
R	x_1, x_{2a}	x_{2b}	D	$H_{11} = h_{11} - h_{12a}(h_{2a2a} + h_{2b2b})^{-1}h_{2a1}$	7.2	7.5
			C	$H_{21} = h_{2a1} - h_{2a2a}(h_{2a2a} + h_{2b2b})^{-1}h_{2a1}$		7.6
			D	$H_{22} = h_{2a2a} - h_{2a2a}(h_{2a2a} + h_{2b2b})^{-1}h_{2a2a}$	7.3	7.10
			C	$H_{12} = h_{12a} - h_{12a}(h_{2a2a} + h_{2b2b})^{-1}h_{2a2a}$		7.11
			D	$H_{1a1a} = h_{1a1a} - h_{1a1a}(h_{1a1a} + h_{1b1b} + \frac{1}{k})^{-1}h_{1a1a}$	7.4	7.14
F	x_{1a}	x_{1b}	C	$H_{1b1a} = h_{1b1b}(h_{1a1a} + h_{1b1b} + \frac{1}{k})^{-1}h_{1a1a}$		7.15
			D	$H_{1b1b} = h_{1b1b} - h_{1b1b}(h_{1a1a} + h_{1b1b} + \frac{1}{k})^{-1}h_{1b1b}$	7.5	7.17
			C	$H_{1a1b} = h_{1a1a}(h_{1a1a} + h_{1b1b} + \frac{1}{k})^{-1}h_{1b1b}$		7.18
			D	$H_{11} = h_{11} - h_{12a}(h_{2a2a} + h_{2b2b} + \frac{1}{k})^{-1}h_{2a1}$	7.6	7.21
F	x_1, x_{2a}	x_{2b}	C	$H_{2a1} = h_{2a1} - h_{2a2a}(h_{2a2a} + h_{2b2b} + \frac{1}{k})^{-1}h_{2a1}$		7.22
			C	$H_{2b1} = h_{2b2b}(h_{2a2a} + h_{2b2b} + \frac{1}{k})^{-1}h_{2a1}$		7.23
			D	$H_{2a2a} = h_{2a2a} - h_{2a2a}(h_{2a2a} + h_{2b2b} + \frac{1}{k})^{-1}h_{2a2a}$	7.7	7.25
			C	$H_{2b2a} = h_{2b2b}(h_{2a2a} + h_{2b2b} + \frac{1}{k})^{-1}h_{2a2a}$		7.26
			C	$H_{12a} = h_{12a} - h_{12a}(h_{2a2a} + h_{2b2b} + \frac{1}{k})^{-1}h_{2a2a}$		7.27
			D	$H_{2b2b} = h_{2b2b} - h_{2b2b}(h_{2a2a} + h_{2b2b} + \frac{1}{k})^{-1}h_{2b2b}$	7.8	7.29
			C	$H_{2a2b} = h_{2a2a}(h_{2a2a} + h_{2b2b} + \frac{1}{k})^{-1}h_{2b2b}$		7.30
			C	$H_{12b} = h_{12a}(h_{2a2a} + h_{2b2b} + \frac{1}{k})^{-1}h_{2b2b}$		7.31

The connection type (labeled C-type) is R, rigid, or F, flexible. The receptance type (labeled R-type) is D, direct, or C, cross. The corresponding figure and equation numbers are also included

$$H_{11} = h_{11} - h_{12a} \left(h_{2a2a} + h_{2b2b} + \frac{1}{k} \right)^{-1} h_{2a1} \quad (7.34)$$

Before proceeding with a numerical example, we present Table 7.1 which summarizes the receptance coupling equations developed in the previous paragraphs.



In a Nutshell

As always, improved accuracy of the model and prediction comes at the expense of increased model complexity and/or measurement requirements. Prediction of the natural frequency of the assembly, for example, does not place the same demands on the model as prediction of the dynamic stiffness (including damping). Accurate frequency response function prediction and, by extension, the corresponding stability lobe diagram require more care.

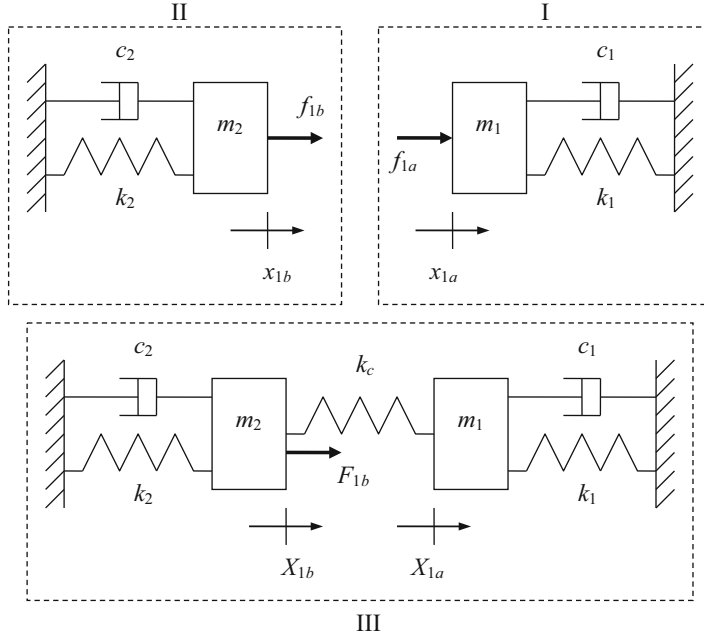


Fig. 7.10 Flexible coupling of spring-mass-damper systems I and II to form the two degree of freedom assembly III

Example 7.1 Comparison of Assembly Modeling Techniques Let's now complete an example where we compare receptance coupling to the methods we discussed in Sects. 2.3 and 2.4: modal analysis and complex matrix inversion. As shown in Fig. 7.10, two single degree of freedom spring-mass-damper systems, I and II, are to be connected using the linear spring element, \$k_c\$, to form the new two degree of freedom assembly, III [16]. The assembled system's equations of motion are determined as shown in Sects. 2.3 and 2.4. The matrix representation of these equations, after substituting the assumed harmonic form of the solution, is provided in Eq. 7.35. This equation takes the same form as Eq. 2.51, \$(s^2[M] + s[C] + [K])\{X\}e^{st} = \{F\}e^{st}\$, where we've substituted the Laplace variable \$s\$ for the product \$i\omega\$ and \$[M]\$, \$[C]\$, and \$[K]\$ are the lumped parameter mass, damping, and stiffness matrices in local coordinates, respectively.

$$\begin{aligned} & \left(s^2 \begin{bmatrix} m_1 & 0 \\ 0 & m_2 \end{bmatrix} + s \begin{bmatrix} c_1 & 0 \\ 0 & c_2 \end{bmatrix} + \begin{bmatrix} k_1 + k_c & -k_c \\ -k_c & k_2 + k_c \end{bmatrix} \right) \begin{Bmatrix} X_{1a} \\ X_{1b} \end{Bmatrix} = \begin{Bmatrix} 0 \\ F_{1b} \end{Bmatrix} \\ & \begin{bmatrix} m_1 s^2 + c_1 s + (k_1 + k_c) & -k_c \\ -k_c & m_2 s^2 + c_2 s + (k_2 + k_c) \end{bmatrix} \begin{Bmatrix} X_{1a} \\ X_{1b} \end{Bmatrix} = \begin{Bmatrix} 0 \\ F_{1b} \end{Bmatrix} \end{aligned} \quad (7.35)$$

Modal Analysis

We can use the equations of motion shown in Eq. 7.35 to find the modal solution for the assembled system. If we assume that proportional damping exists (i.e., $[C] = \alpha[M] + \beta[K]$, where α and β are real numbers), damping can be neglected in the modal solution. Note that this solution is also independent of the external force, F_{1b} . We write the characteristic equation for this system as shown in Eq. 7.36. The quadratic roots of this fourth-order equation, s_1^2 and s_2^2 , give the two eigenvalues ($s_1^2 = -\omega_{n1}^2$ and $s_2^2 = -\omega_{n2}^2$, where $\omega_{n1} < \omega_{n2}$) for the two degree of freedom system.

$$\begin{aligned} (m_1 s^2 + (k_1 + k_c))(m_2 s^2 + (k_2 + k_c)) - k_c^2 &= 0 \\ m_1 m_2 s^4 + (m_1(k_2 + k_c) + m_2(k_1 + k_c))s^2 + (k_1 + k_c)(k_2 + k_c) - k_c^2 &= 0 \end{aligned} \quad (7.36)$$

Substitution of these eigenvalues, normalized to the coordinate of interest (coordinate X_{1b} in this case), into either of the original equations of motion, again neglecting damping and the external force, yields the eigenvectors (mode shapes). Selecting the top equation from Eq. 7.35, for example, gives:

$$\frac{X_{1a}}{X_{1b}} = \frac{k_c}{m_1 s^2 + (k_1 + k_c)} \quad (7.37)$$

The mass, damping, and stiffness matrices are diagonalized using the modal matrix (composed of columns of the eigenvectors), P , defined in Eq. 7.38. Specifically, we have $[M_q] = [P]^T [M] [P] = \begin{bmatrix} m_{q1} & 0 \\ 0 & m_{q2} \end{bmatrix}$, $[C_q] = [P]^T [C] [P] = \begin{bmatrix} c_{q1} & 0 \\ 0 & c_{q2} \end{bmatrix}$, and $[K_q] = [P]^T [K] [P] = \begin{bmatrix} k_{q1} & 0 \\ 0 & k_{q2} \end{bmatrix}$. Based on these modal values, we calculate the associated damping ratios, $\zeta_{q1,2} = \frac{c_{q1,2}}{2\sqrt{k_{q1,2}m_{q1,2}}}$. The modal solution for the direct FRF at coordinate X_{1b} of the assembled system is then expressed as shown in Eq. 7.39, where $r_{1,2} = \frac{\omega}{\omega_{n1,2}}$.

$$P = \begin{bmatrix} \frac{X_{1a}}{X_{1b}}(s_1^2) & \frac{X_{1a}}{X_{1b}}(s_2^2) \\ 1 & 1 \end{bmatrix} \quad (7.38)$$

$$H_{1b1b} = \frac{X_{1b}}{F_{1b}} = \frac{1}{k_{q1}} \left(\frac{(1 - r_1^2) - i(2\zeta_{q1}r_1)}{(1 - r_1^2)^2 + (2\zeta_{q1}r_1)^2} \right) + \frac{1}{k_{q2}} \left(\frac{(1 - r_2^2) - i(2\zeta_{q2}r_2)}{(1 - r_2^2)^2 + (2\zeta_{q2}r_2)^2} \right) \quad (7.39)$$

Complex Matrix Inversion⁷

Equation 7.35 can be compactly written as $[A]\{X\} = \{F\}$. As shown in Sect. 2.4, complex matrix inversion is carried out using $\{X\}\{F\}^{-1} = [A]^{-1}$ to determine the assembly direct and cross FRFs. The inverted $[A]$ matrix for this two degree of freedom example is:

$$\begin{aligned}[A]^{-1} &= \frac{\begin{bmatrix} a_{22} & -a_{12} \\ -a_{21} & a_{11} \end{bmatrix}}{a_{11} \cdot a_{22} - a_{12} \cdot a_{21}} \\ &= \frac{\begin{bmatrix} -\omega^2 m_2 + i\omega c_2 + (k_2 + k_c) & k_c \\ k_c & -\omega^2 m_1 + i\omega c_1 + (k_1 + k_c) \end{bmatrix}}{(-\omega^2 m_1 + i\omega c_1 + (k_1 + k_c))(-\omega^2 m_2 + i\omega c_2 + (k_2 + k_c)) - k_c^2},\end{aligned}$$

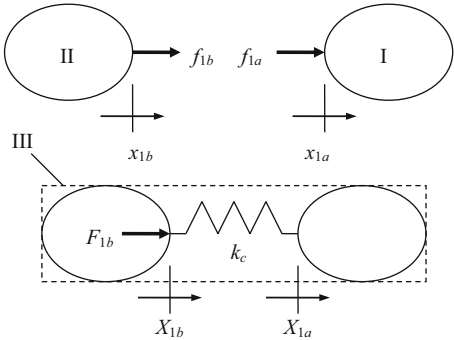
where we've replaced s with $i\omega$ relative to Eq. 7.35. The individual terms in the inverted $[A]$ matrix are:

$$[A]^{-1} = \begin{bmatrix} X_{1a} & X_{1a} \\ F_{1a} & F_{1b} \\ X_{1b} & X_{1b} \\ F_{1a} & F_{1b} \end{bmatrix} = \begin{bmatrix} H_{1a1a} & H_{1a1b} \\ H_{1b1a} & H_{1b1b} \end{bmatrix}. \quad (7.40)$$

Receptance Coupling

This case is the same as the two component flexible coupling example shown in Fig. 7.5. Replacing k with k_c in Eq. 7.17, we obtain Eq. 7.41. See Fig. 7.11.

Fig. 7.11 Receptance coupling representation of joining spring-mass-damper systems I and II to form the two degree of freedom assembly III

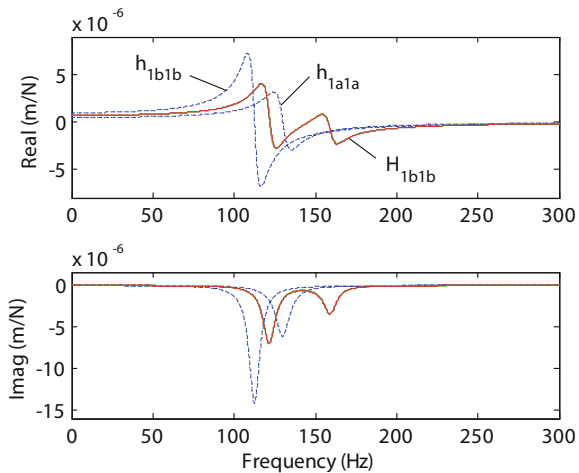


⁷As discussed in Sect. 2.4, complex matrix inversion, rather than modal analysis, is typically applied when the damping may not be proportional.

Table 7.2 Mass, damping, and stiffness values for Example 7.1

Parameter	Value
m_1	3 kg
c_1	200 N s/m
k_1	2×10^6 N/m
m_2	2 kg
c_2	100 N s/m
k_2	1×10^6 N/m
k_c	5×10^5 N/m

Fig. 7.12 Comparison of three methods for H_{1b1b} calculation. It is seen that the modal analysis, complex matrix inversion, and receptance coupling methods nominally agree (superimposed solid lines). The component receptances, h_{1a1a} and h_{1b1b} , are also shown



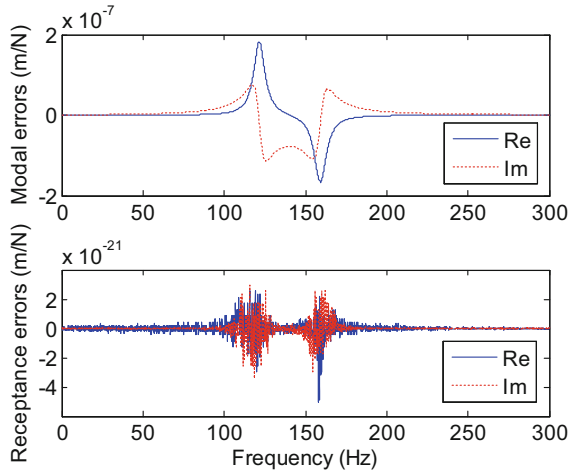
$$\frac{X_{1b}}{F_{1b}} = \frac{x_{1b}}{F_{1b}} = \frac{h_{1b1b}f_{1b}}{F_{1b}} = \frac{h_{1b1b} \left(1 - \left(h_{1a1a} + h_{1b1b} + \frac{1}{k_c} \right)^{-1} h_{1b1b} \right) F_{1b}}{F_{1b}} \quad (7.41)$$

$$\frac{X_{1b}}{F_{1b}} = H_{1b1b} = h_{1b1b} - h_{1b1b} \left(h_{1a1a} + h_{1b1b} + \frac{1}{k_c} \right)^{-1} h_{1b1b}$$

To compare the three methods, we select the mass, damping, and stiffness values shown in Table 7.2 for the model in Fig. 7.10. We note that proportional damping exists ($\alpha = 0$ and $\beta = 1 \times 10^{-4}$) for the selected system, so the modal approach may be applied. The MATLAB® program used to produce Fig. 7.12, which displays both the component receptances and the assembly receptance computed using the three methods, is provided with the textbook as p_7_1_1.m. The frequency dependent differences between the complex matrix inversion result, which was obtained through vector manipulations only by calculating the H_{1b1b} result directly:

$$H_{1b1b} = \frac{-\omega^2 m_1 + i\omega c_1 + (k_1 + k_c)}{(-\omega^2 m_1 + i\omega c_1 + (k_1 + k_c))(-\omega^2 m_2 + i\omega c_2 + (k_2 + k_c)) - k_c^2}$$

Fig. 7.13 Real and imaginary parts of difference between complex matrix inversion and modal analysis (top) and real and imaginary parts of difference between complex matrix inversion and receptance coupling (bottom). Receptance coupling agrees much more closely



and the modal and receptance coupling method results are shown in Fig. 7.13. It is seen that the errors introduced by the modal method (top) are approximately 4×10^{13} times greater than the errors associated with the receptance technique (bottom). The differences between the three techniques are introduced by numerical round off errors in the mathematical manipulations. However, the improved numerical accuracy obtained with receptance coupling (vector manipulations) over modal coupling (matrix manipulations) is another benefit of the receptance coupling approach.

7.3 Advanced Receptance Coupling

The primary difference between the simple examples we've considered so far and tool-holder-spindle-machine modeling is that we now need to consider not only lateral displacements (x_i/X_i) and forces (f_j/F_j) but also rotations about lines perpendicular to the beam axis (θ_i/Θ_i) and bending couples (m_j/M_j).^{8,9} To begin this discussion, let's consider the solid cylinder-prismatic cantilever beam assembly shown in Fig. 7.14. To determine the assembly dynamics, all four bending receptances must be included in the component descriptions (i.e., displacement-to-force, h_{ij} ; displacement-to-couple, l_{ij} ; rotation-to-force, n_{ij} ; and rotation-to-couple, p_{ij}).

Let's summarize the steps required to predict the Fig. 7.14 assembly receptances.

1. Define the components and coordinates for the model. In this simple example, we can select two components: a prismatic beam with fixed-free (or cantilever)

⁸We will not consider axial or torsional vibrations in this analysis.

⁹T. Schmitz acknowledges collaboration with M. Davies in the early application of receptance coupling to tool point FRF prediction.

Fig. 7.14 Rigid coupling of solid cylinder and prismatic beam to form cantilevered assembly

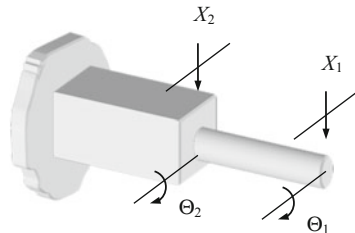
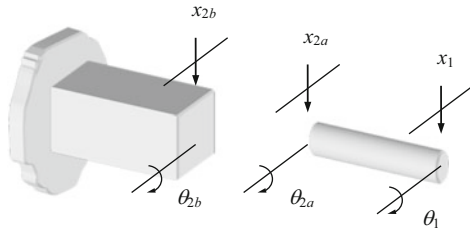


Fig. 7.15 Solid cylinder and prismatic beam components used to form cantilevered assembly



boundary conditions and a cylinder with free-free (or unsupported) boundary conditions; see Fig. 7.15.

2. Determine the component receptances. We can use either measurements or models. For the models, an elegant choice is the closed-form receptances presented by Bishop and Johnson [1] for flexural vibrations of uniform Euler-Bernoulli beams with free, fixed, sliding, and pinned boundary conditions. Of course, the Timoshenko beam model or other approaches may also be applied. See Sect. 7.4. For measurements, we can follow the procedures outlined in Sect. 2.6.
3. Based on the selected model from step 1, express the assembly receptances as a function of the component receptances. As demonstrated in Sect. 7.4, we determine the assembly receptances using the component displacements/rotations, equilibrium conditions, and compatibility conditions.

We begin the analysis of the system shown in Figs. 7.14 and 7.15 by writing the component receptances. Note that we have placed coordinates at the prediction location (1), which would represent the tool point for a tool-holder-spindle assembly, and coupling locations (2a and 2b). For the cylinder, we have the following direct receptances at the coordinate 1 end:

$$h_{11} = \frac{x_1}{f_1} \quad l_{11} = \frac{x_1}{m_1} \quad n_{11} = \frac{\theta_1}{f_1} \quad p_{11} = \frac{\theta_1}{m_1}. \quad (7.42)$$

The corresponding cross receptances at the same location are:

$$h_{12a} = \frac{x_1}{f_{2a}} \quad l_{12a} = \frac{x_1}{m_{2a}} \quad n_{12a} = \frac{\theta_1}{f_{2a}} \quad p_{12a} = \frac{\theta_1}{m_{2a}}. \quad (7.43)$$

At coordinate $2a$ on the cylinder, the direct and cross receptances are written as shown in Eqs. 7.44 and 7.45, respectively.

$$h_{2a2a} = \frac{x_{2a}}{f_{2a}} \quad l_{2a2a} = \frac{x_{2a}}{m_{2a}} \quad n_{2a2a} = \frac{\theta_{2a}}{f_{2a}} \quad p_{2a2a} = \frac{\theta_{2a}}{m_{2a}} \quad (7.44)$$

$$h_{2a1} = \frac{x_{2a}}{f_1} \quad l_{2a1} = \frac{x_{2a}}{m_1} \quad n_{2a1} = \frac{\theta_{2a}}{f_1} \quad p_{2a1} = \frac{\theta_{2a}}{m_1} \quad (7.45)$$

Similarly, for the prismatic beam, the direct receptances at the coupling location $2b$ are described by Eq. 7.46.

$$h_{2b2b} = \frac{x_{2b}}{f_{2b}} \quad l_{2b2b} = \frac{x_{2b}}{m_{2b}} \quad n_{2b2b} = \frac{\theta_{2b}}{f_{2b}} \quad p_{2b2b} = \frac{\theta_{2b}}{m_{2b}} \quad (7.46)$$

To simplify notation, the component receptances can be compactly represented in matrix form as shown in Eqs. 7.47 through 7.50 for the cylinder and Eq. 7.51 for the prismatic beam:

$$\begin{Bmatrix} x_1 \\ \theta_1 \end{Bmatrix} = \begin{bmatrix} h_{11} & l_{11} \\ n_{11} & p_{11} \end{bmatrix} \begin{Bmatrix} f_1 \\ m_1 \end{Bmatrix} \quad \text{or} \quad \{u_1\} = [R_{11}]\{q_1\}, \quad (7.47)$$

$$\begin{Bmatrix} x_{2a} \\ \theta_{2a} \end{Bmatrix} = \begin{bmatrix} h_{2a2a} & l_{2a2a} \\ n_{2a2a} & p_{2a2a} \end{bmatrix} \begin{Bmatrix} f_{2a} \\ m_{2a} \end{Bmatrix} \quad \text{or} \quad \{u_{2a}\} = [R_{2a2a}]\{q_{2a}\}, \quad (7.48)$$

$$\begin{Bmatrix} x_1 \\ \theta_1 \end{Bmatrix} = \begin{bmatrix} h_{12a} & l_{12a} \\ n_{12a} & p_{12a} \end{bmatrix} \begin{Bmatrix} f_{2a} \\ m_{2a} \end{Bmatrix} \quad \text{or} \quad \{u_1\} = [R_{12a}]\{q_{2a}\}, \quad (7.49)$$

$$\begin{Bmatrix} x_{2a} \\ \theta_{2a} \end{Bmatrix} = \begin{bmatrix} h_{2a1} & l_{2a1} \\ n_{2a1} & p_{2a1} \end{bmatrix} \begin{Bmatrix} f_1 \\ m_1 \end{Bmatrix} \quad \text{or} \quad \{u_{2a}\} = [R_{2a1}]\{q_1\}, \quad \text{and} \quad (7.50)$$

$$\begin{Bmatrix} x_{2b} \\ \theta_{2b} \end{Bmatrix} = \begin{bmatrix} h_{2b2b} & l_{2b2b} \\ n_{2b2b} & p_{2b2b} \end{bmatrix} \begin{Bmatrix} f_{2b} \\ m_{2b} \end{Bmatrix} \quad \text{or} \quad \{u_{2b}\} = [R_{2b2b}]\{q_{2b}\}, \quad (7.51)$$

where R_{ij} is the generalized receptance matrix that describes both translational and rotational component behavior [6, 10, 17] and u_i and q_j are the corresponding generalized displacement/rotation and force/couple vectors. To visualize R_{ij} , we can think of each frequency dependent $2 \times 2 R_{ij}$ matrix as a page in a book with every page representing a different frequency value. Flipping through the book from front to back scans the frequency values from low to high through the modeled or measured bandwidth. Naturally, all receptances in the coupling analysis must be based on the same frequency vector (resolution and range).

We write the component receptances, using the new notation, as $u_1 = R_{11}q_1 + R_{12a}q_{2a}$ and $u_{2a} = R_{2a1}q_1 + R_{2a2a}q_{2a}$ for the cylinder and $u_{2b} = R_{2b2b}q_{2b}$ for the prismatic beam. If we apply a rigid connection between the two components, the compatibility condition is $u_{2b} - u_{2a} = 0$. Additionally, if we again specify that the component and assembly coordinates are at the same physical locations, then we have that $u_1 = U_1$ and $u_{2a} = u_{2b} = U_2$ (due to the rigid coupling).

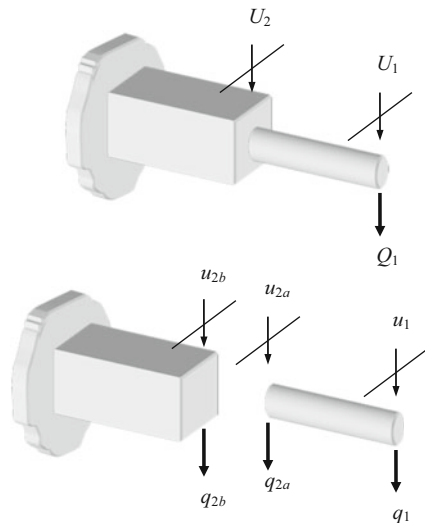
We can write the assembly receptances as shown in Eq. 7.52, which again implements the generalized notation:

$$\begin{Bmatrix} U_1 \\ U_2 \end{Bmatrix} = \begin{bmatrix} G_{11} & G_{12} \\ G_{21} & G_{22} \end{bmatrix} \begin{Bmatrix} Q_1 \\ Q_2 \end{Bmatrix}, \quad (7.52)$$

where $U_i = \begin{Bmatrix} X_i \\ \Theta_i \end{Bmatrix}$, $G_{ij} = \begin{bmatrix} H_{ij} & L_{ij}^{\bar{y}} & P_{ij} \\ N_{ij} & & \end{bmatrix}$, and $Q_j = \begin{Bmatrix} F_j \\ M_j \end{Bmatrix}$. To determine the

assembly receptance at the free end of the cylinder, G_{11} , we apply Q_1 to coordinate U_1 as shown in Fig. 7.16, where the generalized U_i and u_i vectors are shown schematically as “displacements,” although we recognize that they describe both lateral translation and rotation. The associated equilibrium conditions are $q_{2a} + q_{2b} = 0$ and $q_1 = Q_1$. By substituting the component displacements/rotations and equilibrium conditions into the compatibility condition, we obtain the expression for q_{2b} shown in Eq. 7.53. The component force q_{2a} is then determined from the equilibrium condition $q_{2a} = -q_{2b}$. The expression for G_{11} is given by Eq. 7.54. We find the corresponding cross receptance matrix, G_{21} , in a similar manner; see Eq. 7.55. Note that G_{11} and G_{21} comprise the first column of the receptance matrix in Eq. 7.52.

Fig. 7.16 Receptance coupling model for determining G_{11} and G_{21} . Rigid coupling is assumed



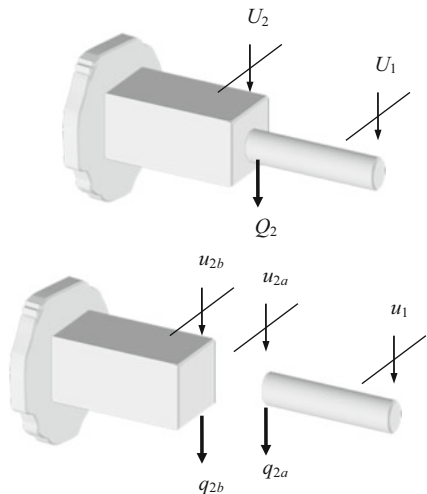
$$\begin{aligned}
u_{2b} - u_{2a} &= 0 \\
R_{2b2b}q_{2b} - R_{2a1}q_1 - R_{2a2a}q_{2a} &= 0 \\
(R_{2a2a} + R_{2b2b})q_{2b} - R_{2a1}Q_1 &= 0 \\
q_{2b} &= (R_{2a2a} + R_{2b2b})^{-1}R_{2a1}Q_1
\end{aligned} \tag{7.53}$$

$$\begin{aligned}
G_{11} &= \frac{U_1}{Q_1} = \frac{u_1}{Q_1} = \frac{R_{11}q_1 + R_{12a}q_{2a}}{Q_1} = \frac{R_{11}Q_1 - R_{12a}(R_{2a2a} + R_{2b2b})^{-1}R_{2a1}Q_1}{Q_1} \\
G_{11} &= R_{11} - R_{12a}(R_{2a2a} + R_{2b2b})^{-1}R_{2a1} = \begin{bmatrix} H_{11} & L_{11} \\ N_{11} & P_{11} \end{bmatrix}
\end{aligned} \tag{7.54}$$

$$\begin{aligned}
G_{21} &= \frac{U_2}{Q_1} = \frac{u_{2a}}{Q_1} = \frac{R_{2a1}q_1 + R_{2a2a}q_{2a}}{Q_1} = \frac{R_{2a1}Q_1 - R_{2a2a}(R_{2a2a} + R_{2b2b})^{-1}R_{2a1}Q_1}{Q_1} \\
G_{21} &= R_{2a1} - R_{2a2a}(R_{2a2a} + R_{2b2b})^{-1}R_{2a1} = \begin{bmatrix} H_{21} & L_{21} \\ N_{21} & P_{21} \end{bmatrix}
\end{aligned} \tag{7.55}$$

To find the receptances in the second column of Eq. 7.52, we apply Q_2 at U_2 , as shown in Fig. 7.17. The component receptances are $u_1 = R_{12a}q_{2a}$ and $u_{2a} = R_{2a2a}q_{2a}$ for the cylinder and $u_{2b} = R_{2b2b}q_{2b}$ for the prismatic beam. For the assumed rigid connection, the compatibility condition is again $u_{2b} - u_{2a} = 0$. The equilibrium condition is $q_{2a} + q_{2b} = Q_2$. By substituting the component displacements/rotations

Fig. 7.17 Receptance coupling model for determining G_{22} and G_{12} . Rigid coupling is assumed



and equilibrium condition into the compatibility condition, we obtain the expression for q_{2b} shown in Eq. 7.56. The component force q_{2a} is then determined from the equilibrium condition $q_{2a} = Q_2 - q_{2b}$. The expression for G_{22} is provided by Eq. 7.57. We find the corresponding cross receptance matrix, G_{12} , in a similar manner as shown in Eq. 7.58.

$$\begin{aligned} u_{2b} - u_{2a} &= 0 \\ R_{2b2b}q_{2b} - R_{2a2a}q_{2a} &= 0 \\ R_{2b2b}q_{2b} - R_{2a2a}Q_2 + R_{2a2a}q_{2b} &= 0 \\ (R_{2a2a} + R_{2b2b})q_{2b} - R_{2a2a}Q_2 &= 0 \\ q_{2b} &= (R_{2a2a} + R_{2b2b})^{-1}R_{2a2a}Q_2 \end{aligned} \quad (7.56)$$

$$\begin{aligned} G_{22} &= \frac{U_2}{Q_2} = \frac{u_{2a}}{Q_2} = \frac{R_{2a2a}q_{2a}}{Q_2} = \frac{R_{2a2a}\left(1 - (R_{2a2a} + R_{2b2b})^{-1}R_{2a2a}\right)Q_2}{Q_2} \\ G_{22} &= R_{2a2a} - R_{2a2a}(R_{2a2a} + R_{2b2b})^{-1}R_{2a2a} = \begin{bmatrix} H_{22} & L_{22} \\ N_{22} & P_{22} \end{bmatrix} \end{aligned} \quad (7.57)$$

$$\begin{aligned} G_{12} &= \frac{U_1}{Q_2} = \frac{u_1}{Q_2} = \frac{R_{12a}q_{2a}}{Q_2} = \frac{R_{12a}\left(1 - (R_{2a2a} + R_{2b2b})^{-1}R_{2a2a}\right)Q_2}{Q_2} \\ G_{12} &= R_{12a} - R_{12a}(R_{2a2a} + R_{2b2b})^{-1}R_{2a2a} = \begin{bmatrix} H_{12} & L_{12} \\ N_{12} & P_{12} \end{bmatrix} \end{aligned} \quad (7.58)$$

We see that the procedure to model the systems with both displacement and rotations is analogous to the examples provided in Sect. 7.2. Let's again summarize the receptance terms in tabular form; see Table 7.3. Due to the clear similarities to Table 7.1, we will not derive the receptances for the other two component coupling cases. The only consideration is that for nonrigid coupling, we replace the scalar

Table 7.3 Direct and cross receptances for generalized two component coupling

C-type	Substructure coordinates		Receptances		Fig.	Eq.
	I	II	R-type			
R	u_1, u_{2a}	u_{2b}	D	$G_{11} = R_{11} - R_{12a}(R_{2a2a} + R_{2b2b})^{-1}R_{2a1}$	7.16	7.13
			C	$G_{21} = R_{2a1} - R_{2a2a}(R_{2a2a} + R_{2b2b})^{-1}R_{2a1}$		
			D	$G_{22} = R_{2a2a} - R_{2a2a}(R_{2a2a} + R_{2b2b})^{-1}R_{2a2a}$	7.17	7.16
			C	$G_{12} = R_{12a} - R_{12a}(R_{2a2a} + R_{2b2b})^{-1}R_{2a2a}$		

The connection type (labeled C-type) is R, rigid. The receptance type (labeled R-type) is D, direct, or C, cross. The figure and equation numbers are also included. Similarities to the corresponding entries in Table 7.1 are evident

stiffness term, $\frac{1}{k}$, from the displacement-to-force analyses with the matrix expression $[\tilde{k}]^{-1}$, where:

$$[\tilde{k}] = \begin{bmatrix} k_{xf} & k_{\theta f} \\ k_{xm} & k_{\theta m} \end{bmatrix}.$$

The subscripts for the stiffness matrix entries indicate their function. For example, $k_{\theta f}$ represents resistance to rotation due to an applied force. As shown in Eq. 7.34, these four real valued stiffness terms are augmented by the corresponding damping expressions if viscous damping is included at the coupling location [11]. The new complex, frequency dependent stiffness matrix is:

$$[\tilde{k}'] = \begin{bmatrix} k_{xf} + i\omega c_{xf} & k_{\theta f} + i\omega c_{\theta f} \\ k_{xm} + i\omega c_{xm} & k_{\theta m} + i\omega c_{\theta m} \end{bmatrix}.$$

7.4 Beam Receptances

To describe the lateral vibration and associated rotation at the ends of uniform beams, we may apply Euler-Bernoulli beam theory. Many sources are available for full equation development, such as [1, 18], and we refer the reader to these texts for a detailed analysis. However, we'll review some of the basic concepts before presenting the closed form equations developed by Bishop and Johnson [1].

For a uniform elastic beam subject to lateral vibrations, y , we can write the differential equation:

$$\frac{\partial^2 y}{\partial t^2} + \frac{EI}{\rho A} \frac{\partial^4 y}{\partial x^4} = 0 \quad (7.59)$$

to describe its lateral motion as a function of time, t , and position along the beam, x , where E is the beam's elastic modulus (N/m^2), I is the second moment of area/area moment of inertia (m^4), ρ is the density (kg/m^3), and A is the cross-sectional area (m^2). This equation assumes that the axis of the undeflected beam lies along the x direction and an infinitesimal slice of the deflected beam is bounded by plane faces. If we assume a harmonic disturbance, we can use the trial function $y = Y(x) \sin(\omega t)$, where ω is the frequency, to eliminate the time dependence. See Eq. 7.60, where $\lambda^4 = \omega^2 \frac{\rho A}{EI}$.

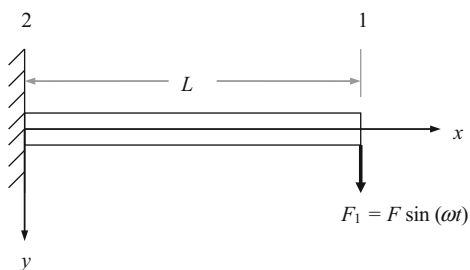
$$\frac{\partial^4 Y}{\partial x^4} - \lambda^4 Y = 0. \quad (7.60)$$

The general solution to Eq. 7.60 is given in Eq. 7.61. In this equation, A , B , C , and D are constants that are determined from the boundary conditions. See Table 7.4.

Table 7.4 Boundary conditions for Euler-Bernoulli beam receptance calculations [1]

End description	Boundary conditions
Clamped	$y = 0, \frac{\partial y}{\partial x} = 0$
Free	$\frac{\partial^2 y}{\partial x^2} = 0, \frac{\partial^3 y}{\partial x^3} = 0$
Pinned	$y = 0, \frac{\partial^2 y}{\partial x^2} = 0$
Sliding	$\frac{\partial y}{\partial x} = 0, \frac{\partial^3 y}{\partial x^3} = 0$
Harmonic force $F \sin(\omega t)$	$\frac{\partial^2 y}{\partial x^2} = 0, \frac{\partial^3 y}{\partial x^3} = -\frac{F}{EI} \sin(\omega t)$
Harmonic bending couple $M \sin(\omega t)$	$\frac{\partial^2 y}{\partial x^2} = \frac{M}{EI} \sin(\omega t), \frac{\partial^3 y}{\partial x^3} = 0$

Fig. 7.18 Clamped-free uniform beam with a harmonic force applied at the free end



$$Y = A \cos(\lambda x) + B \sin(\lambda x) + C \cosh(\lambda x) + D \sinh(\lambda x) \quad (7.61)$$

Example 7.2 Tip Receptances for Clamped-Free Beam In this example, we'll use Eq. 7.61 and Table 7.4 to determine the receptances at the free end of a clamped-free beam. Let's first consider a harmonic force applied in the positive y direction at the free end of the uniform beam of length L as shown in Fig. 7.18 and find $H_{11} = \frac{y_1}{F_1}$ and $N_{11} = \frac{\Omega_1}{F_1}$. From Table 7.4, the boundary conditions at coordinate 2 (clamped), where $x = 0$, are $y = 0$ and $\frac{\partial y}{\partial x} = 0$. At coordinate 1 (free), where $x = L$, the boundary conditions are $\frac{\partial^2 y}{\partial x^2} = 0$ and $\frac{\partial^3 y}{\partial x^3} = -\frac{F}{EI} \sin(\omega t)$. Using these four end conditions, let's determine the four coefficients A , B , C , and D in Eq. 7.61.

At $x = 0$, we have that $y = 0$ and $\frac{\partial y}{\partial x} = 0$. Therefore, we can use Eq. 7.61 directly and substitute $x = 0$ to obtain Eq. 7.62.

$$y|_{x=0} = Y|_{x=0} = A + C = 0 \quad (7.62)$$

This gives $A = -C$. Using the slope boundary condition at $x = 0$, we calculate the first derivative of Eq. 7.61 with respect to y and evaluate it at $x = 0$ to get Eq. 7.63, which yields the relationship $B = -D$.

$$\left. \frac{\partial y}{\partial x} \right|_{x=0} = \left. \frac{\partial Y}{\partial x} \right|_{x=0} = \lambda(B + D) = 0 \quad (7.63)$$

At $x = L$, we first apply $\frac{\partial^2 y}{\partial x^2} = 0$. See Eq. 7.64.

$$\left. \frac{\partial^2 y}{\partial x^2} \right|_{x=L} = \left. \frac{\partial^2 Y}{\partial x^2} \right|_{x=L} = \lambda^2(-A \cos(\lambda L) - B \sin(\lambda L) + C \cosh(\lambda L) + D \sinh(\lambda L)) = 0 \quad (7.64)$$

Substituting for A and B in Eq. 7.64, we obtain:

$$C(\cos(\lambda L) + \cosh(\lambda L)) + D(\sin(\lambda L) + \sinh(\lambda L)) = 0. \quad (7.65)$$

We next use $\frac{\partial^3 y}{\partial x^3} = -\frac{F}{EI} \sin(\omega t)$ at $x = L$ and again substitute for A and B to find:

$$C(-\sin(\lambda L) + \sinh(\lambda L)) + D(\cos(\lambda L) + \cosh(\lambda L)) = -\frac{F}{\lambda^3 EI} \sin(\omega t). \quad (7.66)$$

Let's now rewrite Eqs. 7.65 and 7.66 in matrix form and solve for the coefficients C and D . See Eq. 7.67.

$$\begin{bmatrix} \cos(\lambda L) + \cosh(\lambda L) & \sin(\lambda L) + \sinh(\lambda L) \\ -\sin(\lambda L) + \sinh(\lambda L) & \cos(\lambda L) + \cosh(\lambda L) \end{bmatrix} \begin{Bmatrix} C \\ D \end{Bmatrix} = \begin{Bmatrix} 0 \\ -\frac{F}{\lambda^3 EI} \sin(\omega t) \end{Bmatrix} \quad (7.67)$$

We can use Cramer's rule [19] to determine C and D . Writing Eq. 7.67 in the generic form $[A]\{x\} = \{B\}$, or $\begin{bmatrix} a_{11} & a_{12} \\ a_{21} & a_{22} \end{bmatrix} \begin{Bmatrix} x_1 \\ x_2 \end{Bmatrix} = \begin{Bmatrix} b_1 \\ b_2 \end{Bmatrix}$, we find x_1 by Eq. 7.68 and x_2 by 7.69.

$$x_1 = \frac{\begin{vmatrix} b_1 & a_{12} \\ b_2 & a_{22} \end{vmatrix}}{\begin{vmatrix} a_{11} & a_{12} \\ a_{21} & a_{22} \end{vmatrix}} = \frac{b_1 a_{22} - b_2 a_{12}}{a_{11} a_{22} - a_{21} a_{12}} \quad (7.68)$$

$$x_2 = \frac{\begin{vmatrix} a_{11} & b_1 \\ a_{21} & b_2 \end{vmatrix}}{\begin{vmatrix} a_{11} & a_{12} \\ a_{21} & a_{22} \end{vmatrix}} = \frac{a_{11} b_2 - a_{21} b_1}{a_{11} a_{22} - a_{21} a_{12}} \quad (7.69)$$

Substitution in Eq. 7.68 gives C , while Eq. 7.69 is used to find D . See Eqs. 7.70 and 7.71.

$$\begin{aligned}
C &= \frac{\begin{vmatrix} 0 & \sin(\lambda L) + \sinh(\lambda L) \\ -\frac{F}{\lambda^3 EI} \sin(\omega t) & \cos(\lambda L) + \cosh(\lambda L) \end{vmatrix}}{\begin{vmatrix} \cos(\lambda L) + \cosh(\lambda L) & \sin(\lambda L) + \sinh(\lambda L) \\ -\sin(\lambda L) + \sinh(\lambda L) & \cos(\lambda L) + \cosh(\lambda L) \end{vmatrix}} \\
C &= \frac{\frac{F}{\lambda^3 EI} (\sin(\lambda L) + \sinh(\lambda L))}{(\cos(\lambda L) + \cosh(\lambda L))^2 - (-\sin(\lambda L) + \sinh(\lambda L))(\sin(\lambda L) + \sinh(\lambda L))} \sin(\omega t) \\
C &= \frac{F(\sin(\lambda L) + \sinh(\lambda L))}{2\lambda^3 EI(1 + \cos(\lambda L)\cosh(\lambda L))} \sin(\omega t)
\end{aligned} \tag{7.70}$$

$$\begin{aligned}
D &= \frac{\begin{vmatrix} \cos(\lambda L) + \cosh(\lambda L) & 0 \\ -\sin(\lambda L) + \sinh(\lambda L) & -\frac{F}{\lambda^3 EI} \sin(\omega t) \end{vmatrix}}{\begin{vmatrix} \cos(\lambda L) + \cosh(\lambda L) & \sin(\lambda L) + \sinh(\lambda L) \\ -\sin(\lambda L) + \sinh(\lambda L) & \cos(\lambda L) + \cosh(\lambda L) \end{vmatrix}} \\
D &= \frac{-\frac{F}{\lambda^3 EI} (\cos(\lambda L) + \cosh(\lambda L))}{(\cos(\lambda L) + \cosh(\lambda L))^2 - (-\sin(\lambda L) + \sinh(\lambda L))(\sin(\lambda L) + \sinh(\lambda L))} \sin(\omega t) \\
D &= -\frac{F(\cos(\lambda L) + \cosh(\lambda L))}{2\lambda^3 EI(1 + \cos(\lambda L)\cosh(\lambda L))} \sin(\omega t)
\end{aligned} \tag{7.71}$$

We determine Y_1 by substituting the equations for C and D , together with the relationships $A = -C$ and $B = -D$, in Eq. 7.61. Because $x = L$ at coordinate 1, we also substitute L for x . The result is provided in Eq. 7.72.

$$\begin{aligned}
Y_1 &= A \cos(\lambda L) + B \sin(\lambda L) + C \cosh(\lambda L) + D \sinh(\lambda L) \\
Y_1 &= -C \cos(\lambda L) - D \sin(\lambda L) + C \cosh(\lambda L) + D \sinh(\lambda L) \\
Y_1 &= C(-\cos(\lambda L) + \cosh(\lambda L)) + D(-\sin(\lambda L) + \sinh(\lambda L)) \\
Y_1 &= \frac{F(\sin(\lambda L) + \sinh(\lambda L))}{2\lambda^3 EI(1 + \cos(\lambda L)\cosh(\lambda L))} \sin(\omega t) \times (-\cos(\lambda L) + \cosh(\lambda L)) \\
&\quad - \frac{F(\cos(\lambda L) + \cosh(\lambda L))}{2\lambda^3 EI(1 + \cos(\lambda L)\cosh(\lambda L))} \sin(\omega t) \times (-\sin(\lambda L) + \sinh(\lambda L)) \\
Y_1 &= -\left(\begin{array}{l} \frac{(\sin(\lambda L) + \sinh(\lambda L))(\cos(\lambda L) - \cosh(\lambda L))}{2\lambda^3 EI(1 + \cos(\lambda L)\cosh(\lambda L))} \\ -\frac{(\cos(\lambda L) + \cosh(\lambda L))(\sin(\lambda L) - \sinh(\lambda L))}{2\lambda^3 EI(1 + \cos(\lambda L)\cosh(\lambda L))} \end{array} \right) \times F \sin(\omega t)
\end{aligned} \tag{7.72}$$

Finally, the displacement-to-force tip receptance at the free end of the beam is written as shown in Eq. 7.73.

$$\begin{aligned}
 H_{11} &= \frac{Y_1}{F_1} = \frac{-\left(\begin{array}{c} (\sin(\lambda L) + \sinh(\lambda L))(\cos(\lambda L) - \cosh(\lambda L)) \\ \frac{2\lambda^3 EI(1 + \cos(\lambda L)\cosh(\lambda L))}{ } \end{array} \right)}{\frac{F \sin(\omega t)}{}} \\
 H_{11} &= -\left(\begin{array}{c} (\sin(\lambda L) + \sinh(\lambda L))(\cos(\lambda L) - \cosh(\lambda L)) \\ \frac{2\lambda^3 EI(1 + \cos(\lambda L)\cosh(\lambda L))}{ } \end{array} \right) \\
 H_{11} &= \frac{\sin(\lambda L)\cosh(\lambda L) - \cos(\lambda L)\sinh(\lambda L)}{\lambda^3 EI(1 + \cos(\lambda L)\cosh(\lambda L))} \tag{7.73}
 \end{aligned}$$

To determine the rotation-to-force tip receptance, we return to Eq. 7.61 and substitute for A , B , C , and D .

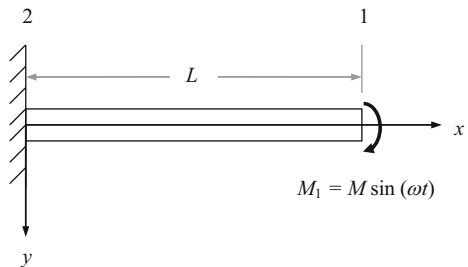
$$Y = (C(-\cos(\lambda x) + \cosh(\lambda x)) + D(-\sin(\lambda x) + \sinh(\lambda x))) \tag{7.74}$$

We then obtain rotation by differentiating Y with respect to x , $\Theta = \frac{dy}{dx}$, and evaluate this expression at $x = L$. Finally, we divide this result by F_1 to find $N_{11} = \frac{\Theta_1}{F_1}$. See Eq. 7.75.

$$N_{11} = \frac{\sin(\lambda L)\sinh(\lambda L)}{\lambda^2 EI(1 + \cos(\lambda L)\cosh(\lambda L))} \tag{7.75}$$

The remaining tip receptances are $L_{11} = \frac{Y_1}{M_1}$ and $P_{11} = \frac{\Theta_1}{M_1}$. We find these terms by applying the harmonic bending couple $M_1 = M \sin(\omega t)$ at coordinate 1 as shown in Fig. 7.19. The boundary conditions at coordinate 2 ($x = 0$) are $y = 0$ and $\frac{\partial y}{\partial x} = 0$. The boundary conditions at coordinate 1 ($x = L$) are $\frac{\partial^2 y}{\partial x^2} = \frac{M}{EI} \sin(\omega t)$ and $\frac{\partial^3 y}{\partial x^3} = 0$. We

Fig. 7.19 Clamped-free uniform beam with a harmonic bending couple applied at the free end



find the coefficients A , B , C , and D from Eq. 7.61 in the same manner as described in the previous paragraphs.

At $x = 0$, the situation is identical to the force application case shown in Fig. 7.18, so we obtain $A = -C$ and $B = -D$. At $x = L$, we first use $\frac{\partial^2 y}{\partial x^2} = \frac{M}{\lambda^2 EI}$ as demonstrated in Eq. 7.76.

$$\left. \frac{\partial^2 y}{\partial x^2} \right|_{x=L} = \left. \frac{\partial^2 Y}{\partial x^2} \right|_{x=L} = \lambda^2 \begin{pmatrix} -A \cos(\lambda L) - B \sin(\lambda L) + \\ C \cosh(\lambda L) + D \sinh(\lambda L) \end{pmatrix} = \frac{M}{\lambda^2 EI} \sin(\omega t) \quad (7.76)$$

Substitution for A and B in Eq. 7.76 gives:

$$C(\cos(\lambda L) + \cosh(\lambda L)) + D(\sin(\lambda L) + \sinh(\lambda L)) = \frac{M}{\lambda^2 EI} \sin(\omega t). \quad (7.77)$$

We next apply $\frac{\partial^3 y}{\partial x^3} = 0$ (at $x = L$) and substitute for A and B to get:

$$C(-\sin(\lambda L) + \sinh(\lambda L)) + D(\cos(\lambda L) + \cosh(\lambda L)) = 0. \quad (7.78)$$

Expressing Eqs. 7.77 and 7.78 in matrix form yields:

$$\begin{bmatrix} \cos(\lambda L) + \cosh(\lambda L) & \sin(\lambda L) + \sinh(\lambda L) \\ -\sin(\lambda L) + \sinh(\lambda L) & \cos(\lambda L) + \cosh(\lambda L) \end{bmatrix} \begin{Bmatrix} C \\ D \end{Bmatrix} = \begin{Bmatrix} \frac{M}{\lambda^2 EI} \\ 0 \end{Bmatrix} \sin(\omega t). \quad (7.79)$$

Again applying Cramer's rule, we obtain equations for C and D .

$$C = \frac{M(\cos(\lambda L) + \cosh(\lambda L))}{2\lambda^2 EI(1 + \cos(\lambda L)\cosh(\lambda L))} \sin(\omega t) \quad (7.80)$$

$$D = -\frac{M(-\sin(\lambda L) + \sinh(\lambda L))}{2\lambda^2 EI(1 + \cos(\lambda L)\cosh(\lambda L))} \sin(\omega t) \quad (7.81)$$

We find Y_1 by substituting Eqs. 7.80 and 7.81, together with the relationships $A = -C$ and $B = -D$, in Eq. 7.61. We also set $x = L$. The result is given in Eq. 7.82.

$$Y_1 = - \left(\begin{array}{l} \frac{(\cos(\lambda L) + \cosh(\lambda L))(\cos(\lambda L) - \cosh(\lambda L))}{2\lambda^2 EI(1 + \cos(\lambda L)\cosh(\lambda L))} + \\ \frac{(\sin(\lambda L) - \sinh(\lambda L))(\sin(\lambda L) - \sinh(\lambda L))}{2\lambda^2 EI(1 + \cos(\lambda L)\cosh(\lambda L))} \end{array} \right) M \sin(\omega t) \quad (7.82)$$

We obtain the displacement-to-couple tip receptance at the free end of the beam by dividing Eq. 7.82 by M_1 . A comparison of Eqs. 7.83 and 7.75 shows us that the displacement-to-couple and rotation-to-force receptances are identical.

$$L_{11} = \frac{Y_1}{M_1} \frac{-\left(\begin{array}{l} \frac{(\cos(\lambda L) + \cosh(\lambda L))(\cos(\lambda L) - \cosh(\lambda L))}{2\lambda^2 EI(1 + \cos(\lambda L)\cosh(\lambda L))} \\ + \frac{(\sin(\lambda L) - \sinh(\lambda L))(\sin(\lambda L) - \sinh(\lambda L))}{2\lambda^2 EI(1 + \cos(\lambda L)\cosh(\lambda L))} \end{array} \right) M \sin(\omega t)}{M \sin(\omega t)}$$

$$L_{11} = -\left(\begin{array}{l} \frac{(\cos(\lambda L) + \cosh(\lambda L))(\cos(\lambda L) - \cosh(\lambda L))}{2\lambda^2 EI(1 + \cos(\lambda L)\cosh(\lambda L))} \\ + \frac{(\sin(\lambda L) - \sinh(\lambda L))(\sin(\lambda L) - \sinh(\lambda L))}{2\lambda^2 EI(1 + \cos(\lambda L)\cosh(\lambda L))} \end{array} \right) \quad (7.83)$$

$$L_{11} = \frac{\sin(\lambda L)\sinh(\lambda L)}{\lambda^2 EI(1 + \cos(\lambda L)\cosh(\lambda L))}$$

To determine the rotation-to-couple tip receptance, we return to Eq. 7.61 and substitute for A , B , C , and D (according to Eqs. 7.80 and 7.81).

$$Y = (C(-\cos(\lambda x) + \cosh(\lambda x)) + D(-\sin(\lambda x) + \sinh(\lambda x))) \quad (7.84)$$

We then find $P_{11} = \frac{\Theta_1}{M_1}$ by (1) differentiating Y with respect to x to obtain rotation $\Theta = \frac{dY}{dx}$; (2) evaluating this expression at $x = L$; and (3) dividing this result by M_1 . See Eq. 7.85.

$$P_{11} = \frac{\sin(\lambda L)\cosh(\lambda L) + \cos(\lambda L)\sinh(\lambda L)}{\lambda EI(1 + \cos(\lambda L)\cosh(\lambda L))} \quad (7.85)$$

This process can be repeated for any of the boundary conditions shown in Table 7.4. The tip receptance results for clamped-free and free-free conditions (see Fig. 7.20) are summarized in Table 7.5, where both direct and cross receptances are included for the free-free beam. No cross receptances are shown for the clamped-free beam because the response at the tip is zero for any excitation at the clamped end and the response is always zero at the clamped end. We should note that the free-free receptances also include the two (zero frequency) rigid body modes for the uniform beam. The first displacement-to-force rigid body mode, for example, represents the motion of the unsupported beam (imagine the beam floating in space) when a force is applied at its mass center and rigid body translation occurs. The second rigid body

Fig. 7.20 Free-free uniform beam

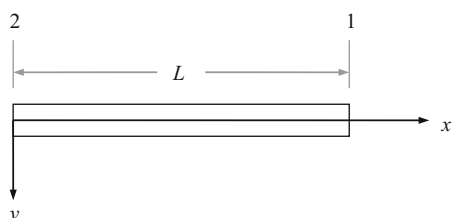


Table 7.5 Euler-Bernoulli beam tip receptances for clamped-free and free-free boundary conditions [1]

H_{22}	N_{22} L_{22}	H_{12} H_{21}	N_{12} L_{21}	P_{22}	L_{12} N_{21}	P_{12} P_{21}	H_{11}	N_{11} L_{11}	P_{11}
<i>Free-free</i>									
$\frac{-c_1}{\lambda^3 c_7}$	$\frac{-c_2}{\lambda^2 c_7}$	$\frac{c_3}{\lambda^3 c_7}$	$\frac{c_4}{\lambda^2 c_7}$	$\frac{c_5}{\lambda c_7}$	$\frac{-c_4}{\lambda^2 c_7}$	$\frac{c_6}{\lambda c_7}$	$\frac{-c_1}{\lambda^3 c_7}$	$\frac{c_2}{\lambda^2 c_7}$	$\frac{c_5}{\lambda c_7}$
<i>Clamped-free</i>									
-	-	-	-	-	-	-	$\frac{-c_1}{\lambda^3 c_8}$	$\frac{c_2}{\lambda^2 c_8}$	$\frac{c_5}{\lambda c_8}$
<i>Terms c_1 through c_8</i>									
$c_1 = \cos(\lambda L) \sinh(\lambda L) - \sin(\lambda L) \cosh(\lambda L)$	$c_5 = \cos(\lambda L) \sinh(\lambda L) + \sin(\lambda L) \cosh(\lambda L)$								
$c_2 = \sin(\lambda L) \sinh(\lambda L)$	$c_6 = \sin(\lambda L) + \sinh(\lambda L)$								
$c_3 = \sin(\lambda L) - \sinh(\lambda L)$	$c_7 = EI(\cos(\lambda L) \cosh(\lambda L) - 1)$								
$c_4 = \cos(\lambda L) - \cosh(\lambda L)$	$c_8 = EI(\cos(\lambda L) \cosh(\lambda L) + 1)$								

Coordinates 1 and 2 are defined in Figs. 7.18 through 7.20. Also, $\lambda^4 = \omega^2 \frac{\rho A}{EI}$ and L is the beam length

mode corresponds to a force applied at any other location, which causes rigid body rotation about the mass center.

An important omission for the receptance expressions provided in Table 7.5 is damping. Because we are considering solid beams under lateral vibration, the energy dissipation occurs within the beam only; there are no joints to introduce damping. As discussed in Sect. 2.1, internal damping is typically classified as solid, or structural, damping [20]. It is conveniently included in our harmonic vibration analysis by replacing EI in λ , c_7 , and c_8 with the complex stiffness term $EI(1 + i\eta)$, where η is the solid damping factor. Representative values for selected engineering materials are provided in [21]. For tool-holder modeling, typical values for steel and sintered carbide components are in the 0.001–0.002 range.

While the closed form Euler-Bernoulli beam tip receptances provided in Table 7.5 are convenient to apply, accurate solutions are obtained only for beams which exhibit small cross-sectional area to length ratios (i.e., long slender beams). An alternative for beams that do not meet this criterion is the Timoshenko beam model [22]. The corresponding differential equation is given by:

$$\left(\frac{\partial^2 y}{\partial t^2} + \frac{EI}{\rho A} \frac{\partial^4 y}{\partial x^4} \right) + \left(\frac{\rho I}{\hat{k}AG} \frac{\partial^4 y}{\partial t^4} + \frac{EI}{\hat{k}AG} \frac{\partial^4 y}{\partial x^2 \partial t^2} \right) - \left(\frac{I}{A} \frac{\partial^4 y}{\partial x^2 \partial t^2} \right) = 0, \quad (7.86)$$

where \hat{k} is a shape factor that depends on the beam cross section [23] and G is the shear modulus. Eq. 7.86 is grouped into three sections (i.e., three parenthetical expressions). We see that the first section matches the Euler-Bernoulli beam equation provided in Eq. 7.59. The second and third sections account for shear deformations and rotary inertia, respectively. While these additional terms improve the model accuracy (particularly at higher frequencies), the trade-off is that a closed form solution is unavailable. Finite element calculations may be applied, but at the expense of computation time. A description of the Timoshenko free-free beam receptances obtained from finite element calculations is given in [24].

7.5 Assembly Receptance Predictions

In Sects. 7.3 and 7.4, we provided the building blocks for assembly receptance predictions. In this section, we'll detail coupling examples to demonstrate their implementation.

Example 7.3 Free-Free Beam Coupled to Rigid Support As a test of the receptance coupling procedure, let's couple a free-free beam to a rigid support (i.e., a wall) to verify that it matches the clamped-free beam response we derived in Sect. 7.4. As described in Sect. 7.3, we have three primary tasks to complete in order to predict the assembly response. First, we must define the components and coordinates for the model. Here we have two components: a uniform beam with free-free boundary conditions and a rigid support (which exhibits zero receptances); see Fig. 7.21. Second, we need to determine the component receptances. We will apply the closed form receptances provided in Table 7.5. Third, based on the selected model, we express the assembly receptances as a function of the component receptances as shown in Table 7.3.

Let's define the free-free beam to be a solid steel cylinder with a diameter of 10 mm and a length of 125 mm. The elastic modulus is 200 GPa and the density is 7800 kg/m³. We'll select the solid damping factor to be 0.01 for plotting purposes, but in practice a value near 0.001 would be more realistic. The free-free cylinder's direct and cross receptance equations are given in Table 7.5, while the wall receptances are zero. To calculate λ , we need the frequency vector, ω (rad/s); cross-sectional area, A ; and second moment of area, I . We'll use a frequency range of 5000 Hz with a resolution of 0.1 Hz. The variables A and I are defined in Eqs. 7.87 and 7.88 for the cylinder, where d is the cylinder diameter. The displacement-to-force free-free receptance for the cylinder, h_{11} , is shown in Fig. 7.22. We see a first bending natural frequency of 2884.9 Hz. The rigid body behavior is exhibited as the dramatic change in the real part as the frequency approaches zero.

Fig. 7.21 Rigid coupling of the free-free cylinder to a wall

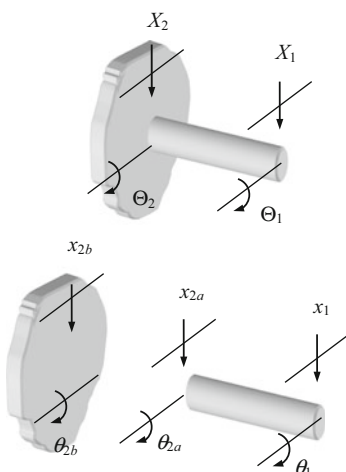
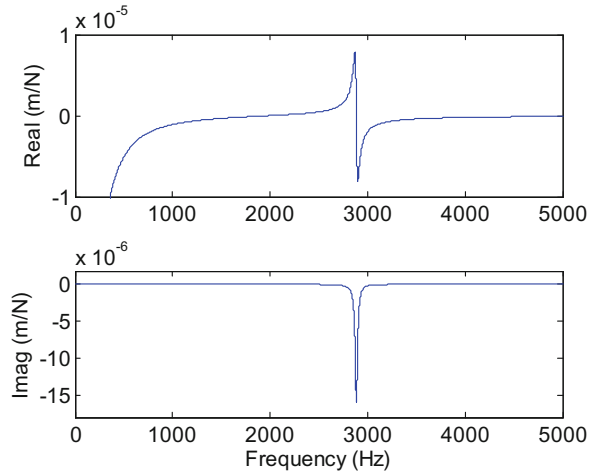


Fig. 7.22 Free-free receptance, h_{11} , for 10 mm diameter by 125 mm long steel cylinder



$$A = \frac{\pi d^2}{4} \quad (7.87)$$

$$I = \frac{\pi d^4}{64} \quad (7.88)$$

To rigidly couple the free-free cylinder to the wall, we apply Eq. 7.54:

$$G_{11} = \begin{bmatrix} H_{11} & L_{11} \\ N_{11} & P_{11} \end{bmatrix} = R_{11} - R_{12a}(R_{2a2a} + R_{2b2b})^{-1}R_{2a1},$$

where the generalized receptance matrices R_{11} , R_{12a} , R_{2a2a} , and R_{2a1} correspond to the cylinder and R_{2b2b} characterizes the wall response. The MATLAB® program p_7_3_1.m is used to complete the receptance coupling procedure. The results are displayed in Figs. 7.23 and 7.24. Figure 7.23 shows the H_{11} response from the $G_{11}(1,1)$ position (solid line). The dotted line in the figure is the clamped-free response, $H_{11} = \frac{-c_1}{\lambda^3 c_8}$, from Table 7.5. We see that the two curves are identical and the rigid body behavior is no longer present due to the coupling conditions. A limited frequency range is displayed in Fig. 7.23 to enable close comparison of the first bending mode. However, all bending modes are included in the Euler-Bernoulli beam receptances. The frequency range is increased in Fig. 7.24 to show the first two assembly bending modes. The vertical axis (response magnitude) is logarithmic in this plot because the second mode magnitude is much smaller than the first. Again, we observe exact agreement between the receptance coupling result (solid) and clamped-free receptance (dotted). An interesting aspect of Fig. 7.24 is that, in addition to the two resonant peaks at 453.4 Hz and 2841.4 Hz, we also see an “antiresonance” at 1988.1 Hz. At this frequency, the response is very small, even for large input force magnitudes.

Fig. 7.23 Comparison of H_{11} receptance coupling result (solid line) and clamped-free response (dotted) for 10 mm diameter by 125 mm long steel cylinder

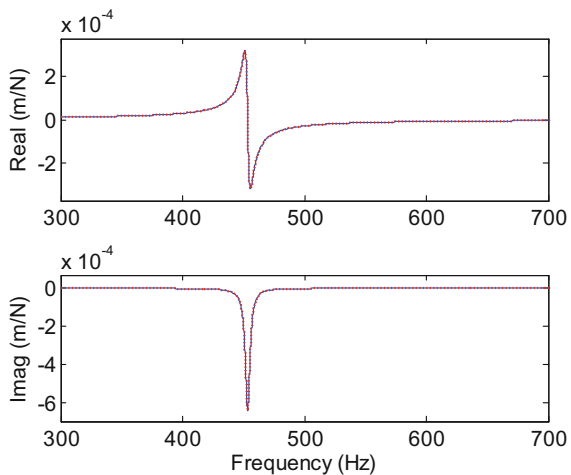
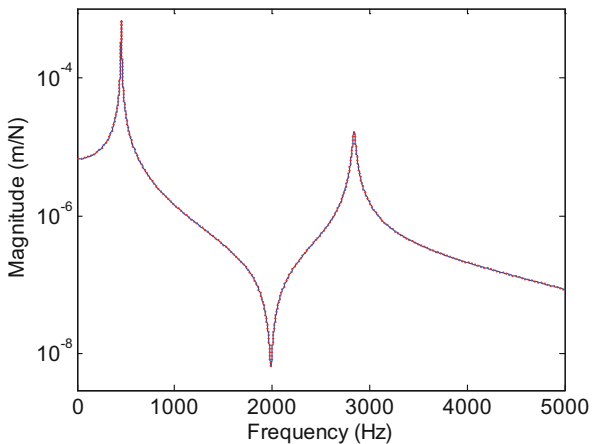


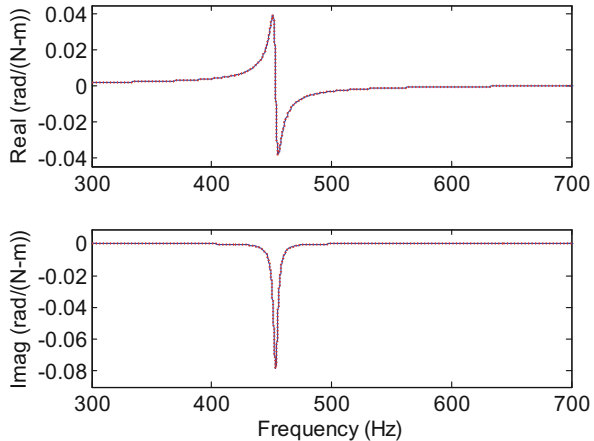
Fig. 7.24 Semilogarithmic plot showing the first two bending modes for H_{11} tip receptances obtained from (1) rigid coupling of free-free beam to wall (solid line); and (2) clamped-free response (dotted)



The rotation-to-couple tip receptance determined from the rigid free-free beam coupling to the wall is also calculated in p_7_3_1.m. This $G_{11}(2,2)$ entry is shown in Fig. 7.25 (solid line). The clamped-free response (dotted line), $P_{11} = \frac{c_s}{\lambda c_8}$, again agrees with the receptance coupling result. We also see that the first mode natural frequency matches the H_{11} result (453.4 Hz), but the magnitude is quite different; note the new units of rad/(N m).

We've already noted that the assembly cross receptances, G_{12} and G_{21} , and the direct receptances at the clamped end, G_{22} , are zero. We can verify this by direct application of Eqs. 7.55, 7.57, and 7.58. For the clamped end direct receptance, Eq. 7.57 simplifies as shown in Eq. 7.89.

Fig. 7.25 Comparison of P_{11} receptance coupling result (solid line) and clamped-free response (dotted) for 10 mm diameter by 125 mm long steel cylinder



$$\begin{aligned} G_{22} &= R_{2a2a} - R_{2a2a}(R_{2a2a} + R_{2b2b})^{-1}R_{2a2a} \\ G_{22} &= R_{2a2a} - R_{2a2a} \left(R_{2a2a} + \begin{bmatrix} 0 & 0 \\ 0 & 0 \end{bmatrix} \right)^{-1} R_{2a2a} \\ G_{22} &= R_{2a2a} - R_{2a2a}(R_{2a2a})^{-1}R_{2a2a} = R_{2a2a} - R_{2a2a} = 0 \end{aligned} \quad (7.89)$$

Similar results are obtained for the cross receptances in Eqs. 7.55 and 7.58 when substituting $R_{2b2b} = \begin{bmatrix} 0 & 0 \\ 0 & 0 \end{bmatrix}$.

Example 7.4 Free-Free Beam Coupled to Clamped-Free Beam Let's now consider the case depicted in Fig. 7.16. A 10 mm diameter by 100 mm long steel cylinder (free-free boundary conditions) is to be rigidly coupled to a clamped-free 50 mm by 50 mm by 200 mm long steel prismatic beam. The steel elastic modulus, density, and solid damping factor are 200 GPa, 7800 kg/m³, and 0.01, respectively. (Again, we selected the solid damping value to be artificially high for display purposes.) The analysis is the same as Example 7.3 except that the R_{2b2b} receptances are no longer zero. They are now defined as shown in Table 7.5, $H_{11} = \frac{-c_1}{\lambda^2 c_8}$, $L_{11} = N_{11} = \frac{c_2}{\lambda^2 c_8}$, and $P_{11} = \frac{c_5}{\lambda c_8}$. We'll again use a frequency range of 5000 Hz with a resolution of 0.1 Hz to calculate λ . The variables A and I are defined in Eqs. 7.90 and 7.91 for the square prismatic beam, where s is the side length of 50 mm. The displacement-to-force free-free receptance for the cylinder, h_{11} , is shown in Fig. 7.26 (solid line). The clamped-free square beam tip receptance, h_{2b2b} , is also displayed (dotted line). We see a first bending natural frequency of 4507.6 Hz for the free-free beam. The clamped-free beam has a first bending frequency of 1022.5 Hz.

$$A = s^2 \quad (7.90)$$

$$I = \frac{s^4}{12} \quad (7.91)$$

Fig. 7.26 Free-free receptance, h_{11} , for 10 mm diameter by 100 mm long steel cylinder (solid line) and clamped-free receptance, h_{2b2b} , for 50 mm square by 200 mm long steel prismatic beam (dotted line)

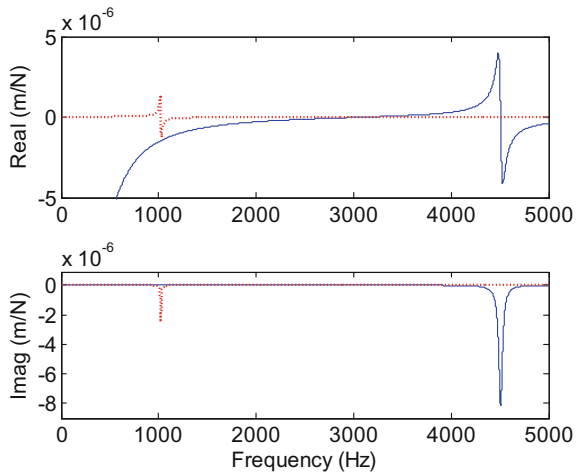
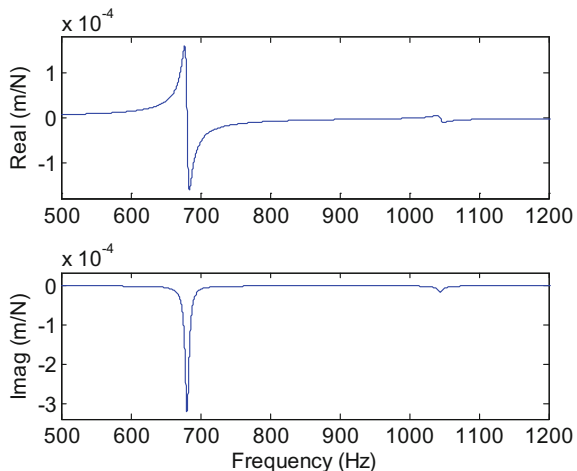


Fig. 7.27 Assembly displacement-to-force tip receptance H_{11} for the rigidly coupled cylinder and prismatic beam shown in Fig. 7.16



The application of Eq. 7.54 to this scenario using program p_7_4_1.m gives Fig. 7.27, which shows H_{11} for the assembly. We see two modes within the 5000 Hz frequency range: one at 1045.2 Hz, near the original clamped-free response and a second more flexible mode at 680.9 Hz due to the now coupled cylinder. Because the prismatic beam is much stiffer than the cylinder, it appears to serve as a nearly rigid support for the cylinder. This may lead us to believe that approximating the assembly as a cylinder clamped to a wall is adequate. However, let's investigate what happens if we modify the prismatic beam to reduce its first bending frequency to a value near the clamped-free cylinder's first bending frequency.

Figure 7.28 displays h_{11} for the free-free cylinder (solid line), as well as h_{2b2b} for a longer clamped-free prismatic beam (dotted line). The cylinder's first bending natural frequency remains at 4507.6 Hz for the free-free boundary conditions.

Fig. 7.28 Free-free receptance, h_{11} , for 10 mm diameter by 100 mm long steel cylinder (solid line) and clamped-free receptance, h_{2b2b} , for 50 mm square by 250 mm long steel prismatic beam (dotted line)

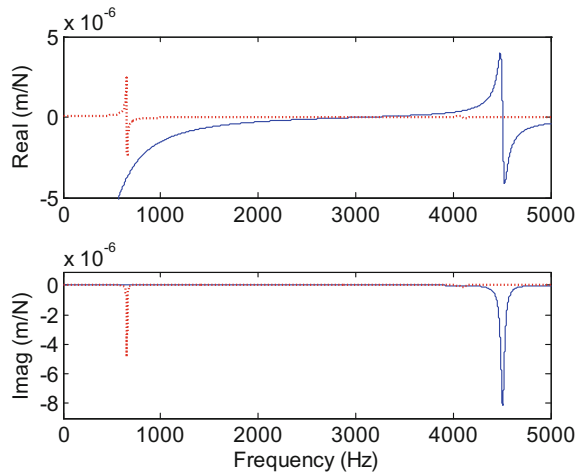
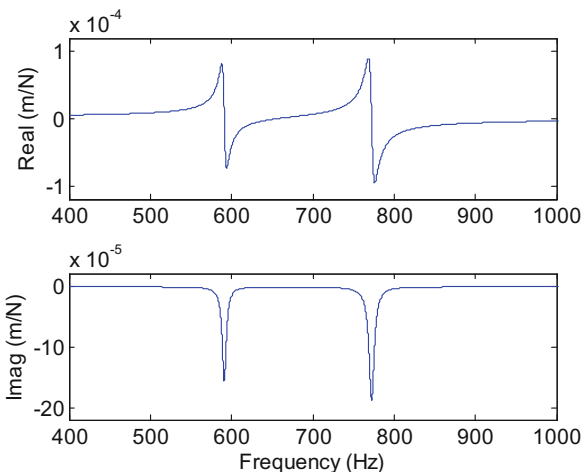


Fig. 7.29 The displacement-to-force tip receptance, H_{11} , for rigid coupling of the 10 mm diameter by 100 mm long cylinder to the 50 mm square by 250 mm long prismatic beam is displayed



However, the first bending frequency for the extended clamped-free beam is reduced to 654.4 Hz. Figure 7.29 shows H_{11} for the cylinder rigidly coupled to a 50 mm square by 250 mm long prismatic beam. The response is now quite different than the assembly receptance shown in Fig. 7.27 for the 200 mm long prismatic beam. Even though the cylinder is coupled to a more flexible base (i.e., a longer clamped-free beam), the assembly response has a smaller peak magnitude. The minimum imaginary value for the new assembly is -1.865×10^{-4} m/N, while the corresponding value for the shorter (and stiffer) prismatic beam assembly is -3.222×10^{-4} m/N; this represents a 42% compliance¹⁰ reduction. The compliance reduction or,

¹⁰Compliance is the inverse of stiffness.

equivalently, the stiffness increase is due to interaction between the two beams in a manner analogous to the well-known dynamic absorber. When the clamped-free prismatic beam's natural frequency is near the coupled cylinder's natural frequency, some energy is able to "pass through" the cylinder and excite the stiffer base. The result is that the energy is more equally partitioned between the two modes and the assembly response appears stiffer [8]. An electrical equivalent is the impedance matching strategy used at cable connections. For example, it is common to use $50\ \Omega$ terminations at all connections to encourage signal transmission and avoid reflection.

One application of this phenomenon is to select tool lengths that encourage the interaction between the clamped-free tool's first bending frequency and one of the spindle natural frequencies (in bending). For slender tools, as the tool overhang length from the holder face is adjusted, its natural frequency can be modified to match a spindle natural frequency. This technique, referred to as "tool length tuning" or simply "tool tuning" [8, 25, 26], can lead to improved dynamic stiffness (i.e., a smaller magnitude for the tool point FRF) and increased allowable axial depths of cut. As we saw with the prismatic beam-cylinder coupling, the surprising outcome is that increasing the tool length can reduce the assembly compliance in some instances. We should also note that forcing this interaction and encouraging the two mode response shown in Fig. 7.29 will generally lead to competing lobes (Sect. 3.4) in the corresponding stability lobe diagram.

7.6 Tool-Holder-Spindle-Machine Receptance Predictions¹¹

As we noted in Sect. 7.2, we can consider the tool-holder-spindle-machine combination as being composed of three parts: the tool, holder, and spindle-machine [7]. This enables us to use the closed form Euler-Bernoulli beam receptances contained in Table 7.5 to describe the tool and holder dynamics; finite element based Timoshenko beam receptances may also be applied, of course. Due to modeling challenges, we measure the spindle-machine response using impact testing techniques. Given the component responses, we then couple their individual FRFs to obtain the assembly response via the receptance coupling substructure analysis (RCSA) approach [7]. Let's now discuss this procedure in more detail.

Figure 7.30 depicts our model composed of the three individual components: I, tool; II, holder; and III, spindle-machine.¹² So far we have not discussed a three component model. However, by sequentially coupling the components, we can limit the analysis to the two component case. For example, we can first couple the free-free holder and tool to form substructures I-II identified in Fig. 7.31. To carry out this step, we begin by defining the components and coordinates as displayed in

¹¹T. Schmitz recognizes the significant contributions of G.S. Duncan to this section.

¹²US Patent No. 8,131,525 B2.

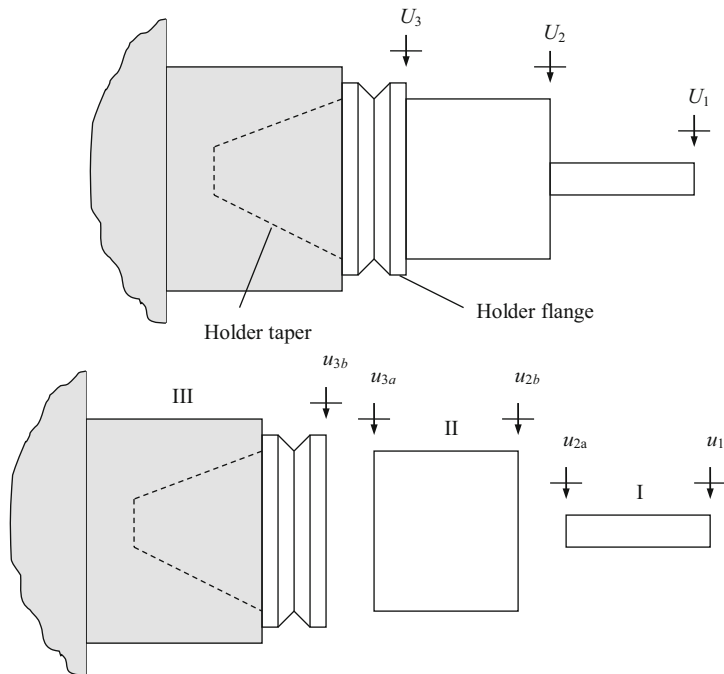


Fig. 7.30 Three component receptance coupling model of tool (I), holder (II), and spindle-machine (III)

Fig. 7.31 (Sub)assembly I-II composed of tool (I) and holder (II). The generalized force Q_1 is applied to U_1 to determine G_{11} and G_{3a1}

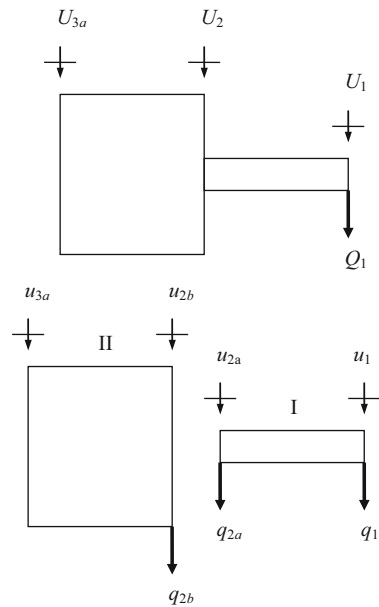


Fig. 7.31. We then calculate the component receptances. If we apply the Euler-Bernoulli receptances described by Bishop and Johnson [1], the appropriate equations are provided in Table 7.5. For I, we have the free-free receptances $h_{11} = \frac{-c_1}{\lambda^3 c_7}$, $l_{11} = n_{11} = \frac{c_2}{\lambda^2 c_7}$, $p_{11} = \frac{c_5}{\lambda c_7}$, $h_{2a2a} = \frac{-c_1}{\lambda^3 c_7}$, $l_{2a2a} = n_{2a2a} = \frac{-c_2}{\lambda^2 c_7}$, $p_{2a2a} = \frac{c_5}{\lambda c_7}$, $h_{12a} = h_{2a1} = \frac{c_3}{\lambda^2 c_7}$, $l_{12a} = n_{2a1} = \frac{-c_4}{\lambda^2 c_7}$, $l_{2a1} = n_{12a} = \frac{c_4}{\lambda^2 c_7}$, and $p_{12a} = p_{2a1} = \frac{c_6}{\lambda c_7}$, where $\lambda^4 = \omega^2 \frac{\rho A}{EI(1+\eta)}$ and L , ρ , A , E , I , and η depend on the tool geometry and material properties. For II, we simply replace coordinate 1 with $2b$ and coordinate $2a$ with $3a$ in the previous equations. Additionally, we must use the holder geometry and material properties to define λ , L , ρ , A , E , I , and η . We will assume a rigid coupling between these two components and follow the approaches described previously to determine the (sub)assembly I-II tip receptances: (direct) G_{11} and G_{3a3a} and (cross) G_{13a} and G_{3a1} .

To find G_{11} and G_{3a1} , we apply Q_1 to coordinate U_1 as shown in Fig. 7.31. The components' displacements/rotations are $u_1 = R_{11}q_1 + R_{12a}q_{2a}$, $u_{2a} = R_{2a1}q_1 + R_{2a2a}q_{2a}$, $u_{2b} = R_{2b2b}q_{2b}$, and $u_{3a} = R_{3a2b}q_{2b}$. The equilibrium conditions are $q_{2a} + q_{2b} = 0$ and $q_1 = Q_1$. We substitute the component displacements/rotations and equilibrium conditions into the compatibility condition, $u_{2b} - u_{2a} = 0$, to obtain the expression for q_{2b} shown in Eq. 7.92. The component force q_{2a} is then determined from the equilibrium condition $q_{2a} = -q_{2b}$. The expression for G_{11} is provided in Eq. 7.93. The cross receptance matrix G_{3a1} is shown in Eq. 7.94.

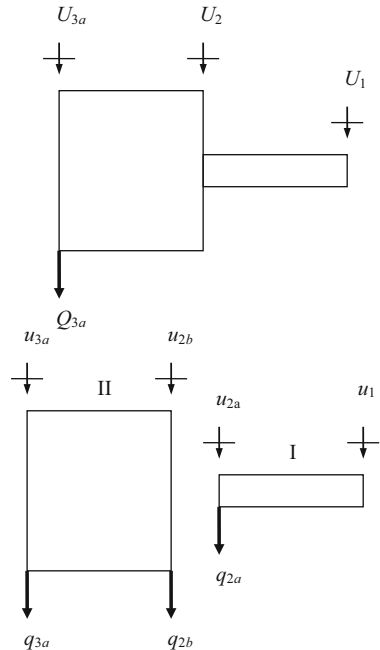
$$\begin{aligned} u_{2b} - u_{2a} &= 0 \\ R_{2b2b}q_{2b} - R_{2a1}q_1 - R_{2a2a}q_{2a} &= 0 \\ (R_{2a2a} + R_{2b2b})q_{2b} - R_{2a1}Q_1 &= 0 \\ q_{2b} &= (R_{2a2a} + R_{2b2b})^{-1}R_{2a1}Q_1 \end{aligned} \tag{7.92}$$

$$\begin{aligned} G_{11} &= \frac{U_1}{Q_1} = \frac{u_1}{Q_1} = \frac{R_{11}q_1 + R_{12a}q_{2a}}{Q_1} = \frac{R_{11}Q_1 - R_{12a}(R_{2a2a} + R_{2b2b})^{-1}R_{2a1}Q_1}{Q_1} \\ G_{11} &= R_{11} - R_{12a}(R_{2a2a} + R_{2b2b})^{-1}R_{2a1} = \begin{bmatrix} H_{11} & L_{11} \\ N_{11} & P_{11} \end{bmatrix} \end{aligned} \tag{7.93}$$

$$\begin{aligned} G_{3a1} &= \frac{U_{3a}}{Q_1} = \frac{u_{3a}}{Q_1} = \frac{R_{3a2b}q_{2b}}{Q_1} = \frac{R_{3a2b}(R_{2a2a} + R_{2b2b})^{-1}R_{2a1}Q_1}{Q_1} \\ G_{3a1} &= R_{3a2b}(R_{2a2a} + R_{2b2b})^{-1}R_{2a1} = \begin{bmatrix} H_{3a1} & L_{3a1} \\ N_{3a1} & P_{3a1} \end{bmatrix} \end{aligned} \tag{7.94}$$

We find the remaining tip receptances G_{3a3a} and G_{13a} by applying Q_{3a} to coordinate U_{3a} as shown in Fig. 7.32. The components displacements/rotations are

Fig. 7.32 (Sub)assembly I-II composed of tool (I) and holder (II). The generalized force Q_{3a} is applied to U_{3a} to determine G_{3a3a} and G_{13a}



$u_1 = R_{12a}q_{2a}$, $u_{2a} = R_{2a2a}q_{2a}$, $u_{2b} = R_{2b2b}q_{2b} + R_{2b3a}q_{3a}$, and $u_{3a} = R_{3a2b}q_{2b} + R_{3a3a}q_{3a}$. The equilibrium conditions are $q_{2a} + q_{2b} = 0$ and $q_{3a} = Q_{3a}$. In the same manner as before, we substitute the component displacements/rotations and equilibrium conditions into the compatibility condition, $u_{2a} - u_{2b} = 0$, to determine q_{2a} ; see Eq. 7.95. The component force q_{2b} is found from $q_{2b} = -q_{2a}$. The equation for the direct receptance G_{3a3a} is shown in Eq. 7.96, while the cross receptance G_{13a} is provided in Eq. 7.97.

$$\begin{aligned} u_{2a} - u_{2b} &= 0 \\ R_{2a2a}q_{2a} - R_{2b2b}q_{2b} - R_{2b3a}q_{3a} &= 0 \\ (R_{2a2a} + R_{2b2b})q_{2a} - R_{2b3a}Q_{3a} &= 0 \\ q_{2a} &= (R_{2a2a} + R_{2b2b})^{-1}R_{2b3a}Q_{3a} \end{aligned} \quad (7.95)$$

$$\begin{aligned} G_{3a3a} &= \frac{U_{3a}}{Q_{3a}} = \frac{u_{3a}}{Q_{3a}} = \frac{R_{3a3a}q_{3a} + R_{3a2b}q_{2b}}{Q_{3a}} = \frac{R_{3a3a}Q_{3a} - R_{3a2b}(R_{2a2a} + R_{2b2b})^{-1}R_{2b3a}Q_{3a}}{Q_{3a}} \\ G_{3a3a} &= R_{3a3a} - R_{3a2b}(R_{2a2a} + R_{2b2b})^{-1}R_{2b3a} = \begin{bmatrix} H_{3a3a} & L_{3a3a} \\ N_{3a3a} & P_{3a3a} \end{bmatrix} \end{aligned} \quad (7.96)$$

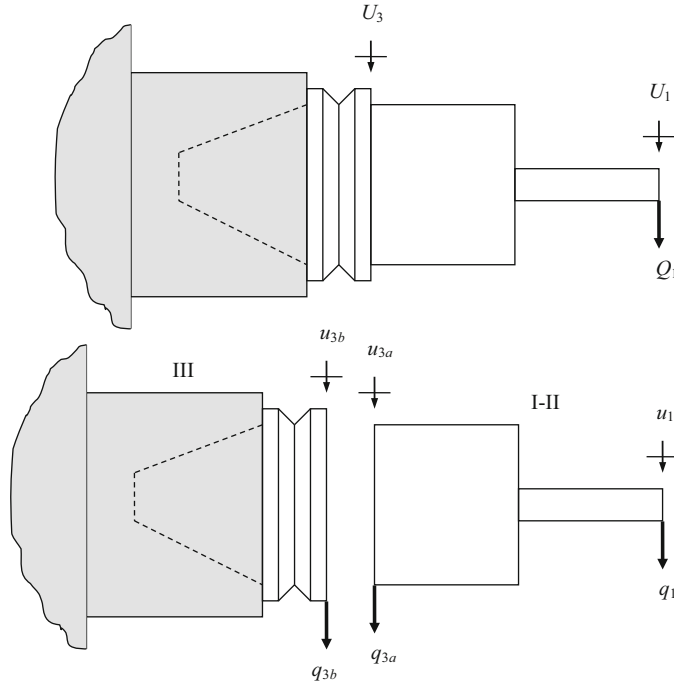


Fig. 7.33 The (sub)assembly I-II is rigidly coupled to the spindle-machine (III) to determine the tool point receptances, G_{11}

$$G_{13a} = \frac{U_1}{Q_{3a}} = \frac{u_1}{Q_{3a}} = \frac{R_{12a}q_{2a}}{Q_{3a}} = \frac{R_{12a}(R_{2a2a} + R_{2b2b})^{-1}R_{2b3a}Q_{3a}}{Q_{3a}} \quad (7.97)$$

$$G_{13a} = R_{12a}(R_{2a2a} + R_{2b2b})^{-1}R_{2b3a} = \begin{bmatrix} H_{13a} & L_{13a} \\ N_{13a} & P_{13a} \end{bmatrix}$$

Now that we've coupled components I and II to form the (sub)assembly I-II, we can rigidly couple this result to the spindle-machine. See Fig. 7.33, which is very similar to Fig. 7.16. To apply Eq. 7.54, we must make minor modifications to the subscripts to match our new coordinates. Relative to the original equation, we see that we must replace coordinate $2a$ with $3a$ and coordinate $2b$ with $3b$. Therefore, the tool point receptances are defined by:

$$G_{11} = R_{11} - R_{13a}(R_{3a3a} + R_{3b3b})^{-1}R_{3a1}, \quad (7.98)$$

where the R_{ij} matrices are the (sub)assembly matrices from the I-II coupling result. Therefore, we have $R_{11} = G_{11}$ from Eq. 7.93, $R_{3a1} = G_{3a1}$ from Eq. 7.94, $R_{3a3a} = G_{3a3a}$ from Eq. 7.96, and $R_{13a} = G_{13a}$ from Eq. 7.97. We still have one matrix in Eq. 7.98 that is unknown, however. We do yet not know the spindle-machine receptances R_{3b3b} .

7.6.1 Spindle-Machine Receptances

Before discussing R_{3b3b} in more detail, let's take another look at the model in Fig. 7.30. We notice that the section of the tool-holder beyond the flange has been artificially separated from the rest of the holder, which includes the portion that is inserted and clamped in the spindle. There are two reasons for this approach. First, for a given spindle, all holders inserted in that spindle will typically have the same flange geometry. In general, it is only the portion of the holder beyond the flange that varies from one holder to the next; this is necessary for automatic tool changes. Second, the portion of the spindle that we need to excite and measure is the spindle shaft itself. Unfortunately, typical spindle designs do not give us access to the spindle shaft. It is located within the spindle housing and interfaces with the holder-spindle coupling mechanism (such as HSK, CAT, or others). Therefore, it is convenient to consider the holder flange and taper to be part of the spindle itself. This also locates potential flexibility in the holder-spindle coupling within the measured spindle receptances so that they do not have to be separately modeled.

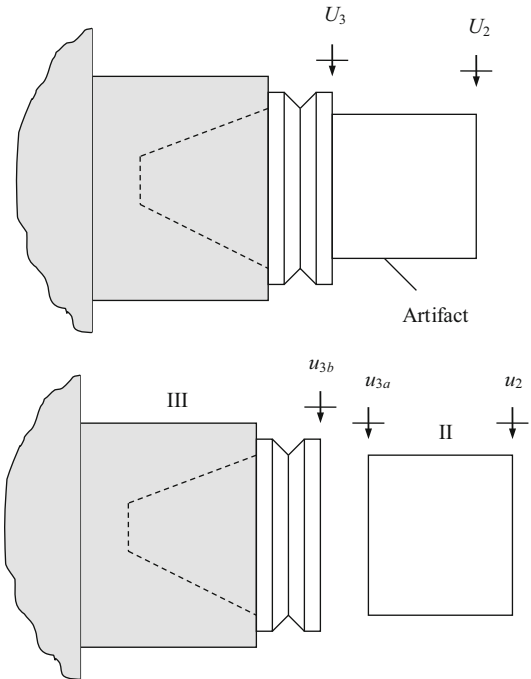
Given our discussion of impact testing in Sect. 2.6, we see that the direct FRF h_{3b3b} would be straightforward to obtain. We'd simply need to modify a holder to remove the portion beyond the flange, place this artifact in the spindle, and then excite spindle machine at the free end of the holder (on the flange) while measuring the response at the same location. However, as we've discussed, we also require the direct displacement-to-couple, rotation-to-force, and rotation-to-couple FRFs to fully populate the R_{3b3b} matrix. These additional receptances are not so easy to obtain experimentally. Exciting the system with an impulsive couple is particularly challenging. Therefore, we can consider a different approach.

Rather than using a measurement artifact that includes only the flange and taper, let's select an artifact that incorporates some length beyond the flange as shown in Fig. 7.34. If we can determine the assembly matrix $G_{22} = \begin{bmatrix} H_{22} & L_{22} \\ N_{22} & P_{22} \end{bmatrix}$ experimentally, then we can use this information, together with a model of the portion of the artifact beyond the flange, to determine R_{3b3b} . By replacing coordinate 1 with 2, coordinate 2a with 3a, and coordinate 2b with 3b in Eq. 7.54, we obtain the free end response for the artifact-spindle-machine assembly:

$$G_{22} = R_{22} - R_{23a}(R_{3a3a} + R_{3b3b})^{-1}R_{3a2}. \quad (7.99)$$

We can rearrange Eq. 7.99 to isolate R_{3b3b} . See Eq. 7.100, where the R_{ij} matrices are obtained from a model of the free-free portion of the artifact beyond the flange (component II in Fig. 7.34) and G_{22} is determined from measurements. We can describe this decomposition process of identifying the substructure receptances, R_{3b3b} , from the measured assembly receptances, G_{22} , and modeled substructure receptances, R_{3a2} , R_{22} , R_{23a} , and R_{3a3a} , as “inverse RCSA.”

Fig. 7.34 Artifact model for G_{22} measurement; these receptances are subsequently used to determine R_{3b3b} by inverse RCSA (Eq. 7.100)

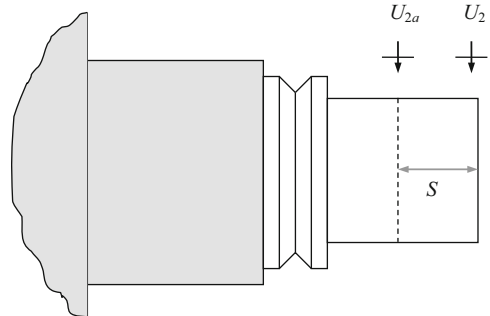


$$\begin{aligned}
 G_{22} - R_{22} &= -R_{23a}(R_{3a3a} + R_{3b3b})^{-1}R_{3a2} \\
 R_{23a}^{-1}(R_{22} - G_{22})R_{3a2}^{-1} &= (R_{3a3a} + R_{3b3b})^{-1} \\
 R_{3a2}(R_{22} - G_{22})^{-1}R_{23a} &= R_{3a3a} + R_{3b3b} \\
 R_{3b3b} &= R_{3a2}(R_{22} - G_{22})^{-1}R_{23a} - R_{3a3a}
 \end{aligned} \tag{7.100}$$

Our only remaining task is to define the G_{22} receptances. The displacement-to-force term $H_{22} = \frac{X_2}{F_2}$ is straightforward to obtain. We simply excite the assembly at coordinate 2, typically via an impact hammer, and record the response at the same location using, for example, an accelerometer, laser vibrometer, or capacitance probe. To find the rotation-to-force receptance $N_{22} = \frac{\Theta_2}{F_2}$, we can implement a first-order finite difference approach [27]. By measuring both the direct FRF H_{22} and cross FRF $H_{2a2} = \frac{X_{2a}}{F_2}$, we can compute N_{22} according to Eq. 7.101. The displacement-to-force cross FRF H_{2a2} is obtained by exciting the assembly at U_2 and measuring the response at coordinate U_{2a} , located a distance S from the artifact's free end, as shown in Fig. 7.35. Equivalently, we could measure H_{22a} , where the linear transducer is placed at U_2 and the force is applied at U_{2a} .

$$N_{22} = \frac{H_{22} - H_{2a2}}{S} = \frac{H_{22} - H_{22a}}{S} \tag{7.101}$$

Fig. 7.35 Locations for direct and cross artifact-spindle-machine assembly measurements



We can assume reciprocity to establish the equality: $L_{22} = N_{22}$. (We see this same behavior for the free-free beam receptances in Table 7.5.) We cannot rely on reciprocity or finite difference computations to find P_{22} . However, using the other three artifact-spindle-machine receptances, we can synthesize P_{22} [28]. See Eq. 7.102. Given P_{22} , we have now fully populated G_{22} , and we can use Eq. 7.100 to obtain R_{3b3b} .

$$P_{22} = \frac{\Theta_2}{M_2} = \frac{F_2}{X_2} \frac{X_2}{M_2} \frac{\Theta_2}{F_2} = \frac{1}{H_{22}} L_{22} N_{22} = \frac{N_{22}^2}{H_{22}} \quad (7.102)$$

Let's conclude the section by summarizing the RCSA steps and discussing implementation considerations. Given the three component model shown in Fig. 7.30, our initial task is to identify the substructure receptances. We find the tool (I) and holder (II) free-free receptances from models. These may be based on Euler-Bernoulli beam theory or finite element computations, for example. We use artifact measurements and inverse RCSA to determine the spindle-machine (III) receptances. Once we have the substructure dynamics defined, we sequentially couple the three component receptance matrices to obtain the tool point FRF, H_{11} , that is required for the stability and surface location error analyses described in Chaps. 4, 5, and 6. A benefit of this technique is that once the spindle-machine receptances have been identified, any tool-holder combination can be coupled to the selected spindle without the need for additional measurements.

A final point for consideration is the tool and holder models. One issue is that a portion of the tool is inserted in the holder; see component III in Fig. 7.36. This gives the potential for cross sections with different material properties between a steel holder and carbide tool, for example. Equivalent structural rigidity, EI_{eq} , and mass per unit length, ρA_{eq} , values can be calculated as shown in Eqs. 7.103 and 7.104, where the h and t subscripts indicate the holder and tool, respectively. These may then be substituted for the EI and ρA products in the Euler-Bernoulli beam receptance equations defined in Table 7.5.

$$EI_{eq} = E_h I_h + E_t I_t \quad (7.103)$$

$$\rho A_{eq} = \rho_h A_h + \rho_t A_t \quad (7.104)$$

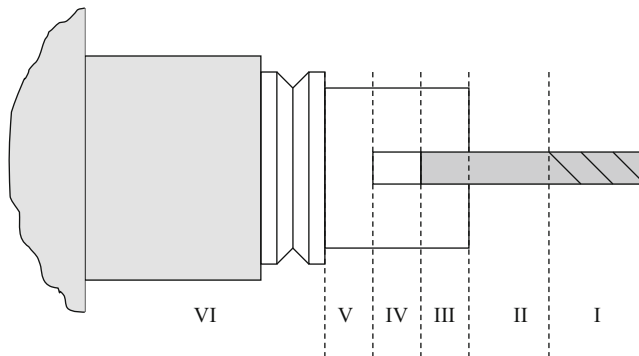


Fig. 7.36 Component definitions to account for changes in cross-sectional dimensions and the portion of the tool inserted in the holder

A second issue for the Euler-Bernoulli receptances is that constant cross-sectional dimensions are required. Changes in cross section can be accommodated by defining a new component for each constant cross-sectional portion. Components I through V are defined in Fig. 7.36 to represent the required tool and holder substructures. Here we see that a separate component, I, was defined for the fluted portion of the tool. This is necessary because the actual second moment of area, I , and area, A , for the helical flutes differ from the cylindrical shank I and A values. One approach is to define an equivalent diameter that is then used in the I and A calculations. See [29, 30], for example.



In a Nutshell

If measurement of the tool tip FRF is convenient for the machine tool user, then the information required for preprocess predictions of machining performance can be directly obtained. However, if FRF measurements are difficult for the user to complete, then receptance coupling offers an alternative.

While receptance coupling requires accurate measurements of the spindle-machine substructure, these measurements certainly fall within the domain of expert consultants. If the spindle-machine response is archived and the computations are embedded in software, then the power of a machine tool user to predict the assembly FRF for a new unmeasured tool is formidable. The predicted FRF can be used to compute stability lobes and surface location error and enable the end user significant advantage because he/she will know which cuts are acceptable and which are not for the selected tool-holder-spindle-machine combination.

The previous scenario highlights the thrust of this book. It is possible to use the techniques described here to predict machining performance with sufficient accuracy that the trial and error process development approach so prevalent in machining operations today can be rendered obsolete.

7.7 Accelerometer Mass Compensation

Let's now discuss a novel application of RCSA in order to improve FRF measurement accuracy. In impact testing, FRFs are measured using an instrumented hammer to excite the system and (typically) an accelerometer to record the response. However, the measured FRF differs slightly from the actual FRF due to (1) the accelerometer and cable mass; and (2) the cable damping effects. To compensate for both mass loading and cable damping, we will implement the inverse RCSA approach. In this approach, a model of the accelerometer cable is decoupled from the measured FRF to isolate the structure's FRF.

As we've demonstrated, RCSA is used to predict an assembly's receptances by coupling receptances from the individual components. The connections between components can be rigid or flexible with or without energy dissipation (damping). An example for rigid coupling of two components is displayed in Fig. 7.37.

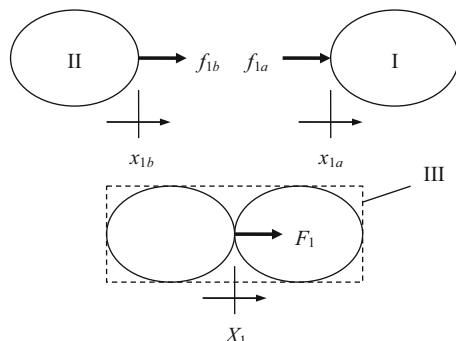
As described in Sect. 7.2, the component direct receptances can be described as $h_{1a1a} = \frac{x_{1a}}{f_{1a}}$ (component I) and $h_{1b1b} = \frac{x_{1b}}{f_{1b}}$ (component II). The compatibility condition for the rigid coupling is $x_{1b} - x_{1a} = 0$. The equilibrium condition, $f_{1a} + f_{1b} = F_1$, relates the internal forces to the external force. The assembly (III) direct receptance, H_{11} , at assembly coordinate X_1 can be expressed as shown in Eq. 7.105.

$$H_{11} = \frac{X_1}{F_1} = h_{1a1a} - h_{1a1a}(h_{1a1a} + h_{1b1b})^{-1}h_{1a1a} \quad (7.105)$$

A tool point FRF may be measured by impact testing as shown in Fig. 7.38a (see also Sect. 2.6). However, the experimental FRF differs from the actual FRF to some extent due to the accelerometer and cable mass for this contact-type measurement. A reduction in the natural frequency(s) and FRF magnitude may be observed, depending on the amount of mass loading and its ratio to the modal mass(es) for the system under test.

The accelerometer-cable mass can be compensated using inverse RCSA, where the corresponding RCSA model is depicted in Fig. 7.38b. In this model, it is assumed that the accelerometer is rigidly coupled to the tool point (using wax or other

Fig. 7.37 Two-component RCSA model: I and II are individual components and III is the assembly. Component coordinates and forces are lower case; assembly coordinates and forces are upper case



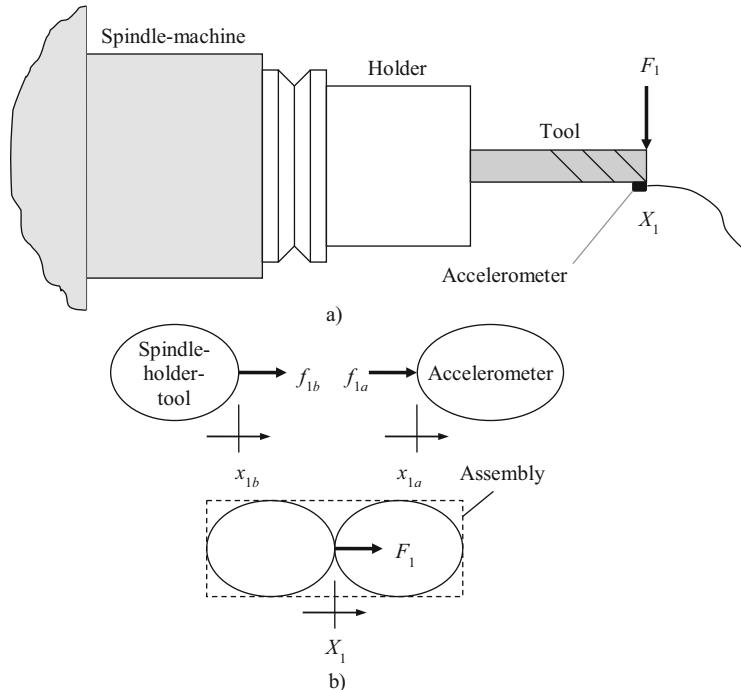


Fig. 7.38 (a) FRF measurement and (b) RCSA model

connection strategy). The measurement provides the assembly receptance, $H_{11} = \frac{X_1}{F_1}$. The accelerometer-cable receptance is $h_{1a1a} = \frac{x_{1a}}{f_{1a}}$, while the unknown tool point receptance is $h_{1b1b} = \frac{x_{1b}}{f_{1b}}$. The tool point receptance can be determined by rearranging Eq. 7.105 as shown in Eq. 7.106. This approach is referred to as inverse RCSA since Eq. 7.106 represents a decoupling, rather than a coupling, operation.

$$h_{1b1b} = -h_{1a1a} + h_{1a1a}(h_{1a1a} - H_{11})^{-1}h_{1a1a} \quad (7.106)$$

For mass compensation only (i.e., mass loading of the structure under test by the accelerometer-cable), the accelerometer-cable may be defined as a point mass. The corresponding receptance (m/N) is provided in Eq. 7.107, where m is the mass (kg) and ω is the frequency (rad/s).

$$h_{1a1a} = \frac{1}{-m\omega^2} \quad (7.107)$$

In addition to mass loading, compensation for energy dissipation by the cable motion may also be included in the inverse RCSA model. In this case, the accelerometer-cable may be defined as a point mass with a lumped parameter (massless) viscous damper. The corresponding receptance (m/N) is provided in Eq. 7.108, where m is the mass (kg), c is the viscous damping coefficient (N s/m),

and ω is the frequency (rad/s). Experimental results for both mass loading and cable damping compensation are presented in [31].

$$h_{1a1a} = \frac{1}{-m\omega^2 + i\omega c} \quad (7.108)$$

7.8 Thin Rib Dynamics

It is common practice to produce monolithic metallic components with thin ribs from solid billets by machining. This enables complex parts with high strength-to-weight ratio to be produced without significant assembly time and cost. Application domains range from aerospace structures to laptop cases. With the recent advances in metal additive manufacturing, it is also possible to produce near net shape parts that require only minimal machining to provide the desired surface finish and dimensional accuracy. This is particularly attractive for titanium alloys due to their high material cost and low machinability. The inherent challenge with this hybrid (i.e., combined additive and subtractive) approach is machining flexible parts. The low dynamic stiffness of the thin, near net shape ribs limits both machining stability (Chap. 4) and part accuracy via the surface location errors that can arise from forced vibrations (Chap. 5).

One option for modeling and predicting the thin rib dynamics is finite element analysis (see Table 7.6 for a selection of prior research efforts). In this section, however, we'll present an analytical approach to describe the stiffness and natural frequency of fixed-free beams, as well as the change in stiffness and natural frequency as material is removed by milling. We address the specific challenge of near net shape machining, where an initially thin rib is machined to produce a thinner rib. We'll use fixed-free beams with stepped profiles to represent the thin rib geometries and subsequent material removal [32]. The advantage of an analytical approach to the system dynamics prediction is that, as the dynamics change, the machining conditions can be selected and updated at less computational expense than a full finite element solution to maximize material removal rate for the current dynamic system. Naturally, these operating parameters change as material is removed, so an analytical updating procedure is beneficial.

In the analytical approach, the free-free receptances for the machined section of the beam are rigidly coupled to the remaining (unmachined) fixed-free section; see Fig. 7.39, where E is the elastic modulus and I is the second moment of area. Using rigid compatibility and equilibrium conditions, the assembly direct receptances, $H_{11} = \frac{Y_1}{F_1}$ and $H_{22} = \frac{Y_2}{F_2}$, at assembly coordinates Y_1 and Y_2 are written as a function of the component receptances at coordinates 1, 2a, and 2b. As in previous sections, the component receptances are identified using lower case variables, while the assembly receptances are represented using upper case variables.

The assembly direct receptances at coordinates 1 and 2 are provided in Eqs. 7.109 and 7.110.

Table 7.6 Prior research in thin rib machining

First author	Year	Ref.	Topic
Y. Altintas	1995	[33]	The authors considered the influence of plate dynamics on the geometric accuracy of machined thin ribs
J. Tlusty	1996	[25]	Techniques for machining thin ribs using relieved shank tooling in a series of axial passes, finishing the rib on every pass, were described
S. Smith	1998	[34]	Tool path strategies for the machining of thin webs which rely on the support of the unmachined workpiece were investigated
H. Ning	2003	[35]	Finite element thin rib part models were used to assess dimensional accuracy during milling
S. Ratchev	2004	[36]	Force induced geometric errors were predicted in thin rib machining using finite element analysis and a voxel transformation model
S. Ratchev	2004	[37]	An adaptive theoretical force finite element analysis deflection model was used to predict thin rib surface errors during milling
U. Bravo	2005	[38]	A three-dimensional stability lobe diagram was presented that considered both the part and tool frequency response functions and the intermediate stages of the rib machining
S. Ratchev	2005	[39]	Finite element models were used to predict and compensate force induced geometric errors in machining of thin rib structures
V. Thevenot	2006	[40]	A three-dimensional stability lobe diagram was presented that incorporated the spatial variation in the thin rib dynamics. Modal testing and finite element analysis were used to identify the thin rib frequency response functions
I. Mañé	2008	[41]	A spindle-tool finite element model that considered the gyroscopic moment of the spindle rotor and the speed dependent bearing stiffness was coupled to a finite element model of the thin rib part to predict milling stability
J.K. Rai	2008	[42]	A finite element based milling process plan verification model was presented. The effects of fixturing, operation sequence, tool path, and operating parameters were considered to predict the thin rib part deflections
S. Seguy	2008	[43]	The authors examined the relationship between chatter instability and surface roughness for thin rib milling. Finite element models were used to describe the rib dynamics
O.B. Adetoro	2009	[44]	Finite element and experimental frequency response functions were used to obtain stable operating parameters for thin rib machining
W. Chen	2009	[45]	The authors considered the effect of machining deformation that occurs in the current layer on the nominal cutting depth in the next layer during thin rib milling
L. Gang	2009	[46]	Three-dimensional finite element models of a helical tool and a thin titanium alloy (6Al-4V) cantilever were used to predict the cutting deformation during milling
L. Arnaud	2011	[47]	Finite element analysis was used to model the part and time domain simulation was used to predict the thin rib machining stability
R. Izamshaw	2011	[48]	A combination of finite element and statistical analyses was used to predict part deflection during thin rib machining

(continued)

Table 7.6 (continued)

First author	Year	Ref.	Topic
S. Smith	2012	[49]	Sacrificial structure preforms that support the part during machining, but are not a part of the finished component, were designed and tested
A. Polishetty	2014	[50]	The trochoidal milling strategy was used for thin rib machining of titanium alloy 6Al-4V

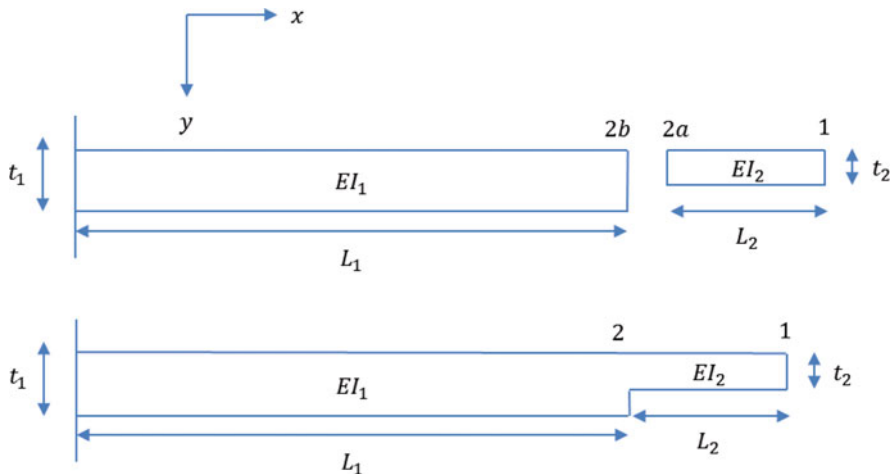


Fig. 7.39 Beam model for RCSA. (Top) The two components and associated coordinates (1 and 2a for the free-free component and 2b for the fixed-free component) are identified. (Bottom) The assembly and associated coordinates (1 and 2) are shown

$$\begin{bmatrix} H_{11} & L_{11} \\ N_{11} & P_{11} \end{bmatrix} = \begin{bmatrix} h_{11} & l_{11} \\ n_{11} & p_{11} \end{bmatrix} - \begin{bmatrix} h_{12a} & l_{12a} \\ n_{12a} & p_{12a} \end{bmatrix} \left(\begin{bmatrix} h_{2a2a} & l_{2a2a} \\ n_{2a2a} & p_{2a2a} \end{bmatrix} + \begin{bmatrix} h_{2b2b} & l_{2b2b} \\ n_{2b2b} & p_{2b2b} \end{bmatrix} \right)^{-1} \begin{bmatrix} h_{2a1} & l_{2a1} \\ n_{2a1} & p_{2a1} \end{bmatrix} \quad (7.109)$$

$$\begin{bmatrix} H_{22} & L_{22} \\ N_{22} & P_{22} \end{bmatrix} = \begin{bmatrix} h_{2a2a} & l_{2a2a} \\ n_{2a2a} & p_{2a2a} \end{bmatrix} - \begin{bmatrix} h_{2a2a} & l_{2a2a} \\ n_{2a2a} & p_{2a2a} \end{bmatrix} \left(\begin{bmatrix} h_{2a2a} & l_{2a2a} \\ n_{2a2a} & p_{2a2a} \end{bmatrix} + \begin{bmatrix} h_{2b2b} & l_{2b2b} \\ n_{2b2b} & p_{2b2b} \end{bmatrix} \right)^{-1} \begin{bmatrix} h_{2a2a} & l_{2a2a} \\ n_{2a2a} & p_{2a2a} \end{bmatrix} \quad (7.110)$$

The component receptances can be obtained from measurements or models. Two modeling options are the Euler-Bernoulli and Timoshenko beams. Let's implement the Timoshenko beam model to find the free-free receptances. This requires a numerical solution of the partial differential equation displayed in Eq. 7.86. To

determine the required fixed-free receptances for the L_1 section component, the free-free receptances for this component are rigidly coupled to a rigid boundary (i.e., zero receptances). Equation 7.109 is also applied for this sub-step, where the 2b coordinate is assigned to the rigid boundary and the 1 and 2a coordinates to the L_1 section component.

To provide a numerical validation of the analytical coupling approach, comparisons between the RCSA predictions and finite element calculations were completed. Multiple beam geometries were tested where the beam thickness was reduced over a varying length, L_2 . In each case, the natural frequency and modal stiffness were extracted by peak picking from the direct receptances (see Sect. 2.5). Natural frequency, f_n , results are presented in Table 7.7 and Fig. 7.40, where the steel beam's elastic modulus was 200 GPa, its width was 20 mm, Poisson's ratio was 0.3, and the density was 7800 kg/m³.

Table 7.7 Comparison of finite element (FE) and RCSA natural frequency predictions

L_1 (mm)	L_2 (mm)	t_1 (mm)	t_2 (mm)	FE f_n (Hz)	RCSA f_n (Hz)	% diff.
150	0	6	6	217.96	217.87	0.04
146	4	6	4	221.79	221.70	0.04
142	8	6	4	225.51	225.42	0.04
132	18	6	4	234.28	234.19	0.04
122	28	6	4	242.03	241.96	0.03
100	50	6	4	253.20	253.37	-0.07
75	75	6	4	248.22	249.26	-0.42
50	100	6	4	219.84	221.82	-0.90
25	125	6	4	180.46	182.63	-1.20
10	140	6	4	157.53	159.54	-1.28
0	150	4	4	145.39	145.34	0.03

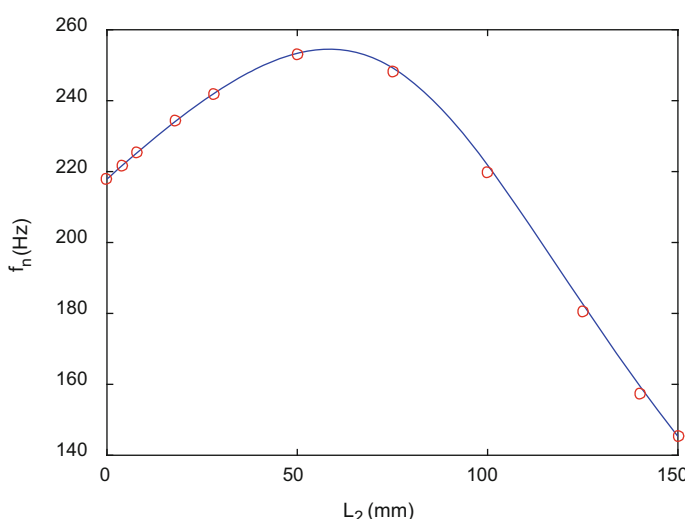
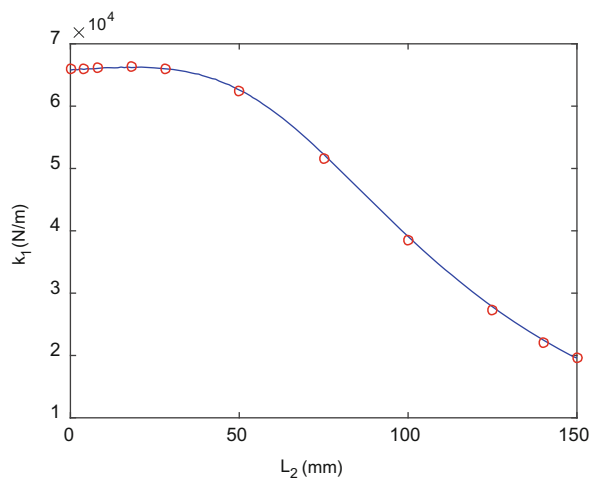


Fig. 7.40 Graphical comparison of FE (circles) and RCSA (line) natural frequency predictions

Table 7.8 Comparison of finite element (FE) and k_1 stiffness predictions

L_1 (mm)	L_2 (mm)	t_1 (mm)	t_2 (mm)	FE k_1 (N/m)	RCSA k_1 (N/m)	% diff.
150	0	6	6	6.5915×10^4	6.5758×10^4	0.24
146	4	6	4	6.6054×10^4	6.5894×10^4	0.24
142	8	6	4	6.6176×10^4	6.6016×10^4	0.24
132	18	6	4	6.6329×10^4	6.6185×10^4	0.22
122	28	6	4	6.6057×10^4	6.5969×10^4	0.13
100	50	6	4	6.2371×10^4	6.2577×10^4	-0.33
75	75	6	4	5.1665×10^4	5.2243×10^4	-1.12
50	100	6	4	3.8433×10^4	3.9059×10^4	-1.63
25	125	6	4	2.7277×10^4	2.7779×10^4	-1.84
10	140	6	4	2.2057×10^4	2.2471×10^4	-1.88
0	150	4	4	1.9537×10^4	1.9513×10^4	0.12

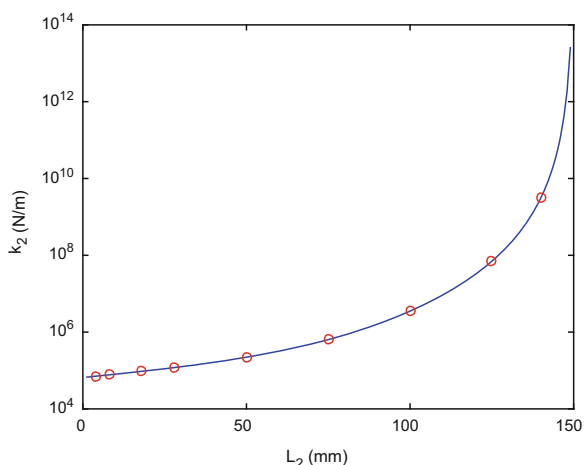
Fig. 7.41 Graphical comparison of FE (circles) and RCSA (line) k_1 stiffness predictions

The k_1 stiffness results from the rib's free end are presented in Table 7.8 and Fig. 7.41. The k_2 stiffness results from the location of the step change in rib thickness are provided in Table 7.9 and Fig. 7.42.

Figures 7.40 through 7.42 deserve discussion. In Fig. 7.40, we observe that the machined rib's first bending natural frequency increases and then decreases as material is removed. This is because the mass is being reduced at the same time as the free end stiffness is being reduced. As we learned in Sect. 2.1, natural frequency depends on the ratio of stiffness to mass. Figure 7.41 shows that the free end stiffness (for the first bending mode) reduces as material is removed, but not linearly with L_2 . In Fig. 7.42, we see that the stiffness at the change in cross section increases dramatically as L_2 approaches zero (note the logarithmic scale on the vertical axis). This stiffness approaches infinity as L_2 goes to zero because we have assumed a rigid base.

Table 7.9 Comparison of finite element (FE) and k_2 stiffness predictions

L_1 (mm)	L_2 (mm)	t_1 (mm)	t_2 (mm)	FE k_2 (N/m)	RCSA k_2 (N/m)	% diff.
150	0	6	6	—	—	—
146	4	6	4	7.1162×10^4	7.0989×10^4	0.24
142	8	6	4	7.7001×10^4	7.6811×10^4	0.25
132	18	6	4	9.4891×10^4	9.4646×10^4	0.26
122	28	6	4	1.1945×10^5	1.1912×10^5	0.28
100	50	6	4	2.2295×10^5	2.2184×10^5	0.50
75	75	6	4	6.4489×10^5	6.3670×10^5	1.27
50	100	6	4	3.6000×10^6	3.5204×10^6	2.21
25	125	6	4	7.1920×10^7	6.9920×10^7	2.78
10	140	6	4	3.2515×10^9	3.1501×10^9	3.12
0	150	4	4	—	—	—

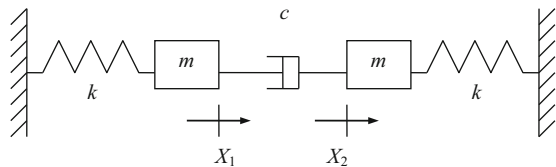
Fig. 7.42 Graphical comparison of FE (circles) and RCSA (line) k_2 stiffness predictions

The corresponding implications for milling stability (Chap. 4) follow. First, the best speeds in the stability lobe diagram will shift first right and then left as the natural frequency varies as depicted in Fig. 7.40. Simultaneously, the stability lobes that represent the free end response will be shifted to lower axial depths of cut as k_1 reduces with L_2 . If the response at the change in cross section is considered, however, the allowable depth of cut increases with k_2 as more material is removed.

Exercises

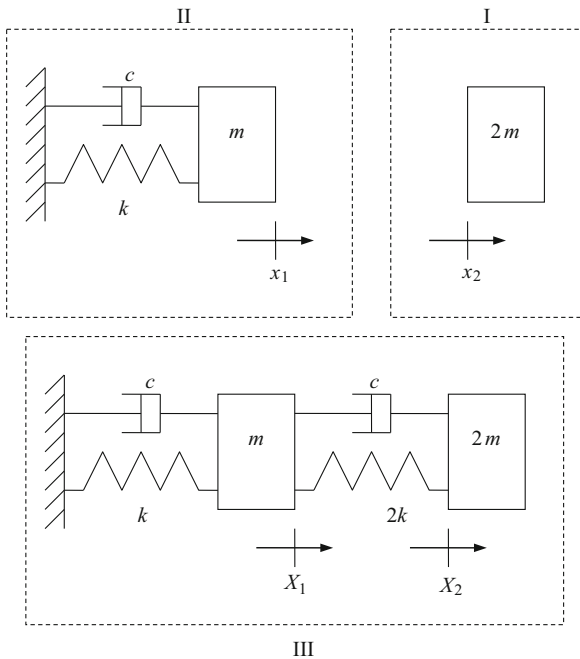
- Determine the direct frequency response function, $\frac{X_2}{F_2}$, for the two degree of freedom system shown in Fig. 7.43 using receptance coupling. Express your final result as a function of m , c , k , and the excitation frequency, ω . You may assume a harmonic forcing function, F_2 , is applied to coordinate X_2 .

Fig. 7.43 Two degree of freedom assembly



2. Determine the direct frequency response function, $\frac{X_1}{F_1}$, for the two degree of freedom system shown in Fig. 7.44 using receptance coupling. Express your final result as a function of m , c , k , and the excitation frequency, ω . You may assume a harmonic forcing function, F_1 , is applied to coordinate X_1 .

Fig. 7.44 Flexible damped coupling of mass (I) to spring-mass-damper (II) to form the two degree of freedom assembly III



3. Plot the displacement-to-force tip receptance for a sintered carbide cylinder with free-free boundary conditions. The beam is described by the following parameters: 19 mm diameter, 150 mm length, 550 GPa elastic modulus, and 15,000 kg/m³ density. Assume a solid damping factor of 0.002. Select a frequency range that encompasses the first three bending modes and display your results as magnitude (m/N) vs. frequency (Hz) in a semi-logarithmic format.
4. Use receptance coupling to rigidly join two free-free beams and find the free-free assembly's displacement-to-force tip receptance. Both steel cylinders are described by the following parameters: 12.7 mm diameter, 100 mm length,

200 GPa elastic modulus, and 7800 kg/m^3 density. Assume a solid damping factor of 0.0015. Once you have determined the assembly response, verify your result against the displacement-to-force tip receptance for a 12.7 mm diameter, 200 mm long free-free steel cylinder with the same material properties. Select a frequency range that encompasses the first three bending modes and display your results as the real (m/N) and imaginary (m/N) parts vs. frequency (Hz) using a linear scale.

5. Determine the fixed-free displacement-to-force tip receptance for a sintered carbide cylinder by coupling the free-free receptances to a rigid wall (with zero receptances). The beam is described by the following parameters: 19 mm diameter, 150 mm length, 550 GPa elastic modulus, and $15,000 \text{ kg/m}^3$ density. Assume a solid damping factor of 0.002. Select a frequency range that encompasses the first two bending modes and display your results as magnitude (m/N) vs. frequency (Hz) in a semi-logarithmic format. Verify your result by comparing it to the displacement-to-force tip receptance for a fixed-free beam with the same dimensions and material properties.
6. For a rigid coupling between two component coordinates x_{1a} and x_{1b} , the compatibility condition is _____.
7. For a flexible coupling (spring stiffness k) between two component coordinates x_{1a} and x_{1b} , the compatibility condition is _____. An external force is applied to the assembly at coordinate X_{1a} .
8. For a flexible-damped coupling (spring stiffness k and damping coefficient c) between two component coordinates x_{1a} and x_{1b} , the compatibility condition is _____. An external force is applied to the assembly at coordinate X_{1a} .
9. What are the units for the rotation-to-couple receptance, p_{ij} , used to describe the transverse vibration of beams?
10. What are the (identical) units for the displacement-to-couple, l_{ij} , and rotation-to-force, n_{ij} , receptances used to describe the transverse vibration of beams?

References

1. Bishop, R., & Johnson, D. (1960). *The mechanics of vibration*. Cambridge: Cambridge University Press.
2. Jetmundsen, B., Bielawa, R., & Flannelly, W. (1988). Generalized frequency domain substructure synthesis. *Journal of the American Helicopter Society*, 33, 55–64.
3. Schmitz, T., & Donaldson, R. (2000). Predicting high-speed machining dynamics by substructure analysis. *Annals of the CIRP*, 49(1), 303–308.
4. Schmitz, T., Davies, M., & Kennedy, M. (2001). Tool point frequency response prediction for high-speed machining by RCSA. *Journal of Manufacturing Science and Engineering*, 123, 700–707.
5. Schmitz, T., Davies, M., Medicus, K., & Snyder, J. (2001). Improving high-speed machining material removal rates by rapid dynamic analysis. *Annals of the CIRP*, 50(1), 263–268.

6. Burns, T., & Schmitz, T. (2004). Receptance coupling study of tool-length dependent dynamic absorber effect. In *Proceedings of American Society of Mechanical Engineers International Mechanical Engineering Congress and Exposition, IMECE2004-60081*, Anaheim, CA.
7. Schmitz, T., & Duncan, G. S. (2005). Three-component receptance coupling substructure analysis for tool point dynamics prediction. *Journal of Manufacturing Science and Engineering*, 127(4), 781–790.
8. Duncan, G. S., Tummond, M., & Schmitz, T. (2005). An investigation of the dynamic absorber effect in high-speed machining. *International Journal of Machine Tools and Manufacture*, 45, 497–507.
9. Cheng, C.-H., Schmitz, T., Arakere, N., & Duncan, G. S. (2005). An approach for micro end mill frequency response predictions. In *Proceedings of American Society of Mechanical Engineers International Mechanical Engineering Congress and Exposition, IMECE2005-81215*, Orlando, FL.
10. Burns, T., & Schmitz, T. (2005). A study of linear joint and tool models in spindle-holder-tool receptance coupling. In *Proceedings of 2005 American Society of Mechanical Engineers International Design Engineering Technical Conferences and Computers and Information in Engineering Conference, DETC2005-85275*, Long Beach, CA.
11. Schmitz, T., Powell, K., Won, D., Duncan, G. S., Sawyer, W. G., & Ziegert, J. (2007). Shrink fit tool holder connection stiffness/damping modeling for frequency response prediction in milling. *International Journal of Machine Tools and Manufacture*, 47(9), 1368–1380.
12. Cheng, C.-H., Duncan, G. S., & Schmitz, T. (2007). Rotating tool point frequency response prediction using RCSA. *Machining Science and Technology*, 11(3), 433–446.
13. Ewins, D. (1986). *Analysis of modified or coupled structures using FRF properties*. Report No. 86,002. Imperial College London, Dynamics Section, Mechanical Engineering, London, England.
14. Ferreira, J., & Ewins, D. (1995). Nonlinear receptance coupling approach based on describing functions. In *Proceedings of the 14th International Modal Analysis Conference* (pp. 1034–1040), Dearborn, MI.
15. Lui, W., & Ewins, D. (2002). Substructure synthesis via elastic media. *Journal of Sound and Vibration*, 257(2), 361–379.
16. Schmitz, T., Davies, M., & Kennedy, M. (2000). High-speed machining frequency response prediction for process optimization. In *Proceedings of the Second International Seminar on Improving Machine Tool Performance*, La Baule, France.
17. Park, S., Altintas, Y., & Movahhedy, M. (2003). Receptance coupling for end mills. *International Journal of Machine Tools and Manufacture*, 43, 889–896.
18. Thomson, W., & Dahleh, M. (1998). *Theory of vibration with application* (5th ed.). Upper Saddle River, NJ: Prentice Hall, Section 9.5.
19. Chapra, S., & Canale, R. (1985). *Numerical methods for engineers with personal computer applications*. New York, NY: McGraw-Hill, Section 7.1.
20. Thomson, W., & Dahleh, M. (1998). *Theory of vibration with application* (5th ed.). Upper Saddle River, NJ: Prentice Hall, Section 3.9.
21. Beards, C. (1996). *Structural vibration: Analysis and damping*. London: Arnold, Section 2.2.5.
22. Weaver Jr., W., Timoshenko, S., & Young, D. (1990). *Vibration problems in engineering* (5th ed.). New York, NY: John Wiley and Sons, Section 5.12.
23. Hutchinson, J. (2001). Shear coefficients for Timoshenko beam theory. *Journal of Applied Mechanics*, 68, 87–92.
24. Schmitz, T., & Duncan, G. S. (2005). Three-component receptance coupling substructure analysis for tool point dynamics prediction. *Journal of Manufacturing Science and Engineering*, 127(4), 781–790, Appendix A: Beam Receptance Modeling.
25. Lustig, J., Smith, S., & Winfough, W. R. (1996). Techniques for the use of long slender end mills in high-speed milling. *Annals of the CIRP*, 45(1), 393–396.
26. Davies, M., Dutterer, B., Pratt, J., & Schaut, A. (1998). On the dynamics of high-speed milling with long, slender endmills. *Annals of the CIRP*, 47(1), 55–60.

27. Sattinger, S. (1980). A method for experimentally determining rotational mobilities of structures. *Shock and Vibration Bulletin*, 50, 17–27.
28. Ewins, D. (2000). *Modal testing: Theory, practice and application* (2nd ed.). Philadelphia, PA: Research Studies Press.
29. Kops, L., & Vo, D. (1990). Determination of the equivalent diameter of an end mill based on its compliance. *Annals of the CIRP*, 39(1), 93–96.
30. Kivanc, E., & Budak, E. (2004). Structural modeling of end mills for form error and stability analysis. *International Journal of Machine Tools and Manufacture*, 44, 1151–1161.
31. Kiran, K., Satyanarayana, H., & Schmitz, T. (2017). Compensation of frequency response function measurements by inverse RCSA. *International Journal of Machine Tools and Manufacture*, 121, 96–100.
32. Honeycutt, A., & Schmitz, T. (2017). Analytical solutions for fixed-free beam dynamics in thin rib machining. *Journal of Manufacturing Processes*, 30, 41–50.
33. Budak, E., & Altintas, Y. (1995). Modeling and avoidance of static form errors in peripheral milling of plates. *International Journal of Machine Tools and Manufacture*, 35, 459–476.
34. Smith, S., & Dvorak, D. (1998). Tool path strategies for high speed milling aluminum workpieces with thin webs. *Mechatronics*, 8, 291–300.
35. Ning, H., Zhigang, W., Chengyu, J., & Bing, Z. (2003). Finite element method analysis and control stratagem for machining deformation of thin-walled components. *Journal of Materials Processing Technology*, 139, 332–336.
36. Ratchev, S., Nikov, S., & Moualek, I. (2004). Material removal simulation of peripheral milling of thin wall low-rigidity structures using FEA. *Advances in Engineering Software*, 35, 481–491.
37. Ratchev, S., Liu, S., Huang, W., & Becker, A. A. (2004). Milling error prediction and compensation in machining of low-rigidity parts. *International Journal of Machine Tools and Manufacture*, 44, 1629–1641.
38. Bravo, U., Altzarra, O., López de Lacalle, L. N., Sánchez, J. A., & Campa, F. J. (2005). Stability limits of milling considering the flexibility of the workpiece and the machine. *International Journal of Machine Tools and Manufacture*, 45, 1669–1680.
39. Ratchev, S., Liu, S., & Becker, A. A. (2005). Error compensation strategy in milling flexible thin-wall parts. *Journal of Materials Processing Technology*, 162–163, 673–681.
40. Thevenot, V., Arnaud, L., Dessein, G., & Cazenave-Larroche, G. (2006). Influence of material removal on the dynamic behavior of thin-walled structures in peripheral milling. *Machining Science and Technology*, 10(3), 275–287.
41. Mañé, I., Gagnol, V., Bougarrou, B. C., & Ray, P. (2008). Stability-based spindle speed control during flexible workpiece high-speed milling. *International Journal of Machine Tools and Manufacture*, 48, 184–194.
42. Rai, J. K., & Xirouchakis, P. (2008). Finite element method based machining simulation environment for analyzing part errors induced during milling of thin-walled components. *International Journal of Machine Tools and Manufacture*, 48, 629–643.
43. Seguy, S., Dessein, G., & Arnaud, L. (2008). Surface roughness variation of thin wall milling, related to modal interactions. *International Journal of Machine Tools and Manufacture*, 48, 261–274.
44. Adetoro, O. B., Wen, P. H., Sim, W. M., & Vepa, R. (2009). Stability lobes prediction in thin wall machining. In *Proceedings of the World Congress on Engineering 2009 Vol I, WCE 2009, July 1–3, 2009*, London, UK.
45. Chen, W., Xue, J., Tang, D., Chen, H., & Qu, S. (2009). Deformation prediction and error compensation in multilayer milling processes for thin-walled parts. *International Journal of Machine Tools and Manufacture*, 49, 859–864.
46. Gang, L. (2009). Study on deformation of titanium thin-walled part in milling process. *Journal of Materials Processing Technology*, 209, 2788–2793.
47. Arnaud, L., Gonzalo, O., Seguy, S., Jauregi, H., & Peigné, G. (2011). Simulation of low rigidity part machining applied to thin-walled structures. *International Journal of Advanced Manufacturing Technology*, 54, 479–488.

48. Izamshah, R., Mo, J. P. T., & Ding, S. (2011). Hybrid deflection prediction on machining thin-wall monolithic aerospace components. *Proceedings of IMechE Part B: Journal of Engineering Manufacture*, 226, 592–605.
49. Smith, S., Wilhelm, R., Dutterer, B., Cherukuri, H., & Goel, G. (2012). Sacrificial structure preforms for thin part machining. *CIRP Annals—Manufacturing Technology*, 61, 379–382.
50. Polishetty, A., Goldberg, M., Littlefair, G., Puttaraju, M., & Patil, P. (2014). A preliminary assessment of machinability of titanium allow Ti 6Al 4V during thin wall machining using trochoidal milling. *Procedia Engineering*, 97, 357–364.

Chapter 8

Machining Tribology



*There are two important things for full success in life:
1. Don't tell everything you know.*

—Albert Einstein

In the previous chapters, we detailed the influence of process dynamics on machining performance. In this chapter, we investigate the role of tribology, or the study of friction, wear, and lubrication, in machining performance. Machining is fundamentally a competition between the defined cutting edge and the workpiece material as it is sheared away in the form of chips to obtain the desired part geometry. Because this material removal occurs at high temperatures, pressures, and velocities, understanding the tribology of the tool-workpiece interface is essential for successful discrete part production. Important considerations include the friction developed at the tool-chip interface, which leads to increased energy consumption, and the tool wear that naturally occurs and must be minimized to achieve high material removal rates at low cost.

Machining tribology poses a significant challenge due to the multiple parameters that must be simultaneously considered to arrive at a cost-minimized solution in production. These include, but are not limited to:

- Machining parameters—chip width, chip thickness, and cutting speed; these are specified by the depth of cut (both axial and radial depth for milling), feed per revolution (or feed per tooth for milling), and spindle speed.
- Tool material and coating—many tool material options with and without single and multilayer coatings are available.
- Tool geometry—basic parameters include side rake angle, clearance angle, cutting edge radius, and number of teeth and spacing (for milling), but actual cutting tools, whether solid or inserted designs, include many additional geometric options.
- Workpiece material and microstructure.
- Cutting fluid type and application method.

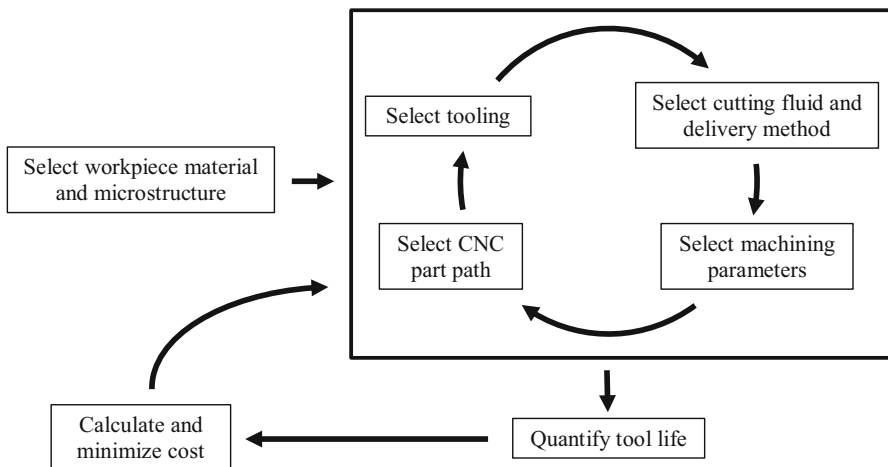


Fig. 8.1 Schematic of parameter selection process for machining

- CNC part path—the strategy used by the computer numerically controlled (CNC) part program can affect the time to machine and the tool wear rate; for example, up or down (conventional or climb) milling and the path geometry, such as spiral in/out, constant radial engagement, trochoidal, and zigzag strategies for milling, must be selected by the process planner.

A schematic of the parameter selection process for machining is provided in Fig. 8.1. It assumes that the workpiece material, as well as the required microstructure (which is produced by the alloy composition/heat treatment and defines the desired material properties), is pre-specified by the application. Given the workpiece material, interrelated selections regarding the tooling, cutting fluid/delivery, machining parameters, and CNC part path are made, where the chatter-free machining parameters depend on the structural dynamics of the machining platform as detailed previously. Based on these decisions, the tool life for the machining parameter range must be assessed. This includes measurements when possible or, at minimum, a literature survey to identify parameters that others have applied successfully. Finally, if the machining parameters and associated tool life are known, the cost can be calculated and minimized. Minimizing the cost may require a modification of the machining parameters (and related selections), so a feedback loop is included in Fig. 8.1.

In the remaining sections of this chapter, we'll identify the tribology-related information required to make informed decisions about machining parameters. This includes:

- The relationships between machining parameters, workpiece material properties, cutting forces, and the corresponding temperature field in the chip.
- Tool life (defined using an empirical model), common wear features, and the relationship between tool life and machining cost.
- Cutting fluids and their effect on tool life.



In a Nutshell

Some of the machining parameters are relatively easy to know. The nominal chip width, chip thickness, and cutting speed can be readily calculated from the nominal workpiece geometry and planned tool motions. The tool material and coating(s), if any, may be challenging to select, but they are known by the time the cutting process starts. The tool geometry is generally clearly specified when the cutting starts. The workpiece material and microstructure should be known, but the microstructure, in particular, may change during processing and may vary at different points within the workpiece. For example, there may be surface layers of oxidation or hard inclusions. The cutting fluid type and application method are selected by the user. The tool path is selected by the programmer and the programming software often helps in the creation of the tool path. However, the software sometimes gives the programmer results that do not match the request. For instance, if a milling tool is used to make a rectangular pocket with a spiral-out tool path and the programmer asks for a radial depth that is half of the tool diameter, then at each internal corner the radial depth momentarily increases to the diameter of the tool.

Other machining parameters are difficult to derive from physical geometry or material properties. The relationship between the cut geometry and the cutting forces must typically be measured. The same is true for the relationship between the cutting parameters and temperature.

8.1 Geometry, Forces, and Temperature

The chip removal characteristics depend on the tool geometry (including its wear state), workpiece material properties, the user-selected machining parameters, and the cutting fluid application, if applicable. To understand the relationships between machining parameters, workpiece material properties, cutting forces, and the corresponding temperature field in the chip, we can idealize the three-dimensional cutting process as two-dimensional. This is referred to as “orthogonal cutting,” where the strains and forces required to form the chip exist in a single plane. We apply this approximation here and develop the corresponding relationships [1]. We can visualize orthogonal cutting as tube turning, where the feed direction is along the tube axis; see Fig. 8.2 and Sect. 3.6.

The top right panel in Fig. 8.2 depicts a sharp cutting tool removing material to form a chip in orthogonal cutting. The uncut material approaches the fixed tool from above with a downward velocity, v (i.e., the cutting speed), and the chip is formed along the rake face of the tool. A positive (side) rake angle, α , is shown, where the rake face is inclined downward from the normal to the uncut surface (i.e., away from the chip). A negative rake angle is achieved when the rake face is inclined upward from the surface normal (toward the chip); a negative rake angle increases the cutting

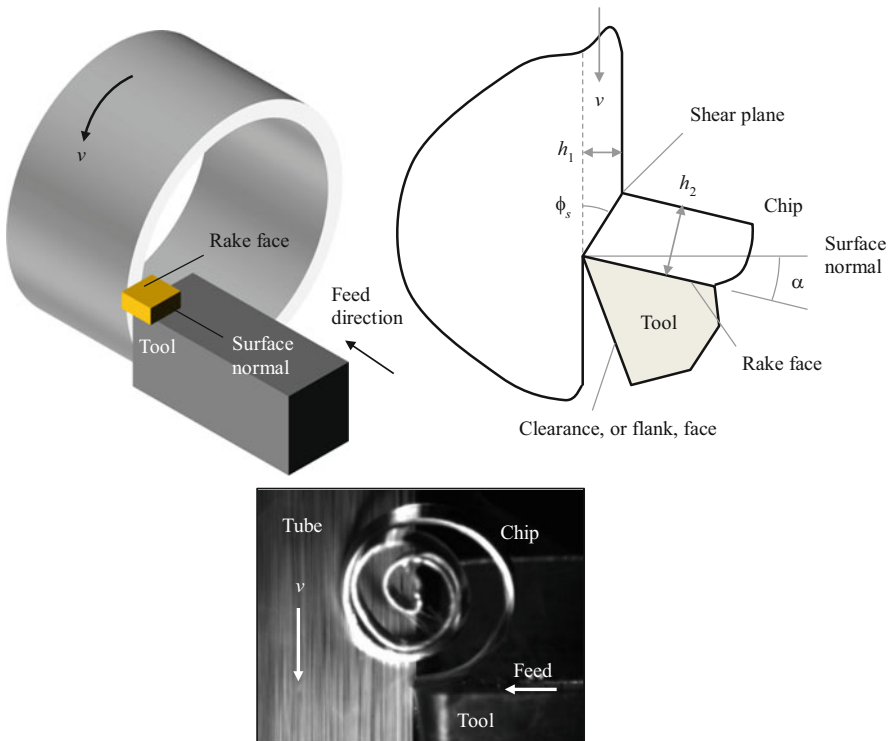


Fig. 8.2 (Top left) Tube turning. (Top right) Chip formation in orthogonal cutting. (Bottom) Photograph of chip formation in tube turning

edge strength but also tends to increase the cutting force. The rake angle is zero when the rake face is aligned with the normal direction (i.e., horizontal in the figure). The commanded (or mean) uncut chip thickness, h_m , is sheared away by the tool to form a chip with a larger deformed thickness, h_d . In turning (Chap. 3), the uncut chip thickness is specified by the feed per revolution. In milling (Chap. 4), it is defined by the feed per tooth and the angle of the rotating cutter as it proceeds through the material.

The shearing action that produces the chip occurs approximately along a plane in orthogonal cutting. The angle of this “shear plane” is ϕ_s and its length is L . The chip width, b , is measured perpendicular to the plane of Fig. 8.2 top right panel and is assumed to remain constant. This chip width is the tube wall thickness in tube turning. A geometric relationship between the shear plane length, uncut chip thickness, and shear plane angle is defined by:

$$L = \frac{h_m}{\sin \phi_s}. \quad (8.1)$$

A companion relationship between the shear plane length, deformed chip thickness, shear plane angle, and rake angle is:

$$L = \frac{h_d}{\cos(\phi_s - \alpha)}. \quad (8.2)$$



In a Nutshell

Note that the rake angle, α , and the uncut chip thickness, h_m , are selected by the user, but not the shear plane angle, ϕ_s . The shear plane angle selects itself, as does, therefore, the deformed chip thickness. The shear plane angle can be determined experimentally by comparing the uncut chip thickness (planned) to the deformed chip thickness (measured on a chip).

Combining Eqs. 8.1 and 8.2 yields the chip ratio, r , which is the ratio of the uncut chip thickness to the deformed chip thickness.

$$r = \frac{h_m}{h_d} = \frac{\sin \phi_s}{\cos(\phi_s - \alpha)} = \frac{\sin \phi_s}{\cos \phi_s \cos \alpha + \sin \phi_s \sin \alpha} \quad (8.3)$$

Equation 8.3 can be rewritten to determine the shear plane angle as a function of the chip ratio and rake angle.

$$\phi_s = \tan^{-1}\left(\frac{r \cos \alpha}{1 - r \sin \alpha}\right) \quad (8.4)$$

If the deformed chip thickness is measured after cutting, r can be determined experimentally and the shear plane angle can be calculated using Eq. 8.4. The chip velocity, v_c , as it slides along the tool's rake face differs from the cutting speed. Its value is determined by mass continuity.

$$v_c = \frac{h_m}{h_d} v = rv \quad (8.5)$$



In a Nutshell

“Mass continuity” means that all of the mass that enters the shear plane exits the shear plane. Alternatively, we can describe the situation as volume in equals volume out, since the density does not change.

Because the chip ratio is less than one, the chip velocity is less than the cutting speed. The velocity along the shear plane, v_s , is determined from geometry. The cutting speed, chip, and shear plane velocity vectors are shown in Fig. 8.3.

$$v_s = v \frac{\cos \alpha}{\cos(\phi_s - \alpha)} \quad (8.6)$$

The force required to shear away the chip is summarized in Fig. 8.4. Its components in the surface normal direction, F_n , and cutting speed or tangential direction, F_t , are shown. Their vector sum is the resultant force, F , which is inclined away from

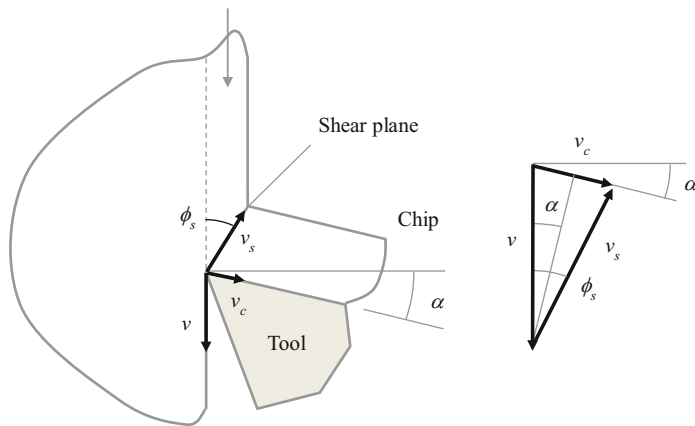
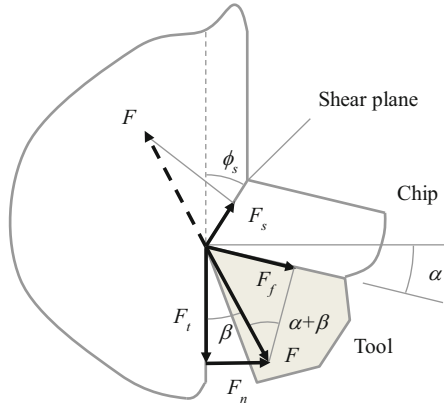


Fig. 8.3 Velocity relationships in machining

Fig. 8.4 Force components



the cutting speed direction by the force angle, β . The force along the shear plane, F_s , and the friction force, F_f , between the sliding chip and tool rake face are also identified.



In a Nutshell

The cutting force is a vector quantity. It has magnitude and direction. It is possible to resolve the cutting force vector into components that are in the direction of the cutting speed, F_c , and perpendicular to the surface, F_n .

The same force can also be resolved into components along the shear plane, F_s , and along the tool-chip contact surface, F_f . The force can be resolved in other directions as well.

Using a mechanistic cutting process description, the normal and tangential components can be related directly to the uncut chip area, which is the product $b h_m$:

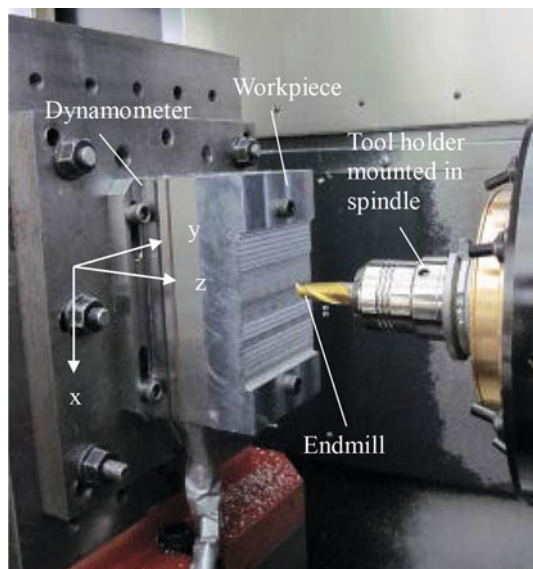
$$F_n = k_n b h_m, \quad (8.7)$$

$$F_t = k_t b h_m \quad (8.8)$$

using the cutting force coefficients k_n and k_t . These values may be obtained from experiments or the literature [e.g., 1]. These coefficients are not workpiece material properties. Rather, they are process properties that depend not only on the workpiece material, but also on the tool geometry and, to a lesser extent, the machining parameters. For example, as the cutting speed increases, the heat generation also increases which tends to soften the material. This, in turn, reduces the workpiece material strength and lowers the cutting force coefficients. As a practical matter, these coefficients have to be determined experimentally by someone. Once determined, they do not change unless the workpiece material (or less influential parameters) changes.

To determine the cutting force coefficients experimentally, there are two primary approaches: linear regression and nonlinear optimization [2]; see Sect. 4.7. Both are based on a measurement of the cutting force components for known machining conditions and comparison of the measured forces to a mechanistic force model (e.g., Eqs. 8.7 and 8.8) to determine the best-fit coefficients [2, 3]. The force measurement is typically completed using a cutting force dynamometer that implements piezoelectric or strain gage-based load cells to record the cutting force components while cutting. An example setup for milling is displayed in Fig. 8.5, where the dynamometer is able to measure the force components in the fixed x , y , and z directions. These may then be related to the normal and tangential force components for the rotating tool. See Fig. 8.6, where F_a is the axial force component

Fig. 8.5 Setup for cutting force coefficient measurement



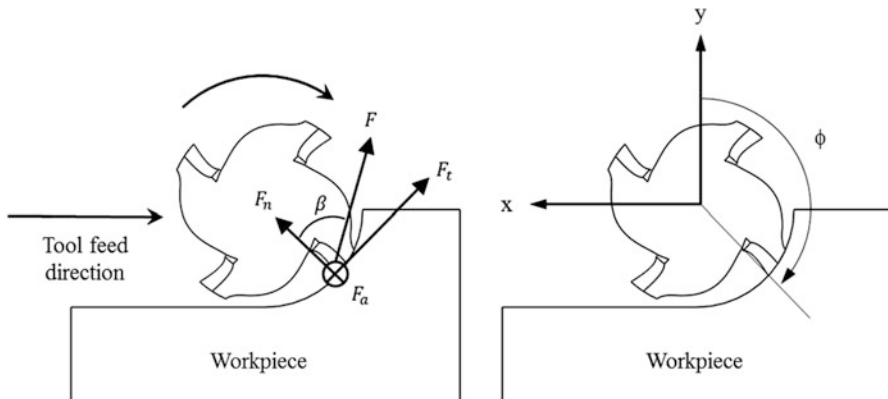


Fig. 8.6 Relationship between rotating and fixed force directions in down milling force measurement

along the tool's axis and ϕ is the cutter rotation angle. This axial component occurs for endmills with a helical cutting edge.



In a Nutshell

Unfortunately, dynamometers are not perfect. The dynamometer enables cutting force measurement, but it also influences the cutting process. The dynamometer is stiff, but not infinitely stiff. To some extent, it acts like a spring-mass system and it therefore has natural frequencies and a bandwidth (i.e., it has a limited range of frequencies for which the measurement is accurate). The bandwidth quoted by the manufacturer is often much higher than that which is obtained in practice because the added mass of the workpiece and fixture lowers the dynamometer's natural frequencies. It is important to check the frequency response function between the dynamometer output and the cutting force input. In general, the workpiece should be light and the cutting force should be well within the dynamometer range. The cutting should also take place as close to the dynamometer surface as possible.

Example results for 6061-T6511 aluminum extruded bar stock are provided in Fig. 8.7 [2]. The tangential cutting force coefficient is presented as a function of the feed per tooth value for three different down milling radial immersions (100% represents slotting or cutting with the tool's full diameter). It is observed that the force coefficient values decrease with increasing feed per tooth and radial immersion. This is attributed to the finite radius on the cutting edge. Due to this nonzero edge radius, the actual rake angle depends on the instantaneous chip thickness. Although the cutting tool may have a positive rake angle at the macroscopic scale for thicker chips, as the commanded feed per tooth approaches the same order of magnitude as the cutting edge radius, the effective rake angle becomes negative; see

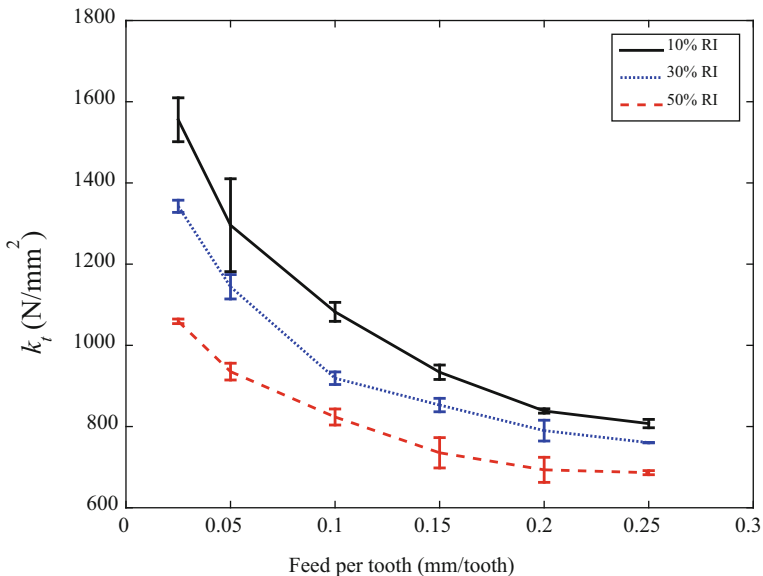


Fig. 8.7 Tangential cutting force coefficient calculated by nonlinear optimization as a function of feed per tooth. Results for three radial immersions (RI) are shown [2]

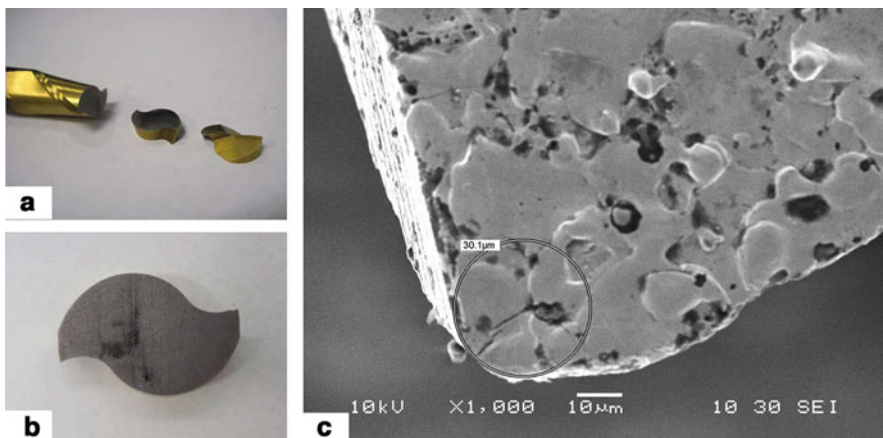


Fig. 8.8 Edge radius measurement for endmill. The endmill was (a) sliced into axial disks to (b) facilitate cutting-edge radius measurements with a scanning electron microscope (c) at $\times 1000$ magnification. In (c) the flank face is on the left and the rake race is on the right. The cutting edge radius is approximately $15 \mu\text{m}$ [2]

Fig. 8.8 for a measurement of the edge radius (approximately $15 \mu\text{m}$) for the endmill used to produce the Fig. 8.7 results [2].

Figure 8.9 depicts the change in effective rake angle with uncut chip thickness due to the finite cutting edge radius. This change in effective rake angle is

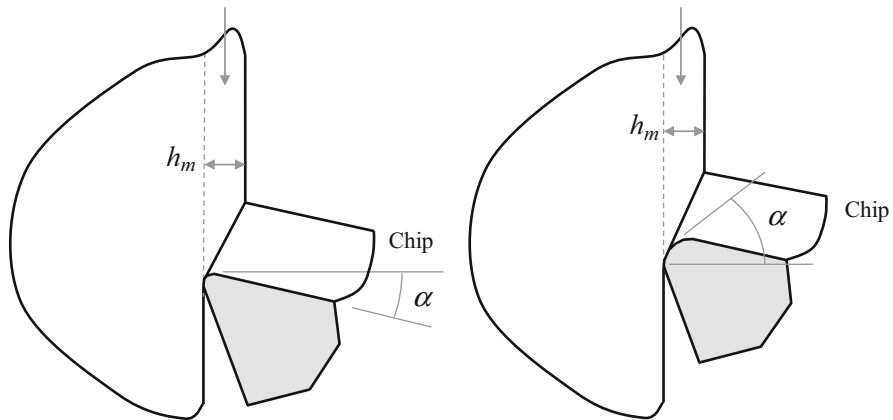


Fig. 8.9 Effect of cutting edge radius on effective rake angle. (Left) When the uncut chip thickness is large relative to the edge radius, the positive macroscopic rake angle defines the chip formation. (Right) When the edge radius is on the same order as the uncut chip thickness, the effective rake angle becomes negative

accompanied by a change in the chip formation [4]. Additionally, the negative rake angle serves to impose compressive stresses on the workpiece surface. These factors contribute to the increase in the cutting force coefficients at low feed per tooth values.

Returning to the force geometry for orthogonal cutting in Fig. 8.4, the resultant cutting force is:

$$F = \sqrt{F_t^2 + F_n^2} = \sqrt{k_t^2 + k_n^2} b h_m = K_s b h_m, \quad (8.9)$$

where K_s is the specific cutting force. The resultant force is also related to the normal and tangential components through the force angle.

$$F_n = F \sin \beta \quad (8.10)$$

$$F_t = F \cos \beta \quad (8.11)$$

The shear and friction force components are related to the resultant force by the Fig. 8.4 geometry.

$$F_s = F \cos (\beta + \phi_s) \quad (8.12)$$

$$F_f = F \sin (\alpha + \beta) \quad (8.13)$$

The corresponding powers are the product of the appropriate force and velocity components. The shear power, P_s , serves to increase the temperature at the shear plane, while the friction power, P_f , increases the temperature along the rake face-chip contact (also referred to as the secondary shear zone). Together, they define the heat inputs to the chip temperature profile.

$$P_s = F_s v_s \quad (8.14)$$

$$P_f = F_f v_c \quad (8.15)$$



In a Nutshell

The cutting operation generates a lot of heat! The chips get hot, the tool gets hot, and the heat makes it into the structure of the machine and workpiece. Some of the heat comes from the intense deformation of shearing and some comes from the friction. Investigation of the heat in metal cutting provided much of the early data for the science of thermodynamics and heat transfer. This heat has important implications for part accuracy and tool wear.

Example 8.1 1035 Steel Orthogonal Cutting To demonstrate these relationships, let's consider orthogonal cutting of 1035 steel with the following parameters: $h_m = 0.2$ mm, $b = 6$ mm, $v = 3$ m/s, $\alpha = 10$ deg, $\phi_s = 28$ deg, $k_t = 2300$ N/mm², and $k_n = 690$ N/mm². The corresponding force angle is:

$$\beta = \tan^{-1} \left(\frac{F_n}{F_t} \right) = \tan^{-1} \left(\frac{k_n}{k_t} \right) = 16.7 \text{ deg} \quad (8.16)$$

and the specific cutting force is:

$$K_s = \sqrt{k_t^2 + k_n^2} = \sqrt{2300^2 + 690^2} = 2401 \text{ N/mm}^2. \quad (8.17)$$

The shear plane length is:

$$L = \frac{h_m}{\sin \phi_s} = \frac{0.2}{\sin 28} = 0.43 \text{ mm}. \quad (8.18)$$

The deformed chip thickness is:

$$h_d = L \cos (\phi_s - \alpha) = 0.43 \cos (28 - 10) = 0.41 \text{ mm} \quad (8.19)$$

and the chip ratio is:

$$r = \frac{h_m}{h_d} = \frac{0.2}{0.41} = 0.49. \quad (8.20)$$

The chip and shearing velocities are:

$$v_c = rv = 0.49(3) = 1.48 \text{ m/s}, \quad (8.21)$$

$$v_s = v \frac{\cos \alpha}{\cos (\phi_s - \alpha)} = 3 \frac{\cos 10}{\cos (28 - 10)} = 3.1 \text{ m/s}. \quad (8.22)$$

The resultant, shear, and friction force components are:

$$F = K_s b h_m = 2401(6)0.2 = 2881 \text{ N}, \quad (8.23)$$

$$F_s = F \cos(\beta + \phi_s) = 2881 \cos(16.7 + 28) = 2048 \text{ N}, \quad (8.24)$$

$$F_f = F \sin(\alpha + \beta) = 2881 \sin(10 + 16.7) = 1294 \text{ N}. \quad (8.25)$$

The corresponding shear and friction power inputs are:

$$P_s = F_s v_s = 2048(3.1) = 6349 \text{ W}, \quad (8.26)$$

$$P_f = F_f v_c = 1294(1.48) = 1915 \text{ W}. \quad (8.27)$$

By summing the shear and friction powers, we see that there is nearly 8.3 kW of power which serves to continuously heat the chip, tool, and workpiece for the selected cut.

Example 8.2 Temperature Field in the Chip To understand how this heat input is propagated into the chip temperature field, let's review results from a finite difference simulation for a simplified single-dimensional transient analysis. The details of this simulation are provided in [1]. Comprehensive finite element analysis (FEA) software packages are also commercially available.



In a Nutshell

We are imagining that successive slices of the chip all pass through the same place and, in steady state, the temperature field can be computed by following one slice.

Let's consider an orthogonal cut in a 7075-T6 aluminum workpiece with $h_m = 0.5 \text{ mm}$, $b = 5 \text{ mm}$, $\alpha = 0$, $\phi_s = 20 \text{ deg}$, $K_s = 775 \text{ N/mm}^2$, and $\beta = 19 \text{ deg}$. Additionally, the thermal conductivity is $140 \text{ N/s} \cdot ^\circ\text{C}$ and the specific heat per unit volume is $2.4 \text{ N/mm}^2 \cdot ^\circ\text{C}$ for the workpiece [1]. The thermal conductivity for the sintered carbide tool is $70 \text{ N/s} \cdot ^\circ\text{C}$. Figure 8.10 shows the predicted chip temperature field for a cutting speed of 5 m/s. The figure uses the same orientation as Fig. 8.4 so that the lower boundary (x direction) is the tool-chip interface and the left boundary (y direction) is the shear plane. The chip temperature profile along the rake face is provided in Fig. 8.11. It is observed that the maximum temperature does not occur at the tool tip (i.e., the left end where $x = 0$). Instead, it appears 1.1 mm from the tool tip along the rake face. The chip gets hot due to the intense shearing, but the temperature increases still more due to the friction. This highest temperature location corresponds to the position of maximum crater wear, should it occur, because the tool wear mechanism that causes crater wear is strongly temperature dependent.

In Fig. 8.12, the cutting speed has been doubled to 10 m/s with all other parameters remaining constant. The maximum temperature increased from $511.9 \text{ }^\circ\text{C}$ to $594.6 \text{ }^\circ\text{C}$. This demonstrates the strong correlation between cutting speed and chip temperature. This increased temperature tends to accelerate tool wear, so it is an important consideration in the tribology of machining.

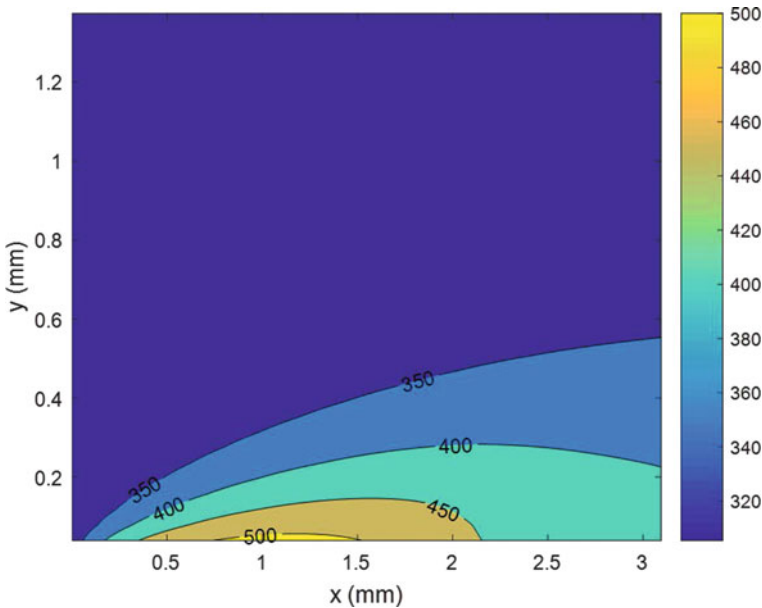


Fig. 8.10 Chip temperature field ($^{\circ}\text{C}$) for 7075-T6 aluminum with $v = 5$ m/s

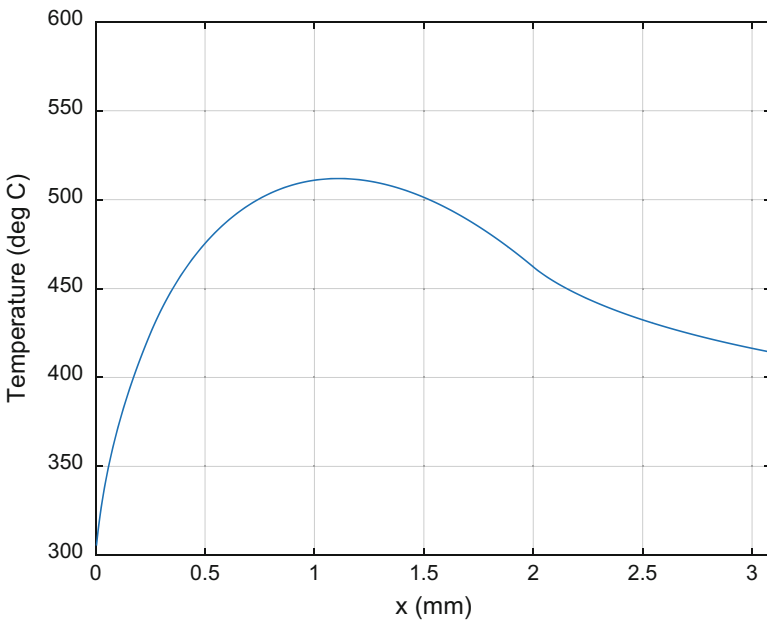


Fig. 8.11 Rake face temperature profile of the chip for 7075-T6 aluminum with $v = 5$ m/s

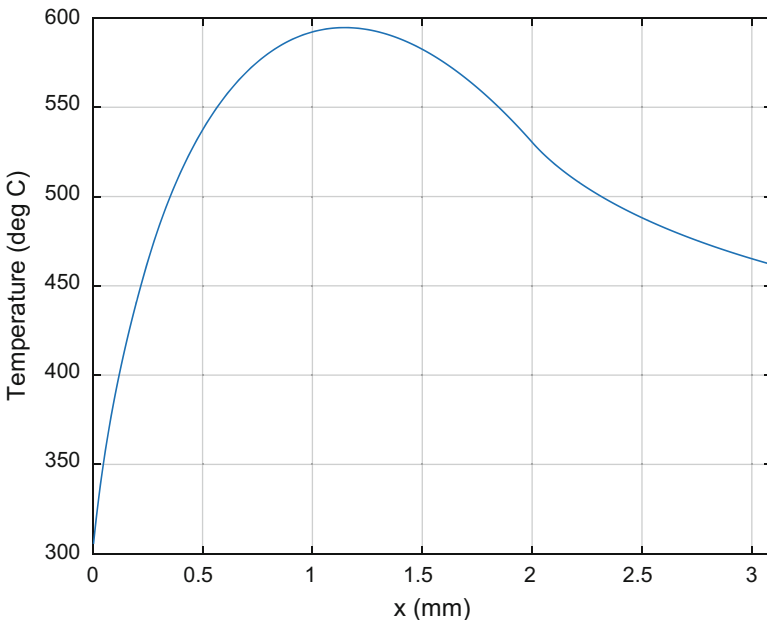


Fig. 8.12 Rake face temperature profile of the chip for 7075-T6 aluminum with $v = 10 \text{ m/s}$

Another important consideration is the thermal conductivity of the workpiece material. If it is low, the heat is not propagated away in the chip as efficiently, and tool wear is accelerated. Figure 8.13 shows simulation results for the original 7075-T6 aluminum machining parameters, but the workpiece thermal properties have been changed to a thermal conductivity of $7 \text{ N/s}\cdot\text{C}$ ($20\times$ lower than 7075-T6 aluminum) and a specific heat per unit volume of $2.7 \text{ J/mm}^3\cdot\text{C}$. These values correspond to 6Al-4V titanium [1]. The specific cutting force is $K_s = 2000 \text{ N/mm}^2$ with $\beta = 19 \text{ deg}$. The maximum temperature is now 2234.7°C (this actually exceeds the melting temperature of 6Al-4 V titanium). It is seen that the temperature profile has “flattened out” and the heat remains at the tool-chip interface, rather than conducting away in the chip. This is a primary cause for the high wear rates and low machinability of titanium alloys relative to aluminum alloys.

The chip temperature results shown in Figs. 8.10 through 8.13 are for an orthogonal cutting model. In practice, the chip formation is three-dimensional. Turning and boring, for example, typically form continuous three-dimensional chips. This can be a challenge when the long stringy chip becomes entangled with the cutting tool and causes damage to the machined surface, tool, or both. For this reason, features are often added to the rake face to curl and intentionally break the continuous chip (i.e., chip breaker geometries). Drilling can also produce a continuous chip that follows the helical flutes. Drilling mechanics are generally more complicated than turning or boring, however, due to the rubbing along the margins (side surfaces in contact with the drilled hole) and plowing/indentation at the chisel point in the drill center [3]. For these continuous chip cases with constant uncut chip

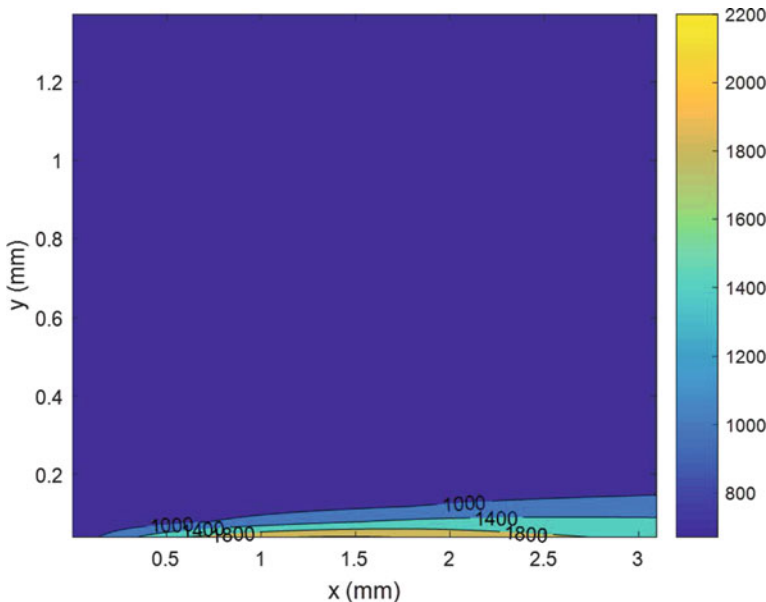


Fig. 8.13 Chip temperature field ($^{\circ}\text{C}$) for 6Al-4V titanium with $v = 5 \text{ m/s}$

thickness, the heat generated in the primary and secondary shear zones enters the chip under approximately steady-state conditions.

Milling, on the other hand, produces discontinuous chips as the teeth continually enter and exit the cut. For down milling, the uncut chip thickness reduces as the cut proceeds from entry to exit for each tooth. For up milling, the opposite is true. Not only is the chip discontinuous in milling, but the teeth are also not engaged in the cut for a portion of each tool revolution. The heat generation is therefore inherently transient in nature. The time out of the cut allows each tooth to cool prior to reentering the cut, either through convection only or aided by cutting fluid application. This periodic cooling can increase tool life, particularly for low radial immersions, but it can also lead to fatigue fracture and premature failure if the temperature difference in and out of the cut is too high. This “thermal cycling” can occur when a low temperature cutting fluid is applied outside the cut, but the maximum temperature inside the cut remains unchanged.

8.2 Tool Life

Tool wear in machining leads to finite tool life, which is often measured in minutes rather than hours. Because tool costs can be significant, selecting a process plan that limits tool wear to an acceptable level is an important activity for part production by machining. Tool wear is driven by:

- High temperatures at the tool-chip interface, which can lead to softening of the tool material.
- Intimate contact between the chip and tool rake face, which encourages diffusion between the chip and tool materials, particularly at high temperatures (e.g., this can cause the carbon-greedy steel chip to rapidly wear an uncoated tungsten carbide cutting tool).
- Hard inclusions in the workpiece material, which can abrade the tool material.
- Large cutting forces and pressures, which can cause plastic deformation and fracture of the tool edge.
- Thermal cycling in interrupted cuts, which can cause cracking and catastrophic tool failure due to thermal fatigue.



In a Nutshell

The tool life is often selected based on cost, but it may also be selected so that the tool lasts through one workpiece or one shift, for example.

Several wear mechanisms have been identified in metal cutting. These include abrasion, adhesion, diffusion, and attrition [1, 3]. We'll discuss them individually in the following paragraphs.

Abrasion occurs when hard particles in the workpiece material scratch the tool surface as the chip is sheared away. It can also occur when small particles of the hard tool material are dislodged and carried away with the chip, again scratching the tool surface. The hard particles can be carbides, oxides, or nitrides, for example [3].

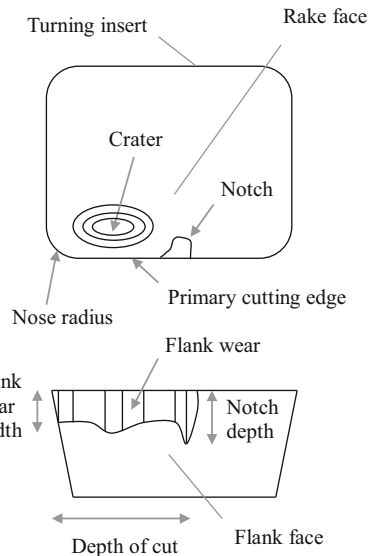
Adhesive wear occurs when the work material locally welds to the tool surface due to the high temperatures and pressures and then tears away tool material as it is removed during the chip formation process. Adhesion is also the mechanism for built-up edge (BUE), which is typically observed at lower cutting speeds. BUE occurs near the tool point where the tool-chip interface temperature is lower and the harder material tends to seize against the tool rake face. Farther along the contact, the temperature is higher and the softer chip slides more easily. The BUE can change the effective rake angle at the tool point, which affects the cutting force magnitude [3].

Diffusion depends on the chemical affinity between the tool and workpiece. Its rate, which is defined by the number of atoms of the tool or workpiece material that penetrates the other at the intimate, high-pressure rake face contact, is strongly temperature dependent, so diffusion often dominates at high cutting speeds where the tool-chip interface temperature is also high. Diffusion is therefore a mechanism for crater wear, which occurs where the temperature is highest (see Fig. 8.10), although adhesion and abrasion can also contribute to crater development. Additionally, diffusion participates in flank wear.

Attrition occurs when tool material grains near cutting edge are broken out by contact with the chip and machined surface. It is a primary mechanism for flank wear and can dominate at low cutting speeds with nonuniform chip flow.

These wear mechanisms combine to form characteristic wear features on the cutting tool surfaces. Common wear features include flank, crater, and notch wear.

Fig. 8.14 Common wear features in metal cutting



These are depicted in Fig. 8.14. In many cases, a single wear feature will dominate, such as flank wear, but all may occur simultaneously.

The tool wear rate naturally depends on the cutting tool material and any coatings applied to the wear surfaces. Fundamental tool material requirements include:

- A higher hardness than the work material at the cutting temperature.
- High strength to resist cutting stresses.
- High toughness to avoid breakage under impact loads.
- Low reactivity (i.e., chemically inert).

Tool materials have progressed from high-speed steels in the 1900s to sintered carbides, such as tungsten carbide or WC and titanium carbide or TiC (1930s); to ceramics, such as Al_2O_3 , cubic boron nitride or CBN, and polycrystalline diamond or PCD (1960s); and to coated steels and carbides (1970s). Coatings are now routinely applied by chemical vapor deposition (CVD) and physical vapor deposition (PVD). Common examples include TiC, TiN, Al_2O_3 , and combinations of these in alternating layers. One important issue for coating life is the cutting edge preparation. Edge honing can be used to increase the coating persistence at the sharp edge.

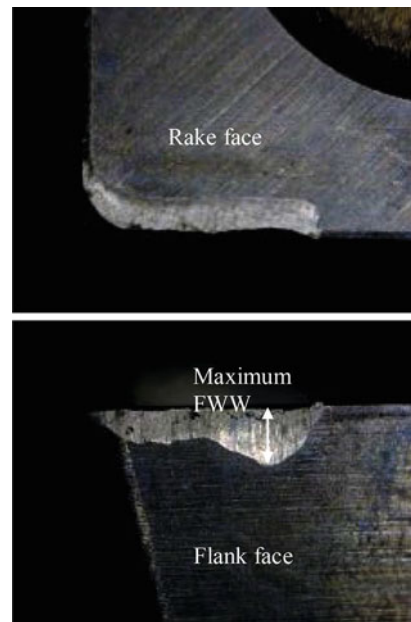
Although it has been understood since the early 1900s that the rate of tool wear depends strongly on the cutting speed, as well as other process parameters, and tool geometry, its preprocess prediction remains elusive [5]. Empirical modeling efforts are therefore common. However, we notice some common behaviors in the experimental work. The Taylor-type tool life model, named for the pioneering work by F.W. Taylor, can be expressed for turning operations as:

$$C = v^p f_r^q T, \quad (8.28)$$

where C , p , and q are constants that depend on the tool and workpiece materials, tool geometry, coolant use, and process parameters. They are empirical. The parameters v , f_r , and T are the cutting speed, feed per revolution, and tool life, respectively, and they are set by the machinist. Other parameters may be added as well, including the depth of cut, for example. The tool life may be defined by the cutting time required to reach a predetermined level for a particular wear feature (Fig. 8.14).

One common tool life indicator is flank wear since increased levels of flank wear lead to higher friction between the insert flank face and the machined surface. This higher friction, in turn, accelerates the tool wear due to increased temperatures. To establish the tool life, an allowable flank wear width, FWW (also denoted Verschleissmarken Breite, or VB, in German), is established, and tests are performed at a given combination of process parameters (v and f_r from Eq. 8.28). The time to reach the predetermined flank wear width is then recorded and defined as the tool life for the selected machining conditions. In practice, we cut for some time and then measure the FWW. We then cut some more and measure again. It is a time consuming, laborious effort. This sequence is repeated at different process parameters in order to determine the best-fit constants for Eq. 8.28. The ranges for the experimental process parameters may be collected from tool supplier recommendations, which often provide a good baseline. Photographs for a flank wear dominated case are provided in Fig. 8.15. Fundamental limitations of this empirical approach are (1) a new testing sequence is required for each change in tool geometry, tool material, workpiece material, or coolant delivery; (2) the data cannot, in general, be extrapolated outside the testing range; and (3) only the limiting tool life is

Fig. 8.15 Flank wear example for a turning insert



examined—the process variation (e.g., in force or power) which naturally occurs due to the tool degradation is not typically evaluated.

While measurement of a wear feature provides an identifiable metric to define tool life, it can be inconvenient to obtain this data in production environments. An alternative approach is to monitor an accessible process signal, such as spindle power, cutting force, or acoustic emission, and compare this signal level to the nominal value for a new tool throughout the selected CNC part program. This approach is often referred to as “indirect” sensing because a signal which is believed to be indicative of tool wear is queried, rather than a direct physical feature such as the machined surface finish [6–8]. The primary challenges associated with indirect sensing are (1) defining the baseline behavior; and (2) setting the limits at which the tool is considered to be worn while avoiding false alarms.

Once a tool life model is identified, the tool life can be related to the machining cost, and the process parameters can be optimized to arrive at a minimum cost solution. The cost per part, C_p , can be written as:

$$C_p = t_m r_m + \frac{(t_{\text{tch}} r_m + C_{\text{te}}) t_m}{T}, \quad (8.29)$$

where t_m is the machining time (min), r_m is the rate for using the machine tool (\$/min), t_{tch} is the tool changing time (min), C_{te} is the cost per tool edge, and T is Taylor-type tool life ($T = Cv^p f_r^q$) [1]. Since the machining time for turning can be written as $t_m = \frac{A}{vf_r}$ where A is the cross-sectional area of the volume removed, Eq. 8.29 can be rewritten as:

$$C_p = \frac{Ar_m}{vf_r} + \left(\frac{C_{\text{tr}} A}{vf_r} \right) \left(\frac{v^p f_r^q}{C} \right) = A \left(\frac{r_m}{vf_r} + \frac{C_{\text{tr}} v^{p-1} f_r^{q-1}}{C} \right), \quad (8.30)$$

where the tool-related cost is $C_{\text{tr}} = t_{\text{tch}} r_m + C_{\text{te}}$. The optimum values of the cutting speed, v_{opt} , and feed rate, $f_{r,\text{opt}}$, can be determined by calculating the partial derivatives of Eq. 8.30 with respect to v and f_r and setting them equal to zero, respectively. The optimum cutting speed is provided in Eq. 8.31, where the feed per revolution is typically selected as the maximum permissible value (e.g., based on the desired surface finish).

$$\begin{aligned} \frac{\partial C_p}{\partial v} &= A \left(\frac{-r_m}{v^2 f_r} + \frac{(p-1)C_{\text{tr}} v^{p-2} f_r^{q-1}}{C} \right) = 0 \\ v_{\text{opt}}^p f_r^q &= \frac{Cr_m}{(p-1)C_{\text{tr}}} \\ v_{\text{opt}} &= \left[\frac{Cr_m}{(p-1)C_{\text{tr}} f_r^q} \right]^{\frac{1}{p}} \end{aligned} \quad (8.31)$$

The optimum feed rate is given by Eq. 8.32.

$$\begin{aligned}\frac{\partial C_p}{\partial f_r} &= A \left(\frac{-r_m}{v f_r^2} + \frac{(q-1)C_{tr} v^{p-1} f_r^{q-2}}{C} \right) = 0 \\ v^p f_{r,\text{opt}}^q &= \frac{Cr_m}{(q-1)C_{tr}} \\ f_{r,\text{opt}} &= \left[\frac{Cr_m}{(q-1)C_{tr} v^p} \right]^{\frac{1}{q}}\end{aligned}\quad (8.32)$$

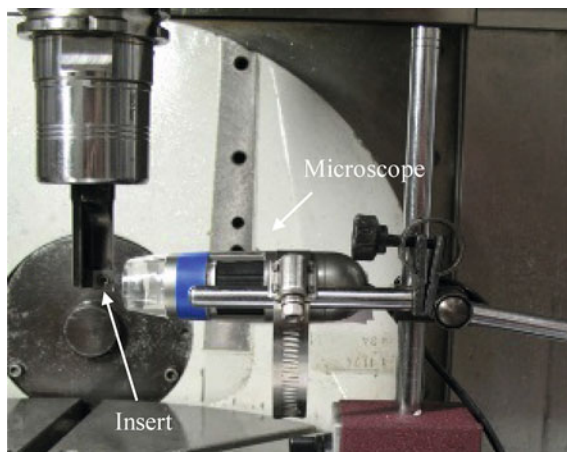


In a Nutshell

Clearly this optimization of the cutting parameters is only justifiable if many parts are going to be made. There are many cases (automobile components, for example) where even a small savings in tool costs translates into tremendous savings for the company.

Example 8.3 Tool Life Model To demonstrate the procedure for identifying an empirical tool life model, let's examine experimental results from a milling study.¹ Tool wear tests were completed using a 19.1 mm diameter, single insert endmill (uncoated carbide) to machine 1018 steel. The tool life model was $vT^n = C$, where n is equivalent to $\frac{1}{p}$ in Eq. 8.28. The experimental setup is displayed in Fig. 8.16. A digital microscope was mounted to the machine table and used to measure the FWW on the carbide insert at intervals of 12 cm³ of volume removed (no significant crater or notch wear was observed). The milling parameters were radial depth of 4.76 mm (25% RI), axial depth of 3 mm, and feed per tooth of 0.06 mm/tooth.

Fig. 8.16 Tool wear measurement setup for milling



¹T. Schmitz recognizes the contributions of J. Karandikar to this experimental study.

Fig. 8.17 Tool life measurement results. (Top) Example FWW measurements using the digital microscope. (Bottom) FWW vs. cutting time. The tool life was defined by the time to reach a FWW of 0.3 mm

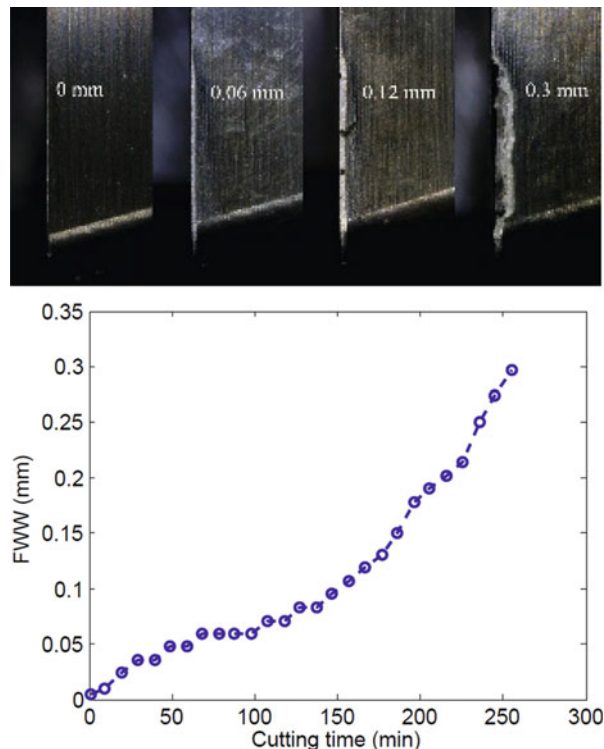
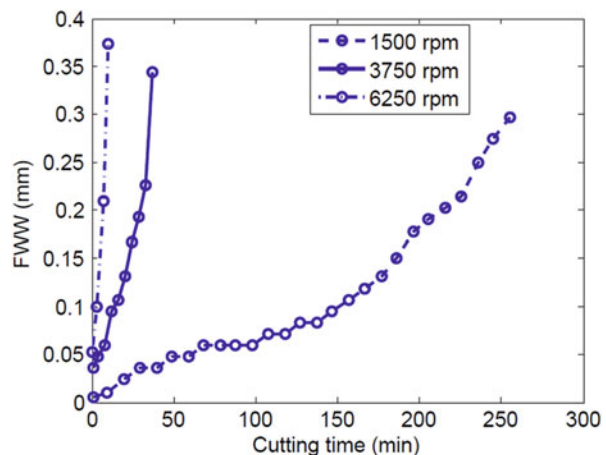


Fig. 8.18 FWW vs. cutting time for all three spindle speeds. The tool wear rate increases rapidly with increasing spindle speed



The FWW progression for a single test at a spindle speed of 1500 rpm is shown in Fig. 8.17. The tool life was defined as the time required to reach a FWW of 0.3 mm. Additional results for 3750 rpm and 6250 rpm are displayed in Fig. 8.18. As expected, the tool life decreased with the increased cutting speed (and temperature). The test results are summarized in Table 8.1.

Table 8.1 Test results for milling 1018 steel with an uncoated carbide insert

Test number	Spindle speed (rpm)	v (m/min)	T (min)
1	1500	89.8	255.3
2	3750	224.4	35.5
3	6250	374.0	8.5

Fig. 8.19 Tool life model (solid line) and experimental data points (\times) for 1018 steel tool wear tests

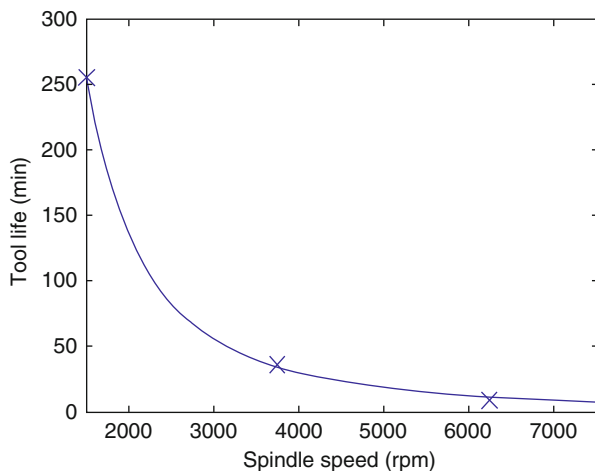


Table 8.2 Test results for turning low carbon steel with a coated carbide insert

Test number	v (in/sec)	f_r (in/rev)	T (min)
1	126 (v_0)	0.020 (f_{r0})	11.46
2	152 (1.2 v_0)	0.020 (f_{r0})	5.68
3	152 (1.2 v_0)	0.024 (1.2 f_{r0})	2.03
4	126 (v_0)	0.024 (1.2 f_{r0})	6.52
5	101 (0.8 v_0)	0.020 (f_{r0})	22.47

The tool life model constants were determined from a least-squares best-fit to the data: $vT^{0.455} = 1120$. The data points and fit are presented in Fig. 8.19.

Example 8.4 Cost Optimization To demonstrate the cost optimization procedure, let's review results for a turning case study.² Outside diameter turning tests were completed on carbon steel workpieces using coated carbide inserts. Five trials were completed to determine the empirical tool life model constants: $v^p f_r^q T = C$. The depth of cut was set at 4.1 mm (0.16 in.), while the cutting speed and feed per revolution were varied. The conditions and results are shown in Table 8.2. The tool life was defined as the cutting time required to reach a FWW of 0.4 mm. The variation in FWW with volume of material removed is displayed in Fig. 8.20.

²T. Schmitz recognizes the contributions of H.S. Kim to this case study.

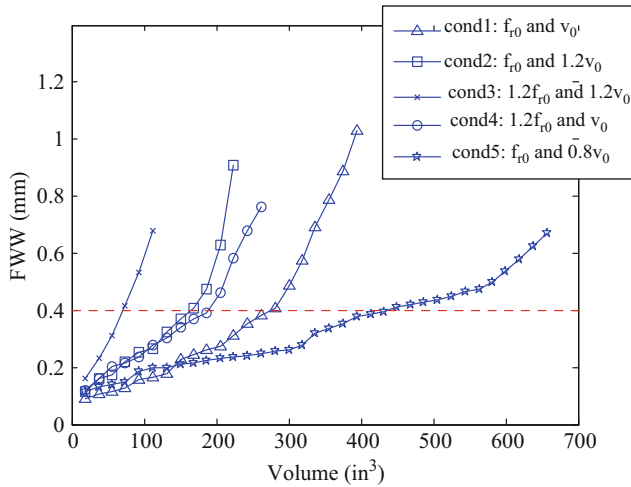


Fig. 8.20 FWW vs. volume of material removed for all five turning test conditions

To determine p , q , and C , a least-squares best-fit procedure was used. The calculation details follow. The Taylor-type tool life can be rewritten as shown in Eq. 8.33.

$$\begin{aligned} T &= Cv^{-p}f_r^{-q} \\ \ln T &= \ln C + \ln v^{-p} + \ln f_r^{-q} \\ \ln T &= \ln C - p \ln v - q \ln f_r \end{aligned} \quad (8.33)$$

Defining $C^* = \ln C$, Eq. 8.33 is rewritten as shown in Eq. 8.34.

$$\ln T = C^* + p(-\ln v) + q(-\ln f_r) \quad (8.34)$$

Substituting for v , f_r , and T from the five data sets gives the following.

$$\begin{aligned} \ln T_1 &= C^* + p(-\ln v_1) + q(-\ln f_{r1}) \\ &\vdots \\ \ln T_5 &= C^* + p(-\ln v_5) + q(-\ln f_{r5}) \end{aligned} \quad (8.35)$$

This set of equations is rewritten in matrix form to obtain Eq. 8.36.

$$\begin{bmatrix} \ln T_1 \\ \ln T_2 \\ \ln T_3 \\ \ln T_4 \\ \ln T_5 \end{bmatrix} = \begin{bmatrix} 1 & -\ln v_1 & -\ln f_{r1} \\ 1 & -\ln v_2 & -\ln f_{r2} \\ 1 & -\ln v_3 & -\ln f_{r3} \\ 1 & -\ln v_4 & -\ln f_{r4} \\ 1 & -\ln v_5 & -\ln f_{r5} \end{bmatrix} \begin{bmatrix} C^* \\ p \\ q \end{bmatrix} \quad (8.36)$$

$y = AB$

In this equation, y and A are known and B contains the unknown coefficients. The vector B is determined using the pseudo-inverse, where T is the transpose operator and -1 indicates the matrix inverse in Eq. 8.37.

$$B = (A^T A)^{-1} A^T y. \quad (8.37)$$

Once B is known, C is determined using:

$$C = \exp C^*. \quad (8.38)$$

Using the data in Table 8.2, the constants are $C = 197$, $p = 3.85$, and $q = 4.02$. The corresponding Taylor-type tool life model is $v^{3.85} f_r^{4.02} T = 197$. This is a somewhat unusual results because the feed rate affects tool life slightly more than cutting speed ($q > p$). Typically, $p > q$.

To check the tool life repeatability, test cuts at operating points 1 and 3 were again completed. These results are shown in Fig. 8.21. The predicted tool life using $v^{3.85} f_r^{4.02} T = 197$ is also identified for the two cases (\times for case 1 and Δ for case 3). Using all seven data sets, the new model constants are $C = 212$, $p = 3.90$, and $q = 4.06$, and the updated tool life model is $v^{3.90} f_r^{4.06} T = 212$. To calculate the cost per part, the parameters in Table 8.3 are required. These are representative of industry values.

The optimum feed rate at the nominal cutting speed (v_0) and the optimum cutting speed at the nominal feed per revolution (f_{r0}) were calculated using

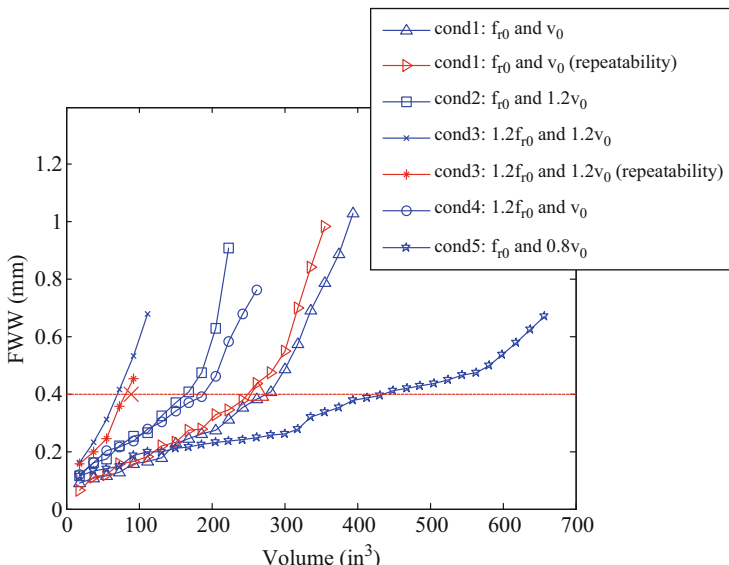
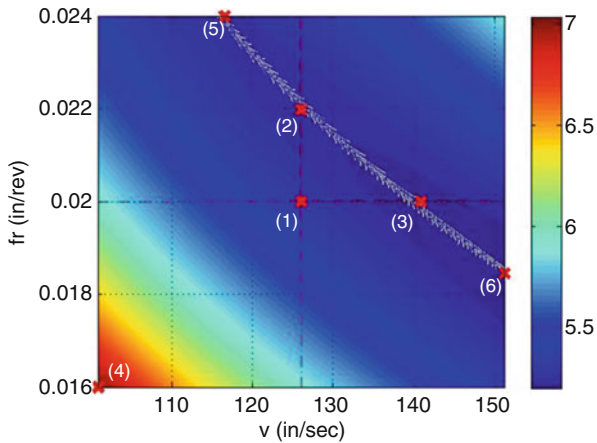


Fig. 8.21 FWW vs. volume of material removed for all five turning test conditions including repeats at conditions 1 and 3

Table 8.3 Cost parameters

Variable	Value
r_m	1.79 (\$/min)
t_{tc}	1.27 (min)
C_{te}	\$2.01/tool edge

Fig. 8.22 Contour plot for the cost per part (\$) as a function of cutting speed and feed per revolution



Eqs. 8.31 and 8.32, respectively. The cost per part for both conditions were then determined using Eq. 8.30. The cost per part at the nominal condition ($v_0 = 126$ in/sec and $f_{r0} = 0.02$ in/rev) was also calculated to compare with the optimum conditions. In the range of $v = 101$ in/sec to 152 in/sec and $f_r = 0.016$ in/rev to 0.024 in/rev which are $\pm 20\%$ from the nominal condition, the minimum and maximum costs per part were also determined. Figure 8.22 provides a contour plot showing the cost per part as a function of cutting speed and feed per revolution. In the figure, the white band indicates the minimum cost for particular combinations of cutting speed and feed per revolution. For example, if the nominal cutting speed ($v_0 = 126$ in/sec) is used, the cost is the minimum at $f_r = 0.022$ in/rev, where the white band intersects with the vertical line associated with the selected cutting speed. Likewise, the cost is minimum at $v = 141$ in/sec if the nominal feed per revolution ($f_{r0} = 0.020$ in/rev) is used. Therefore, the plot provides the optimum cutting condition (either v_{opt} or $f_{r, opt}$) based on preselected feed per revolution or cutting speed to minimize the cost.

As shown in Table 8.4, the cost is minimized at the higher cutting speed (6) rather than at the higher feed rate (5). This is because $q > p$ in the Taylor-type tool life model. The percent difference for the cost between the maximum (4) and optimum condition (6) is 26.1%.

Table 8.4 Cost per part for selected cutting conditions

Point in Fig. 8.21	v (in/sec)	f_r (in/rev)	C_p (\$)
1	126 (v_0)	0.020 (f_{r0})	5.31 (nominal)
2	126	0.022	5.24
3	141	0.020	5.22
4	101	0.016	7.04 (maximum)
5	117	0.024	5.27
6	152	0.018	5.20 (minimum)

8.3 Cutting Fluids

Cutting fluids are used to:

- Prevent the tool, workpiece, and machine from overheating and distorting.
- Increase tool life.
- Improve surface finish.
- Prevent oxidation.
- Clear away chips.

They can serve as a coolant, lubricant, or both. Due to the high pressures between the chip and rake face, this interface is generally inaccessible to externally applied cutting fluids, particularly for continuous cutting. Note that the specific cutting force, K_s , is essentially the pressure between the tool and chip in the cutting zone. Compare it to atmospheric pressure, and it will be clear that the cutting fluid reaches this zone only (possibly) by capillary action. Nevertheless, new tool designs that include high-pressure streams directed at the tool-chip interface are being introduced in an effort to lubricate and cool this location while encouraging chip breakage for continuous cutting operations. The two primary fluid types are:

- Water-based (oil/synthetic/organic and water emulsion)—these serve as an effective coolant, often directed at the highest temperature location to flood the cutting zone with tens of liters per minute; it is also possible to target the hot zones using mist delivery at much lower flow rates.
- Neat cutting oils—these serve as an effective lubricant, can improve surface finish, reduce forces, extend tool life, and reduce BUE.

Cutting fluids are applied manually, by flooding, by mist application, and by high-pressure directed nozzles. Flooding is typically carried out at flow rates of approximately 5 to 10 liters per minute (lpm) and pressures of hundreds of kPa. For mist application, the fluid consumption rate is orders of magnitude smaller, approximately 1 liter per hour.

High-pressure coolant is a more recent approach and is carried out at flow rates that may exceed 100 lpm with pressures up to 200 MPa. Tooling with integrated coolant nozzles is available. A commercial example is displayed in Fig. 8.23 [9]. Selection of the flow rate (lpm) depends on the power (kW) consumed in the cut. A rule of thumb is 2.5 lpm/kW [10]. The required coolant jet orifice diameter is

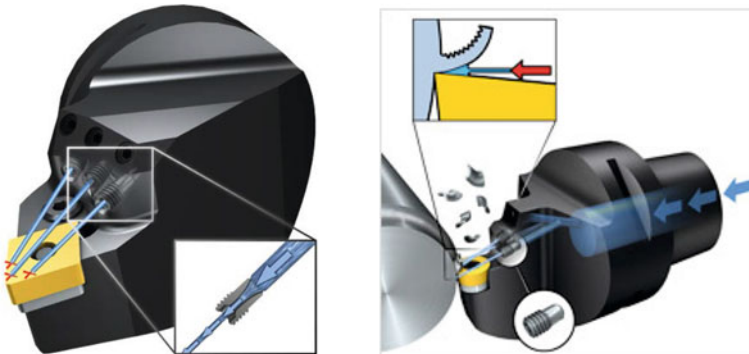


Fig. 8.23 Example of high-pressure coolant turning tools with integrated delivery nozzles [9]

Table 8.5 Example of specific cutting force values

Material	K_s (N/mm ²)
6061-T6 aluminum	750
1020 steel	2400
304 stainless steel	3500
Titanium (6Al-4V)	2100
Inconel 718	3600

directly related to the velocity, pressure, and flow rate. Tabulated values for these relationships are available [11]. For a selected orifice diameter and pressure, the flow velocity, flow rate, and power are listed. Therefore, given the anticipated power and a selected pressure, the appropriate orifice diameter can be chosen.

The approximate power can be estimated using the mean material removal rate and specific cutting force for the workpiece material-tool combination. The average material removal rate, MRR (mm³/min), for milling is defined in Eq. 8.39, where:

- a is the radial depth of cut (mm).
- b is the axial depth of cut (mm).
- f_t is the feed per tooth (mm/tooth).
- N_t is the number of teeth.
- Ω is the spindle speed (rpm).

$$\text{MRR} = abf_t N_t \Omega \quad (8.39)$$

$$P = \frac{K_s \text{MRR}}{6 \times 10^4} \quad (8.40)$$

The corresponding power, P (W), is defined in Eq. 8.40, where K_s is the specific cutting force (N/mm²). Example values are provided in Table 8.5; note that these values will vary with the material microstructure and tool geometry and should be considered as representative of the alloy. For improved estimates, cutting trials can be completed to identify the specific cutting force experimentally.



In a Nutshell

It is useful to have these numbers readily at hand. For many kinds of cutting operations (e.g., milling, turning, boring, and sawing), the required power is proportional to the MRR by these values.

High-pressure coolant research and development are motivated by the shortcomings of existing technology. It is proposed that low-pressure flood coolant fails because a vapor barrier is created when the coolant is rapidly heated above its boiling point due to contact with the primary shear zone. It is suggested that high-pressure coolant penetrates this barrier and is, therefore, capable of removing the heat that is generated by the cutting process. The ability to select the high-pressure coolant application point and direction is therefore important.

Research articles that investigate high-pressure coolant include [12–23]. More work has been completed for turning than for milling due to the continuous heat generation and difficulty in introducing coolant into the tool-chip interface in continuous cutting. In general, improved performance was observed when using high-pressure coolant. However, critical evaluations of the effect of jet orientation on machining performance are not currently available. The pressure and flow rate were varied in a few studies, but a complete understanding of their effects have not been reported. Based on the results in the literature, it appears that performance improves up to a process-dependent pressure and then less improvement is achieved with increased pressure.

Tool wear for hard-to-machine materials, such as nickel based alloys, is a particular challenge. Oil emulsion and water-based cutting fluids are the conventional cooling/lubrication approach in these cases. However, the environmental and health concerns associated with the use of these fluids are driving the demand for alternative machining strategies. These strategies include, for example, dry machining using ceramic cutters, minimum quantity lubrication, chilled air, and cryogenic machining [24].

Among these methods, the use of cryogenic fluids offers an attractive cooling alternative and has received significant attention in the literature. Cryogenic fluids cool the cutting zone to very low temperatures using liquefied gases, such as liquid nitrogen (N_2), helium (He), or carbon dioxide (CO_2). Investigations involving cryogenic cooling are leading to improved tool performance and overall part quality. The influence of cryogenic nitrogen machining, for example, has notably improved the tool life, surface finish, and residual compressive stresses in the turning of magnesium alloys, NiTi shape memory alloys, and titanium alloys [25–27].

CO_2 cooling has been shown to improve the tool life in polycrystalline diamond (PCD) turning of compacted graphite iron (CGI), but the performance is highly dependent on grain size and binder content of the tool material [28]. It has also been shown to also suppress burr formation and limit notch wear in the turning of β -titanium alloys by a factor of two over conventional emulsion flood coolant [29].

Predominately, cryogenic cooling has positively impacted the cutting performance of hard-to-machine materials during uninterrupted cutting operations. Its

effect on interrupted cutting operations, such as milling, is not well understood, although some studies are reported in the literature. For example, Su et al. observed improved tool life in the high-speed milling of titanium 6Al-4V using compressed nitrogen gas but also observed instances of dramatically reduced tool life due to thermal fatigue cracking of the tool [30].

A recent study examined the cutting performance of milling Hastelloy X using two cooling/lubricating strategies [31]. The effects on tool life, cutting forces, and cutting temperatures were examined using an aqueous-based MQL coolant and external cryogenic CO₂ spray. Digital microscope images, SEM images, cutting force data, and thermal images were used to compare the effectiveness of the two cooling methods. Results showed an approximately 89% longer tool life when using MQL compared to CO₂ for the selected cutting conditions. From microscope images, a clear edge chipping phenomenon occurred when using CO₂. This led to larger cutting forces and, ultimately, sudden catastrophic failure of the tool edge. Possible explanations for the adverse cutting performance using CO₂ include thermal fatigue cycling, material adhesion to the cutting edge, coating failure, and changes in workpiece material properties. The periodic large variations in temperature for the in-cut and out-of-cut times are proposed to have caused brittle cracking of the cutting edge.

8.4 Relationship to Machining Dynamics

In this chapter, we extended our study beyond process dynamics to include machining tribology (i.e., the study of friction, wear, and lubrication). We derived relationships between the cut geometry, cutting forces, velocities, and powers in order to estimate the temperature rise caused by chip formation. We described an empirical procedure for relating tool life to machining parameters, referred to as the Taylor-type tool life model, and determined optimal operating conditions to minimize cost using this model. Finally, we examined the role of cutting fluids in maximizing tool life and increasing machining productivity.

To relate machining tribology to our prior examination of machining stability, it is generally agreed that relative vibration between the tool and workpiece tends to increase tool wear. This is particularly true for chatter, where the forces and vibrations are large. It can lead to chipping and premature failure of the cutting edge, for example. A study of tool wear (characterized using FWW) for turning and milling under both stable and unstable conditions was completed in [32], where it was shown that chatter, as well as its amplitude (moderate to severe conditions), significantly reduces tool life. One solution is to use conservative chip width values to avoid chatter. However, the penalty is higher cost per part. As discussed previously, the limiting chip width (without chatter) is strongly dependent on spindle speed, particularly at high spindle speed values. The incorporation of the stability lobe diagram in stable machining parameter selection at the process planning stage can therefore not only increase material removal rates but also avoid the high tool wear rates imposed by unstable cutting conditions.

Exercises

1. Tribology is the study of _____.
2. Consider orthogonal cutting of 304 stainless steel with the following parameters: $h_m = 0.1 \text{ mm}$, $b = 4 \text{ mm}$, $v = 2 \text{ m/s}$, $\alpha = 12 \text{ deg}$, $\phi_s = 26 \text{ deg}$, $k_t = 3200 \text{ N/mm}^2$, and $k_n = 1200 \text{ N/mm}^2$. Calculate the following parameters.
 - $K_s (\text{N/mm}^2)$
 - $\beta (\text{deg})$
 - $L (\text{mm})$
 - $h_d (\text{mm})$
 - r
 - $v_c (\text{m/s})$
 - $v_s (\text{m/s})$
 - $F (\text{N})$
 - $F_s (\text{N})$
 - $F_f (\text{N})$
 - $P_s (\text{W})$
 - $P_f (\text{W})$
3. An increase in cutting speed tends to increase the chip temperature. T/F
4. Built-up edge can cause the effective rake angle to change during a cutting operation. T/F
5. Consider the Taylor-type tool life model: $C = v^p f_r^q T$, where C , p , and q are constants. Tests were performed and the tool life was measured; the data is provided in Table 8.6. Using this data determine the constants for the tool life model.
6. Using the populated tool life model from problem 5, plot the cutting speed (horizontal axis) versus the tool life on a log-log scale for feed values of 0.1 mm and 0.2 mm. Use a cutting speed range of 50 m/min to 300 m/min for the horizontal axis and a tool life range of 2 min to 4000 min on the vertical axis.
7. Using the data from Table 8.6, determine the optimum cutting speed (m/min) by applying Eq. 8.31. For your calculation, use the cost parameters from Table 8.3 and a maximum permissible feed of 0.2 mm.

Table 8.6 Tool life testing data

$v (\text{m/min})$	$f_r (\text{mm})$	$T (\text{min})$
100	0.2	80
200	0.2	10
200	0.1	40

8. Calculate the mean power (kW) consumed in the following milling operation: Aluminum alloy workpiece with a specific cutting force of 710 N/mm^2 , slotting, 19.1 mm diameter endmill with four teeth, 8000 rpm, 3 mm axial depth, and 0.15 mm feed per tooth.
9. Define the acronym MQL.
10. Tool life is not affected by the machining stability. T/F

References

1. Lusty, G. (2000). *Manufacturing processes and equipment, chapter 8: Cutting mechanics*. Upper Saddle River, NJ: Prentice Hall.
2. Rubeo, M., & Schmitz, T. (2016). Milling force modeling: A comparison of two approaches. *Procedia Manufacturing*, 5, 90–105.
3. Altintas, Y. (2000). *Manufacturing automation: metal cutting mechanics, machine tool vibrations, and CNC design*. Cambridge, UK: Cambridge University Press.
4. Gunay, M., Aslan, E., Korkut, I., & Seker, U. (2004). Investigation of the effect of rake angle on main cutting force. *International Journal of Machine Tools and Manufacture*, 44, 953–959.
5. Taylor, F. W. (1907). On the art of cutting metals. *Transactions of the ASME*, 28, 31–350.
6. Teti, R. (1995). A review of tool condition monitoring literature database. *Annals of the CIRP*, 44(2), 659–666.
7. Dimla, D. E. (2000). Sensor signals for tool-wear monitoring in metal cutting operations—A review of methods. *International Journal of Machine Tools and Manufacture*, 40, 1073–1098.
8. Sick, B. (2002). On-line and indirect tool wear monitoring in turning with artificial neural networks: A review of more than a decade of research. *Mechanical Systems and Signal Processing*, 16(4), 487–546.
9. Retrieved April 1, 2017, from <http://www.sandvik.coromant.com/en-us/knowledge/featured-articles/pages/benefits-of-high-pressure-coolant.aspx>
10. Retrieved April 1, 2017, from https://www.youtube.com/watch?v=QwoI_F4Xed0
11. Retrieved April 1, 2017, from <http://www.chipblaster.com/orifice-reference-chart>
12. Machado, A. R., & Wallbank, J. (1994). The effects of a high-pressure coolant jet on machining. *Proceedings of the Institution of Mechanical Engineers*, 208, 29–38.
13. Exugwu, E. O., Da Silva, R. B., Bonney, J., & Machado, A. R. (2005). Evaluation of the performance of CBN tools when turning Ti-6Al-4V alloy with high pressure coolant supplies. *International Journal of Machine Tools and Manufacture*, 45, 1009–1014.
14. Nandy, A. K., Gowrishankar, M. C., & Paul, S. (2009). Some studies on high-pressure cooling in turning of Ti-6Al-4V. *International Journal of Machine Tools and Manufacture*, 49, 182–198.
15. Fadare, D. A., Ezugwu, E. O., & Bonney, J. (2009). Modeling of tool wear parameters in high-pressure coolant assisted turning of titanium alloy Ti-6Al-4V using artificial neural networks. *The Pacific Journal of Science and Technology*, 10(2), 68–76.
16. Ezugwu, E. O., Bonney, J., Da Silva, B., & Cakir, O. (2007). Surface integrity of finished turned Ti-6Al-4V alloy with PCD tools using conventional and high pressure coolant supplies. *International Journal of Machine Tools and Manufacture*, 47, 884–891.
17. Sharma, V., Dogra, M., & Suri, N. M. (2009). Cooling techniques for improved productivity in turning. *International Journal of Machine Tools and Manufacture*, 49, 435–453.
18. Lopez de Lacalle, L. N., Perez-Bilbatua, J., Sanchez, J. A., Llorente, I., Gutierrez, A., & Alboniga, J. (2000). Using high pressure coolant in the drilling and turning of low machinability alloys. *International Journal of Advanced Manufacturing Technology*, 16, 85–91.
19. Palanisamy, S., McDonald, S. D., & Dargusch, M. S. (2009). Effects of coolant pressure on chip formation while turning Ti6Al4V alloy. *International Journal of Machine Tools and Manufacture*, 49, 739–743.
20. Kaminski, J., & Alvelid, B. (2000). Temperature reduction in the cutting zone in water-jet assisted turning. *Journal of Materials Processing Technology*, 106, 68–73.
21. Kovacevic, R., Cherukuthota, C., & Mazurkiewicz, M. (1995). High pressure waterjet cooling/lubrication to improve machining efficiency in milling. *International Journal of Machine Tools and Manufacture*, 35(10), 1459–1473.
22. Rahman, M., Kumar, A. S., & Choudhury, M. R. (2000). Identification of effective zones for high pressure coolant in milling. *Annals of the CIRP*, 49(1), 47–52.
23. Kumar, A. S., Rahman, M., & Ng, S. L. (2002). Effect of high-pressure coolant on machining performance. *International Journal of Advanced Manufacturing Technology*, 20, 83–91.

24. Shokrani, A., Dhokia, V., & Newman, S. T. (2012). Environmentally conscious machining of difficult-to-machine materials with regard to cutting fluids. *International Journal of Machine Tools and Manufacture*, 57, 83–101.
25. Pu, Z., Outeirob, J. C., Batista, A. C., Dillon Jr., O. W., Puleo, D. A., & Jawahir, I. S. (2012). Enhanced surface integrity of AZ31B Mg alloy by cryogenic machining towards improved functional performance of machined components. *International Journal of Machine Tools and Manufacture*, 56, 17–27.
26. Kaynak, Y., Karaca, H. E., Noebe, R. D., & Jawahir, I. S. (2013). Tool-wear analysis in cryogenic machining of NiTi shape memory alloys: A comparison of tool-wear performance with dry and MQL machining. *Wear*, 306, 51–63.
27. Wang, Z. Y., & Rajurkar, K. P. (2000). Cryogenic machining of hard-to-cut materials. *Wear*, 239(2), 168–175.
28. Abele, E., & Schramm, B. (2008). Using PCD for machining CGI with a CO₂ coolant system. *Production Engineering*, 2(2), 165–169.
29. Machai, C., & Biermann, D. (2011). Machining of β-titanium-alloy Ti-10V-2Fe-3Al under cryogenic conditions: Cooling with carbon dioxide snow. *Journal of Materials Processing Technology*, 211(6), 1175–1183.
30. Su, Y., He, N., Li, L., & Li, X. L. (2006). An experimental investigation of effects of cooling/lubrication conditions on tool wear in high-speed end milling of Ti-6Al-4V. *Wear*, 261(7), 760–766.
31. Tyler, C., & Schmitz, T. (2014). Examining the effects of cooling/lubrication conditions on tool wear in milling Hastelloy X. *Transactions of the NAMRI/SME*, 42, 1–8.
32. Kayhan, M., & Budak, E. (2009). An experimental investigation of chatter effects on tool life. *Proceedings of the Institution of Mechanical Engineers, Part B: Journal of Engineering Manufacture*, 223(11), 1455–1463.

Index

A

- Accelerometer, 331–333
- Additive manufacturing (AM)
 - digital thread/communication framework, 1
 - digital twin, 1
 - and HM, 1
- Argand diagram, 23
- Artifact-spindle-machine assembly, 327
- Associated cybersecurity, 2

B

- Ball milling time domain simulation, 186–190
- Bifurcation diagrams, 270–271, 273
- Built-up edge (BUE), 360, 370

C

- Capacitance probe (CP), 272
- Chemical vapor deposition (CVD), 361
- Chip
 - 6Al-4V titanium, 359
 - formation, 348
 - nonuniform chip flow, 360
 - ratio, 355
 - shearing velocities, 355
 - 7075-T6 aluminum, 357, 358
 - temperature field, 356
 - thickness, 355
- Circular tool path, 131
- Clamped-free beam, 309, 310, 312–314
- Cloud computing, 2
- Compacted graphite iron (CGI), 372
- Computer aided design (CAD), 1, 67
- Computer aided manufacturing (CAM), 1, 67
- Computer numerically controlled (CNC), 67, 346, 363
- Computer simulation, 4
- Coulomb damping, 16–17
- Cubic boron nitride (CBN), 361
- Cutting force, 4, 348, 350–355, 358, 360, 363, 370, 371, 373
- Cutting force coefficient, 351–353
- Cyberattack, 2
- Cycloidal tool path simulation, 260
- Cycloidal tool path time domain simulation
 - axial slices, 233
 - chip thickness reduction condition, 231
 - cutting parameters, 229
 - helical cutting edge, 232
 - instantaneous chip thickness, 229–231
 - linear interpolation, 230
 - machined surface, 234, 235
 - modal parameters, 232
 - nonlinearity, 230
 - numerical integration, 229
 - peak-picking method, 229
 - radial immersion, 231, 232
 - SLE, 236
 - specifications, 233
 - stability lobe diagram, 233
 - tangential and normal force components, 232
 - time plots, 233
 - transients, 233
 - y direction force and displacement, 233, 234

D

- Damped coupling, 296–302
 Diffusion, 360
 Direction displacements
 plot, 268, 269
 time history, 267–269
 Directional orientation factor, 83
 Dynamometer, 198

E

- Eddy current damper, 14–16
 Edge effect, 191
 Eigensolution, 32, 35, 36
 Endmill, 353, 364
 Energy dissipation, 8
 Euler-Bernoulli beam receptances, 317, 322,
 324, 329, 330
 Euler-Bernoulli beam theory, 303, 308,
 309, 315
 Experimental cutting force coefficients
 dynamometer, 198
 FRF measurement, 199
 linear regression, 193–196
 nonlinear optimization, 196–198
 significant complexity, 199
 tooth passing frequency, 198
 updated force model, 190–193
 Exponential form, 12, 19

F

- Fast Fourier transform (FFT), 110
 Finite element (FE), 284, 315, 322, 329, 333,
 334, 336–338
 First natural frequency, 28, 31, 34
 Flank wear width (FWW), 362
 carbide insert, 364
 vs. cutting time, 365
 digital microscope, 365
 spindle speed, 365
 Verschleissmarken Breite, 362
 vs. volume of material, 367, 368
 Flexible coupling, 296–302
 Force components, 350
 Force dynamometer, 3
 Force model, 3
 Force reconstruction, 219
 Force spectrum, 223
 Fourier force model, 217–219
 Fourier series approach
 angular orientation, 154
 average tooth angle approach, 158

closed loop dynamic milling system, 159

- dynamic milling equation, 159
 Euler identity, 160
 force expressions, 157
 frequency-dependent equation, 160
 FRFs, 158
 impulse-like, 158
 nontrivial solution, 159
 notation, 155
 oriented FRF, 161
 quadratic equation, 160
 radial direction, 155
 spindle speeds, 161
 stability analysis, 158
 stability lobe diagram, 162, 163
 tangential and normal (radial) force
 components, 155, 156
 time-varying directional dynamic force
 coefficients, 157
 trigonometric identities, 156

Fourier series force dependence, 218

Fourier series integrals, 218

Free-free beam

- clamped-free beam, 319, 320, 322
 rigid support, 316–319

Frequency domain approach, 3, 5

Frequency domain solution, 219–223
 assertions, 216
 assumptions, 216

Fourier force model, 217–219

SLE (*see* Surface location error (SLE))

Frequency response function (FRF), 3,

- 242–245, 251, 252, 275

 amplitudes, 48

 machining productivity, 7

 magnitude and phase, 21

 measurement, 37

 modal analysis, 42

 modal fitting, 34

 peak-picking method, 42

 real and imaginary parts, 21, 40

 steady-state responses, 37

 vector representation, 24

Fused deposition modeling, 1

G

Game-changing innovations, 1

H

Helical square endmills, 243

Home stereo system, 139

Hopf bifurcation, 266
Hybrid manufacturing (HM), 1

I

Industrial Internet of Things, 2
Interior-reflective Newton approach, 197

L

Laser tachometer (LT), 272
Laser vibrometer (LV), 272
Linear regression, 193–196
Lumped parameter model, no damping, 10–13
Lumped parameter systems, 13, 38

M

Machining dynamics
 factors, 2
 FRF, 3
 parameter selection, 2
Machining tribology
 cost-minimized solution, 345
 cost optimization, 366–370
 cutting fluids, 370–373
 feedback loop, 346
 geometry, forces and temperature, 347–359
 parameter selection process, 346
 relationship, 373
 steel orthogonal cutting, 355, 356
 temperature field in chip, 356, 358, 359
 tool life, 359–369
 tool-workpiece interface, 345
 tribology-related information, 346, 347
 workpiece material, 346
Magnesium alloys, 372
Material removal rate (MRR), 371
MATLAB® diff function, 263
MATLAB® sound function, 256
Measurement uncertainties, 58–59
Mechanical vibrations, 7, 23
Metal cutting, 355, 360, 361
Microphone-amplifier-speaker systems, 74
Milling dynamics
 angle geometry, 132
 applications and tool geometries, 131
 automated stability identification, 129
 axis milling machine, 130
 chip thickness variation, 132
 circular tool path approximation, 131
 cutter angle, 132
 cutting force, 134

cutting tools and holders, 130
endmills, 130
feed per tooth, 132
force expressions, 129
multiple teeth in cut, 140–142
normal and tangential components, 134
parameters, 136
projection, 134
radial immersion, 136, 137
regenerative chatter, 141–145
rigid tool and workpiece, 133, 135
solid body cutters, 131
start and end angle, 133
tool-holder-spindle, 129, 130
tooth passing frequency, 137–139
turning operations, 133

Milling process

 actual cycloidal tool path, 241
 bifurcation diagrams, 270–271
 frequency content, 241–256
 instance, 243–247, 249, 250
 nutshell, 250, 251, 253, 254, 256–258
 period- n bifurcations, 265–274
 Poincaré maps, 270
 radial immersion milling, 241
 runout, 256–261
 simulation modification, 259–261
 stability maps, 271–274
 teeth spacing, 262–265
 uncertainty propagation, 274–276

Milling signals, 254, 256

Milling time domain simulation
 analytical stability boundaries, 169
 assumptions, 164
 chatter frequency, 174
 chip thickness calculation, 164–167
 cutter rotation, 165
 displacement calculation, 167–168
 force calculation, 167
 Fourier series approach, 169
 FRF mode, 182
 helical teeth, 178–185
 implementation, 168–175
 interrupted cutting, 174
 local cutting force/tool vibrations, 164
 modal parameters, 164
 numerical integration, 164
 orthogonality, 172
 periodic sampling, 175–177
 resultant cutting force vs. time, 183, 185
 resultant force, 171, 173
 and sampling, 177, 178
 stability metric, 176, 177

- Milling time domain simulation (*cont.*)
 stable cutting, 173
 tooth angle definition, 166, 167
 tooth passing frequency and harmonics, 174
 x direction force and displacement,
 169–172
 y direction force and displacement, 169–174
 Modal analysis, 36–40
 Modal fitting, 7, 34, 49–52
 Modal matrices, 47
 Modal testing equipment, 52–58
 force input, 53
 vibration measurement, 54–58
 Modal testing techniques, 3
 Modulated tool path (MTP)
 chip buildup, 101
 chip thickness, 104, 105
 continuous cutting processes, 101
 experimental setup, 108–113
 frequency domain analysis, 102
 oscillation frequency and amplitude, 101
 periodic sampling, 102, 112, 175
 spindle revolutions, 103
 stability analysis, 104–108
 stability metric values, 113
 thrust direction acceleration, 114
 thrust direction force, 113
 thrust direction velocity, 114
 tool point FRF, 110
 tube turning setup, 109
 user-defined parameters, 102
 Monte Carlo simulation, 275
- N**
 National Institute of Standards and Technology (NIST), 275
 Natural frequency, 9
 NiTi-shape memory alloys, 372
 Nonlinear optimization, 196–198
- O**
 Orthogonal cutting, 68, 347, 348, 355, 358
 Oscillations per revolution (OPR), 102
- P**
 Parameter selection process, 346
 Peak-picking method, 42
 Peak-picking modal fit, 44
 Period- n bifurcations, 265–274
 Photopolymerization, 1
- Physical vapor deposition (PVD), 361
 Piezo-accelerometer (PA), 272
 Poincaré map, 270
 period-2 bifurcation, 272
 period-3 bifurcation, 273
 period-8 bifurcation, 273
 Polycrystalline diamond (PCD), 361, 372
 Process coefficients, 4
 Process damping, 200–206
 chatter-free chip widths, 115
 description, 115–117, 199–200
 energy dissipation, 115
 single degree of freedom turning model,
 117, 119–121
 stability algorithm, 117–122
 down milling, 202–204
 regenerative chatter, 200
 time domain simulation, 203–206
 up milling, 201, 204
 time domain simulation, 120, 122
 turning and milling operations, 115
 two degree of freedom turning
 model, 121
- R**
 Radial immersions (RI), 352, 353, 359
 Radial immersion stability, 266, 269
 Receptance coupling substructure analysis (RCSA), 3, 285, 322, 327–329, 331, 332, 335–338
 Receptance coupling technique
 assembly modeling techniques, 298
 and clamped-free response, 318, 319
 complex matrix inversion, 300
 component, 300, 301
 component flexible and damped
 coupling, 296–302
 component flexible coupling, 289–296
 component rigid coupling, 285–289
 H_{1b1b} calculation, 301
 mass, damping and stiffness values, 301
 matrix manipulations, 302
 modal analysis, 299, 302
 tool-holder-spindle-machine, 284–286, 323
 vector manipulations, 302
 Regeneration of waviness, 71
 Regenerative chatter, 141–145
 Roadmap, 4–5
 Runout
 forces, 259, 260
 frequency content, 257, 258
 harmonics and chatter frequencies, 258

S

- Second natural frequency, 31, 34
Self-excited vibrations, 4
Semi-logarithmic plot, 318
Shear plane, 348–350, 354–356
Single degree of freedom, 10–13, 17–19,
 22–25, 27, 33, 271
 coulomb damping, 16–17
 forced vibration, 9, 10, 19–25
 free vibration, 8, 9
 FRF, 22–25
 lumped parameter model, no damping,
 10–13
 lumped parameter model, viscous
 damping, 17–19
 self-excited vibration, 10
 solid damping, 17
 viscous damping, 13–16
Sinusoidal forces, 20
Solid cylinder
 and prismatic beam, 303
Solid damping, 17
Spindle-machine receptances, 327–330
Spindle speeds
 chatter frequency, 244, 246–251
 competing lobes, 251, 253–255
Spring-mass-damper model, 19, 25, 35
Spring-mass-damper systems, 298, 300
Stability lobe diagrams, 73, 147–149, 154–163
 average tooth angle approach, 145–147, 182
 competing lobe effect, 154
 directional orientation factors
 down milling, 148
 slotting, 147, 148
 up milling, 149
 Fourier series (*see* Fourier series approach)
 Fourier series approach, 183
 oriented FRF, 147–154
 radial immersion down milling, 152
 slotting calculation, 149, 150
 turning operation (*see* Turning dynamics)
Stereolithography, 1
Surface location error (SLE)
 axial location, 225–228
 calculations, 219, 220
 CNC programming packages, 215
 constant *y* direction cutting force and
 displacement, 227
 down milling cut, 214, 215
 force magnitude, 222
 frequency response function, 216
 helical endmill geometry, 225
 higher *N* value stability lobes, 222

- machine-spindle-holder-tool, 214
 overcut condition, 214, 215
 pusher and swing, 216
 radial depth of cut, 223, 224
 rectangular stable zone, 221
 spindle speed range, 222
 stability, 228–229
 stability lobe diagram, 220, 221
 steps, 219
 thermal deformation, 214
 tool's dynamic displacement, 227
 tooth passing frequency, 214, 223, 224
 undercut condition, 214, 215
 up and down milling, 220
 variable cutting force, 216
 variation, 222
 visual explanation, 214
 workpiece geometric inaccuracies, 213

System identification, 42–52
 modal fitting, 42–47
 modal truncation, 49–52
 model definition, 47–49

T

- Taylor's tool life model, 4
Taylor-type tool life model, 361, 368, 369, 373
Teeth spacing cutter
 uniform, 265
 variable, 265
Thin rib dynamics, 333–338
Time domain simulation strategy, 3
Titanium alloys, 358, 372
Tlusty model, 83
Tool-chip interface, 345, 356, 358, 360,
 370, 372
Tool-holder-spindle-machine modeling, 284,
 302, 322–330
Tool point
 FRFs, 283
 stability and surface location error, 283
 tool-holder-spindle-machine, 284
Tooth passing frequency, 137–139
Trimming algorithm, 234, 235
Tube turning, 348
Turning dynamics
 automatic control, 67
 cutting force dynamometer, 69
 cutting force vector, 69
 force angle, 69
 instantaneous chip thickness calculation, 72
 K_s values, 69, 70
 less favorable phase relationship, 72, 73

- Turning dynamics (*cont.*)
- manual lathe, 68
 - oriented FRF, 83–91
 - orthogonal cutting operation, 68
 - regenerative chatter, 70–73
 - revolution-to-revolution alignment, 73
 - sharp cutting edge, 67
 - specific (or per unit chip area) force, 69
 - spindle speeds, 89
 - stability lobe diagrams
 - chatter frequency, 74, 78
 - chip thickness variation, 77
 - chip width, 74
 - governing relationships, 73
 - inphase, 77
 - instantaneous chip thickness, 75
 - length of vector difference, 76
 - minimum b_{\lim} value, 77
 - multiple degree of freedom systems, 82
 - oriented FRF, 82
 - requirements, 75
 - revolution to revolution, 73
 - single degree of freedom system, 82, 83
 - spindle speed, 79, 80
 - time dependent tool deflections, 77
 - tool deflections, 74, 76
 - tool point natural frequency, 81
 - unit normal force, 76
 - vector representation, 77
 - vector sum, 75
 - vibration levels, 75
 - waviness, 81
 - workpiece revolutions, 78, 79
- surface waviness, 72
- vibrating cutter, 71
- vibrations, 71
- Turning time domain simulation, 101–113
- chip thickness calculation, 91–93
 - directional orientation factors, 94
 - displacement calculation, 94–99
 - force and displacement values, 97–99
 - force calculation, 93
 - MTP (*see* Modulated tool path (MTP))
 - multiple degree of freedom modeling, 99–101
 - numerical integration, 92, 93
 - oriented FRF, 95, 96
 - stability evaluation, 94, 96, 97
- Two degree of freedom
- complex coefficients, 29–32
 - complex matrix inversion, 40–41
 - forced vibration, 35, 36
 - free vibration, 25–35
 - modal analysis, 32–40
- U**
- Updated force model, 190–193
- V**
- Vector of angles, 165
- Velocity, 350
- Verschleissmarken Breite (VB), 362
- Vibrating systems, 7
- Vibration transducers, 54
- Viscous damping, 13–16